

Modelling the Behaviour of Helical Screw Piles



Samuel A. Stanier

Department of Civil and Structural Engineering
University of Sheffield

A thesis submitted for the degree of

Doctor of Philosophy

May 2011

Declaration

I, Samuel Anthony Stanier, hereby confirm that all work presented here is my own. Where information has been used from other sources, I confirm that this has been clearly stated within the thesis.

Signed,

May 2011

Abstract

The research described in this thesis concerns modelling the behaviour of helical screw piles using both physical and numerical modelling techniques. A review of published literature highlighted that the influence of the geometry of helical screw piles on their performance and failure mechanisms is not definitively known. Development of transparent synthetic soils has facilitated observation of soil displacements around helical screw piles during both installation and load testing using small scale $1g$ physical models. This allowed the failure mechanisms to be identified for helical screw piles of varying geometry and comparison to be drawn with parallel numerical simulations.

The transparent soil utilised was representative of soft clay and allowed non-intrusive measurement of displacements on a plane highlighted by a sheet of laser light allowing a digital camera to record movement of the soil. This enabled Particle Image Velocimetry to be used to measure the displacement of the soil on the target plane. This allowed observation of both the installation induced disturbance and the displacement and shear strain fields mobilised around deeply installed helical screw piles with $20mm$ diameter helical plates on a $5mm$ diameter shaft, under compressive and tensile loading. The results of the physical model tests demonstrated that the geometry of helical screw piles significantly impacted on their behaviour in soft clay soils. The installation disturbance induced by helical screw pile installation was shown to be related to the volume of the pile and that most disturbance was caused by the installation of the lowermost helical plate. Additional helical plates following the installation path of the lowermost plate caused less disturbance. Under loading the spacing of the helical plates was shown to control the stiffness of the piles' load-deflection response and the distance between the uppermost and lowermost helical plates, was shown to govern the ultimate capacity. The compressive and tensile capacities of deeply installed helical screw piles were demonstrated to be very similar.

The geotechnical properties of the transparent soil beds tested were assessed by performing in-situ hand vane shear tests and Undrained Unconsolidated (UU) triaxial tests on extracted specimens. A novel method of assessing the non-linear stress-strain characteristics of the transparent soil based upon the Mobilisable Strength Design (MSD) method of Osman & Bolton (2005) was then investigated using the same non-intrusive modelling techniques as for the helical screw piles. From this collection of property data a simple elasto-plastic constitutive model was calibrated that described the stress-strain response of the transparent soil used in the physical models. This allowed comparative Finite Element (FE) simulations of the model footing tests to be created. In general the agreement between the physical model and FE model was good. However, the deformation mechanism assumed by Osman & Bolton (2005) was somewhat different to that observed in the physical model tests or numerical simulations.

FE simulations of the helical screw pile tests were also performed with the helical plate geometry simplified as flat circular plates and the piles were ‘wished’ into place. Hence, installation induced effects were not reproduced in the FE simulations. Comparisons of the displacement and shear strain fields between the physical models and numerical simulations were generally good for both compressive and tensile loading. However, comparison of the load-deflection responses indicated that the FE simulations underpredicted the initial stiffness of the load-deflection responses for all helical screw piles. The general trends related to the effect of the geometry of the helical screw piles observed in the physical models were preserved in the FE simulations.

Lastly, a simple analytical model was shown to provide adequate prediction of ultimate capacity for helical screw piles loaded in compression or tension. Design methodologies including Eurocode 7, the traditional permissible stress approach and a method based upon reserving base or uplift capacity were then used to calculate design capacities. This highlighted the importance of minimising the spacing between the helical plates to optimise performance and the importance of separate serviceability limit state checks if maximum economy is sought in design.

Keywords: Helical screw piles, transparent soil, Particle Image Velocimetry, Mobilisable Strength Design, physical modelling, numerical modelling.

Acknowledgements

I would like to express my gratitude to Dr. Charles Hird and Dr. Jonathan Black for their supervision and guidance throughout my postgraduate research. Their advice and feedback over the last three years has been exceptional. I particularly thank Dr. Charles Hird for continuing to support me long after retirement and Dr. Jonathan Black for providing additional experiences and opportunities that have helped me to broaden my research interests.

I thank Prof. Adrian Hyde for his interest in my research and career. I am particularly grateful for the help he afforded me when looking for an academic position upon completion of this research. I thank Dr. Sam Clarke for his companionship, support and encouragement. I also thank the remaining staff and students of the Geotechnical Engineering Group for their engaging discussion and camaraderie during my time as a member of the group.

I would like to acknowledge the technical and support staff in the Department of Civil and Structural Engineering. Notably I thank Mr. Paul Osborne, Mr. Mark Foster, Mr. David Callaghan and Mr. Alex Cargill for their excellent support in the laboratory; they were always eager to help as and when required and for this I am most grateful.

Finally, I would like to thank my friends and family for their continued backing and faith in my abilities. Their encouragement throughout my education has been invaluable and will not be forgotten.

Contents

Declaration	i
Abstract	ii
Acknowledgements	iv
Contents	x
List of Figures	xxi
List of Tables	xxiv
List of Symbols	xxv
List of Abbreviations	xxxii
1 Introduction	1
1.1 Background	1
1.2 Objectives	2
1.3 Thesis Structure	3
2 Literature Review	5
2.1 Introduction	5
2.2 Helical Screw Piles	6
2.2.1 Behaviour in Sands	6
2.2.2 Behaviour in Clays	13
2.3 Physical Modelling	21
2.3.1 1g Modelling	21
2.3.2 Centrifuge Modelling	22
2.3.3 Scaling Laws	23
2.3.4 Boundary Effects	23
2.3.5 Displacement Measurement	25

2.3.5.1	Review of Previous Measurement Techniques	25
2.3.5.2	Particle Image Velocimetry	29
2.3.5.3	GeoPIV	30
2.3.5.4	Photogrammetry	32
2.3.5.5	System Accuracy and Precision	35
2.3.6	Materials	35
2.4	Transparent Synthetic Soils	37
2.4.1	Coarse Grained Transparent Synthetic Soils	37
2.4.1.1	Crushed Glass	37
2.4.1.2	Silica Gel	39
2.4.2	Fine Grained Transparent Synthetic Soils	44
2.4.2.1	Precipitated Amorphous Silica	44
2.4.2.2	Fumed Amorphous Silica	48
2.5	Potential for Further Research	55
3	Laboratory Schemes	57
3.1	Introduction	57
3.2	Transparent Soil Development	58
3.2.1	Methodology	58
3.2.2	Precipitated Amorphous Silica	60
3.2.3	Fumed Amorphous Silica	60
3.2.4	Consolidated Transparency	61
3.3	Equipment	64
3.3.1	Test Chamber	64
3.3.1.1	Design	64
3.3.1.2	Surface Finish	65
3.3.1.3	Assembly	67
3.3.2	Consolidation Apparatus	68
3.3.3	Laser Aided Tomography Apparatus	69
3.3.3.1	Laser	69
3.3.3.2	Digital Camera	70
3.3.3.3	Control Points	71
3.3.4	Pile Driving Apparatus	73
3.3.4.1	Pile Driving Rig	73
3.3.4.2	Stepper Motors	74
3.3.4.3	Stepper Motor Controllers	74
3.3.5	Model Helical Screw Piles	75

3.3.6	Measurement Devices	77
3.3.6.1	Load Cell	77
3.3.6.2	Linear Variable Differential Transformer (LVDT) . .	78
3.3.6.3	Draw-wire LVDT	78
3.3.7	Data Acquisition Device	80
3.3.7.1	Signal Amplification	80
3.4	Control Software	81
3.4.1	Nimbus	81
3.4.2	LabVIEW	81
3.5	Calibrations	84
3.5.1	Laser Aided Tomography Apparatus	84
3.5.1.1	Laser	84
3.5.1.2	Digital Camera	84
3.5.1.3	Control Points	87
3.5.2	Pile Driving Rig	91
3.5.2.1	Vertical Drive	92
3.5.2.2	Rotational Drive	92
3.5.3	Transducers	95
3.5.3.1	Load Cell	95
3.5.3.2	LVDT	97
3.5.3.3	Draw-wire LVDT	98
3.6	Sample Preparation	101
3.6.1	Consolidation	104
3.6.1.1	Results	106
3.6.1.2	Discussion	115
3.7	Test Procedure	119
4	Particle Image Velocimetry, Photogrammetry and Post-Processing	124
4.1	Introduction	124
4.2	Particle Image Velocimetry (PIV)	125
4.2.1	Calibration	126
4.2.1.1	Transparent Synthetic Soil	127
4.2.1.2	Control Point Calibration	127
4.2.1.3	Pile Displacement Calibration	129
4.2.1.4	Footing Displacement Calibration	130
4.2.1.5	Discussion	130
4.3	Photogrammetry	133

4.3.1	Internal Correction	133
4.3.2	External Correction	135
4.3.3	Scale Correction	137
4.3.4	Validation	138
4.3.4.1	Calibration Target	139
4.3.4.1.1	Centroiding	140
4.3.4.1.2	GeoPIV	143
4.3.4.2	Camera Calibration	144
4.3.4.3	Process	147
4.3.4.4	Results	150
4.3.5	Camera-Soil Movement Error Reduction	157
4.3.6	Shear Strain Computation	163
4.4	Post-Processing	164
5	Physical Modelling of Helical Screw Piles	167
5.1	Introduction	167
5.2	Installation	169
5.2.1	Analysis Method	169
5.2.2	Data Appraisal	170
5.2.3	Displacement and Shear Strain Fields	173
5.2.4	Observations	178
5.2.4.1	Breakout	178
5.2.4.2	Lateral Disturbance	179
5.2.4.3	Vertical Disturbance	179
5.2.4.4	Shear Strains	180
5.2.5	Repeatability	181
5.3	Performance	185
5.3.1	Load-Deflection Response	185
5.3.2	Analysis Method	188
5.3.3	Data Appraisal	190
5.3.4	Displacement and Shear Strain Fields	197
5.3.4.1	Compression Results	197
5.3.4.2	Tension Results	235
5.3.5	Observations	272
5.3.5.1	Displacement Asymmetry	272
5.3.5.2	Development of Ultimate Limit State (ULS)	272
5.3.5.3	Effect of Spacing Ratio	275

5.3.5.4	Effect of Active Length	276
5.3.5.5	Soil-Shaft Interface Behaviour	277
5.3.5.6	Compressive-Tensile Comparison	277
5.3.6	Repeatability	279
5.4	Summary	284
6	Derivation of Stress-Strain Characteristics of Transparent Soil	285
6.1	Introduction	285
6.2	Post-Test Investigation of Sample Properties	286
6.3	Mobilisable Strength Design (MSD)	290
6.3.1	Previous Validation	292
6.4	Physical Modelling of Undrained Settlement of a Circular Footing on Clay	297
6.4.1	Load-Deflection Response	297
6.4.2	Analysis Method	298
6.4.3	Data Appraisal	300
6.4.4	Displacement and Shear Strain Fields	300
6.4.5	Observations	310
6.4.5.1	Development of Ultimate Limit State	310
6.4.5.2	Soil-Footing Interface	311
6.4.5.3	Depth of Deformation Mechanism	312
6.4.6	Repeatability	312
6.5	Comparison with MSD Mechanism	317
6.6	Derivation of Stress-Strain Response	320
6.7	Finite Element Simulation	324
6.7.1	Load-Deflection Response	326
6.7.2	Displacement and Shear Strain Fields	327
6.7.3	Observations	338
6.7.3.1	Displacement Field Discrepancy	338
6.7.3.2	Development of Ultimate Limit State	338
6.7.3.3	Soil Footing Interface	339
6.7.3.4	Depth of Deformation Mechanism	339
6.7.3.5	Heave at Toe of Footing	339
6.7.4	Sensitivity of Finite Element Simulation	340
6.8	Summary	341

7 Numerical Modelling of Helical Screw Piles	343
7.1 Introduction	343
7.2 Finite Element Simulation	344
7.2.1 Load-Deflection Response	349
7.2.2 Comparison of Displacement and Shear Strain Fields	356
7.2.3 Observations	357
7.2.3.1 Initial Displacement Increment	357
7.2.3.2 Development of Ultimate Limit State	367
7.2.3.3 Comparison of ULS Deformation Mechanisms	375
7.2.4 Sensitivity of Finite Element Simulation	387
7.3 Analytical Model	393
7.4 Discussion	400
7.5 Design Methodology	403
7.5.1 Permissible Stress	403
7.5.2 Uplift/Base Capacity in Reserve	404
7.5.3 Eurocode 7	405
7.5.4 Comparison of Methods	411
7.6 Summary	417
8 Conclusion	421
8.1 Introduction	421
8.2 Research Outcomes	421
8.3 Recommendations for Further Research	430
References	442

List of Figures

1.1 Example of partially installed helical screw pile	1
2.1 Examples of model single and multi helix screw piles	6
2.2 Ultimate tensile capacity of group single helical piles in sand	7
2.3 Installation torque versus ultimate tensile capacity for single helix piles in dense, medium and loose sands	8
2.4 Installation torque in dry and saturated sands with net upward ground-water flow	9
2.5 Ultimate tensile capacity of inclined single helical screw piles in sand	10
2.6 Proposed failure mechanism of helical screw piles in tension	12
2.7 Failure modes with installation depth	14
2.8 Effect of plate spacing on compressive and tensile capacity of small model helical screw piles installed to deep embedment depths	15
2.9 Evidence of changing failure mechanism with differing helical plate spacing ratio after tensile test	16
2.10 Assessment of predicted capacities compared to experimental capacities of helical screw piles by normalisation	16
2.11 Cylindrical failure theory compared to field data	17
2.12 Individual bearing failure theory compared to experimental data . .	18
2.13 Torque factor correlation for silts and clays	19
2.14 Shear strain field around a cantilever wall in sand	26
2.15 Photographic measurement of model displacements	27
2.16 Strain around a model penetrometer in transparent clay	28
2.17 Graphical concept of PIV process conducted by GeoPIV	31
2.18 Interpolation of cross correlation peak to sub pixel resolution	33
2.19 Pinhole camera model	34
2.20 Physical modelling of a submerged embankment under seismic loading using crushed glass and Laser Aided Tomography	39

2.21 Fine angular and coarse rounded silica gels used in investigation of transparent synthetic soils to model sands	40
2.22 Compressibility of fine angular and coarse rounded silica gels	42
2.23 Displacement fields and vertical strains above open faced tunnels with various depths of cover	43
2.24 Transmission Electron Microscope (TEM) image of precipitated amorphous silica	44
2.25 Consolidation of precipitated amorphous silica	45
2.26 Stress-strain and volume change relationships for precipitated amorphous silica from consolidated undrained and drained triaxial tests .	46
2.27 Permeability of amorphous silica based transparent synthetic soil . .	47
2.28 Displacements around a continuous flight auger in transparent synthetic soil	49
2.29 Displacements around a continuous flight auger compared with SSPM .	49
2.30 Comparison of octahedral shear strains caused by driven pile installation and predicted by SSPM theory	50
2.31 Undrained shear strength of fumed amorphous silica transparent soil with consolidation pressure	52
2.32 Permeability of fumed amorphous silica based transparent synthetic soil	53
2.33 Images from investigations conducted using fumed amorphous silica based transparent synthetic soils	54
3.1 Transparency test card	59
3.2 Transparency test viewing depths	60
3.3 Transparency of Hi-Sil T600 precipitated amorphous silica transparent soil	61
3.4 Transparency of fumed amorphous silica transparent soil	62
3.5 Comparison of consolidated transparency of amorphous and fumed silica.	63
3.6 Equipment schematic	64
3.7 Test chamber	66
3.8 Drainage channels	67
3.9 Assembled consolidation apparatus	69
3.10 Laser Apparatus	70
3.11 Control points used in previous PIV research	72
3.12 Light Emitting Diode (LED) control points	73

3.13	Pile driving rig	74
3.14	Helical screw pile configurations	76
3.15	Load-cell connectors	78
3.16	LVDT mounting bracket	79
3.17	Draw-wire LVDT mounting points	79
3.18	LabVIEW control software interface	83
3.19	Exposure calibration	87
3.20	LED 12V calibration analysis	88
3.21	LED 15V calibration analysis	89
3.22	LED 17V calibration analysis	90
3.23	Vertical drive calibration and residual error	93
3.24	Rotational drive calibration and residual error	94
3.25	Load cell calibration	96
3.26	25 mm LVDT calibration	97
3.27	50 mm LVDT calibration	99
3.28	Draw-wire calibration	100
3.29	Soil mixing and de-airing apparatus	101
3.30	Sheet aluminium divider and removal	103
3.31	Air entrainment caused by swift unloading of consolidation pressures	105
3.32	Consolidation plot for 0.0kPa to 6.25kPa increment	107
3.33	Consolidation plot for 6.25kPa to 12.5kPa increment	107
3.34	Consolidation plot for 12.5kPa to 25.0kPa increment	108
3.35	Consolidation plot for 25.0kPa to 50.0kPa increment	108
3.36	Consolidation plot for 50.0kPa to 100.0kPa increment	109
3.37	Void ratio plot derived from consolidation data	115
3.38	Void ratio plot compared to previous investigations	117
3.39	Alignment assessment	120
3.40	Normalised velocity based estimation of pore pressure dissipation below a circular footing during uplift	121
3.41	Locations of hand vane shear measurements	123
3.42	Hand vane shear apparatus	123
4.1	Standard error of transparent soil tracking	128
4.2	Standard error of control point tracking with 15.0V supply voltage .	128
4.3	Standard error of pile displacement tracking	131
4.4	Standard error of footing displacement tracking	131
4.5	Calibration target	139

4.6	Control point	140
4.7	Intensity of control point before and after Gaussian smoothing	141
4.8	Typical centroid deviation	142
4.9	Histograms of all horizontal and vertical centroid deviations	142
4.10	Standard error of target panel control point tracking	143
4.11	Calibration target images	145
4.12	Residual error for each control point in all six calibration images using the calibration target	146
4.13	Secondary calibration target images	148
4.14	Residual error using secondary calibration target	149
4.15	Amplified (100 times) residual vectorial errors from camera calibration validation	151
4.16	Residual errors from photogrammetric correction validation	152
4.17	Standard error of residual errors from photogrammetry validation . .	153
4.18	Mean residual error from camera calibration validation	154
4.19	Mean residual error from zero soil movement analysis	155
4.20	Mean residual error from repeat zero soil movement analysis	156
4.21	Mean and maximum absolute residual error with increasing histogram bin width from modal movement correction for calibration panel validation	158
4.22	Mean and maximum absolute residual error with increasing histogram bin width from modal movement correction for zero soil movement validation	159
4.23	Mean and maximum absolute residual error with increasing histogram bin width from modal movement correction for repeat zero soil movement validation	159
4.24	Percentage of measurements coincident with the modal movement magnitude for calibration target validation	160
4.25	Percentage of measurements coincident with the modal movement magnitude for zero soil movement validation	161
4.26	Percentage of measurements coincident with the modal movement magnitude for repeat zero soil movement validation	161
4.27	Mean residual error from calibration target validation after modal movement correction	162
4.28	Mean residual error from zero soil movement validation after modal movement correction	162

4.29	Mean residual error from repeat zero soil movement validation after modal movement correction	163
4.30	Typical raw output plots prior to post-processing	165
4.31	Typical post-processed output plots	166
5.1	Comparison of uncorrected and corrected installation disturbance displacement contours to depth of 7D for double helix pile with active length of 30mm (C2-30)	172
5.2	Installation disturbance to depth of 7D for single helix pile (C1) . .	174
5.3	Installation disturbance to depth of 7D for double helix pile with active length of 30mm (C2-30)	175
5.4	Installation disturbance to depth of 7D for double helix pile with active length of 60mm (C2-60)	176
5.5	Installation disturbance to depth of 7D for triple helix pile with active length of 60mm (C3)	177
5.6	Installation disturbance to depth of 7D for double helix pile repeat with active length of 30mm (T2-30)	184
5.7	Comparison of load-deflection response for helical screw pile configurations	185
5.8	Effect of active length on absolute ultimate capacity	186
5.9	Uncorrected cumulative displacement contours at 3mm compressive displacement for a double helix pile with 30mm active length	194
5.10	Uncorrected cumulative displacement contours at 3mm tensile displacement for a double helix pile with 30mm active length	195
5.11	Assessment of pile tracking methodology	197
5.12	C1 cumulative PIV results for 1mm axial compressive displacement .	199
5.13	C1 incremental PIV results from 1mm to 2mm axial compressive displacement	200
5.14	C1 cumulative PIV results for 2mm axial compressive displacement .	201
5.15	C1 incremental PIV results from 2mm to 3mm axial compressive displacement	202
5.16	C1 cumulative PIV results for 3mm axial compressive displacement .	203
5.17	C1 incremental PIV results from 3mm to 4mm axial compressive displacement	204
5.18	C1 cumulative PIV results for 4mm axial compressive displacement .	205
5.19	C1 incremental PIV results from 4mm to 5mm axial compressive displacement	206

5.20 C1 cumulative PIV results for 5mm axial compressive displacement .	207
5.21 C2-30 cumulative PIV results for 1mm axial compressive displacement	208
5.22 C2-30 incremental PIV results from 1mm to 2mm axial compressive displacement .	209
5.23 C2-30 cumulative PIV results for 2mm axial compressive displacement	210
5.24 C2-30 incremental PIV results from 2mm to 3mm axial compressive displacement .	211
5.25 C2-30 cumulative PIV results for 3mm axial compressive displacement	212
5.26 C2-30 incremental PIV results from 3mm to 4mm axial compressive displacement .	213
5.27 C2-30 cumulative PIV results for 4mm axial compressive displacement	214
5.28 C2-30 incremental PIV results from 4mm to 5mm axial compressive displacement .	215
5.29 C2-30 cumulative PIV results for 5mm axial compressive displacement	216
5.30 C2-60 cumulative PIV results for 1mm axial compressive displacement	217
5.31 C2-60 incremental PIV results from 1mm to 2mm axial compressive displacement .	218
5.32 C2-60 cumulative PIV results for 2mm axial compressive displacement	219
5.33 C2-60 incremental PIV results from 2mm to 3mm axial compressive displacement .	220
5.34 C2-60 cumulative PIV results for 3mm axial compressive displacement	221
5.35 C2-60 incremental PIV results from 3mm to 4mm axial compressive displacement .	222
5.36 C2-60 cumulative PIV results for 4mm axial compressive displacement	223
5.37 C2-60 incremental PIV results from 4mm to 5mm axial compressive displacement .	224
5.38 C2-60 cumulative PIV results for 5mm axial compressive displacement	225
5.39 C3 cumulative PIV results for 1mm axial compressive displacement .	226
5.40 C3 incremental PIV results from 1mm to 2mm axial compressive displacement .	227
5.41 C3 cumulative PIV results for 2mm axial compressive displacement .	228
5.42 C3 incremental PIV results from 2mm to 3mm axial compressive displacement .	229
5.43 C3 cumulative PIV results for 3mm axial compressive displacement .	230
5.44 C3 incremental PIV results from 3mm to 4mm axial compressive displacement .	231

5.45 C3 cumulative PIV results for 4mm axial compressive displacement	232
5.46 C3 incremental PIV results from 4mm to 5mm axial compressive displacement	233
5.47 C3 cumulative PIV results for 5mm axial compressive displacement	234
5.48 T1 cumulative PIV results for 1mm axial tensile displacement	236
5.49 T1 incremental PIV results from 1mm to 2mm axial tensile displacement	237
5.50 T1 cumulative PIV results for 2mm axial tensile displacement	238
5.51 T1 incremental PIV results from 2mm to 3mm axial tensile displacement	239
5.52 T1 cumulative PIV results for 3mm axial tensile displacement	240
5.53 T1 incremental PIV results from 3mm to 4mm axial tensile displacement	241
5.54 T1 cumulative PIV results for 4mm axial tensile displacement	242
5.55 T1 incremental PIV results from 4mm to 5mm axial tensile displacement	243
5.56 T1 cumulative PIV results for 5mm axial tensile displacement	244
5.57 T2-30 cumulative PIV results for 1mm axial tensile displacement	245
5.58 T2-30 incremental PIV results from 1mm to 2mm axial tensile displacement	246
5.59 T2-30 cumulative PIV results for 2mm axial tensile displacement	247
5.60 T2-30 incremental PIV results from 2mm to 3mm axial tensile displacement	248
5.61 T2-30 cumulative PIV results for 3mm axial tensile displacement	249
5.62 T2-30 incremental PIV results from 3mm to 4mm axial tensile displacement	250
5.63 T2-30 cumulative PIV results for 4mm axial tensile displacement	251
5.64 T2-30 incremental PIV results from 4mm to 5mm axial tensile displacement	252
5.65 T2-30 cumulative PIV results for 5mm axial tensile displacement	253
5.66 T2-60 cumulative PIV results for 1mm axial tensile displacement	254
5.67 T2-60 incremental PIV results from 1mm to 2mm axial tensile displacement	255
5.68 T2-60 cumulative PIV results for 2mm axial tensile displacement	256
5.69 T2-60 incremental PIV results from 2mm to 3mm axial tensile displacement	257
5.70 T2-60 cumulative PIV results for 3mm axial tensile displacement	258
5.71 T2-60 incremental PIV results from 3mm to 4mm axial tensile displacement	259
5.72 T2-60 cumulative PIV results for 4mm axial tensile displacement	260

5.73 T2-60 incremental PIV results from 4mm to 5mm axial tensile displacement	261
5.74 T2-60 cumulative PIV results for 5mm axial tensile displacement	262
5.75 T3 cumulative PIV results for 1mm axial tensile displacement	263
5.76 T3 incremental PIV results from 1mm to 2mm axial tensile displacement	264
5.77 T3 cumulative PIV results for 2mm axial tensile displacement	265
5.78 T3 incremental PIV results from 2mm to 3mm axial tensile displacement	266
5.79 T3 cumulative PIV results for 3mm axial tensile displacement	267
5.80 T3 incremental PIV results from 3mm to 4mm axial tensile displacement	268
5.81 T3 cumulative PIV results for 4mm axial tensile displacement	269
5.82 T3 incremental PIV results from 4mm to 5mm axial tensile displacement	270
5.83 T3 cumulative PIV results for 5mm axial tensile displacement	271
5.84 Repeatability of performance of model helical screw piles	280
5.85 C1-R cumulative PIV results for 5mm axial compressive displacement	282
5.86 C3-R cumulative PIV results for 5mm axial compressive displacement	283
6.1 Triaxial response of transparent soil from UU test	287
6.2 Single helix pile installation modal correction magnitude and percentage of vectors with modal magnitude	288
6.3 Single helix pile installation modal correction magnitude and percentage of vectors with modal magnitude	289
6.4 Plastic deformation mechanism for shallow circular foundation on clay	291
6.5 Stiffness response and K_0 profile assumed in FE validation of MSD concept by Osman and Bolton (2005)	292
6.6 Variation of soil stiffness, undrained shear strength and representative stress-strain curve selected by Osman and Bolton (2005)	294
6.7 Displacement vector field at a bearing pressure of 100kPa and the effect of choice of representative depth on settlement predictions from Osman and Bolton (2005)	295
6.8 Comparison of MSD settlement predictions and field measurements at Bothkennar and Kinnegar from Osman and Bolton (2005)	296
6.9 Curved sample surface and resultant uneven initial contact of footing	298
6.10 Footing load-deflection response under axial compressive loading before and after correction to account for bedding errors	298
6.11 Footing test (F) PIV results for 2mm settlement	301
6.12 Footing test (F) PIV results for 2-4mm settlement increment	302
6.13 Footing test (F) PIV results for 4mm settlement	303

6.14	Footing test (F) PIV results for 4-6mm settlement increment	304
6.15	Footing test (F) PIV results for 6mm settlement	305
6.16	Footing test (F) PIV results for 6-8mm settlement increment	306
6.17	Footing test (F) PIV results for 8mm settlement	307
6.18	Footing test (F) PIV results for 8-10mm settlement increment	308
6.19	Footing test (F) PIV results for 10mm settlement	309
6.20	Footing repeat load-deflection response under axial compressive load-ing before and after correction to account for bedding errors	312
6.21	Repeatability of footing test response	313
6.22	Repeat footing test (F-R) PIV results for 10mm settlement	316
6.23	MSD deformation mechanism results for 2mm settlement increment	319
6.24	Deformation mechanisms beneath smooth and rough strip footings on soft clay with reducing strength with depth	321
6.25	MSD derived theoretical triaxial response	321
6.26	Strength derived from reverse MSD compared to lower, upper and mean strength profiles derived from post-test vane shear data and UU triaxial data	322
6.27	FE regions and mesh	326
6.28	Comparison of FE and experimental footing response	328
6.29	Baseline FE analysis results for 2mm settlement	329
6.30	Baseline FE analysis results for 2-4mm settlement increment	330
6.31	Baseline FE analysis results for 4mm settlement	331
6.32	Baseline FE analysis results for 4-6mm settlement increment	332
6.33	Baseline FE analysis results for 6mm settlement	333
6.34	Baseline FE analysis results for 6-8mm settlement increment	334
6.35	Baseline FE analysis results for 8mm settlement	335
6.36	Baseline FE analysis results for 8-10mm settlement increment	336
6.37	Baseline FE analysis results for 10mm settlement	337
7.1	Axisymmetric mesh regions for helical screw pile baseline FE models	346
7.2	Axisymmetric meshes for helical screw pile baseline FE models . . .	347
7.3	Comparison of experimental and ‘Baseline’ FE derived load deflection response for a single helix pile and double helix pile with 30mm active length	351
7.4	Comparison of experimental and ‘Baseline’ FE derived load deflection response for double and triple helix piles with 60mm active length .	352
7.5	Effect of active length on absolute ultimate capacity of FE validation	353

7.6	Comparison of normalised load deflection response of deeply embedded circular foundations in a uniform clay using small strain and LDPE methods from Wang et al. (2010)	355
7.7	Comparison of initial horizontal displacement increment from FE and PIV for C1-T1 test pair	358
7.8	Comparison of initial horizontal displacement increment from FE and PIV for C2-30-T2-30 test pair	359
7.9	Comparison of initial horizontal displacement increment from FE and PIV for C2-60-T2-60 test pair	360
7.10	Comparison of initial horizontal displacement increment from FE and PIV for C3-T3 test pair	361
7.11	Comparison of initial vertical displacement increment from FE and PIV for C1-T1 test pair	363
7.12	Comparison of initial vertical displacement increment from FE and PIV for C2-30-T2-30 test pair	364
7.13	Comparison of initial vertical displacement increment from FE and PIV for C2-60-T2-60 test pair	365
7.14	Comparison of initial vertical displacement increment from FE and PIV for C3-T3 test pair	366
7.15	Comparison of FE and PIV derived shear strain fields at 1mm cumulative displacement for C1-T1 test pair	368
7.16	Comparison of FE and PIV derived shear strain fields at 1mm cumulative displacement for C2-30-T2-30 test pair	369
7.17	Comparison of FE and PIV derived shear strain fields at 1mm cumulative displacement for C2-60-T2-60 test pair	370
7.18	Comparison of FE and PIV derived shear strain fields at 1mm cumulative displacement for C3-T3 test pair	371
7.19	Comparison of FE and PIV derived shear strain fields for 1-2mm and 2-3mm incremental displacements for C2-30-T2-30 test pair	373
7.20	Comparison of FE and PIV derived shear strain fields for 3-4mm and 4-5mm cumulative displacement for C2-30-T2-30 test pair	374
7.21	Comparison of ULS horizontal displacement field for 4-5mm displacement increment from FE and PIV for C1-T1 test pair	376
7.22	Comparison of ULS vertical displacement field for 4-5mm displacement increment from FE and PIV for C1-T1 test pair	377

7.23 Comparison of ULS shear strain field for 4-5mm displacement increment from FE and PIV for C1-T1 test pair	378
7.24 Comparison of ULS horizontal displacement field for 4-5mm displacement increment from FE and PIV for C2-30-T2-30 test pair	380
7.25 Comparison of ULS vertical displacement field for 4-5mm displacement increment from FE and PIV for C2-30-T2-30 test pair	381
7.26 Comparison of ULS shear strain field for 4-5mm displacement increment from FE and PIV for C2-30-T2-30 test pair	382
7.27 Comparison of ULS horizontal displacement field for 4-5mm displacement increment from FE and PIV for C2-60-T2-60 test pair	384
7.28 Comparison of ULS vertical displacement field for 4-5mm displacement increment from FE and PIV for C2-60-T2-60 test pair	385
7.29 Comparison of ULS shear strain field for 4-5mm displacement increment from FE and PIV for C2-60-T2-60 test pair	386
7.30 Comparison of ULS horizontal displacement field for 4-5mm displacement increment from FE and PIV for C3-T3 test pair	388
7.31 Comparison of ULS vertical displacement field for 4-5mm displacement increment from FE and PIV for C3-T3 test pair	389
7.32 Comparison of ULS shear strain field for 4-5mm displacement increment from FE and PIV for C3-T3 test pair	390
7.33 Spacing ratio factor relationship	395
7.34 Discrepancy summary	400
7.35 Idealised load-settlement and load-transfer phenomena for compressive loading of a pile to failure	404
7.36 Experimental/design capacity for various design methodologies . . .	412
7.37 Load-deflection curves for model piles after correction for the effect of the post-installation residual force	414
7.38 Estimation of immediate displacement of model piles for design capacities calculated using various design methodologies	416
7.39 Percentage absolute immediate displacement as a function of helical plate diameter estimated using design capacities derived using various design methodologies and the corresponding load-deflection response from the model tests	418

List of Tables

2.1	Coefficients a and b proposed by different researchers	22
2.2	Physical modelling scaling factors	24
2.3	Shear strength of fine angular and coarse rounded silica gels	40
2.4	Stiffness of loose and dense, fine angular and coarse rounded silica gels	40
2.5	Physical properties of precipitated amorphous silicas	44
2.6	Bulk properties of fumed amorphous silica	51
3.1	Estimation of maximum achievable consolidation pressure	68
3.2	Pentax K10D digital camera specification	71
3.3	Model helical screw pile configurations	76
3.4	Vertical drive calibration error	93
3.5	Rotational drive calibration error	94
3.6	Transparent synthetic soil mix proportions per batch (two of each being required for each model)	102
3.7	Consolidation and unloading stages	105
3.8	Coefficient of consolidation summary	109
3.9	Coefficient of compressibility summary	110
3.10	Hydraulic conductivity summary	111
3.11	Measured and assumed component densities	111
3.12	Percentage slurry loss and final consolidated sample heights	112
3.13	Compression index	114
3.14	Swelling index	114
3.15	Comparison of aspect ratio of various consolidation apparatus	116
3.16	Drainage estimation using normalised velocity based approximation for helical screw pile tests	122
4.1	Camera calibration parameters derived using calibration panel and centroiding	146

4.2 Camera calibration parameters derived using secondary calibration panel and corner extraction	149
5.1 Contours of displacement and shear strain presented in helical screw pile installation contour plots	170
5.2 Magnitude of horizontal and vertical correction specified by modal movement correction process for installation analyses alongside the percentage of vectors of modal magnitude	171
5.3 Residual forces induced by model helical screw pile installation . . .	182
5.4 Magnitude of horizontal and vertical correction specified by modal movement correction process for the double helix pile with 30mm active length repeat installation (T2-30) analysis alongside the percentage of vectors of modal magnitude	182
5.5 Percentage discrepancy between compressive and tensile capacity of helical screw piles	187
5.6 Contours of displacement and shear strain presented in helical screw pile load-deflection contour plots	188
5.7 Magnitude of horizontal and vertical correction specified by modal movement correction process for compressive response tests	191
5.8 Magnitude of horizontal and vertical correction specified by modal movement correction process for tensile response tests	192
5.9 Capacity of model pile in test T1 after each displacement increment	273
5.10 Magnitude of horizontal and vertical correction specified by modal movement correction process for repeat compressive response tests .	281
6.1 Drainage estimation using normalised velocity based approximation for footing tests	297
6.2 Contours of displacement and shear strain presented in footing test contour plots	299
6.3 Magnitude of horizontal and vertical correction specified by modal movement correction process for footing test	300
6.4 Magnitude of horizontal and vertical correction specified by modal movement correction process for repeat footing test	314
6.5 Stiffness, strength and rigidity index derived using reversed MSD method for smooth and rough bearing capacity factors	322
7.1 Helical screw pile axisymmetric mesh aspect ratio summary	348

LIST OF TABLES

7.2	Percentage discrepancy between experimental and FE validation derived absolute capacity of helical screw piles at ULS	350
7.3	Percentage discrepancy between FE validation derived compressive and tensile capacity of helical screw piles	353
7.4	Absolute compressive capacity calculated using analytical methods and mean strength bound	398
7.5	Absolute tensile capacity calculated using analytical methods and mean strength bound	398
7.6	Parameters common to all analytical calculations	399
7.7	Percentage discrepancy between experimental and analytical validation derived absolute capacity of helical screw piles at ULS	399
7.8	Partial factors for actions as specified by EN 1997-1	407
7.9	Partial factors for resistance specified by EN 1997-1	407
7.10	Correlation factors specified by EN 1997-1	407
7.11	Partial factors for material properties as specified by EN 1997-1	407
7.12	Mean and minimum soil surface shear strength and gradients	408
7.13	Partial factors for resistances generated by helical screw piles proposed by the author	409
7.14	Eurocode 7 Design Approach partial factor sets and primary variables	410
7.15	Design capacities calculated using various design methodologies	413
7.16	Standard deviation of percentage immediate displacement estimated to be caused by application of design loads using different design methodologies	417

List of Symbols

A	Area of helical plate.
A	Total area of calibration target control point in pixels.
A	Area of plate anchor.
A	Amphere.
A_1	Projected area top helical plate.
A_c	Area of cylindrical failure surface.
A_p	Projected area of helical plate.
A_s	Area of pile shaft.
A_t	Area of tip of pile shaft.
α	Material type scaling factor.
α	Adhesion factor.
α	CCD non-squareness aspect ratio.
B	Average diameter of lower helical plates.
bar	Unit of pressure equal to 100kPa.
bit	Unit of digital data or binary digit.
C	Celsius.
C_c	Compression index.
C_s	Swelling index.
C_u	Centroid horizontal coordinate.
C_v	Centroid vertical coordinate.
c'	Effective cohesion.
c_{mob}	Mobilised shear stress.
c_v	Coefficient of Consolidation.
D	Diameter.
D	Depth to bottom helical plate.
D_1	Depth to top helical plate.
d/D	Shaft to helical plate diameter ratio.
d	Pile shaft diameter.
\bar{d}	Average length of drainage path.
$^\circ$	Degree.
Δ	Delta.
δ	Displacement.
δ	Displacement of footing.
$\delta_{u^{radial}}$	Horizontal radial distortion.

$\delta_{u^{tangential}}$	Horizontal tangential distortion.
$\delta_{v^{radial}}$	Vertical radial distortion.
$\delta_{v^{tangential}}$	Vertical tangential distortion.
E	Young's modulus.
E_u	Young's modulus.
e	Void ratio.
e_0	Initial void ratio.
e_f	Final void ratio.
ϵ_a	Axial strain.
ϵ_s	Engineering shear strain.
$\epsilon_{s,mob}$	Average engineering shear strain mobilised.
F	Capacity of circular plate anchor.
f_d	Bearing capacity correction factor for embedment depth.
F	Permissible stress safety factor.
F_d	Design action to Eurocode 7.
F_k	Characteristic action to Eurocode 7.
F_{k_G}	Characteristic unfavourable permanent action to Eurocode 7.
G	Giga.
g	Gram.
g	Gravitational acceleration of $9.81m/s^2$.
γ	Engineering shear strain.
γ	Unit weight.
γ_b	Eurocode 7 partial factor for base resistance.
$\gamma_{c'}$	Eurocode 7 partial factor for effective cohesion.
γ_F	Eurocode 7 partial factors for actions.
γ_G	Eurocode 7 partial factor for permanent unfavourable action.
$\gamma_{G_{fav}}$	Eurocode 7 partial factor for permanent favourable action.
γ_l	Unit weight of pore fluid.
γ_M	Eurocode 7 partial factors for material properties.
γ_ϕ	Eurocode 7 partial factor for angle of friction.
γ_Q	Eurocode 7 partial factor for unfavourable variable action.
$\gamma_{Q_{fav}}$	Eurocode 7 partial factor for favourable variable action.
γ_{q_u}	Eurocode 7 partial factor for unconfined compressive strength.
γ_R	Eurocode 7 partial factors for resistances.
γ_s	Eurocode 7 partial factor for shaft resistance.
γ_{sh}	Eurocode 7 partial factor for cylindrical failure surface resistance proposed by the author.
γ_{st}	Eurocode 7 partial factor for tensile resistance.
γ_{S_u}	Eurocode 7 partial factor for undrained shear strength.
γ_t	Eurocode 7 partial factor for total resistance.
γ_u	Eurocode 7 partial factor for uplift resistance proposed by the author.
γ_γ	Eurocode 7 partial factor for unit weight.
H	Height of soil.

H_{consol}	Height of sample during consolidation process.
H/D	Embedment ratio or height of soil divided by plate diameter.
H_{eff}	Effective length of shaft contributing to pile capacity.
Hz	Frequency or number of cycles per second.
h_0	Height of sample at beginning of consolidation increment.
h_f	Height of sample at completion of consolidation increment.
I_R	Rigidity Index.
I_{search}	Search interrogation patch.
I_{test}	Test interrogation patch.
K_0	Earth pressure coefficient.
k	Kilo or thousand.
k	Hydraulic conductivity.
k	Shear strength gradient with depth.
k_f	Coefficient of lateral earth pressure.
k_1	Primary radial distortion coefficient.
k_2	Secondary radial distortion coefficient.
κ	Eulerian rotation angle.
L	Length of side of test patch.
L_a	Active length or distance between uppermost and lowermost helical plates.
l	Left hand side.
l	Litre.
λ	Linear scaling factor.
M	Mega.
M	Dummy test patch.
MB	Megabyte.
M_c	Compatability factor.
m	Mass.
m	Metre.
m_f	Mass of pore fluid component of transparent synthetic soil.
ml	Millilitre.
mm	Millimetre.
m_s	Mass of fumed silica component of transparent synthetic soil.
m_{scorr}	Mass of fumed silica component of transparent synthetic soil corrected to account for losses during pouring.
mV	Millivolt.
m_v	Coefficient of compressibility.
N	Newton.
N_c	Bearing capacity factor.
N_{cu}	Uplift capacity factor.
N_{qu}	Uplift capacity factor.
n	Geometric scale factor.
n	Nano.

ω	Swept angular velocity.
ω	Eulerian rotation angle.
Pa	Pascal.
p_1	Primary tangential distortion coefficient.
p_2	Secondary tangential distortion coefficient.
p	Helix pitch.
px	Pixel.
$\%$	Percent.
$\%_{loss}$	Percentage Loss.
$\%_u$	Percentage vectors passing for horizontal camera-soil movement correction.
$\%_v$	Percentage vectors passing for vertical camera-soil movement correction.
ϕ	Angle of friction.
ϕ	Eulerian rotation angle.
Q_{base}	Ultimate capacity due to bearing capacity of lowermost helical plate.
Q_c	Compressive ultimate capacity.
$Q_{c\ d}$	Compressive ultimate design capacity.
Q_g	Gross ultimate capacity.
Q_{shaft}	Ultimate capacity due to pile shaft adhesion.
Q_{shear}	Ultimate capacity due to shearing resistance of cylindrical failure surface between uppermost and lowermost helical plates.
Q_t	Tensile ultimate capacity.
$Q_{t\ d}$	Tensile ultimate design capacity.
Q_u	Ultimate capacity.
Q_{uplift}	Ultimate capacity due to uplift capacity of uppermost helical plate.
q	Deviator stress.
q_{mob}	Mobilised deviatoric stress.
q_u	Unconfined compressive strength.
R	Radius.
R	Rotation matrix.
R_b	Base resistance to Eurocode 7.
R_{cal}	Calculated resistance to Eurocode 7.
$R_{cal\ base}$	Calculated helical pile base resistance to Eurocode 7.
$R_{cal\ shaft}$	Calculated helical pile shaft resistance to Eurocode 7.
$R_{cal\ shear}$	Calculated helical pile shear resistance to Eurocode 7.
$R_{cal\ uplift}$	Calculated helical pile uplift resistance to Eurocode 7.
$R_{c\ cal}$	Calculated compressive resistance to Eurocode 7.
$R_{c\ d}$	Design compressive resistance to Eurocode 7.
R_d	Design resistance to Eurocode 7.
R_k	Characteristic resistance to Eurocode 7.
$R_{k\ base}$	Characteristic base resistance to Eurocode 7.
$R_{k\ shaft}$	Characteristic shaft resistance to Eurocode 7.
$R_{k\ shear}$	Characteristic cylindrical shear resistance to Eurocode 7.

R_{k_uplift}	Characteristic uplift resistance to Eurocode 7.
$R_n(s)$	Normalised cross correlation estimator.
R_s	Shaft resistance to Eurocode 7.
$R(s)$	Cross correlation estimator.
R_{st}	Tensile resistance to Eurocode 7.
R_{sh}	Cylindrical failure surface resistance proposed by the author for use with Eurocode 7 for helical screw pile design.
R_t	Total resistance to Eurocode 7.
$R_{t\ cal}$	Calculated tensile helical pile resistance to Eurocode 7.
$R_{t\ d}$	Design tensile resistance to Eurocode 7.
R_u	Uplift resistance proposed by the author for use with Eurocode 7 for helical screw pile design.
r	Radial distance from principal point in recorded image.
r	Radial distance in MSD mechanism.
r	Right hand side.
rps	Rotations per second.
ρ	Density.
ρ_f	Density of blended pore fluid.
ρ_s	Density of fumed silica.
S	Samples.
S_a	Surface area of pile shaft.
S_f	Helical plate spacing ratio factor.
S_u	Undrained shear strength.
$S_{u_{lower}}$	Undrained shear strength at base of helical pile.
$S_{u_{shaft}}$	Undrained shear strength along shaft of helical pile.
$S_{u_{shear}}$	Undrained shear strength along cylindrical failure surface between uppermost and lowermost helical plates.
$S_{u_{surface}}$	Undrained shear strength at sample surface.
$S_{u_{upper}}$	Undrained shear strength at uppermost helical plate.
s	Second.
s	Displacement of test patch center from original position.
s/D	Helical plate spacing ratio or distance between plates divided by plate diameter.
s_{max}	Maximum displacement of test patch center from original position.
s_{peak}	Peak displacement of test patch center from original position.
σ'_v	Vertical effective stress.
σ_f	Final vertical consolidation stress.
σ_i	Initial vertical consolidation stress.
σ_{mob}	Mobilised stress.
T	Installation torque.
T	Sample thickness.
T_{v90}	Time factor at 90% average degree of consolidation.
t	Translation vector.
t_x	Horizontal translation.
t_y	Vertical translation.
t_z	Depth translation.

t_{90}	Time at which 90% of consolidation is complete.
U	Location of interrogation patch.
u	Image space horizontal coordinate.
u_c	Horizontal modal correction magnitude.
u_i	Image space horizontal coordinate corrected for intrinsic camera induced error.
u_{ie}	Image space horizontal coordinate corrected for intrinsic and extrinsic camera induced errors.
u_0	Image space horizontal principal point coordinate.
μ	Micro or thousandth.
V	Normalised velocity.
V	Volume.
V	Volt.
V_f	Volume of fluids.
V_{in}	Input Voltage.
V_s	Volume of solids.
V_v	Volume of voids.
v	Image space vertical coordinate.
v_c	Vertical modal correction magnitude.
v_f	Footing uplift velocity.
v_i	Image space vertical coordinate corrected for intrinsic camera induced error.
v_{ie}	Image space vertical coordinate corrected for intrinsic and extrinsic camera induced errors.
v_0	Image space vertical principal point coordinate.
ν	Poisson's ratio.
W	Watt.
W_a	Force due to self-weight of pile.
w	Displacement of circular plate anchor.
X	Object space horizontal coordinate.
ξ	Correlation factors to Eurocode 7.
Y	Object space vertical coordinate.
z	Depth in MSD mechanism.
z	Depth in model.
z_{ie}	Image space depth coordinate corrected for intrinsic and extrinsic camera induced errors.

List of Abbreviations

ACC	Adaptive Cross Correlation.
BASIC	Programming Language.
BMAD	Block Matching Method.
C1	Single helix pile loaded in compression.
C1-R	Repeat single helix pile loaded in compression.
C2-30	Double helix pile with an active length of 30mm loaded in compression.
C2-60	Double helix pile with an active length of 60mm loaded in compression.
C3	Triple helix pile loaded in compression.
C3-R	Repeat triple helix pile loaded in compression.
CCD	Charge Coupled Device.
CFA	Continuous Flight Auger.
CNC	Computer Numerical Control.
DA	Design Approach.
DAQ	Data Acquisition.
DC	Direct Current.
D	Depth.
DIC	Digital Image Correlation.
DSLR	Digital Single Lens Reflex.
EMF	Electro Magnetic Feedback.
EV	Exposure Value.
F	Footing test.
F-R	Repeat footing test.
FE	Finite Element.
FGSP	Flo-Gard SP Amorphous Silica.
FOV	Field Of View.
fps	Frames per second.
GUI	Graphical User Interface.
H	Height.

HST600	Hi-Sil T600 Amorphous Silica.
I/O	Input/Output.
ISO	International Standardisation Organisation Film Speed.
JPEG	JPEG.
LAT	Laser Aided Tomography.
LDFE	Large Deformation Finite Element.
LED	Light Emitting Diode.
LSF	Linear Scale Factor.
LVDT	Linear Variable Differential Transformer.
M	Million.
MSD	Mobilisable Strength Design.
MUEM	Modified Unique Element Method.
OCR	Over Consolidation Ratio.
PIV	Particle Image Velocimetry.
PSU	Power Supply Unit.
PTV	Particle Tracking Velocimetry.
PVC	Poly Vinyl Chloride.
PVD	Prefabricated Vertical Drain.
REP	Recovered Equilibrium of Patches.
RI	Refractive Index.
RITSS	Remeshing and Interpolation Technique with Small Strain.
SD	Secure Digital.
SDMCC	Strain Dependent Modified Cam Clay.
SLS	Serviceability Limit State.
SSPM	Shallow Strain Path Method.
T1	Single helix pile loaded in tension.
T2-30	Double helix pile with an active length of 30mm loaded in tension.
T2-60	Double helix pile with an active length of 60mm loaded in tension.
T3	Triple helix pile loaded in tension.
TCD	Trinity College Dublin.
TEM	Transmission Electron Microscope.
ULS	Ultimate Limit State.
UU	Unconsolidated Undrained.
W	Width.

Chapter 1

Introduction

1.1 Background

Helical screw piles consist of a tubular or solid shaft onto which regularly spaced helical plates of up to $0.4m$ diameter (D) are welded. All the plates are of the same pitch so minimum disturbance is assumed to be caused during installation. An example of an helical screw pile is shown during installation.



Figure 1.1: An example of an helical screw pile partially installed on a construction site from GTL Partnership Ltd. (2008).

Helical screw piles were patented by Alexander Mitchell in 1833 and became popular almost immediately as a method of creating anchors in marine environments. This was primarily because the piles could be easily installed using a capstan to screw in the pile to a sufficient depth or refusal. They were typically used to support marine structures such as lighthouses and piers (Parkes, 2003).

Recently they have regained popularity and are now used for a wide range of applications including: marine anchors and pier supports, temporary structure supports due to their ease of removal, support for road and rail signage and more recently as foundations for oil and gas pipelines (GTL Partnership Ltd., 2008). Their wide range of uses stems from their ability to support loads both in compression and tension when installed to a suitable depth.

However, in all cases the design methods used to predict helical screw pile capacity, are dependent upon correctly assuming the failure mechanism. In coarse grained soils the interaction of multiple helical plates has been investigated and it has been suggested that a cylindrical shear band is formed between the uppermost and lowermost helical plates (Clemence and Pepe, 1984). In fine grained soils the helical plate spacing ratio (s/D) has been suggested to affect the failure mechanism (Rao et al., 1991; Rao and Prasad, 1993; Rao et al., 1993a). However, limited experimental evidence of this behaviour has been reported.

Recent development of transparent synthetic soils (Iskander et al., 1994; Sadek et al., 2002) and Particle Image Velocimetry (PIV) allows measurement of the displacement of soil (White et al., 2005a), non-intrusively, within a body of soil (Hird et al., 2008; Ni et al., 2010). These methods potentially allow observation of the failure mechanisms of helical screw piles. Enhanced understanding of their failure mechanisms would allow rational choices to be made during the formulation of the design methods used to predict the capacities of helical screw piles in practice.

1.2 Objectives

The principal objective of this investigation was to enhance understanding of the failure mechanisms and load-deflection performance of helical screw piles. To meet this objective the following goals were developed, using which the success of the investigation may be measured:

1. To assess the potential capacity of transparent soils for the investigation of geotechnical problems using small scale physical modelling by conducting a thorough review of published literature.
2. To design small scale physical modelling experiments that maximise the modelling capacity of transparent soils and allow observation of the failure mechanisms of helical screw piles.

3. To measure accurately the displacement and shear strain fields generated during loading of model helical screw piles of varying geometry using Particle Image Velocimetry (PIV) and photogrammetry.
4. To derive suitable soil parameters to allow calibration of a suitable constitutive model for use in Finite Element (FE) simulations of the physical model tests.
5. To perform FE simulations of the physical models to allow comparison of the experimentally derived load-deflection performance and displacement and shear strain fields with a numerically derived solution.
6. To assess the validity of capacity prediction methods reported in published literature by comparing the predictions with capacities derived from the physical modelling experiments and FE simulations.
7. To utilise the findings of the research to guide industrial practice relating to the prediction of helical screw pile capacities and definition of appropriate pile geometries during design.

1.3 Thesis Structure

This thesis is comprised of eight chapters. Excluding Chapter 1, the following paragraphs outline the contents of each chapter.

Chapter 2 reviews the research previously conducted on helical screw pile behaviour in both coarse and fine grained soils. An introduction to state of the art physical modelling techniques, including PIV and photogrammetry is presented. The chapter concludes with a thorough overview of transparent synthetic soils, their development and research reported in the literature in which they have been utilised.

Chapter 3 outlines the laboratory techniques used in the physical modelling of helical screw pile behaviour. This includes development of the transparent soil used in this investigation and an overview of the experimental apparatus, measurement devices and data acquisition equipment used. Generation of transparent soil models is discussed and consolidation derived material properties are presented. The chapter concludes by outlining the experimental procedure adopted during testing.

Chapter 4 first describes the implementation of PIV, including its accuracy and precision in relation to this investigation. The photogrammetric correction procedure adopted to convert image space measurements to object space is described. Lastly, the post-processing method used to interpret the data yielded from the physical modelling process is outlined.

Chapter 5 presents the results of the physical modelling tests. First, the installation disturbance for four configurations of helical screw pile is assessed. Next, the performance of the four configurations of helical screw pile is assessed under compressive and tensile loading. The load-deflection performance is presented alongside displacement and shear strain fields for increments of axial displacement until the Ultimate Limit State (ULS) is reached.

Chapter 6 concerns the derivation of the stress-strain response of the transparent soil used in the physical models, so that a Finite Element (FE) model could be developed to simulate the physical modelling observations. This involved taking post-test measurements of undrained shear strength using the hand vane and performing Unconsolidated Undrained (UU) triaxial tests. A novel method of deriving the stress-strain relationship was also proposed, based upon employing the Mobilisable Strength Design (MSD) theory of Osman and Bolton (2005) in reverse. The validity of this concept was assessed using transparent soils in a small scale physical model with parallel simulation using the FE method.

Chapter 7 presents numerical modelling of helical screw pile behaviour. FE simulations of the physical models are presented with comparison of the results with the experimental data. An analytical method of estimating the ultimate capacity of helical screw piles is then introduced and appraised. Lastly, different design methodologies are compared and appropriate design practice discussed.

Chapter 8 contains a summary of the findings of the investigation before recommending areas requiring further research.

Chapter 2

Literature Review

2.1 Introduction

In this chapter a review of previous research into the behaviour of helical screw piles in both sands and clay soils is presented. Single helix and multi-helix piles have been investigated by researchers at various scales using different geometries of piles, leading to the proposal of suitable design equations to allow prediction of capacities. However there has been relatively little research concerning the deformation mechanisms mobilised as helical screw piles are loaded.

To investigate the deformation behaviour of helical screw piles a suitable experimental method is required. Physical models have often been used by researchers interested in geotechnical phenomena and an overview of modern physical modelling techniques, laws of similitude and measurement techniques is provided. Recent development of PIV and photogrammetry has allowed measurement of deformation behaviour to a very high resolution for plane strain and axisymmetric problems against a Perspex viewing window. These techniques are described in depth before introducing some of the materials used in physical models to represent the soil.

One relatively recently developed material is transparent soil. This material, typically formulated from silica aggregates and mineral oils, has allowed non-intrusive measurement of displacements and computation of strains without the impact of an adjacent boundary such as a Perspex viewing window. The development of these transparent materials is described before the potential for future research using the material and associated techniques is proposed.

2.2 Helical Screw Piles

Research into helical screw piles in recent years can broadly be split into the soil types within which they have been investigated: sands and clays. The following two sections contain a review of previous research conducted on helical screw piles in these two materials.

2.2.1 Behaviour in Sands

The pullout resistance of single and multi helix screw piles (see Figure 2.1) has been studied theoretically by Ghaly and Hanna (1994) and later by Hanna et al. (2007), and experimentally by Ghaly and Hanna (1992). Results from the studies were compared with field results published in the literature, for multi-helix and single helix helical screw piles loaded in tension. The results indicated reasonable agreement allowing theoretical mechanisms for shallow, transition and deep behaviour to be developed. Hanna et al. (2007) used these initial observations to develop theories to predict the ultimate tensile capacity of single helix screw piles. The results were compared with previous experimental data and design charts were presented for practical use.

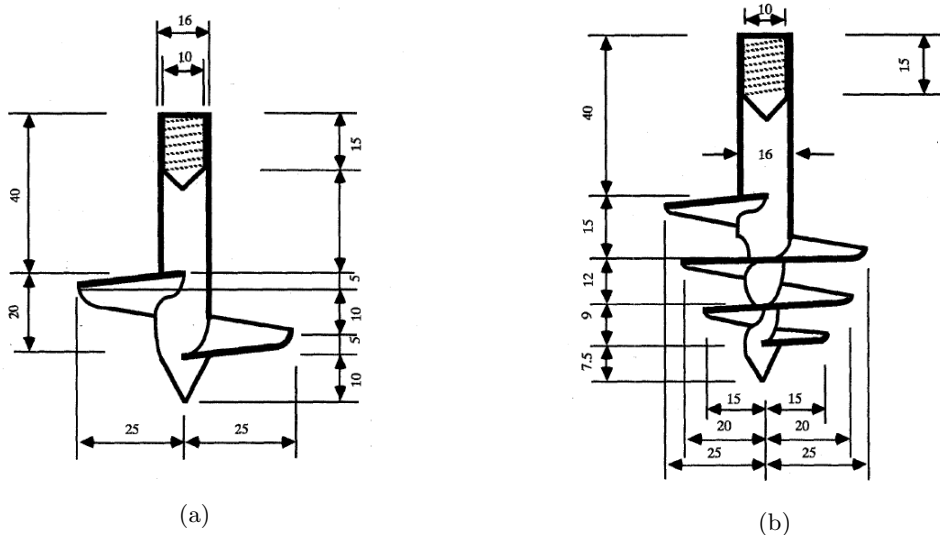


Figure 2.1: Examples of model single (a) and multi (b) helix screw piles with dimensions in mm, from Ghaly and Hanna (1992).

The tensile performance of grouped single helical screw piles in sand was studied by Ghaly and Hanna (1994a) and Hanna and Ghaly (2007) using similar theoretical and experimental techniques. They concluded that close grouping of a large number of screw piles leads to a significant increase in the overall capacity of the group. It was

suggested that this was due to interaction of the individual piles' zones of influence, possible densification and increase of the angle of friction of the sand in these zones, that may be caused by the installation process. This caused increasing disagreement between the theoretical and experimental studies where more than three piles were installed in close proximity as illustrated by the results presented in Figure 2.2 where the predictions and performance of 3 and 9 pile groups are compared.

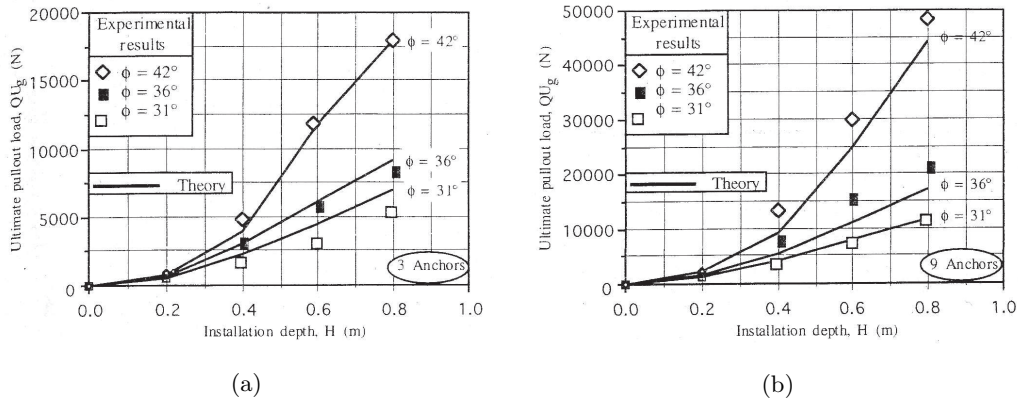


Figure 2.2: Ultimate tensile capacity of group single helical screw piles in sand compared to theoretical predictions, for three (a) and nine (b) pile groups installed at spacings of $3D$ in dense, medium and loose sands, from Ghaly and Hanna (1994a).

It has been suggested that the final installation torque measured during helical screw pile installation should relate to its ultimate tensile capacity. The possibility of this was investigated in sands (Ghaly et al., 1991; Ghaly and Hanna, 1991a) by measuring the installation torque required to install helical screw piles of varying geometry into sand. Single and multi-pitch helical screw piles were investigated in dense, medium dense and loose sands to investigate the possibility of a relationship between measured installation torque and ultimate tensile capacity. Results were compared against theoretical predictions with reasonable agreement, suggesting that the final refusal torque can be a reasonable indicator of ultimate tensile capacity in sands.

From the experimental results (see Figure 2.3), Ghaly and Hanna (1991a) used logarithmic curve fitting to develop the relationship in Equation 2.1 where Q_u is the tensile capacity, A is the helix area, H is the depth of installation, p is the helix pitch, T is the measured installation torque and γ is the bulk unit weight of the sand.

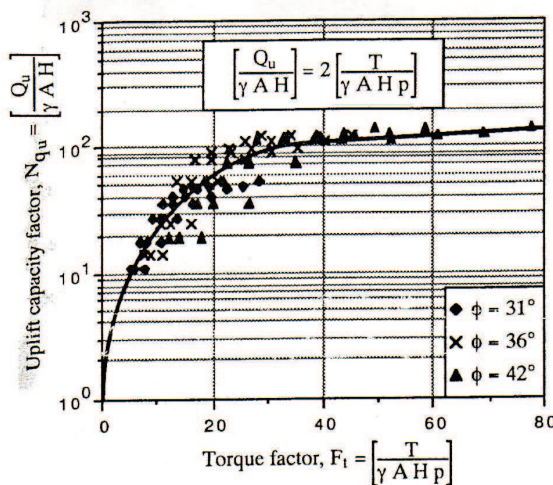


Figure 2.3: Installation torque versus ultimate tensile capacity for single helix piles in dense, medium and loose sands, from Ghaly and Hanna (1991a).

$$\left[\frac{Q_u}{\gamma \cdot A \cdot H} \right] = 2 \cdot \left[\frac{T}{\gamma \cdot A \cdot H \cdot p} \right] \quad (2.1)$$

This is an interesting method of assessing the potential capacity of helical screw piles using in-situ installation torque measurements. However, it is not particularly useful where a known load needs to be supported by a helical screw pile because the installation torque is measured during installation. During design the installation torque would have to be assumed unless field trial tests are performed. Furthermore, relying on the installation torque in certain conditions may present further problems. For example, in heterogeneous soils the measured installation torque may appear to be higher than would be expected, generating false confidence regarding the helical screw piles' capacity. An example of this from full-scale testing is reported by Livneh and El Naggar (2008), where erroneous torque measurement was caused by the striking of a cobble within the ground. Stress development within the sand was also measured at certain locations (Ghaly and Hanna, 1991a; Ghaly and Hanna, 1992) using earth pressure cells. These indicated that a larger helix pitch and shaft diameter to helix diameter (d/D) increased the stress measured within the soil. Therefore, these factors have a significant impact on the required installation torque and should be considered carefully when estimating the capacity of a helical screw pile in sand using the installation torque as an indicator of capacity.

Comparison of helical screw pile behaviour in dry and saturated sand in hydrostatic and groundwater flow conditions (Ghaly et al., 1991b; Ghaly et al., 1991c; Ghaly et al., 1991d; Ghaly, 1995a) has led to suggestions that if a specific installation torque is to be targeted during installation as an indicator of capacity, a correction should be applied since installation torque reduces in saturated soil conditions and further with net upward groundwater flow (see Figure 2.4). This is due to a reduction in effective stress. It is particularly important when helical screw piles are employed as anchors in a marine environment, such as in dry docks or navigation locks as seepage could cause a significant reduction in capacity.

Ghaly et al. (1991b) investigated the effects of surcharge on single helix screw pile behaviour in dry and submerged sands. The work concluded that the application of surcharge causes a significant increase in tensile capacity which diminished with increasing installation depth. The application of surcharge in marine environments may offset some of the loss of capacity experienced due to reduction in effective stress caused by saturation of the ground or net upward groundwater flow.

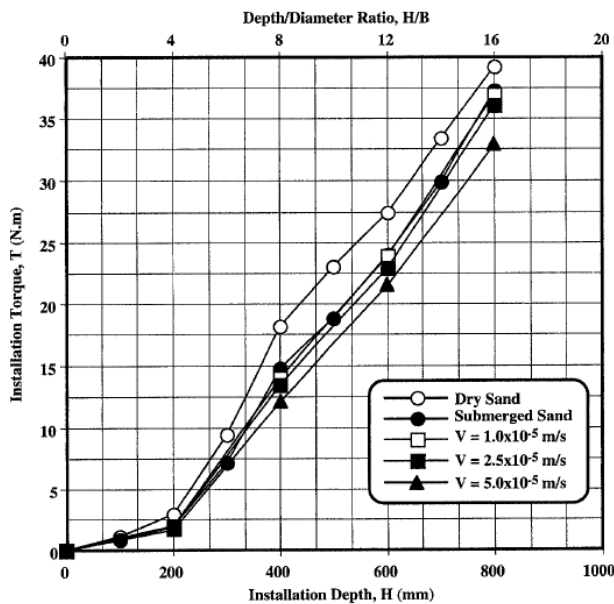


Figure 2.4: Installation torque for single helical screw pile installed in dry, saturated and net upward groundwater flow conditions in sand from Ghaly (1995a).

The performance of inclined helical screw piles in sand has been studied by Ghaly and Clemence (1998) using the same model single helical screw piles as in most of the work described above. The piles were inclined at various angles and installed to varying embedment depths before analysing the failure mechanism and ultimate

tensile capacity. This is a useful development since helical screw piles could be used to anchor back retaining walls if predicted capacities are accurate. They developed a theoretical analysis to predict the ultimate tensile capacity (Q_u) for inclined single helical screw piles based upon observations from physical models. The theoretical predictions and experimental capacities were then compared. They concluded that inclined helical screw pile tensile capacity is dependent on installation depth, inclination angle, the relative depth ratio and sand characteristics. They found that their theoretical predictions appeared to be reasonably accurate for angles of inclination up to 45° from vertical, as illustrated by the results in Figure 2.5.

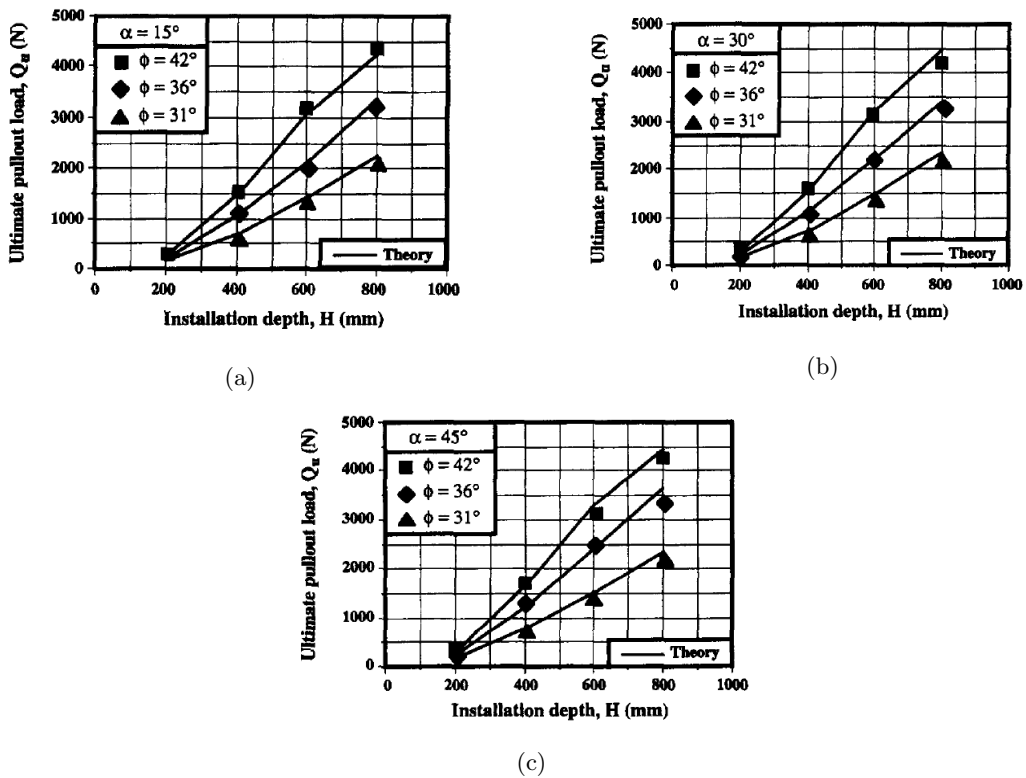


Figure 2.5: Ultimate tensile capacity of inclined single helical screw piles in dense, medium and loose sands, with angles of inclination of 15° (a), 30° (b) and 45° (c), from Ghaly and Clemence (1998).

All of the aforementioned research was conducted by the same group of authors over a number of years, using a single set of model single helical screw piles and sand, in a relatively large test chamber. However the helical screw piles that are used in engineering practice today, tend to have more than one helical plate regularly spaced over the length of the shaft (GTL Partnership Ltd., 2008; ScrewFast Foundations UK Ltd., 2008; Chance Construction Ltd., 2008).

Clemence and Pepe (1984) investigated the development of stresses and strains around a one quarter scale model of a triple helix screw pile supplied by Chance Construction Ltd. They used earth pressure cells buried at various locations around the pile to measure the change in in-situ stress caused by installation and tensile loading to failure in dense and medium dense sands. They found that the increase in lateral stress around the pile was proportional to the density of the sand and the depth of installation. When installed in deep conditions much higher stresses were developed in the surrounding sand than for piles installed to shallow depths. From these results they assessed the accuracy of a helical screw pile design method proposed by Udwari et al. (1979) in Equation 2.2, which relates to the geometry illustrated in Figure 2.6.

$$Q_u = \gamma \cdot D_1 \cdot A_1 \cdot N_{qu} + (\pi/2) \cdot B \cdot \gamma \cdot (D^2 - D_1^2) \cdot k_f \cdot \tan \phi + S_a \cdot [\gamma \cdot (D_1/2)] \cdot k_f \cdot \tan \phi \quad (2.2)$$

where D_1 is the depth to the top helical plate, A_1 is the projected area of the top helical plate, N_{qu} is the uplift capacity factor (typically 1.18), B is the average diameter of the lower helical plates, k_f is the coefficient of lateral earth pressure, D is the depth to the bottom helical plate, ϕ is the angle of friction of the sand and S_a is the surface area of the pile shaft. It is assumed that the ultimate tensile capacity is dependent upon the bearing capacity above the top of the pile, the frictional resistance of the cylinder of sand constrained by the helical plates and the friction on the shaft of the pile. By comparing their experimental results with this theoretical model they found that the coefficients of lateral earth pressure were 30-40% lower than those previously published in the literature. They concluded that this was likely to be due to disturbance caused by pile installation.

This is a more useful method of design for the practicing engineer than the installation torque method proposed by Ghaly and Hanna (1991a), since estimates of ultimate capacity can be made from site investigation data rather than in-situ data derived during pile installation. However, there is much uncertainty regarding the prediction of ultimate tensile capacity of helical screw piles, since in both this design method and the installation torque prediction method proposed by Ghaly and Hanna (1991a), significant empiricism is employed.

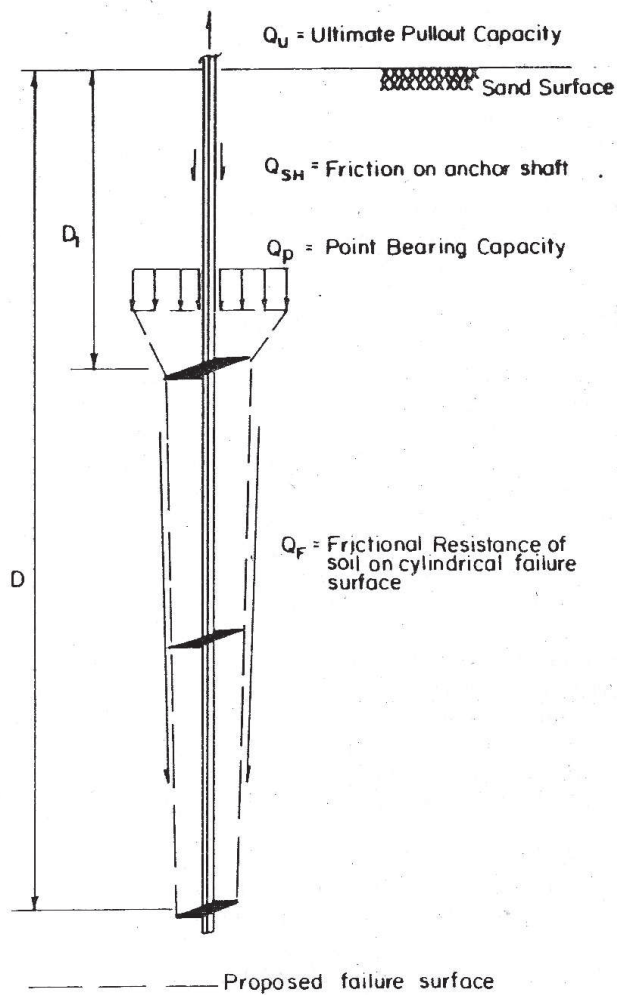


Figure 2.6: Proposed failure mechanism of helical screw piles in tension after Clemence and Pepe (1984).

Livneh and El Naggar (2008) performed full-scale field tests on a triple helix screw pile manufactured by AB Chance Ltd. in sand. The pile, comprised of three helical plates spaced at intervals of $3D$ and was deeply installed. Installation torque was measured and used to estimate the ultimate loads to be applied to the piles during testing. Both compressive and tensile tests were performed. A Finite Element (FE) model of the helical screw pile tested was developed, which assumed the helical plates could be idealised as circular plates. Soil parameters were derived from limited in-situ testing, before being finely calibrated by modifying the parameters assumed, until a good match was apparent between the load-deflection responses from the FE analysis and field testing. The failure mechanisms from the FE analysis indicated that a cylindrical failure mechanism was dominant, as was suggested by Clemence

and Pepe (1984). Minimum pile spacing of $4-5D$ was suggested to ensure that the full capacity of the individual piles is mobilised when groups of helical piles are used.

Further full-scale field testing was reported by Sakr (2010). Double helix piles with plate spacing equal to $3D$, were installed to deep embedment depths in oil sand deposits in Canada. They were subsequently loaded to failure in compression and tension. Lateral capacity was also assessed. In contrast to the work reported by Livneh and El Naggar (2008) the failure mechanism was thought to comprise of individual plate bearing rather than a cylindrical failure surface, though no evidence was provided to prove this was the case. This demonstrates the uncertainty surrounding the failure mechanisms assumed for helical screw piles in sands, indicating that further research into the failure mechanisms in sands, of helical screw piles with similar geometry to those used in practice, would be of interest.

The majority of this research has been focused on the behaviour of helical screw piles when loaded in tension. This leaves much scope for future work since one of the major advantages of helical screw piles over other forms of low capacity piling is the fact that they are able to resist both compressive and tensile loads.

2.2.2 Behaviour in Clays

Research related to the behaviour of helical screw piles in clays reported by Rao et al. (1991), Rao and Prasad (1993) and Rao et al. (1993a), has focused upon the behaviour of multi-helix screw piles loaded in both compression and tension with varying embedment depth (H), diameter (D) and helical plate spacing ratio (s/D). A number of interesting observations are made in these three publications. Firstly, varying the embedment ratio H/D allowed the authors to define shallow, transition and deep installation zones for helical screw piles in soft clay in terms of the diameter of the helical plate as follows:

- Shallow Zone - $H \leq 2D$
- Transition Zone - $2D < H < 4D$
- Deep Zone - $H \geq 4D$

The assumed failure modes varied with installation depth as illustrated in Figure 2.7.

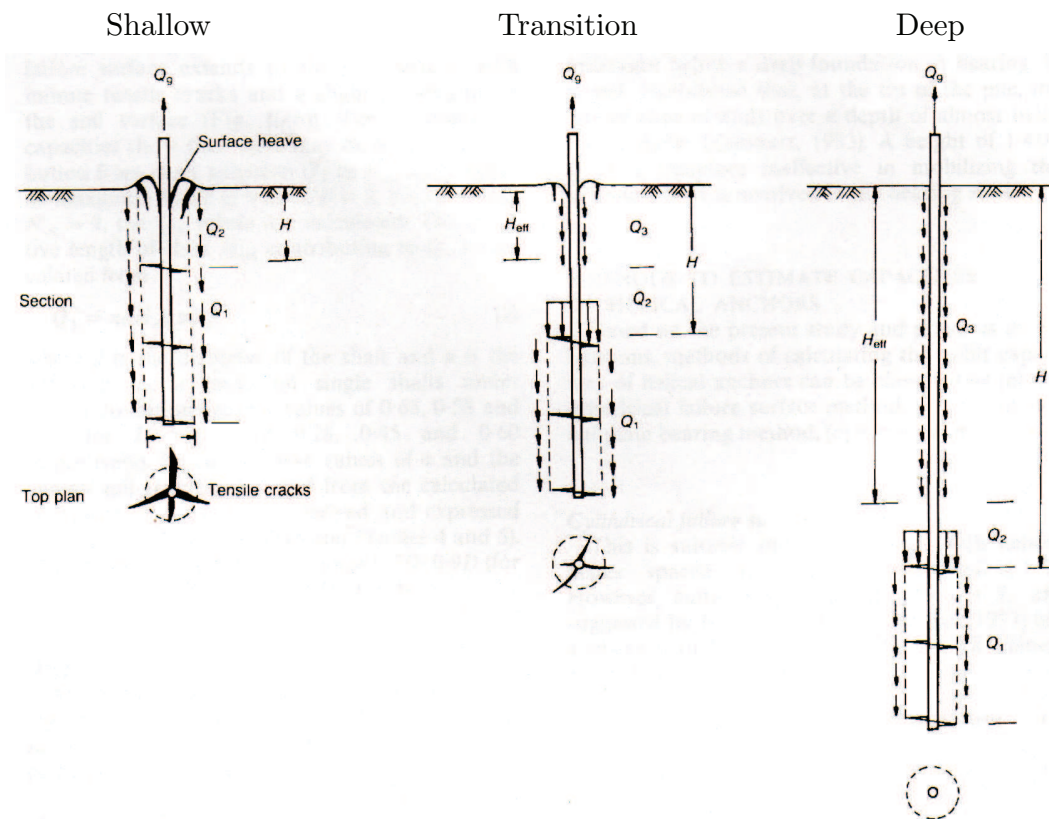


Figure 2.7: Assumed failure modes with installation depth from Rao et al. (1993a).

Secondly, the effect of the number of helical plates over a fixed length of pile installed to a deep condition ($H/D \geq 4$) was investigated using a set of small model helical screw piles with helical plate diameter of 75mm, as shown by the results in Figure 2.8. The results suggest that the number of plates over a fixed length of helical screw pile significantly affects the ultimate capacity and stiffness response of the pile. The authors concluded that in order to achieve maximum capacities using helical screw piles in soft to medium stiff clays, s/D ought to be between 1.0 and 1.5, as from photographic evidence taken during post-test analysis of the model piles (Figure 2.9) the failure surface was nearly cylindrical for this range of spacing ratios, yet was less cylindrical between the helical plates for $s/D > 1.5$.

The authors thus proposed simple design equations (Rao et al., 1991) for the ultimate capacity of helical screw piles loaded in compression and tension, assuming a cylindrical failure surface between the uppermost and lowermost helical plates which are given by Equations 2.3 and 2.4.

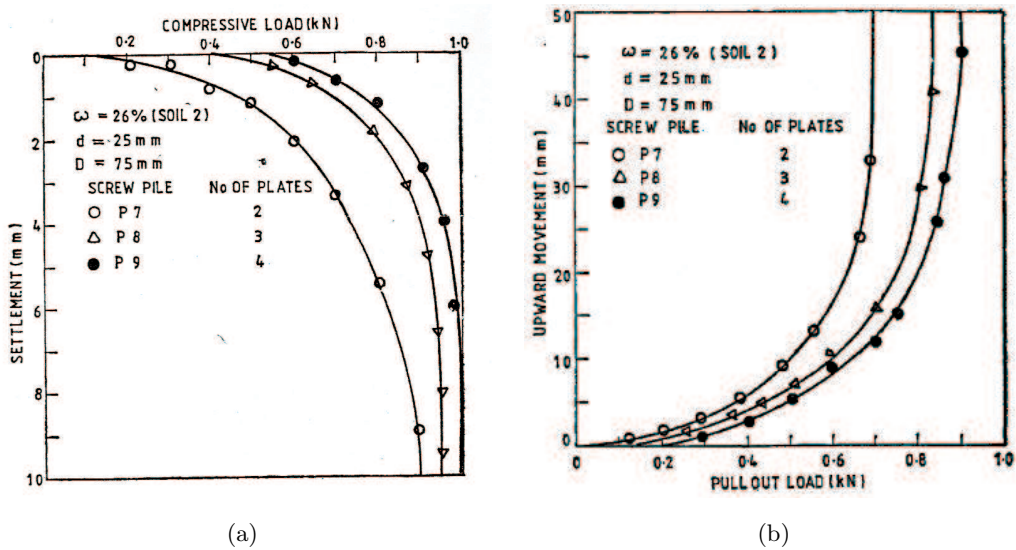


Figure 2.8: Compressive (a) and tensile (b) for deeply embedded helical screw piles with s/D of 4, 2 and 1.3, where the number of helical plates is 2, 3 and 4 respectively, from Rao et al. (1991).

$$Q_c = A_p \cdot N_c \cdot S_u + A_t \cdot N_c \cdot S_u + A_c \cdot S_u + \alpha \cdot A_s \cdot S_u \quad (2.3)$$

$$Q_t = A_p \cdot N_{cu} \cdot S_u + A_c \cdot S_u + \alpha \cdot A_s \cdot S_u \quad (2.4)$$

where S_u is the average undrained shear strength of the soil bed, A_p is the projected area of the helical plate, A_t is the area of the pile shaft tip, A_c is the area of the cylindrical failure surface, A_s is the area of the pile shaft, α is the adhesion factor and N_c and N_{cu} are the bearing capacity and uplift factors. Assessment of the predictions of capacity made using the above design equations compared to the measured experimental capacities is summarised in Figure 2.10 with respect to s/D .

The results indicated that the theoretical predictions were good for s/D over the range 1.0-1.5, but led to overprediction of capacity for piles with $s/D > 1.5$. This led to Rao and Prasad (1993) and Rao et al. (1993a) refining the design equations to incorporate a correction factor which was related to s/D , to account for the weight of the pile and to account for the assumption that some proportion of the shaft will be ineffective.

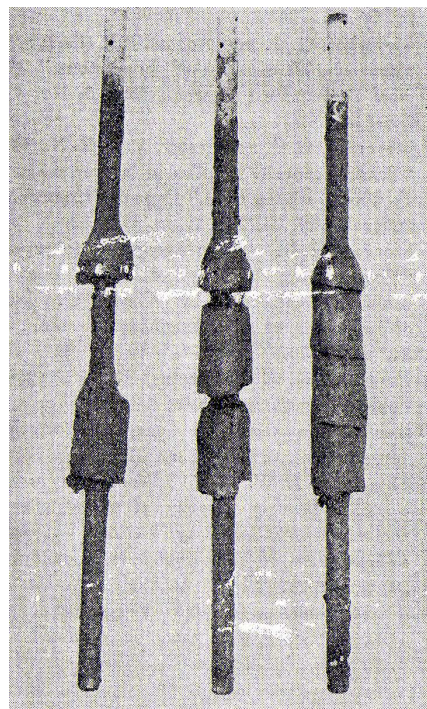


Figure 2.9: Evidence of changing failure mechanism after tensile test of deep helical screw piles with s/D of 4.0, 2.0 and 1.3 where the number of helical plates is 2, 3 and 4 respectively, from Rao et al. (1991).

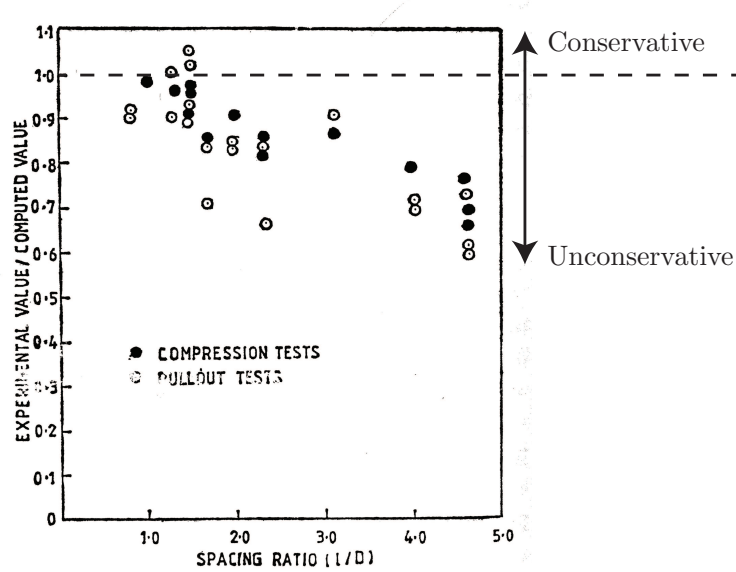


Figure 2.10: Assessment of predicted capacities compared to experimental capacities of helical screw piles from Rao et al. (1991) by normalisation.

Equation 2.5 is the refined formulation proposed to estimate the tensile capacity of helical screw piles:

$$Q_g = S_f \cdot A_c \cdot S_u + A_p \cdot (N_{cu} \cdot S_u + \gamma \cdot H) + \pi \cdot d \cdot H_{eff} \cdot \alpha \cdot S_u + W_a + \text{Suction Force} \quad (2.5)$$

where Q_g is the gross capacity, H is the depth of soil overlying the uppermost helical plate, H_{eff} is the assumed effective shaft length and W_a is the weight of the pile and S_u , A_p , A_t , A_c , A_s , α , N_c and N_{cu} are as defined for Equation 2.3 and 2.4. The correction factor S_f was defined as follows:

$$\begin{aligned} s/D \leq 1.5 &\Rightarrow S_f = 1.0 \\ 1.5 \leq s/D \leq 3.5 &\Rightarrow S_f = 0.863 + 0.069(3.5 - s/D) \\ 3.5 \leq s/D \leq 4.6 &\Rightarrow S_f = 0.700 + 0.148(4.6 - s/D) \end{aligned} \quad (2.6)$$

These factors were fitted empirically using the experimental results reported in Rao et al. (1991) and compared to limited field data from full scale tensile loading tests on helical screw piles from previous publications as shown in Figure 2.11 with good agreement.

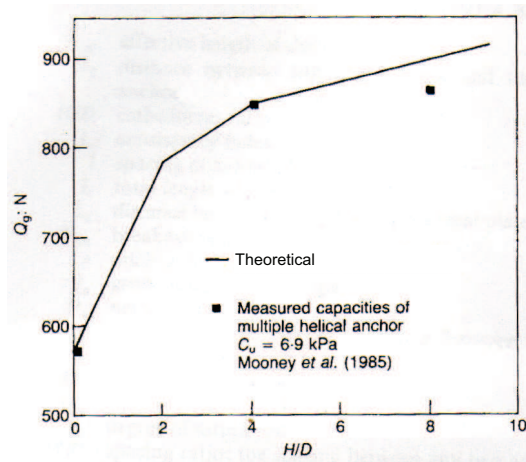


Figure 2.11: Cylindrical failure theory proposed by Rao et al. (1993a) compared to field data.

The authors also presented a brief investigation of the applicability of the assumption that, where $s/D \geq 2$, the bearing capacity of the individual helical plates can

be summated. The results are presented in Figure 2.12, showing that assuming that the failure mechanism around each helical plate is independent, leads to a maximum underestimation of capacity of 20%. Thus, it is possible that using these two design methodologies dependent on the s/D of the pile, the ultimate capacity can be estimated with reasonable confidence.

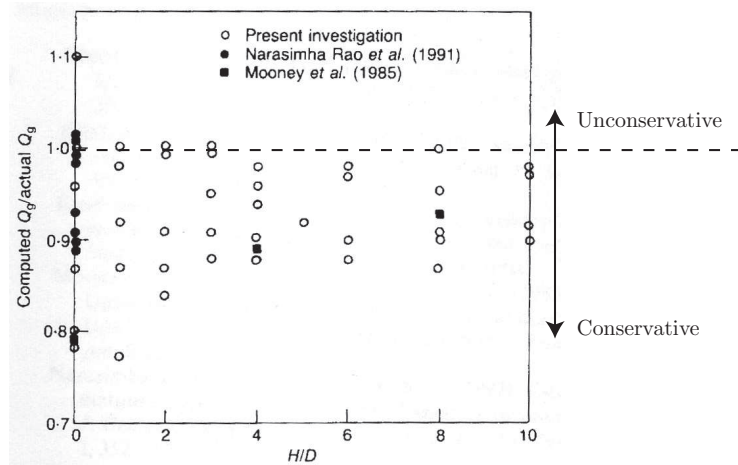


Figure 2.12: Individual bearing failure theory compared to experimental data from Rao et al. (1993a).

The significance of this was highlighted during discussions with helical screw piling contractors GTL Partnership Ltd. and ScrewFast Foundations Ltd. as their experiences suggested that rules such as those proposed by Rao et al. (1991) and Rao et al. (1993a), are not necessarily adhered to in practice. The s/D used in helical pile design in practice ranges from 1.0 to as much as 6.0, and yet the pile capacities are often estimated using the same methodology regardless of s/D . Design methods also differ between different helical screw piling consultancies, with some assuming that helical screw piles fail with a cylindrical failure surface between the helical plates and some assuming that each individual helical plate will fail by mobilising bearing capacity individually.

If the failure mechanisms are affected by s/D then there is, at worst, a possibility of unsafe design, or, at best, uneconomical design if the wrong failure mechanism is assumed by the designer. More worryingly, some contractors appear to use the measured installation torque to define whether adequate capacity has been mobilised upon installation. Using the installation torque in this way was suggested by Prasad (1996a) by proposing correlation of a torque factor for silts and clays similar to that

proposed by Ghaly (1995a) for sands. This was achieved using model and field test data from previously published results. Figure 2.13 presents the torque factor correlation suggested in comparison to that for sands.

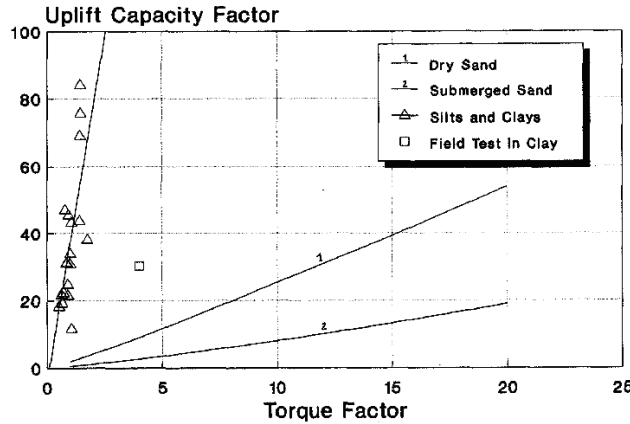


Figure 2.13: Torque factor correlation for silts and clays from Prasad (1996a).

However, the slope of the correlation line proposed to relate torque factor to ultimate capacity factor is very large. Hence a small variation in the slope of the torque factor correlation line proposed would cause a large range of predicted capacities. Therefore in practice small changes in the measured installation torque could lead to wildly varying capacity predictions. This adds risk since the installation torque would be highly sensitive to heterogeneities within the soil. For this reason, even with the relatively small scatter in the data presented, the author thought it improper to propose an equation for the relationship. This serves as a demonstration of the potential danger of relying on installation torque to predict the capacity of helical piles in clays. This also highlights the need for improved understanding of the failure mechanics of helical screw piles, particularly in fine grained soils, where in-situ measurements of installation torque cannot be relied upon to indicate that the pile will achieve the required design capacity under loading.

Prasad and Rao (1994) investigated the effects of lateral cyclic loading on the tensile capacity of helical screw piles in clay using the same laboratory soil and model piles as Rao et al. (1991). They found that if lateral deflections were less than 10% of the shaft diameter of the helical screw pile there was no reduction in capacity and performance was significantly better than for a comparable straight shafted pile of the same shaft diameter. This work is particularly relevant to industrial practice since a principal use of helical screw piles in recent years in the UK has been to support

road signs on highways. Typically in these applications, a single pile is used and thus a helical screw pile is favourable due to its increased lateral loading capacity (Prasad and Rao, 1994).

Field testing of helical screw piles in clay has been reported by Lutenegger (2008). Single helix piles were installed to deep embedment depths in clay, before loading in tension. The load-deflection results obtained suggested that the ultimate capacity of single helix piles subjected to tensile loading ought to be defined as the load apparent at a displacement of $0.1D$. The author further proposes that, in homogeneous clay soils, the load-deflection response of deeply embedded single helix screw piles of differing geometry can be predicted using a normalisation approach. A simple power relationship coupled with an accurate estimate of the ultimate capacity of the pile can be coupled to estimate the load-deflection response. Further research into the viability of this approach is ongoing.

2.3 Physical Modelling

Physical modelling of geotechnical problems in the laboratory at reduced scale, is a powerful method for researchers to increase their knowledge of the behaviour of soils, and their interaction with geotechnical structures during loading. According to White (2008) in a review of contributions made to *Géotechnique* since 1948, approximately 200 papers primarily concerning physical modelling of geotechnical problems have been published in the journal. These used techniques ranging from simple plane-strain modelling at $1g$ (White and Bolton, 2004) to centrifuge modelling of problems where the self-weight of the soil was artificially increased by imposing levels of gravitational acceleration in excess of $1g$ (Lyndon and Schofield, 1970). Using these techniques, many quintessential geotechnical engineering problems have been investigated, such as slope failures (Lyndon and Schofield, 1970), stability of shallow circular tunnels (Atkinson and Potts, 1977) and the collapse of diaphragm walls retaining clay (Bolton and Powrie, 1987). Latterly, the advent of digital cameras and powerful computational analysis techniques have been used to investigate the displacements and strains caused by pile installation in plane-strain conditions (White and Bolton, 2004) and the influence of seasonal moisture cycles on clay slopes (Take, 2003).

2.3.1 1g Modelling

Physical modelling at $1g$ is a popular method of investigating the behaviour of field scale problems at small scale within the laboratory. This is due to its inherent simplicity and low relative risk and running costs. The size of the models is usually reduced by a scale factor n . At $1g$ coarse grained soil models can be prepared by pluviation to achieve a target density and repeatable sample generation. Fine grained models can be generated by pre-consolidation of the model via application of an effective stress, such that after consolidation a target undrained strength is achieved. One method of estimating the undrained shear strength of a fine grained soil, consolidated at a given pre-consolidation pressure and known Over Consolidation Ratio (OCR), is by using a normalised undrained shear strength relationship such as that in Equation 2.7 from Ladd and Foott (1977).

$$\frac{S_u}{\sigma'_v} = a \cdot \text{OCR}^b \quad (2.7)$$

This relates the undrained shear strength S_u with the OCR and pre-consolidation pressure (σ'_v), where the coefficients a and b are empirically derived and some reported values for which are summarised in Table 2.1.

Table 2.1: Coefficients a and b proposed by different researchers.

Researcher	a	b
Philips and Valsangkar (1987)	0.19	0.67
Nunez (1989)	0.22	0.62
Springman (1989)	0.22	0.71

Fine grained models formed in a consolidometer at $1g$ typically exhibit high OCR and relatively uniform S_u with depth, because σ'_v is almost uniform with depth. However, Tani and Craig (1995) have shown that by using a Rowe Cell consolidometer (Rowe and Barden, 1966) and the hydraulic gradient similarity method (Zelikson, 1969), samples with linearly increasing strength with depth can be formed at $1g$. This is of particular importance in relation to offshore geotechnical problems, where fine grained soils are generally normally consolidated and thus exhibit linearly increasing strength with depth.

One drawback with small scale $1g$ physical models is the lack of similarity of stress profile between the model and prototype. If a field problem is scaled down by a geometric scale factor n at $1g$, the stresses at coincident points in the model and prototype are different by a factor of n . Therefore, if the behaviour of the soil used in the model is strongly dependent on the stress level, the field behaviour would not be correctly reproduced in the $1g$ model. This shortcoming is less problematic when modelling with fine grained soil such as clay, since the soil strength is not stress dependent under undrained deformation. The dissimilarity of stress profile within the model then only impacts upon the apparent self weight of the soil within the model.

2.3.2 Centrifuge Modelling

Centrifuges designed to carry a soil model as its payload, have been used in geotechnical research to artificially increase the weight of the soil within the model. The general principle of the mechanics of the geotechnical centrifuge is that a soil body of mass m is rotated at a constant radius R with a velocity v . To maintain a circular orbit the soil model must be subjected to a constant centripetal acceleration $R\omega^2$, where ω is the swept angular velocity. This requires the soil model to experience a

radial force equal to $mR\omega^2$, which can be normalised by g . The soil is thus described to be subjected to acceleration ng , where the scale factor n is equal to $\frac{R\omega^2}{g}$. This has the effect of increasing the weight of the soil within the model by the factor n . Hence, when a model reduced in scale by n , is subjected to an acceleration ng , the stress profile in the model is identical to that of the prototype at geometrically equivalent locations (Wood, 2004).

This is advantageous for models comprised of soil with stress level dependent behaviour, as the mechanical response of the soil should be more realistically reproduced in a model subjected to acceleration of ng , compared to the same small scale model subjected to $1g$. In the words of Roscoe (1970) the geotechnical centrifuge is “the only satisfactory method for modelling to scale a prototype problem in which the self-weight of the soil is significant”. It also allows normally consolidated deposits of fine grained soils to be formed from slurry in flight (White et al., 2010).

The major drawback with centrifuge modelling is its complexity and increased risk when compared to $1g$ modelling. The apparatus and setup costs are considerable. Furthermore significant payloads revolving at high speeds require expert supervision and stringent health and safety considerations. Thus the running costs are also high.

2.3.3 Scaling Laws

In order for a scale model to be deemed fit for purpose it must be geometrically, kinematically and dynamically similar. Scaling laws have been derived in order to attain similitude in physical models, as presented by Wood (2004) in Table 2.2, where n is the scaling factor and α is dependent on material type: typically α of 0.5 for sand and α of 1.0 for clay.

2.3.4 Boundary Effects

With regard to modelling the behaviour of deep foundations such as piles, the ratio of pile diameter to boundary distance requires some consideration. Utilising a large test chamber in relation to the model pile reduces the possibility of boundary effects and increases the likelihood of the ideal conditions of zero stress change and deflection being present at the boundary.

Boundary effects in sands have been investigated by Gui et al. (1998) by performing cone penetration tests with varying chamber size and probe diameter. Both

Table 2.2: Scale factors from Wood (2004).

Quantity	Scale Factors		
	General	$1g$	ng
Length	n_l	$1/n$	$1/n$
Mass Density	n_ρ	1	1
Acceleration	n_g	1	n
Stiffness	n_G	$1/n^\alpha$	1
Stress	$n_p n_g n_l$	$1/n$	1
Force	$n_p n_g n_l^3$	$1/n^3$	$1/n^2$
Force/Length	$n_p n_g n_l^2$	$1/n^2$	$1/n$
Strain	$n_p n_g n_l / n_G$	$1/n^{1-\alpha}$	1
Displacement	$n_p n_g n_l^2 / n_G$	$1/n^{2-\alpha}$	$1/n$
Time (Diffusion)	$n_\mu n_l^2 / n_G$	$1/n^{2-\alpha}$	$1/n^2$
Time (Creep)	1	1	1
Time (Dynamic)	$n_l (n_\rho / n_G)^{1/2}$	$1/n^{2-\alpha/2}$	$1/n$

rectangular and cylindrical chambers were investigated with the required boundary distance to achieve minimal boundary effects being twenty probe diameters in a cylindrical chamber and fifteen probe diameters in a rectangular chamber. Following further work on cone penetration tests in cylindrical calibration chambers, Bolton et al. (1999) proposed that the minimum boundary distance required to eliminate boundary effects should be fifteen probe diameters. Klotz and Coop (2001) conducted model pile tests in the centrifuge with a boundary distance of nineteen pile diameters in loose carbonate and silica sands with no reported boundary effects, except where dense silica sand was used and increased base resistance was experienced.

Boundary effects in test chambers containing clays were estimated by Smith (1993), by assuming an elastic-perfectly plastic soil response and using cylindrical cavity expansion theory to calculate the radius of the elasto-plastic boundary for a cylindrical penetrating object. The calculation suggested that a boundary distance of at least twenty probe diameters is required to minimise boundary effects. Brown et al. (2004) utilised a flexible wall boundary in a calibration chamber to investigate statnamic testing of model piles in clay. Using the same methods as Smith (1993) they calculated that a boundary distance of as little as three pile diameters should adequately simulate a semi-infinite soil mass, when a flexible stress controlled boundary is employed.

In the modelling of penetrating objects such as piles, boundary effects are thus very much dependent on the nature of the boundary and material properties. However,

it is also apparent that a balance is required, between minimising boundary effects and maintaining reasonable economy when conducting physical modelling, by not using samples that are larger than is necessary.

2.3.5 Displacement Measurement

Displacement measurement in physical models has traditionally been conducted at points of interest using Linear Variable Displacement Transducers (LVDT). Displacements occurring throughout the soil mass of a physical model are much more difficult to record, yet are vital to developing an understanding of the failure mechanisms of many geotechnical problems. Ultimate Limit State (ULS) failure modes can often be inferred by careful inspection of the post-failure dissected model. However, in many instances, particularly in the modelling of field scale problems where ultimate failure must never occur, the Serviceability Limit State (SLS) behaviour is of greater interest. Comparison of pre-failure and post-failure geometric conditions of a physical model offers no insight into the development of displacements and strains during loading of a geotechnical model to its ultimate capacity. If pre-failure deformations are to be measured, a pertinent question is what is the required resolution of the measuring technique? White (2002a) states that it is strains in the range of 0.01 to 1.0% that are of most interest in investigating the behaviour of geotechnical models since this typically encompasses both “serviceability and pre-failure deformations”. This requires the capability to measure displacements with a resolution and precision that allows strains to be calculated in the order of 0.01%.

2.3.5.1 Review of Previous Measurement Techniques

One method originally used to measure displacements in physical models utilised X-rays to create a radiograph of a sample of sand containing a planar grid of lead shot. Taking radiographs at intervals during deformation of the physical model, allowed analysis of the development of displacements within the soil by measuring the positions of each of the markers relative to the radiograph of the original geometric condition. Figure 2.14 is a strain field plot presented by Bransby and Milligan (1975) that was calculated using displacements derived from X-ray radiograph measuring techniques. In this instance the radiograph measurements were able to define the positions of the lead shot with an accuracy of $\pm 34\mu m$, allowing strain contours to be plotted at intervals of 1%. Some drawbacks with X-ray based displacement measurement include that the apparatus is expensive and health and safety considerations regarding sources of radiation are anything but trivial. Furthermore, its

rate of capture is limited to the time required to develop a radiograph, plus the time required to change the film. The addition of lead shot into the soil continuum may cause arching around these foreign bodies. The difference in density between lead and soil in the physical model and differences in the mechanical deformation behaviour of the two materials will also influence the behaviour observed.

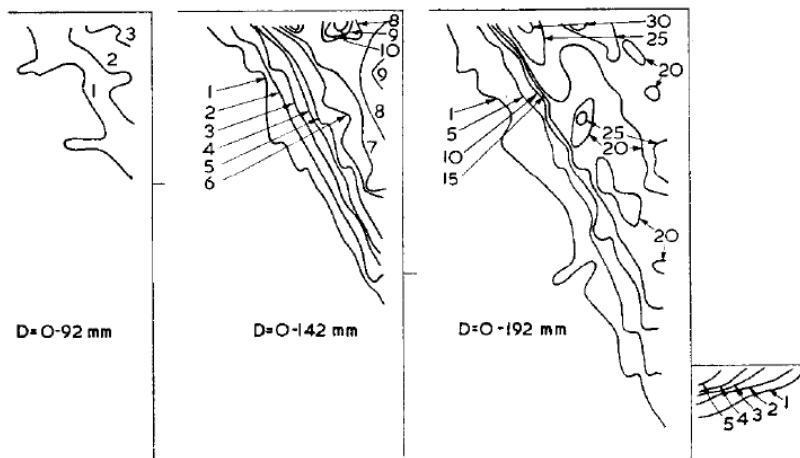


Figure 2.14: Shear strains, γ , expressed as a percentage, around a cantilever wall in sand, derived from displacements measured using X-ray radiograph measuring techniques by Bransby and Milligan (1975).

Photographic measuring techniques were the next logical step in measuring displacements within a soil body, where a simple camera is used to expose an image of a plane strain physical model onto ordinary film, by virtue of a glass or Perspex viewing pane. The primary advantages of this method are that it does not require a source of radiation and can be incorporated simply into a geotechnical centrifuge. Butterfield et al. (1970) proposed a method of analysis of the photographic images called stereo-photogrammetry where two images of the model at sequential incremental displacements are compared over a light box, allowing the displacements of distinct features such as distinct groups of sand grains to be manually measured. The technique was originally stated to be able to measure displacements with an accuracy of $10\mu m$. Further development by Andrawes and Butterfield (1973) led to the accuracy being refined such that displacements as small as $5\mu m$ could be accurately measured by tracing the movements of individual sand grains, as illustrated in Figure 2.15.

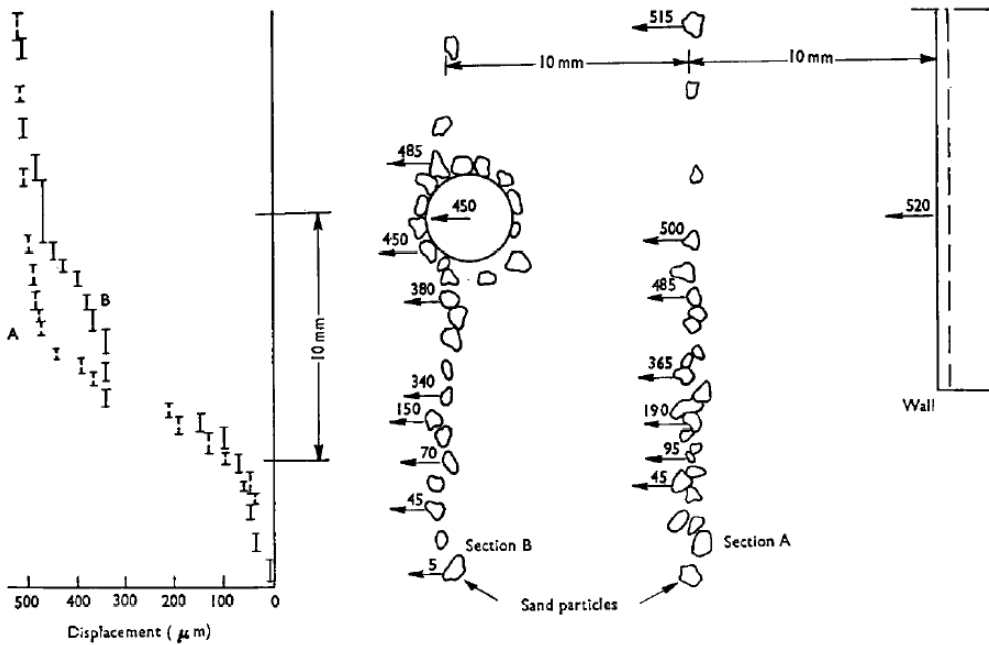


Figure 2.15: Displacement of individual sand grains measured using stereo-photogrammetry, from Andrawes and Butterfield (1973).

The advent of digital video cameras and their much improved image capture rate negated the use of traditional film in photographic measurement techniques and the laborious processes attached to them. Centroiding allows tracking of markers within a digital image to be conducted automatically and reliably by a computer. Video extensometry is an alternative and improved method of analysing the movement of target markers using digital video. The principal advantage is that this technique differentiates between target markers that contrast with the background of the image creating digital signatures for each target. These digital signatures are dynamically adaptive, so that changes in contrast or shape of the target are accounted for during tracking.

Gill (1999) used a video extensometer to investigate the movement of target markers (black beads) during the installation of a penetrometer in transparent synthetic clay (see Section 2.4 for further information on transparent synthetic soils). The video extensometer used in the investigation was capable of tracking 100 markers at a rate of $25Hz$ and real time averaging was used between penetration increments to improve the resolution of the displacement measuring technique, such that the quoted accuracy was $0.004mm$ in the $200mm$ field of view (Gill and Lehane, 2001; Lehane and Gill, 2004). Figure 2.16 presents the radial and vertical strain contours,

normalised by penetrometer radius, caused by installation of a model penetrometer in transparent synthetic clay. In this instance strain contours of 0.5% were computed.

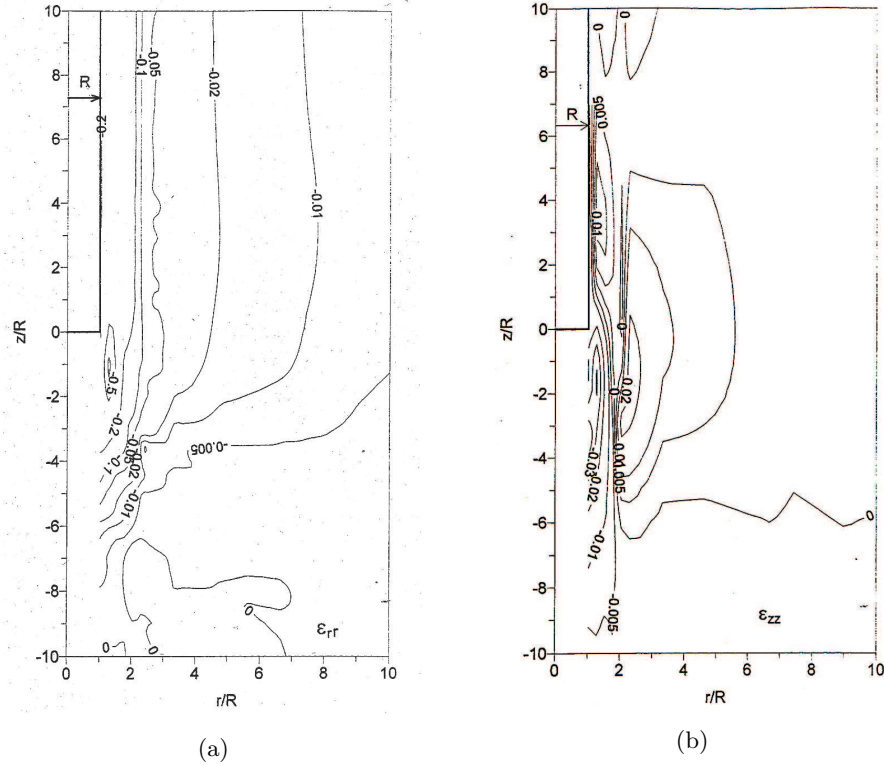


Figure 2.16: Radial (a) and vertical (b) strain contours around a model penetrometer in transparent clay from Gill (1999).

Irrespective of the achievable accuracy of the video extensometry technique, its major drawback in common with X-ray and photographic displacement measurement techniques is the reliance on discrete target markers to allow calculation of displacements, as this generates numerous problems including (after White (2002a)):

- The reinforcing effect of target markers is unknown.
- Detail in areas of large strain is unsatisfactory.
- Measurement reliability is reduced if target markers are obscured.
- Points of interest must be chosen before construction of the physical model.

These reasons were the motivation for White et al. (2003) to develop a new system of measuring displacements in geotechnical physical models, using the existing techniques of digital photography, Particle Image Velocimetry or PIV and photogrammetry. This system is not reliant on discrete target markers within the soil and computes displacements with greater accuracy and precision than previously achieved.

The product was the now widely known piece of software called GeoPIV (White et al., 2001; White et al., 2001a; White and Take, 2002; White et al., 2003a). The following sections will include a brief overview of PIV, the development of GeoPIV and photogrammetry techniques.

2.3.5.2 Particle Image Velocimetry

Particle Image Velocimetry or PIV was originally developed by Adrian (1991), to determine the velocity of fluid flows by tracking the movements of seeding particles illuminated by a light sheet, using a photographic camera to capture images of the light sheet perpendicular to the optical axis of the camera. Single image pairs are created using multiple flashes or pulses of the light sheet. Correlation algorithms are used to either track movement of individual particles within the image if the seeding particle density is low, which is known as Particle Tracking Velocimetry (PTV), or by splitting the image up into interrogation patches which contain multiple particles if the seeding density is high, which is known as High Image Density PIV (Adrian, 1991). Results are usually presented in the form of velocity fields.

Adrian (2005), in his review of the development of PIV techniques over the past twenty years, suggests that it has been the lack of the technology required to conduct PIV that has held back its development until the latter decades of the 20th century, rather than a lack of awareness of the underlying concept. Thus it is the recent rapid development of digital cameras and the vast increase of the computational power of computers that has led to an explosion of interest and activity in PIV techniques, not just limited in application to experimental fluid mechanics but also including: chemical engineering (Ali et al., 2008), food engineering (Laguerre et al., 2009), respiratory physiology (Chung and Kim, 2008), nuclear engineering (Hassan and Dominguez-Ontiveros, 2008) and building and the environment (Kang and Lee, 2008).

In fluid mechanics the movement of seeding particles within fluid flows are tracked within a planar section of the model at high velocities. In geotechnical engineering research the application of the concept is slightly different. The planar section of interest is usually a cross-section of the model with the soil exposed using a glass or Perspex viewing window. Texture is provided in the photographic images recorded by the contrasting colouration. In sands this texture may be provided by different coloured sand grains (White, 2002a), whilst in clays it may be due to flocking of

the exposed plane with a coloured material (White and Take, 2002; Effendi, 2007). In fluid mechanics a snapshot of the velocity field at different flow rates is usually the target of a PIV investigation, yet in geotechnical modelling the interest is in the incremental nature of deformation at different strains. Thus, rather than capturing single image pairs, capturing a sequence of images at incremental strains during testing is preferable to allow analysis of the development of failure conditions.

Implementation of PIV to geotechnical modelling was reported by Guler et al. (1999) as the block-matching method (BMAD), which split images into interrogation patches and used correlation algorithms to identify the likely positions of the patches in sequential images, subsequently allowing calculation of displacements. White (2002a) utilised PIV to investigate the displacement of soil during pile installation, which led to the development and release into the academic community of GeoPIV, which is an implementation of PIV specifically for the calculation of displacements in geotechnical physical models. Another implementation of PIV for geotechnical research purposes, independent of GeoPIV, is that of Sadek et al. (2003), where the method was termed as Digital Image Correlation (DIC), but the concept was fundamentally the same. Liu and Iskander (2004) further developed DIC to create a process known as Adaptive Cross Correlation (ACC) that allows the interrogation patch sizes and positions to be refined during analysis to reduce the proliferation of spurious wild random vectors caused by loss of texture between sequential images. In recent years due to its availability and rigorous calibration (White, 2002a), GeoPIV has become widely used by researchers for measuring displacement in geotechnical models and thus, Section 2.3.5.3 contains a brief review of the implementation of PIV within GeoPIV.

2.3.5.3 GeoPIV

White et al. (2003) implemented PIV into GeoPIV in the form of a modified version of cross correlation. Cross correlation differs from auto correlation in that two interrogation patches are defined rather than one, such that I_{test} is a matrix of pixel intensities apparent in an initial patch taken from the original image and I_{search} is a matrix of pixel intensities in a search patch in sequential images. The cross correlation estimator $R(s)$ is defined by Equation 2.8, given that U is the location of the test patch and s is the displacement experienced by the patch.

$$R(s) = \sum_{(U)} I_{test}(U) \cdot I_{search}(U+s) \quad (2.8)$$

White (2002a) felt that this formulation of cross correlation was not ideal for geotechnical modelling purposes since it causes texture or particle images which move from within the zone of the original patch U to be defined as null or void in I_{search} , and thus not contribute to the correlation process. Therefore this process requires that the maximum displacement between sequential images s_{max} be limited to half the patch length, $L/2$.

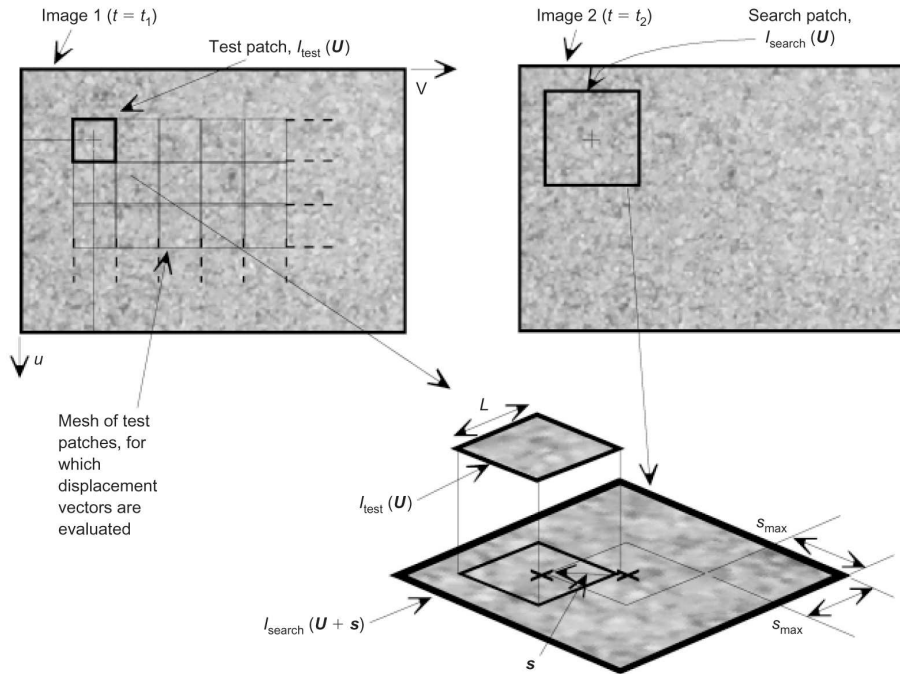


Figure 2.17: Graphical concept of PIV process conducted by GeoPIV from White et al. (2003).

Figure 2.17 illustrates the concept of PIV utilised in GeoPIV in a graphical format. To tackle the problem of texture or particle image loss White (2002a) proposed that a normalised estimator $R_n(s)$ can be defined as shown in Equation 2.9, where a dummy test patch $M(U)$ of uniform intensity allows a “degree of match” to be calculated over the search area defined by I_{search} , regardless of discrepancies in size between I_{test} and I_{search} .

$$R_n(s) = \frac{R(s)}{\sum_{(U)} [I_{test}(U) \cdot I_{search}(U+s)] M(U)} \quad (2.9)$$

The best degree of match is defined by the vector s_{peak} , which is a discrete interval vector in pixel terms between the original position $I_{test}(U)$ and the peak of the correlation function. By performing bicubic spline interpolation around the peak of the correlation function at intervals of $1/100^{th}$ of a pixel, sub pixel resolution can be achieved as illustrated by Figure 2.18. This interval according to White et al. (2003) is typically $1/200^{th}$, giving a system resolution of 0.005 pixels. Reducing the interval improves the resolution, with a corresponding increase in the computational burden, yet is not required since the errors associated with the PIV process are usually larger.

GeoPIV outputs within a text file, the coordinates of I_{test} and the correlation peak within I_{search} defined by the vector s_{peak} , as well as computed vertical and horizontal displacements for each interrogation patch in pixel terms. This result file can then be used in post-processing to calculate and convert image space displacements to object space using photogrammetry.

2.3.5.4 Photogrammetry

Displacements from PIV analyses are output in terms of pixels. Subsequently they require photogrammetric manipulation to convert them from image space in pixels to object space coordinates in metric units. Previously, since measurable strains in physical models have been of the order of 1%, photogrammetric correction consisted of using a Linear Scale Factor (LSF) to convert image space coordinates, and hence displacements, to object space. The development of GeoPIV has seen the capability to measure strains in physical models increase significantly and thus the assumption that a LSF can be used to perform this conversion is no longer valid since the errors associated are larger than those attributed to the PIV technique. A number of distortional effects need to be accounted for in photogrammetric correction including internal and external camera induced distortions.

Internal distortions are caused by lens imperfections including radial and barrel distortion (Slama, 1980), lens focal length and Charge Coupled Device (CCD) aspect ratio. External distortions are caused by non-coplanarity of the object and the CCD

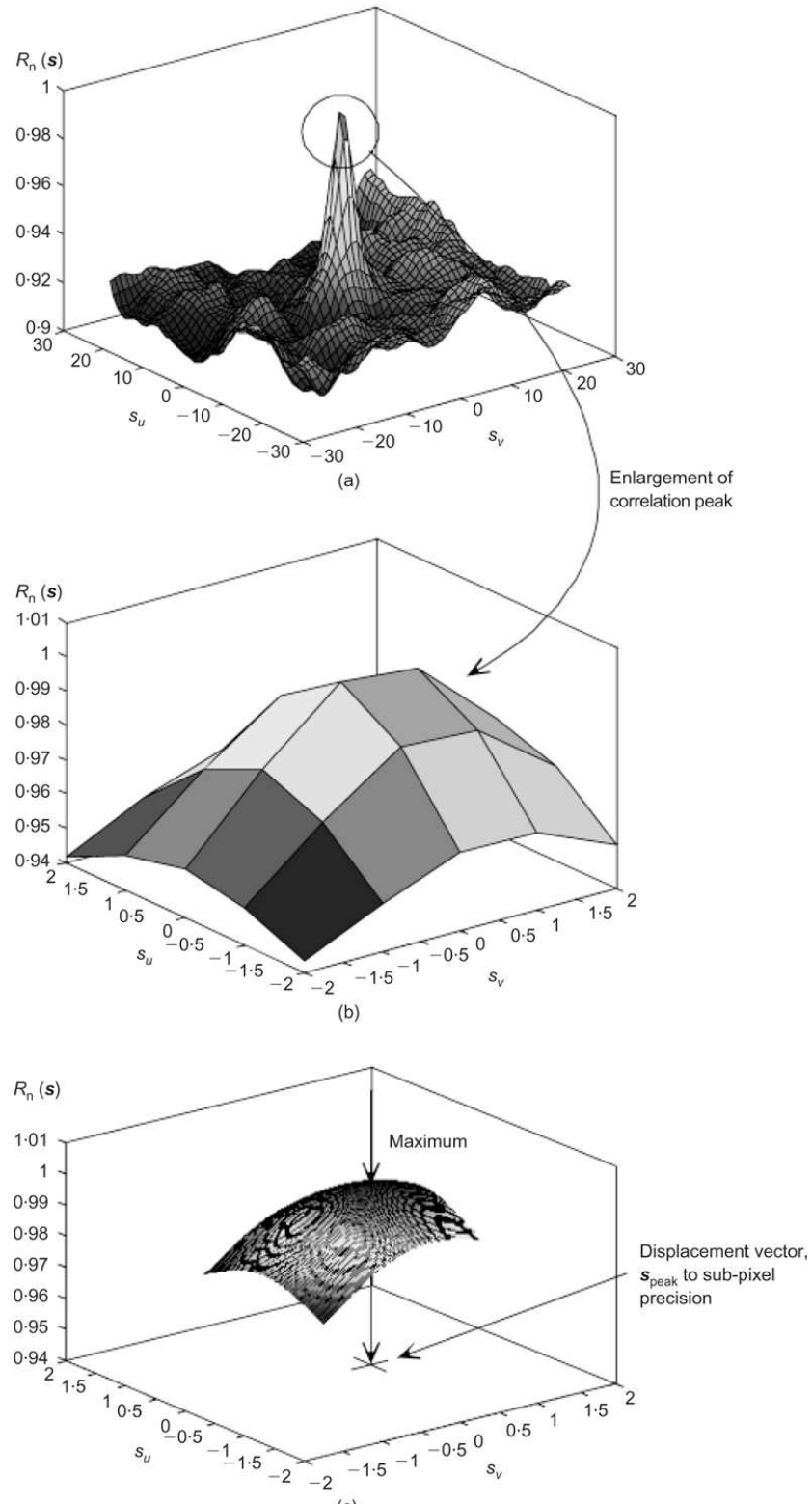


Figure 2.18: Correlation peak (a), enlarged correlation peak (b) and bi-cubic spline interpolation of cross correlation peak (c) to define spatial coordinates from White et al. (2003).

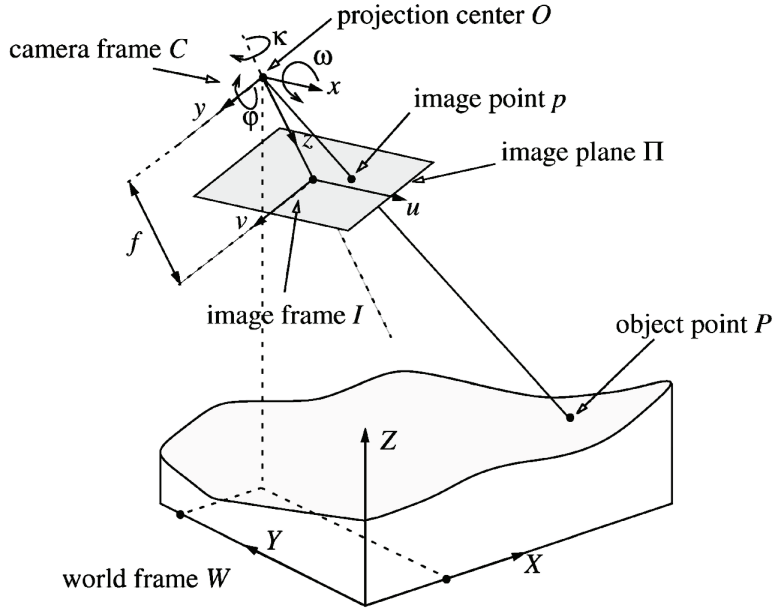


Figure 2.19: Pinhole camera model from Heikkilä (2000).

caused by translation and rotation of the camera, as illustrated by the pinhole camera model in Figure 2.19, which assumes a pure perspective projection through a perfect lens at the projection center O . Camera translation is defined in the pinhole camera model as the spatial difference between object space (X , Y and Z) and image space (x , y and z) and camera rotation is defined with Eulerian angles ω , φ and κ .

White (2002a) utilised the procedure for photogrammetric correction proposed by Heikkilä and Silvén (1997) to transform coordinates and displacements from image space to object space. This was achieved using a Matlab toolbox released by Heikkilä (2000a) to calculate parameters describing internal and external camera induced distortions. This process is known as camera calibration and in the method used by White (2002a), fourteen independent parameters need to be derived to describe the camera calibration. Target markers of known size and position are usually incorporated into the physical model to allow assessment of the success of photogrammetric correction. White (2002a) used target markers consisting of a black laser printed circle within a white square background between the Perspex and glass layers of the viewing window. A similar methodology was employed by Effendi (2007), except that white circular markers were used against a black background.

Refraction caused by the viewing window is another consideration when quantifying external distortions and has been investigated by both White (2002a) and Effendi (2007). The viewing window causes a scaling distortion caused by the differing Refractive Index (RI) of the viewing window compared to the surrounding atmosphere. Both investigations found that linear scaling based corrections could be applied. In the procedure used by White (2002a) this adds a further two parameters that require calibration. However, if the photogrammetric control points are situated on the back face of the viewing window, transformation from image space to object space coordinates is conducted after the influence of the viewing window. This negates the need for a correction to specifically deal with viewing window induced scaling errors.

The precision of a camera calibration procedure is unique to the model of camera used and its optical properties, the light conditions, the camera position and geometric properties of the apparatus. It is important therefore that photogrammetric correction be conducted for every specific physical modelling application.

2.3.5.5 System Accuracy and Precision

White (2002a) compared the normalised system accuracy and precision of his analysis procedure using GeoPIV and close range photogrammetry with previous studies, concluding that the new technique was superior. Over a field of view of 300mm by 200mm, with patch size of 50 x 50 pixels and control point size of 25 x 25 pixels, the quoted accuracy was $16.7\mu m$ with a precision of $4.6\mu m$. This is a significant improvement on any previous soil displacement measuring technique as it allows pre-failure strains to be quantified with vastly increased measurement point density and without introducing discrete markers into the soil model using the method proposed by Gill (1999).

2.3.6 Materials

Typically in physical models, a material is chosen due to its availability and knowledge of its geotechnical properties and uniformity. The uniformity of the material is particularly important since in physical modelling investigations it is usual to conduct a parametric study of the effects of altering a particular parameter in the model whether geometric (e.g. dimension) or material property (e.g. strength of soil).

To model coarse grained soils, sands such as Leighton Buzzard or Fontainebleau sand, have been used in physical models in laboratory research for more than 50 years and many publications are available that contain studies of their properties (White, 2002a). Similarly, to model fine grained soils, Speswhite kaolin clay is often used as this material is produced by the ceramics industry to a set specification, affording some confidence of repeatability. The properties of this material has been shown to be similar to those of many natural clays (Effendi, 2007).

The main drawback with laboratory sands and clays is the fact that the materials are opaque and it is only possible to model problems that are planar in nature or have a natural line of symmetry. Examples include plane strain pile installation (White, 2002a; White and Bolton, 2004), settlement interaction of neighbouring buildings in plane strain (Effendi, 2007), plane strain movement of buried pipelines (Cheuk et al., 2008) and punch through of Spudcan foundations in an axisymmetric half-space (Hossain and Randolph, 2009).

Relatively recent development of both granular and cohesive transparent synthetic soils has allowed the investigation of axisymmetric and three dimensional geotechnical problems. As in the application of PIV in fluid mechanics, a laser light sheet can be used to highlight a plane within the physical model of transparent material. The following section is dedicated to transparent synthetic soils, their inception, development and application to physical modelling.

2.4 Transparent Synthetic Soils

Transparent synthetic soil has been developed over the past twenty five years to allow the modelling of axisymmetric and three dimensional geotechnical problems. They are two phase continua containing an aggregate and a fluid component. Non-saturation causes a loss of transparency since the RI of air differs significantly from those of the constituent aggregates and fluids. Both coarse and fine grained soils can be modeled using transparent aggregates of different forms, mixed with a fluid of matched RI; typically a mineral oil or brine.

2.4.1 Coarse Grained Transparent Synthetic Soils

2.4.1.1 Crushed Glass

The first use of a transparent two phase continuum as a model for soil in the laboratory was that of Allersma (1982), where crushed borosilicate glass (RI of 1.469) was mixed with risella oil (RI of 1.475), which is a white oil. This was used to allow modelling of the stress and strain distributions caused by installation of a penetrometer, utilising the photoelastic properties of the glass for the former and photographic measurement techniques for the latter. The aggregates in this instance were either 1-2mm or 2-3mm in diameter and were created and sorted using custom built crushing and riddling machines.

One significant issue when using glass as a sand replacement material is the possibility for crushing, yet Allersma (1982) reports that, although during triaxial testing crushing sounds were heard, particle size distribution analysis suggested little crushing occurred. The density of the crushed material was $22.3kN/m^3$, which is similar to natural sand. However, the particle shape of the crushed glass is somewhat different, since natural sand grains are weathered over time and crushed glass is created almost instantaneously by the crushing process. To reduce the significance of this a screening process was used to remove extremely irregular shape fragments or shards. However, this apparent difference in particle shape may still have affected the shear behaviour, as triaxial data derived under an isotropic stress of $81kPa$ suggested the angle of friction (ϕ) of the crushed glass in a medium-dense sample was 33° and 40° for particle size ranges of 1-2mm and 2-3mm respectively. This was larger than that derived for fine gravel and sand in similar states in the same apparatus of 33° and 31° respectively.

The crushed glass soil used by Allersma (1982), proved to be no more than translucent due to the slightly differing RI's of the aggregate and fluid components. Allersma (1982) did note that other fluids with more closely matching RI, such as Sunflower oil (RI of 1.468), and Peanut oil (RI of 1.469) were available, yet unsuitable due to their chemical instability when exposed to air. More optically sensitive glass was also precluded from use, presumably due to a suitable fluid with matching RI not being available. This ultimately limited the use of the material to modelling problems in two dimensions in plane strain.

However, Konagai et al. (1992) were able to use a more optically sensitive glass to model the stability of a submerged slope exposed to seismic excitation and the penetration of a cylindrical penetrometer into a bed of the material in three dimensions. A mixture of tetralin oil (RI of 1.546-1.557) and turpentine oil (RI of 1.481-1.491) was used as the matched RI fluid. The RI of the fluids was measured over a range of temperatures and under various wavelengths of laser light, to allow for optical calibration of the mixture in an environment representative of the testing environment.

The optical glass chosen was Schott BK-7 (RI of 1.5194), as it was readily available and inexpensive. The glass was crushed in a mechanical jaw crusher. The improved transparency of the optical glass, coupled with careful matching of the RI of the fluid created a material capable of allowing measurements on a plane within a three dimensional problem. A laser light sheet highlights the surfaces of crushed glass particles in its path, since the crushing process used to prepare the glass optically strained the surface of the particles and it is this optical discrepancy that was highlighted. This technique is known as Laser Aided Tomography or LAT.

Figure 2.20 shows the experimental setup used by Konagai et al. (1992) and three cross sections of the embankment that were photographed. To indicate the scale of the model, the slope height was 200mm and the individual glass aggregates were 2-5mm in size. The authors also created a model to represent penetration of a cylindrical pile. In this instance the crushed glass was less than 1mm in size, and thus more representative of natural sands. However, with particles this small it was not possible to identify the outline of the individual aggregates and layers of fine glass powder were added to improve visualisation of movements. At the time of writing, the authors had no access to PIV techniques so the results of its application on LAT derived images of crushed glass particles is unknown.

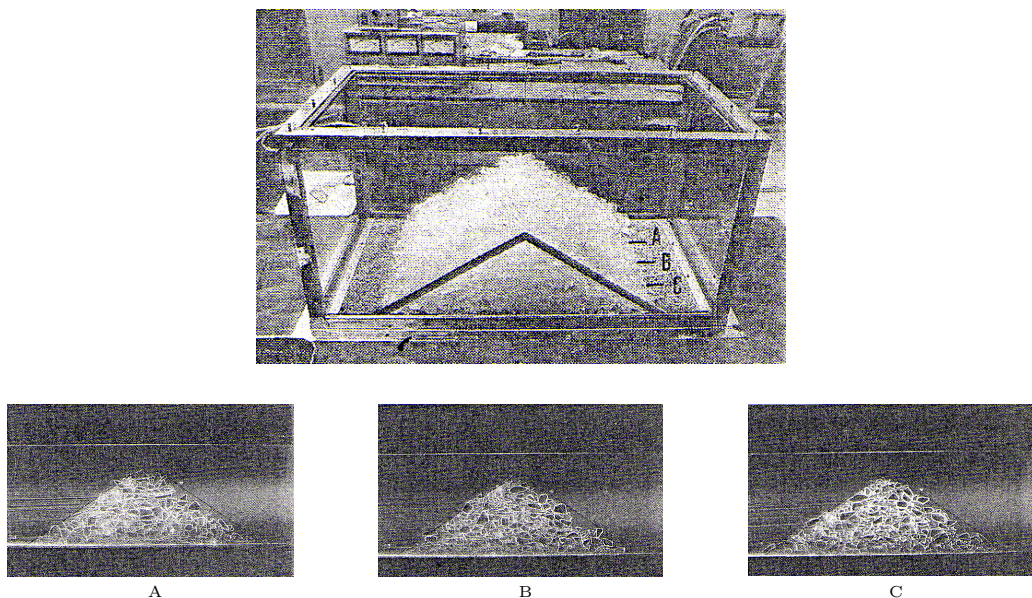


Figure 2.20: Physical modelling of a submerged embankment under seismic loading using crushed glass, a matched RI pore fluid and LAT, from Konagai et al. (1992).

2.4.1.2 Silica Gel

Silica gel in both rounded and angular forms (see Figure 2.21) has been investigated as a transparent analogue for sand in physical models (Sadek et al., 2002; Iskander et al., 2002a; Iskander et al., 2002b; Liu et al., 2002; Iskander et al., 2003). Two sizes of aggregates were investigated with particle diameter ranges of 0.5-1.5mm and 2.0-5.0mm. The specific gravity was 2.2 (around 80% of that of natural sands). They were thus, representative of medium and coarse sands respectively.

In these previous studies the matched RI fluid was typically a mixture of mineral oil and a paraffinic solvent, blended to have a RI of 1.447 at 25°C, although experimentation with a brine solution with a RI of 1.448 at 25°C was also mentioned.

Silica gel is a colloidal form of silica such that silica gel aggregates are made up of an array of micro particles with size of the order of $0.02\mu m$. The size of these micro-particles enables a transparent continuum to be formed when silica gels are saturated in a matched RI fluid, since the micro particles are smaller than the wavelength of light (Iskander et al., 1994). Also the voids between them are hygroscopic and thus encourage saturation of the voids with the fluid. After mixing, the transparent synthetic soil was de-aired under vacuum to maximise transparency.



Figure 2.21: Fine angular and coarse rounded silica gels used by Sadek et al. (2002) to model sands, with particle diameters of 0.5–1.5mm and 0.2–0.5mm respectively.

Table 2.3: Shear strength of fine angular and coarse rounded silica gels, after Sadek et al. (2002).

Silica Gel	Particle Size Range (mm)	Angle of Friction (ϕ)	
		Triaxial Compression	Direct Shear
Fine Angular	0.5 – 1.5	29 – 36°	32 – 46°
Coarse Rounded	2.0 – 5.0	31 – 42°	37 – 52°

Table 2.4: Stiffness of loose and dense, fine angular and coarse rounded silica gels, after Sadek et al. (2002).

Silica Gel	Particle Size Range (mm)	Stiffness (MPa)		Confining Pressure (kPa)
		Loose	Dense	
Fine Angular	0.5 – 1.5	15 – 22	26 – 32	70 – 420
Coarse Rounded	2.0 – 5.0	24 – 52	36 – 84	70 – 420

Triaxial compression and direct shear tests were conducted to attain the angle of friction and stiffness of the silica gel, yielding the results shown in Tables 2.3 and 2.4, which appear consistent with those of natural sands. The stress-strain behaviour exhibited post-peak softening for dense samples and the residual strength tended to that of the loose samples for both silica gel types. Peak strength occurred at higher strain than in natural sands, owing to the high compressibility of the silica gel. This was acutely evident for the fine angular silica gel.

Figure 2.22 shows that the fine angular silica gel was far more compressible than natural sands, whereas coarse rounded silica gel compressibility is more consistent with the behaviour of natural sands. This may be a significant drawback for fine silica gel based transparent soils. However, utilising coarse materials in a physical model at reduced scale may induce particle size effects due to the discrepancy in scale. Also, using perfectly rounded particles is not ideal, since no natural sand is perfectly rounded. Furthermore, Sadek et al. (2002) report that particle breakage could be heard during triaxial compression tests at high normal pressures. This was confirmed by Iskander et al. (2002a) as grain size distribution plots before and after triaxial compression tests indicated that significant particle breakage had occurred. This phenomenon is another consideration when assessing silica gel's suitability for the representation of sand in a geotechnical model, although particle breakage also occurs in natural sands (Yasufuku and Hyde, 1995).

In later research silica gel was used to model a number of geotechnical phenomena using PIV (or Digital Image Correlation or DIC) and LAT. Pile penetration was investigated by Iskander et al. (2002a). Settlement of square and round footings was reported by Liu et al. (2002). Liu and Iskander (2010) presented comparisons of displacement fields measured using PIV in silica gel transparent soil and natural sand, indicating that the results were similar. Ahmed and Iskander (2010) used silica gel transparent soil to investigate tunnelling induced settlements. The PIV analysis is apparently able to track movement of the silica gel due to the interaction between the laser light and silica gel which appears to produce a distinctive speckle pattern.

Figure 2.23 shows displacement and vertical strain fields induced by volume loss of an open faced tunnel in silica gel transparent soil, computed using PIV by Ahmed and Iskander (2010). These results were derived from images of an internal section of the model, highlighted by a 0.035W laser. The model comprised of a 25.4mm diameter

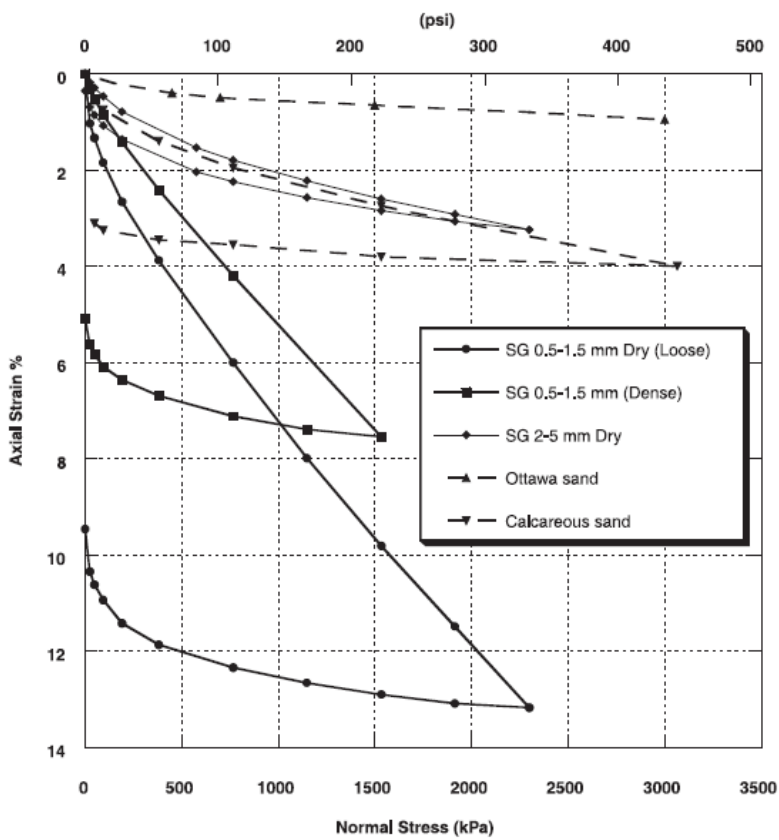


Figure 2.22: Compressibility of fine angular and coarse rounded silica from Sadek et al. (2002).

PVC tunnel, inside a bed of silica gel transparent soil with width of 254mm, depth of 304.8mm and height of 203.2mm (camera perspective). The quoted measurement accuracy was 0.01mm. The depth of cover from the front of the test chamber to the open face of the tunnel was not stated. However, the work demonstrates that relatively large models can be created, allowing non-intrusive measurement of displacements within a body of soil. This potentially allows the investigation of many 3D problems.

A major advantage of the silica gels is their extremely close chemical formulation to powdered variants of silica, such as amorphous and fumed amorphous silica. These alternative aggregates can be used to model fine grained soils. The fact that both silica gel and powdered forms of silica are chemically identical means they have the same RI. This potentially allows layered samples to be created. The following sections will review in further depth fine grained transparent synthetic soils and their development.

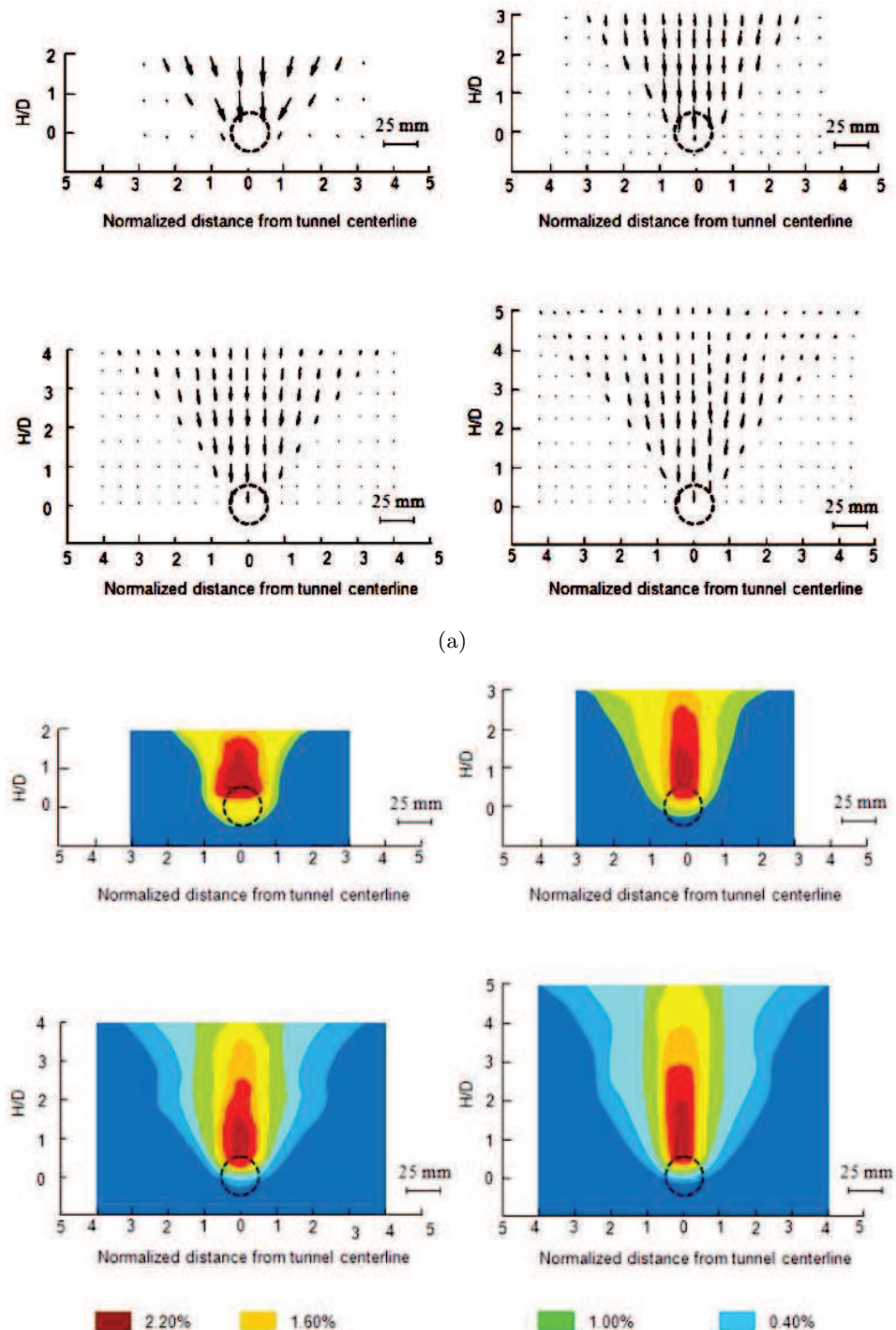


Figure 2.23: Displacement fields (a) and vertical strains (b) above open faced tunnels with various depths of cover from Ahmed and Iskander (2010).

2.4.2 Fine Grained Transparent Synthetic Soils

2.4.2.1 Precipitated Amorphous Silica

Precipitated amorphous silica was the first silicate material to be utilised as an aggregate in a transparent synthetic soil and the properties of the combination of precipitated amorphous silica and matched RI mineral oils and brine has been researched extensively (Iskander et al., 1994; Iskander et al., 2002; Sadek et al., 2002; Liu et al., 2003). The precipitated amorphous silica materials investigated in these studies were sourced from PPG Industries and Table 2.5 contains a summary of their product names and physical properties. One of the major advantages of using silicates as aggregates to create transparent soil is the size of the micro particles which make up the individual aggregates. Figure 2.24 is a Transmission Electron Microscope (TEM) image of Flo-Gard SP (FGSP) showing the composition of the $25\mu\text{m}$ aggregates with micro particles approximately $0.02\mu\text{m}$ in size.

Table 2.5: Physical properties of precipitated amorphous silicas from PPG Industries from Iskander et al. (2002a).

Material	Median aggregate size (μm)	Surface area (m^2/g)	Oil absorption ($\text{mL}/100 \text{ g}$)	Specific gravity	Bulk density (kg/m^3)
Hi-Sil T600 (HST600)	1.4	150	150	2.1	56
Flo-Gard FF (FGFF)	10	180	210	2.0	128
Flo-Gard SP (FGSP)	25	220	260	2.0	144
Hi-Sil SC-72 (SC72)	175	150	200–350	2.0	230

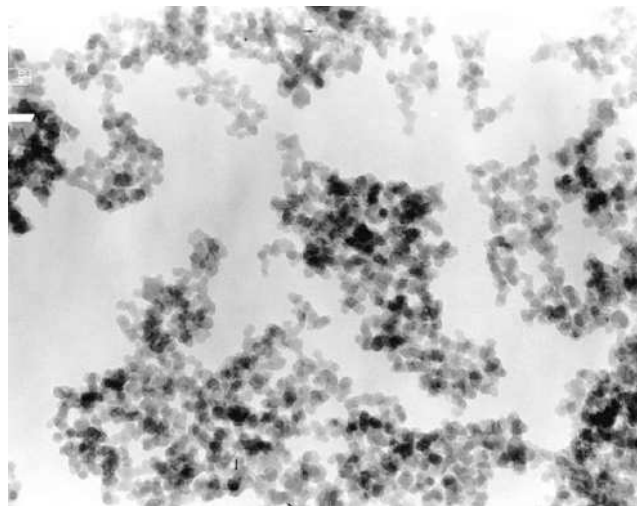


Figure 2.24: Transmission Electron Microscope (TEM) image of FGSP precipitated amorphous silica showing aggregates and micro particles from Sadek et al. (2002).

Samples are created by mixing the precipitated amorphous silica powder with the matched RI fluid at concentrations by mass ranging from 9-20% (with lesser concentrations being used for finer grades of precipitated amorphous silica to preserve workability), before de-airing the mixture in a vacuum and consolidating in a one dimensional consolidometer.

Consolidation of precipitated amorphous silica was studied by Iskander et al. (1994) in the oedometer to pressures in the range of 70-1500 kPa. Significant secondary consolidation was apparent when compared with predictions made using Terzaghi's conventional theory of consolidation as shown in Figure 2.25. Iskander et al. (1994) suggest that primary consolidation in precipitated amorphous silica transparent soils is due to volume change within the voids of the material and secondary consolidation is due to volume change within the aggregates. The compression indices derived are higher than may be expected for natural clays due to this high component of secondary consolidation, but comparisons with consolidation properties for natural clays were generally favourable (Iskander et al., 1994; Iskander et al., 2002a; Sadek et al., 2002; Liu et al., 2003). The coefficient of consolidation c_v was found to be in the range of 3.15-6.31 m²/year, which is similar to typical values for natural clays (Iskander et al., 1994).

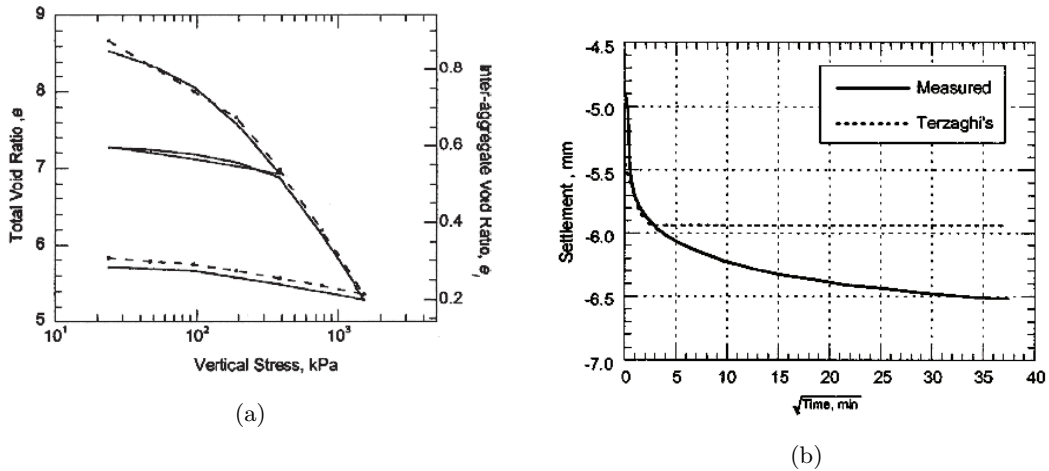


Figure 2.25: Consolidation of FGSP precipitated amorphous silica showing repeatability (a) and components of primary and secondary consolidation (b) when compared with Terzaghi's conventional theory of consolidation, from Liu et al. (2003).

Iskander et al. (1994) conducted a set of consolidated undrained and drained triaxial tests on precipitated amorphous silica transparent soils and Figure 2.26 shows

the stress-strain and volume change relationships for these tests. The behaviour observed is similar to that of natural clays except that the axial and volumetric strains are perhaps larger than would be expected for a natural clay. This was attributed to the large oil volume present within the aggregates affording them high compressibility.

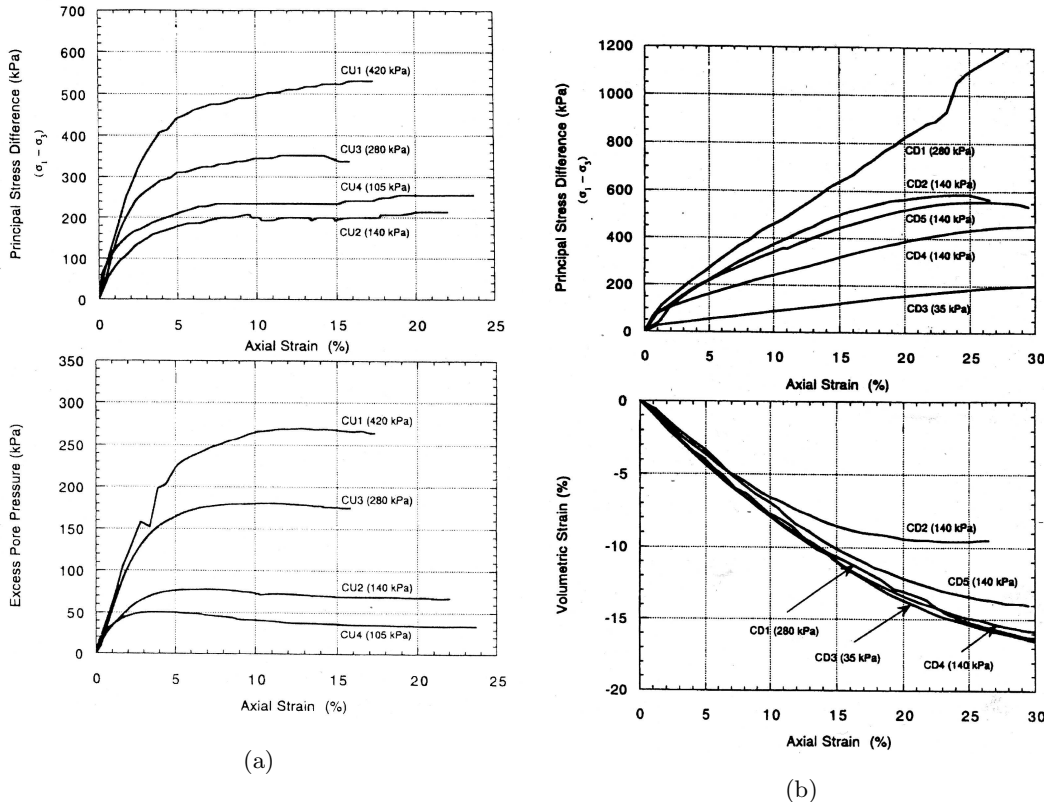


Figure 2.26: Stress-strain and volume change relationships for precipitated amorphous silica from consolidated undrained (a) and drained (b) triaxial tests, from Iskander et al. (1994).

Over consolidated undrained triaxial tests were performed by Iskander et al. (2002a) and illustrated that precipitated amorphous silica exhibited similar strain softening with increasing OCR, as is observed in natural clays. Normalised strength and pore pressure behaviour was also shown to be similar to natural clays, suggesting that this material may be suitable for physical modelling in the laboratory. More detailed analysis of the shear strength of precipitated amorphous silica transparent synthetic soils is presented in Iskander et al. (2002a) and Sadek et al. (2002).

An important consideration when assessing the suitability of a material to model clay in a physical model is its permeability. When creating a physical model using a fine grained soil, a slurry mixture is usually consolidated to create the clay bed, and the permeability of the consolidated material will affect the rate at which consolidation can occur. As can be seen in Figure 2.27 the finer precipitated amorphous silica, Hi-Sil T600 or HST600 ($1.6\mu m$) has far lower permeability for a given consolidation pressure than the coarser Flo-Gard SP or FGSP ($25\mu m$), and thus would take longer to consolidate in the laboratory to a given strength. An in depth investigation of the consolidation and permeability of precipitated amorphous silica is presented by Liu et al. (2003).

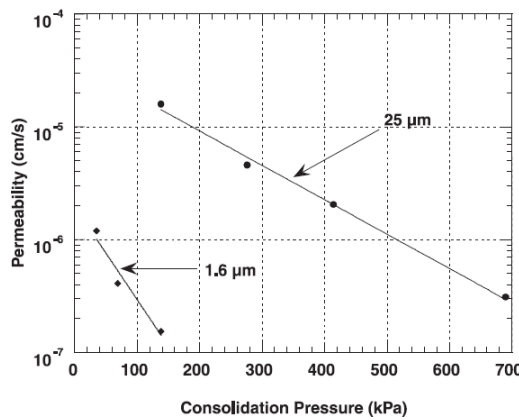


Figure 2.27: Permeability of FGSP ($25\mu m$) and HST600 ($1.6\mu m$) amorphous silicas with consolidation pressure from Sadek et al. (2002).

Precipitated amorphous silica based transparent synthetic soils have been used by a number of researchers, including investigations into: the flow into a Prefabricated Vertical Drain or PVD (Welker et al., 1999), deformations below pad footings (Liu et al., 2002), the shear vane test (Stanier, 2006), three dimensional imaging of particle motion during penetrometer testing (Toiya et al., 2007), displacements around continuous augers in clay (Hird et al., 2008) and displacement and strain fields induced by driven pile installation (Ni et al., 2010). This latter research represents the current state of the art using precipitated amorphous silica based transparent soil to model deformations non-intrusively using digital imaging and PIV analysis techniques. Titanium oxide coated mica seeding particles, which are highly reflective, were added to the rearward half of the model to provide texture, thus enhancing the ability of PIV to measure soil displacements. Figures 2.28 and 2.29 present displacement fields measured using PIV and comparison with displacement fields predicted

by the Shallow Strain Path Method (SSPM) of Sagaseta et al. (1997).

Figure 2.30 provides a comparison of the octahedral shear strains measured within the transparent soil using PIV, compared to those predicted by the SSPM theory. These studies demonstrate one of the major advantages of using transparent soils to perform non-intrusive measurements within a body of soil, as they allow insight into the behaviour of soil around rotating objects such as CFA piles, which would not be possible against a window in plane strain or half-space axisymmetry.

Hird et al. (2008) utilised a physical model 100mm by 100mm in size on plan view, with a depth of approximately 200mm comprising HST600 precipitated amorphous silica and a matched RI pore fluid. Considering an auger with flight diameter of 20mm was used, boundary effects may have been significant since the minimum boundary distance was only $4R$ (see Section 2.3.4). It was not possible to enlarge the models due to a significant degradation of transparency at a larger scale. This highlights one of the main limitations of the material: its limited transparency. Iskander et al. (1994) stated that precipitated amorphous silica based transparent synthetic soils were “truly transparent, not merely translucent” yet in the above research sufficient transparency was only achieved in very small physical models in both studies. More accurate matching of the RI of the pore fluid and improved temperature control within the laboratory may lead to improvements in the transparency of larger samples.

2.4.2.2 Fumed Amorphous Silica

Gill (1999) created a fine grained transparent soil using fumed amorphous silica supplied by Sigma, as opposed to precipitated amorphous silica. This transparent soil, referred to as Trinity College Dublin or TCD soil, was then used to investigate the deformations and strains caused by installation of a penetrometer in clay (see Figure 2.16). The particles that constitute fumed amorphous silica differ from precipitated amorphous silica in the way in which they are created. Fumed amorphous silica is formed at high temperatures and recovered by condensing the silica from the gaseous phase as a fine powder, whereas the precipitated amorphous silica described in Section 2.4.2.1 is precipitated in an aqueous solution as the silica micro particles coagulate allowing it to be recovered, washed and dried. An investigation into the performance of vibro-stone reinforced columns in clays by McKelvey (2002) used fumed amorphous silica similar to that of Gill (1999). Physical properties typical of

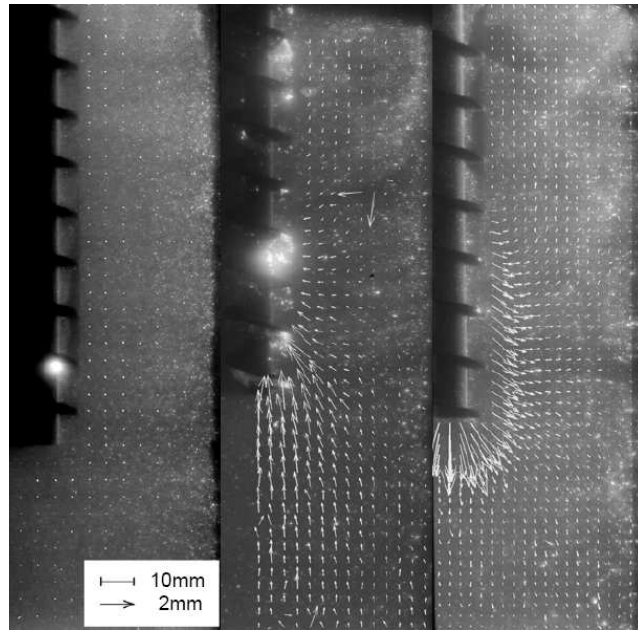


Figure 2.28: Displacements around a CFA pile during (from left to right) neutral, over-rotating and under-rotating installation rates, from Hird et al. (2008).

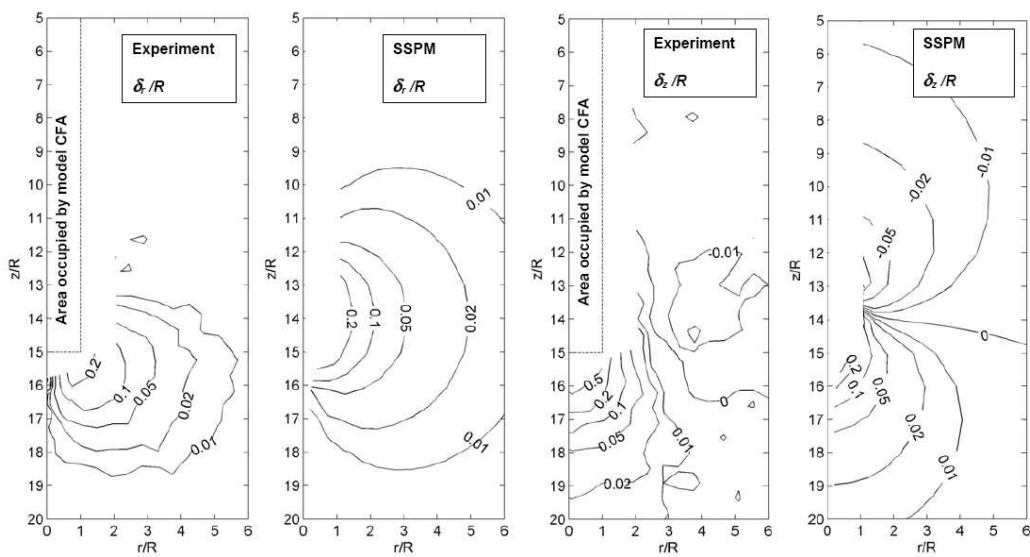


Figure 2.29: Comparison of horizontal and vertical displacements during under-rotating continuous flight augering in transparent synthetic soil with SSPM predictions, from Hird et al. (2008).

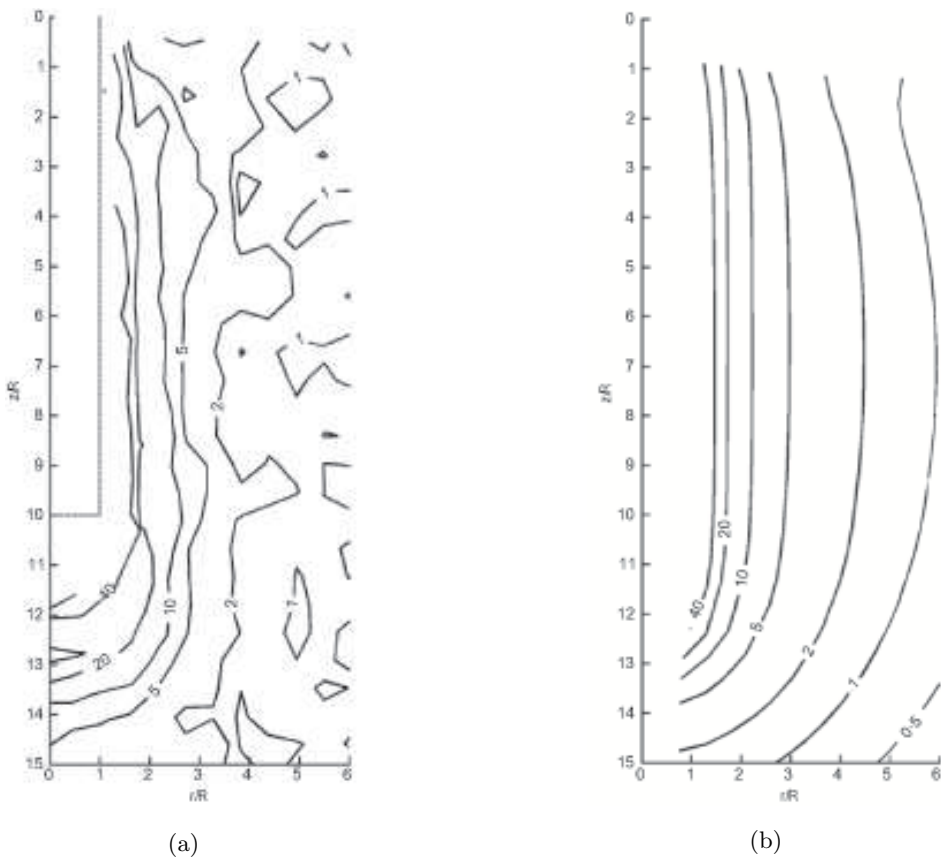


Figure 2.30: Comparison of octahedral shear strains caused by driven pile installation (a) and predicted by SSPM theory (b), from Ni et al. (2010).

fumed amorphous silica are presented in Table 2.6.

The particle size quoted is for that of the micro particles that form the aggregates and is not directly comparable with the particle sizes for the precipitated amorphous silicas in Table 2.5. Gill (1999) examined the fumed amorphous silica aggregates using an electron microscope, finding that the aggregates were approximately $0.08\text{-}0.35\mu\text{m}$ in diameter after consolidation to 225kPa . The micro structure apparently differed to that of natural clays in that the particles were predominantly spherical, whereas in a natural clay the particles are usually ‘plate-like’.

The matched RI fluid used by both Gill (1999) and McKelvey (2002) was composed of a mixture of crystal light liquid paraffin and mineral spirits in a ratio of 70:30. Transparency was assessed by placing beakers of slurries with different mixes of pore fluid over a fine target grid and qualitatively assessing the clarity of the grid at room temperature. The fumed amorphous silica transparent synthetic soil used in both

Table 2.6: Bulk properties of fumed amorphous silica used by Gill (1999) and McKelvey (2002).

Property	Fumed Amorphous Silica
Bulk Density (kg/m^3)	36.8
Particle Density (kg/m^3)	2200
Refractive Index (RI)	1.46
Particle Size (μm)	0.014
Surface Area (m^2/g)	200 ± 25

the aforementioned studies was mixed and consolidated using similar methods as for precipitated amorphous silica based materials as documented in Section 2.4.2.1. However, due to the smaller particle size Gill (1999) found that the concentration of fumed amorphous silica to fluid should be no more than 7% by mass to preserve workability and to allow successful de-airing.

Consolidation properties were investigated by Gill (1999) in a 60mm square shear box, prior to shearing and by McKelvey (2002) using a 150mm Rowe Cell, with both series of testing producing similar results for consolidation over the range of 25-250kPa. The coefficient of consolidation c_v was found to be in the range of 0.24-1.65m²/year, which was found to be consistent with that of normally consolidated alluvial clays. The coefficient of compressibility m_v was found to be in the range of 1.18-5.4m²/MN which is typical of a range for normally consolidated alluvial clays (0.3-1.5m²/MN), very organic alluvial clays and peat (>1.5m²/MN). The compression index C_c was found to be in the range of 5.4-7.0 by Gill (1999) which would be considered very high for a natural clay. Of greater significance is the over consolidated behaviour investigated by Gill (1999) using a sample consolidated to 200kPa and then tested at an effective stress of 25kPa giving an OCR of 8, since soil in physical models tested at 1g is usually in an over consolidated state. The values of c_v (0.93m²/year), m_v (0.42m²/MN) and compression index C_c (0.34) were consistent with values expected for soft clays.

The shear strength of fumed amorphous silica transparent soil has been investigated using direct shear, triaxial compression and hand vane shear tests (Gill, 1999), and triaxial compression and Geonor cone penetrometer tests (McKelvey, 2002). Direct shear tests conducted by Gill (1999) indicated that the soil exhibited an effective angle of friction of 37° at peak and 31° post rupture, which is similar to soft normally consolidated or lightly over consolidated natural clays. Undrained behaviour was

investigated by Gill (1999) using the hand vane at various depths within the model bed and triaxial compression tests using samples taken from the top 100mm of the physical model post-testing. These tests yielded hand vane shear strengths in the range of 19.5-30kPa and UU triaxial shear strengths in the range of 38.1-44.5kPa. These strengths at a consolidation pressure of 200kPa, were thought by Gill (1999) to be rather high due to the low plasticity of the silica particles. McKelvey (2002) conducted UU triaxial compression tests on samples taken from the Rowe Cell, after consolidation to pressures in the range of 75-150kPa. A series of Geonor cone penetrometer tests were also conducted to estimate the undrained shear strength. Figure 2.31 is a plot of the undrained shear strength derived from both tests compared to the shear strength of kaolin. This shows that the undrained shear strength changes fairly linearly with consolidation pressure. The undrained shear strength of fumed amorphous silica transparent soil is similar to that of kaolin in its response to consolidation pressure.

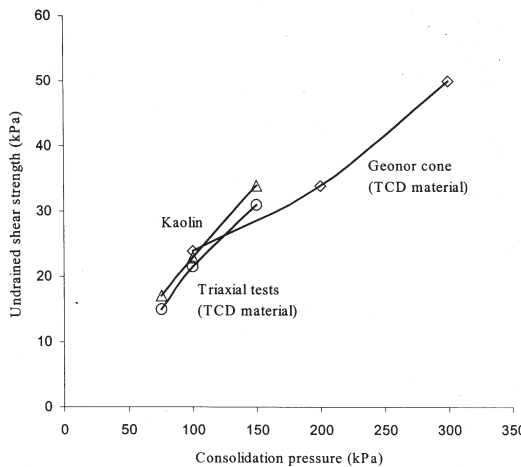


Figure 2.31: Undrained shear strength of fumed amorphous silica transparent soil with consolidation pressure, from McKelvey (2002).

Due to the smaller micro particle size of fumed amorphous silica compared to precipitated amorphous silica, the post-consolidation permeability of fumed amorphous silica transparent soil is less than that of the precipitated amorphous silica transparent soil. This is illustrated by the plot of hydraulic conductivity k in Figure 2.32. This suggests that there is a direct link between the aggregate size and the permeability with increasing consolidation pressure. Since the permeability is much lower in the material used by Gill (1999) compared to that investigated by Iskander et al. (1994), more time would be required to fully consolidate a sample to a given

consolidation pressure with fumed amorphous silica aggregates than precipitated amorphous silica aggregates.

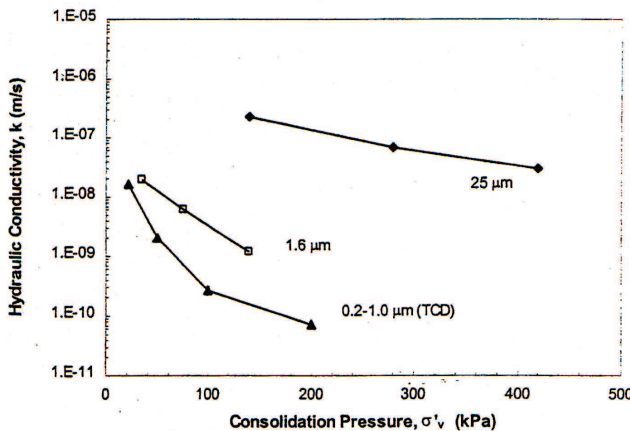


Figure 2.32: Permeability of TCD transparent synthetic soil with consolidation pressure compared with FGSP ($25\mu m$) and HST600 ($1.6\mu m$) precipitated amorphous silica based transparent synthetic soils from Gill (1999).

A limitation of precipitated amorphous silica transparent soil was the imperfect transparency which restrains the size of physical models that can utilise the material. The fumed amorphous silica based transparent synthetic soil used by Gill (1999) and McKelvey (2002) was used in physical models of larger geometry. The chamber utilised by Gill (1999) was 160mm by 280mm in size on plan and 775mm deep allowing a consolidated sample depth of up to 400mm. The 12mm diameter penetrometer was installed at the centre of the chamber. Thus the penetrometer was viewed through a minimum depth of soil of 74mm. This is a significantly larger viewing depth than achieved using precipitated amorphous silica transparent soil (Hird et al., 2008; Ni et al., 2010) and thus boundary effects should be reduced. In this instance the minimum boundary distance was $12.33R$.

McKelvey (2002) conducted physical modelling of vibro stone columns at an altogether larger scale in a chamber with a diameter of 413mm and vibro stone column reinforced zone with a diameter of 150mm, giving a minimum viewing depth of 131.5mm. However, no digital image based analyses were conducted on images recorded of the deformation process, so it is not clear whether the soil would be sufficiently transparent at this scale to allow tracking of soil movements. Figure 2.33 contains two sets of images from the testing conducted by Gill (1999) and McKelvey

(2002), which illustrate the achievable transparency at larger scale. Further publications on the use of fumed amorphous silica transparent soil include Gill and Lehane (2001), Lehane and Gill (2004), McKelvey et al. (2004) and Song et al. (2010).

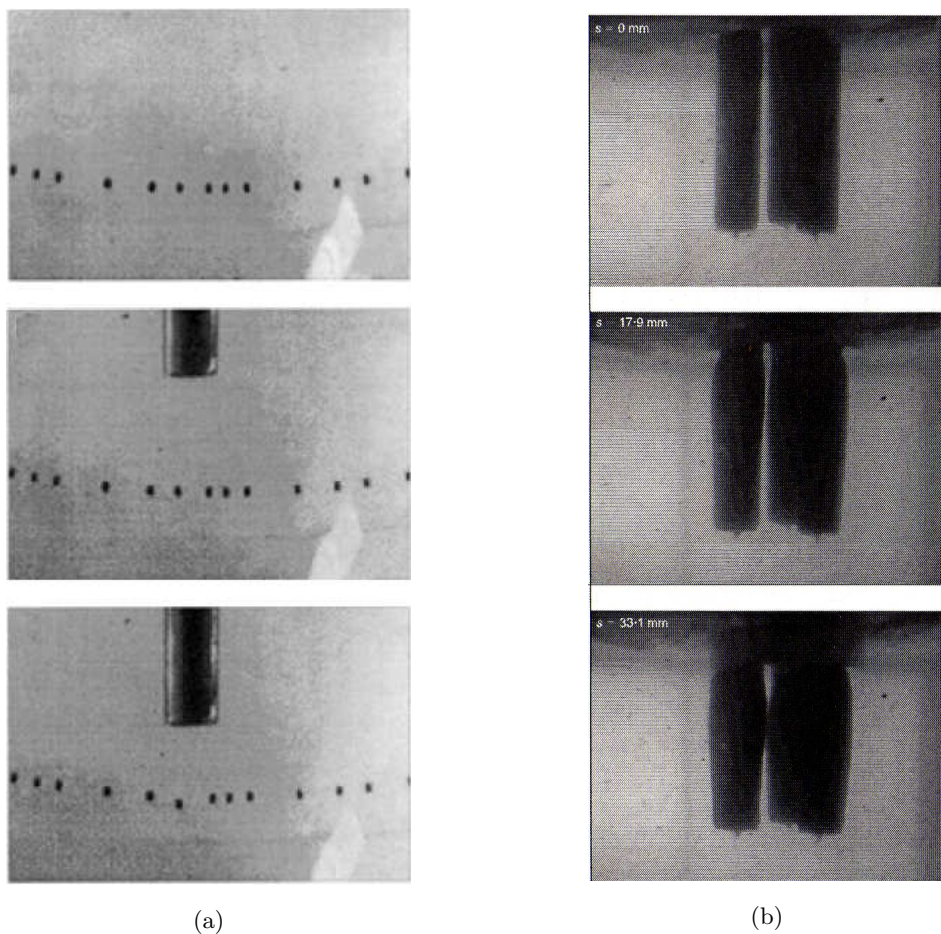


Figure 2.33: Images from investigations conducted by (a) Gill and Lehane (2001) and (b) McKelvey et al. (2004).

2.5 Potential for Further Research

The previous studies outlined here highlight a number of areas with scope for further research. Investigation into helical screw pile failure mechanisms is perhaps the most important area requiring further research, since all methods of capacity estimation currently rely upon correctly assuming the failure mechanism. In the field most helical screw piles are deeply embedded, so the behaviour of helical screw piles installed to deep depths is of primary interest. Utilisation of PIV and transparent soils can now allow the non-intrusive investigation of both the installation induced disturbance and the failure mechanisms of helical screw piles of varying geometry. The transparent soil material with the greatest potential in relation to model size is fumed amorphous silica based transparent soil, which can be used to model fine grained soils such as soft clays. Therefore in summary, the following investigation is focussed on the following objectives:

1. Develop fine grained transparent soil to allow modelling of geotechnical problems at an adequate scale to allow PIV measurements of soil displacements.
 - Investigate:
 - Transparency and model size achievable using precipitated and fumed amorphous silica aggregates.
2. Conduct physical modelling of deeply embedded helical screw pile installation induced disturbance in fine grained soil.
 - Investigate:
 - Installation induced disturbance caused by various geometries of helical screw pile using PIV.
3. Conduct physical modelling of the performance and failure mechanisms of deeply embedded helical screw piles in fine grained soil.
 - Investigate:
 - Single helical screw pile behaviour.
 - The affect of the number of helical plates.
 - The affect of s/D on performance.
 - The importance of L_a in respect to capacity.
 - The similarity of compressive and tensile behaviour.

- Failure mechanisms of various geometries of helical screw pile using PIV.
4. Assess similarity of the performance and failure mechanisms of helical screw piles with small strain FE simulations of the experiments.
- Investigate:
 - The ability of the small strain FE simulations to predict the behaviour observed in the physical models.
 - The sensitivity of FE simulations.
5. Assess the validity of existing analytical capacity prediction methods based on the observations made from the physical modelling and accompanying FE simulations.
- Investigate:
 - The validity of the assumptions made by existing analytical capacity prediction methods using PIV derived measurements.
 - Comparison of the ULS capacity predicted by simple analytical methods and observed in the physical models.
 - Potential strategies for safe prediction of the ultimate capacity of helical screw piles in practice.
6. Assess the application of different design methodologies for use in practice to estimate design loads for helical screw piles using simple calculation models.
- Investigate:
 - Traditional ‘permissible stress’ design approaches.
 - Other simple alternative design approaches suitable specifically for helical screw pile design.
 - Eurocode 7 partial factor based design methods.

Chapter 3

Laboratory Schemes

3.1 Introduction

The following chapter first concerns the development of a fine grained transparent synthetic soil, allowing increased model size in conjunction with non-intrusive PIV measurements compared to those most recently reported (Hird et al., 2008; Ni et al., 2010).

An overview of pre-existent equipment and further development to meet the needs of the proposed investigation is then presented including: discussion of the design of the test chamber, consolidation apparatus, LAT apparatus, pile driving apparatus, model helical screw piles, measurement devices and data acquisition devices. Calibrations for all the aforementioned equipment are also documented where applicable.

Next, sample preparation procedures are reported and consolidation derived material parameters are compared to those reported in the literature for transparent soils (Gill, 1999; McKelvey, 2002). Lastly the test procedure adopted is described.

3.2 Transparent Soil Development

Hird et al. (2008) and Ni et al. (2010) reported physical modelling of CFA pile installation and driven-pile penetration in precipitated amorphous silica transparent soil, concluding that model size was restricted by the limited transparency of the soil. To allow PIV measurements of soil movements to be captured between the helical plates of small model helical screw piles, the maximum size of model achievable required improvement if boundary effects were to be minimised.

Gill (1999) and McKelvey (2002) reported the use of fumed amorphous silica aggregates in transparent soil in much larger models than those reported using precipitated amorphous silica aggregates. As a result a sample of the material used by McKelvey (2002) was sourced from the Queen's University, Belfast, to allow comparison of the transparency achievable with the two forms of silica aggregate.

3.2.1 Methodology

To assess the transparency of the fumed and amorphous silica based transparent soils, a simple qualitative assessment method was developed. The test card shown in Figure 3.1, consisting of a random selection of Times New Roman characters in a range of font sizes, was used to determine the minimum visible font size when viewed through a sample of de-aired transparent soil slurry.

The test card was viewed in two directions through a Perspex enclosure with internal dimensions of 50mm and 150mm on plan. The thickness of the Perspex was 10mm, therefore, the text was viewed through two 10mm layers of Perspex and either 50mm or 150mm of transparent soil. The qualitative assessment process is illustrated in Figure 3.2. The test was conducted for a range of pore fluid compositions with constant aggregate content for each material at 20°C. Smaller visible font size indicated improved transparency.

The aggregate content used in the calibrations was 6% by mass, as this allowed for relatively fast de-airing of the slurry mixture after thorough stirring to ensure homogeneity. This is less than the proportion reported by Ni et al. (2010) of 9%, however, the reduction was necessary to allow full de-airing of the mixtures in a reasonable time period in a vacuum chamber. As pore fluid oil constituents were added to the

Test Card Example	Point Size
54521	72
21036	48
27147	36
78828	28
61638	26
20728	24
87650	22
88776	20
46302	18
73101	16
64458	14
43376	12
34241	10
11620	9
82747	8
77218	7
58538	6
24735	5
32414	4
13598	3
40112	2
—	1

Figure 3.1: Test card used to qualitatively assess transparency of transparent synthetic soils (not to scale).

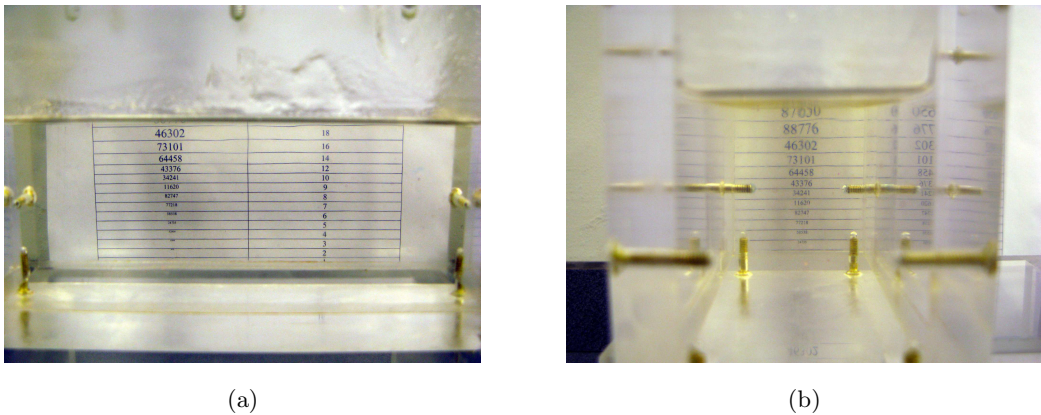


Figure 3.2: View of test card during transparency test through (a) 50mm and (b) 150mm depths of transparent soil slurry.

composition to change the RI, a proportion of additional aggregate was added to maintain the percentage content during the transparency assessment process. After every addition of oil and aggregate the composition was mixed thoroughly and de-aired before assessment.

3.2.2 Precipitated Amorphous Silica

The precipitated amorphous silica aggregate used was the same as the aggregate used by Hird et al. (2008) and Ni et al. (2010). The matched RI pore fluid was blended from two mineral oils: Technical White Oil ISO 15 and N-Paraffin C10-C13, both of which were supplied by Aztec Oils, Chesterfield, UK. The results of the transparency assessment are presented in Figure 3.3. The optimum paraffin content was found to be 43% of the pore fluid. The minimum visible font size was 3 when the test card was viewed through a 150mm depth of transparent soil. This is similar to the result reported by Ni et al. (2010) (font size equal to 4) using the same test methodology when viewed through a 110mm depth of transparent soil slurry with 9% silica content. Therefore, the transparent soil assessed here is at least as transparent as that previously reported in the literature for precipitated amorphous silica transparent soil.

3.2.3 Fumed Amorphous Silica

The fumed amorphous silica aggregate used was similar to that used by Gill (1999) and McKelvey (2002). The matched RI pore fluid was blended from two mineral oils: Baylube WOM 15 supplied by Bayford Oils, Leeds UK and N-Paraffin C10-C13 supplied by Aztec Oils, Chesterfield, UK. The decision to change one of the oils from

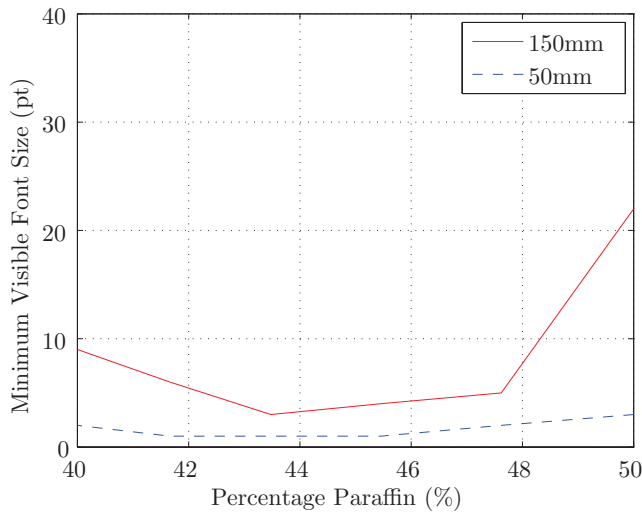


Figure 3.3: Transparency of HST600 precipitated amorphous silica transparent soil through 50mm and 150mm depths of material.

Technical White Oil ISO 15 to Baylube WOM 15 was due to the improved clarity of the latter oil. Therefore the transparency assessment presented here is a comparison of the optimum transparency attainable using the formulation of transparent soil used by Hird et al. (2008) and Ni et al. (2010) and the new formulation using fumed amorphous silica aggregates and a different composition of pore fluid. The results of the transparency assessment are presented in Figure 3.4 and indicate a slightly improved transparency as the minimum visible font size clearly visible through 150mm of slurry was 2. The optimum paraffin content was found to be 23% of the pore fluid.

3.2.4 Consolidated Transparency

Comparison of the transparency assessments in Figures 3.3 and 3.4 indicates that it is difficult to assess the difference in the potential model size achievable using such a method. The qualitative assessment method is therefore best suited to being used to check material quality before the pouring of the slurry in preparation for the commencement of consolidation. Therefore, to provide a more direct appraisal of soil transparency, consolidated samples were formed in a test chamber with plan internal dimensions of 200mm by 200mm (described in greater detail in Section 3.3.1). The consolidation process causes any deficiency in transparency to be exacerbated. Hence assessment of the transparency of a consolidated sample provides a better indicator of sample optical quality.

3.2 Transparent Soil Development

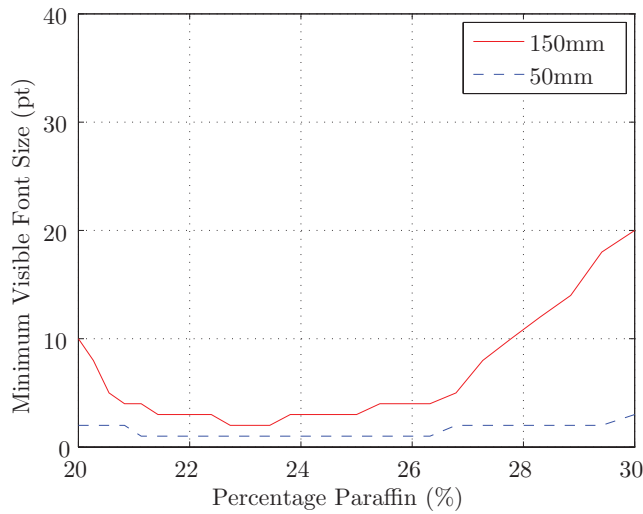


Figure 3.4: Transparency of fumed amorphous silica transparent soil through 50mm and 100mm depths of material.

Samples were formed using a sheet aluminium divider such that the rear 52.5% of the sample could be seeded with highly reflective particles to provide texture. The seeding material used was supplied under the product name Timiron by EMD Chemicals Inc., Gibbstown, USA. It consists of platy mica particles coated in titanium oxide, in the size range of 10-60 μm . 0.02% was added to the seeded slurry as a function of the aggregate content by mass. The front 47.5% of the model was left unseeded to maintain optimum transparency in the front portion of the model.

Each sample was consolidated under an effective vertical stress σ'_v of 100kPa. The transparency was assessed by passing a laser light sheet (apparatus described in detail in Sections 3.3.3.1 and 3.5.1.1) through the model at the mid-depth. Therefore the highlighted target plane is viewed through a 100mm depth of material plus the viewing window which was 10mm thick Perspex. A 12mm diameter straight pile, painted matt black to reduce laser light reflections, was inserted into the samples to provide a reference. Comparison of the transparency of the two formulations of transparent soil was conducted in a darkroom.

Figure 3.5 shows the marked difference in transparency between the two materials as the model pile and seeding is barely visible when viewed through the 100mm depth of precipitated amorphous silica soil. In contrast the model pile and seeding is clearly visible when viewed through the same depth of fumed amorphous silica soil.

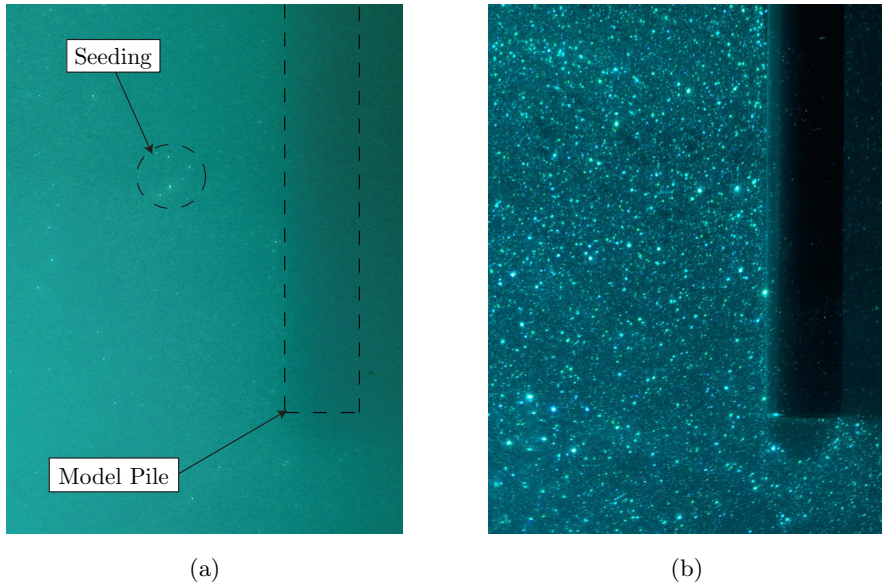


Figure 3.5: Comparison of transparency of amorphous silica (a) and fumed silica (b) consolidated to $100kPa$. Pile visible is $12mm$ diameter straight pile viewed through $100mm$ of transparent synthetic soil.

This is a significant improvement, since it now means that a larger test chamber than those previously described (Hird et al., 2008; Ni et al., 2010) can be used. The transparent soil models reported by Hird et al. (2008) were $100mm$ by $100mm$ on plan, with a depth of $200mm$. The CFA pile installed in the model had a radius of $9mm$, hence, the minimum free boundary distance was $41mm$ or about $4.5R$. If the same pile were installed in the fumed amorphous silica soil in the larger test chamber, the minimum free boundary distance would be $91mm$ or about $10R$. This represents a significant improvement and should significantly reduce the boundary effects.

3.3 Equipment

Figure 3.6 shows a schematic of the setup of the measurement devices used during this investigation. Central to the technique is the use of a computer to log data from the transducers during testing, control the pile-driving rig and act as a file store for digital images captured by the digital camera during the various stages of testing.

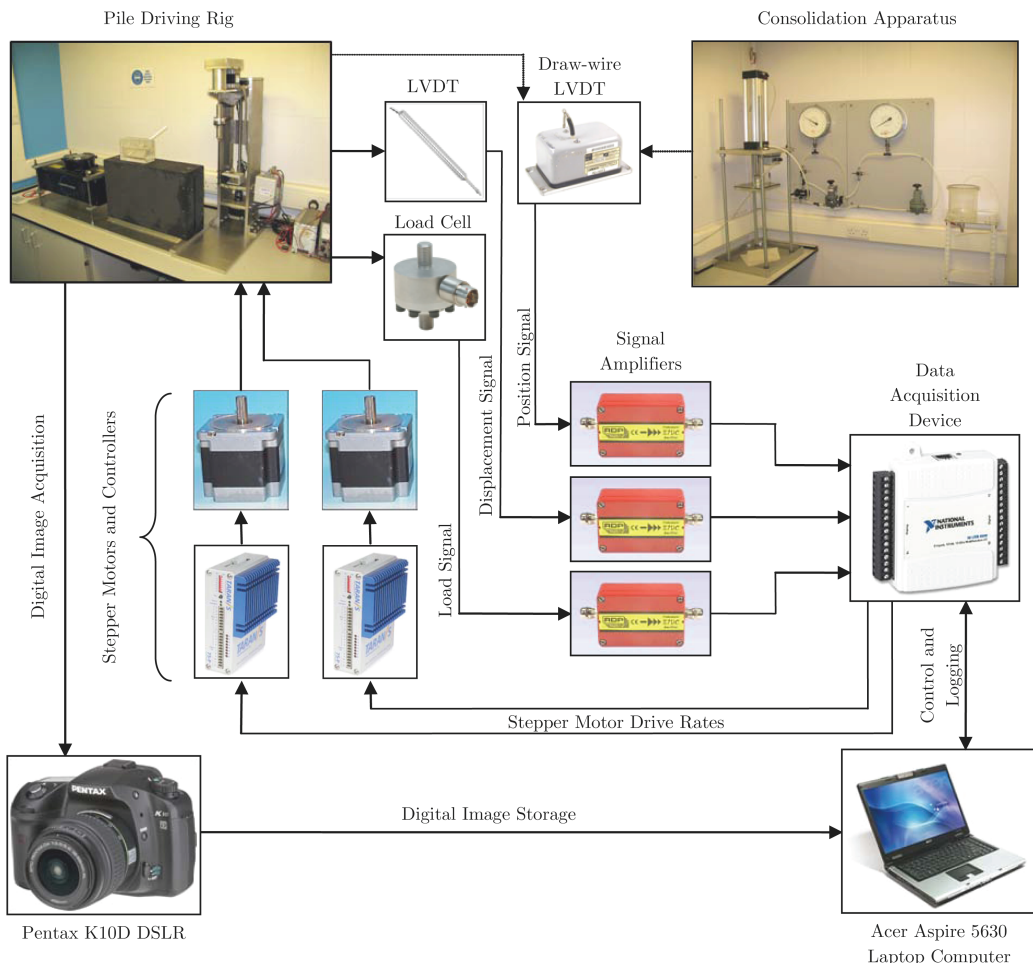


Figure 3.6: Equipment schematic.

3.3.1 Test Chamber

3.3.1.1 Design

The test chamber used in this investigation was originally commissioned for a previous investigation into ‘Strain fields around augered piles in clay soils’ and is shown in Figure 3.7(a). The internal dimensions are 200mm width, 200mm length and

480mm depth, allowing consolidation of samples with final height between 200mm and 240mm. In the research reported by Hird et al. (2008) and Ni et al. (2010), the transparency of the soil was limited, thus the chamber was not used. However, the improved transparency observed by using fumed amorphous silica soil allows the use of this larger chamber.

The chamber walls are manufactured from 20mm aluminium sheet, bolted together using M8 set screws at regular intervals of about 40mm. Viewing windows are provided in adjacent chamber walls. 10mm thick Perspex panels are sealed into slots 10mm larger than the viewing window itself, such that the inner faces of the aluminium chamber wall and viewing panel are flush, as seen in Figure 3.7(b). Consolidation pressures reinforce the seal during consolidation. The reinforcing panels shown in Figure 3.7(c) are machined from 20mm sheet aluminium and provide support to the Perspex windows during consolidation. They sit flush with Perspex viewing panels and have a 15mm overlap of 10mm depth, which allows them to be secured onto the chamber walls using M6 set screws at regular intervals of about 40mm. The removable panel shown in Figure 3.7(d) is provided on the rear of the enclosure to allow access for the pile-driving rig to the surface of the sample. This panel constrains the maximum sample height to 240mm.

Drainage is provided through the base of the chamber and the consolidation piston via a series of linked concentric semi-cylindrical channels, as shown in Figure 3.8. The consolidation piston is sealed using a square seal constructed from 4mm cylindrical rubber section, bonded at 45° mitred corners using cyano-acrylate adhesive. This provides a reasonably effective seal that reduces the passage of slurry around the perimeter of the sample during the early stages of the consolidation process. As consolidation progresses the effectiveness of this seal improves as consolidated material becomes trapped in any gaps present, in a similar fashion to that observed by Gill (1999). The test chamber was originally specified to allow consolidation of transparent synthetic soil samples up to consolidation pressures in excess of 200kPa.

3.3.1.2 Surface Finish

When recording digital image data for use in PIV analysis, it was important to minimise light captured from sources other than the laser illuminated plane of interest. Reflection of the laser sheet from the boundaries of the box had to be minimised

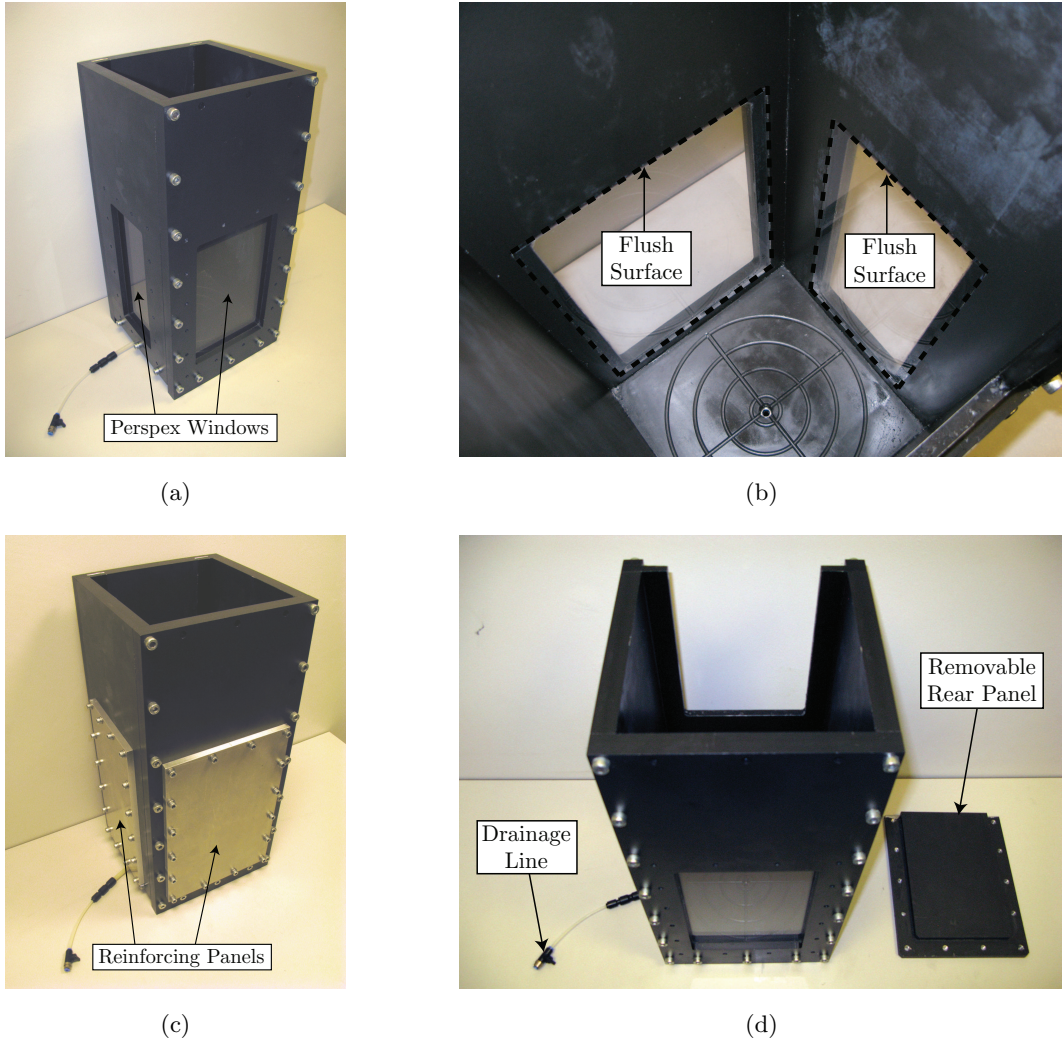


Figure 3.7: Images of 200 mm x 200 mm x 500 mm (internal dimensions) test chamber: (a) with viewing windows installed; (b) inner detail of viewing windows showing flush fit; (c) with consolidation reinforcement panels installed; and, (d) with rear panel removed to allow access for pile-driving rig to the top of the consolidated sample.

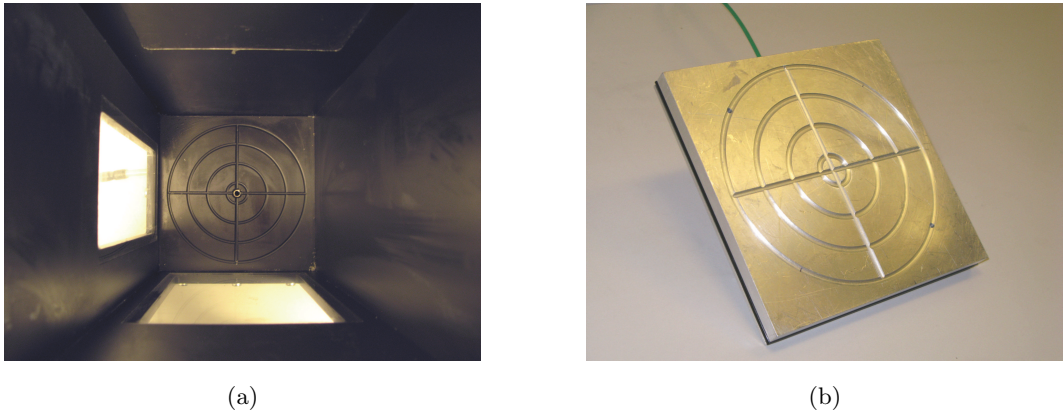


Figure 3.8: Drainage channels: (a) on the base plate of the test chamber; and, (b) on the consolidation piston showing the piston seal in-situ.

to safeguard this. The interior of the aluminium test chamber had previously been painted with matt black paint. However, after only one soil bed was consolidated within the enclosure it was observed that significant damage had occurred and it was deemed necessary to coat the interior of the chamber with a harder wearing surface. Heywood Metal Finishers (<http://www.hmfld.co.uk>), Huddersfield, were employed to hard anodise the chamber walls in black, providing a hard wearing matt black finish that minimised reflection of laser light.

3.3.1.3 Assembly

Firstly, the Perspex viewing windows were bonded into the corresponding test chamber walls using silicone sealant and loaded using 4kg weights during curing to ensure an adequate seal was generated. Secondly, after the viewing windows were in position, the four sides and base of the test chamber were given a light application of silicone sealant on all the mating surfaces, and the test chamber was assembled. The set screws were gently tightened in an opposing sequence to ensure even sealing of the mating surfaces. Any excess silicone sealant was allowed to cure. Thirdly, the removable rear panel of the chamber was given a light application of silicone sealant and pressed into position, before being fixed using set screws.

This rear panel was removed after consolidation, so grooves were provided at the top of the mating surfaces to allow use of a lever to break the silicone seal after removal of the set screws. The remaining sealant was then removed to allow a fresh application of sealant upon reassembly, before generation of the next soil bed. The excess silicone sealant was allowed to cure on all mating surfaces before removal, as

wiping off excess silicone sealant would leave a glossy residue over the interior of the chamber that would reflect light undesirably. A scalpel was used to carefully remove the cured excess silicone sealant without damaging either the seal or the anodised finish on the interior of the chamber. Lastly, the drainage lines were installed in the base of the test chamber and on the consolidation piston using push-fit fittings and flexible 4mm nylon tubing, such that draining pore fluid could be collected in a reservoir.

3.3.2 Consolidation Apparatus

Consolidation of the transparent synthetic soil sample was achieved using a 320mm stroke, 100mm diameter double action pneumatic cylinder, manufactured by Parker Hannifin Corporation (PIE100-320). The maximum pressure that could safely be sustained by the cylinder was 10 bar, which is greater than the maximum pressure of the system provided in the laboratories at the University of Sheffield, which is limited to 7 bar or 700kPa. By comparing the areas of the pneumatic cylinder and consolidation piston, the maximum consolidation pressure, assuming frictionless conditions, was estimated as summarised in Table 3.1. Thus the maximum consolidation pressure achievable was approximately 137kPa which allowed the consolidation of transparent to achieve soil with shear strength of around 15-20kPa, which is representative of very soft clay.

Table 3.1: Estimation of maximum achievable consolidation pressure.

Pneumatic Cylinder Diameter(m)	0.1
Pneumatic Cylinder Area (m^2)	0.0078
System Pressure (kPa)	700
Maximum Force (kN)	5.5
Consolidation Piston Size (m)	0.2
Consolidation Piston Area (m^2)	0.04
Maximum Consolidation Pressure (kPa)	137.5

The consolidation apparatus consisted of two aluminium end-plates separated by four 20mm diameter threaded steel bars. The pneumatic cylinder was mounted centrally on the upper end-plate with the consolidation piston attached to the end of the shaft. The test chamber was placed on the lower end-plate and aligned with the consolidation piston such that the piston could move freely vertically. The pneumatic cylinder was controlled using a two-way valve, a pair of regulators and Budenberg dial gauges, allowing accurate control of pneumatic cylinder pressure at both lower

(0-100kPa) and upper (100-700kPa) pressure ranges. This setup allowed the consolidation piston to be both raised and lowered during the soil bed preparation process. The assembled consolidation apparatus can be seen in Figure 3.9.

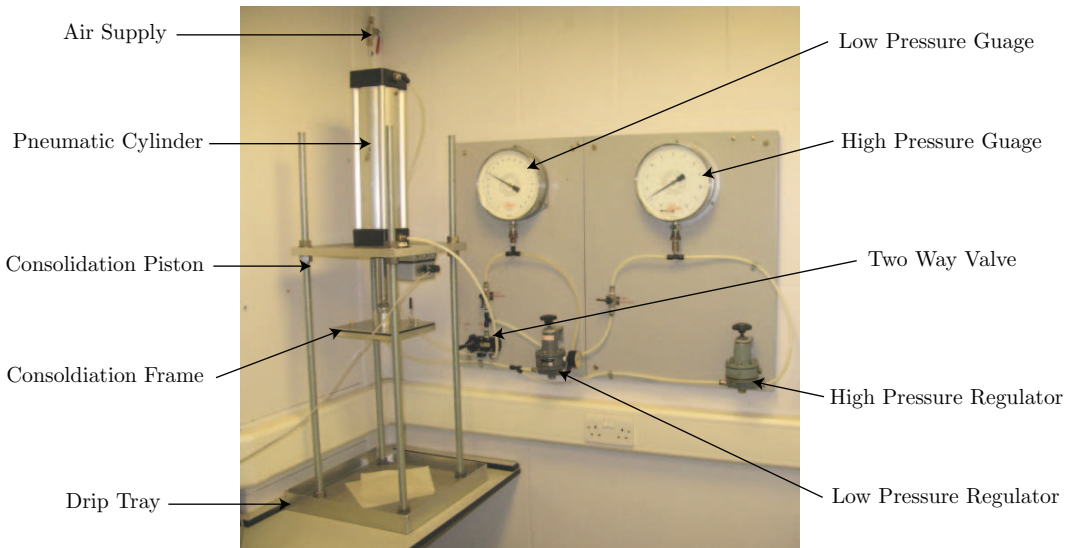


Figure 3.9: Assembled consolidation apparatus.

Two-way one dimensional drainage was provided through the surface and base of the test chamber, via the drainage channels described in Section 3.3.1.1. To minimise loss of aggregates through these drainage channels and to alleviate the risk of blockage, porous plastic sheets were cut to fit into the base of the test chamber and to cover the area of the consolidation piston. The consolidation process was monitored using a draw-wire Linear Variable Displacement Transducer (LVDT) that is described in Section 3.3.6.3.

3.3.3 Laser Aided Tomography Apparatus

LAT requires the use of a laser to highlight a plane of interest within a transparent medium to allow capture of movements using a digital camera. The following subsections describe the apparatus specific to the LAT based geotechnical modelling techniques.

3.3.3.1 Laser

The laser utilised in this investigation was a class IV air cooled Argon laser, manufactured by Laser Physics UK Ltd. with a 1W maximum power output and wavelength range of 457-514nm. The laser provided a beam of 0.95mm diameter which was then

shaped, using a top-hat beam-shaper manufactured by Dantec Dynamics Ltd. with 23.5° spread angle, into a sheet of approximately uniform intensity. To minimise the required shutter period required to attain sufficient exposure in captured digital images, the laser was used on its maximum setting during testing. However, for health and safety considerations, all alignments were conducted using the minimum output power.

Figure 3.10 shows the laser unit in-situ in the laboratory alongside the beam-shaper. The laser aperture and beam-shaper was raised 150mm above the base plate of the apparatus on threaded bars and secured by aluminium crossbars. The beam-shaper lens was 630mm from the centreline of the pile driving rig (described in Section 3.3.4.1), so that the minimum height of laser light sheet generated within the model was 220mm.



Figure 3.10: Laser apparatus consisting of 1W laser and top-hat beam shaper mounted on an aluminium frame.

3.3.3.2 Digital Camera

Capturing of digital images for the PIV analysis process was conducted using a Pentax K10D Digital Single Lens Reflex (DSLR) camera mounted on a Manfrotto 055XPROB tripod and swivel ball head. Digital cameras utilise a Charge Coupled Device (CCD) which is light sensitive, in lieu of film. Digital images were recorded on a SanDisk Extreme III SD memory card capable of transferring data at speeds of about $20MB/s$, which allows for continuous capture, at a rate of 3.3fps, of JPEG images of the maximum resolution which the camera is able to record (10 megapix-

els). A summary of the specification of the digital camera is contained in Table 3.2. The camera settings used are highly dependent on the experimental setup and so are outlined in Section 3.5.1.2 concerning digital camera calibration.

Table 3.2: Pentax K10D digital camera specification.

<i>Image Sensor</i>	
Type	CCD
Maximum Resolution	3872 x 2592 px
Effective Pixels	10.0 M
Size	23.5 x 15.7 mm
Image Ratio (W:H)	3 : 2
Image Stabilisation	Gyroscopic
<i>Lens</i>	
Focal Length Range	18.0 – 55.0 mm
Aperture Range	F3.5 – 38.0
<i>Exposure Control</i>	
Shutter Duration	1/4000 – 30 s
Exposure Compensation	-3 to +3 EV
ISO Speed Equivalent	AUTO, 100, 200, 400, 800, 1600
<i>Storage</i>	
Format	SecureDigital™ Memory Card
<i>Capture Rate</i>	
Maximum Rate	3.3 fps

3.3.3.3 Control Points

Differential movement between the digital camera and plane of interest generates errors in any data generated by PIV analyses, so some technique is required to mitigate these errors. This is typically achieved by using a set of control points that are stationary throughout testing in relation to the plane of interest. These can then be tracked using PIV and any movement errors can then be corrected in a process known as registration.

White and Bolton (2004) used black target circles printed on an acetate sheet by a laser printer with square white backgrounds formed from paper behind each individual marker, generating contrast as shown in Figure 3.11(a). The centre of each marker is calculated using a centroiding process and then the metric positions are calculated by comparison with a photogrammetric calibration target, to the certificated accuracy of the calibration target of $200\mu m$. Alternatively Effendi (2007) utilised an array of control points consisting of a thin Perspex sheet drilled with

3mm diameter blind holes using a milling machine, to a quoted accuracy of $\pm 10\mu m$. These were then filled with Tipp-ExTM fluid and backed with a square of black electrical tape as shown in Figure 3.11(b).

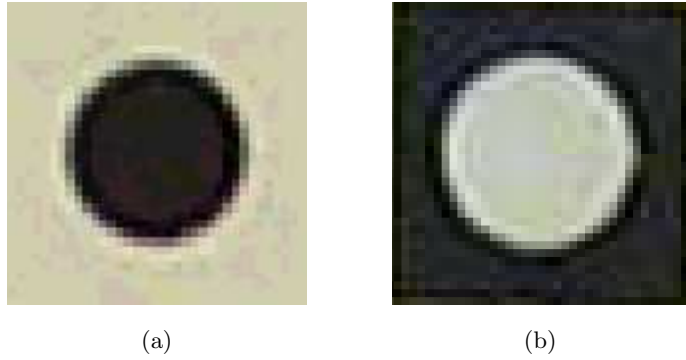


Figure 3.11: Control points used by: (a) White and Bolton (2004); and (b) Effendi (2007).

Both of these forms of control point rely on the contrast between the circular target and background colour, of black against white. In both cases PIV is used to track the movements of the individual markers during testing allowing correction of movement errors during photogrammetric correction of the output data. However, both types of control point require that there is sufficient ambient light to evenly illuminate the control points to allow centroiding to be conducted accurately. When modelling using transparent soil it is imperative that the laboratory be completely dark during testing so that only soil on the plane of interest is illuminated by the laser sheet. Hence the above control points are unsuitable.

Hird et al. (2008) and Ni et al. (2010) describe an array of control points consisting of sixteen light emitting diodes or LED's mounted in two groups of eight within separate vertical panels manufactured from Perspex. These were mounted using Pritt-StickTM, to either side of the front viewing window of the test chamber. The LED's on each of the panels were wired in series and powered by a Direct Current (DC) Power Supply Unit (PSU). The voltage supplied to these control point panels can then be calibrated to generate maximum contrast with minimal light bleeding or overexposure, as is explored in Section 3.5.1.3.

Two improvements have been made to these control point panels for this investigation. Firstly the panels themselves have been painted matt black to generate maximum contrast and minimise erroneous transmission of light from the LED's.

Secondly, one of the panels has been stepped out by 10mm such that when one panel is mounted on the viewing window and the other is mounted on the side of the test chamber itself, the two panels are coplanar. This is critical for accurate correction of movement errors as is discussed in Chapter 4. The control point panels can be seen in Figure 3.12.

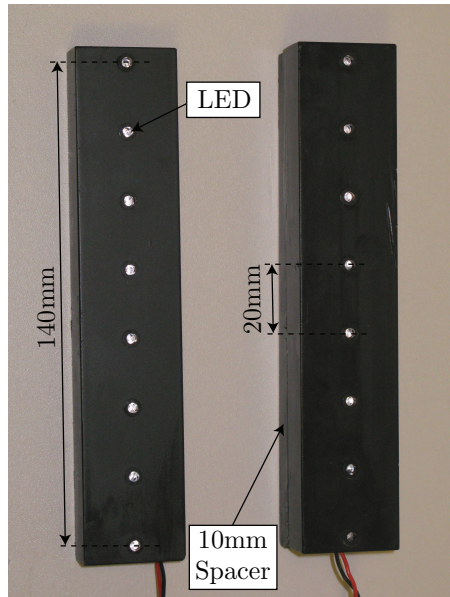


Figure 3.12: Light Emitting Diode (LED) based control points used in this investigation.

3.3.4 Pile Driving Apparatus

The apparatus required to install model helical screw piles must afford the user control of both rotational and vertical movement of the pile drive head precisely if true screw installation is to be achieved. In this investigation a pre-existent pile-driving rig that was developed to install CFA piles in transparent synthetic soils has been utilised, and is shown in Figure 3.13. Details of its construction, drive and control systems are outlined in the following sub-sections.

3.3.4.1 Pile Driving Rig

The pile driving rig itself consists of a frame machined from 10mm sheet aluminium that is braced at regular intervals to allow housing of bearing units for the vertical drive system. This system comprises of a 5mm Hepco ballscrew driven using a stepper motor and guide rail on which a cantilever arm slides vertically up or down dependent on the direction of rotation of the motor. Rotational control is provided

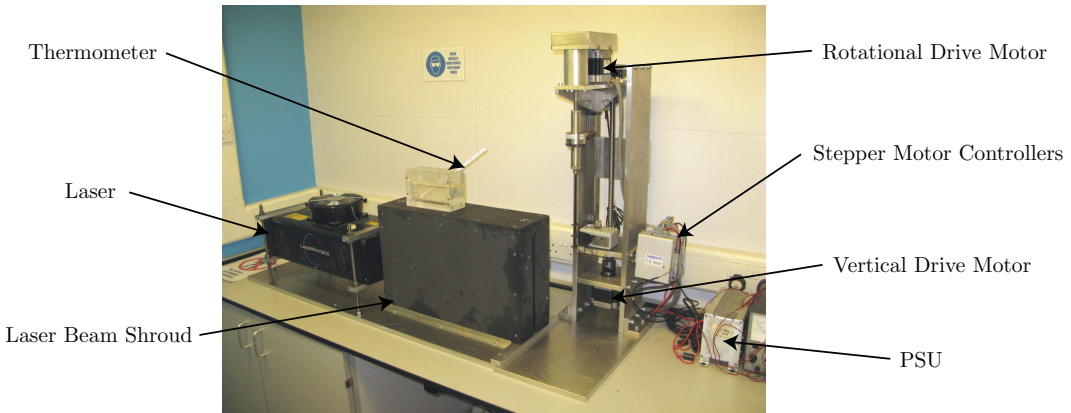


Figure 3.13: Pile driving rig used in this investigation.

on the cantilever arm using a second stepper motor and 1:1 belt and pulley system to drive the pile drive-shaft. The frame itself was originally designed to resist vertical loads in excess of $1kN$.

3.3.4.2 Stepper Motors

The stepper motors are 34 frame, 1.8° , high torque, rare earth magnet motors (model no. SMR-341-064-G-FN) that were supplied by SmartDrive Ltd., Cambridge, UK. They are capable of supplying $3.45Nm$ of holding torque from a supply current of $4.5A$. This is sufficient to provide a vertical driving force of around $1kN$. For simplicity the same specification stepper motor was used for both vertical and rotational drive.

3.3.4.3 Stepper Motor Controllers

Integrated drive and controller units were also supplied by SmartDrive Ltd. in the form of their Taranis™ system, which can drive stepper motors with current draw up to $7.5A$, generating ultra smooth motion with 51200 microsteps per revolution. This equates to a maximum control accuracy of $0.0977\mu m$ for the vertical drive and 0.007° in rotation. The Taranis control units can either be controlled using pre-defined programs that can be stored on the Flash EPROM memory of the device or controlled in real-time using an RS232 serial port connection to a suitable computer. In addition, the control unit has ten digital I/O's that can be used to convey signals from either transducers or data acquisition devices to the embedded control program. This can subsequently be used to control the stepper motors. The stepper motor controllers and the stepper motors are supplied by a PSU that is specifically suited for the purpose and is capable of powering both drive systems simultaneously.

3.3.5 Model Helical Screw Piles

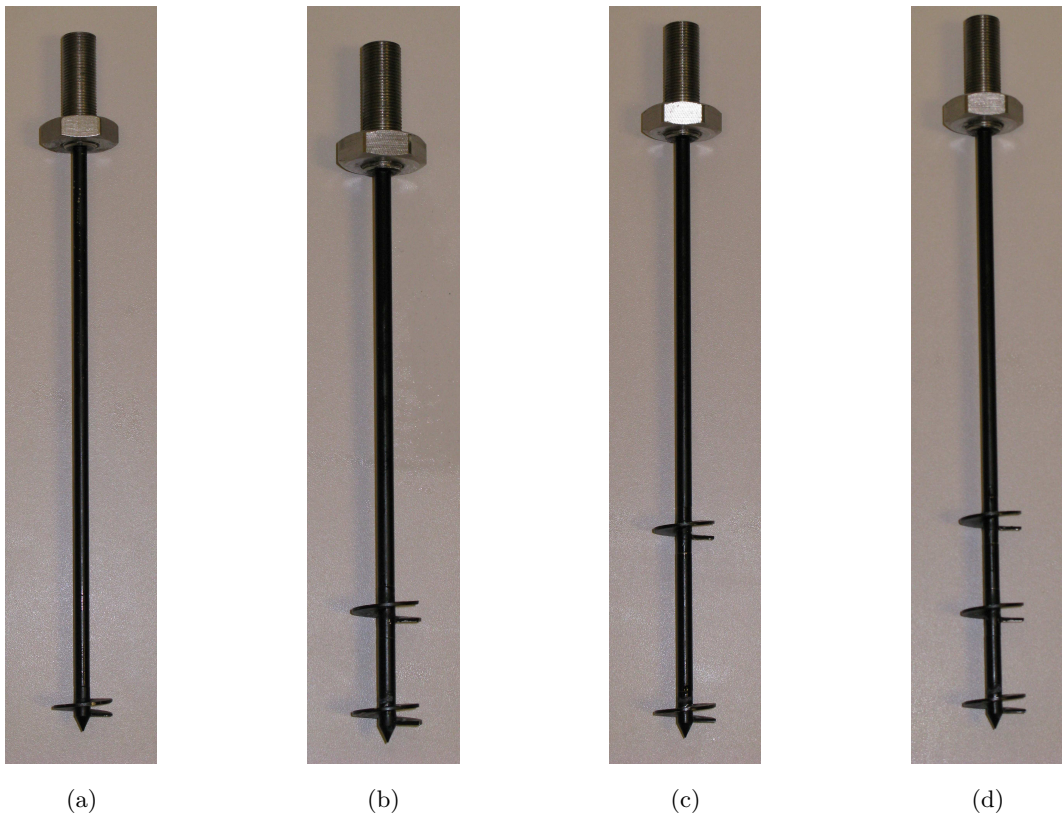
In designing the model helical screw piles to be used in this investigation a number of considerations had to be made regarding the proposed scope of research. Model piles were required to allow investigations into the areas highlighted in Section 2.5 as having potential for further research. A deep installation condition as outlined by Rao et al. (1993a) entails installation of the helical screw pile until the coverage of soil above the uppermost helical plate is equal to or greater than four times the diameter of the helical plate ($4D$). A range of helical plate spacing ratios (s/D) was proposed for investigation to incorporate ratios that are closely spaced ($s/D=1.0\text{--}1.5$) and well-spaced ($s/D=1.5\text{--}3.5$). A series of suitable test geometries was specified based on a helical screw pile with plates of $20mm$ diameter and $5mm$ pitch tested in a soil bed of $220mm$ depth. Thus the total soil height is $11D$. If H/D is a minimum of $4D$, the maximum active length (L_a) is $3D$ assuming that the free soil depth beneath the model pile is equal to the overburden depth of $4D$. The pile shaft was designed to be sufficiently rigid during testing to resist buckling. This allowed the set of tests outlined in Table 3.3 to be performed. The model piles described here allow all of the objectives outlined in Section 2.5 to be investigated.

Essentially four separate pile geometries are required to conduct this sequence of tests. Due to the complex nature of a helix and the need for maximum geometric similarity between helices on each of the model piles, it was decided to commission the machining of the helical plates themselves using Computer Numerical Control (CNC) machining techniques.

This raised the possibility of designing the model piles such that the different configurations could be assembled from a pool of common parts. In order to achieve this it was decided that the helical plates and adjoining sections of shaft $5mm$ above and below each plate would be machined using CNC machining techniques from a billet of aluminium. Interconnecting shafts of $5mm$ diameter were then machined such that the desired s/D ratios and L_a values could be achieved. These were connected to the helical plate sections using $2mm$ stainless steel threads, permanently inserted using threadlock into the helical plate sections. Two types of helical plate were required: terminating and intermediate. The terminating helical plate had a conical end of $5mm$ length to aid installation and the intermediate helical plate had shaft attachments at either end.

Table 3.3: Model helical screw pile configurations.

Series	No. Plates	Loading	d (mm)	D (mm)	d/D	L_a (mm)	H/D	s/D
C1	1	Compression	5.0	20.0	4	0.0	7	∞
C2-30	2	Compression	5.0	20.0	4	30.0	5.5	1.5
C2-60	2	Compression	5.0	20.0	4	60.0	4	3.0
C3	3	Compression	5.0	20.0	4	60.0	4	1.5
T1	1	Tension	5.0	20.0	4	0.0	7	∞
T2-30	2	Tension	5.0	20.0	4	30.0	5.5	1.5
T2-60	2	Tension	5.0	20.0	4	60.0	4	3.0
T3	3	Tension	5.0	20.0	4	60.0	4	1.5

Figure 3.14: Helical screw pile configurations: (a) single helix pile; (b) double helix pile where L_a is 30mm; (c) double helix pile where L_a is 60mm; and (d) triple helix pile where L_a is 60mm.

The intermediate and terminating helical plates were drawn using SolidWorks by Dr. Qing Ni of the University of Warwick and machined by technicians at the same institution. After manufacture, all components were painted matt black to minimise laser light reflection during testing and to give the differing materials from which the piles were constructed uniform surface properties. The assembled configurations of model screw pile can be seen in Figure 3.14. Care had to be taken during assembly to ensure that all helical plates aligned at the same point on the pile, thus ensuring that the anticipated L_a was achieved. At the top of the pile shaft a M12F threaded section was provided to allow connection of the model pile to the pile-driving rig.

3.3.6 Measurement Devices

3.3.6.1 Load Cell

By consulting Table 3.3 it was tentatively assumed that the largest resistance to be measured would be generated by the C3/T3 series of tests where s/D was minimal and L_a was maximal. The required capacity of the load cell was estimated using Equations 2.3 and 2.4, assuming S_u of $20kPa$, α of 1.0, N_c of 9.0, N_{cu} of 9.0, γ of $9.24kN/m^3$ and H_{eff} equal to the shaft height H of $0.08m$.

Based upon these assumptions the minimum required capacity was calculated as about $\pm 157N$. Hence, assuming the suction force and weight of the model pile combined was less than approximately 30% of the total capacity of the model pile then a load cell with capacity of around $\pm 200N$ was required. An LCM213-200N tension-compression load cell from Omega Engineering Ltd. was chosen to monitor the load applied to the piles. The transducer was certified with a capacity of $\pm 200N$, safe overload capacity of $\pm 300N$ and ultimate overload capacity of $\pm 600N$. It therefore afforded a good margin for error without risk of damage.

The quoted accuracy of the transducer was $\pm 0.15\%$ of the total capacity, which equated to $\pm 0.3N$. The transducer required a DC supply of 10-15V and generated an output signal of $2mV/V_{in}$. The load cell was connected to the pile-driving rig and model helical screw piles using a pair of stainless steel connectors of 30mm diameter, half threaded with M12F threads to allow connection to the pile-driving rig and model piles and half threaded with M12 threads to allow connection to the load-cell itself as shown in Figure 3.15.

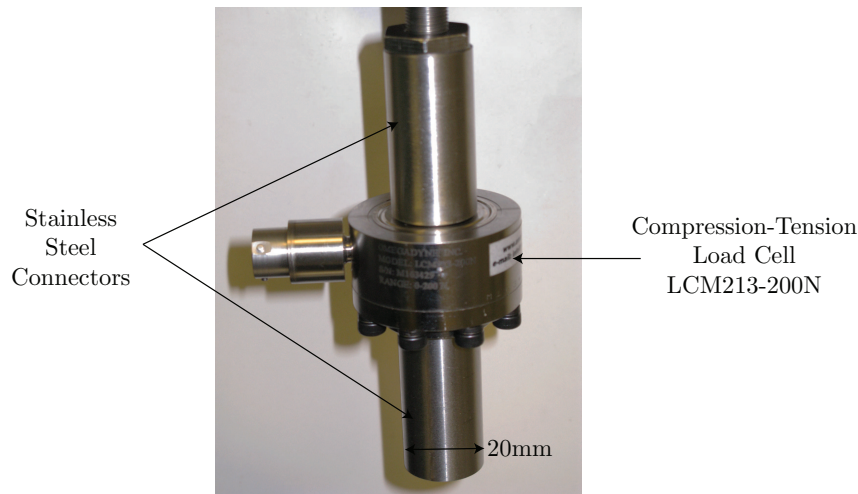


Figure 3.15: Load-cell connectors.

3.3.6.2 Linear Variable Differential Transformer (LVDT)

To measure the vertical displacement experienced by the model pile during load testing, the differential displacement between the pile-driving rig frame and cantilever arm (see Figure 3.13) was measured using a 25mm LVDT supplied by MPE Electronics Ltd. which required a DC supply voltage of 1.5-10V to output a signal of $5.3mV/V_{in}$. The reported accuracy of the transducer was $\pm 0.1\%$ of the range or $\pm 0.025mm$. The LVDT was mounted to the pile-driving rig using a pair of machined aluminium brackets as shown in Figure 3.16. The bracket was designed such that the LVDT could be in place during testing without interfering with the test chamber.

3.3.6.3 Draw-wire LVDT

A Celesco PT101-0025 draw-wire LVDT was used to monitor the consolidation process and helical screw pile installation progress. This transducer had a range of 560mm and was mounted to the top plate of the consolidation frame during consolidation and adjacent to the ballscrew on the pile-driving rig frame during pile installation as shown in Figure 3.17. This transducer required a 1.5-30V DC supply to create an output signal of $94\% \pm 4\%$ of the input voltage, with accuracy of $\pm 0.1\%$ of the range or $\pm 0.45mm$. To facilitate simple transfer of the draw-wire LVDT from one application to the other a mounting plate was created from a section of 90° angle aluminium, that was then secured to either the consolidation or pile-driving rig frame using three M4 set screws.

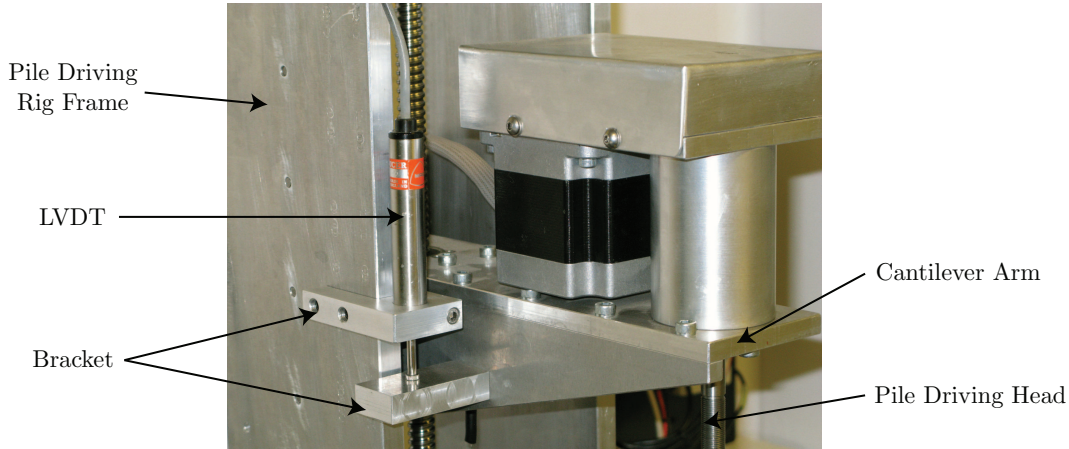


Figure 3.16: LVDT mounting bracket.

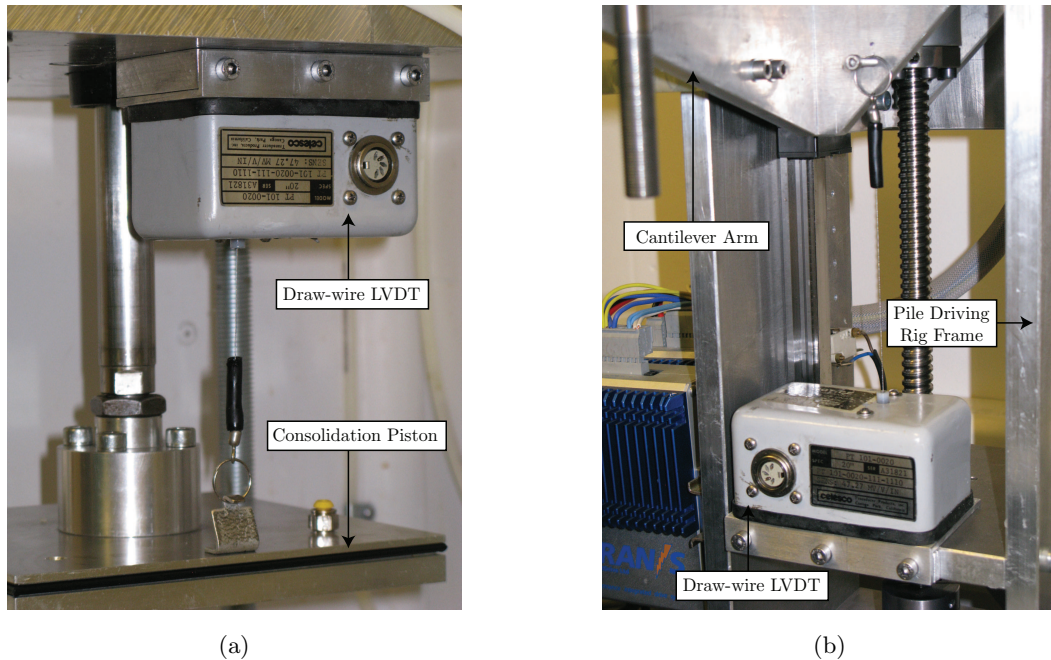


Figure 3.17: Draw-wire LVDT mounted on: (a) the consolidation apparatus top plate; and (b) the pile-driving rig frame.

3.3.7 Data Acquisition Device

To record measurements using the afore described transducers and to control the pile-driving rig, a National Instruments NI USB-6009 Data Acquisition Device (DAQ) was utilised. This device had eight analog inputs in the range of $\pm 1.0 - 20.0V$ with a maximum sampling rate of $48kS/s$ and *14 bit* resolution. Two analog outputs could supply a signal of $0.0-5.0V$ at a rate of $150Hz$ which was used to control the two stepper motor drive rates. Twelve digital input/output (I/O) lines were also provided that could be used as trigger inputs on the Taranis stepper motor controllers, to provide boolean signals to the control software described in Section 3.4.1. Recording the data measured by the transducers, controlling of the data sampling rate and control of the pile-driving rig were all achieved using LabVIEW, the details of which can be found in Section 3.4.2.

3.3.7.1 Signal Amplification

Due to the output signal from a number of the transducers being in the order of mV/V_{in} and the DAQ not being sufficiently sensitive to capture the signal accurately, inline signal amplifiers were required. For this purpose RDP S7DC inline DC amplifiers were employed in conjunction with a stable $15V$ DC power supply to excite the output signals from the transducers such that the final output was in the range of about $\pm 5V$ and thus measurable accurately using the DAQ.

3.4 Control Software

3.4.1 Nimbus

Nimbus is the software used to program the Taranis stepper motor controllers. Using BASIC type programming Nimbus is used to create a program that can be uploaded to their Flash EPROM memory onboard each controller using a serial port connection. The control program is required to control the following:

- Speed control.
- On/off toggle.
- Directional toggle.
- End point stop toggle for the vertical drive stepper motor.

Speed control for the two stepper motors was provided using the 0.0-5.0V output channels from the DAQ. The on/off and directional controls were provided using the digital I/O channels of the DAQ. Lastly, the end point stop control for the vertical drive motor was triggered using a pair of micro switches at the limits of the vertical drive frame. Using these inputs a control program was created by Mr. David Martin of SmartDrive Ltd. to control the stepper motors, which was permanently uploaded to the Flash EPROM memory on each controller.

3.4.2 LabVIEW

LabVIEW is software developed by National Instruments that utilises a graphical programming language to sample data, control analog output channels and switch digital I/O channels. This software was chosen for use in this investigation since it is capable of real-time control as well as data sampling and recording. Hence control of the pile-driving rig and the recording of measurements could be conducted simultaneously. It was also convenient that, since the DAQ and LabVIEW are supplied by the same manufacturer, their integration was seamless.

Data sampling during load-deflection testing was conducted at a rate of $1kHz$ in 100 sample batches. This is far in excess of the sampling rate required. However, due to Electro Magnetic Feedback (EMF) from the stepper motors, controllers and power supply it was deemed necessary to employ a digital low-pass bandwidth filter to the input signal of $1Hz$ for all transducers (except the draw-wire LVDT where a $0.25Hz$ filter was employed for increased signal stability), followed by averaging of each 100

sample batch to generate an effective output signal frequency of $10Hz$. The same system was employed in the sampling of consolidation displacements except that the sampling frequency was $10Hz$ such that the effective signal output frequency was $0.1Hz$. This system of filtration and averaging generated output signals that were sufficiently free of noise generated by the EMF. Other precautions were taken with the wiring of the hardware by ensuring that all grounds were common and all transducer cables suitably shielded. All calibrations presented in Section 3.5.3 were conducted using the same system of digital signal filters with the pile-driving rig stepper motors energised to recreate the test conditions.

Output signals were simultaneously written to an output file in tab-delimited format that could be read by many analysis software packages such as MATLABTM or Microsoft ExcelTM and used to control the pile-driving rig. The signal from the draw-wire LVDT was used to indicate the position of the pile-driving head, such that a comparison could be performed against a user-defined required driving depth. This output was used to control a digital I/O channel on the DAQ, which was wired to the digital I/O channel on the stepper motor controllers corresponding to the on/off switch programmed into the controllers using the Nimbus package. This was achieved by supplying $0V$ or $5V$ to the corresponding digital channel on the appropriate controller. Digital switches were used within the LabVIEW environment in the same way to control the on/off toggle and directional toggle for each stepper motor such that they could be controlled digitally by the user in real-time, thus providing a manual override if necessary. Figure 3.18 shows a screenshot of the Graphical User Interface (GUI) developed by the author to satisfy the requirements of this investigation, showing the data-logging, real-time plotting and digital control facilities of the pile-driving rig.

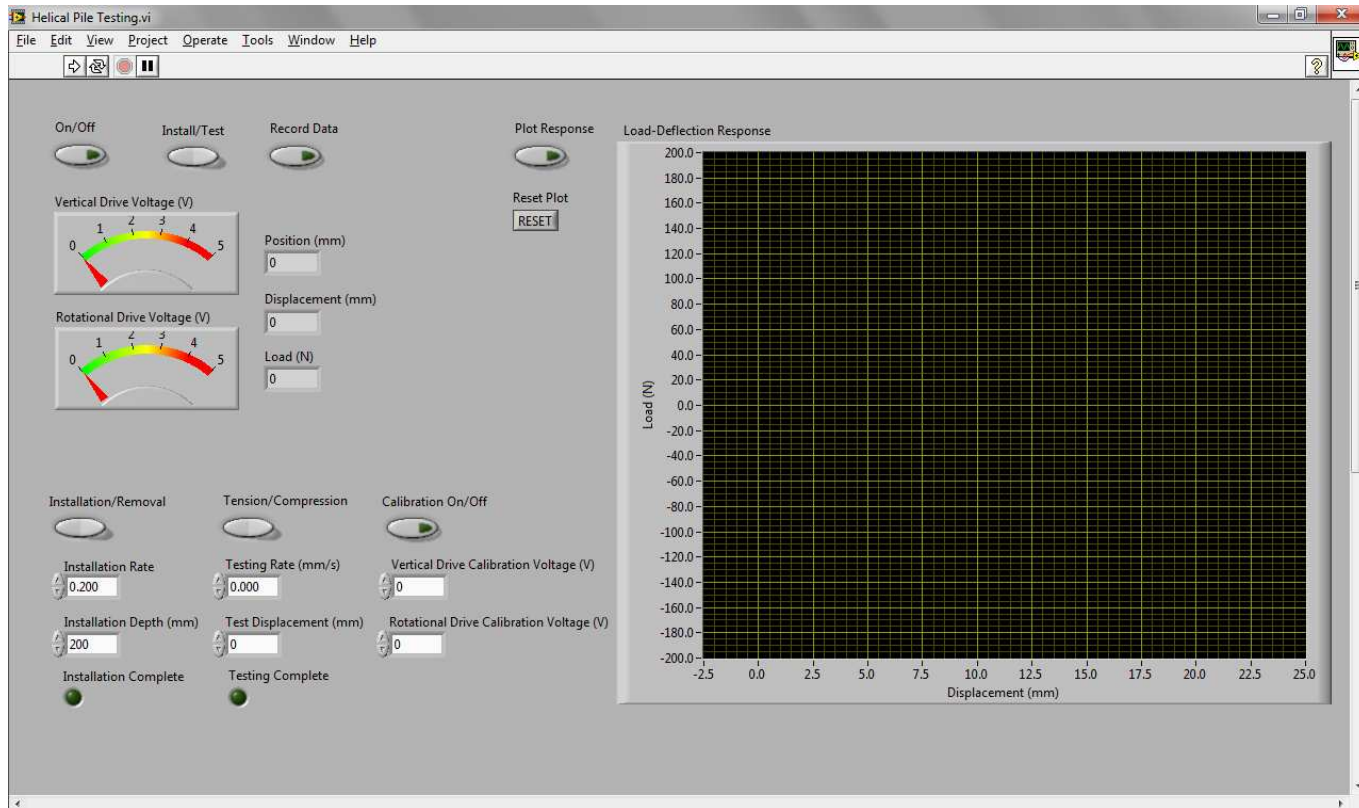


Figure 3.18: LabVIEW control software interface for data sampling and real-time control of the pile-driving rig.

3.5 Calibrations

3.5.1 Laser Aided Tomography Apparatus

3.5.1.1 Laser

To minimise the exposure time required to record each image the laser brightness was maximised. However, for health and safety reasons all alignment work was conducted with the laser set to minimum output. The power was only increased once all safety apparatus was in place and operational and testing was ready to commence. This safety apparatus consisted of a set of high density goggles and laboratory over-coat for the laser operator. A door lock was used to safeguard the room whilst the laser was active and an illuminated ‘laser in use sign’ was employed to inform other laboratory users of the fact that the laser was active. The laser laboratory was designed such that once the door was closed no light was emitted from the laboratory during testing.

Alignment of the laser was achieved by mounting the laser on four threaded bars and aluminium cross-members set onto a 20mm thick sheet of aluminium that constituted the laser apparatus frame. This allowed vertical height and longitudinal position to be adjusted so that the laser beam passed through the center of the envisaged soil sample height of 220mm, whilst remaining in alignment with the pile-driving head. Next, the top-hat beam shaper was positioned using adjacent pairs of threads in the laser apparatus frame to generate a laser sheet covering the visible plane of interest when viewed through the test chamber viewing window. Lastly, the alignment of the top hat beam shaper was assessed by checking that the laser sheet produced was vertical and aligned with the pile-driving head.

3.5.1.2 Digital Camera

After alignment of the laser apparatus the settings of the digital camera were calibrated by using a consolidated transparent soil sample (see Section 3.6.1 for an overview of the consolidation procedure) to determine the optimum settings for the digital camera. Firstly, the position of the camera was chosen. In this investigation the laser sheet is aligned with the central axis of the model pile and thus all soil in the sample beyond the model pile was not illuminated by the laser sheet. Thus the digital camera was positioned so that only a little over half of the model was captured in the image and pseudo-axisymmetric deformation was assumed to exist.

The digital camera was fitted with an 18-55mm zoom lens, so a suitable focal length had to be chosen. To ensure repeatability only 18mm or 55mm zoom lengths were considered, as it was impossible to ensure any intermediate value was consistently reproduced between tests and this uncertainty would have undermined the camera calibration process outlined in Chapter 4. In this investigation a zoom length of 55mm was assumed in all tests, since this positioned the camera at a more convenient distance from the test enclosure and reduced the maximum angle between the plane of interest and the CCD of the digital camera, thus reducing the radial and tangential lens distortions recorded in the image.

As previously mentioned the laser output was maximised so that minimum exposure times were required of the digital camera. However, there are a range of inter-dependent settings on a camera that require careful consideration as they all affect the exposure characteristics of the image recorded. These include:

- Shutter duration.
- Aperture size.
- ISO sensitivity.
- White balance.

Shutter duration is simply the length of time that the shutter of the camera is opened and the CCD of the camera is exposed to the field of view. To minimise entrainment of movement of the soil in images during testing, the shutter duration should be minimised.

Aperture size is the size of the lens aperture through which light passes to the CCD, which is quantified in terms of f-stop or focal ratio. This is a dimensionless expression of the lens speed and is essentially the focal length divided by the effective aperture diameter. Thus as the aperture dimension increases the f-stop reduces. The shutter duration and aperture size are essentially coupled and together control the overall exposure of the recorded image, whereby a large f-stop and long shutter duration generates a similarly exposed image as a small f-stop and short shutter duration. However, depth of field also increases with f-stop, so that a small f-stop generates an image with a very small range of focus. Conversely, a large f-stop generates hyperfocal focus, where foreground, target and background all remain in focus.

This means that balance must be achieved between short shutter durations and small aperture sizes such that a well exposed image can be recorded in a suitably short duration. The sensitivity (ISO) could be used to achieve this by amplifying the recorded light allowing shorter shutter durations and smaller apertures to be used to generate a suitably exposed image. This is similar to using faster reacting photosensitive film in a traditional camera. However, the main drawback with this mitigation is the generation of noise in the output image, as high ISO has a propensity to generate a number of pixels that are erroneous which contaminate the image. The pixels affected by the noise are random and change between subsequently recorded images, so may influence the PIV analysis process in a negative fashion. For this reason in all tests the ISO used was the minimum of 100 in order to minimise the random noise recorded in the images. For similar reasons no white balance manipulations were performed before recording of the digital image data in JPEG format.

To define appropriate parameters for these settings first a suitable exposure of the image needed to be defined. In LAT based PIV modelling of geotechnical problems the soil highlighted by the laser sheet is of primary importance. The seeding particles within the rearward portion of the consolidated model generate texture in the recorded image. Under-exposure can be defined as where the texture generated by the seeding is not sufficiently distinct. Over-exposure can be defined as where the light reflected by the seeding is so prevalent that whole areas of the image are overly bright and the texture is lost. These two scenarios need to be avoided as PIV is reliant on even contrast over the field of interest if accurate measurement is to be assured over the whole FOV.

Thus different combinations of shutter duration and aperture size were tested to generate a range of images, until the most evenly contrasting and exposed setting could be qualitatively chosen. Figure 3.19 illustrates an under-exposed, correctly-exposed and over-exposed image of seeded transparent synthetic soil. The shutter duration and aperture size for the correctly exposed image were 1/10th of a second and F8.0 respectively. These settings were used in all photogrammetric calibrations and all model tests, and it is important to note that the camera was manually focussed prior to every test to ensure the images recorded were sharply focussed.

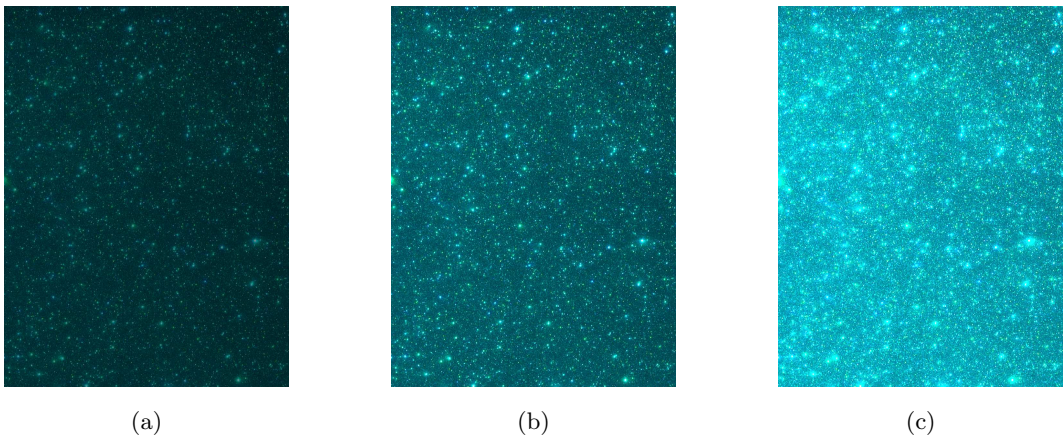


Figure 3.19: Exposure calibration of transparent synthetic soil: (a) under-exposed; (b) correctly-exposed; and (c) over-exposed;

3.5.1.3 Control Points

After defining suitable settings for the digital camera to ensure optimum exposure of the plane of interest, the control points were calibrated by altering the voltage supplied to the LED control panels. The control points were powered by a DC PSU with each eight LED panel wired in series and the two panels connected to the PSU in parallel. The supply voltage was varied between 12.0V and 17.0V in 0.5V increments, whilst images were recorded at each supply voltage with the camera in the position used during testing and with the settings described in Section 3.5.1.2. Each image was then loaded into MATLABTM for analysis.

To ensure optimum tracking of each LED control point the contrast between the LED and background panel must be maximised. This needs to be achieved without flares of light emanating from the LED's that may impact on the image of the highlighted plane of interest. Figures 3.20 to 3.22 shows an LED control point supplied with 12.0V, 15.0V and 17.0V in mono image form over a 100 x 100 pixel area accompanied by a light intensity plot (where 0 represents absolute black and 255 represents absolute white) and an intensity histogram in terms of normalised frequency (sum is equal to unity) indicating the range of light intensities present within the image excerpt.

In Figure 3.20(a) using a 12V DC supply voltage the output from the LED is very faint and thus indicates low light intensity of about 40, as illustrated by the light intensity plot presented in Figure 3.20(b). The intensity histogram in Figure 3.20(c)

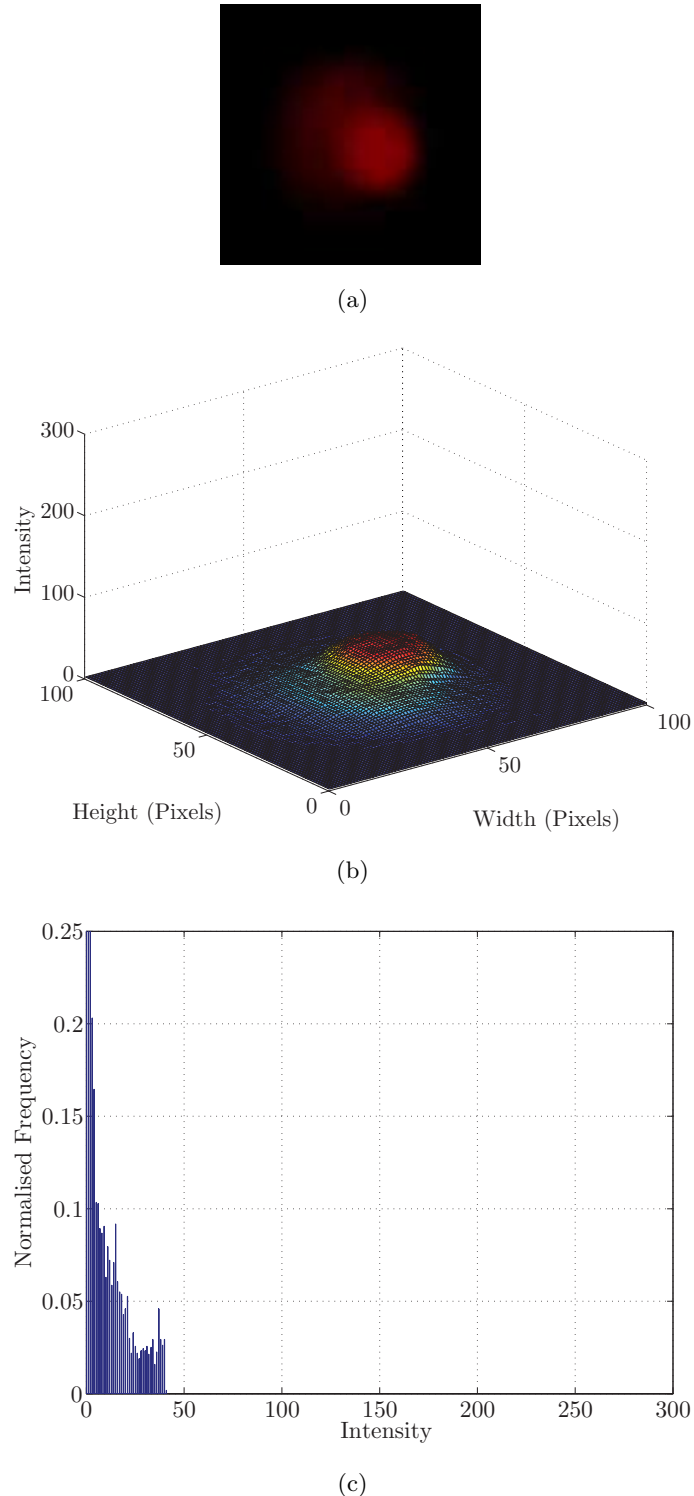


Figure 3.20: LED calibration analysis with 12V supply: (a) image of LED output; (b) intensity plot of LED output; and, (c) histogram of LED output intensity.

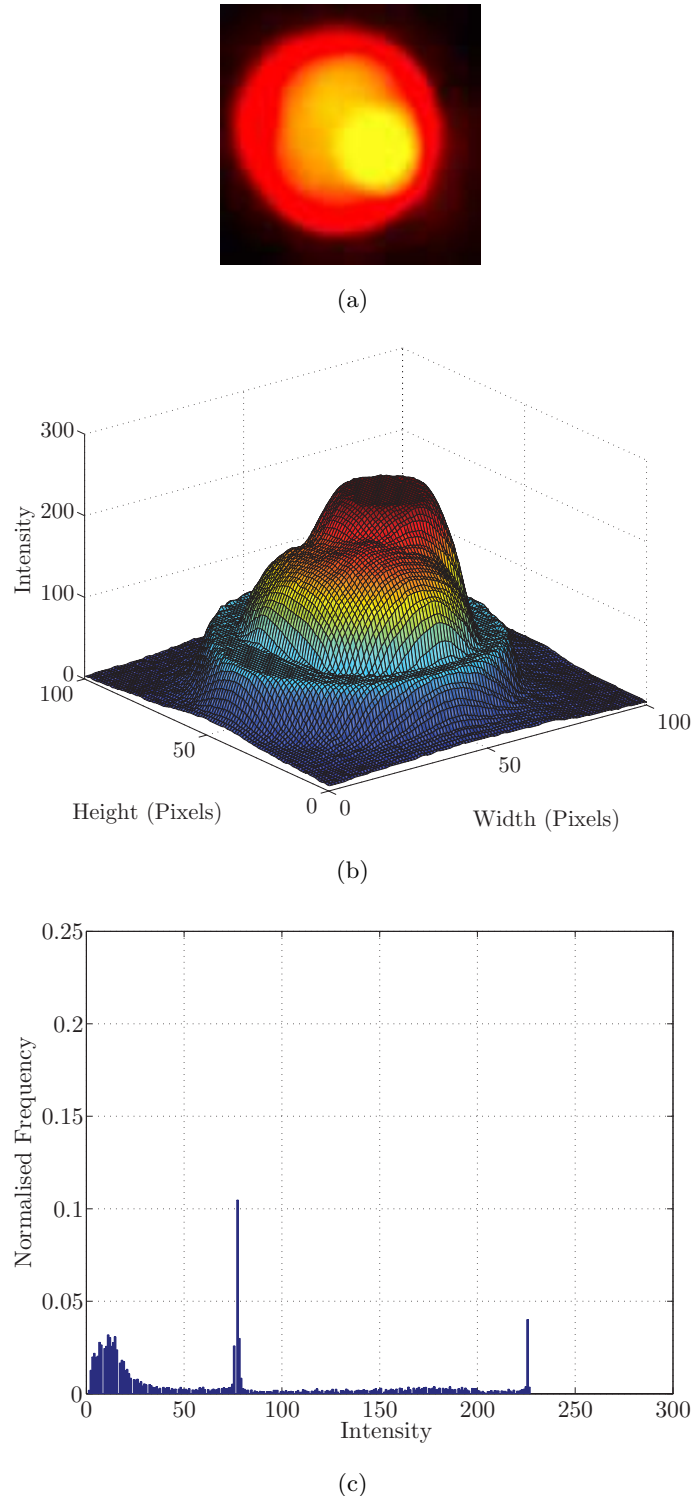


Figure 3.21: LED calibration analysis with 15V supply: (a) image of LED output; (b) intensity plot of LED output; and, (c) histogram of LED output intensity.

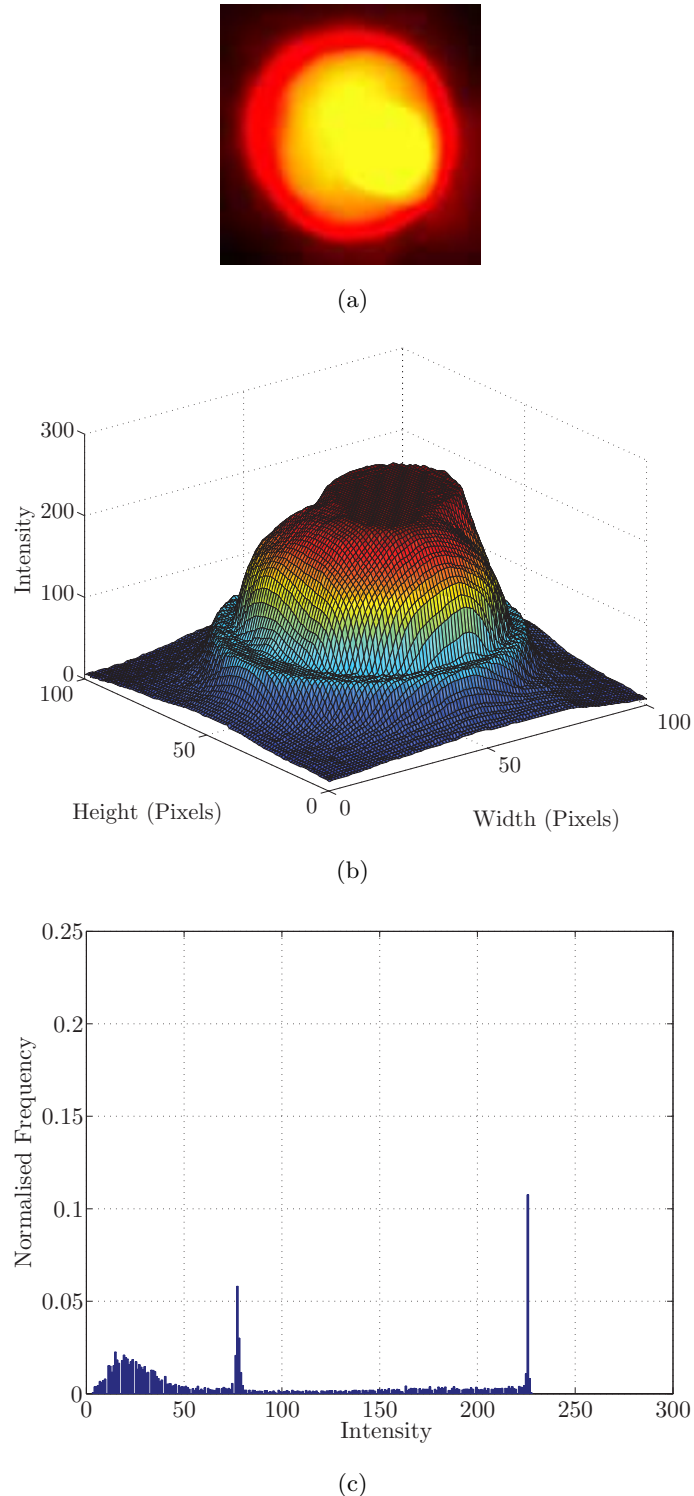


Figure 3.22: LED calibration analysis with 17V supply: (a) image of LED output; (b) intensity plot of LED output; and, (c) histogram of LED output intensity.

indicates that there is a very narrow range of intensities emitted by the LED and PIV analysis would therefore be susceptible to errors due to the lack of contrast.

In comparison Figure 3.22(a) shows a very brightly lit LED when supplied with 17V DC, with maximal intensity of about 228 indicated by the light intensity plot in Figure 3.22(b). The light intensity histogram in Figure 3.22(c) shows the much improved range of intensity generated by the higher supply voltage and as a result the differential movement between the camera and control points ought to be more accurately measured by PIV. However, close study of Figure 3.22(a) shows that there is significant excess light emitted by the LED that may cause ‘contamination’ of data recorded on the plane of interest at the center of the test chamber.

Figure 3.21(a) indicates that this light flaring at the periphery of the LED is reduced when the supply voltage is reduced to 15V DC without compromising the maximum intensity, indicated in Figure 3.21(b). The intensity range illustrated by Figure 3.21(c) shows that even with this reduction in supply voltage the range of intensities remains unchanged and the distribution of intensity becomes more even. Thus the contrast produced by the LED at the 15V DC supply voltage is increased, and hence this was the supply voltage used for testing. Analysis of the effectiveness of PIV tracking of control point movement is covered in Section 4.2.1.2 of Chapter 4.

3.5.2 Pile Driving Rig

Calibration of the pile driving rig was conducted by supplying a voltage to each stepper motor controller using the DAQ and then measuring the corresponding velocity by observing the time taken to drive a chosen vertical distance or complete a finite number of revolutions. This was accomplished in 0.25V increments with three repeats per supply voltage and observation of the vertical drive distances and number of rotations for between 30 and 160 seconds.

From these observations the velocities for both vertical and rotational drives were calculated in mm/s and rps respectively allowing equations to be fitted to describe each relationship. These could then be used in programming the pile-driving rig control software to convert required velocities to the appropriate output voltages required by the stepper motor controllers. Sections 3.5.2.1 and 3.5.2.2 explain the choice of relationship chosen to achieve this. Unlike the transducer calibrations signal drift was not envisaged to be problematic since the DAQ supplies a regulated

voltage output and is not reliant upon any external amplification. Hence a repeat calibration such as those conducted for all strain-gauge based transducers at the end of the test schedule was deemed unnecessary.

3.5.2.1 Vertical Drive

Figure 3.23(a) is a plot of the vertical drive calibration data, showing supply voltage versus measured velocity with linear, second order and third order equations fitted to the data using the method of least squares. Figure 3.23(b) shows the corresponding residual error for each of these relationships indicating that the relationship deviates from linearity at the extreme supply voltages around zero and five volts. The mean and standard residual errors for each order of calibration relationship are presented in Table 3.4.

The errors reduce considerably when using a higher order calibration relationship so for this reason a cubic relationship, as presented in Equation 3.1, with a correlation coefficient of 0.99, has been utilised to convert required velocities to suitable DAQ output voltages for the vertical drive system.

$$\text{Velocity (mm/s)} = -0.0018V^3 + 0.0081V^2 + 0.3448V - 0.0147 \quad (3.1)$$

3.5.2.2 Rotational Drive

Similarly, Figures 3.24(a) and 3.24(b) show the calibration data, fitted calibration relationships and residual errors for the rotational drive. The mean and standard residual errors are presented in Table 3.5, demonstrating that the use of a higher order calibration relationship was also highly beneficial in this case.

A cubic relationship was used to convert the required velocities to suitable DAQ output voltages for the rotational drive system. Equation 3.2 presents the calibration relationship used, yielding a correlation coefficient of 0.99:

$$\text{Velocity (rps)} = -0.0009V^3 + 0.0065V^2 + 0.0612V - 0.0119 \quad (3.2)$$

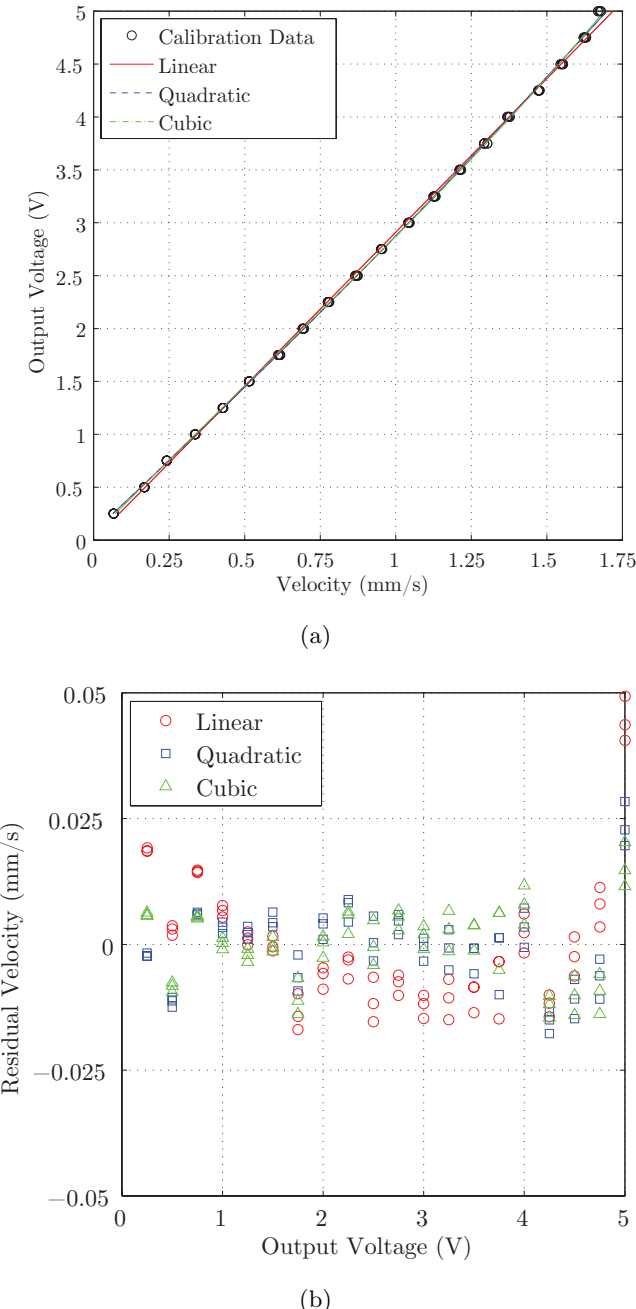


Figure 3.23: Vertical drive: (a) calibration and first, second and third order polynomial fit; and, (b) corresponding residual errors.

Table 3.4: Vertical drive calibration error.

Calibration Relationship	Mean Residual Error (mm/s)	Standard Deviation (mm/s)
Linear	0.0100	0.0139
Quadratic	0.0063	0.0086
Cubic	0.0060	0.0075

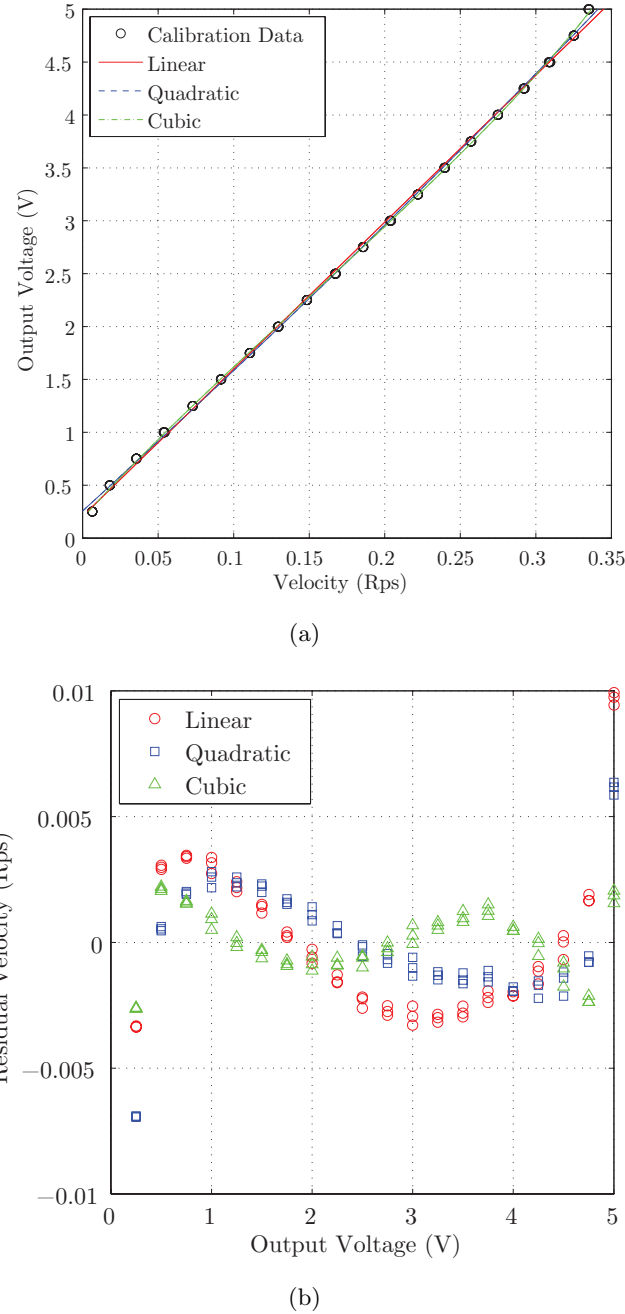


Figure 3.24: Rotational drive: (a) calibration and first, second and third order polynomial fit; and, (b) corresponding residual errors.

Table 3.5: Rotational calibration error.

Calibration Relationship	Mean Residual Error (rps)	Standard Deviation (rps)
Linear	0.0025	0.0032
Quadratic	0.0019	0.0026
Cubic	0.0010	0.0013

3.5.3 Transducers

Calibration of the transducers first entailed setting the excitation voltage, gain and center on all S7DC transducer signal amplifiers such that the output of the transducer at the extremes of the range of each transducer was about $\pm 5V$. This ensured that the maximum resolution of the DAQ was utilised during data capture. Due to EMF interference from the stepper motor drive system, as outlined in Section 3.4.2, it was important to perform all calibrations whilst the drive system was energised such that the accuracy and precision of the calibrations were representative of the data capture system during testing.

One concern with the test system assembled, where separate transducer amplifiers and DAQ were used, was that drift in the signal amplification may cause the residual errors generated for each transducer to become larger with time. To check this the calibration process was conducted twice, once before the test schedule commenced and once upon its completion, so that transducer calibration drift could be assessed. Sections 3.5.3.1 to 3.5.3.3 outline the methodologies and results of the calibrations conducted for the transducers.

3.5.3.1 Load Cell

Due to the low capacity of the load-cell and both its compressive and tensile capacity, traditional calibration using a dead weight tester was not possible. Instead a series of 4 *kg* weights was added to a hanger system attached to the load-cell whilst installed on the energised pile-driving rig for tensile loading and with the load cell fixed to the frame with the hanger system inverted during compressive loading. The self-weight of the load-cell was considered in both cases, with measurement of the load-cell, hanger system and laboratory weight masses conducted to $\pm 1.0g$ using a digital mass balance. The calibration process entailed first loading the load-cell to the two compressive and tensile extremes of its range in two cycles whilst checking the gain of the transducer signal amplifier was appropriate. Loads were then applied in 4 *kg* increments up to a maximum loading of about 24 *kg* in compression and tension in two cycles. The signal from the transducer was then recorded for a period of one minute per increment and cycle to generate the initial (03/2009) and repeat (04/2010) calibration datasets presented in Figure 3.25.

The initial calibration (03/2009) was suitably linear and a first order relationship was fitted to generate the relationship in Equation 3.3, with a correlation coefficient of

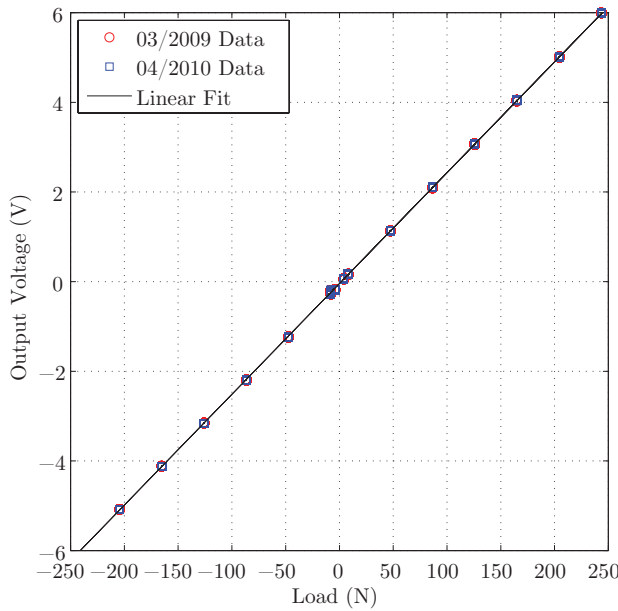


Figure 3.25: Load cell calibration.

0.99. The mean residual error was $0.5411N$ and the standard deviation was $0.7021N$. The mean residual error is a little over the quoted accuracy of the transducer of $\pm 0.3N$ (see Section 3.3.6.1) but this can be attributed mainly to the noise caused by EMF interference from the stepper motor drive system and in any case was deemed adequate. Higher order calibration relationships did not significantly improve the residual errors due to the random nature of the interference.

$$\text{Load } (N) = 40.4457V + 1.6930 \quad (3.3)$$

The calibration check (04/2010) conducted after completion of the test schedule was used to recalculate the residual errors. The mean residual error was $0.6203N$ and the standard deviation was $0.7713N$. This suggests that some minor drift had occurred during the period of the investigation and is possibly a product of voltage fluctuation from the PSU used to power the transducer signal amplifiers. However, the correlation coefficient was not affected as it remained 0.99. Therefore, the effect in this instance was not overly significant, since a change in mean residual error of $0.08N$ is equal to 0.02% of the quoted range of the transducer of $\pm 200N$. Therefore the calibration relationship in Equation 3.3 was used for all analyses.

3.5.3.2 LVDT

The LVDT used to measure pile head displacement was calibrated using a Mitutoyo Corporation digital micrometer calibrator. The LVDT was fixed to the calibrator frame and taken through two full range cycles to check the gain of the transducer signal amplifier. The calibration was then conducted in 2.5mm increments, set to a resolution of 0.001mm using the digital output of the calibrator, over two full cycles, whilst recording data for one minute for each increment in each cycle. Figure 3.26 shows the initial (03/2009) and repeat (04/2010) calibration data along with a linear calibration relationship fitted using the least squares method to the initial calibration (03/2009).

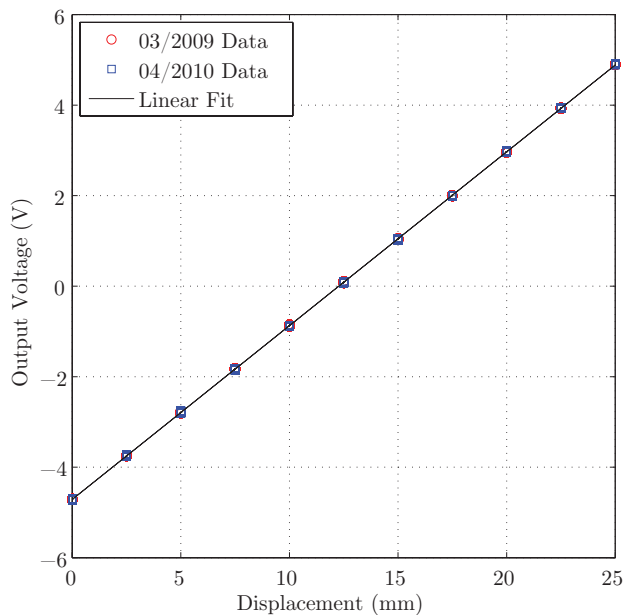


Figure 3.26: 25 mm LVDT calibration.

$$\text{Displacement (mm)} = 2.6038V + 12.2712 \quad (3.4)$$

The linear relationship in Equation 3.4 generated a correlation coefficient of 0.99, with residual mean error of 0.0201mm and standard deviation of 0.0290 mm . These compare favourably with the quoted accuracy of the transducer of $\pm 0.025\text{mm}$ (see Section 3.3.6.2) and thus it was deemed unnecessary to use higher order calibration relationships. Drift of the transducer signal was checked using a set of data captured

upon completion of the testing schedule (04/2010) using the same methodology, which yielded a mean error of $0.0235mm$ and standard residual error of $0.0356mm$ and the correlation coefficient remained 0.99. Thus signal drift was not significant, as the mean residual error drifted by only $0.0034mm$, which equates to 0.014% of the range of the LVDT. Hence the initial calibration was maintained in the analysis of all datasets.

3.5.3.3 Draw-wire LVDT

Ideally a draw-wire LVDT would be calibrated over its full range using a dedicated device, but since no such device was available a staged calibration methodology was developed. This involved using the pile-driving rig in conjunction with a $50mm$ LVDT. With the draw-wire LVDT installed on the pile-driving rig and the cantilever arm at its uppermost position, calibration was conducted in increments of about $50mm$ to the accuracy of the $50mm$ LVDT. Before the calibration commenced both the draw-wire LVDT and $50mm$ LVDT were cycled through two full displacement cycles. The calibration itself entailed taking simultaneous measurements for a period of one minute from both transducers in the initial position (draw-wire LVDT fully extended and $50mm$ LVDT almost fully depressed), before moving the cantilever arm vertically downwards by about $50mm$, without leaving the range of the $50mm$ LVDT. A second set of measurements was then taken at this point for one minute, before moving the LVDT bracket mount such that the $50mm$ LVDT became almost fully depressed once again, after which a third set of measurements was taken for the same time period. This process was repeated over the full range of draw-wire LVDT.

Analysing the calibration data entailed firstly calibrating the $50mm$ LVDT using the same calibrator and process as described in Section 3.5.3.2, generating the calibration dataset (03/2009) and linear calibration relationship in Figure 3.27. Equation 3.5 is the linear calibration relationship which had a correlation coefficient of 0.99, indicating a suitably linear relationship. The mean residual error was 0.0605 mm and the standard deviation was 0.0942mm . Accuracy was favourably comparable with the quoted accuracy of the transducer of $\pm 0.15\%$ of the range, or $\pm 0.6\text{mm}$.

$$\text{Displacement (mm)} = 5.2329V + 26.0577 \quad (3.5)$$

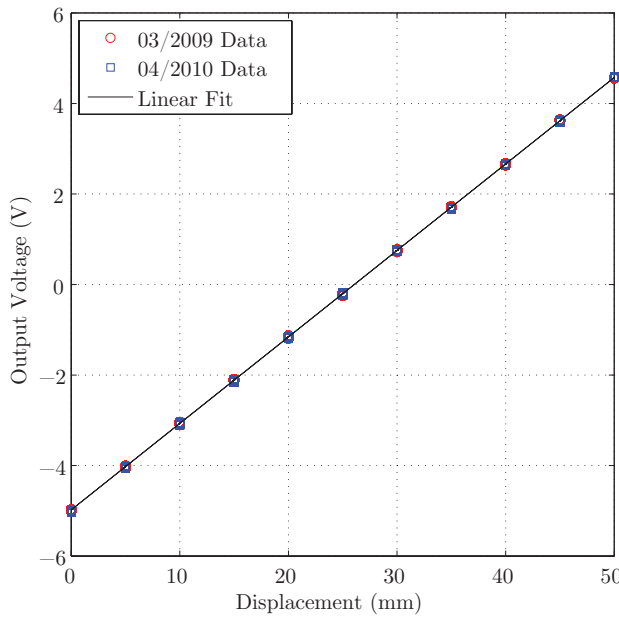


Figure 3.27: 50 mm LVDT calibration.

A repeat calibration (04/2010) was conducted, giving a mean residual error of 0.0696mm and standard residual error of 0.0896mm when analysed using the original calibration relationship (Equation 3.5), demonstrating that the mean drift was 0.0091mm or 0.02% of the range of the transducer and thus is reasonably insignificant. Therefore, the original calibration relationship was used in both the initial and repeat calibration of the draw-wire transducer.

Using the calibration for the 50mm transducer, the voltages recorded were converted to displacements using a MATLABTM routine that utilised logic to determine the positions of the 50mm LVDT (extended or depressed) and compute a summation of the displacements from each increment of the calibration process. This generated a plot of cumulative displacement and corresponding voltage output from the draw-wire LVDT shown in Figure 3.28 and yielded the linear relationship in Equation 3.6. The corresponding correlation coefficient was 0.99.

$$\text{Displacement (mm)} = -30.8054V + 154.6489 \quad (3.6)$$

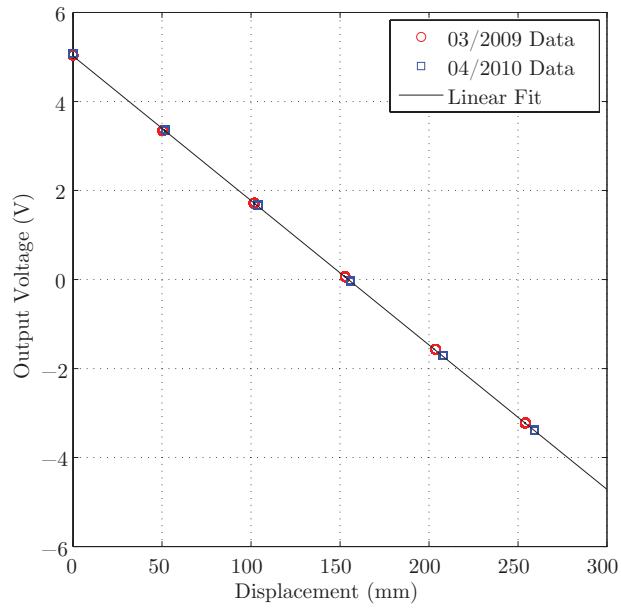


Figure 3.28: Draw-wire LVDT calibration.

The mean residual error of the initial calibration (03/2009) was 0.5384mm and the standard deviation was 0.6474mm . This is slightly greater than the quoted accuracy of $\pm 0.45\text{ mm}$ but in any case was deemed adequate. Drift was checked upon completion of the testing schedule with a repeat calibration (04/2010), where the mean residual error was 0.6751mm and the standard deviation was 0.6893mm when using the original calibration relationship (Equation 3.6), which equates to a mean drift of 0.14mm or 0.025% of the range of the transducer, demonstrating that drift was not particularly significant over the duration of the test schedule.

3.6 Sample Preparation

Transparent synthetic soil slurry was created by mixing the aggregate, fumed amorphous silica, and matched RI pore fluid. After initial mixing the slurry typically contained a large volume of entrained air. This was subsequently removed prior to consolidation under vacuum. The apparatus required to achieve this consisted of the test chamber, porous plastic filters, consolidation piston, whisk, spatula, palette knife, four 10l mixing buckets, petri dishes, vacuum chamber, vacuum pump and measuring cylinders shown in Figure 3.29. Before use the cleanliness and dryness of all this apparatus needs to be checked as any contamination with water causes serious degradation of transparency of the resulting material.

The volume of slurry required to create a 200mm (W) by 200mm (D) by 220mm (H) sample was mixed in four parts, two seeded with Timiron and two unseeded batches, which were mixed in 10 l plastic buckets in the proportions summarised in Table 3.6. The pore fluid was mixed in the proportion of 77:23 of white oil:paraffin oil, as this was the optimum oil ratio. The fumed amorphous silica content was 6% by mass compared to the pore fluid and correspondingly the Timiron seeding proportion was 0.02% by mass compared to the fumed silica content. The seeding proportion was chosen due to positive results found during calibration of GeoPIV as demonstrated in Chapter 4 and because it was the proportion predominantly used successfully in previous investigations (Hird et al., 2008; Ni et al., 2010).



Figure 3.29: Soil mixing and de-airing apparatus.

The mineral oil components were measured using measuring cylinders and the fumed amorphous silica and Timiron using appropriately accurate mass balances. After each of the components was measured the slurry was mixed by hand using a whisk

Table 3.6: Transparent synthetic soil mix proportions per batch of material (two of each being required for each model).

Batch	Seeded	Non-seeded
Risella Oil Volume (<i>ml</i>)	4446.75	4023.25
Paraffin Oil Volume (<i>ml</i>)	1328.25	1201.75
Fumed Silica (<i>g</i>)	286.13	259.19
Timiron (<i>g</i>)	0.0572	0

until the Timiron was well dispersed within the seeded batches and all the fumed amorphous silica was completely wetted with oil for all batches. This generated a three phase material containing fumed amorphous silica, pore fluid of matched RI and entrained air with differing RI. Hence the mixture at this stage was translucent rather than transparent. To maximise transparency a vacuum pump and chamber was used to remove the air from the mixture. The vacuum chamber consisted of a 300mm diameter stainless steel cylinder with sealed end plates, the lower end plate permanently bolted closed and the upper with a seal generated and maintained by the applied vacuum. Each batch was de-aired for a period of one hour or until the sample was completely devoid of visible entrained air.

Upon completion of mixing and de-airing the four batches of material were poured into the test chamber. To minimise the entrainment of air during this process the test chamber was tilted during pouring. To ensure that a planar interface between seeded and non-seeded material was present in the consolidated sample a sheet aluminium divider was used to keep the two types of material separate until equal volumes were poured and the sheet aluminium divider was removed. Figure 3.30 shows the sheet aluminium divider in position before pouring of the slurry and during removal after pouring. The sheet aluminium divider segregates the test chamber such that the rearward 52.5% of the sample was seeded and the foremost 47.5% of the sample was unseeded.

Before pouring of the slurry a small volume of pore-fluid was poured into the base of the test chamber and drainage allowed to ensure saturation of the system. The drainage line was then closed before the soil slurry was poured into the test chamber in four batches in alternating order: seeded followed by unseeded. This ensured that minimal flow of slurry occurred around the sheet aluminium divider.

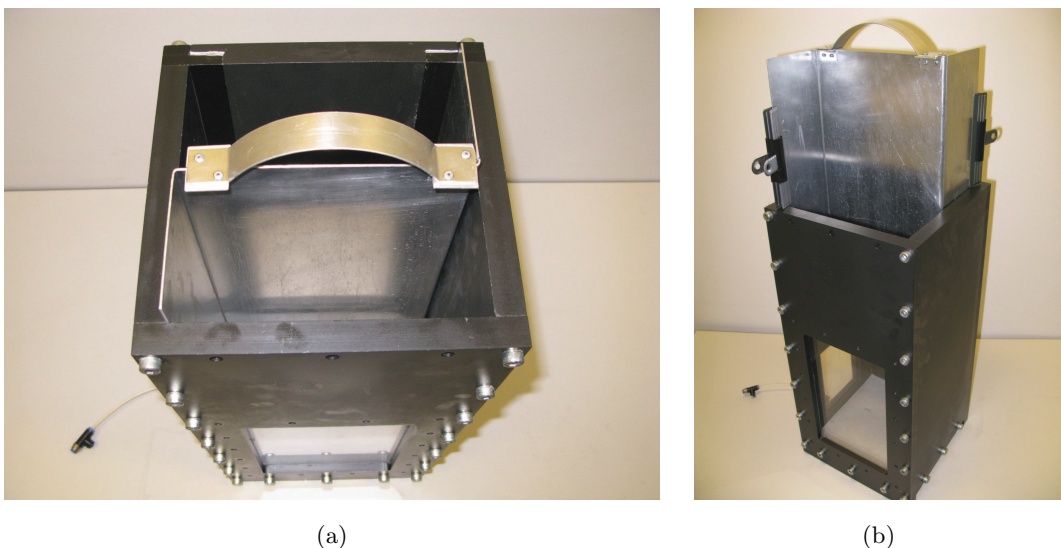


Figure 3.30: Sheet aluminium divider: (a) installed prior to pouring of slurry; and, (b) during removal after pouring of slurry.

The total internal volume of the test chamber was about 20 litres and since the total volume of slurry poured was about 22 litres, pouring was conducted in stages, allowing intermediate drainage of pore fluid from the base of the test chamber to achieve consolidation under gravity similar to the procedure adopted by Gill (1999). This enabled all slurry to be poured into the sample before removal of the sheet aluminium divider and application of surcharge. It was observed that during this consolidation under gravity stage the volume of pore fluid drained off in a 72 hour period was as much as 30% of the total pore fluid content. To improve the sustainability of the investigation all pore-fluid drained off during consolidation was collected and recycled in subsequent samples.

Consolidation under gravity was allowed until all the slurry was poured into the test chamber with sufficient clearance that the consolidation piston could be lowered into the test chamber, without spillage of material over the sides of the test chamber. Upon completion of pouring and consolidation under gravity, the drainage line at the base of the sample was closed so that during removal of the sheet aluminium divider, no air would be pulled into the sample through the drainage line by any suction generated. Removal of the sheet aluminium divider was conducted in stages using Bulldog™ clips to hold it in an elevated position (see Figure 3.30(b)), allowing a palette knife to be used to remove material stuck to the sheet aluminium divider, thus minimising wastage of material.

Once the sheet aluminium divider was completely removed the upper porous plastic filter was placed above the slurry and the reinforcement plates were installed onto the two viewing windows. The mass of slurry remaining in the mixing containers, on all mixing apparatus and the sheet aluminium divider was measured such that the volume of slurry inside the test chamber before consolidation was known and a percentage loss could be calculated. This was later used to estimate the void ratio of the consolidated soil.

3.6.1 Consolidation

To begin the consolidation process the test chamber was installed in the consolidation frame. The consolidation piston was then lowered carefully into position inside the test chamber until contact with the slurry surface was achieved. The draw-wire LVDT was then mounted on the upper consolidation frame plate and the draw-wire attached to the consolidation piston. Upper and lower drainage lines were then connected using push-fittings and a drainage reservoir provided in the form of a 25l plastic barrel, allowing collection of drained pore-fluid and recycling of pore fluid in later tests. More than 50% of the pore-fluid could be recycled in this way, significantly reducing the total volume of oil required for a given number of samples and the total environmental impact of disposal. No degradation in transparency was observed by recycling the pore fluid. To minimise the risk of drying of the surface of the sample a layer of pore fluid was added to the top of the sample above the consolidation piston. Consolidation was then commenced following the schedule outlined in Table 3.7. Thus the test schedule was run on a three week cycle.

This schedule was designed to take advantage of natural breaks imposed by weekends by allowing the sample to be either consolidating under gravitational loading, consolidating at 100kPa or resting at 0kPa over each weekend period. Slow unloading of the sample, using the same pressures (in reverse) as the consolidation stages, ensured that minimal air was drawn into the sample during unloading. Unacceptable air entrainment was observed in an early test sample, shown in Figure 3.31, where air was thought to have entered the sample through the viewing window seals due to unloading being too rapid.

Table 3.7: Consolidation and unloading stages.

Week	Day	Pressure (kPa)
1	Friday	0.0
	Saturday	0.0
	Sunday	0.0
	Monday	6.25
	Tuesday	12.5
	Wednesday	25.0
	Thursday	50
2	Friday	100
	Saturday	100
	Sunday	100
	Monday	50
	Tuesday	25.0
	Wednesday	12.5
	Thursday	6.25
3	Friday	0.0
	Saturday	0.0
	Sunday	0.0
	Monday	0.0
	Tuesday	0.0
	Wednesday	Testing
	Thursday	Testing



Figure 3.31: Air entrainment caused by swift unloading of consolidation pressures.

3.6.1.1 Results

Figures 3.32 to 3.36 are typical plots of the consolidation process taken from consolidation of the sample used for test C1 over the five increments from $0kPa$ to $100kPa$, plotted against the square root of time in minutes. Also shown is the graphical derivation of the coefficient of consolidation (c_v) using Taylor's method, where a routine created in MATLABTM was used to perform the graphical construction required. The coefficient of consolidation was then derived using Equation 3.7.

$$c_v = \frac{T_{v90} \cdot \bar{d}^2}{\sqrt{t_{90}}} \quad (3.7)$$

$$\bar{d} = \frac{h_0 + h_f}{4} \quad (3.8)$$

where t_{90} is the time at which 90% consolidation had occurred, T_{v90} is the time factor at 90% average degree of consolidation which is equal to 0.848, \bar{d} is the average drainage path length for the consolidation increment and h_0 and h_f are the sample heights at the start and completion of the consolidation increment. Table 3.8 contains the coefficient of consolidation derived for all five consolidation increments for all fourteen samples tested. The 'C' (compressive loading) and 'T' (tensile loading) series of tests were introduced previously in Section 3.3.5. The 'F' series refers to footing tests conducted to assist in the derivation of the stress-strain response of the transparent synthetic soil (see Chapter 6) and all 'R' suffixes refer to repeat tests performed to assess the repeatability of the modelling process.

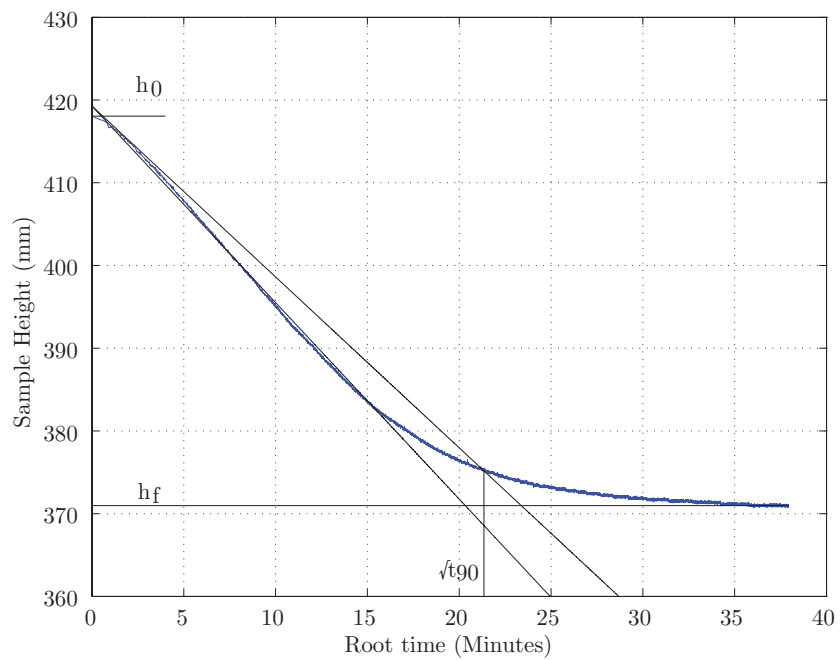


Figure 3.32: Consolidation plot for 0.0kPa to 6.25kPa increment expressed in terms of displacement.

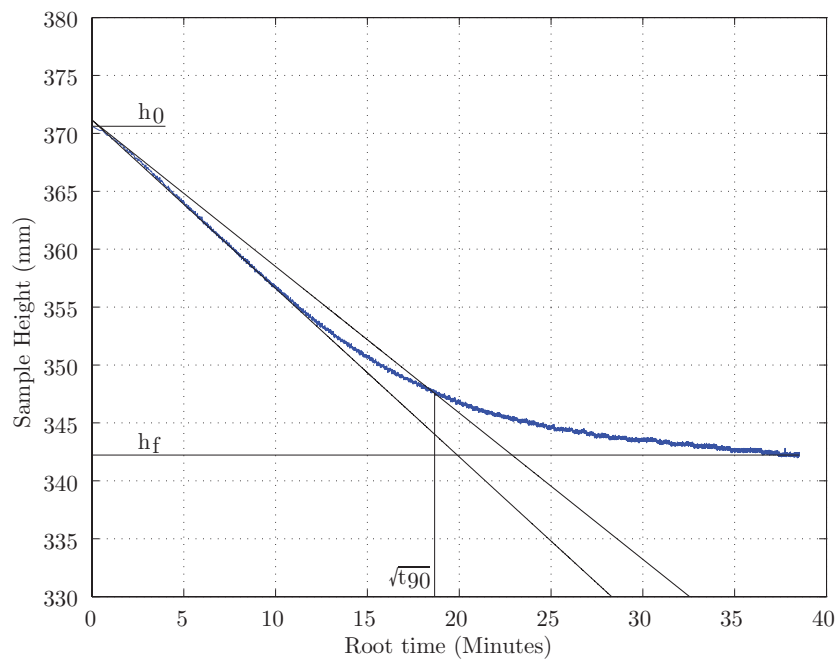


Figure 3.33: Consolidation plot for 6.25kPa to 12.5kPa increment expressed in terms of displacement.

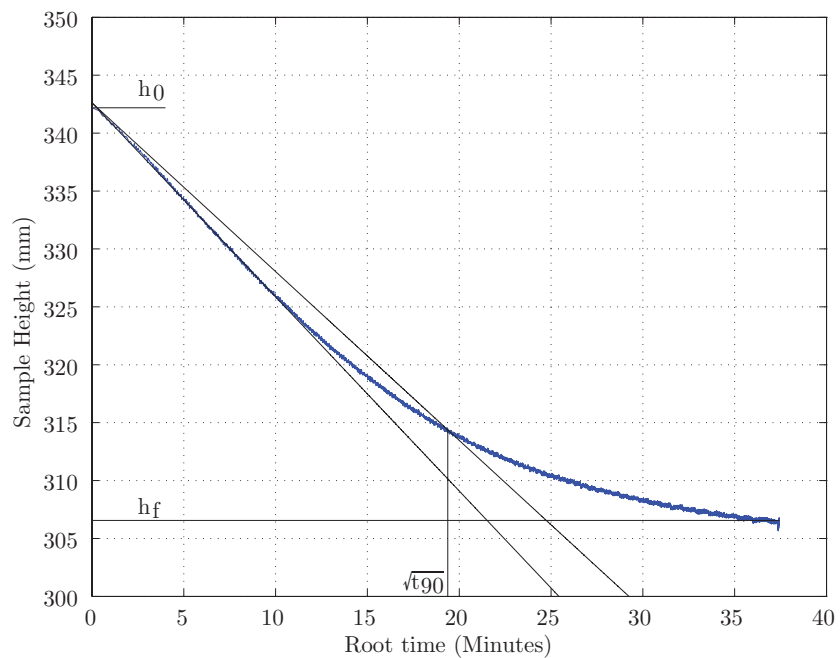


Figure 3.34: Consolidation plot for 12.5kPa to 25.0kPa increment expressed in terms of displacement.

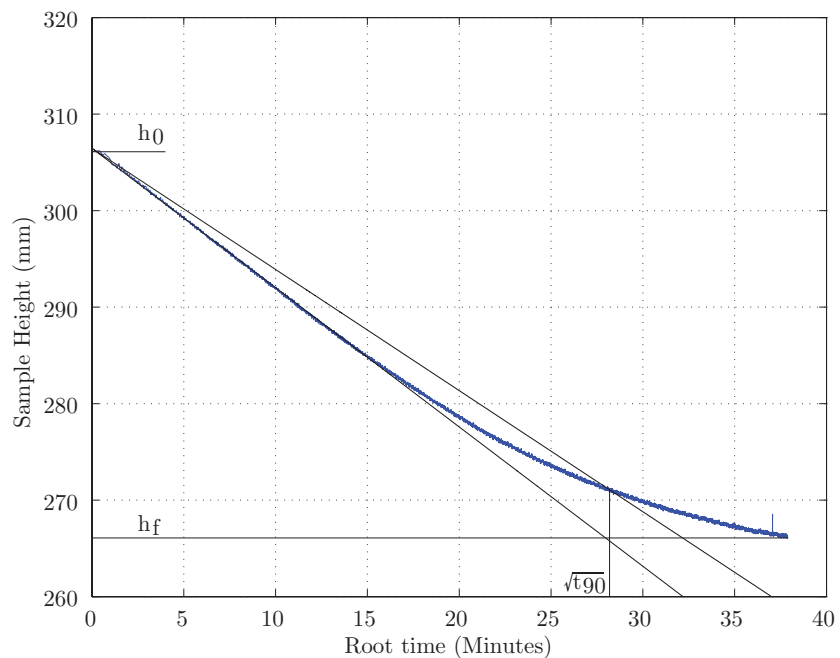


Figure 3.35: Consolidation plot for 25.0kPa to 50.0kPa increment expressed in terms of displacement.

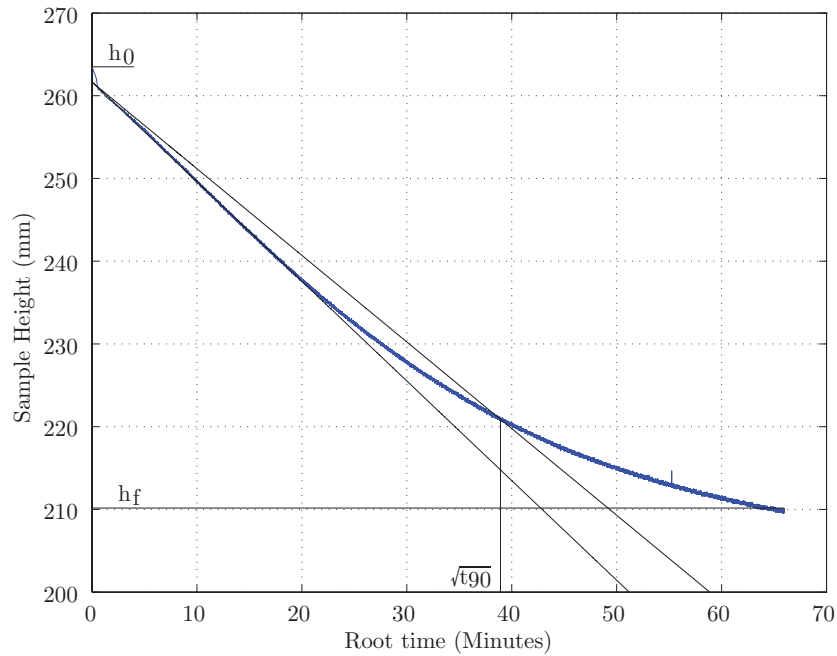


Figure 3.36: Consolidation plot for 50.0kPa to 100.0kPa increment expressed in terms of displacement.

Table 3.8: Summary of coefficients of consolidation, c_v , expressed in m^2/year , derived for all consolidation increments and all samples tested during the investigation.

Test	Consolidation Increment (kPa)				
	0.0-6.25	6.25-12.5	12.5-25.0	25.0-50.0	50.0-100.0
C1	41.94	40.74	29.75	12.40	4.05
C2-30	64.39	55.13	38.60	15.84	4.41
C2-60	92.23	53.78	39.39	16.60	4.84
C3	58.07	49.15	24.42	13.47	2.85
T1	24.20	27.36	21.07	8.75	3.32
T2-30	37.16	54.08	26.04	22.02	4.43
T2-60	112.17	40.39	29.50	14.14	3.63
T3	62.81	46.74	28.69	15.54	4.04
F	137.22	31.83	28.50	13.91	4.11
F-R	107.88	39.67	36.25	19.01	4.14
C1-R	122.71	59.97	38.14	11.64	3.80
C3-R	154.75	42.95	45.10	20.42	4.65
Standard Deviation	42.44	9.83	7.21	3.80	0.56
Range	130.56	32.61	24.02	13.27	1.98
Mean	84.63	45.15	32.12	15.31	4.02

3.6 Sample Preparation

From the same data the coefficient of compressibility (m_v) can be derived:

$$m_v = \frac{h_0 - h_f}{h_0} \cdot \frac{1}{\sigma_f - \sigma_i} \quad (3.9)$$

where σ_i and σ_f are the initial and final pressures for the consolidation increment. Table 3.9 contains a summary of m_v values for all samples generated.

Table 3.9: Summary of coefficients of compressibility, m_v , expressed in m^2/kN , derived for all consolidation increments and all samples tested during the investigation.

Test	Consolidation Increment (kPa)				
	0.0-6.25	6.25-12.5	12.5-25.0	25.0-50.0	50.0-100.0
C1	1.80E - 02	1.23E - 02	8.30E - 03	5.20E - 03	4.00E - 03
C2-30	1.67E - 02	9.80E - 03	7.00E - 03	5.30E - 03	4.10E - 03
C2-60	2.90E - 02	9.90E - 03	6.40E - 03	5.70E - 03	3.90E - 03
C3	2.63E - 02	1.17E - 02	8.20E - 03	5.10E - 03	4.00E - 03
T1	6.40E - 02	9.90E - 03	7.50E - 03	5.30E - 03	4.20E - 03
T2-30	1.86E - 02	9.82E - 03	8.12E - 03	4.98E - 03	3.98E - 03
T2-60	2.17E - 02	1.73E - 02	7.30E - 03	5.10E - 03	3.90E - 03
T3	2.28E - 02	1.02E - 02	7.60E - 03	5.10E - 03	4.00E - 03
F	2.22E - 02	1.04E - 02	7.70E - 03	5.20E - 03	4.10E - 03
F-R	2.69E - 02	1.32E - 02	7.30E - 03	5.00E - 03	3.80E - 03
C1-R	2.30E - 02	9.48E - 02	7.16E - 03	5.10E - 03	3.85E - 03
C3-R	3.00E - 02	9.03E - 02	6.66E - 03	4.98E - 03	3.75E - 03
Standard Deviation	6.43E - 03	2.32E - 3	5.94E - 04	2.00E - 04	1.32E - 04
Range	2.36E - 02	8.27E - 03	1.90E - 03	7.23E - 04	4.51E - 04
Mean	2.18E - 02	1.11E - 02	7.44E - 03	5.17E - 03	3.96E - 03

Once c_v and m_v have been derived the hydraulic conductivity (k) can be estimated:

$$k = c_v \cdot m_v \cdot \gamma_l \quad (3.10)$$

where γ_l is the unit weight of the pore fluid, calculated knowing the density of the pore fluid (ρ_f - see Table 3.11). Table 3.10 contains a summary of the hydraulic conductivity values derived from each sample consolidated.

Upon completion of consolidation and unloading, the final height of the sample was measured, allowing calculation of an estimate of the void ratio of the sample using

Table 3.10: Summary of hydraulic conductivity, k , expressed in m/s , derived for all consolidation increments and all samples tested during the investigation.

Test	Consolidation Increment (kPa)				
	0.0-6.25	6.25-12.5	12.5-25.0	25.0-50.0	50.0-100.0
C1	$1.93E - 07$	$1.27E - 07$	$6.31E - 08$	$1.65E - 08$	$4.20E - 09$
C2-30	$2.74E - 07$	$1.37E - 07$	$6.89E - 08$	$2.12E - 08$	$4.60E - 09$
C2-60	$6.83E - 07$	$1.36E - 07$	$6.42E - 08$	$2.42E - 08$	$4.80E - 09$
C3	$3.89E - 07$	$1.47E - 07$	$5.10E - 08$	$1.74E - 08$	$2.90E - 09$
T1	$3.94E - 08$	$6.91E - 08$	$4.04E - 08$	$1.17E - 08$	$3.56E - 09$
T2-30	$1.76E - 07$	$1.35E - 07$	$5.39E - 08$	$2.79E - 08$	$4.49E - 09$
T2-60	$6.19E - 07$	$1.78E - 07$	$5.50E - 08$	$1.83E - 08$	$3.60E - 09$
T3	$3.55E - 07$	$1.27E - 07$	$6.97E - 08$	$2.18E - 08$	$4.00E - 09$
F	$7.76E - 07$	$8.45E - 08$	$5.59E - 08$	$1.83E - 08$	$4.30E - 09$
F-R	$7.39E - 07$	$1.34E - 07$	$6.71E - 08$	$2.43E - 08$	$4.02E - 09$
C1-R	$7.21E - 07$	$1.45E - 07$	$6.96E - 08$	$1.53E - 08$	$3.73E - 09$
C3-R	$1.18E - 06$	$9.88E - 08$	$7.65E - 08$	$2.59E - 08$	$4.44E - 09$
Standard Deviation	$3.29E - 07$	$2.95E - 08$	$1.02E - 08$	$4.82E - 09$	$5.36E - 10$
Range	$1.14E - 06$	$1.09E - 07$	$3.62E - 08$	$1.62E - 08$	$1.90E - 09$
Mean	$5.12E - 07$	$1.27E - 07$	$6.13E - 08$	$2.02E - 08$	$4.05E - 09$

the percentage loss estimate discussed in Section 3.6. The loss is expressed as a percentage of the total mass of slurry mixed. To calculate the total mass of slurry mixed the volume of each oil was multiplied by its measured density which can be found in Table 3.11. The density of each pore fluid constituent and the matched RI blended pore fluid was derived by measuring the mass of a control volume of fluid. The density of fumed silica assumed was taken from the material data sheet provided by the supplier. The discrepancy between the measured density of the matched RI pore fluid and its theoretical density, calculated using the experimentally derived densities of the two constituent oils, was less than 0.9%. The percentage loss and final consolidated bed heights are summarised in Table 3.12.

Table 3.11: Measured and assumed component densities.

Material	Density (kg/m^3)
White Oil	845.48
Paraffin Oil	764.24
Matched RI Pore Fluid	819.32
Fumed Silica	2200.00

The standard deviation of the final sample heights was $1.04mm$, the range was $3.20mm$ and the percentage range of sample height with respect to the target sample height was 1.45%. The target sample height ($220mm$) was exceeded in all cases.

Table 3.12: Percentage slurry loss and final consolidated sample heights.

Test	Mass Slurry Loss (g)	Percentage Loss ($\%_{loss}$)	Final Height (mm)
C1	268.7	1.53	220.8
C2-30	247.7	1.41	221.2
C2-60	287.0	1.63	221.4
C3	260.2	1.48	221.0
T1	241.1	1.37	221.2
T2-30	238.2	1.36	223.1
T2-60	234.5	1.33	221.6
T3	271.4	1.54	220.4
F	341.5	1.94	220.2
F-R	234.4	1.33	222.8
C1-R	258.3	1.47	221.8
C3-R	251.8	1.43	223.4

Generally as the percentage slurry loss increased, the final sample height decreased. From the final heights and percentage losses, the change of void ratio with consolidation pressure was calculated. The mass (m_s) and density (ρ_s) of fumed silica and mass (m_f) and density (ρ_f) of the pore fluid were known during sample preparation. Using the appropriate percentage loss ($\%_{loss}$) for each test in Table 3.12 the mass of fumed silica (m_{scorr}) in the test chamber after slurry pouring was estimated using:

$$m_{scorr} = m_s \cdot \left(\frac{100 - \%_{loss}}{100} \right) \quad (3.11)$$

Hence the volume of solids (V_s) was calculated using:

$$V_s = \frac{m_{scorr}}{\rho_s} \quad (3.12)$$

Due to the test chamber being square on plan it was difficult to achieve an effective seal around the perimeter of the consolidation piston, so during consolidation fluid was left atop the consolidation piston to safeguard against air infiltration into the sample. This meant that measuring the volume or mass drained during consolidation was not possible. For this reason the position of the consolidation piston (H_{consol}) was used to calculate the total volume (V) of the sample at any given stage of consolidation. Hence the volume of pore fluid could be calculated from the total volume of the sample, given that the chamber was 0.2m by 0.2m on plan (W=D=0.2m),

using Equations 3.13 and 3.14 where V_f is the volume of fluids, which is equal to the volume of voids (V_v) given that the soil is saturated, and V_s is the volume of solids.

$$V = H_{consol} \cdot W \cdot D \quad (3.13)$$

$$V_f = V - V_s \quad (3.14)$$

Hence the void ratio (e) was calculated using:

$$e = \frac{V_f}{V_s} \quad (3.15)$$

By doing this it does not matter if fluid egresses from the sample around the consolidation piston seal as it no longer affects the calculation of void ratio. However, it must be assumed that there is no loss of solids through either of the drainage lines, such that the volume of solids is preserved during consolidation, and that the transparent soil components are incompressible.

It would have been possible to determine a final voids ratio by taking a sample of material and measuring its density in a manner similar to that used by Gill (1999) but this was avoided so that the sample was in a completely virgin state prior to testing. Figure 3.37 shows the final void ratio upon completion of each consolidation increment for all tests plotted against consolidation pressure on a logarithmic scale, alongside a mean relationship derived from the average void ratio at each pressure.

From this plot the compression index (C_c) and swelling index (C_s) can be calculated by considering the average slope of the normal consolidation line and swelling line respectively using the relationship in Equation 3.16 where e_0 is the initial void ratio, e_f is the final void ratio, σ_i is the initial pressure and σ_f is the final pressure.

$$C_c \text{ or } C_s = \frac{e_0 - e_f}{\log(\frac{\sigma_f}{\sigma_i})} \quad (3.16)$$

Tables 3.13 and 3.14 contain summaries of the compression index and swelling index for all samples. This produces an average C_c of 10.0 and C_s of 0.530.

Table 3.13: Summary of compression index, C_c , derived for all consolidation increments and all samples tested during the investigation.

Test	Consolidation Increment (kPa)			
	6.25-12.5	12.5-25.0	25.0-50.0	50.0-100.0
C1	7.31	9.70	10.89	14.52
C2-30	5.94	7.98	10.91	14.56
C2-60	6.09	7.32	12.02	13.95
C3	7.22	9.36	10.39	14.15
T1	6.15	8.73	11.06	15.26
T2-30	5.97	9.27	10.20	14.26
T2-60	10.89	8.22	10.33	14.02
T3	6.17	8.66	10.34	14.36
F	6.43	8.86	10.77	14.76
F-R	8.01	8.06	10.11	13.43
C1-R	5.58	7.92	10.26	13.5
C3-R	5.22	7.26	9.93	13.09
Standard Deviation	1.55	0.73	0.57	0.50
Range	4.96	2.38	1.92	1.83
Mean	7.06	8.62	10.70	14.33

Table 3.14: Summary of swelling index, C_s , derived for all consolidation increments and all samples tested during the investigation.

Test	Consolidation Increment (kPa)			
	12.5-6.25	25.0-12.5	50.0-25.0	100.0-50.0
C1	0.341	0.650	0.564	0.405
C2-30	0.585	0.628	0.638	0.372
C2-60	0.490	0.533	0.650	0.298
C3	0.458	0.543	0.458	0.543
T1	0.436	0.595	0.723	0.319
T2-30	0.490	0.875	0.384	0.181
T2-60	0.563	0.542	0.670	0.489
T3	0.298	0.639	0.586	0.373
F	0.531	0.616	0.468	0.223
F-R	0.535	0.428	0.663	0.481
C1-R	0.553	0.818	0.743	0.515
C3-R	0.570	0.652	0.850	0.479
Standard Deviation	0.091	0.122	0.133	0.117
Range	0.287	0.447	0.466	0.361
Mean	0.488	0.626	0.616	0.390

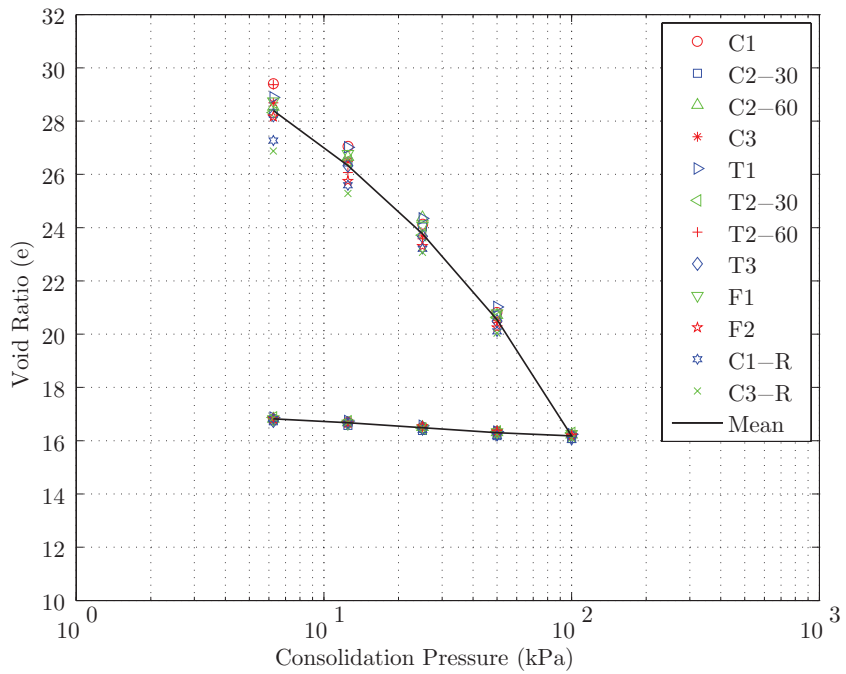


Figure 3.37: Void ratio data derived from consolidation process.

3.6.1.2 Discussion

The consolidation process produced consistent samples due to the care taken in ensuring that the durations used for each stress increment were identical for each sample. However, there is some variation in the void ratios, coefficients of consolidation and compressibility and hydraulic conductivity during the early consolidation stages. This is due to the fact that conducting part of the consolidation process under gravity offers little control.

This lack of control and the range of percentage material loss observed during the series of tests, led to the samples all beginning the consolidation process with differing sample heights. Consequently, some samples exhibited higher initial void ratios, higher coefficients for consolidation and compressibility and higher hydraulic conductivity in the early consolidation stages, before converging with the other samples.

Another possible cause of the variations observed is the potential effect of misalignment of the consolidation piston. Although the consolidation piston was carefully aligned with the test chamber prior to commencement of consolidation, there may have been some variation in the piston friction between different samples. However, the effect of this ought to have dissipated with increasing consolidation pressure, due

to its diminishing magnitude compared to the applied pressure. The variation of parameters in the early consolidation stages is expressed by the significant range in e and increase in standard deviation and range of c_v , m_v and k at low consolidation pressures.

The void ratios obtained in this investigation are similar to those observed by Gill (1999) and McKelvey (2002) as illustrated by Figure 3.38. However, there is a range of void ratios for any given primary consolidation pressure that is difficult to account for. Table 3.15 presents the aspect ratio, diameter:thickness ($D:T$) or width:thickness ($W:T$) for apparatus previously used to measure the consolidation properties of fumed amorphous silica soil compared to that of a typical oedometer. The range of aspect ratio present is one possible explanation for the range of void ratio calculated for a given primary consolidation pressure. High aspect ratios indicate a short and wide sample where sidewall friction would be less prevalent, meaning consolidation may be more extensive over a similar time period. The hypothesis here is that the sidewalls of the chamber reduce the effective stress applied to the aggregates during consolidation, with increasing magnitude with depth from the consolidation piston. Hence, consolidation is decreasingly complete with increasing depth from the consolidation piston. Evidence of the validity of this hypothesis is provided in Chapter 6, where the strength profile is repeatedly shown to reduce with depth in the chamber, indicating that the soil at the bottom of the chamber is less consolidated than that near to the top of the chamber. Further evidence of this has been reported by Black (2007), where comparison of the effective stresses applied by a consolidation piston and measured at the base of kaolin samples indicated that wall friction reduced the effective stress applied with depth during 1D consolidation.

Table 3.15: Comparison of aspect ratio of various consolidation apparatus used in consolidation analyses on fumed silica based transparent synthetic soil.

Apparatus	D/W (mm)	T (mm)	Aspect Ratio ($D/W:T$)
Typical Oedometer	75	20	3.75 : 1
Current Investigation	200	480	0.42 : 1
Rowe Cell - McKelvey (2002)	150	200	0.75 : 1
Shear Box - Gill (1999)	60	40	1.50 : 1
Test Chamber - Gill (1999)	180	800	0.23 : 1

The test chamber based consolidation test performed by Gill (1999) had the smallest aspect ratio of 0.23:1 and exhibited the largest void ratio at a primary consolidation pressure of 100kPa at around 18.4. The test chamber used in this investigation had

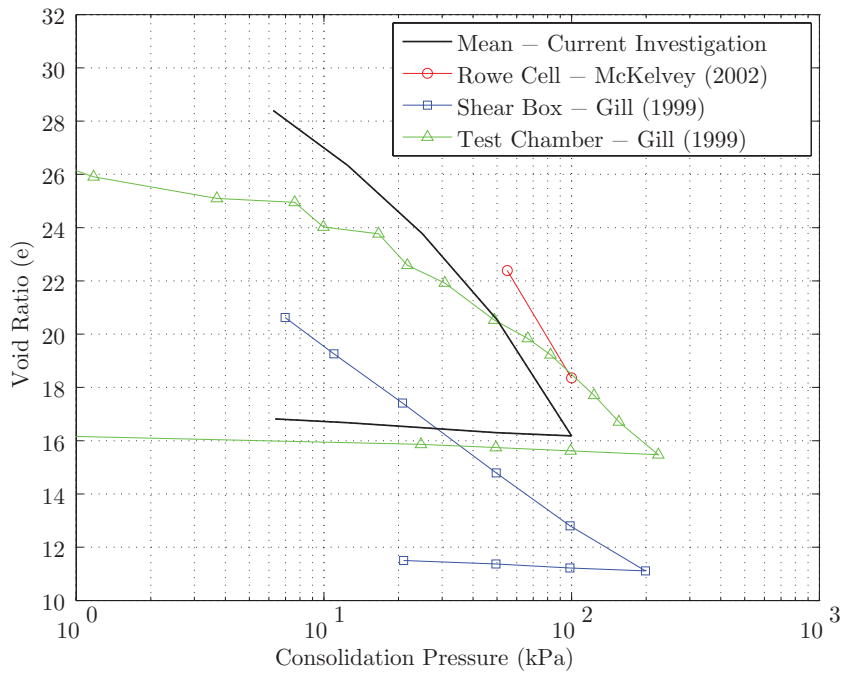


Figure 3.38: Void ratio data compared to previous investigations using fumed silica based transparent synthetic soils.

an aspect ratio of 0.42:1 and showed a void ratio of 16.19 at the same consolidation pressure. The largest aspect ratio was from the shear box test performed by Gill (1999) and produced the lowest void ratio of around 12.8. However, the test performed in a Rowe Cell by McKelvey (2002) yielded a final void ratio of 18.35 at 100kPa, yet had the second largest aspect ratio of 0.75:1, which is not in agreement with the hypothesis concerning the effect of aspect ratio.

Another possible cause for the variation in void ratio may be the method of measurement. McKelvey (2002) states that the mass of fluid drained was measured and converted to a volume using its measured density. Conversely Gill (1999) estimated the void ratio by measuring the density of the consolidated soil. As previously described, in this investigation the estimated void ratio depended on a volumetric measurement of the soil, assuming no loss of aggregates after pouring of the slurry. It is likely that a combination of these differences in void ratio measurement and the effect of consolidation chamber aspect ratio has affected the void ratio estimated for each set of data.

The coefficients of consolidation (Table 3.8) appear to be significantly higher than

those measured by either Gill (1999) or McKelvey (2002) using the shear box apparatus or Rowe Cell ($0.24\text{-}1.65m^2/\text{year}$) for equivalent consolidation pressures ($25\text{-}100kPa$). This is possibly caused by the very small aspect ratio used in this investigation as during the early stages of consolidation sidewall friction may account for a large proportion of the applied consolidation pressure, particularly during the early consolidation increments. However, the c_v values at a consolidation pressure of $100kPa$ were also greater than those previously reported (Gill, 1999; McKelvey, 2002). This discrepancy is most likely attributable to the different apparatus used to derive the consolidation properties of the transparent soil.

No coefficients for consolidation derived inside the test chamber are given by Gill (1999) or McKelvey (2002), which would have been more directly comparable with the data presented here. The coefficients of compressibility are also larger than those measured in previous investigations ($1.18\text{-}5.4E-03m^2/kN$) again, the aspect ratio of the test chamber may be a cause. Hydraulic conductivity follows the same pattern with generally higher values presented here compared to those quoted by Gill (1999) of between $1.66E-8\text{-}2.74E-10m/s$.

The transparent soil used in this investigation exhibits consolidation behaviour similar to that of soft normally consolidated alluvial clays ($c_v = 0.4\text{-}1.7m^2/\text{year}$) and a compressibility comparable with that of very high organic content clays and peats ($m_v > 1.5E-03m^2/kN$), in agreement with observations made by Gill (1999).

3.7 Test Procedure

In preparation for testing, the viewing window reinforcement plates were removed from the test chamber. The consolidation piston was then withdrawn after removal of the draw-wire transducer from the consolidation frame. The rear panel of the test chamber was then removed to allow access for the pile driving rig cantilever arm. The test chamber was then wiped clean of any residual oil before the centre line of the test chamber was marked using a non-permanent marker on each viewing window. A line was then drawn 20mm to the right of the centreline marks on the front viewing window to allow positioning of the viewing window control point array, which was glued using Pritt-StickTM to the viewing window 20mm above its base. This ensured that the viewing panel was central in the images recorded once the camera was correctly positioned to view the target area of the viewing window. The second control point array was then fixed in similar fashion to the left hand side of the box at the same height, before the alignment marks were removed.

After donning all required personal protective equipment (goggles and overcoat) and ensuring that the laboratory was securely locked and that the ‘laser in use light’ was illuminated, the laser was powered up on its minimum setting to allow alignment of the test chamber. The laser light sheet produced was aligned with the aforementioned non-permanent marks thus ensuring that the sheet passed through the centre of the model. The digital camera was then placed upon the tripod and positioned such that the target area of the soil sample and the two control point arrays were visible within the images recorded. Next the test chamber was removed and replaced with the alignment target seen in Figure 3.39(a), so that the vertical and horizontal perpendicularity of the camera and plane of interest could be assessed. The target consisted of two Perspex sheets separated by 5mm wide, 10mm thick aluminium spacers. A grid of holes was drilled at identical locations on each of the two sheets and then joined by red lines on one sheet and blue lines on the other using a permanent marker. The alignment target was placed parallel with the laser sheet. If alignment was successful, the red and blue lines closest to the principal point (centre) of the image were overlapping, both vertically and horizontally, as shown in Figure 3.39(b), allowing the test chamber to be replaced.

Correct alignment was critical in ensuring that any photogrammetric corrections conducted were of optimal accuracy, as discussed in Chapter 4. After alignment was completed the laser power was reset to full power and the LED control points

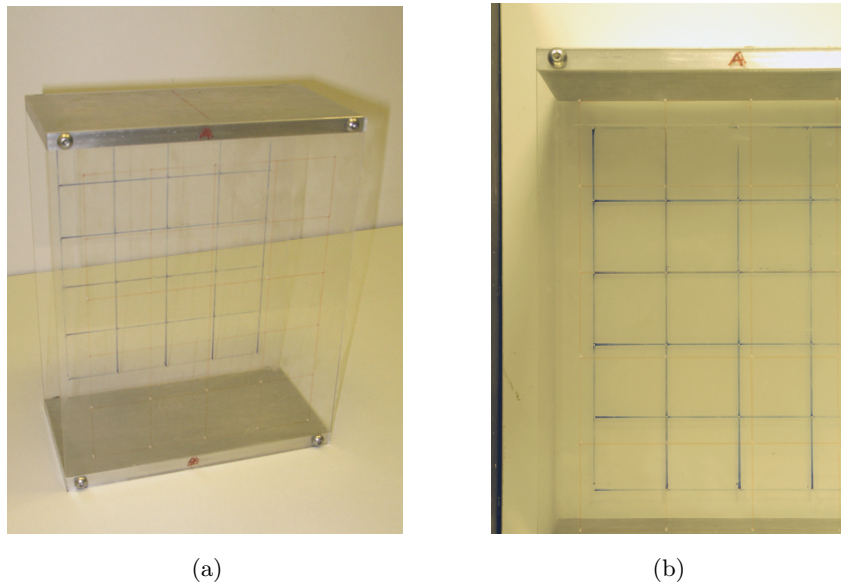


Figure 3.39: Alignment assessment: (a) alignment target; and, (b) alignment target indicating correct alignment.

were energised and visibility checked. The camera was now turned on and set to manual capture mode and manual focus. The settings of F8.0 aperture and 1/10th of a second exposure time were set on the camera and the focus was manually set. Focussing correctly was the most important stage in producing quality images suitable for PIV analysis. Lastly with regard to the camera, the battery was checked for sufficient charge and settings double checked for errors.

The model helical screw pile was then assembled and attached to the pile driving rig along with the load cell. Before installation the output of the load cell was noted. The pile was then installed into the soil bed at a vertical rate of 0.2mm/s and rotational rate of 0.04rps , such that the pile was installed at a rate of one flight pitch per revolution. Image data was recorded to facilitate investigation of the installation process at a continuous rate of 3fps, and the images were downloaded to the personal computer upon completion of installation. The installation terminated with the midpoint of the lowest helical plate at a depth of $7D$. After downloading of all image data the camera memory card was formatted and camera battery checked for sufficient power to complete the load-deflection testing. Next, the load cell was connected to the DAQ and the output from all transducers was checked. Before the commencement of load-deflection testing the recording of data using LabVIEW was also checked.

In order to define the installation and load-deflection testing rates for the proposed scheme of pile testing some estimation of the extent of drainage occurring around the model pile was required. Lehane et al. (2008) developed a normalised velocity based estimation of pore pressure dissipation below a circular footing during uplift assuming that failure occurs at a strain of 2-10% of the footing diameter as shown in Figure 3.40. This approach was used to estimate the pore pressure dissipation below the helical screw pile during uplift loading, with the lower plate of the pile idealised as an impermeable circular plate of 20mm diameter. Using Equation 3.17, given that $V < 0.01$ is considered to be drained and $V > 20$ is considered undrained, no more than 10% of the excess pore pressure beneath the circular plate was expected to dissipate.

$$V = \frac{v_f \cdot D}{c_v} \quad (3.17)$$

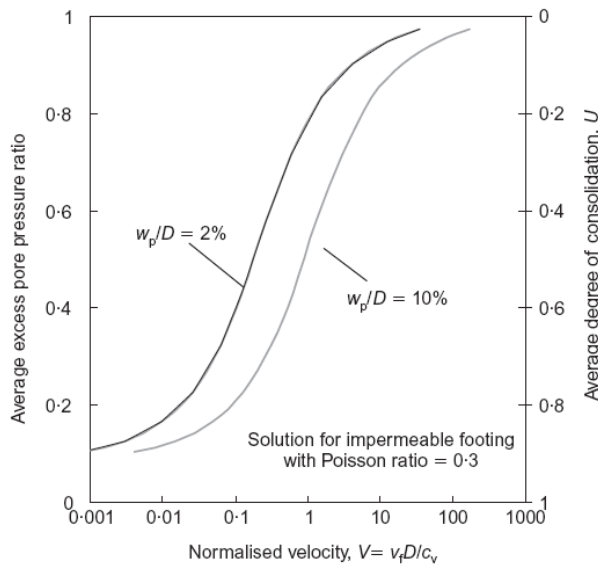


Figure 3.40: Normalised velocity based estimation of pore pressure dissipation below a circular footing during uplift from Lehane et al. (2008).

Using this relationship and the c_v of the consolidated material derived from the consolidation data (see Table 3.8) for the 50.0-100.0kPa stress increment, the proposed testing rate of 0.2mm/s for undrained testing can be checked for its suitability on a sample by sample basis. Table 3.16 summarises the dimensionless velocity factors calculated for all helical screw pile samples. V is always greater than 20, which is acceptable.

Table 3.16: Drainage estimation using normalised velocity approximation from Lehane et al. (2008) for helical screw pile tests.

Test	Dimensionless Velocity (V)
C1	31.17
C2-30	28.61
C2-60	26.07
C3	44.20
T1	38.03
T2-30	28.49
C2-60	34.76
C3	31.20
C1-R	33.20
C3-R	27.14

Once the test rate was set, the test direction (compression or tension) was configured along with a maximum driving distance of 20mm at which the test was to be terminated. The control points, laser sheet position, laser power output, transducer signals and other settings were checked before beginning to drive the model and record load-deflection data and digital images. Upon completion of the test all images and data were transferred to the personal computer and a backup made.

Hand vane shear tests were then performed in the sample in the four corners of the test chamber, 1/4 of the test chamber width from each side and at 1/3 and 2/3 depth in the sample, as illustrated by Figure 3.41. This was conducted using a 33mm Pilcon hand vane shown in Figure 3.42, operated following the procedure outlined by BS1377-9:1990 (1990), in order to assess the undrained strength as well as the uniformity of the sample.

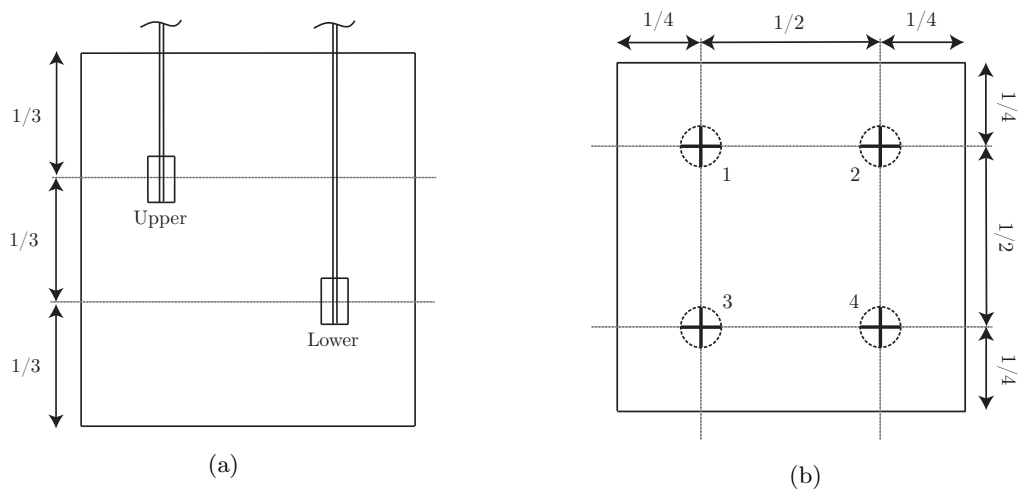


Figure 3.41: Location of hand vane shear measurements: (a) front view and (b) and plan view.

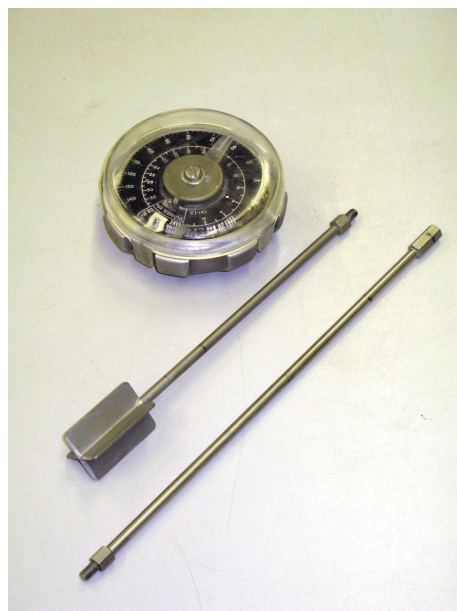


Figure 3.42: Hand vane shear apparatus.

Chapter 4

Particle Image Velocimetry, Photogrammetry and Post-Processing

4.1 Introduction

This chapter outlines the processes required to derive displacements and strains from a series of digital images recorded during loading of a geotechnical structure in a transparent soil model. Firstly PIV is used to derive displacements in image space (px). Next, the data is corrected for radial and tangential lens distortion, camera-soil differential movement and lastly scaling, thus generating displacements in object space (mm).

Typically control points are used where data can be obtained accurately for both image space and object space coordinates of each control point by centroiding. However, due to the nature of the LED control points required in this investigation, given the dark room testing conditions, it was not possible to generate concurrent image space and object space coordinates. An alternative technique is presented here, that relies on only two points with concurrent image and object space data to allow conversion of image space measurements to object space.

This chapter presents calibrations for the PIV analysis software used, calibration and validation of the photogrammetric correction technique developed and a summary of the post-processing techniques used to generate clear output. All analyses were conducted using algorithms developed in MATLABTM and post-processing was conducted manually using appropriate software.

4.2 Particle Image Velocimetry (PIV)

Section 3.7 describes how digital images of the plane of interest are recorded during testing to allow calculation of displacements using PIV. GeoPIV, a MATLABTM based module developed by White and Take (2002) specifically for geotechnical applications, was used to perform this analysis. This module allows a range of analysis parameters to be set including:

- Patch size.
- Searchzone.
- Leapfrog.

In reverse order, ‘leapfrog’ controls the number of sequential computations performed using any one set of initial patch coordinates. Hence if ‘leapfrog’ is equal to one the initial positions for the patches are derived from the final positions of the patches from the previous computation increment. Alternatively if ‘leapfrog’ is equal to 10, the first ten computations will be conducted using the initial coordinates from the first image, the second series of ten images will be conducted from the final coordinates from the tenth image, and so on. This facility is provided as an attempt to reduce the contribution of random walk errors in generating noise within test data.

In this investigation leapfrog was set such that in all analyses a series of no more than seventy computations was used to calculate the displacement increments for each data set. For helical screw pile tests the leapfrog parameter was set to one so that all computations were sequential. The footing tests presented in Chapter 6 were conducted at 40% of the loading rate used for model piles (discussed in Section 6.4). Thus a larger series of images was recorded at the maximum capture rate of 3fps, so to maintain low levels of random walk generated noise the value for leapfrog for these tests was increased to ten.

The ‘searchzone’ parameter controls the distance beyond the initial patch within which GeoPIV searches for the most positively correlated match. This value ought to be set so that it is greater than the maximum anticipated displacement, to ensure accurate displacements are output by GeoPIV. However, with increased ‘searchzone’ comes increased computation time, so the ‘searchzone’ ought also be kept as small as possible to ensure prompt computation of displacements. Due to the fast rate of capture of digital images during testing (3fps), it was found that a ‘searchzone’ of

10 pixels was sufficient for both the model pile and footing series of tests. Had the ‘searchzone’ been too small, wild random vectors would have been prevalent in the output, which was not apparent when a value of 10 was adopted.

Lastly, the patch size is the parameter that most greatly affects the accuracy of output from GeoPIV. The patch size is a direct control on the amount of digital data used in the computation of the displacement of each patch. However, the quality of this data is also key. Good texture and contrast is vital in ensuring accurate PIV calculations. In plane strain or axisymmetric half-space physical models the natural texture of sand or flocked kaolin is used to provide this texture and contrast. In non-intrusive physical modelling it is the Timiron seeding particles that generate texture and contrast. A successful PIV analysis utilises the smallest amount of data (patch size) with maximal quality (texture and contrast), as this provides the maximum number of measurement points on the digital image.

The following sub sections present calibrations performed on all types of target analysed during this investigation, alongside justification and appraisal of the amount and quality of data utilised in the computations of displacements in each case.

4.2.1 Calibration

The calibration process conducted to assess the accuracy of GeoPIV in tracking a known displacement was similar to that employed by White (2002a), whereby an image was digitally translated 10 pixels in the horizontal direction using the image processing toolbox within MATLABTM. The manipulated image was then saved so that an image pair existed, where the displacement between the two images was known. GeoPIV was then used to compute the displacements of a number of patches for a range of patch sizes.

It should be noted that for this calibration process, the ‘searchzone’ parameter was raised to 20 pixels to allow accurate computation of the displacements. The residual errors were then calculated and the standard deviation derived and compared with the upper bound proposed for GeoPIV by White (2002a). In this calibration sixteen individual patches were used, since there were sixteen LED control points. Preservation of an equal number of calculation points ensured fair comparison of displacement tracking accuracy of different components of the measurement process.

In the case of the transparent synthetic soil calibration the patches were chosen at random within a user-defined window, using a simple algorithm that generated random pairs of coordinates. Patch sizes from 5 to 100 pixels in 5 pixel increments were calibrated and compared in all cases. All calibrations are presented here in image space units (px) since no photogrammetric correction processes were conducted at this stage. Therefore the data output is a direct measure of the accuracy of GeoPIV, rather than a combination of errors emanating from GeoPIV and the subsequent analysis procedures used to generate object space output data from image space input data (i.e. photogrammetric correction). The error was quantified in all cases as the standard deviation of the displacement measurement errors, so that the results were comparable with the upper bound proposed by White (2002a).

4.2.1.1 Transparent Synthetic Soil

The transparent soil represents the most important target for the PIV analysis, since it is the medium being used to represent soil in the model. Figure 4.1 presents the calibration of GeoPIV for the laser sheet highlighted plane of interest within the model. The standard errors yielded are comparable with the upper bound equation proposed by White (2002a), for patch sizes greater than 40 pixels. There is only a small improvement in GeoPIV accuracy for patch sizes greater than 40 pixels. However, to provide some margin for inferior patch quality, a 50 pixel patch size was chosen for tracking displacements within the soil yielding standard errors of about 0.01 pixels on average. Using an approximate scaling ratio, derived by calculating the image space distance between the tip of the pile at the commencement and completion of pile installation, of 1:15.5 ($mm:px$), this equates to an error of about $0.65\mu m$. It is important to note that this calibration is only valid for the camera position, seeding density and laser intensity used in this investigation.

4.2.1.2 Control Point Calibration

The control points described in Section 3.3.3.3 allow removal of systematic camera-soil movement errors from the PIV data and so are the next most important target for the PIV analysis. Section 3.5.1.3 described the rationale behind the supply voltage choice for these control points in terms of maximising the range of intensity present, whilst avoiding over-exposure at the centre of the LED. The analysis presented here consists of picking the centre of the LED for each control point and analysing the effect of patch size. Figure 4.2 presents the results of the calibration.

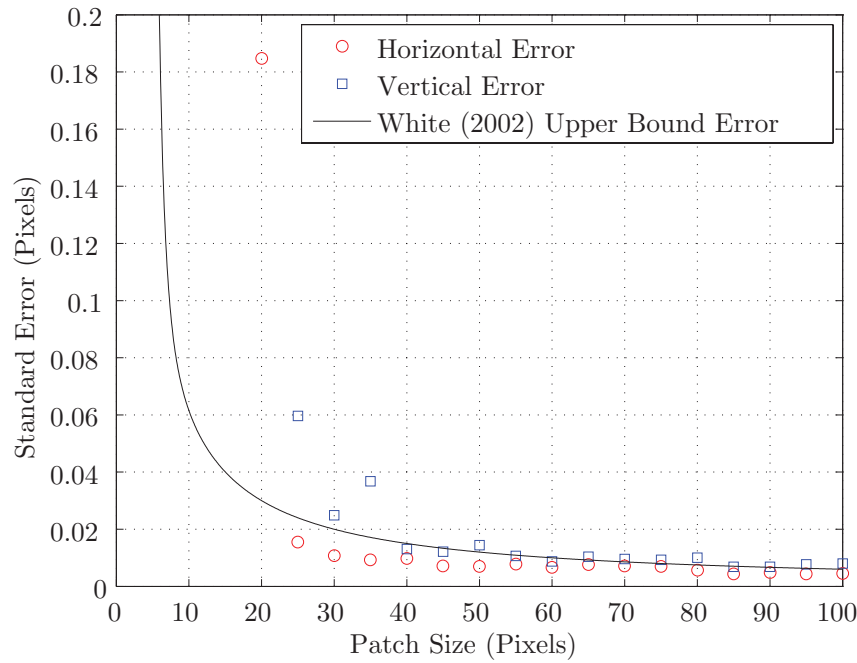


Figure 4.1: Standard error of transparent soil tracking.

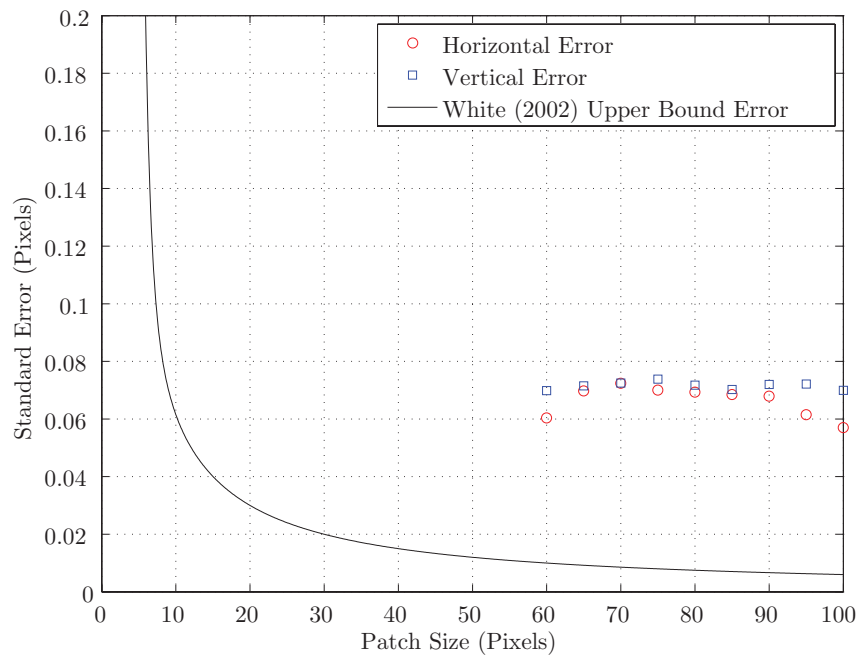


Figure 4.2: Standard error of control point tracking with 15.0V supply voltage.

The results show that the LED was very poorly tracked for patch sizes less than 60px. This was due to the size of the LED in the images necessitating a patch of at least 60px to ensure full coverage of the LED, which ensures there is contrast in the patch between the LED and black background. Due to the background behind the LED's being matt black, there is no penalty associated with using patches larger than 60px, so 100px patches were adopted here.

The 15.0V supply voltage and 100px patch size exhibits an average standard error of about 0.065px, or using the aforementioned approximate scaling ratio of 1:15.5 ($mm:px$), a standard error of $4.19\mu m$. This is higher than the upper bound proposed by White (2002a), or the accuracy of tracking control points presented in the same reference. In the present test configuration this was difficult to mitigate, since as explained in Section 3.3.3.3 traditional control points could not be utilised.

4.2.1.3 Pile Displacement Calibration

To derive the axial displacement applied to the model pile during load-deflection testing and link it to an appropriate image number, it was necessary to track a number of patches intersecting the lower helix of the model pile. Soil in this area was assumed to move purely axially in the direction of loading, with the same magnitude of displacement as the pile driving head. The pile was assumed to be incompressible in comparison to the soil. The time stamp recorded by the digital camera when an image was recorded was not sufficiently accurate to allow correlation of axial pile displacement and image numbers.

A series of sixteen manually selected patches were used in conjunction with the same procedure as for the soil and control points, to estimate the accuracy of this process. Figure 4.3 presents the results of this calibration, indicating that the standard error associated with pile tracking was within the upper bound of White (2002a) for patch sizes greater than 70 pixels. For a patch size of 100 pixels the average standard error was as little as about 0.002 pixels, or using the scaling ratio of 1:15.5 ($mm:px$), about $0.13\mu m$, thus this was the patch size utilised for all pile analyses. This is greater than the accuracy of tracking the transparent soil for an equivalent patch size and is likely to be as a result of the additional contrast between the helix of the model pile and the surrounding soil. Tracking pile movements of the helical screw pile in this way can therefore be expected to be sufficiently accurate to generate a plot of image

number versus axial pile displacement. This is advantageous as it allows selection of images representative of a given displacement increment during analysis.

4.2.1.4 Footing Displacement Calibration

Similarly the axial displacement of the footing described in Chapter 6 also needed to be monitored using PIV, so that the image numbers could be related to the axial displacement. For this process, sixteen patches were manually placed at the intersection of the footing and soil at its centre. It was assumed there is no lateral displacement beneath the centre of a circular footing, an assumption that was assessed using the data generated by the footing tests presented in Chapter 6. Half of each patch covered the footing and the other half covered the underlying soil.

Figure 4.4 presents the results of the calibration, indicating that tracking the footing settlement was less accurate than tracking the model pile displacement. This is likely to be due to the fact that the footing was a simpler shape than the model pile, so the information recorded in the tracking patch was less distinct. For patch sizes between 80 and 100 pixels the average standard error was about 0.009 pixels or, using the scaling ratio of 1:15.5 ($mm:px$), about $0.58\mu m$. This is similar to the upper bound from White (2002a), indicating adequate performance. A patch size of 100px was adopted for the analysis process.

4.2.1.5 Discussion

In the above GeoPIV calibrations the displacement between each image pair was synthesised digitally. In reality the displacement of targets will be far less uniform, so the calibrations presented here represent an optimistic approximation of the errors inherent in the PIV measurements. However, the alternative of physically displacing either the camera or target accurately by a chosen distance is difficult to achieve in the laboratory. Furthermore, any data derived from such an image pair would require photogrammetric correction in order to generate object space displacement measurements unaffected by camera induced distortions. Therefore, any calibration conducted in this fashion would contain errors from both GeoPIV displacement measurement and the photogrammetric correction process.

Therefore, the calibration data presented here, in pixels, is a quantitative appraisal of the accuracy of PIV tracking of the various targets of the PIV analyses, allowing comparison of the performance of GeoPIV for each. In addition, in three of the four

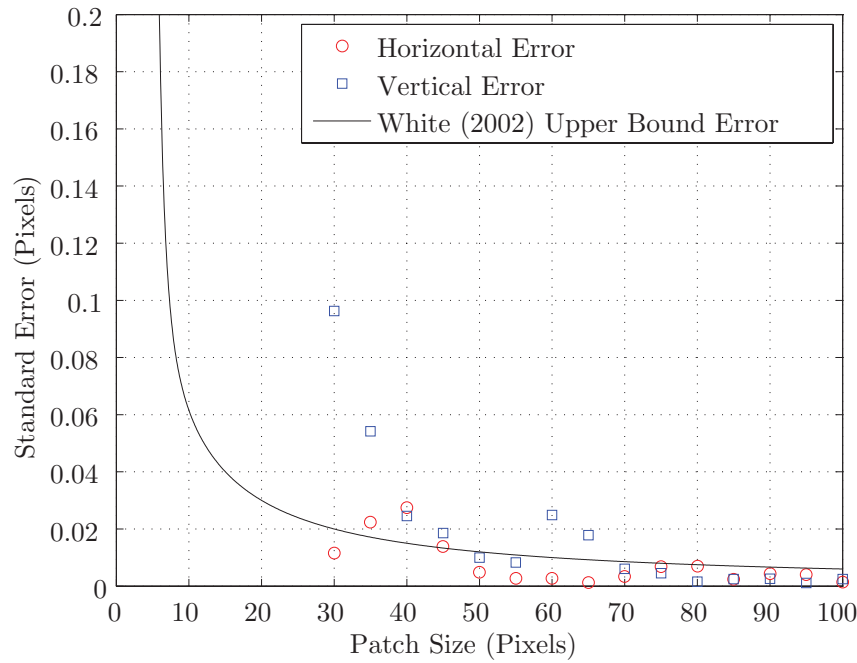


Figure 4.3: Standard error of pile displacement tracking.

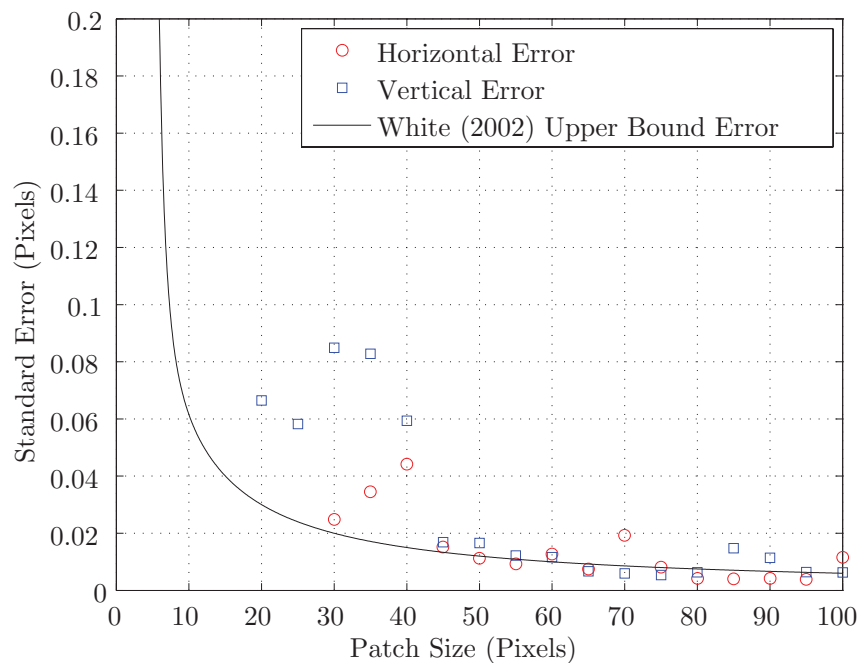


Figure 4.4: Standard error of footing displacement tracking.

4.2 Particle Image Velocimetry (PIV)

calibrations presented, it would be plainly apparent if the calibrations were overly optimistic, as it would be evident in the output. In the case of the control point tracking, poor tracking would lead to camera-soil movement correction errors, which are systematic and therefore easily spotted in the form of erroneous zero contour positions in the output data. Similarly, the model pile and footing displacement tracking accuracy could be assessed, by comparing the maximum PIV computed displacement and the known displacement recorded by the transducers described in Section 3.3.6.

4.3 Photogrammetry

Photogrammetry is the process used to convert image space (pixel) measurements into object space (metric) units via a series of mathematical transformations. The following sections present the method of photogrammetric correction employed starting with camera induced errors, then camera-soil movement induced errors and lastly scaling. White and Take (2002) distribute a package of supplementary algorithms with GeoPIV that can be used for these purposes, so long as concurrent image space and object space coordinates for a series of control points is known. This is not possible in this application due to the use of LED control points (see Section 3.3.3.3) so a less direct method must be used. For all processes presented, image space measurements will be referred to in terms of u and v for horizontal and vertical coordinates, and object space coordinates will be referred to in terms of X and Y respectively.

4.3.1 Internal Correction

Internal corrections are defined in this instance as distortions caused by the camera itself and include a number of phenomena including radial and tangential lens distortion, pixel non-squareness and non-colinearity of the centre of the recorded image and the principal point of the camera lens.

Radial lens distortion is the process of radial deflection of light passing through the lens of the digital camera (Slama, 1980) and is often referred to as a ‘fisheye’ effect. Radial distortion can be calculated using Equation 4.1 if the radial distortion components k_1 and k_2 are known from camera calibration, where the radial distance, r , from the principal point, u_0 , v_0 , is derived using Equation 4.2 (Slama, 1980). u and v are the coordinates of a point in image space and $\delta_{u^{radial}}$ and $\delta_{v^{radial}}$ represent the radial distortion components due to the lens.

$$\begin{bmatrix} \delta_{u^{radial}} \\ \delta_{v^{radial}} \end{bmatrix} = \begin{bmatrix} u(k_1.r^2 + k_2.r^4) \\ v(k_1.r^2 + k_2.r^4) \end{bmatrix} \quad (4.1)$$

$$r = \sqrt{(u-u_0)^2 + (v-v_0)^2} \quad (4.2)$$

Tangential lens distortion is a product of the centres of curvature of the inner and outer surface of the lens not being colinear and hence a second distortion is induced. This type of distortion is most prevalent in multiple lens configurations as was used here. The tangential distortion components $\delta_{u^{tangential}}$ and $\delta_{v^{tangential}}$ due to the lens can be calculated using Equation 4.3 if the tangential distortion components p_1 and p_2 are known from camera calibration, again with radial distance calculated using Equation 4.2 (Slama, 1980).

$$\begin{bmatrix} \delta_{u^{tangential}} \\ \delta_{v^{tangential}} \end{bmatrix} = \begin{bmatrix} 2p_1.u.v + p_2(r^2 + 2u.r^2) \\ p_1(r^2 + 2v.r^2) + 2p_2.u.v \end{bmatrix} \quad (4.3)$$

The lens distortion also effects the positioning of the principal point of the recorded image and thus has both radial and tangential components (Slama, 1980). To correct for both radial and tangential lens distortions the principal point (u_0, v_0) must also be known.

The last form of camera induced distortion is far less significant and caused by non-squareness of the individual pixels that form the CCD within the digital camera. This distortion is typically linear and assumed to be constant over the area of the CCD. It is described mathematically by the aspect ratio, α , which is pixel width divided by height.

Hence, after derivation of the calibration parameters $(u_0, v_0, k_1, k_2, p_1, p_2, \alpha)$ via a camera calibration such as that presented later in Section 4.3.4.2, image space coordinates of measurement points can be corrected to generate the adjusted coordinates (u_i, v_i) , as shown in Equation 4.4.

$$\begin{bmatrix} u_i \\ v_i \end{bmatrix} = \begin{bmatrix} \left[\frac{(u-u_0)}{\alpha} \right] - (\delta_{u^{radial}} + \delta_{u^{tangential}}) \\ (v-v_0) - (\delta_{v^{radial}} + \delta_{v^{tangential}}) \end{bmatrix} \quad (4.4)$$

Take (2003) noted that significant changes to camera calibration parameters were observed for a Kodak DC280 digital camera during centrifuge testing, which is probably due to the flexible lens configuration found in many digital cameras to facilitate zoom. However, all tests in this investigation were conducted at $1g$, hence it was deemed acceptable to perform one single camera calibration at the beginning of

testing, the results of which are presented in Section 4.3.4.2. This assumes that the camera settings (focal length, shutter duration, aperture, ISO, zoom length, position) are kept constant between successive images and every test. The tests themselves are also of a very short duration (minutes). Hence temperature variation and consequent contraction or expansion of the lens assembly was not deemed to pose a significant threat to the validity of the camera calibration. The calibration was conducted in the same laboratory as testing, which was temperature controlled by air conditioning to maintain a temperature of 20°C.

4.3.2 External Correction

External corrections are defined as the systematic errors emanating from differential movement between the camera and the plane of interest, that is differential movement between the CCD plane and the centre of the soil model in this case. This type of error can be readily seen when a series of images are captured of a stationary object using the continuous shoot mode of a digital camera appear to show movement of the object. It is this systematic error that needs to be removed from the data computed using PIV.

A pin-hole camera model or perspective projection is used to achieve this by manipulating the coordinates corrected for internal camera induced distortions (u_i, v_i) to image space coordinates corrected for both internal and external camera induced errors (u_{ie}, v_{ie}). Typically (White, 2002a; Effendi, 2007; Heikkilä and Silvén, 1997) this is achieved using a transformation matrix that also incorporates the effect of scale such that image space data is converted to object space output in one calculation step. However, this requires concurrent image and object space coordinates for a set of control points, which were not available in this instance due to the type of control points used (see Section 3.3.3.3). If the scaling term is removed from the transformation at this stage, a simpler image space to image space transformation is generated, allowing scaling to be applied as an additional step, described in Section 4.3.3.

This form of transformation assumes that the image space and object space planes are coplanar, such that any point in image space can be projected through the projective centre to an equivalent position in object space. This projection is powerful in that it accounts for non-coplanarity between the control point plane and the CCD between sequential images, allowing the camera movements to be accounted for in

terms of both rigid body motion and translation simultaneously. This is achieved using a transformation matrix system such as that in Equation 4.5, which consists of a normalised camera matrix, a rotation matrix R described in terms of Eulerian rotation angles (ϕ, ω, κ), and a translation vector t with components of displacement for the three principal axes (t_x, t_y, t_z). The image space coordinates after correction for both internal and external induced camera errors are derived from the inverse of this equation matrix.

$$\begin{bmatrix} u_i \\ v_i \\ 1 \end{bmatrix} = \begin{bmatrix} 1 & 0 & 0 & 0 \\ 0 & 1 & 0 & 0 \\ 0 & 0 & 1 & 0 \end{bmatrix} \begin{bmatrix} R & t \\ 0 & 1 \end{bmatrix} \begin{bmatrix} u_{ie} \\ v_{ie} \\ z_{ie} \\ 1 \end{bmatrix} \quad (4.5)$$

$$R = \begin{bmatrix} r_{11} & r_{12} & r_{13} \\ r_{21} & r_{22} & r_{23} \\ r_{31} & r_{32} & r_{33} \end{bmatrix} \quad (4.6)$$

$$\begin{aligned} r_{11} &= \cos \phi \cos \kappa \\ r_{12} &= -\sin \kappa \cos \omega + \cos \kappa \sin \phi \sin \omega \\ r_{13} &= \sin \kappa \sin \omega + \cos \kappa \sin \phi \cos \omega \\ r_{21} &= \sin \kappa \cos \phi \\ r_{22} &= \cos \kappa \cos \omega + \sin \kappa \sin \phi \sin \omega \\ r_{23} &= -\cos \kappa \sin \omega + \sin \kappa \sin \phi \cos \omega \\ r_{31} &= -\sin \phi \\ r_{32} &= \cos \phi \sin \omega \\ r_{33} &= \cos \phi \cos \omega \end{aligned}$$

$$t = \begin{bmatrix} t_x \\ t_y \\ t_z \end{bmatrix} \quad (4.7)$$

This process was conducted using the digital image processing toolbox within MATLABTM which incorporates a perspective projection algorithm that uses pairs of control point coordinates to ascertain the rotation and translation parameters. To generate this data, GeoPIV was used to track the displacements of the control points throughout the sequence of images. The rotation and translation parameters were then derived to describe the movement of the camera between the first image, and all sequential images in turn. The inverse function of the transformation matrix system was then used to correct all data for systematic camera-soil movement induced, or external errors. However, this process assumes that the camera CCD and control point plane are perfectly coplanar upon commencement of testing and recording of the first digital image, hence the use of the alignment target described in Section 3.7.

4.3.3 Scale Correction

After internal and camera induced errors have been removed from the dataset, the data is still in image space or pixel units. In order for the data to be interpreted fully a conversion to real world scale (object space) is required. Typically in previous geotechnical studies involving PIV and close range photogrammetry, scaling was conducted as part of the transformation system using the pin-hole camera model, which was followed by a correction for refraction induced distortions where soil deformations were viewed through a Perspex window. To tackle this a mathematical construct was presented by White (2002a) to correct data for refraction though both a single layer and double layer viewing window. The double layer formulation was required since part of the viewing window utilised by White (2002a) was glass and part was Perspex, and the two materials exhibit different RI.

The magnitude of such a refraction correction is proportional to the radial distance from the principal point of the recorded image. Scaling correction is therefore analogous to linear scaling. In the case of White (2002a), and later Effendi (2007), the RI of the Perspex or glass used was either assumed and validated, or calibrated. In both cases the refraction correction had to be implemented since scaling occurred at the control point plane, that is before the effect of refraction induced errors. However, in this investigation scaling cannot occur at the control point plane since concurrent image space and object space coordinates are not available for the LED control points. Instead two points with known coordinates are used to calculate a

linear scaling factor, λ , at the plane of interest and hence refraction errors are automatically accounted for by a single factor. For the pile test two points were taken for the derivation of the linear scaling factor, λ , these being the initial position and final position of the tip of the model pile during installation, the displacement of which was measured accurately using the draw-wire LVDT. The scaling factor was then utilised to convert image space data, corrected for both internal and external camera induced errors, to object space output data using Equation 4.8.

$$\begin{bmatrix} X \\ Y \end{bmatrix} = \begin{bmatrix} \lambda u_{ie} \\ \lambda v_{ie} \end{bmatrix} \quad (4.8)$$

In the case of the footing tests outlined in Chapter 6, the edges of the footing were used as the two points required to derive the scaling factor, λ . Here the linear scale factor was determined from a single image, so the image space coordinates in this case need only be corrected for internal camera induced errors.

4.3.4 Validation

The photogrammetric correction procedure described in Section 4.3 requires validation in order to assess its suitability for purpose. The validation process presented here focusses on two key aspects of the system performance, accuracy and precision. White (2002a) defined accuracy and precision in respect to geotechnical modelling as follows:

1. Accuracy

- The systematic difference between the coordinates of an object as predicted through camera calibration, and the true coordinates of that object.

2. Precision

- The random difference between multiple measurements of the same object.

Assessment of these two performance criteria was achieved by commissioning the manufacture of a calibration target that would sit at the centre of the test chamber and replicate the plane of interest, when surrounded by pore fluid of matched RI to the transparent soil. The following sections outline the design and derivation

of concurrent image space and object space coordinates for the individual control points on the calibration target.

4.3.4.1 Calibration Target

A calibration target (see Figure 4.5) was machined at the University of Sheffield from Perspex sheets, such that the central sheet of the calibration target was coincident with the centreline of the test chamber. The target was then drilled with 252 3mm diameter blind holes to an accuracy of $\pm 10\mu m$ at 15mm centres. The target was then painted matt black before the blind holes were backfilled with white Tipp-ExTM fluid to generate the control points.



Figure 4.5: Calibration target.

Figure 4.6 shows a cropped image of an individual control point when viewed through 100mm of fluid. The contrast in intensity between the black background and the white circle allows centroiding to be conducted to generate image space coordinates for each control point, whilst the object space coordinates are known from the design specification.

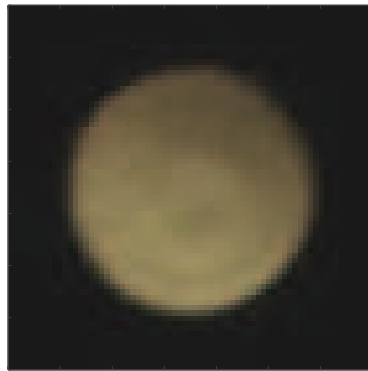


Figure 4.6: Control point consisting of blind-hole filled with Tipp-Ex™ and backed with matt black paint.

4.3.4.1.1 Centroiding The coordinates of the control points (C_u , C_v) on the calibration target in image space were deduced, following Effendi (2007), by using the ratio of the area moment of the individual pixels to the total area (A). As the intensity of the control point in Figure 4.6 is not axisymmetric in profile about the centre of the control point, this method was preferred to the pixel intensity method of centroiding used by Take (2003).

$$C_u = \frac{\int(u) dA}{A} \quad (4.9)$$

$$C_v = \frac{\int(v) dA}{A} \quad (4.10)$$

The first stage in the centroiding process was to isolate each control point by cropping reasonably closely to its centre. This process was made simple by the constant black background behind the control points. As a result the choice of cropping size was arbitrary, so long as the whole of the white area of each control point was contained in the cropped area. Following cropping, the intensity of each of the control points was passed through a Gaussian smoothing algorithm to reduce noise at the control point-background interface (Haralick and Shapiro, 1992; Jain et al., 1995; Davies, 2005), consisting of a 2D convolution operator with a kernel representing the Gaussian bell shape, with a standard deviation $\sigma = 1$ and mean (0,0) as used by Effendi (2007). The effect of this smoothing shown in Figures 4.7 and was less pronounced than that observed by Effendi (2007) because the background surrounding the control points in this instance was more uniform.

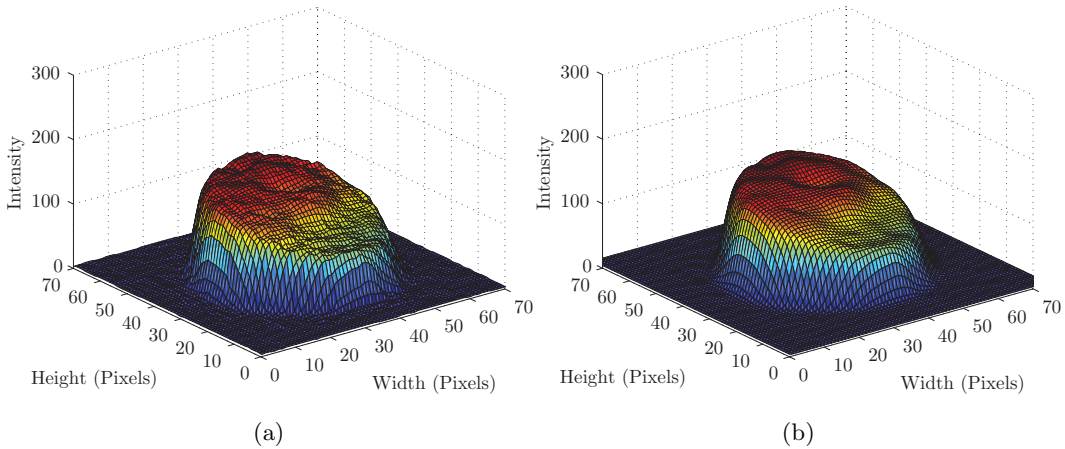


Figure 4.7: Effect of Gaussian smoothing on control point: (a) before; and, (b) after smoothing.

The centroid was then calculated by performing an area moment computation at a range of thresholds over the available intensity range. The upper and lower 30% of the intensity range was excluded for each control point, between which 50 individual thresholds were used to derive the average centroid coordinates (C_u , C_v). The intensity range used was therefore less than that of Effendi (2007), where only the upper and lower 10% were excluded. This was required since the uniformity of intensities observed for different control points, and across the area of each individual control point, was reduced compared to the investigation by Effendi (2007).

Reducing the thresholding range in this manner ensured that centroiding computations were performed only on sections that exhibited a broadly circular profile, thus reducing scatter in the range of centroids calculated. This requirement was probably a product of the low level light conditions present in the centre of the test chamber in the laboratory. For each threshold, intensities were converted to binary form, where intensities greater than the threshold assume a binary value of 1 (white), whereas those less than the threshold assume a binary value of 0 (black). Erroneous pixels outside of the area of the control point were modified using a cavity filling technique, although noise was less prevalent around the lower thresholds than in the investigation by Effendi (2007), so this was seldom utilised. Figure 4.8 illustrates the typical deviation of the threshold centroids around the centroid coordinates (C_u , C_v) for a single control point, indicating horizontal and vertical standard deviations of about 0.05 pixels. This is similar to the deviation quoted by Effendi (2007) of 0.04 pixels. Figure 4.9 summarises the deviations graphically.

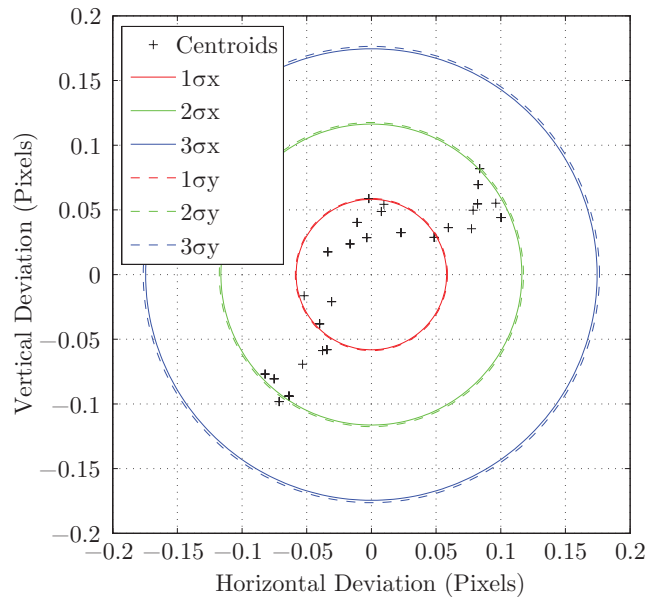


Figure 4.8: Typical centroid deviation.

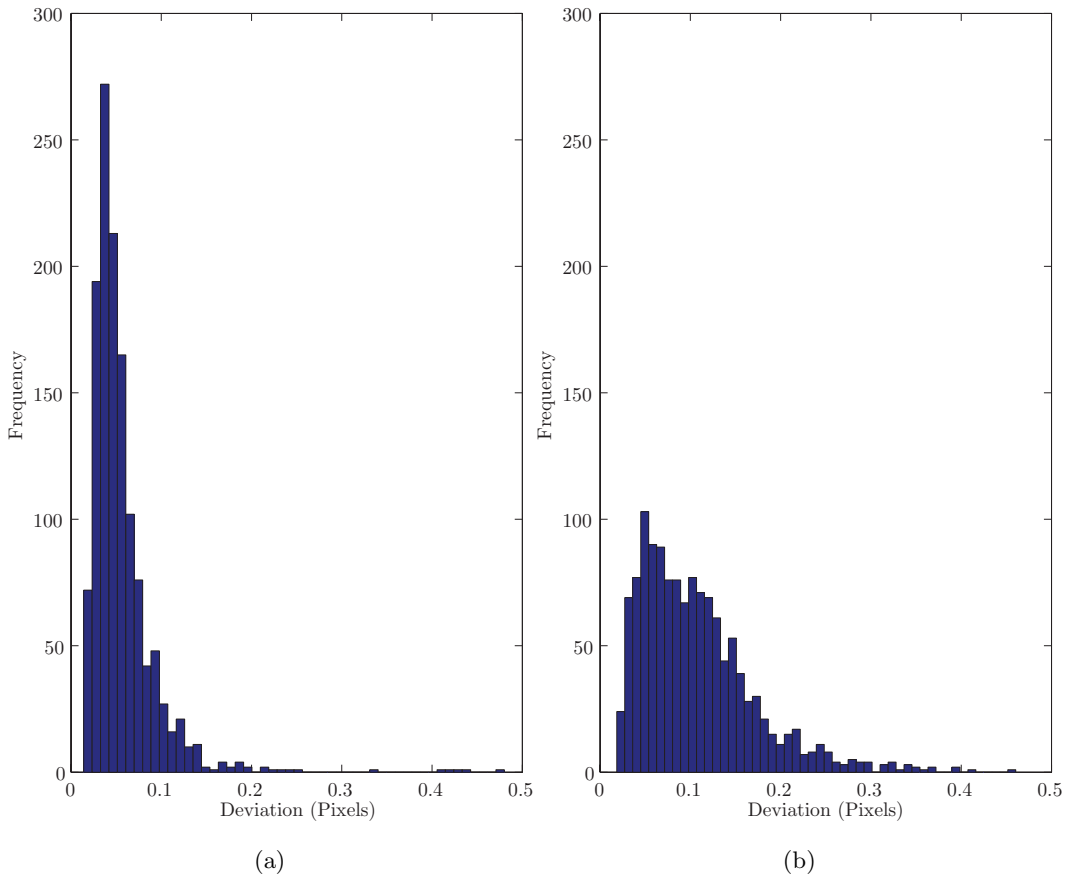


Figure 4.9: Histograms of all centroid deviations: (a) horizontal; and, (b) vertical.

4.3.4.1.2 GeoPIV The centroids in image space for the control points of the calibration target and the known drill hole positions provided concurrent image and object space data. Thus the calibration target could be used to validate the accuracy of the photogrammetric system using a single image. However, assessment of precision required multiple images of the same target, and therefore the image space coordinates of each of the target markers were required in each of the images recorded. This posed the question of whether to use centroiding to deduce the coordinates at each stage of the calculation process or PIV.

To answer this question the accuracy of PIV tracking of the control points on the calibration panel had to be assessed. This was achieved using the same methodology as that presented in Section 4.2.1, where the coordinates of 16 control points were chosen at random and tracked through a synthesised 10 pixel displacement. The results are presented in Figure 4.10 showing that the standard deviation of tracking using GeoPIV was much less than that from centroiding. The mean standard deviation was about 0.02 pixels for patch sizes greater than 60 pixels, and due to the black background the choice of patch size was arbitrary so long as the whole control point was covered by the patch.

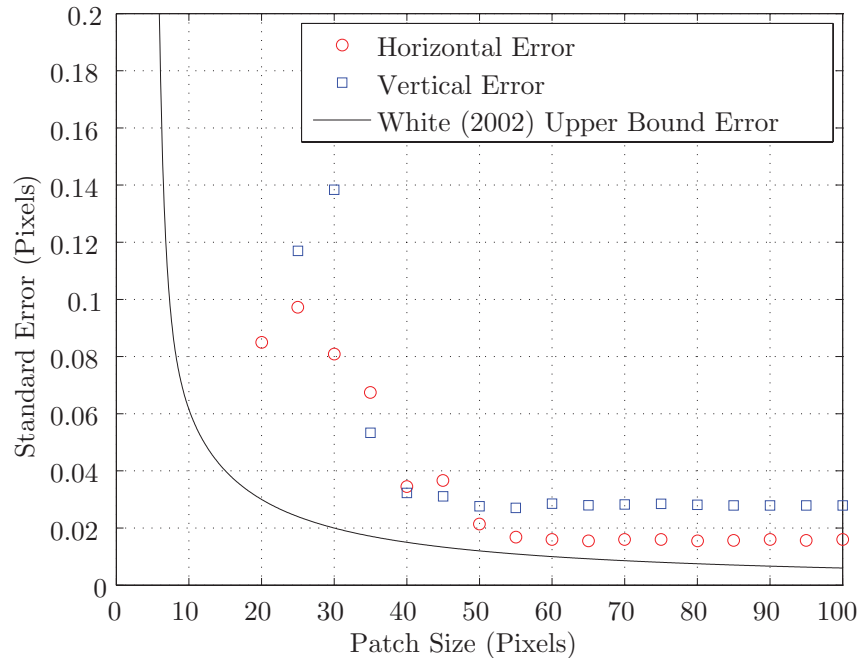


Figure 4.10: Standard error of target panel control point tracking.

This result means that it was best to use centroiding to determine the positions of the control point centroids in the first image, followed by using GeoPIV to track the movement of the control points throughout the remainder of the validation process.

4.3.4.2 Camera Calibration

The calibration of the camera was conducted using a toolbox for MATLABTM (Heikkilä, 2000a), available on the Internet. This uses two or more images with control points on a single plane, with known image space and object space coordinates, to calibrate the internal distortions and external positions of the camera. Alternatively the algorithm is also capable of using a single image with control points on multiple planes. The former technique is used here in conjunction with the calibration target described in Section 4.3.4.1.

The calibration target was positioned such that the camera viewed the target from a similar distance to that used in the testing process except that the calibration target in this instance was not surrounded by the test chamber or matched refractive index pore fluid. The camera settings remained the same as those used in validation and testing and the camera was manually focussed so that the calibration panel was sharply in focus. Six images of the calibration panel were then taken with the calibration panel at different angles and positions relative to the camera in each. These images are presented in Figure 4.11.

Centroiding was then performed on all the control points in each image to generate a set of image space and object space coordinates for each of the six images. These were then passed to the camera calibration subroutine and the intrinsic distortion parameters derived using a non-linear (Levenberg-Marquardt) optimisation process (Heikkilä, 2000a). Table 4.1 contains the camera calibration parameters derived using this process, that are subsequently used to correct internal camera induced errors in test data. The horizontal standard deviation was 0.46 pixels and the vertical standard deviation was 0.54 pixels, which, when using the approximate linear scaling factor introduced in Section 4.2.1 of 1:15.5 ($mm:px$), equates to $29.68\mu m$ and $34.84\mu m$ respectively. This is greater than the quoted accuracy of the drilling of the control points of $\pm 10\mu m$ and likely limits the accuracy of the photogrammetric correction system. Figure 4.12 presents the residual errors for all six images and all control points used in the camera calibration process.

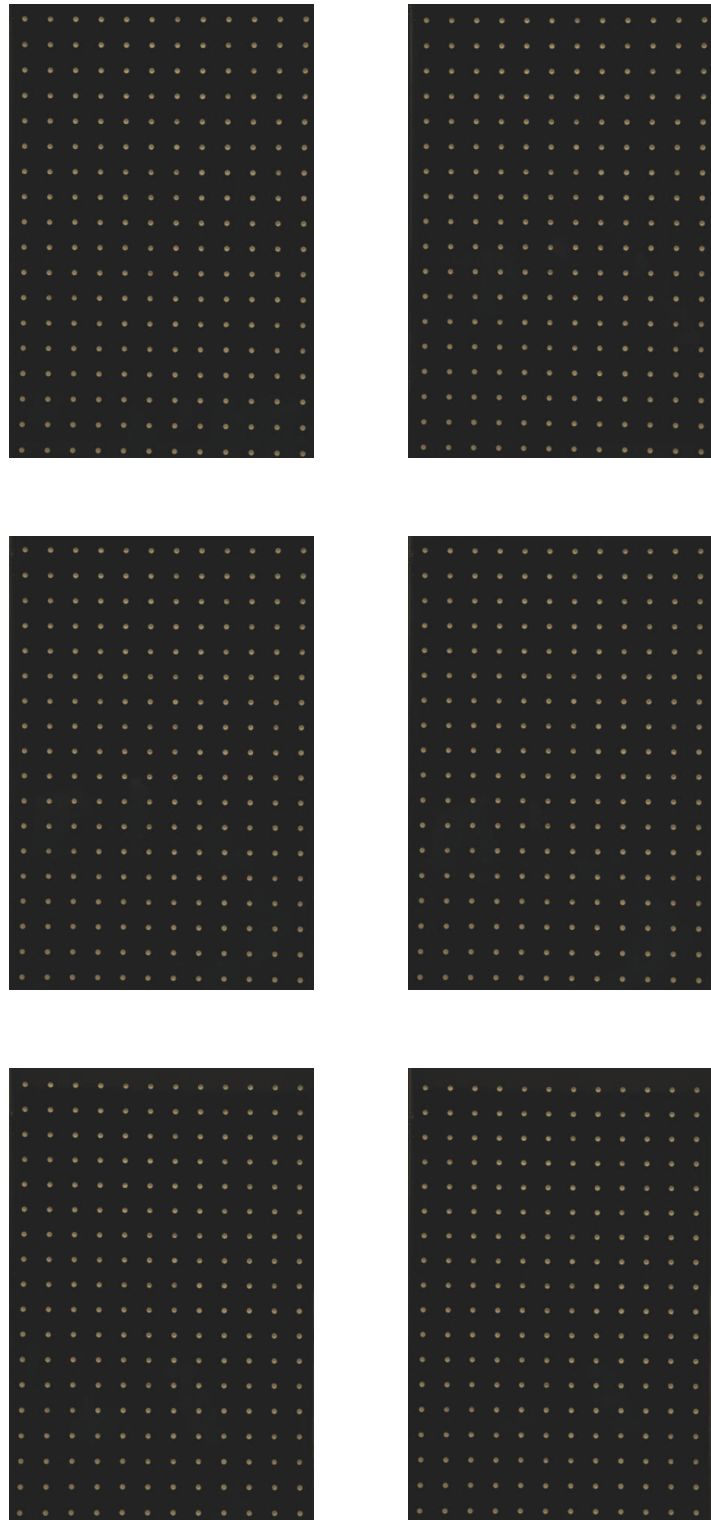


Figure 4.11: Calibration target (FOV of 255mm by 180mm) images.

Table 4.1: Camera calibration parameters derived using calibration panel and centroiding.

α	0.9981
u_0	1315.9820
v_0	1961.6814
k_1	$-3.813107e - 5$
k_2	$-4.438600e - 8$
p_1	$-3.944712e - 6$
p_2	$-1.384821e - 5$

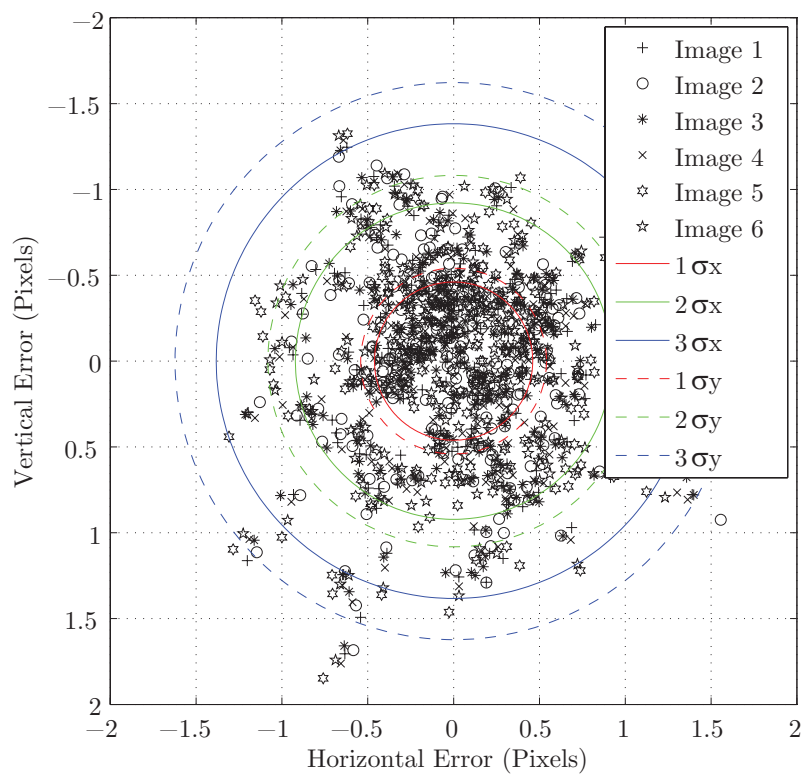


Figure 4.12: Residual error for each control point in all six calibration images using the calibration target.

To provide a check of the validity of the parameters derived from this calibration, the process was repeated using a different set of calibration images of a secondary calibration target. This calibration target was created using a template supplied online (Bouget, 2008) as part of an alternative camera calibration toolbox, consisting of a grid of 30mm by 30mm black and white squares. This was printed at full scale on a laser printer and mounted on a board using spray adhesive. A series of six images (see Figure 4.13) were taken of this secondary calibration panel using the same process as previously described. Corner extraction algorithms provided as part of the alternative camera calibration toolbox were then used to derive image and object space coordinates for each of the intersections of the squares. These were then passed to the same calibration toolbox as previously used for the initial calibration and the intrinsic camera parameters were derived.

Table 4.2 shows the camera calibration parameters derived from this secondary calibration process. The results are generally similar, with a horizontal standard deviation of 0.38 pixels and a vertical standard deviation of 0.62 pixels, which, when using the approximate linear scaling factor introduced in Section 4.2.1 of 1:15.5 (mm:px), equates to $24.52\mu m$ and $40.00\mu m$ respectively. Figure 4.14 presents a plot of the residual error from the secondary calibration process.

The results from these two camera calibrations, using two different methods of extracting image space and object space coordinates for the control points are reassuring in that they are similar. It was not possible to reduce the standard errors further, so it was felt the limit of the system was reached in this instance. Due to the greater number of control points used in the initial calibration, and the fact the residual errors were more consistent (range of 0.08 pixels versus 0.24 pixels), it was these parameters that were used throughout the analysis of both validation and test data.

4.3.4.3 Process

The apparatus used to validate the photogrammetric correction process was essentially the same as that used during testing, except that the transparent soil was replaced by the calibration target surrounded by matched RI pore fluid, and that the light was left on and the laser was not energised. This allowed the traditional control points used on the calibration target to be visible.

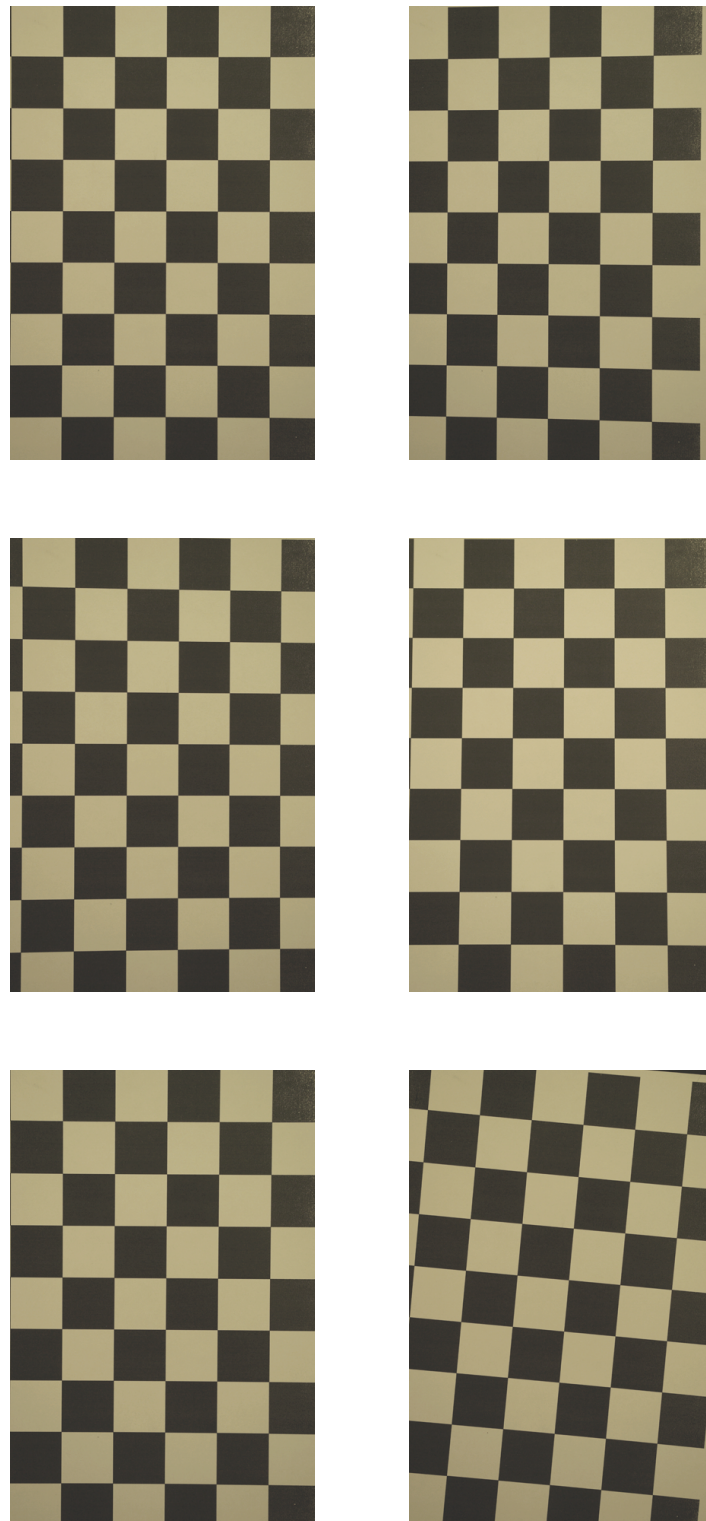


Figure 4.13: Secondary calibration target images of 30mm by 30mm black and white squares.

Table 4.2: Camera calibration parameters derived using secondary calibration panel and corner extraction.

α	1.0012
u_0	1320.2380
v_0	1871.1358
k_1	$-3.153304e - 5$
k_2	$-6.056349e - 8$
p_1	$9.370068e - 5$
p_2	$-9.066078e - 6$

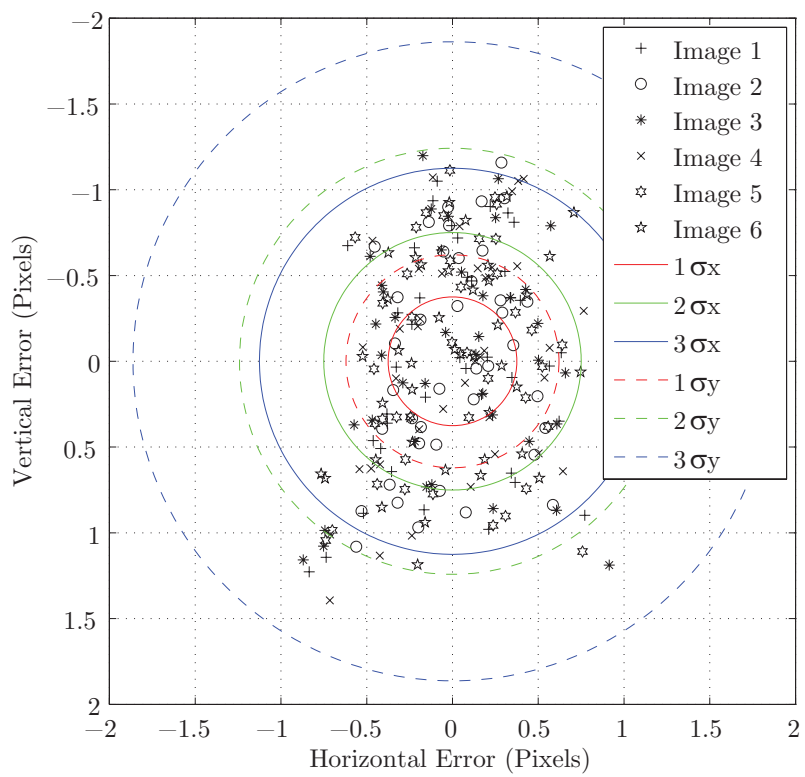


Figure 4.14: Residual error using secondary calibration target.

The apparatus was setup following the procedures outlined in Section 3.7, to ensure the calibration target was perpendicular to the optical axis. The camera was manually focussed on the calibration panel so that the control points were sharply in focus. A series of 70 images was then recorded of the test chamber with the LED control points energised such that the analysis process proposed to be used on test data could be replicated. Apparent positions of the control points on the calibration panel were derived using the photogrammetric correction process. The actual positions were then compared in the first image to define initial system accuracy, and over a sequence of images to define system precision.

4.3.4.4 Results

In total 98 of the 252 control points available were visible in the target area of the test chamber, and all results presented in this section concern the data yielded from this selection of control points. The number of control points visible was reduced in the validation because the FOV of the camera was set to be the same as that adopted during testing. It should be noted that this validation includes centroiding induced errors, which are not a component of the testing process, where concurrent image space and object space data were derived from the initial and final position of the pile tip during installation, allowing calculation of the linear scale factor, λ . In this validation, the coordinates of two control points, at a similar location to the pile during testing, were used to define λ . Therefore the validation could only be as accurate as the drilling of the control points on the calibration panel, which was quoted as $\pm 10\mu m$.

Figure 4.15 is a plot of the amplified (100 times) vectorial residual error between the apparent, or photogrammetry derived, and actual, or known positions of each of the visible control points in the first recorded image. This is a direct assessment of the accuracy of the photogrammetric correction process in a single computation. The vectorial residual errors show no obvious systematic pattern, which suggests that the camera calibration used to correct for internal induced camera errors is suitable for purpose.

Figure 4.16 presents the same data with all coordinates normalised to the datum, such that the data points plotted indicate the horizontal and vertical residual errors for each control point. The standard deviations were about $38.0\mu m$ and $65.0\mu m$ for the horizontal and vertical residual errors respectively. These errors were larger

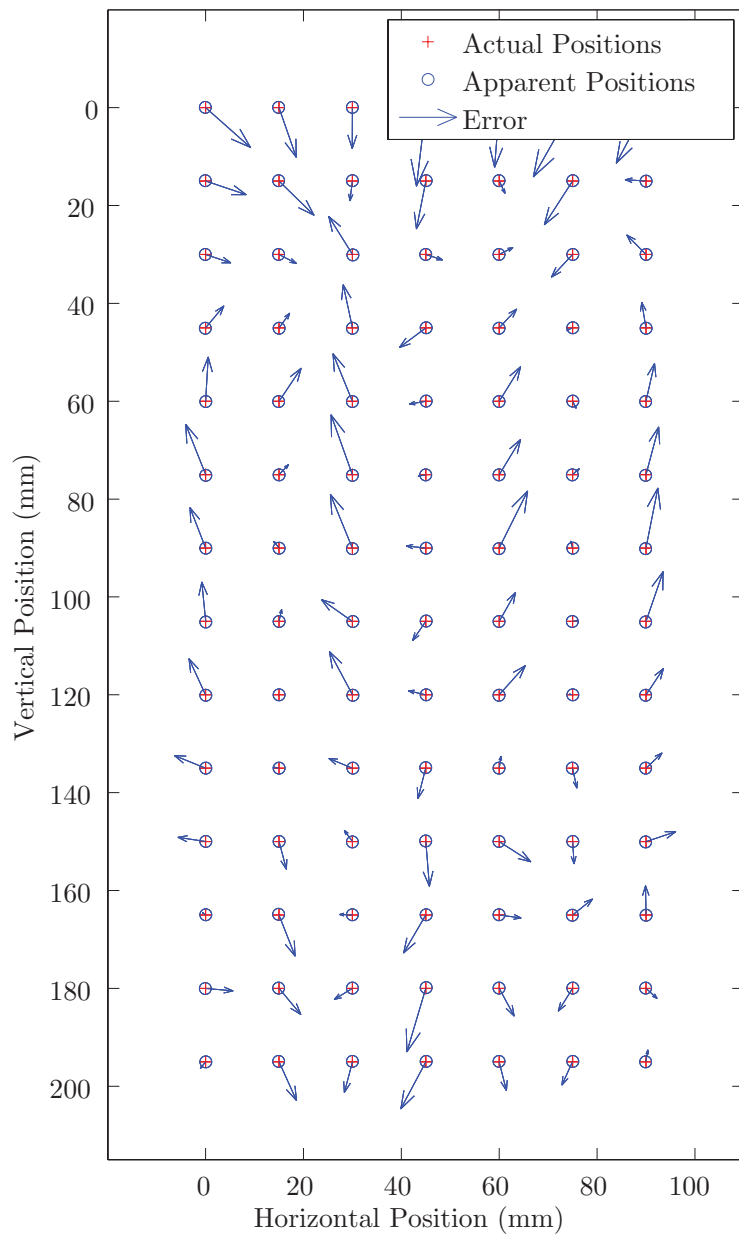


Figure 4.15: Amplified (x 100) residual vectorial errors from camera calibration validation.

than those quoted by White (2002a) with $16.7\mu m$ system accuracy and by Effendi (2007) with $21.0\mu m$ horizontal and $31.0\mu m$ vertical system accuracy, yet was an improvement on simple linear scaling also investigated by White (2002a), for which an accuracy of $107.6\mu m$ was quoted.

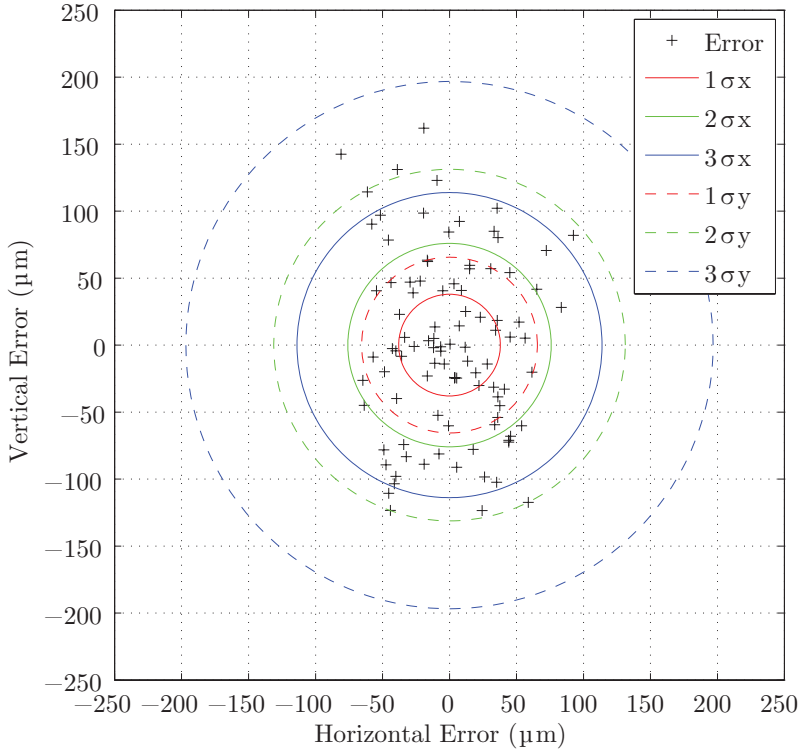


Figure 4.16: Residual errors from photogrammetric correction validation.

The accuracy of the photogrammetric correction system is therefore limited by the camera induced distortion correction. Improvement of the fit of the camera calibration, resulting in a reduction in residual errors would yield improved accuracy of results. However, in regard to PIV measurements for the assessment of geotechnical problems, how important is the accuracy of the photogrammetric correction system?

Typically, physical modellers of geotechnical problems are interested in patterns of behaviour that help generate insight into soil behaviour and geotechnical structure performance. The accuracy to which the movement of an element (patch in PIV terms) can be tracked is of critical importance when the results are to be scaled directly, thus magnifying any errors. The precision of measurements is of key importance when the results are used to assess the development of failure mechanisms around geotechnical structures subjected to increasing load. Figure 4.17 is a plot

of the temporal evolution of the standard deviation, or in this case the number of sequential PIV computations conducted.

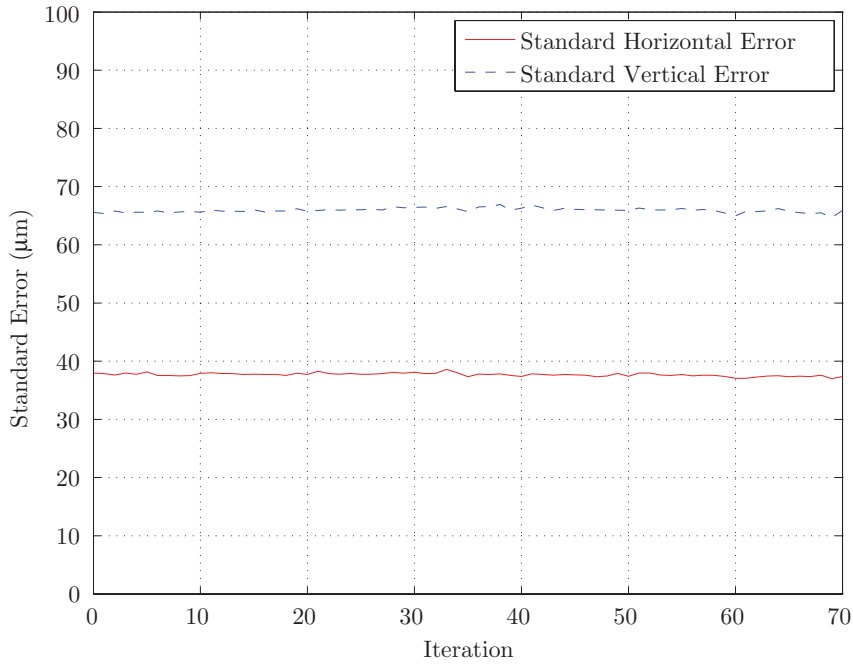


Figure 4.17: Standard error of residual errors from photogrammetry validation.

The standard deviation of the residual errors observed appears to be stable with increasing numbers of PIV computations. This confirms that the correction of internal camera induced distortion is consistent and that the photogrammetric correction system as a whole is precise.

Of more interest are the mean residual errors presented in Figure 4.18. Since the control points are stationary during calibration in relation to the LED control points and test chamber, this represents graphically the camera-soil movement errors that are not removed by the external correction process described in Section 4.3.2. These errors are far more significant. The maximum error in either horizontal or vertical component is about $25\mu m$. So, for example, if the minimum displacement contour plotted is $25\mu m$, then it can only be stated with confidence that it is representative of a displacement magnitude of $25\pm 25\mu m$. This renders contours of displacement of this magnitude meaningless. It also means that there is uncertainty regarding the position of the datum or zero contour, which could lead to confusion when interpreting the results.

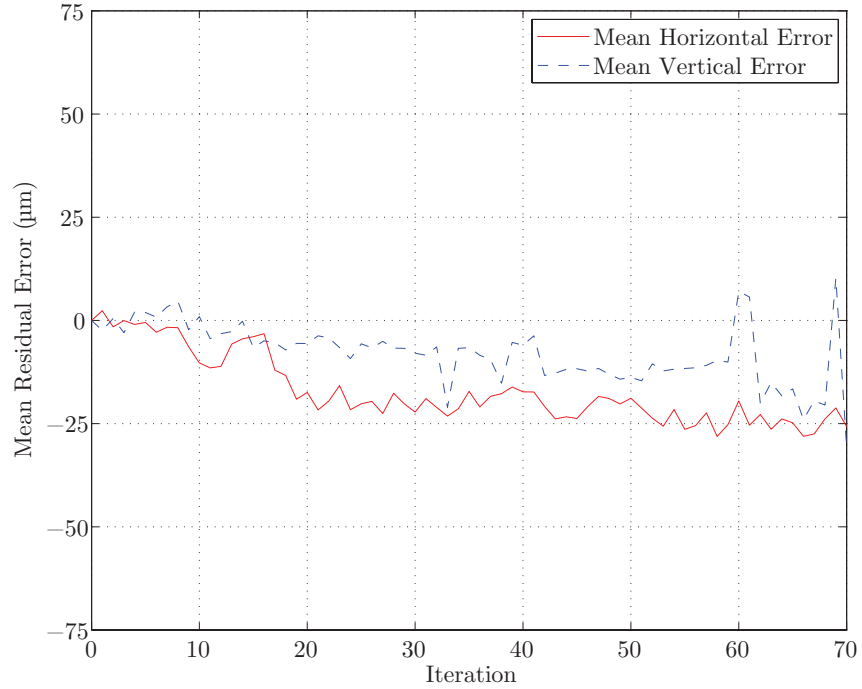


Figure 4.18: Mean residual error from camera calibration validation.

Given that the GeoPIV calibrations demonstrated that tracking of transparent soil was more accurate than that of the control points on the calibration target (compare Figures 4.1 and 4.10), it was deemed necessary to investigate the camera-soil movement errors using a consolidated sample of transparent soil rather than the calibration target. A sample created for a model pile test was utilised for this purpose before model pile testing. After alignment of the camera, a series of 70 images of the plane of interest, highlighted by the laser light sheet, was recorded using the digital camera. GeoPIV was then used to track the movement of 98 randomly selected 50 pixel patches throughout the series of images. Due to the camera being setup and left in-situ for the model pile test, after the camera-soil movement assessment, it was possible to deduce the scaling factor λ from the pile tip position at the start and end of installation, and thus present the camera-soil movement errors in μm . Figure 4.19 presents the residual errors assuming zero soil movement.

The mean residual errors in this instance are very similar to those observed in the validation using the calibration panel. The precision of the photogrammetric correction system was demonstrated by the consistency of the standard deviation of the residual errors presented in Figure 4.17. However, the precision is shown

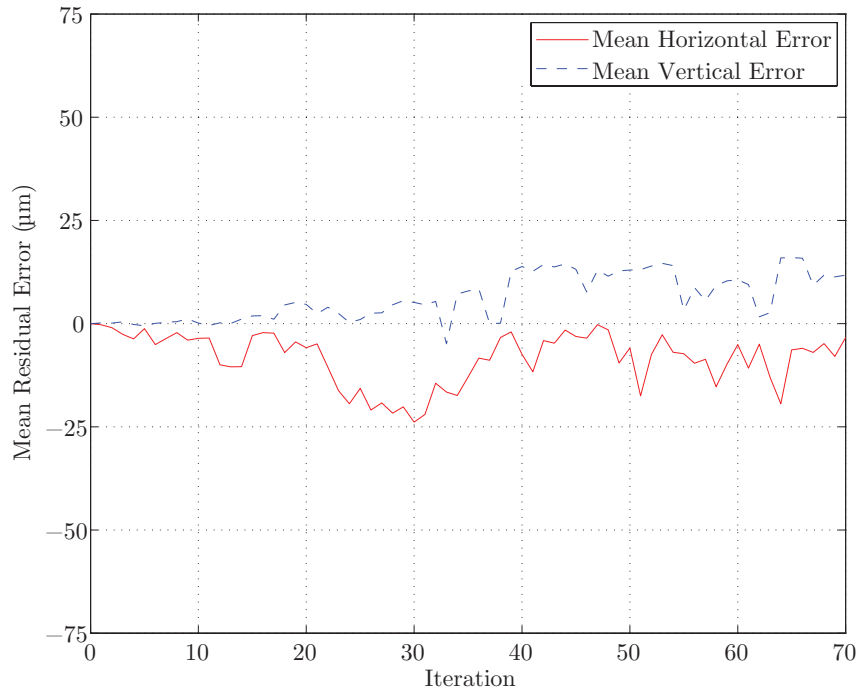


Figure 4.19: Mean residual error from zero soil movement analysis.

in Figures 4.18 and 4.19 to be about $\pm 20\mu m$. It was important to ascertain why the mean error was unstable and not zero as was expected, given that camera-soil movement induced errors were corrected using the procedure described in Section 4.3.2.

In the system utilised by White (2002a), the photogrammetric system converted measurements in pixels recorded on the CCD plane, to metric measurements at the control point plane, or the front of the test chamber. Target plane measurements for movement on the front surface of the soil sample were then derived by correcting the control point plane data for refraction. The distance between the non-coplanar control point plane and target plane was 50mm. In this investigation the distance between the control point plane and the target plane is half the depth of the soil model, plus the depth of the Perspex viewing window, plus the depth of the LED control point panels. This totalled 140mm. It is this increased non-coplanarity between the control point plane and target plane that is the source of the errors seen in Figures 4.18 and 4.19. Since the control point plane is used to correct for camera-soil induced movement errors, and it is not coplanar with the target plane, where the measurements of soil movement are recorded, movement errors are introduced into the dataset. Unfortunately, due to the configuration of the

apparatus and the lack of paired image space and object space coordinates for the LED control points, it is impossible to create a closed form correction for this non-coplanarity, even though the perpendicular distance between the control point and target planes is known.

To serve as a further check on the precision of the system a repeat test was conducted using another consolidated sample of transparent soil. Figure 4.20 indicates that the residual errors in this case were even greater than in the previous two validations.

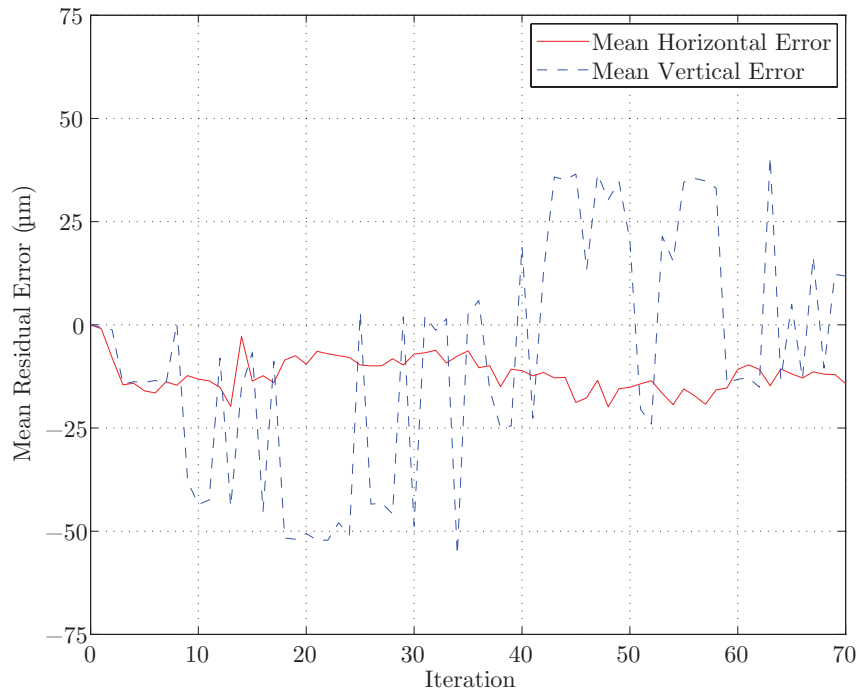


Figure 4.20: Mean residual error from repeat zero soil movement analysis.

This observation significantly increased the need for some form of movement error reduction, in order to allow the full accuracy of GeoPIV to be realised when tracking movements non-intrusively in transparent soil. It was also clearly apparent that the experimental apparatus is susceptible to any local vibrations. In Figure 4.20 the vertical errors are far greater than the horizontal errors, suggesting that vibrations were transmitted through the floor of the laboratory, and subsequently through the legs of the camera tripod. Therefore, to minimise vibrations in the laboratory, all tests from this point forward were conducted out of normal laboratory working hours.

4.3.5 Camera-Soil Movement Error Reduction

In the three validations presented in Section 4.3.4.4, there is zero movement on the plane of interest so the camera-target movement errors could be directly assessed. In this instance the modal magnitude of the mean residual error could be used to correct the data, since the modal magnitude should be identical to the camera-target movement error. Fortunately, this technique can also be used for a physical model test, such as the model pile and footing tests presented in Chapters 5 and 6, assuming that:

1. The boundary effects are minimised by ensuring there is sufficient free boundary distance.
2. Displacement of the geotechnical structure is used to induce displacements within the soil continuum.
3. The surface area of the geotechnical structure is significantly smaller than the surface area of the boundary of the physical model.
4. PIV analysis patches are uniformly spaced throughout the model and encompass areas of the model where zero soil movement is anticipated.

If these constraints are met, the gradient of displacement within the soil continuum is a maximum at the interface with the geotechnical structure that is applying displacement to the soil. Similarly, the gradient of displacement is a minimum where there is zero soil movement. In these circumstances, it can be assumed that modal magnitudes of displacement for both vertical and horizontal components will be equal to the residual camera-target movement error. If the modal magnitude, for both horizontal and vertical components, is calculated for each image in the PIV analysis process, it can be removed universally to generate data where the residual movement errors will be reduced.

To derive the modal movement magnitude for horizontal and vertical movements a simple histogram can be used for each displacement component. The bin width of the histogram is the only subjective choice that needs to be made in the movement error reduction process, and thus requires justification. If a very large bin width is specified the frequency of the modal bin width will be very large. Similarly if a very small bin width is chosen the frequency of the modal bin width will be very small, and critically may not equal the movement error if there is significant

noise entrained in the data through the PIV analysis. Hence, a balance must be sought, where the bin width chosen is small enough that the resolution of the ensuing correction is good enough to have an influence on the output, yet large enough that the modal bin has a frequency that is significantly greater than those of the other bins, thus generating confidence in the method. Figures 4.21, 4.22 and 4.23 present the mean and maximum absolute residual error after correction for all control points or soil patches, from the calibration target, zero soil movement and repeat zero soil movement validations, with increasing histogram bin width, for all 70 images used in each case.

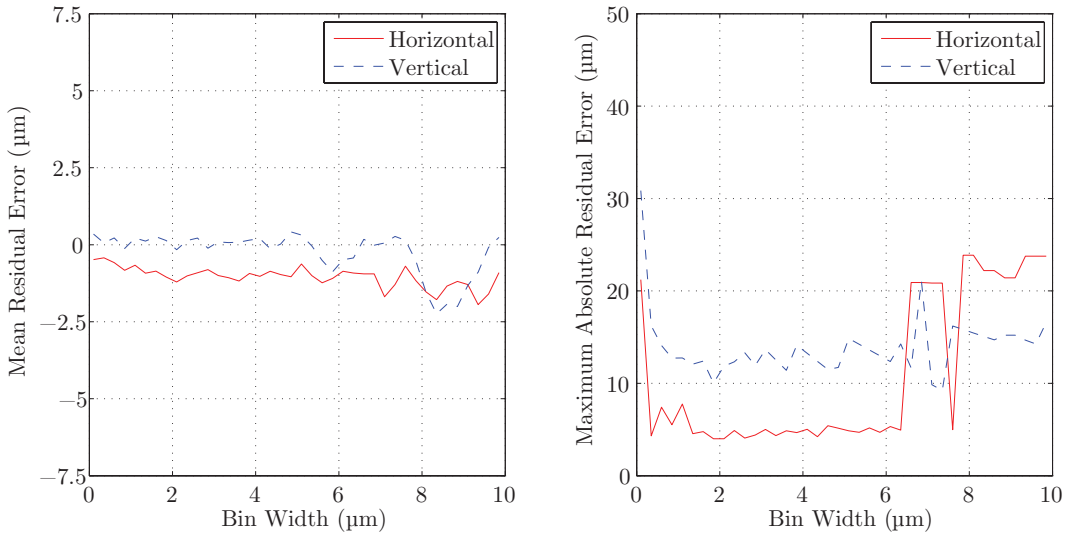


Figure 4.21: Mean and maximum absolute residual error with increasing histogram bin width from modal movement correction for calibration panel validation.

The data presented shows that the optimum bin width for this investigation is $2\mu\text{m}$ as it is the smallest bin width for which both the mean and maximum absolute residual errors remain small in all three cases. The choice of bin width is unique to each experimental setup, so the value proposed here is specific to this investigation (where the position of the camera relative to the target remains constant). A bin width of $2\mu\text{m}$ has been used for all data analysed in the remainder of this thesis.

One method of assessing the confidence that can be placed in the modal magnitude of movement calculated, and thus corrected in this way, is by calculating the percentage of measurement points that have magnitudes equal to the calculated modal magnitudes. Figures 4.24, 4.25 and 4.26 show that in all three validation cases the percentage of measurement points equal to the modal magnitudes reduces rapidly

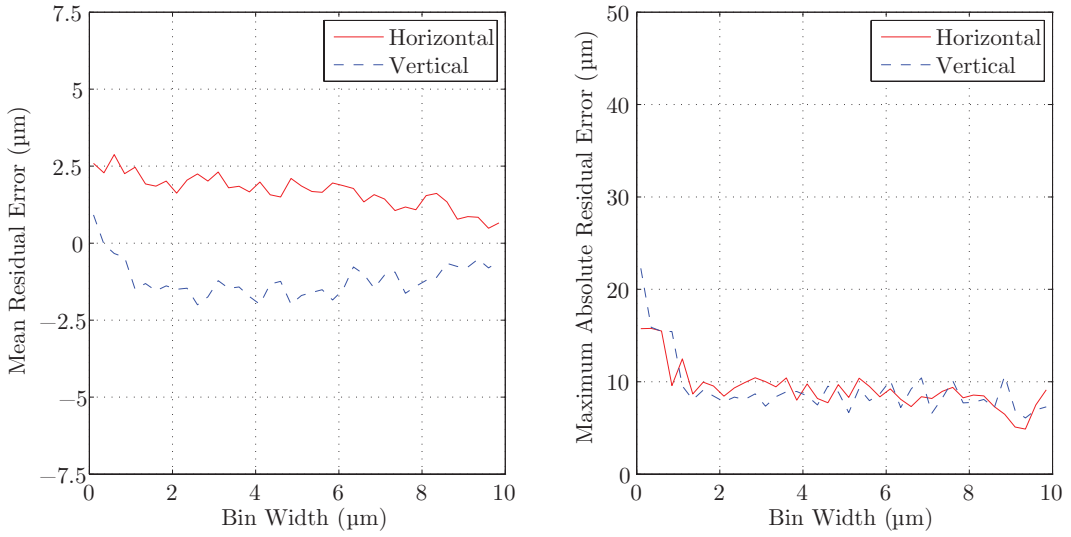


Figure 4.22: Mean and maximum absolute residual error with increasing histogram bin width from modal movement correction for zero soil movement validation.

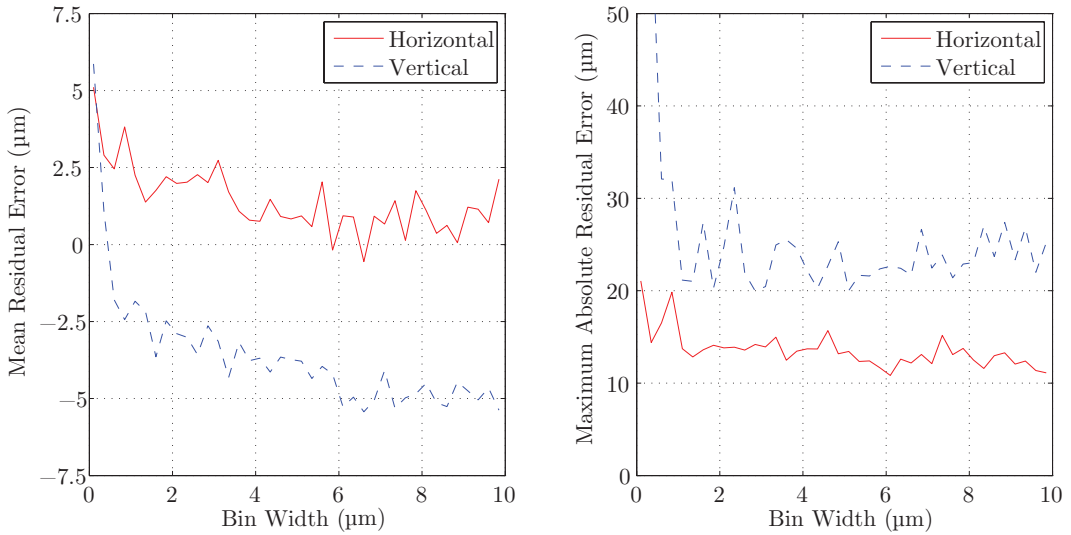


Figure 4.23: Mean and maximum absolute residual error with increasing histogram bin width from modal movement correction for repeat zero soil movement validation.

to a steady 10-20%. In an actual test, where the soil is experiencing differential displacements induced by a geotechnical structure, this percentage may be expected to be lower. It is also highly dependent on bin width, since a small bin width increases the chance of the noise generated by GeoPIV adversely affecting the correct calculation of the modal movement components.

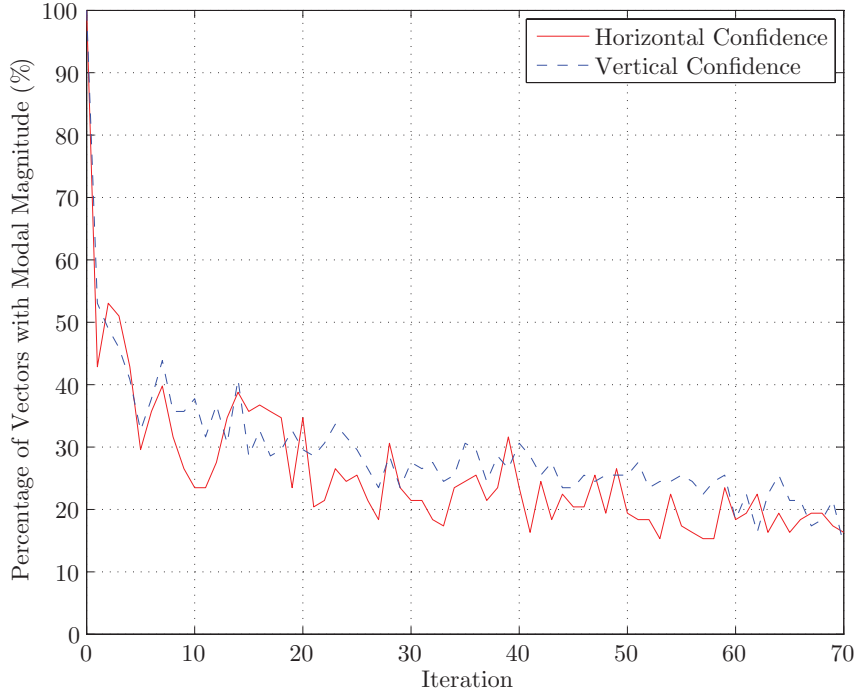


Figure 4.24: Percentage of measurements coincident with the modal movement magnitude for calibration target validation.

The effect that this modal movement correction has on the precision of the photogrammetric correction system is quite dramatic, as demonstrated by the data in Figures 4.27, 4.28 and 4.29. The average residual error present in these three validations is $5\text{-}20\mu\text{m}$ and thus the enhanced precision of the system is comparable with that presented by White (2002a). The application of this modal movement correction can also be observed, when used on actual test data, by monitoring the magnitudes of the horizontal and vertical movement corrections and the corresponding percentage of measurements equal to the modal magnitude. These observations are presented and discussed in Chapters 5 and 6 for the model pile and footing tests respectively.

The modal movement correction presented here helps to mitigate the effect of camera-soil movement errors in a PIV derived dataset, and particularly improves

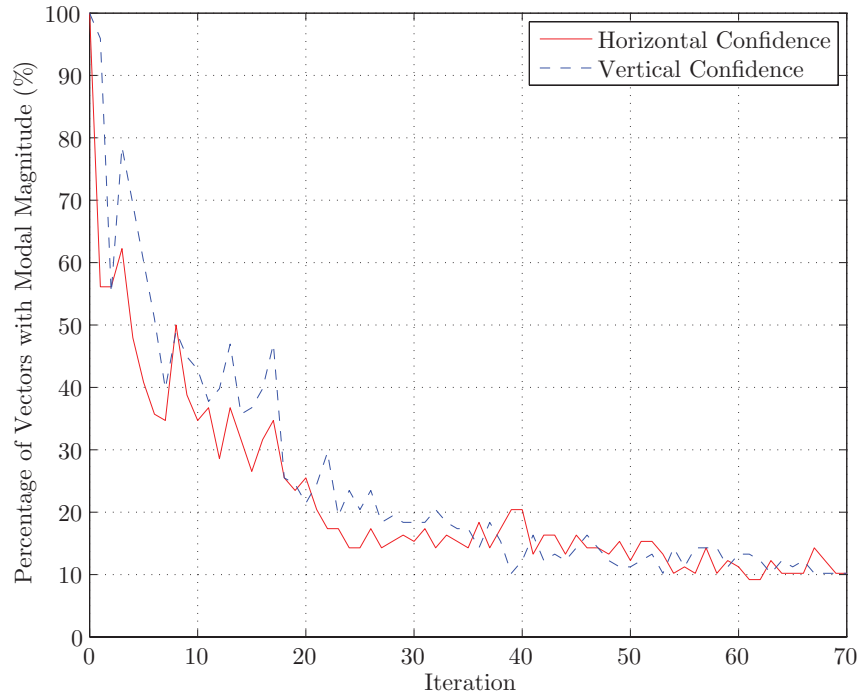


Figure 4.25: Percentage of measurements coincident with the modal movement magnitude for zero soil movement validation.

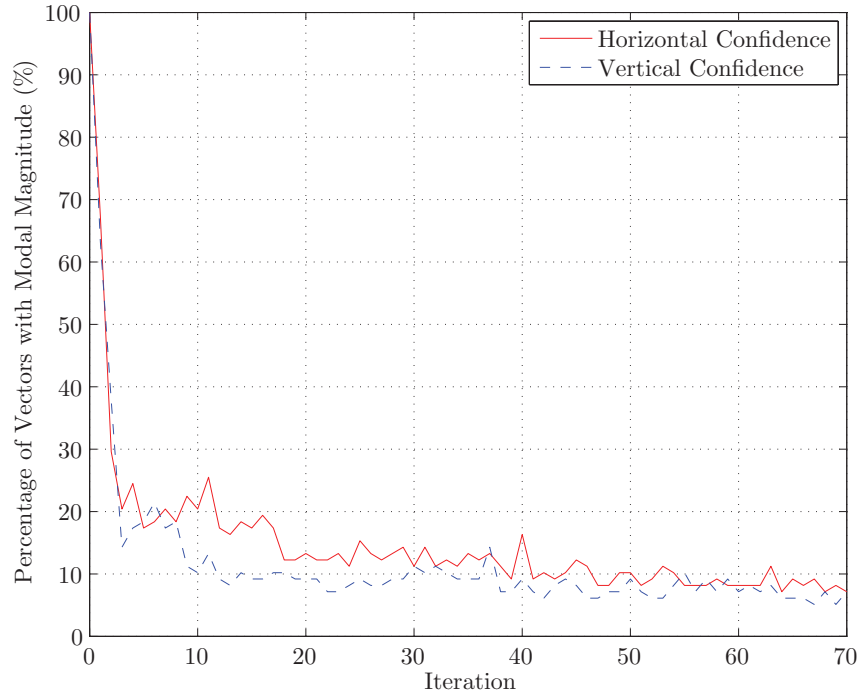


Figure 4.26: Percentage of measurements coincident with the modal movement magnitude for repeat zero soil movement validation.

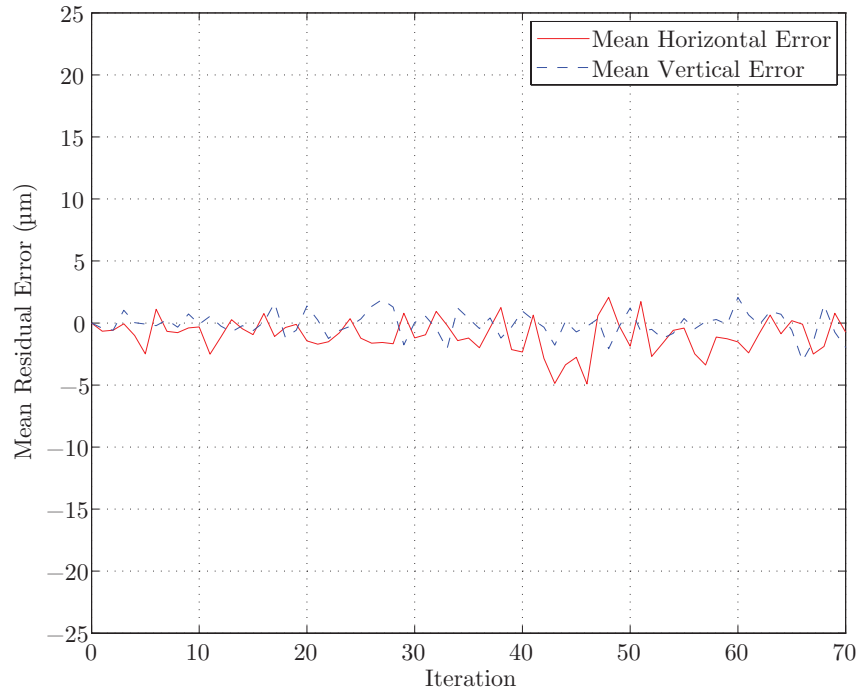


Figure 4.27: Mean residual error from calibration target validation after modal movement correction.

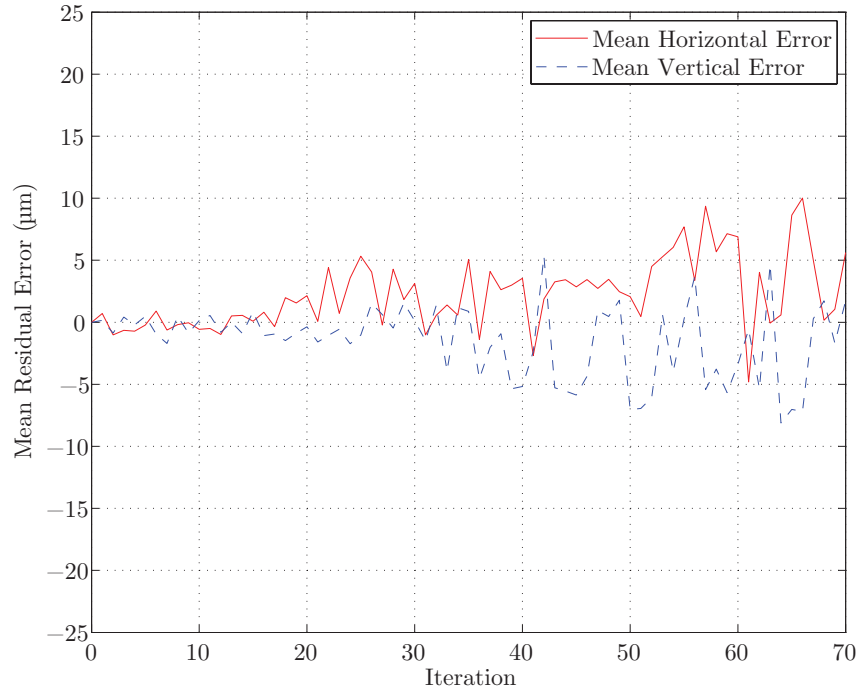


Figure 4.28: Mean residual error from zero soil movement validation after modal movement correction.

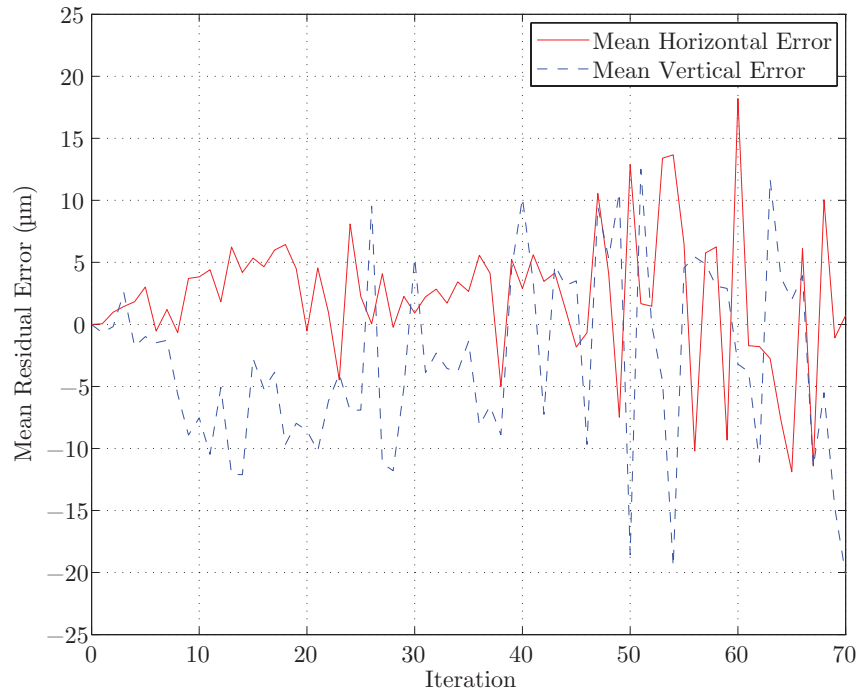


Figure 4.29: Mean residual error from repeat zero soil movement validation after modal movement correction.

precision in tests where vibrations cause camera-soil movements. Case studies are presented in Chapter 5 that illustrate the impact of this correction on the data output and interpretation of the results would be more difficult were it not employed.

4.3.6 Shear Strain Computation

To complement displacement field data, engineering shear strains have been calculated to indicate areas of high shearing occurring within the soil. This has been achieved using the rotating reference frame approach described by White (2002a), using groups of three PIV measurement points to form a strain triangle. The centroid of each triangle defines the strain measurement point, and the three measurement points are used to form a displacement gradient matrix. This is then converted into a deformation gradient matrix from which cumulative and incremental strain components can be extracted. This process was achieved by using the ‘GeoSTRAINS’ package supplied by White and Take (2002). A detailed explanation of the generation and conversion of the displacement gradient matrix into a deformation gradient matrix, followed by the extraction of strain components can be found in Appendix 1 of White (2002a), and thus is not described in greater detail here.

4.4 Post-Processing

Some post-processing was required so that the data derived from the PIV analyses was presented in a clear and concise format. Firstly random vectors were removed from the dataset manually. These were generally vectors that were greater in magnitude than the displacement applied to the geotechnical structure at that point in the test. Some vectors became wild due to a loss of texture at some stage in the analysis, and these were deleted from the full sequence of data. This was accomplished using a modified version of the ‘GeoWILD’ routine distributed by White and Take (2002). Typically 1-2% of the measurement points were deleted in this process.

The second process involved post-processing of the output plots created using MATLABTM typically including:

- Vectorial displacement plot.
- Horizontal displacement contour plot.
- Vertical displacement contour plot.
- Shear strain contour plot.

Figure 4.4 shows typical raw output from MATLABTM prior to post-processing. The zero displacement contour is very noisy due to the random walk error generated by GeoPIV. This creates slightly non-zero displacements where zero displacement may be expected. Hence, there is a high prevalence of zero contours in that region, particularly in the horizontal contour plot in Figure 4.30(b).

Using Adobe Illustrator this noise has been manually removed from the output data, in order to generate clearer output. All continuous contours except closed loop contours of zero displacement magnitude were left untouched. This process is by nature subjective, but due to the low magnitudes of movement being observed, particularly the horizontal displacements, it was considered unavoidable if clear output data was to be generated for analysis. To improve clarity further the contours have also been manually labelled to reduce the reproduction of contour labels seen in the raw data in Figure 4.4. Lastly, the typeset and formatting has been modified using a batch process. Figure 4.4 is an example of the final output, generated by post-processing the data from Figure 4.4.

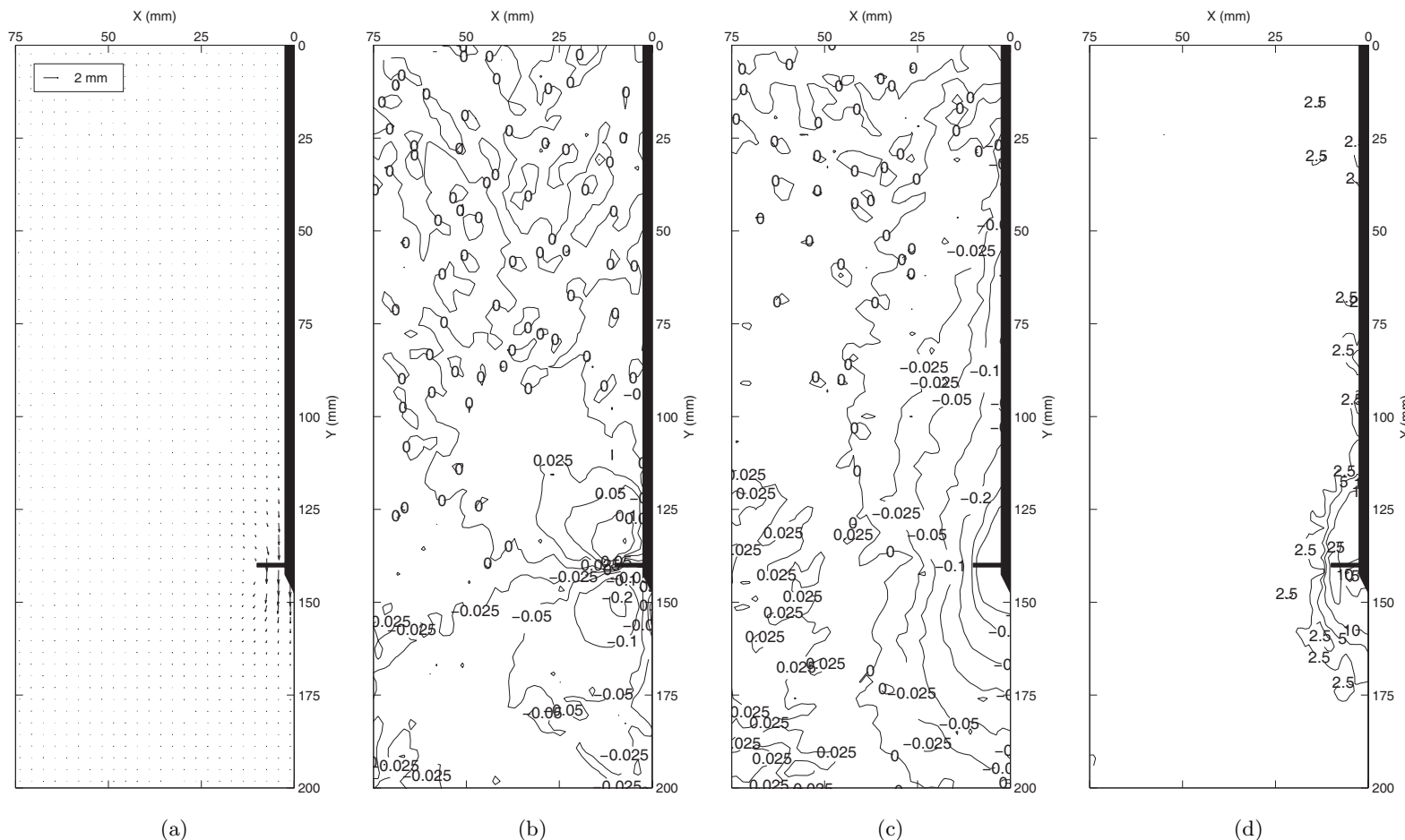


Figure 4.30: Typical raw output plots prior to post-processing: vector (a), horizontal displacement (b), vertical displacement (c) and shear strain contours (d) with displacements in mm and shear strains expressed as a percentage.

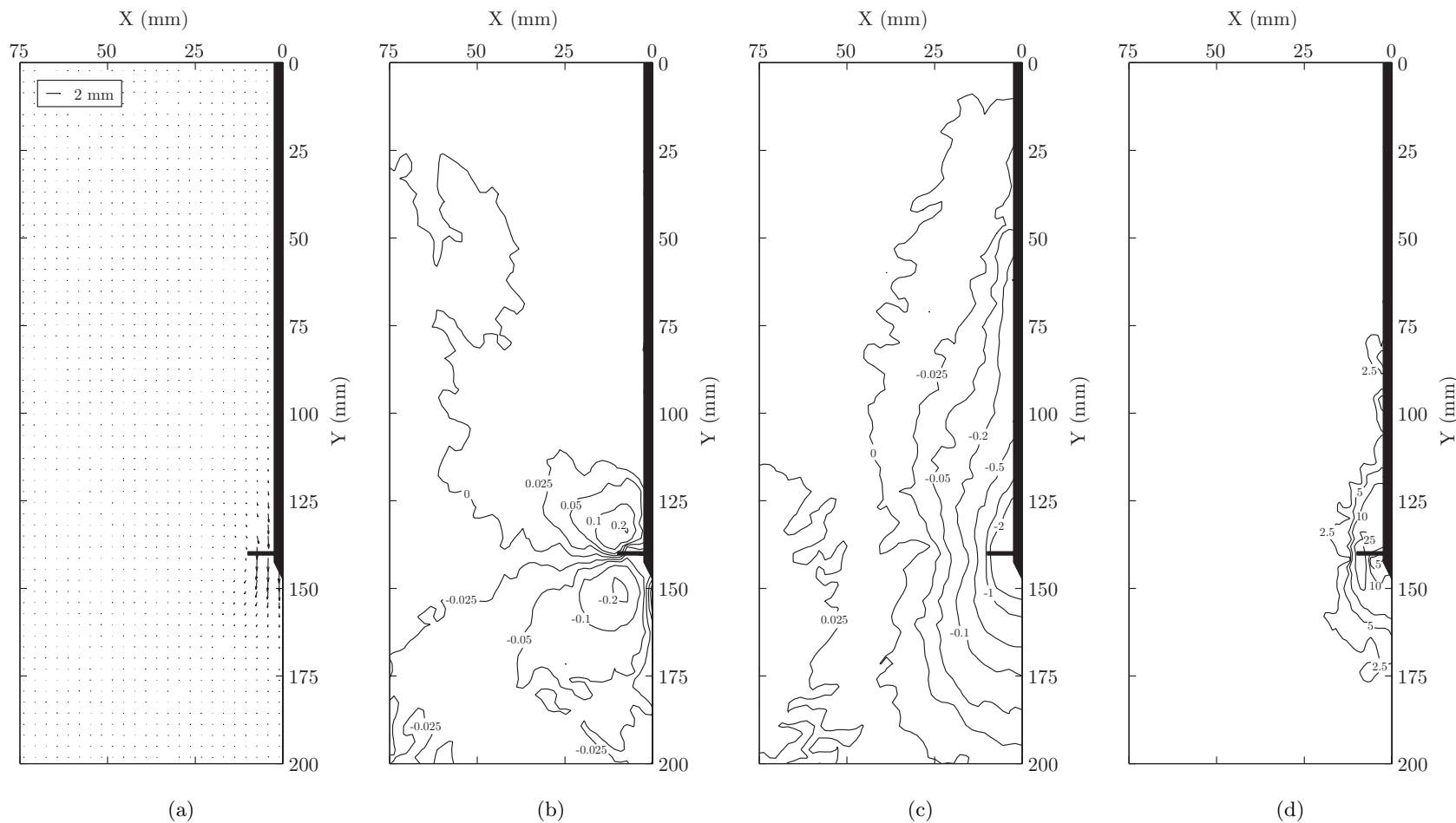


Figure 4.31: Typical post-processed output plots: vector (a), horizontal displacement (b), vertical displacement (c) and shear strain contours (d) with displacements in mm and shear strains expressed as a percentage.

Chapter 5

Physical Modelling of Helical Screw Piles

5.1 Introduction

The results from laboratory testing of model helical screw piles are presented in this chapter. Throughout, PIV analysis is used to assess displacement and shear strain fields apparent within a transparent soil sample.

The convention for the labelling of the graphical output deviates from the common assumption that settlement is positive, since both compressive and tensile loading scenarios are considered. Instead, in the vertical displacement contour plots, positive contours indicate heave and negative contours indicate settlement. Similarly, in the horizontal displacement contour plots, positive contours indicate rightward movement and negative contours indicate leftward movement.

Section 5.2 considers the disturbance caused by installation of the four configurations of helical screw pile as introduced in Section 3.3. Repeatability of installation is considered both in terms of the residual force apparent due to installation and the resultant disturbance caused by installation for the least repeatable case. Observations drawn from the data are presented, which will be of greater relevance when comparisons are made between the performance of the physical models and numerical models of the experiments, which are presented in Chapter 7.

Section 5.3 presents data from the compressive and tensile loading tests. The load-deflection performance for all configurations is presented alongside displacement and shear strain fields for both cumulative and incremental displacements,

during mobilisation of the Ultimate Limit State (ULS). Repeatability of the testing process is considered by comparing the load-deflection response and displacement and shear strain fields, at the ULS, for two repeat tests.

Section 5.3.5 discusses general observations yielded using the laboratory tests that are used to guide assumptions made during development of the FE method based simulations of the physical modelling tests, which are presented in Chapter 7.

5.2 Installation

5.2.1 Analysis Method

Digital images were recorded at a rate of 3fps during installation of the model helical screw piles in a 220mm deep bed of transparent soil, to a depth of 7D, measured from the soil surface to the depth of the mid-flight of the lowermost helical plate. As outlined in Chapter 3, the vertical drive speed was 0.2mm/s with a corresponding rotational speed of 0.04rps, implying one full revolution per helix pitch increment of vertical displacement, given the 5mm helix pitch. Typically, this yielded a series of about 1800 images from commencement of installation to completion, from which displacement and shear strain fields were derived using PIV.

It was not possible to track movements within the installation path of the model piles during installation due to the out of plane movement of soil induced by the rotational nature of the installation process. This meant that only displacement and shear strains in the soil outside of the path of the helices of the pile could be tracked accurately. As a result, the range of displacement apparent in the region analysed was relatively small (< 2mm), allowing a small subset of images to be selected from the dataset for PIV analysis.

The effect of this was two-fold: it reduced the computation time required to assess the total installation disturbance dramatically and effectively increased the value of ‘leapfrog’ used by GeoPIV to approximately 250. This allows very small displacement and shear strains to be computed accurately since the number of iterations required in the PIV calculation process is reduced and the subsequent summated random walk error due to GeoPIV is minimised (White, 2002a).

The ‘searchzone’ parameter within GeoPIV was set to 10px or 0.65mm when converted to metric units using the approximate linear scaling factor introduced in Chapter 4, which is considerably greater than the maximum displacement observed for any single 1D installation increment. This value for ‘searchzone’ was chosen since it allowed computation of a plausible displacement field, with very few wild random datapoints outside the installation path of the model pile. Given that displacements could not be observed within the installation path where the magnitudes of displacement could be expected to be larger, increasing the value of this parameter was not necessary. Table 5.1 presents the displacement and shear strain contours plotted in

the installation data presented. All data is plotted relative to the initial coordinates of the element of soil it is describing. Vectorial displacement plots are amplified by a factor of five for clarity.

Table 5.1: Contours of displacement and shear strain presented in helical screw pile installation contour plots.

Plot	Increments
Horizontal Displacement (mm)	-2, -1, -0.5, -0.2, -0.1, -0.05, -0.025, 0, 0.025, 0.05, 0.1, 0.2, 0.5 ,1, 2
Vertical Displacement (mm)	-2, -1, -0.5, -0.2, -0.1, -0.05, -0.025, 0, 0.025, 0.05, 0.1, 0.2, 0.5 ,1, 2
Shear Strain, γ (%)	1, 2.5, 5, 10, 25

5.2.2 Data Appraisal

Given the use of a statistical camera-soil movement correction framework (see Section 4.3.5) it is important to assess the magnitude of correction applied to the dataset at each point of PIV analysis presented. This allows qualitative appraisal of each dataset. Large camera-soil movement corrections indicate a noisy dataset where camera-soil movements were large and significantly contaminated the dataset with systematic errors. Conversely, low magnitudes of correction indicate that the magnitude of camera-soil movements were small. Table 5.2 presents the horizontal and vertical correction magnitudes applied to the four installation disturbance analyses presented here. The actual test during which the installation data was recorded is noted in the table for clarity. Since the pile geometry was identical for the compressive and tensile test pairs (i.e. tests C1 and T1 being one test pair and tests C2-30 and T2-30 being another) regardless of whether the loading applied after installation and setup was compressive or tensile, the installation disturbance presented herein is representative of that caused by piles of similar geometry loaded either in compression or tension.

As hypothesised in Section 4.3.5, the percentages of vectors equal to the modal magnitude of movement for both horizontal and vertical corrections are significantly less than the percentages observed during the target and zero-soil movement validations (see Figures 4.24, 4.25 and 4.26). This is due to the development of a displacement field due to movement of the model pile. No such movements were evident in the initial validations in Section 4.3.5 and hence the percentage of vectors with modal magnitude was larger. The consistency of the percentage

Table 5.2: Magnitude of horizontal and vertical (u_c , v_c) correction specified by modal movement correction process for installation analyses, alongside the corresponding percentage of vectors of modal magnitude ($\%_u$, $\%_v$).

Test	Correction			
	Horizontal		Vertical	
	u_c (μm)	$\%_u$	v_c (μm)	$\%_v$
Single Helix Pile - C1	17	2.0	-77	1.3
Double Helix Pile - C2-30 ($L_a=30mm$)	19	2.3	-85	1.8
Double Helix Pile - C2-60 ($L_a=60mm$)	27	2.5	-69	1.6
Triple Helix Pile - C3 ($L_a=30mm$)	11	1.5	-87	1.8

of vectors equal to the modal magnitude, at an installation depth of $7D$, is an indication that the camera-soil movement correction applied is functioning in a consistent manner. Comparison of the zero contour position in the results presented in Section 5.2.3 and the potential positions had the correction not been applied, serves as an indication of the range of uncertainty inherent in the output data.

To demonstrate this, the output from installation of a double helix pile with $30mm$ active length (C2-30) is considered at an installation depth of $7D$. The magnitudes of horizontal and vertical correction are $19\mu m$ and $-85\mu m$. Removing these corrections from the horizontal and vertical contour plots demonstrates the effect of the camera-soil movement correction. Figures 5.1(a) and 5.1(b) present the uncorrected displacement contours, which can be directly compared to Figures 5.1(c) and 5.1(d) to assess the effect of the correction.

The vector plot is not noticeably affected by the corrections applied and therefore, has not been presented. The horizontal contour plot in Figure 5.1(a) is not vastly changed by the correction, since there is only a small movement of the zero contour that is generated by the correction. In contrast, the vertical displacement contours in Figure 5.1(b) are significantly affected by the correction at low displacement magnitudes ($< 0.1mm$). The magnitude of the effect of the correction reduces with increasing displacement contour magnitude, such that the vertical displacements adjacent to the installation path of the pile are not noticeably different to those in the corrected output. Strains are calculated from the gradient of displacement so, given that the camera-soil movement correction is systematic in nature and the strain caused by a systematic displacement of an element of soil must be zero, the strain based output remains the same and thus is not presented here.

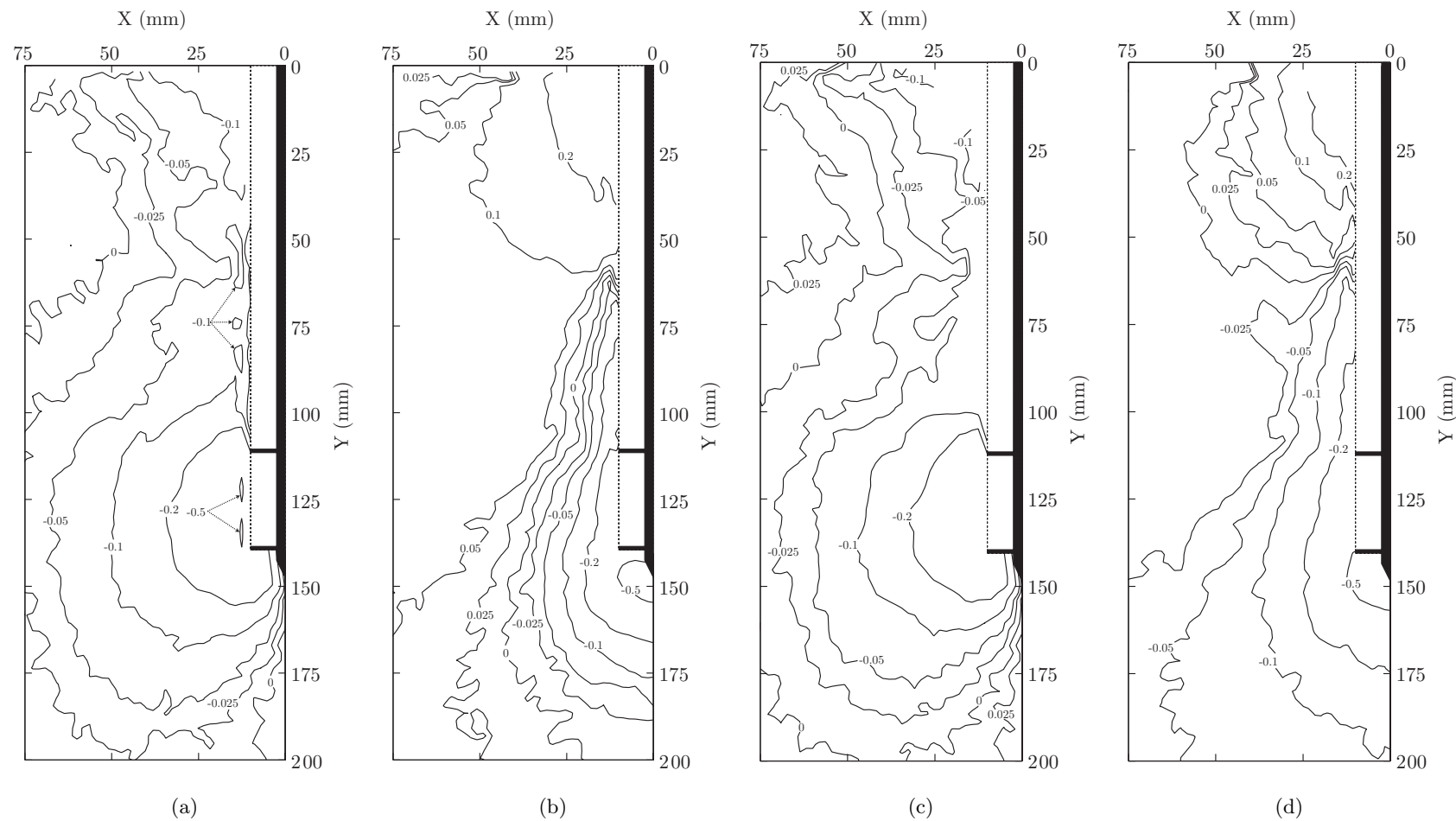


Figure 5.1: Installation disturbance displacement contours to depth of $7D$ for double helix pile with L_a of 30mm (C2-30): uncorrected horizontal (a) and vertical (b) displacement and corrected horizontal (c) and vertical(d) displacement contours in mm .

5.2.3 Displacement and Shear Strain Fields

Figures 5.2, 5.3, 5.4 and 5.5 present the displacement and shear strain fields caused by installation of a single helix pile (C1), double helix pile with L_a of 30mm (C2-30), double helix pile with L_a of 60mm (C2-60) and triple helix pile with L_a of 60mm (C3) respectively. The following sections describe behaviour observed from the installation data.

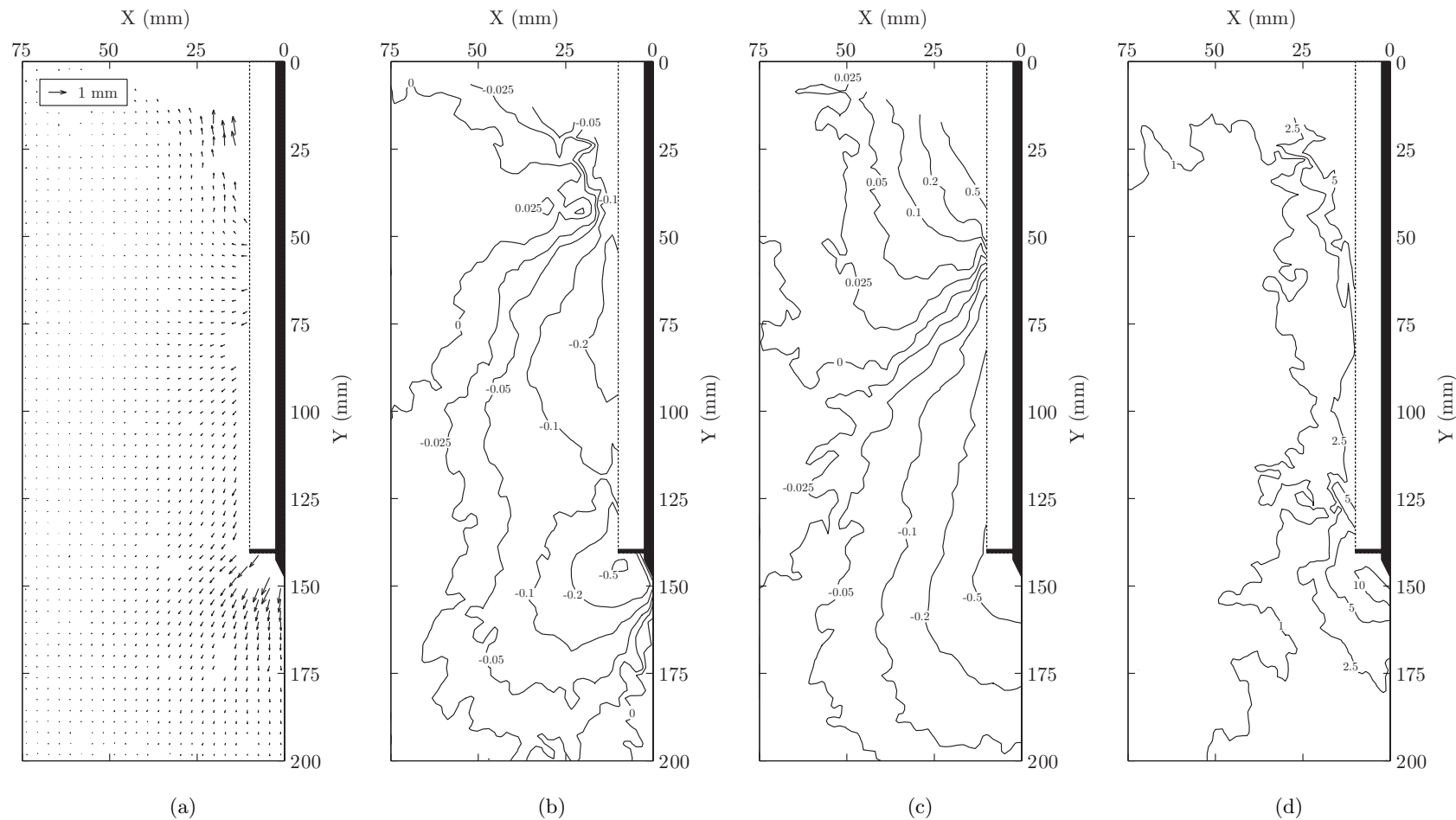


Figure 5.2: Installation disturbance to depth of $7D$ for single helix pile (C1): vector (a), horizontal displacement (b), vertical displacement (c) and shear strain contours (d) with displacements in mm and shear strains expressed as a percentage.

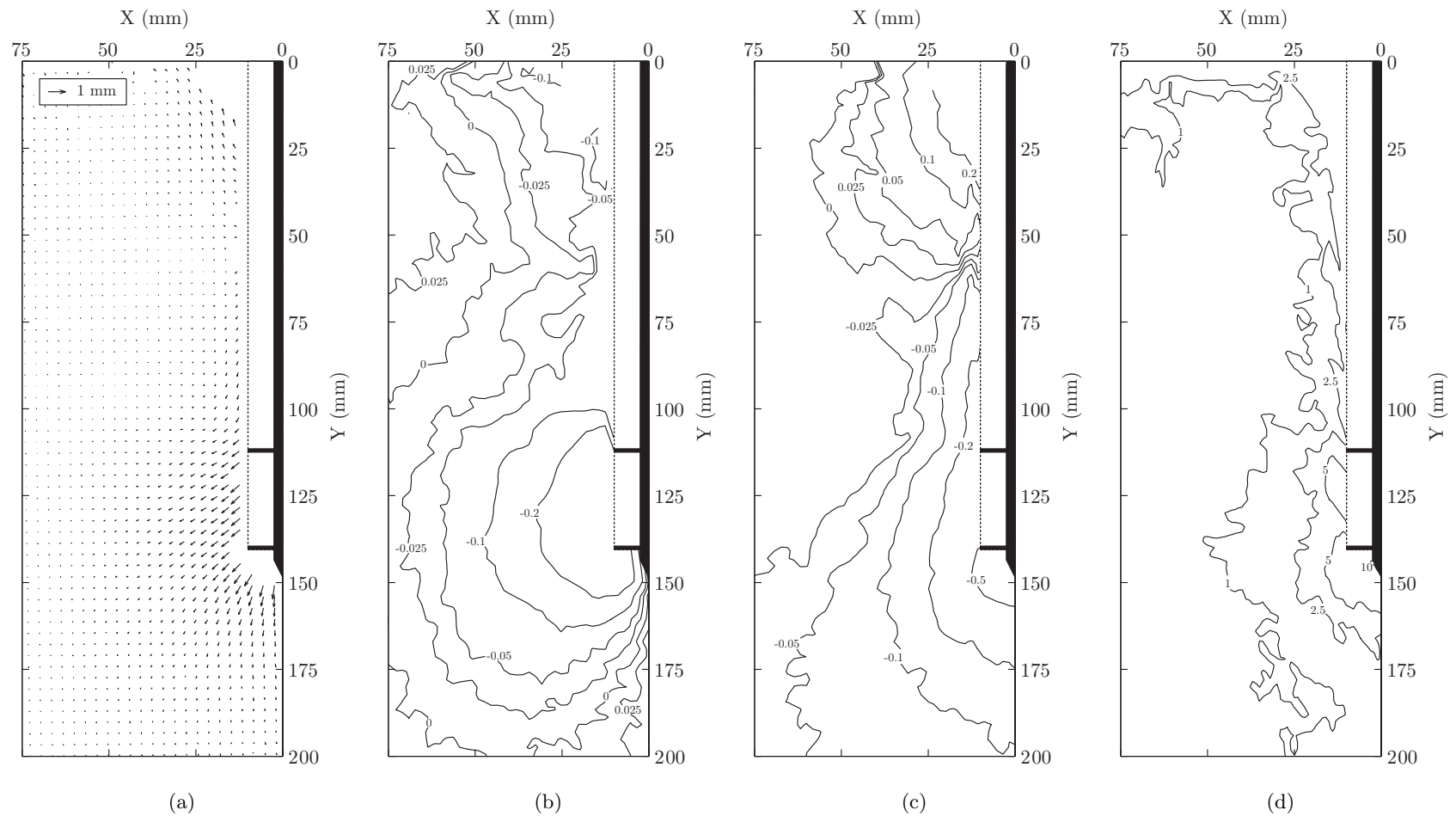


Figure 5.3: Installation disturbance to depth of $7D$ for double helix pile with L_a of 30mm (C2-30): vector (a), horizontal displacement (b), vertical displacement (c) and shear strain contours (d) with displacements in mm and shear strains expressed as a percentage.

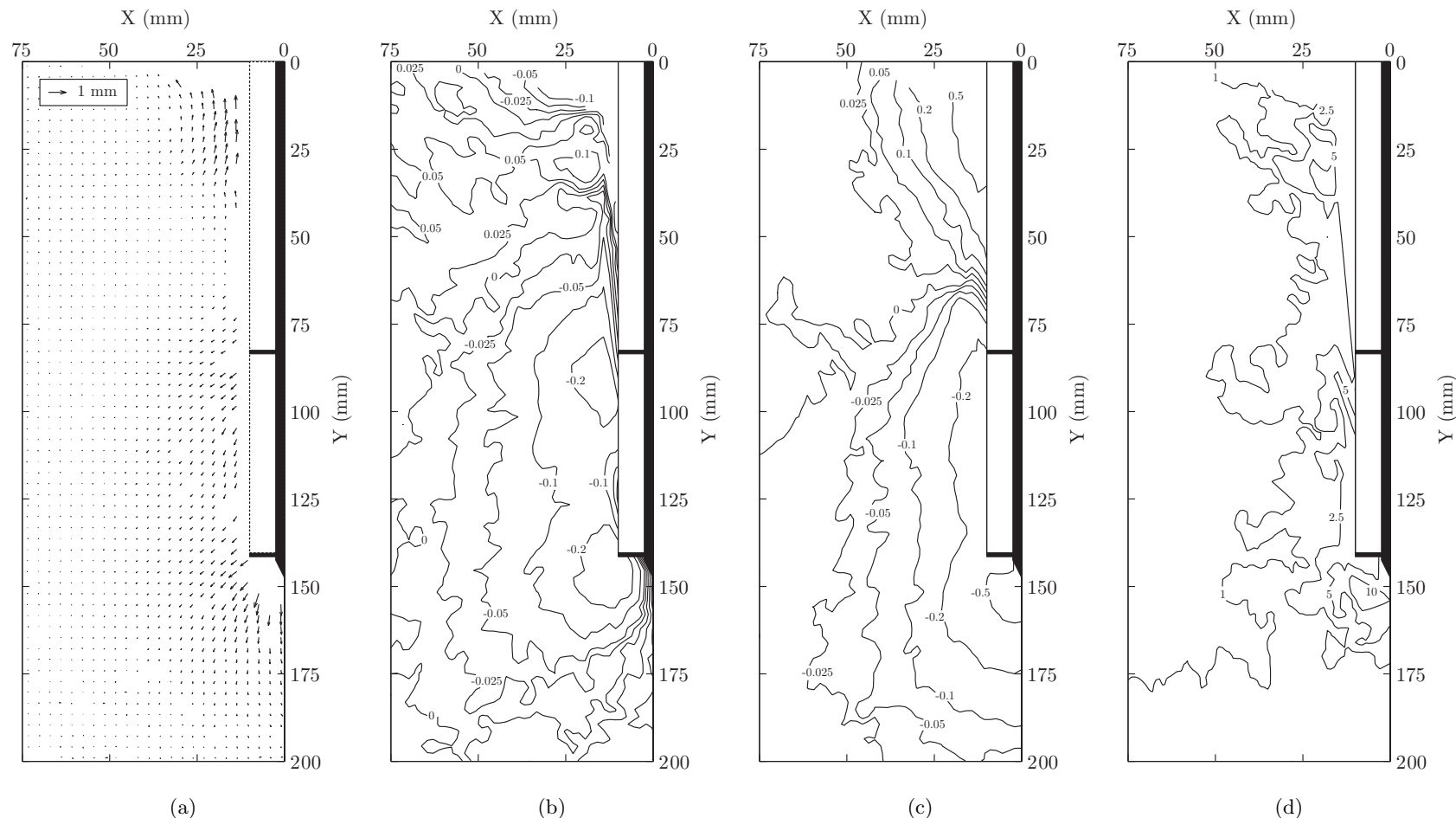


Figure 5.4: Installation disturbance to depth of $7D$ for double helix pile with L_a of 60mm (C2-60): vector (a), horizontal displacement (b), vertical displacement (c) and shear strain contours (d) with displacements in mm and shear strains expressed as a percentage.

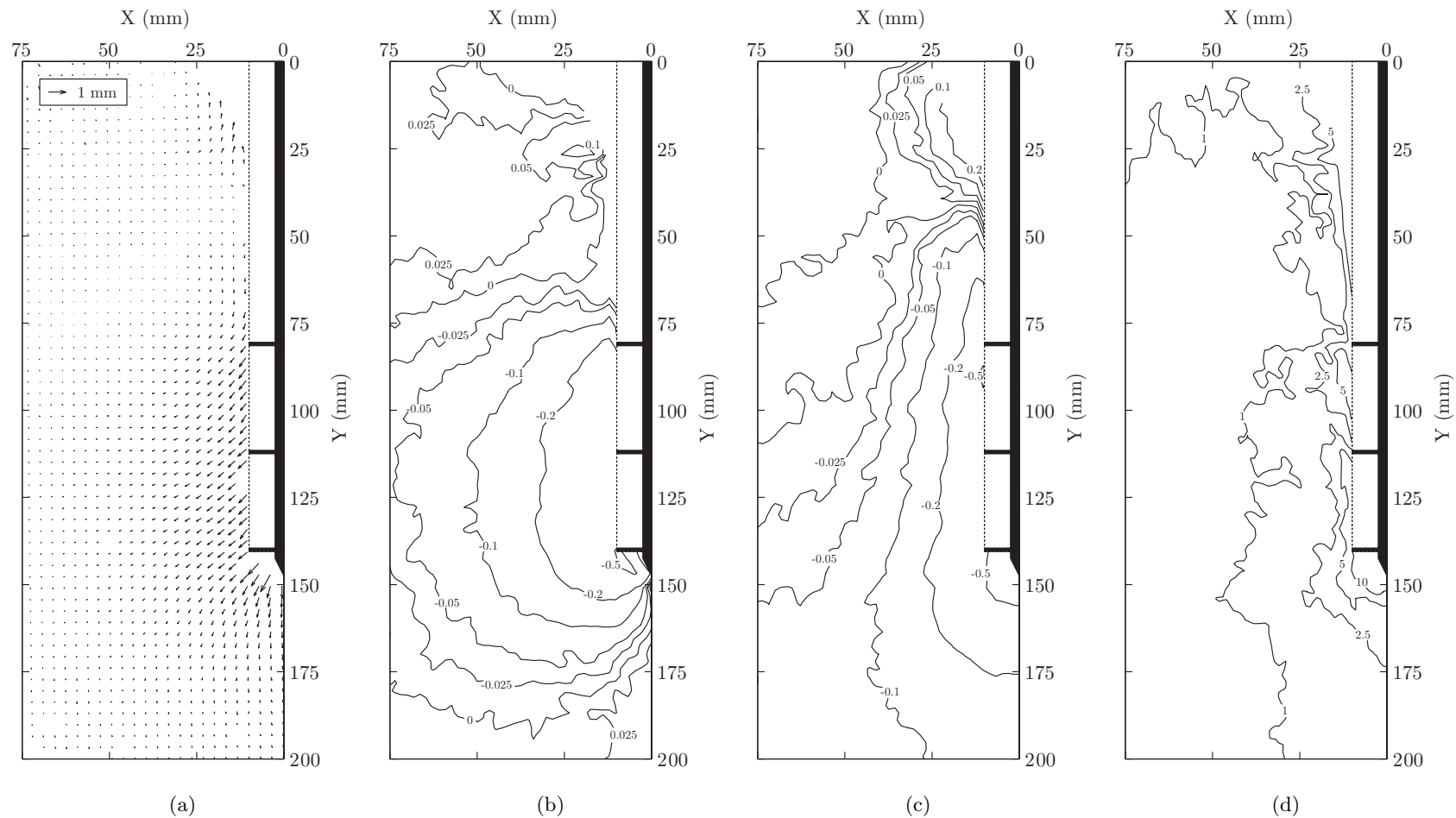


Figure 5.5: Installation disturbance to depth of $7D$ for triple helix pile with L_a of 60mm (C3): vector (a), horizontal displacement (b), vertical displacement (c) and shear strain contours (d) with displacements in mm and shear strains expressed as a percentage.

5.2.4 Observations

5.2.4.1 Breakout

Breakout was observed at the soil surface for all pile configurations, although the magnitude of breakout differed greatly between tests. Figure 5.2(a) is a vector plot showing the displacement caused by installation of the single helix screw pile. The absence of vectors towards the surface is a result of loss of data owing to breakout of soil at the surface of the sample. In contrast the other installation tests showed lesser signs of breakout adjacent to the pile shaft at the soil surface. The double helix pile installation with L_a of 60mm in Figure 5.4(a) is a case where the breakout caused by installation was less prevalent.

The vectors in this region of breakout were removed from the presented data since they appeared to be wild. This is due to the breakout occurring suddenly, over a single 1D installation increment, such that the pixel displacement of the breakout region was greater than the specified ‘searchzone’ command within GeoPIV, which led to erroneous selection of final positions of the patches within the breakout region. Increasing the number of images used in the analysis may have led to capturing the breakout behaviour. However, this would have been at the expense of increasing the summated random walk error produced by GeoPIV, as the effective ‘leapfrog’ value would have been reduced. Given the small magnitudes of displacement being measured within the model during installation, this was avoided.

The breakout phenomenon is most likely a product of the combination of the stress history of the soil and experimental setup. During formation of the model the soil was consolidated to a past maximum effective stress of 100kPa before unloading to an effective stress at the soil surface of zero. Therefore, in relation to the critical state concept, the soil bed generated was heavily overconsolidated and thus on the ‘dry’ side of the critical state line. This could explain the brittle rather than ductile nature of the soil deformation during loading, which facilitated breakout at the soil surface. This was exacerbated by the low stress profiles apparent in models tested due to the 1g test procedure and the relatively low unit weight of the consolidated transparent soil of 9.24kN/m³, compared to a natural soft clay which could have a unit weight in the range of 17-20kN/m³.

5.2.4.2 Lateral Disturbance

Lateral disturbance can be assessed by comparing Figures 5.2(b), 5.3(b), 5.4(b), 5.5(b). The largest lateral displacements are consistently apparent adjacent to the helical plates in all cases. For widely spaced helical plates ($s/D > 1.5$) such as the double helix with L_a of 60mm pile in Figure 5.4(b), the lateral displacement between the helical plates reduces. This is not observed in the closely spaced ($s/D \leq 1.5$) cases, in Figures 5.3(b) and 5.5(b). This is because the increased volume displaced by the additional helical plate causes increased lateral displacement, such that the zones of influence due to each helical plate can be seen to overlap. Thus it may be concluded that the volume of each helical plate is responsible for the peak lateral displacement observed during installation.

It is interesting to observe that above the final position of the pile in each case, the magnitude of lateral displacement reduces significantly. Also, as L_a increases the position of the zero lateral displacement contour moves upwards within the sample, which is further evidence that the volume of the pile is directly related to the lateral disturbance. In the single helix pile case in Figure 5.2(b), which had the smallest volume, the extent of the lateral displacement field is much smaller than the other configurations where the pile volume was increased, through the addition of one or more helical plates. In the double helix pile cases the effect of L_a is evident. In these two cases the pile volume was identical but the centre of volume is lower for the case where L_a was 30mm in Figure 5.3(b). As a result more lateral disturbance is induced at greater depth compared to where L_a was 60mm in Figure 5.4(b), where the lateral displacements are more evenly spread throughout the sample. Lastly in the triple helix pile case with L_a of 60mm the total lateral disturbance is greater again, forcing the point of zero lateral disturbance even higher within the sample.

5.2.4.3 Vertical Disturbance

Vertical disturbance caused by helical screw pile installation is illustrated in Figures 5.2(c), 5.3(c), 5.4(c), 5.5(c). Due to the screwed installation, where the pile advances vertically by the pitch of the helical plate per revolution, the general trend is that significant downward displacement is apparent along the length of the model piles. Maximum vertical displacement is typically apparent underneath the lowermost helical plate for each configuration of pile. Heave at the soil surface is

also apparent in all cases. The position of reversal of vertical displacement direction is consistent for all configurations of pile, at a depth of about $2-3D$.

The extent of vertical displacement is greater for cases with closely spaced ($s/D \leq 1.5$) helical plates due to the increased confinement caused by the close spacing. The effect of this can be seen by comparing Figures 5.4(c) and 5.5(c), where the third helical plate in the triple helix pile, where s/D was 1.5, causes larger vertical displacements over a greater area than for the double helix case, where s/D was 3.0. This is further evidence that the volume of the pile is directly related to the disturbance induced during installation and the generation of the residual force, which is further discussed in Section 5.2.5.

5.2.4.4 Shear Strains

Figures 5.2(d), 5.3(d), 5.4(d), 5.5(d) present the shear strains caused by helical screw pile installation. The results show that disturbance is generally limited to the installation path of the pile and adjacent soil within a distance of $2D$ from the centreline of the model. Maximum shearing is apparent below the lowermost helical plate. However, it ought to be noted that in reality the maximum shear strain would be apparent within the installation path of the helical pile since soil in this region would be significantly disturbed. As previously mentioned, it was not possible to track displacements within the installation path of the pile, due to out of plane soil movements induced by the pile rotation.

Of most interest is the comparison of shear strains induced by installation of the double helix pile with 60mm active length in Figure 5.4(d) and triple helix pile of equal active length in Figure 5.5(d). The magnitude of shear strain caused by installation of these two configurations is not significantly different. This means that the addition of a third helical plate at the mid-height of the active length does not significantly increase disturbance caused by the installation process. This is due to the screw rate of installation. The initial helical plate causes the majority of disturbance as it advances through the soil. Subsequent helical plates follow the same path as the lowermost helical plate, so long as the screw rate of installation is maintained.

This is of importance to helical screw pile contractors as it demonstrates that if minimal disturbance to the ground is desirable, then a screw rate of installation needs to be steadfastly maintained to ensure that all helical plates pass through the

same installation path. Helical piles ought to be designed such that the helical plates are spaced so that they all pass through the same installation path at a screw rate of installation. Potentially, ensuring this will maximise the load-bearing potential of the helical screw piles as the fabric of the soil is minimally disturbed.

5.2.5 Repeatability

Assessment of the repeatability was first achieved by comparing the residual force generated by installation of the helical screw piles for all cases. This is the force measured by the load cell positioned between the helical pile and the pile driving rig post-installation of the model pile. To attain this measurement the load cell was connected and the output noted immediately before commencement of installation. Due to the lack of data acquisition slip-rings or telemetry, the load cell had to be disconnected during installation. However, upon completion of the installation process the load cell was reconnected. The output of the load cell immediately prior to load deflection testing is referred to here as the post-installation residual force and is equal to the difference in force measured before and after installation.

In total 10 helical screw pile tests were conducted (8 tests and 2 repeats) and the residual force for each case is presented in Table 5.3 alongside the appropriate test nomenclature in brackets for clarity. In this instance, since the installation process for a given geometric configuration of pile was identical regardless of the loading direction specified (compressive or tensile), the installation data yielded from both the compressive (C series) and tensile (T series) tests can be considered as repeat datasets where an explicit repeat test (R suffix) was not conducted. Hence, even though only repeat tests on single and triple helix piles loaded in compression were conducted in their entirety, repeat installation datasets were available for all pile geometries.

The range of residual force and the corresponding percentage of the mean residual force indicate the repeatability of the installation process. The residual force appears to be related to the number of helical plates on the pile. This means that the residual force is a function of the volume of the pile and is generated by displacement of soil to accommodate the volume of the pile during installation, confirming the validity of the observations made in Sections 5.2.4.2 and 5.2.4.3.

Table 5.3: Residual force induced by model helical screw pile installation: mean, range and percentage of mean residual force.

Configuration	Single Helix	Double Helix ($L_a = 30mm$)	Double Helix ($L_a = 60mm$)	Triple Helix ($L_a = 60mm$)
Compression (N)	10.30 (C1)	20.16 (C2-30)	22.60 (C2-60)	35.75 (C3)
Tension (N)	9.97 (T1)	23.52 (T2-30)	23.30 (T2-60)	35.43 (T3)
Repeat (N)	9.40 (C1-R)	N/A	N/A	34.55 (C3-R)
Mean (N)	9.89	21.84	22.95	35.24
Range (N)	0.90	3.36	0.71	1.20
Percentage (%)	9.12	15.38	3.07	3.42

The least repeatable installation process, based on this measure, is the double helix pile with $30mm$ active length, where the range of residual force was $3.36N$ or 15.38% of the mean residual force. To assess the impact of this difference in residual force the displacement and shear strain fields induced by installation of a double helix pile with $30mm$ L_a were reassessed using data from a repeat installation. Table 5.4 presents the camera-soil movement correction magnitudes for a repeat dataset for a double helix pile with L_a of $30mm$ (T2-30), which indicates that data quality was similar to that of the other installation datasets shown in Table 5.2.

Table 5.4: Magnitude of horizontal and vertical (u_c , v_c) correction specified by modal movement correction process for the double helix pile with L_a of $30mm$ repeat installation analysis (T2-30), alongside the corresponding percentage of vectors of modal magnitude ($\%_u$, $\%_v$).

Test	Correction			
	Horizontal		Vertical	
	u_c (μm)	$\%_u$	v_c (μm)	$\%_v$
Double Helix Pile - T2-30 ($L_a=30mm$) Repeat	7	2.02	-69	1.42

Figure 5.6 presents the displacement and shear strain fields induced by repeat installation of the double helix pile with L_a of $30mm$. The displacement and shear strain fields are generally very similar to those obtained previously. Notable discrepancies compared to the data presented in Figure 5.3 are limited to slightly greater maximum lateral and vertical displacement and shear strain beneath the lowermost helical plate and differing breakout behaviour at the soil surface. The discrepancy in the displacement and shear strain magnitudes is caused by fewer vectors being removed manually from the repeat installation dataset so displacement closer to the pile (and subsequently shear strains) has been observed in the repeat case. The

breakout observed in the repeat test, where a thin layer has broken away at the soil surface is similar to that observed during the single helix pile installation process, but has been tracked in the PIV analysis process because it occurred gradually during installation rather than suddenly over a single $1D$ increment as was the case during single helix pile installation. Since this is the case with the largest range of installation induced residual stress, it can be concluded that the installation process used is repeatable and thus, suitable for the purpose of observing and comparing both compressive and tensile loading of helical screw piles of the same geometric configuration in different samples with identical stress history. The observations made here, relating to soil displacement and shear strains will be recalled when comparing the physical modelling derived load-deflection responses for both geometries and loading configurations tested and the numerical analyses presented in Chapter 7.

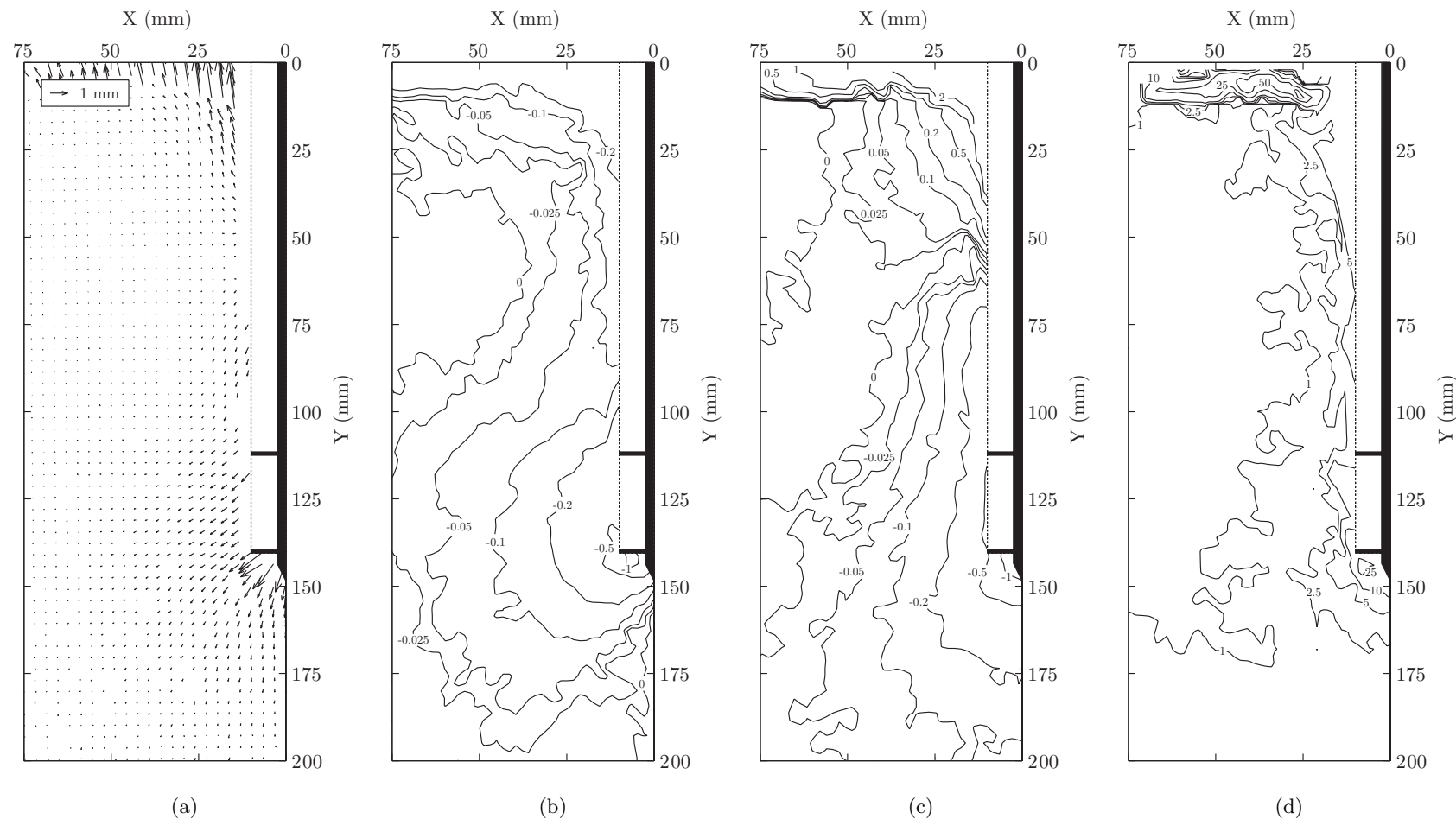


Figure 5.6: Installation disturbance to depth of $7D$ for double helix pile with L_a of 30mm) repeat (T2-30): vector (a), horizontal displacement (b), vertical displacement (c) and shear strain contours (d) with displacements in mm and shear strains expressed as a percentage.

5.3 Performance

The following sections present data recorded during loading of the installed helical screw piles after a holding period of 24 hours allowed for setup. This setup period was intended to allow equilibration of excess pore pressures induced by the installation process. Data was recorded in two separate datastreams: load and displacement measurement, via a load cell and LVDT, and digital images to facilitate PIV analysis of soil movements as the pile was displaced through the soil.

5.3.1 Load-Deflection Response

Figure 5.7 presents the load-deflection response for all four configurations of helical screw pile, loaded in compression and tension. Tests C1 and T1 are the benchmark cases of a pile with a single helix at the end of the shaft (depth of cover of $7D$) to which all other configurations are compared to deduce the following observations.

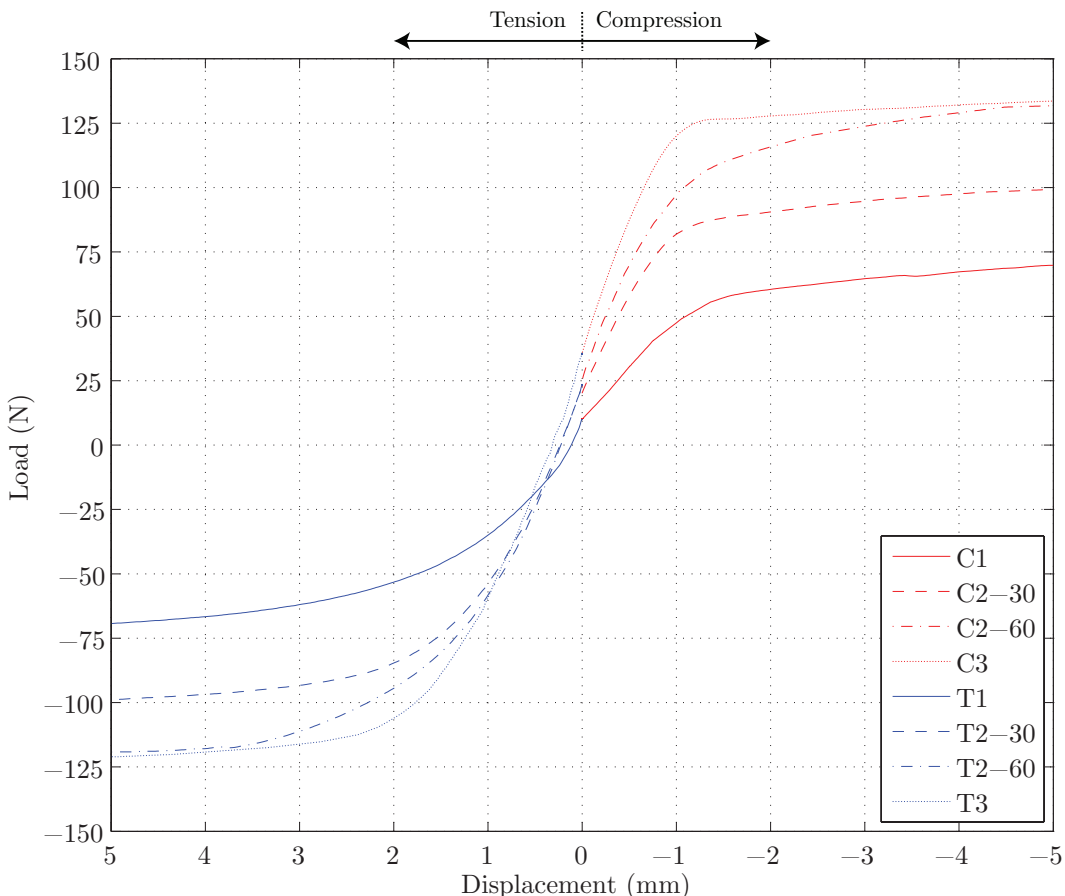


Figure 5.7: Comparison of load-deflection response for helical screw pile configurations.

The active length appears to govern the ultimate capacity of the helical screw pile for both compressive and tensile loading. An increase in ultimate capacity (displacement, $\delta=\pm 5mm$) is observed if the response for tests C1 and T1 and C2-30 and T2-30, where the L_a has been increased by 30mm, are compared. If the distance between the helical plates is doubled, thereby doubling L_a , we notice a further almost identical increase in ultimate capacity when the response for tests C2-30 and T2-30 and C3 and T3 are compared. Adding a third helical plate whilst maintaining L_a appears not to effect the ultimate capacity. Therefore L_a appears to control the ultimate capacity of the helical screw pile. This observation is illustrated in Figure 5.8 by plotting the active length versus the absolute ultimate capacity for both compressive and tensile loading.

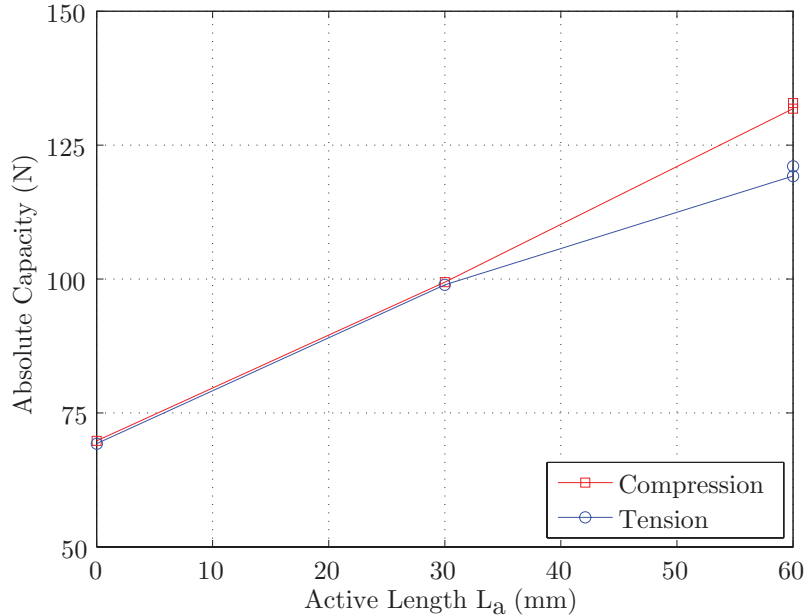


Figure 5.8: Effect of L_a on absolute ultimate capacity.

The helical plate spacing ratio s/D affects performance in a different manner. Comparison of the performance for tests C2-60 and T2-60 and C3 and T3 shows that the addition of a third helical plate and the resultant reduction in s/D from 3.0 to 1.5, increases the stiffness of the response of the helical pile such that for any given pre-ULS load the pile experiences reduced displacement. This suggests that reducing s/D is important if capacity is to be maximised for a given allowable axial displacement.

The load-deflection data generally shows that the compressive and tensile response of helical screw piles in a soft clay type soil is very similar. However, at L_a of 60mm, tensile capacity is slightly reduced compared to the comparable compression test. This is summarised in Table 5.5 where the percentage discrepancy has been calculated with respect to the ultimate compressive capacity where $\delta=\pm 5\text{mm}$ and both compressive and tensile capacities are assumed to be absolute. This is presented alongside the embedment ratio H/D .

Table 5.5: Percentage discrepancy between compressive and tensile capacity of helical screw piles, expressed as a percentage of the ultimate compressive capacity ($\delta=\pm 5\text{mm}$).

Test	H/D	Absolute Capacity (N)	Discrepancy (%)
C1	7	69.8	0.72
T1	7	69.3	
C2-30	5.5	99.4	0.48
T2-30	5.5	98.9	
C2-60	4	131.8	9.55
T2-60	4	119.2	
C3	4	132.8	8.90
T3	4	121.0	

It is evident that the tensile capacity reduces most significantly when H/D is reduced to 4. The consistency of this trend indicates that the cause is likely to be systematic and a result of the test procedure adopted. One possible cause is the configuration of the test. A distance of $4D$ is allowed for cover above and below the uppermost and lowermost helical plates where L_a is 60mm. During compressive loading the pile is advancing towards the base of the test chamber, thus increasing H/D . In contrast during tensile loading the pile is advancing towards the free soil surface, thus reducing H/D . Ideally a smaller model pile or larger test chamber ought to have been specified to alleviate this problem by allowing greater H/D . However, further miniaturisation of the model pile would have led to reduced density of PIV derived measurements across the width of the pile and a larger test chamber was not available. An alternative potential cause is the reduction of H/D demonstrated to be caused by installation induced breakout as was discussed in Section 5.2.4.1. In some cases this breakout was shown to be at least 10mm and thus caused a reduction of H/D of at least 0.5.

5.3.2 Analysis Method

During loading of the helical screw piles digital images were again recorded at a rate of 3fps up to a maximum axial displacement of $\pm 20mm$. This typically yielded a series of about 300 images from the commencement of loading to completion. The ULS was mobilised (identified by a levelling off in the load-deflection response) in all cases by an axial displacement of $\pm 5mm$. This meant that a series of about 70 images could be identified, over which PIV analysis was conducted to assess the development of the ULS in increments of $1mm$ axial displacement.

The ‘leapfrog’ parameter within GeoPIV was set to unity for analysis of images recorded during load-deflection testing. The ‘searchzone’ parameter was set to 10px or $0.65mm$ when converted to metric units using the approximate linear scaling factor introduced in Chapter 4. Since the axial displacement rate was $0.2mm/s$ and the camera frame rate was 3fps, the maximum displacement present within the model must be less than the axial displacement rate divided by the camera frame rate, or about $0.06mm$. This is smaller than the ‘searchzone’ defined with a significant margin for error hence indicating that the ‘searchzone’ chosen was suitable for the analysis. Table 5.6 presents the displacement and shear strain contours plotted in the PIV analyses of helical screw pile performance. Vectorial displacement plots are amplified by a factor of two for clarity.

Table 5.6: Contours of displacement and shear strain presented in helical screw pile load-deflection contour plots.

Plot	Increments
Horizontal Displacement (mm)	-1, -0.5, -0.2, -0.1, -0.05, -0.025, 0, 0.025, 0.05, 0.1, 0.2, 0.5 ,1
Vertical Displacement (mm)	-5, -4, -3, -2, -1, -0.5, -0.2, -0.1, -0.05, -0.025, 0, 0.025, 0.05, 0.1, 0.2, 0.5 ,1, 2, 3, 4, 5
Shear Strain, γ (%)	1 ^a , 2.5, 5, 10, 25, 50, 75, 100, 125

^aOmitted from cumulative shear strain plots due to noise.

Unfortunately, it was not possible to plot the 1% shear strain contour for the cumulative shear strain plots. This is due to the summated random walk error inherent in GeoPIV generating too much noise for the contour to be clearly plotted. Attempts were made to increase the value of ‘leapfrog’ to 2, thereby reducing the number of computation iterations required by half, resulting in a reduction in the summated random walk error. This was successful in that it allowed the 1% shear

strain contour to be plotted clearly. However, it also generated significant wild random vectors in the area of maximum shear strain which were the product of erroneous correlations within GeoPIV, which is reliant on correlations between two sets of image intensity data. First, the image intensity data from the initial patch and second, the image intensity data in the interrogation zone (the area defined by the position and size of the initial patch plus the ‘searchzone’ pixel distance) in the final image. GeoPIV calculates the correlation between the initial patch and the corresponding image intensity data for all possible positions of the initial patch in the interrogation zone in the final image, before selecting the position with the highest correlation. This process is reliant on the initial patch being similar to some area of the interrogation area in the final image.

In a process where soil within a patch is experiencing significant shearing, the correlation is likely to be significantly reduced. Hence, to track displacements in an area experiencing a large amount of shearing, images are required at small intervals to preserve the similarity between the initial patch and interrogation area. In this instance the summated random walk error will be relatively large, as a large number of computations are required to cover the development of a failure mechanism.

However, in an area of high shearing the displacements observed tend to be large, so the summated random walk error may not be significant. In areas of the model where the amount of shearing is small the displacements observed are, conversely, likely to be small. In this instance the summated random walk error is far more significant and may be a similar order of magnitude to the measurements. This leads to the generation of noise in the computation of shear strains, as was observed in this investigation.

Given that an aim of the project was to assess the validity of the assumption that a cylindrical failure surface is generated between regularly spaced helical plates on a helical screw pile, the decision was made to omit the 1% shear strain contour so as to preserve data clarity recorded in the region between the helical plates, where maximum shearing was observed.

It ought to be possible to mitigate this problem in a number of ways. Firstly, regions could be defined over which different values of ‘leapfrog’ could be utilised by GeoPIV, in order to minimise the summated random walk error in sensitive (low

shearing) areas of the model. This relies on the user identifying in advance areas of high and low shearing within the soil model and then assigning an appropriate value of ‘leapfrog’. Due to this subjective input and the associated difficulty with assigning appropriate values of ‘leapfrog’, this method was not adopted here.

A more elegant solution would be to force GeoPIV to refine the analysis in a loop, with displacement increments between iterations being re-calculated with increasing values of ‘leapfrog’ until the measurement calculated deviates ‘wildly’ from the computation conducted in the previous cycle. Some calibration of the minimum correlation required would be needed to define a ‘wild’ deviation. However, with this it would be possible to ensure that a maximum value of ‘leapfrog’ is assumed for each and every data point within the analysis mesh, ensuring that both small and large displacements and strains could be observed accurately in the same model. The only user input required would be a magnitude of deviation that when surpassed, would inform GeoPIV that the measurement had become random. This would then be repeated for all data points within the analysis mesh, allowing output to be generated with varying ‘leapfrog’, thus allowing areas of both high and low shearing to be computed accurately. However, due to the complexity of this mitigation, the ‘black box’ nature of GeoPIV and time constraints this approach was not investigated.

5.3.3 Data Appraisal

Data quality has been assessed in the same manner as for the installation data presented in Section 5.2.2. Tables 5.7 and 5.8 contain a summary of the horizontal and vertical camera-soil movement correction magnitudes applied to the PIV derived displacement fields for the compressive and tensile loading tests respectively.

The magnitudes of the corrections are generally smaller than those applied to the installation data due to the reduced number of images recorded during load-deflection testing (approximately 70 compared to 1800 for the installation analyses). Thus less camera-soil movement is evident. There appears to be no particular trend in the magnitude of correction applied between different increments, suggesting that the correction magnitude required is random and caused by vibration of the camera.

The percentage of vectors of modal magnitude ($\%_u$, $\%_v$) is generally larger for the horizontal correction than the vertical correction. This is due to the geometry of the helical screw piles and the configuration of loading. Since the helical screw

Table 5.7: Magnitude of horizontal (u_c) and vertical (v_c) correction specified by modal movement correction process for compressive response tests.

Test	δ (mm)	Correction			
		Horizontal		Vertical	
		u_c (μm)	$\%_u$	v_c (μm)	$\%_v$
C1	-1	-4	6.97	11	5.42
	-2	-28	7.18	21	5.01
	-3	-36	4.55	36	3.46
	-4	-46	4.03	46	2.94
	-5	-41	3.15	27	2.53
C2-30	-1	-42	7.14	16	4.16
	-2	-50	5.04	26	4.67
	-3	-67	4.19	19	2.47
	-4	-50	2.95	23	2.79
	-5	-71	2.85	47	1.99
C2-60	-1	-21	5.35	-4	3.96
	-2	-19	3.90	-8	2.83
	-3	-23	2.89	-13	2.89
	-4	-15	2.46	-28	2.19
	-5	-43	2.14	-33	1.87
C3	-1	-3	3.22	-1	1.84
	-2	-2	2.99	-27	1.79
	-3	-3	2.30	-78	1.27
	-4	-7	2.13	-9	1.61
	-5	6	2.13	-64	1.48

Table 5.8: Magnitude of horizontal and vertical (u_c, v_c) correction specified by modal movement correction process for tensile response tests, alongside the corresponding percentage of vectors of modal magnitude ($\%_u, \%_v$).

Test	δ (mm)	Correction			
		Horizontal		Vertical	
		u_c (μm)	$\%_u$	v_c (μm)	$\%_v$
T1	1	0	7.57	6	4.11
	2	2	6.25	6	3.40
	3	-6	4.05	-3	3.57
	4	-1	3.13	1	2.52
	5	-13	2.67	-5	2.41
T2-30	1	4	6.29	-2	3.67
	2	10	4.65	-2	3.07
	3	-67	4.10	0	2.41
	4	11	3.39	1	2.30
	5	18	2.46	5	2.03
T2-60	1	4	6.92	-2	3.99
	2	-59	3.40	11	2.67
	3	-94	3.19	13	2.67
	4	-93	2.52	-12	1.36
	5	-125	2.47	31	1.73
T3	1	-16	4.29	5	2.90
	2	-17	3.01	6	2.29
	3	-22	3.12	13	1.95
	4	-60	2.34	18	1.50
	5	-46	2.12	3	1.62

piles have a relatively large plan area and they are loaded axially, the majority of soil displacement mobilised is vertical rather than horizontal. Hence a smaller area of soil experiences zero vertical movement than horizontal movement. This is illustrated by the greater vertical displacement magnitudes observed when horizontal and vertical contour plots are compared for all pile configurations for both compressive and tensile loading presented in Sections 5.3.4.1 and 5.3.4.2.

Assessment of the validity of the correction is demonstrated in the same manner as for the installation analyses (Section 5.2.2) by comparing the uncorrected displacement contour output for tests C2-30 and T2-30 at a displacement of $\pm 3\text{mm}$ in Figures 5.9(a) and 5.9(b) with the corresponding corrected output in Figures 5.9(c) and 5.9(d). For test C2-30 the magnitudes of horizontal and vertical correction were $-67\mu\text{m}$ and $19\mu\text{m}$. Similarly, for test T2-30 the magnitudes of correction were $12\mu\text{m}$ and $0\mu\text{m}$. The double helix pile with 30mm active length was specifically chosen to demonstrate that the camera-soil movement correction methodology does not negatively impact on instances where no differential residual camera-soil movement is evident.

The uncorrected data demonstrates that without the camera-soil movement correction the data is not plausible for either test C2-30 or T2-30. In Figure 5.9(a) the zero contour is a closed contour within which leftward movement of soil is apparent. Almost all of the rest of the soil volume is moving rightward and given the fixed horizontal and vertical boundary of the test chamber this result is unreasonable. The same is apparent in Figure 5.10(a), where only a small proportion of the soil is displacing leftwards. In both cases the result is indicative of a systematic camera-soil movement error and is evidence that the correction framework introduced in Chapter 4 is positively mitigating the effect of camera-soil movement errors caused by non-coplanarity of the control and target planes. To demonstrate the stability of the camera-soil movement correction the vertical displacement contour plots for the same two tests can be considered in an uncorrected state. Figure 5.9(b) indicates that without correction the zero contour would be placed in a less reasonable position than in the corrected output when compared with Figure 5.9(d). Lastly, Figure 5.10(b) when compared with Figure 5.10(d) illustrates that the correction is stable even when the camera-soil movement error is equal to zero, since the output remains identical.

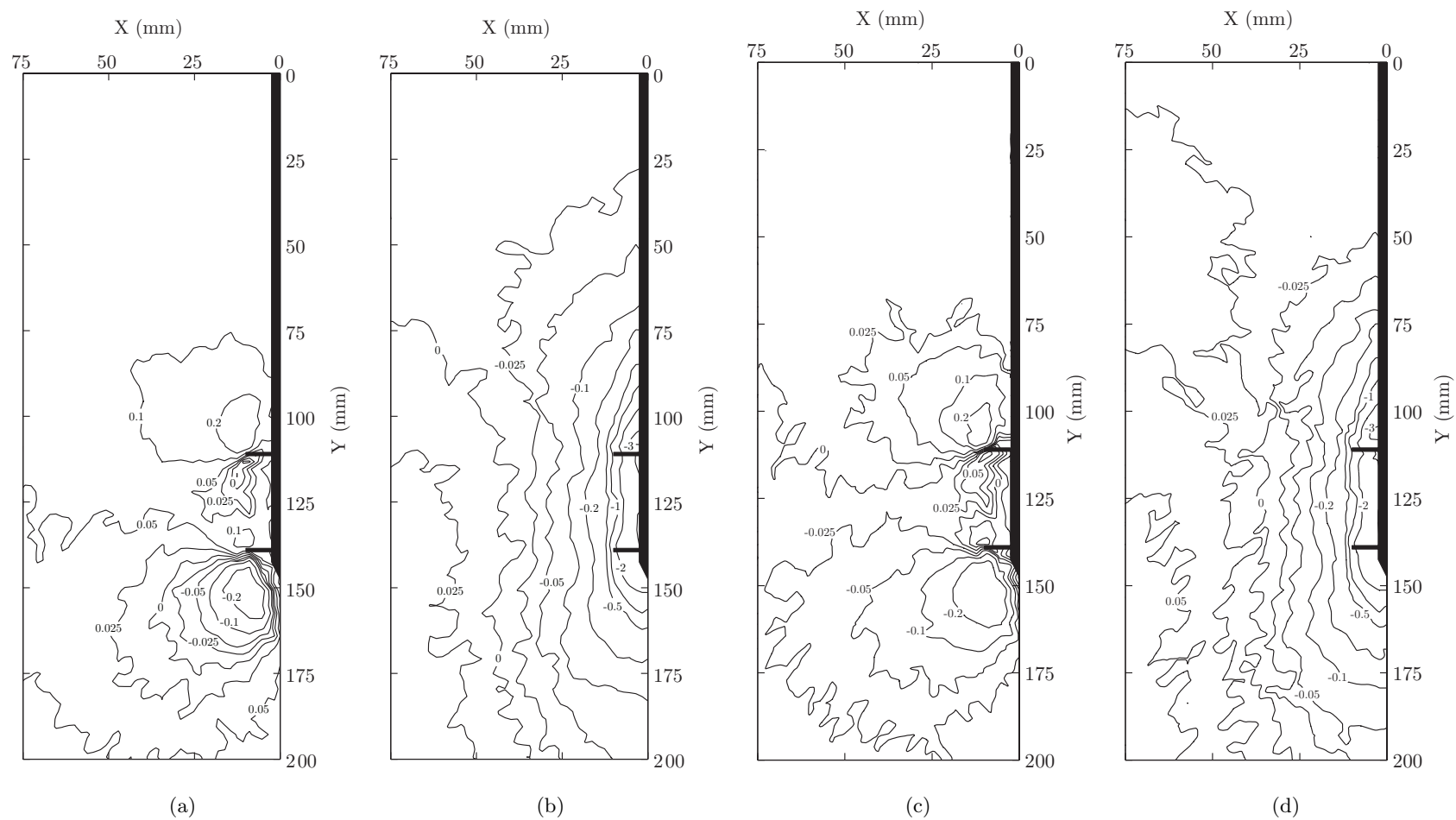


Figure 5.9: Displacement contours at 3mm compressive displacement for a double helix pile with 30mm active length (C2-30): uncorrected horizontal (a) and vertical (b) displacement and corrected horizontal (c) and vertical (d) displacement, with displacements in mm.

195

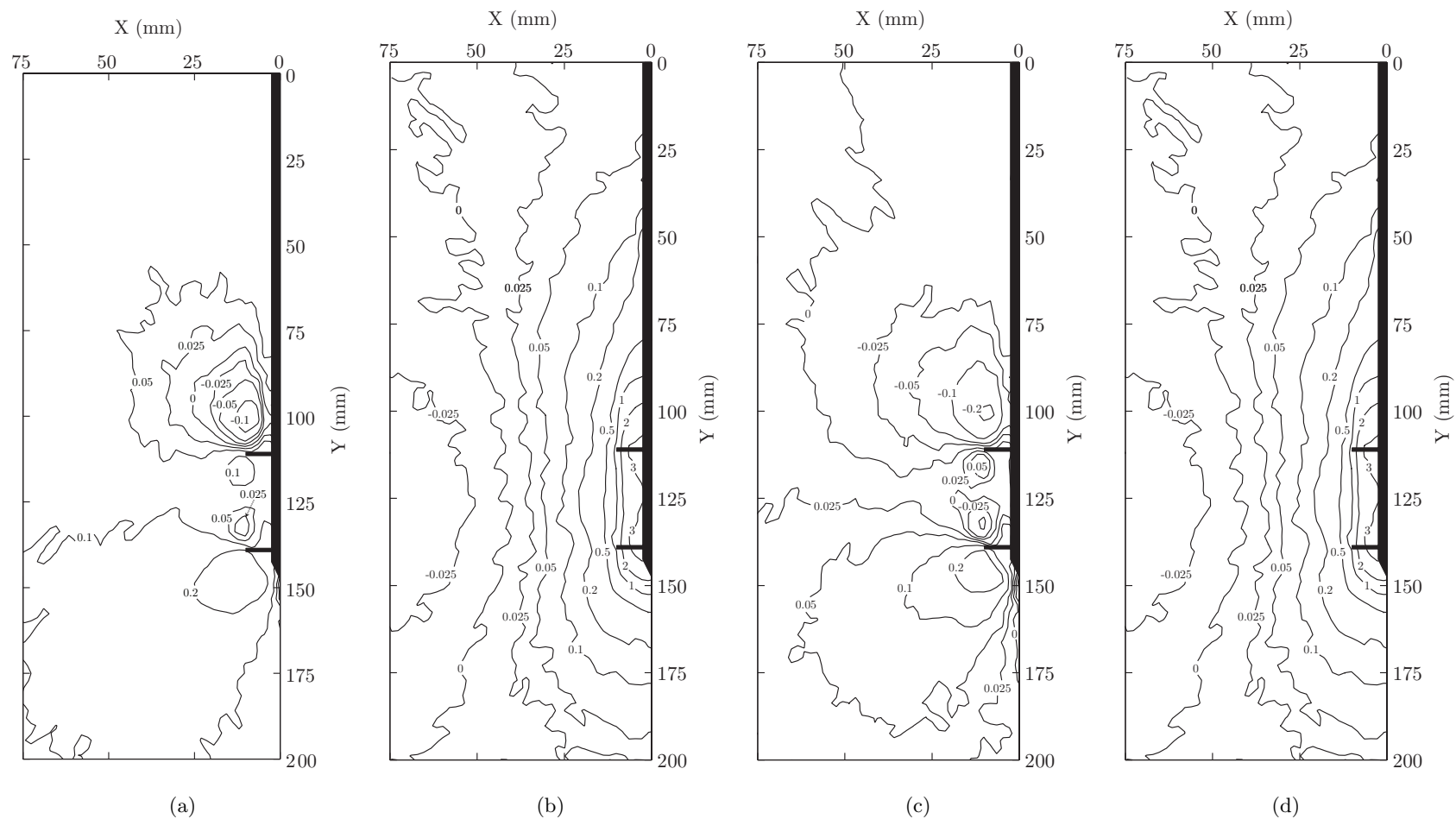


Figure 5.10: Displacement contours at 3mm tensile displacement for a double helix pile with 30mm active length (T2-30): uncorrected horizontal (a) and vertical (b) displacement and corrected horizontal (c) and vertical (d) displacement, with displacements in mm.

It must be noted, that although the positions of the zero displacement contours after correction appear to be plausible in most instances for the cumulative displacement fields, this is less true for incremental results. This is because incremental displacement fields are calculated by subtracting the displacement fields at two points in the test to yield the displacement field due to the resulting increment of axial displacement. Therefore, the systematic camera-soil movement error evident after correction is equal to the sum of the residual post-correction error for the two sets of cumulative displacement data utilised to calculate the incremental displacement field. This coupled with the small displacement gradients apparent in the far field in the incremental data, leads to increased wander in the position of the zero displacement contour for incremental displacement fields compared to cumulative displacement fields.

Another aspect of the analysis process which requires appraisal is the pile displacement measurement methodology described in Section 4.2.1.3. It is reasonable to assume that the configuration of model pile for which this method of displacement measurement would be least accurate would be a single helix pile. This is because the ratio of lateral displacement to vertical displacement is likely to be largest in this case due to the lack of confinement that would have been provided by additional helical plates on the pile shaft for multi helix piles. Reduced magnitudes of horizontal displacement compared to vertical displacement are evident for the multi helix piles in the PIV output presented later in this chapter.

Figure 5.11 is a plot of image number versus measured displacement for tests C1 and T1. Initially for the first few images recorded there is minimal displacement since the camera was triggered to begin capturing images before loading of the model pile was initiated. The linear relationships observed once loading has commenced is reassuring evidence that the tracking of the model pile was reasonably successful. However, it should be noted that this assessment is only valid if the capture rate of the camera used is constant throughout the test. This is ensured by using a memory card with a faster data transfer rate than the capture rate of the camera.

This method, although demonstrated to be reasonably successful is not ideal. In some vertical displacement contour plots, a contour is evident that is equal to the magnitude of axial displacement applied to the model pile, suggesting that some soil within the model has experienced a displacement greater than that

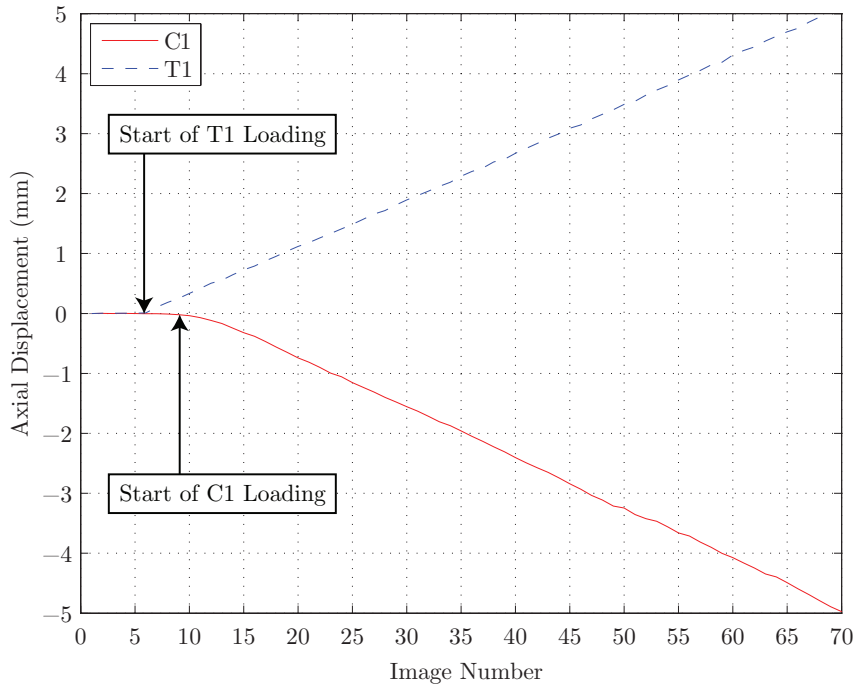


Figure 5.11: Assessment of pile tracking methodology.

applied to the model pile, which is clearly inadmissible. These occurrences must therefore be a product of erroneous measurement of pile displacement. Hence, if improvement is sought, a camera is required that can time stamp each image recorded synchronously with the LVDT used to monitor axial displacement of the pile. Unfortunately this facility was not available during this investigation.

To conclude, the evidence presented here indicates that the effect of the correction is positive and allows measurement resolutions to be significantly increased without rendering the output unclear, even when non-coplanarity exists in the experimental apparatus.

5.3.4 Displacement and Shear Strain Fields

5.3.4.1 Compression Results

The following section contains PIV derived displacement and shear strain fields of compressive loading tests conducted on helical screw piles. Figures 5.12-5.20 relate to test C1. Figures 5.21-5.29 relate to test C2-30. Figures 5.30-5.38 relate to test C2-60. Lastly, figures 5.39-5.47 relate to test C3.

For all tests cumulative displacements and shear strain fields are presented for axial compressive displacements of 1, 2, 3, 4 and 5mm. In addition, incremental results are shown for 1-2mm, 2-3mm, 3-4mm and 4-5mm axial compressive displacement, since these results best demonstrate development of the ULS failure mechanism, where successive incremental displacement and shear strain fields are similar.

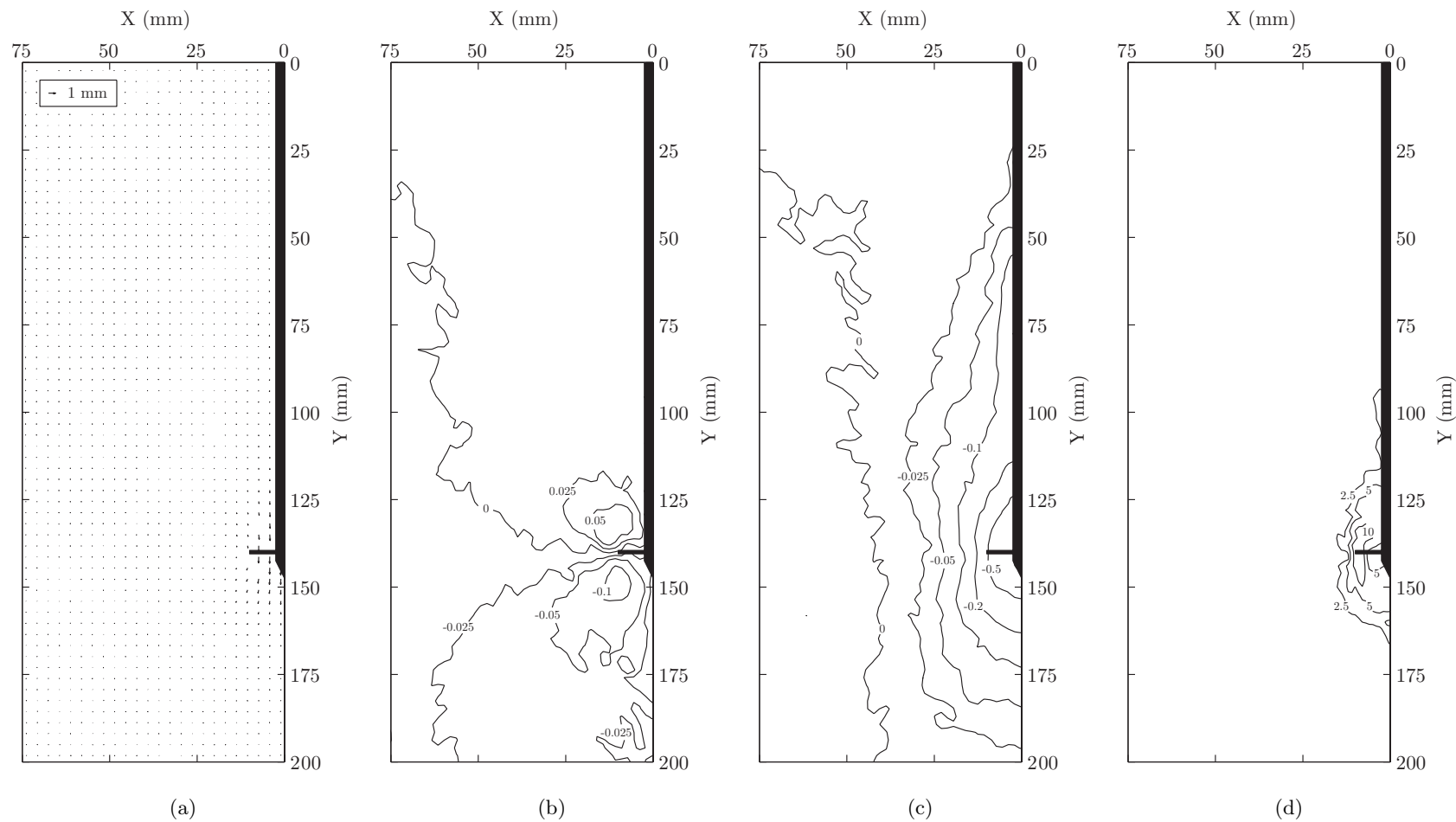


Figure 5.12: C1 cumulative PIV results at 1mm axial compressive displacement: vector (a), horizontal displacement (b), vertical displacement (c) and shear strain contours (d) with displacements in *mm* and shear strains expressed as a percentage.

200

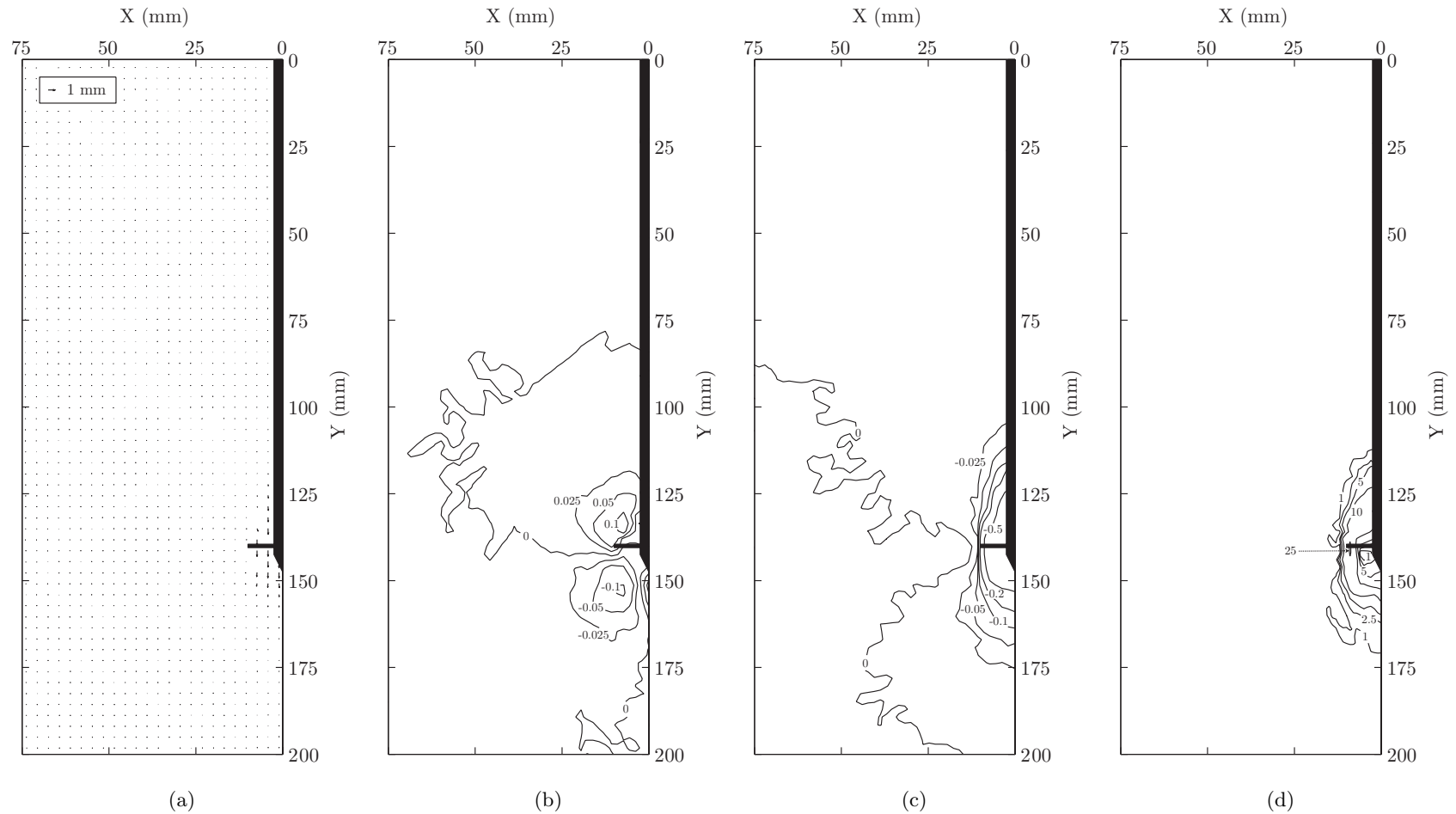


Figure 5.13: C1 incremental PIV results from 1mm to 2mm axial compressive displacement: vector (a), horizontal displacement (b), vertical displacement (c) and shear strain contours (d) with displacements in mm and shear strains expressed as a percentage.

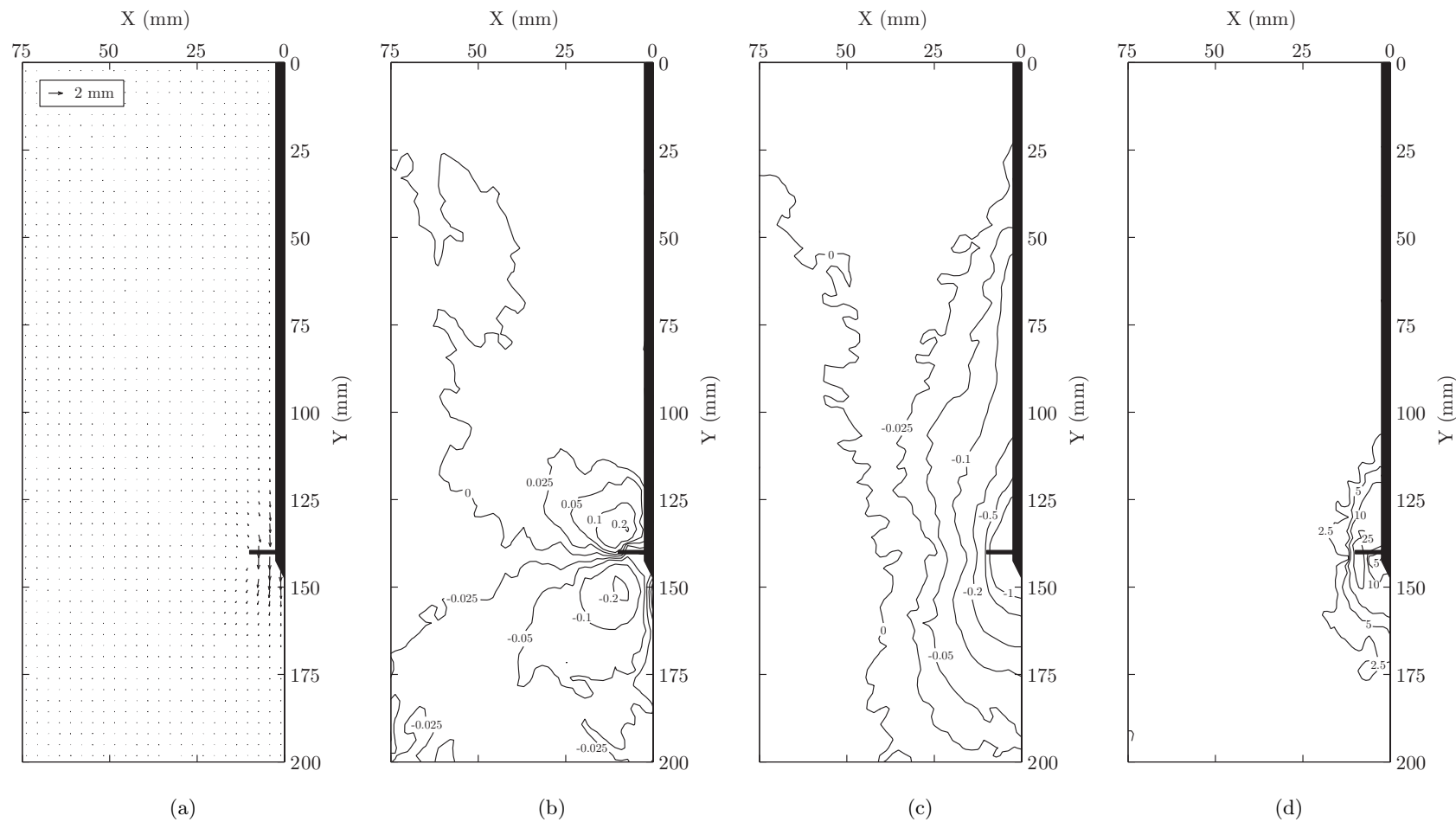


Figure 5.14: C1 cumulative PIV results at 2mm axial compressive displacement: vector (a), horizontal displacement (b), vertical displacement (c) and shear strain contours (d) with displacements in mm and shear strains expressed as a percentage.

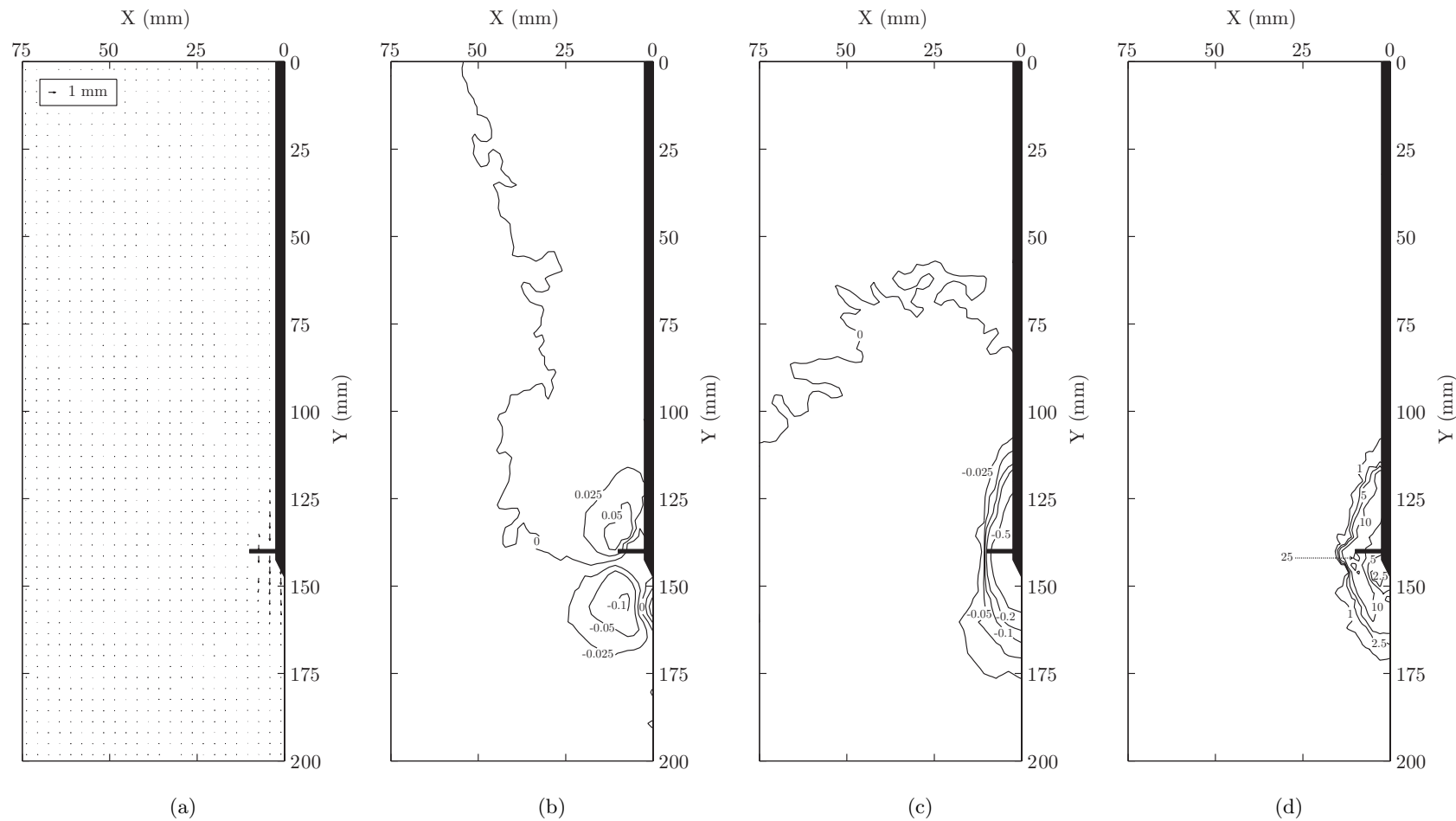


Figure 5.15: C1 incremental PIV results from 2mm to 3mm axial compressive displacement: vector (a), horizontal displacement (b), vertical displacement (c) and shear strain contours (d) with displacements in mm and shear strains expressed as a percentage.

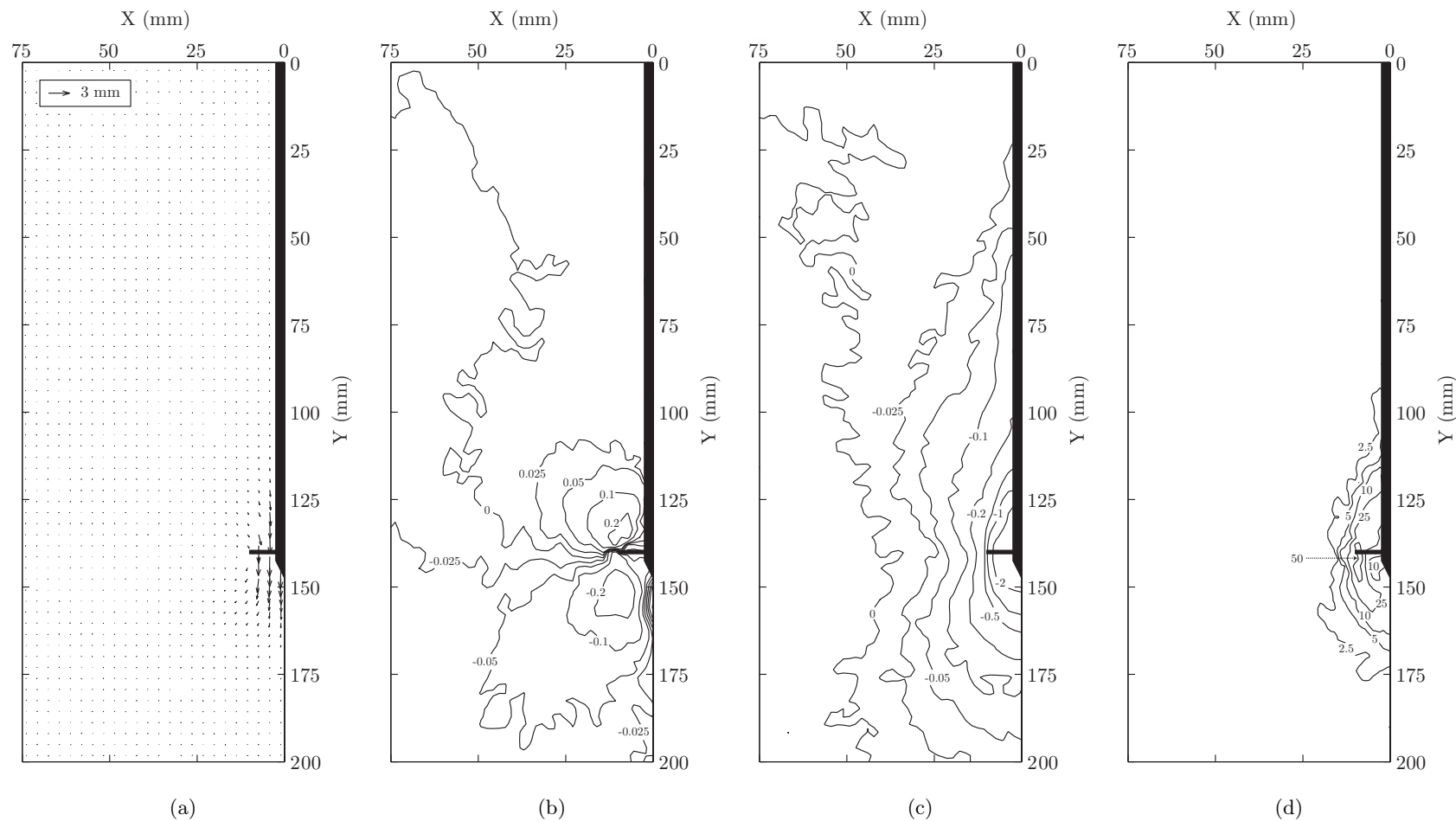


Figure 5.16: C1 cumulative PIV results at 3mm axial compressive displacement: vector (a), horizontal displacement (b), vertical displacement (c) and shear strain contours (d) with displacements in mm and shear strains expressed as a percentage.

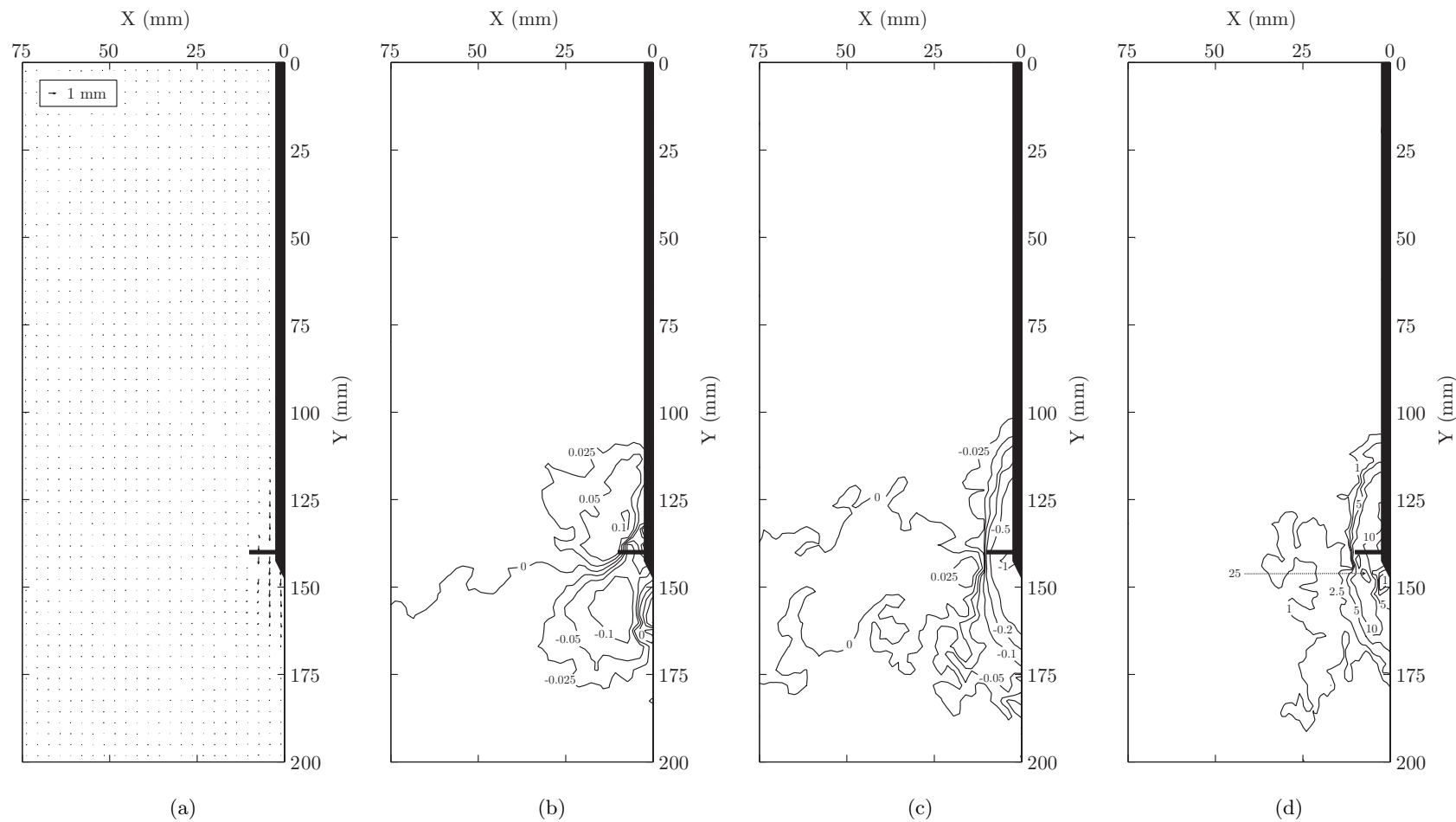


Figure 5.17: C1 incremental PIV results from 3mm to 4mm axial compressive displacement: vector (a), horizontal displacement (b), vertical displacement (c) and shear strain contours (d) with displacements in mm and shear strains expressed as a percentage.

205

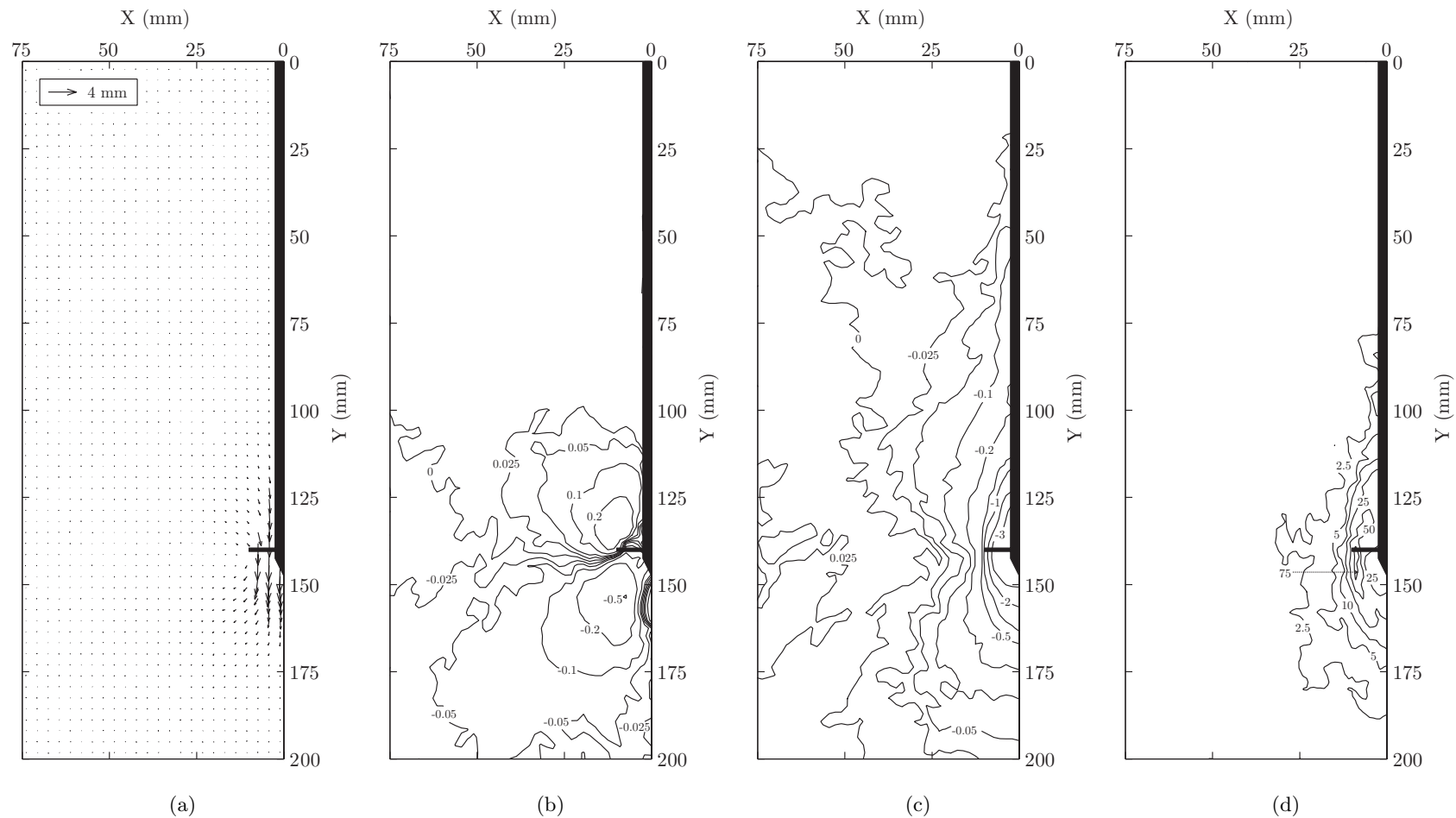


Figure 5.18: C1 cumulative PIV results at 4mm axial compressive displacement: vector (a), horizontal displacement (b), vertical displacement (c) and shear strain contours (d) with displacements in mm and shear strains expressed as a percentage.

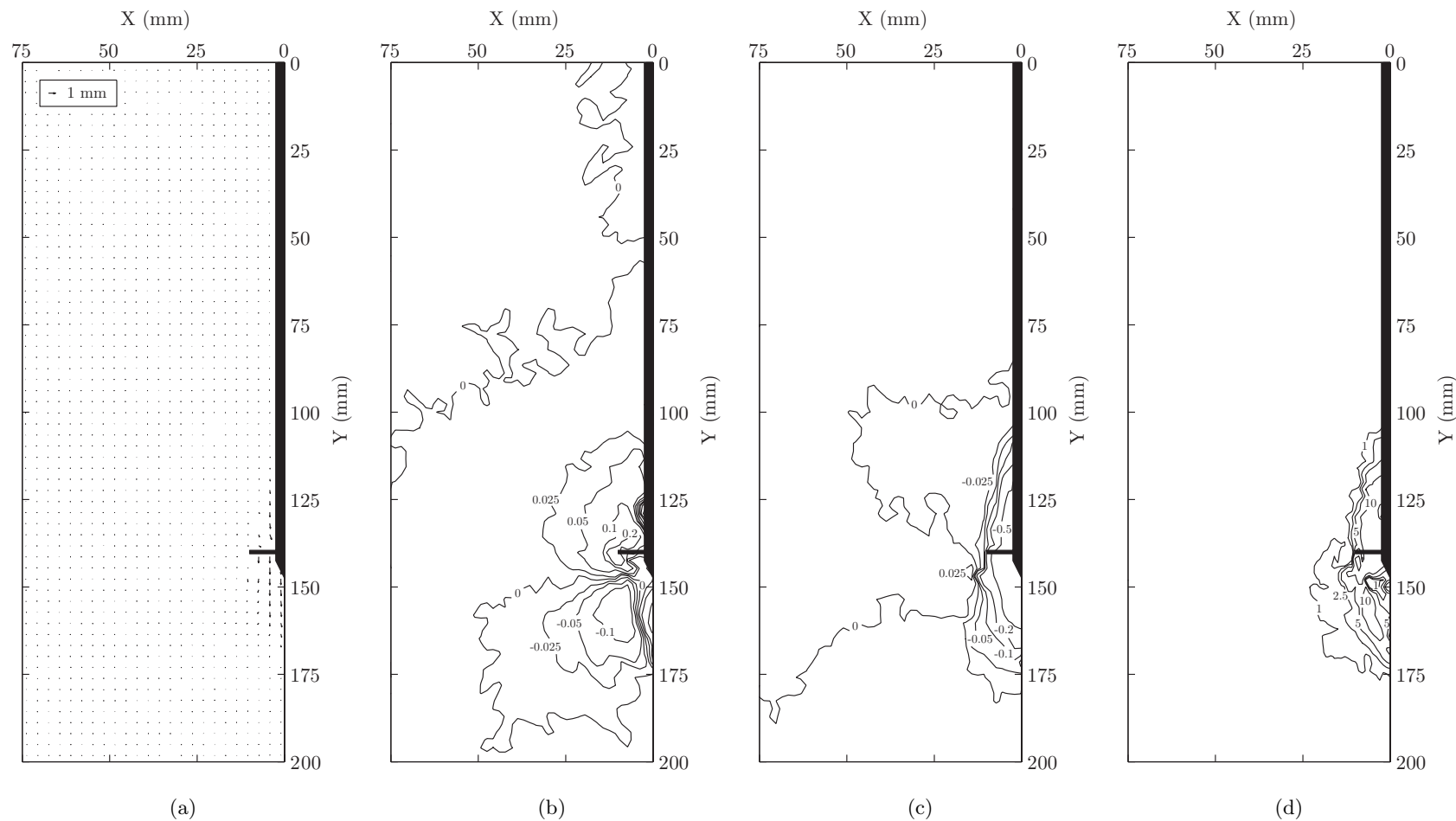


Figure 5.19: C1 incremental PIV results from 4mm to 5mm axial compressive displacement: vector (a), horizontal displacement (b), vertical displacement (c) and shear strain contours (d) with displacements in mm and shear strains expressed as a percentage.

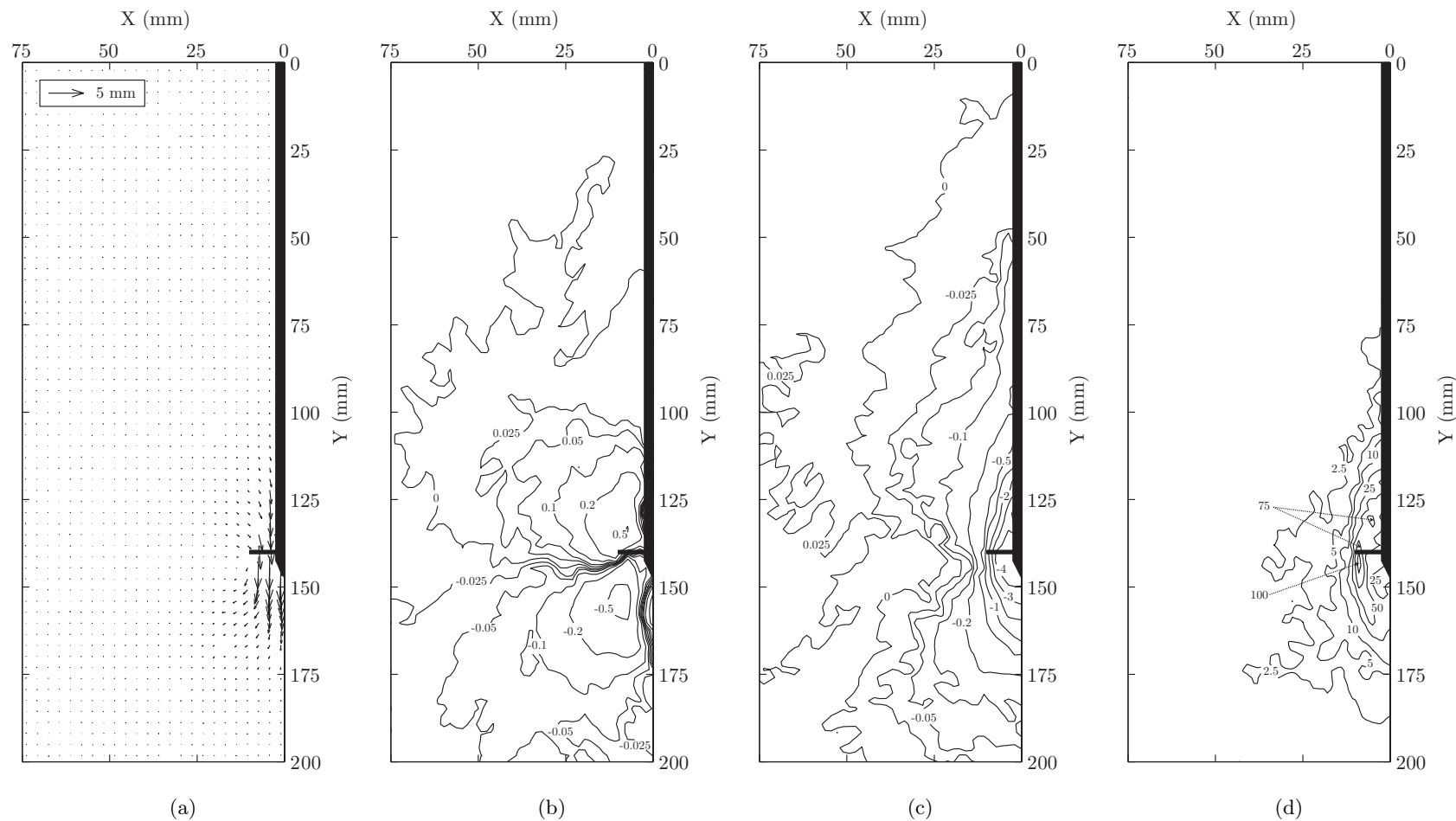


Figure 5.20: C1 cumulative PIV results at 5mm axial compressive displacement: vector (a), horizontal displacement (b), vertical displacement (c) and shear strain contours (d) with displacements in mm and shear strains expressed as a percentage.

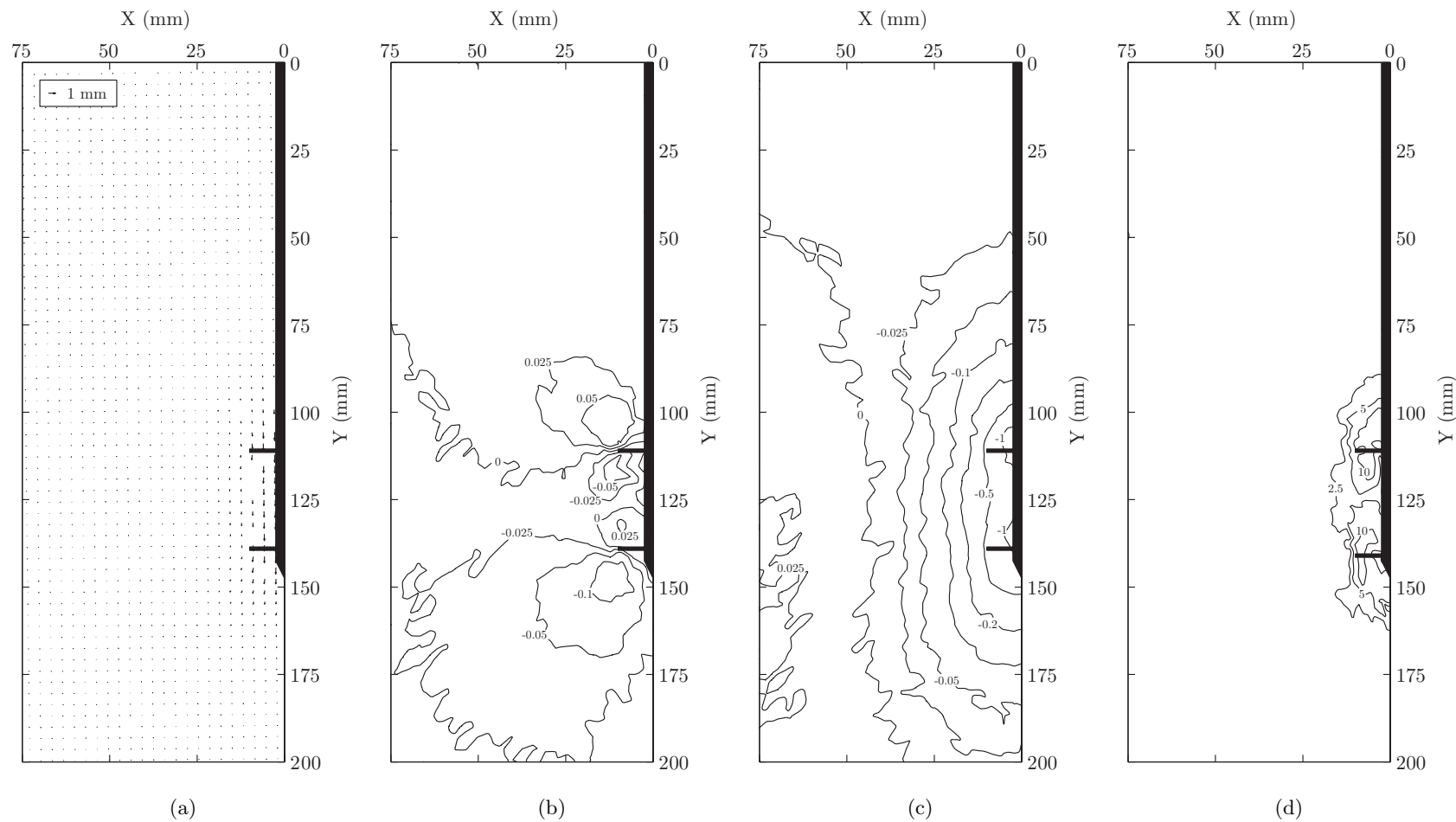


Figure 5.21: C2-30 cumulative PIV results at 1mm axial compressive displacement: vector (a), horizontal displacement (b), vertical displacement (c) and shear strain contours (d) with displacements in mm and shear strains expressed as a percentage.

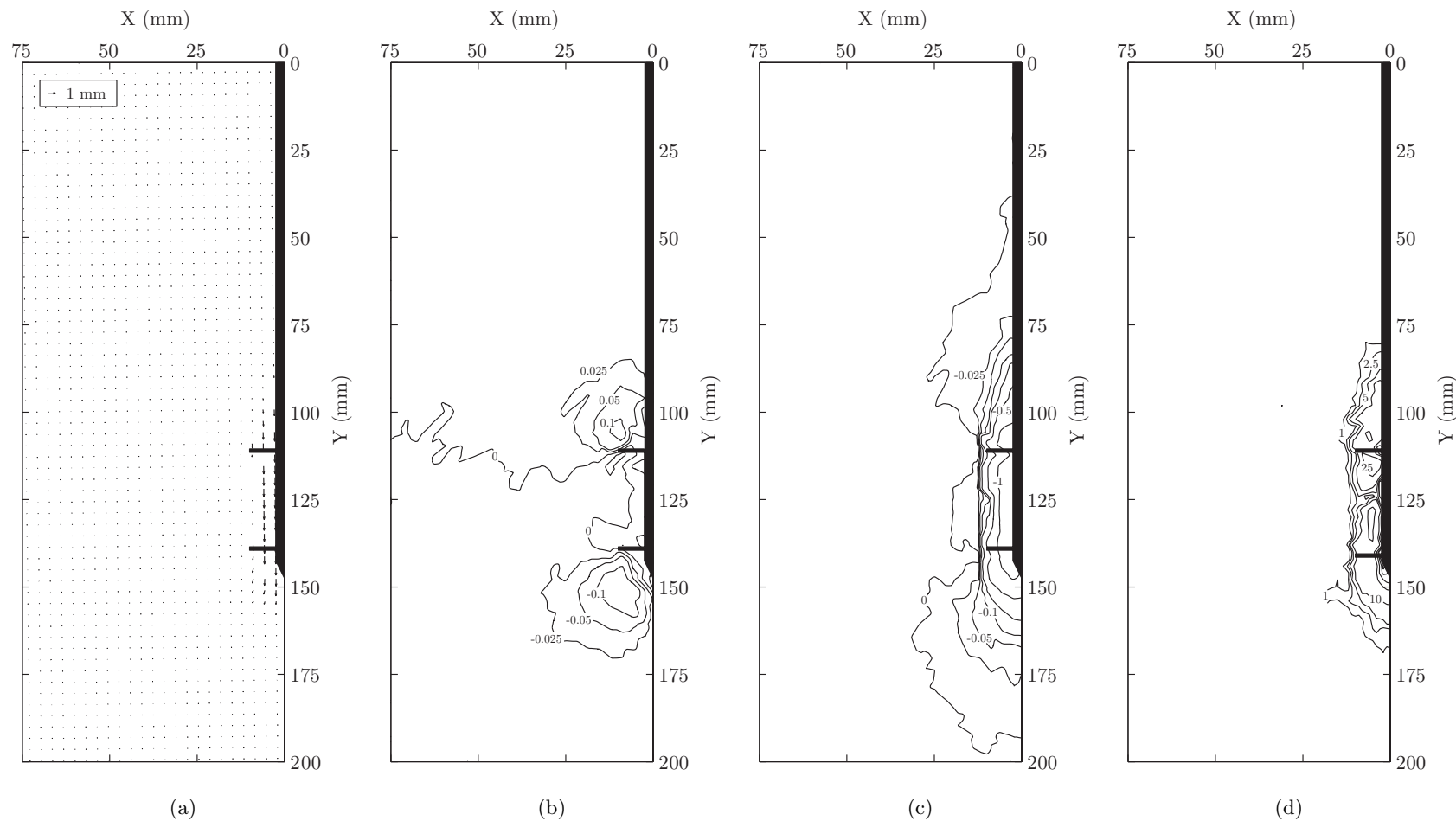


Figure 5.22: C2-30 incremental PIV results from 1mm to 2mm axial compressive displacement: vector (a), horizontal displacement (b), vertical displacement (c) and shear strain contours (d) with displacements in mm and shear strains expressed as a percentage.

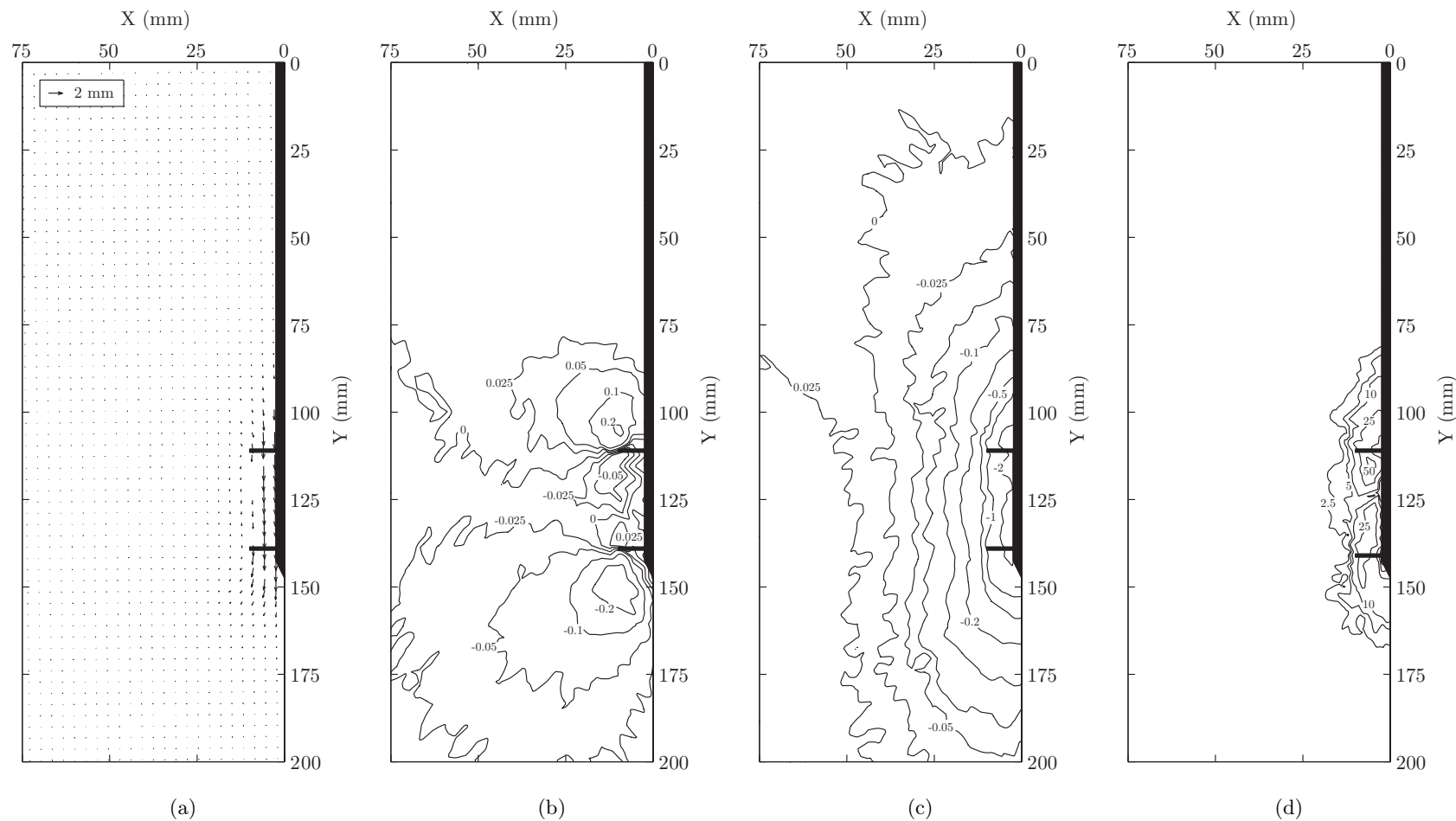


Figure 5.23: C2-30 cumulative PIV results at 2mm axial compressive displacement: vector (a), horizontal displacement (b), vertical displacement (c) and shear strain contours (d) with displacements in mm and shear strains expressed as a percentage.

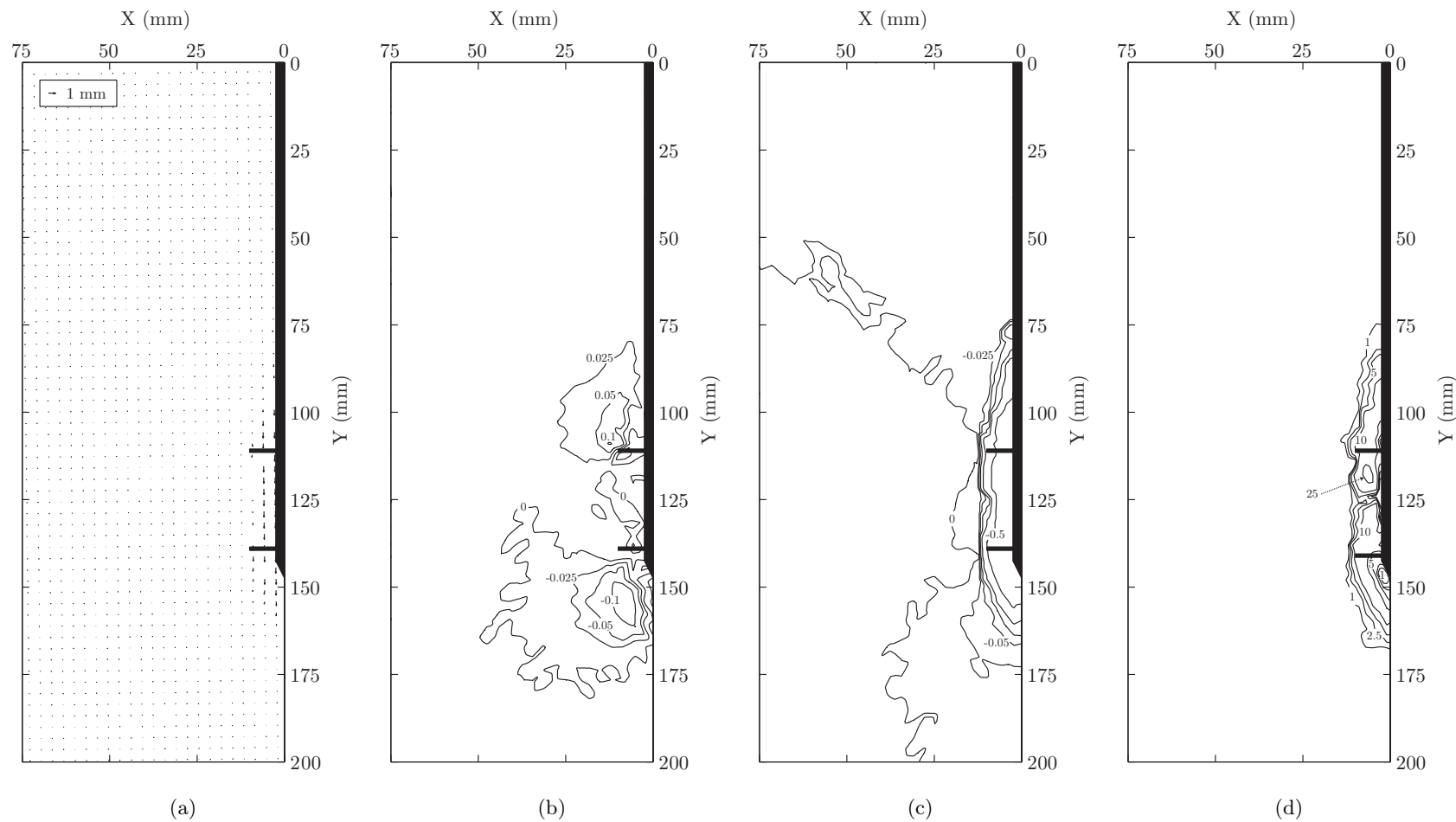


Figure 5.24: C2-30 incremental PIV results from 2mm to 3mm axial compressive displacement: vector (a), horizontal displacement (b), vertical displacement (c) and shear strain contours (d) with displacements in mm and shear strains expressed as a percentage.

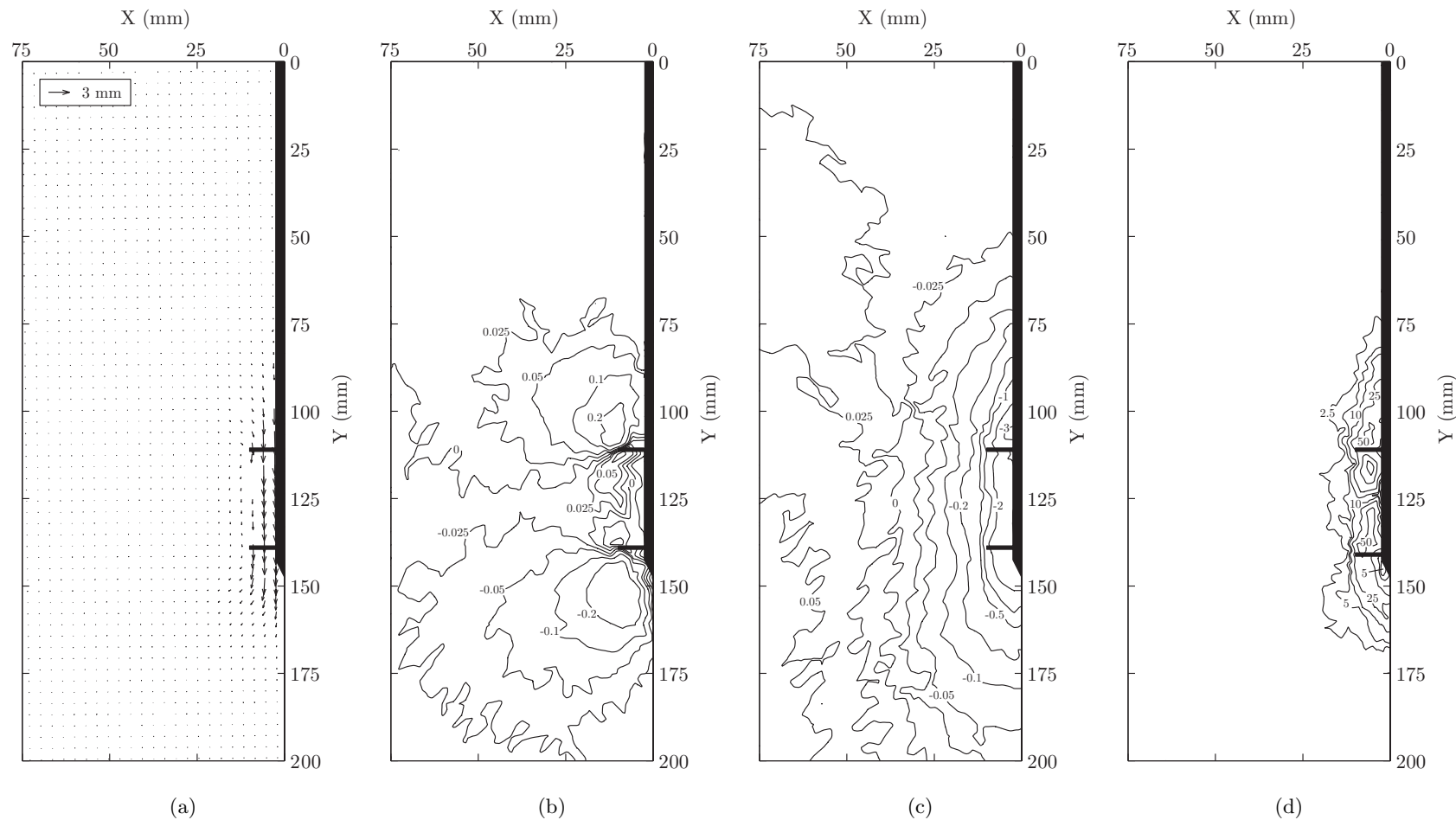


Figure 5.25: C2-30 cumulative PIV results at 3mm axial compressive displacement: vector (a), horizontal displacement (b), vertical displacement (c) and shear strain contours (d) with displacements in mm and shear strains expressed as a percentage.

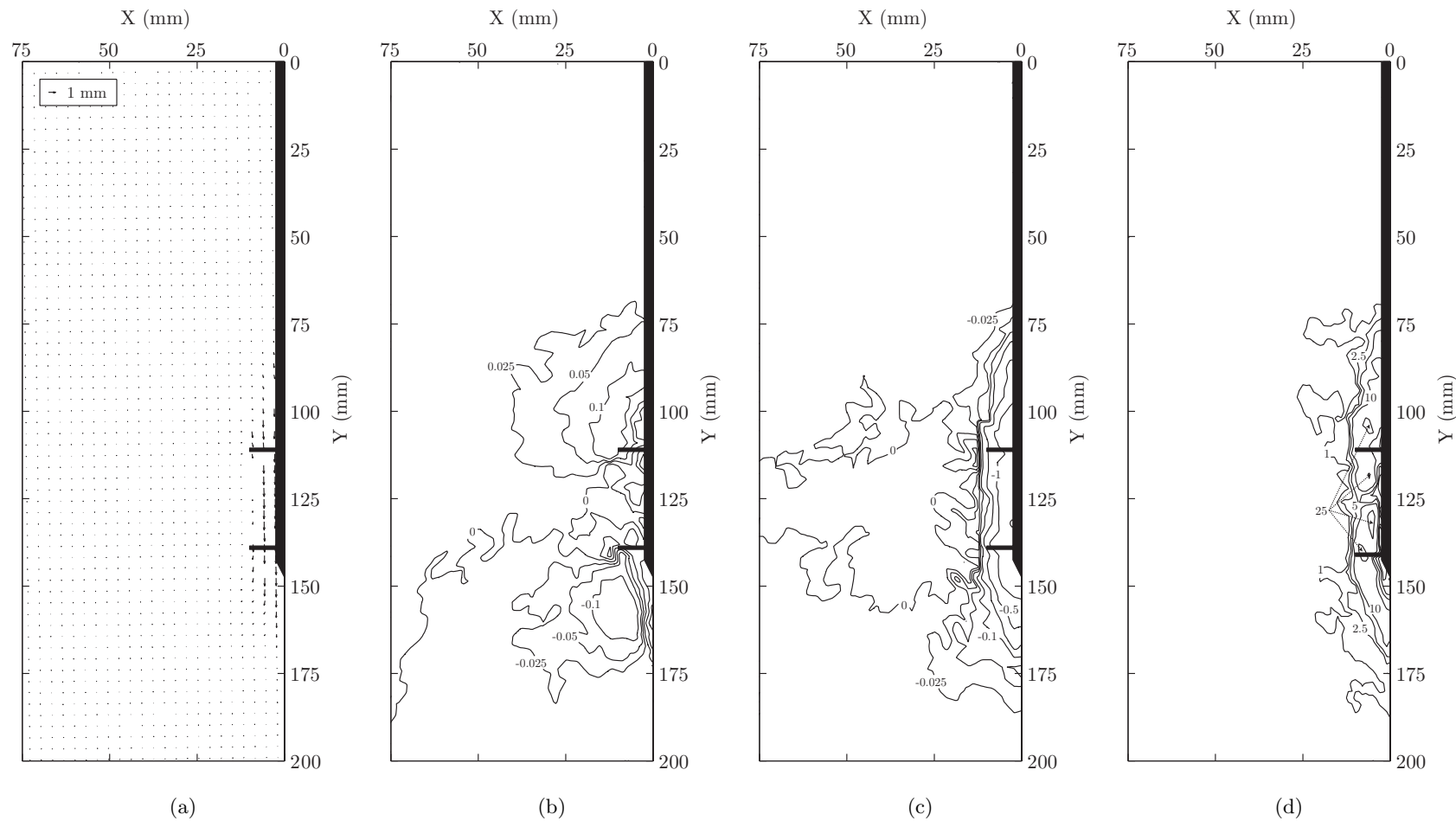


Figure 5.26: C2-30 incremental PIV results from 3mm to 4mm axial compressive displacement: vector (a), horizontal displacement (b), vertical displacement (c) and shear strain contours (d) with displacements in mm and shear strains expressed as a percentage.

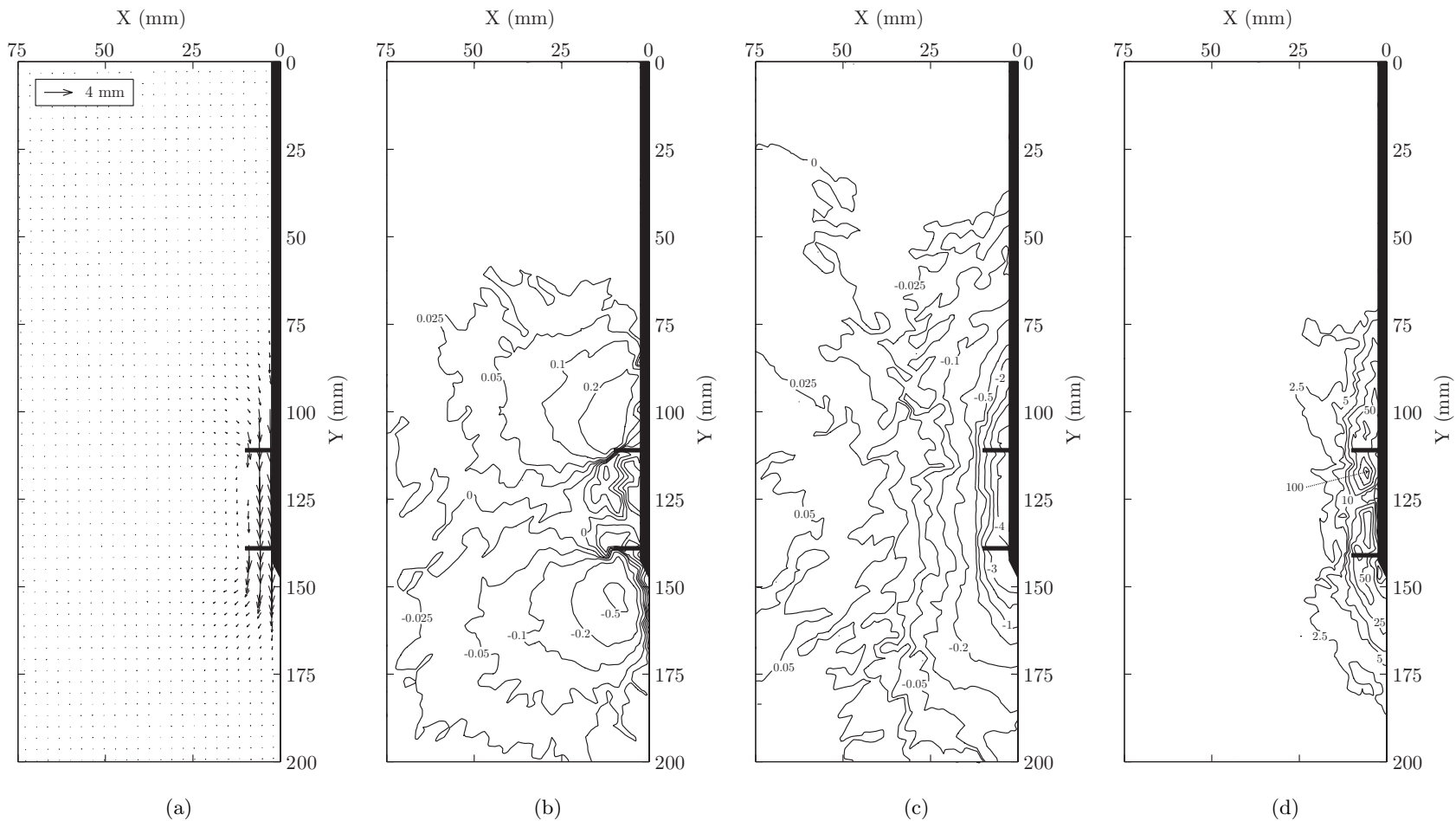


Figure 5.27: C2-30 cumulative PIV results at 4mm axial compressive displacement: vector (a), horizontal displacement (b), vertical displacement (c) and shear strain contours (d) with displacements in mm and shear strains expressed as a percentage.

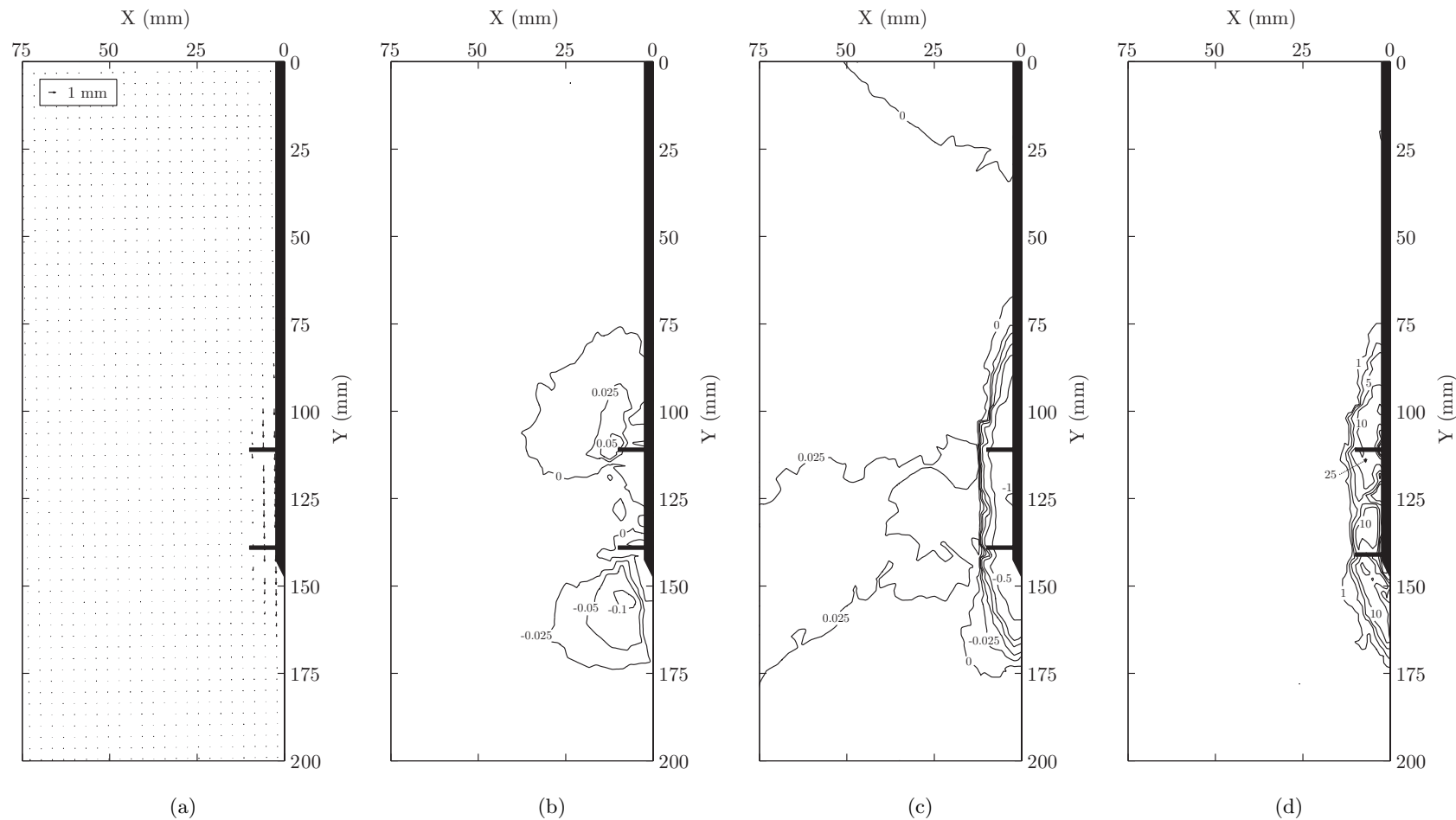


Figure 5.28: C2-30 incremental PIV results from 4mm to 5mm axial compressive displacement: vector (a), horizontal displacement (b), vertical displacement (c) and shear strain contours (d) with displacements in mm and shear strains expressed as a percentage.

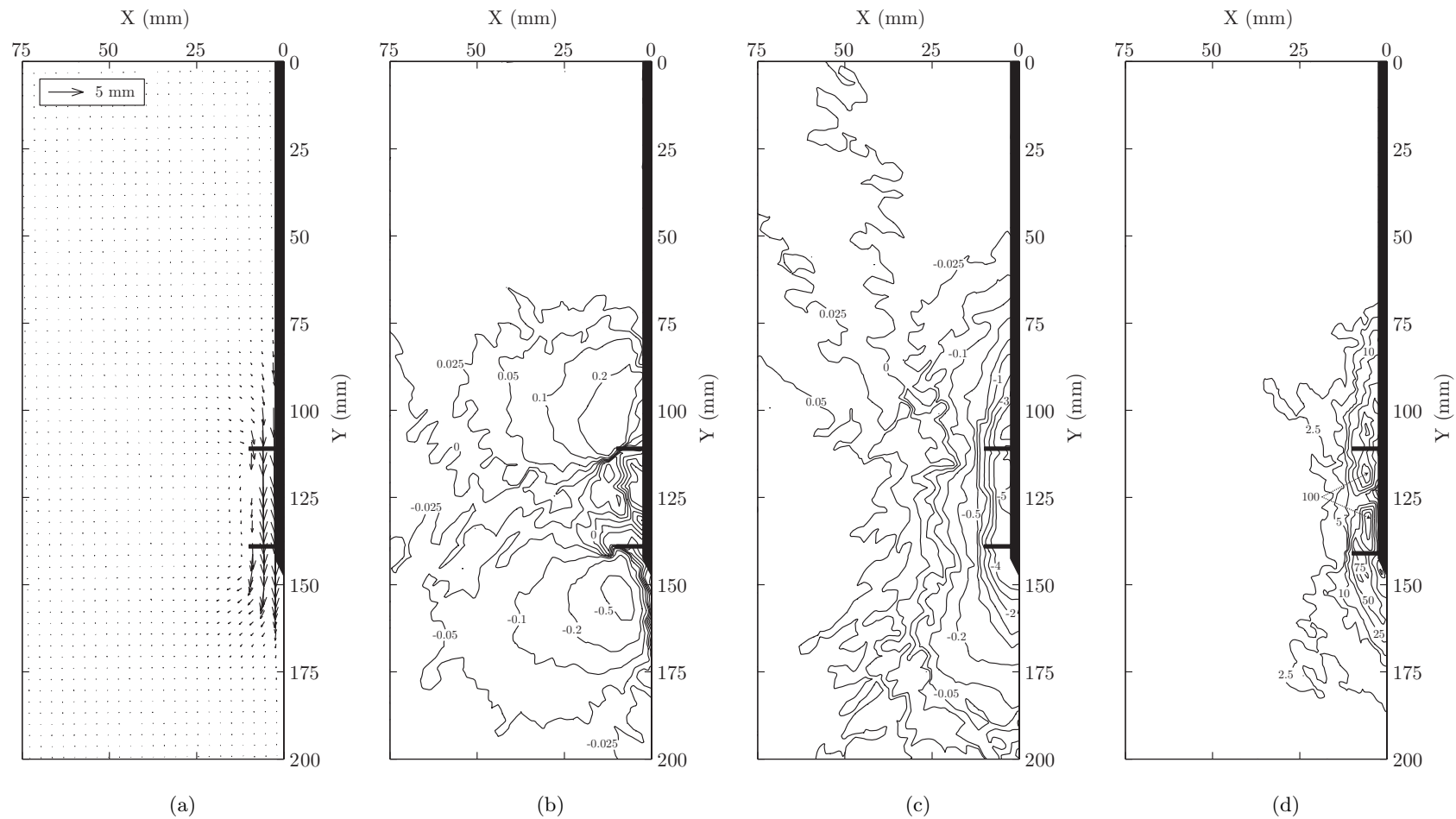


Figure 5.29: C2-30 cumulative PIV results at 5mm axial compressive displacement: vector (a), horizontal displacement (b), vertical displacement (c) and shear strain contours (d) with displacements in mm and shear strains expressed as a percentage.

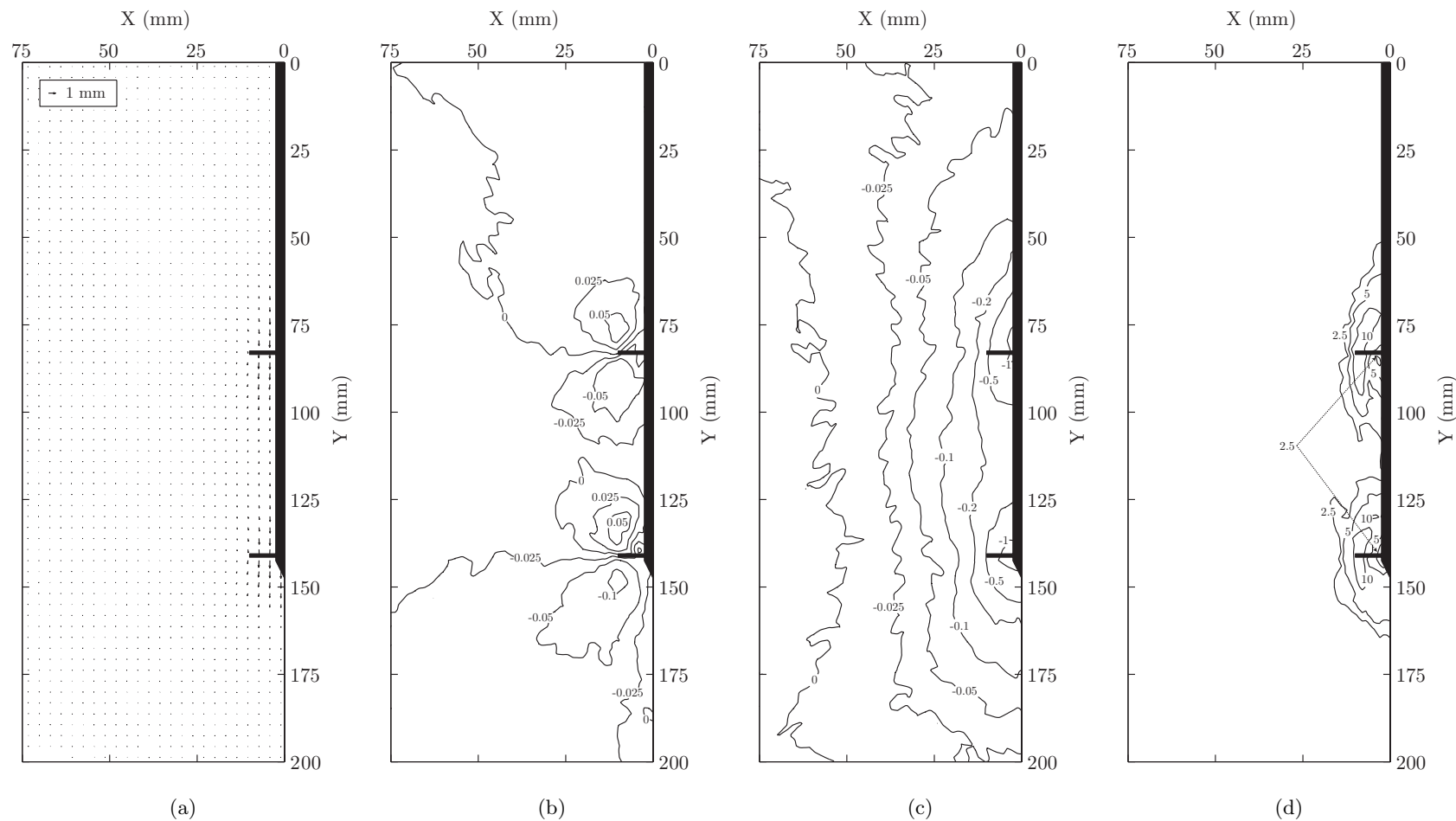


Figure 5.30: C2-60 cumulative PIV results at 1mm axial compressive displacement: vector (a), horizontal displacement (b), vertical displacement (c) and shear strain contours (d) with displacements in mm and shear strains expressed as a percentage.

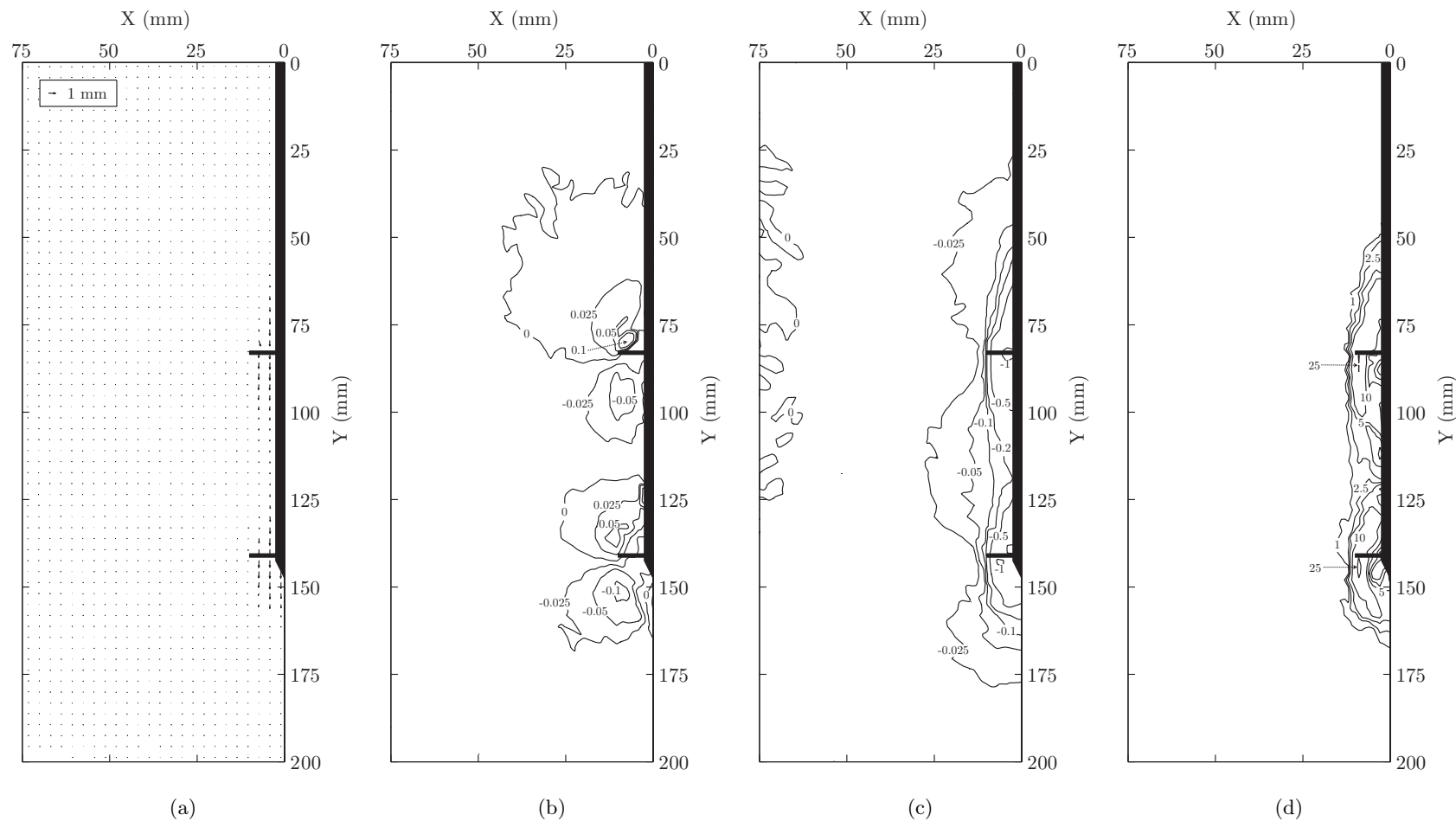


Figure 5.31: C2-60 incremental PIV results from 1mm to 2mm axial compressive displacement: vector (a), horizontal displacement (b), vertical displacement (c) and shear strain contours (d) with displacements in mm and shear strains expressed as a percentage.

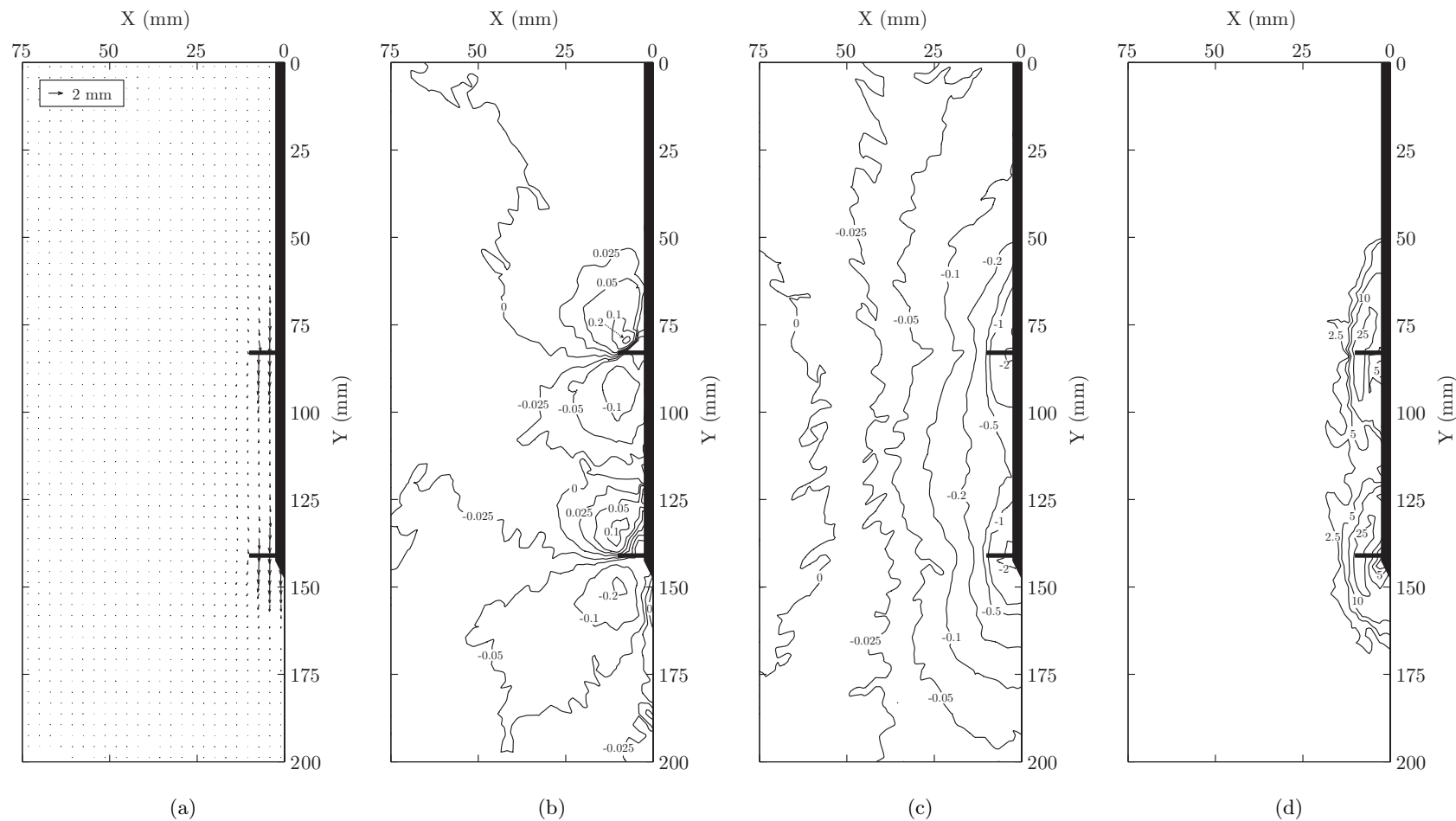


Figure 5.32: C2-60 cumulative PIV results at 2mm axial compressive displacement: vector (a), horizontal displacement (b), vertical displacement (c) and shear strain contours (d) with displacements in mm and shear strains expressed as a percentage.

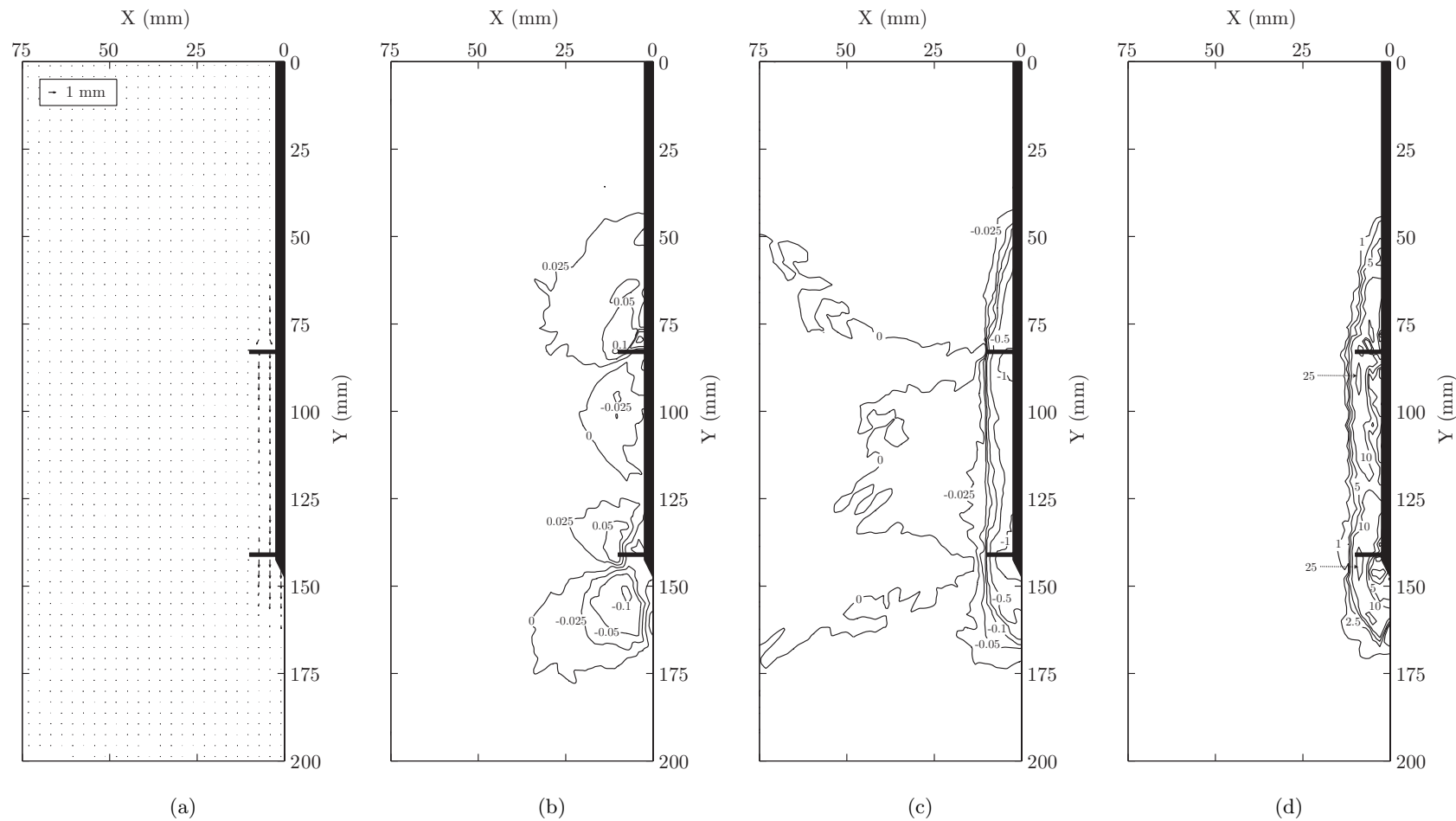


Figure 5.33: C2-60 incremental PIV results from 2mm to 3mm axial compressive displacement: vector (a), horizontal displacement (b), vertical displacement (c) and shear strain contours (d) with displacements in mm and shear strains expressed as a percentage.

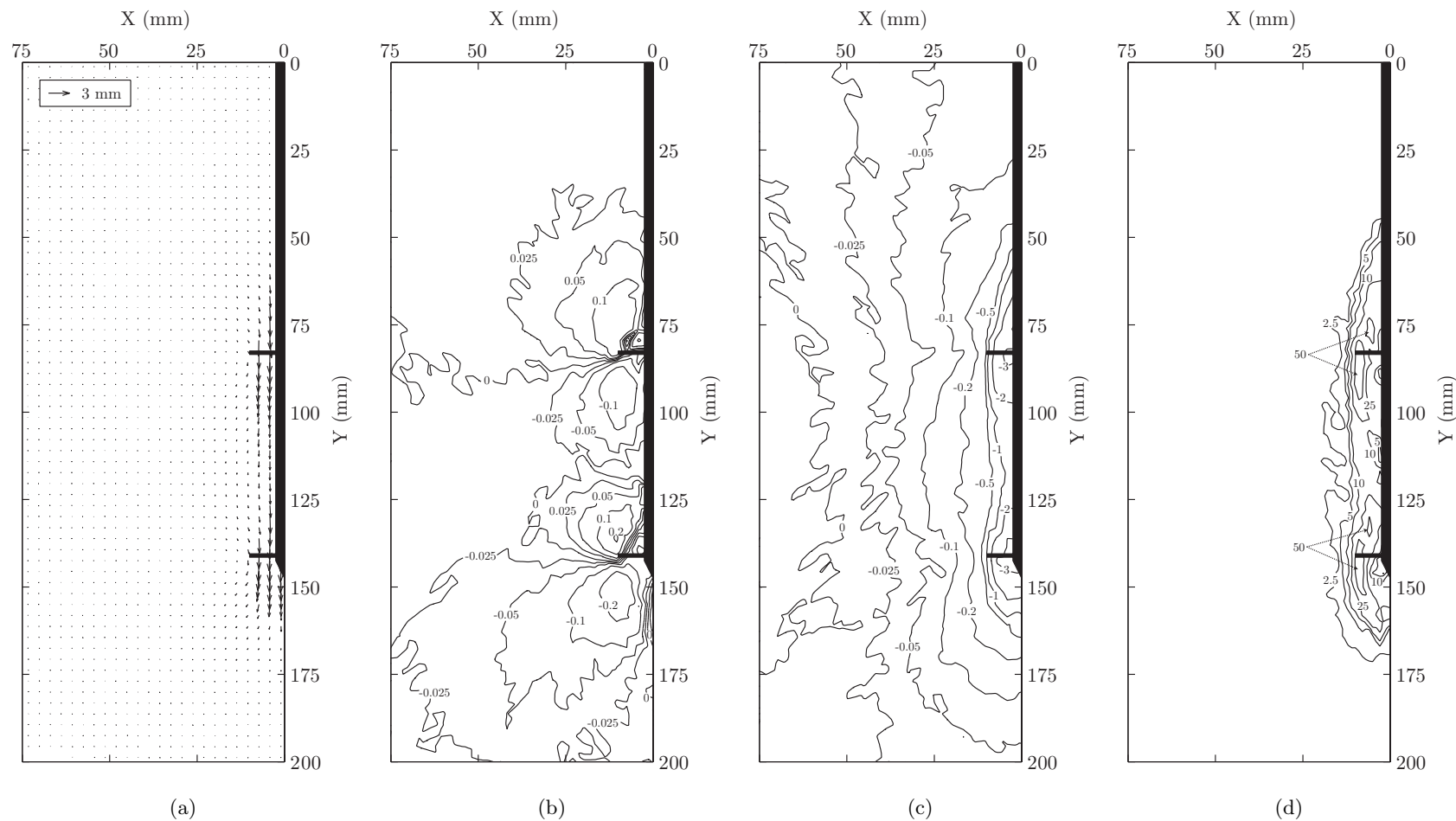


Figure 5.34: C2-60 cumulative PIV results at 3mm axial compressive displacement: vector (a), horizontal displacement (b), vertical displacement (c) and shear strain contours (d) with displacements in mm and shear strains expressed as a percentage.

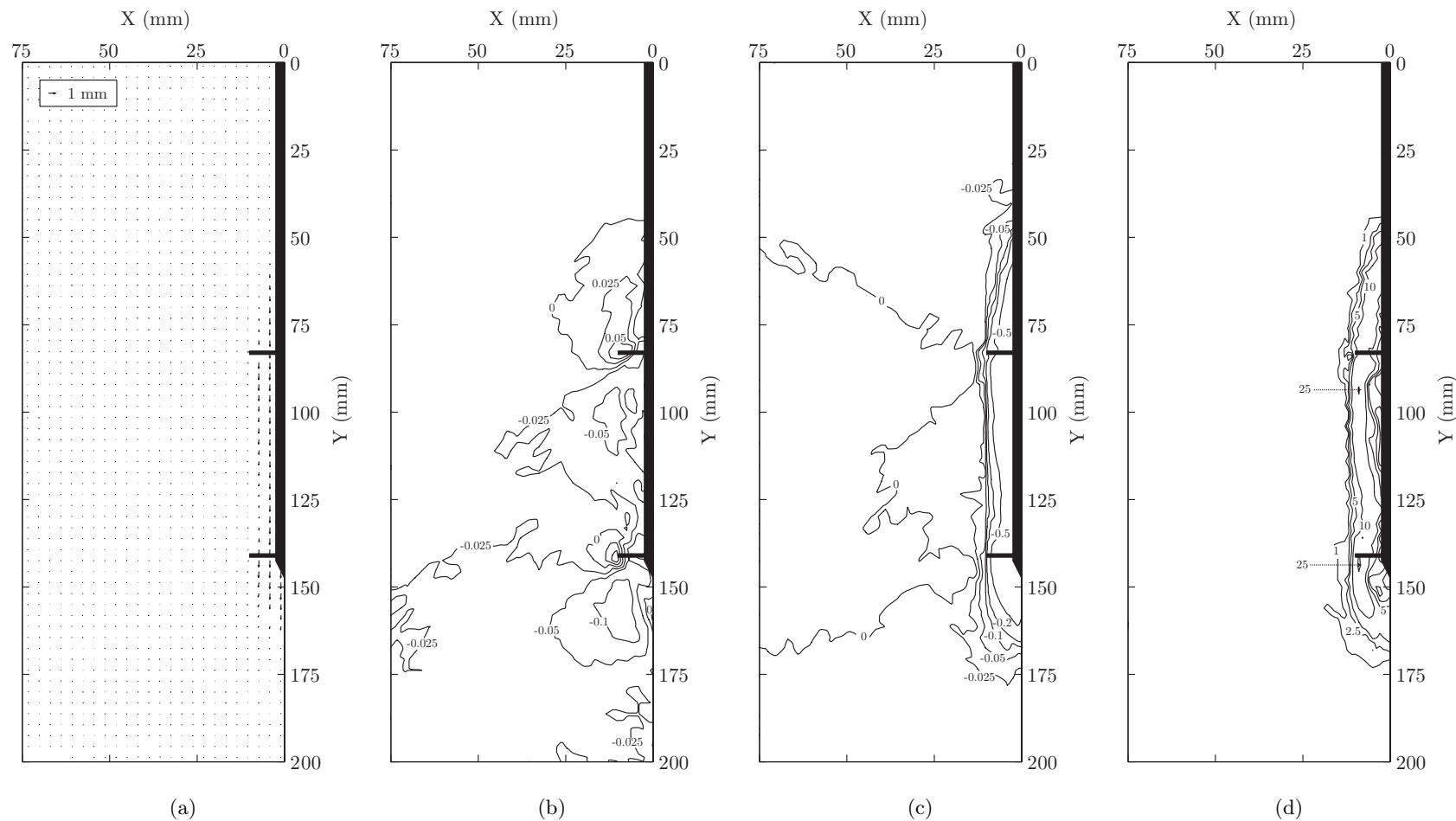


Figure 5.35: C2-60 incremental PIV results from 3mm to 4mm axial compressive displacement: vector (a), horizontal displacement (b), vertical displacement (c) and shear strain contours (d) with displacements in mm and shear strains expressed as a percentage.

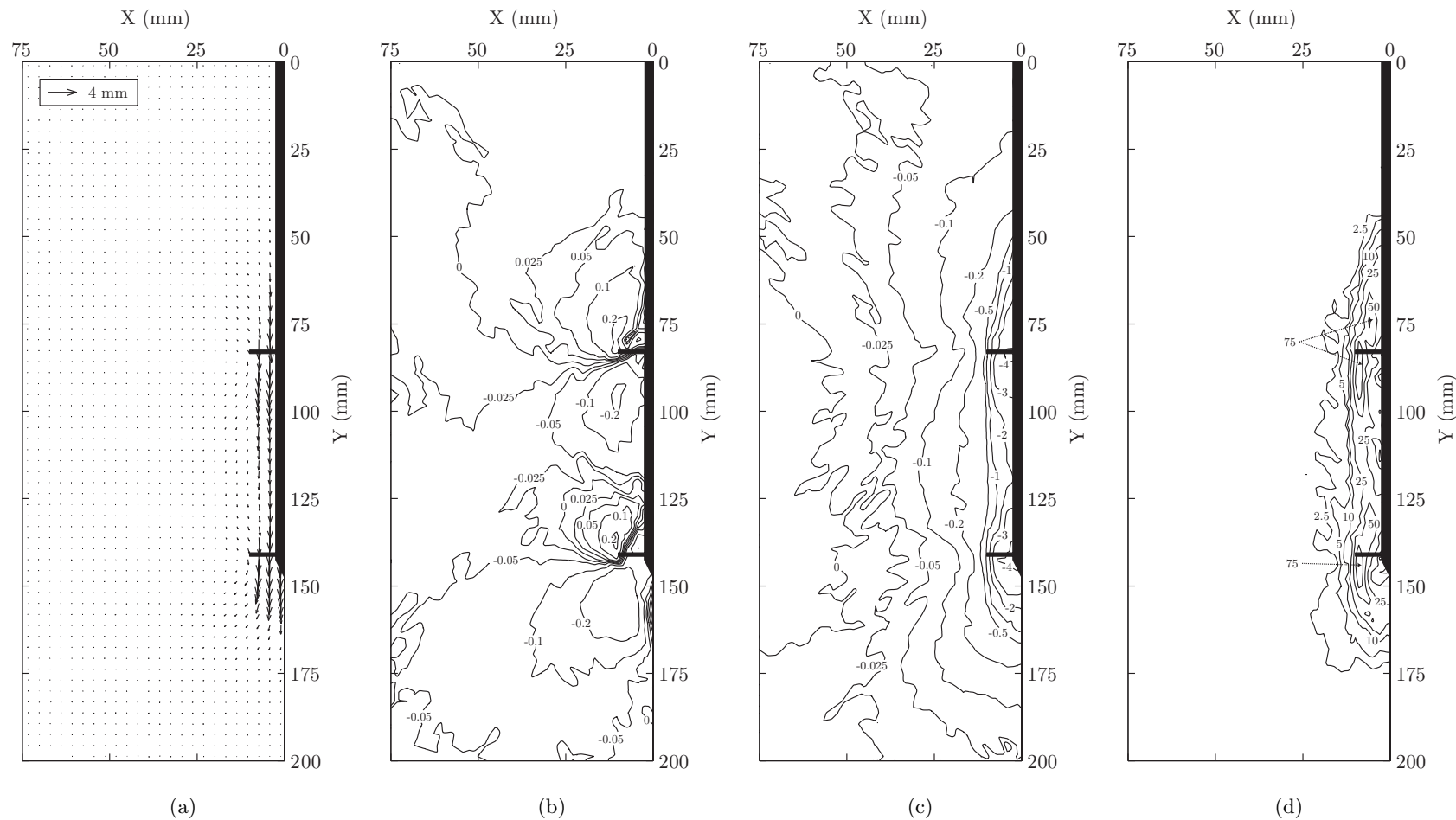


Figure 5.36: C2-60 cumulative PIV results at 4mm axial compressive displacement: vector (a), horizontal displacement (b), vertical displacement (c) and shear strain contours (d) with displacements in mm and shear strains expressed as a percentage.

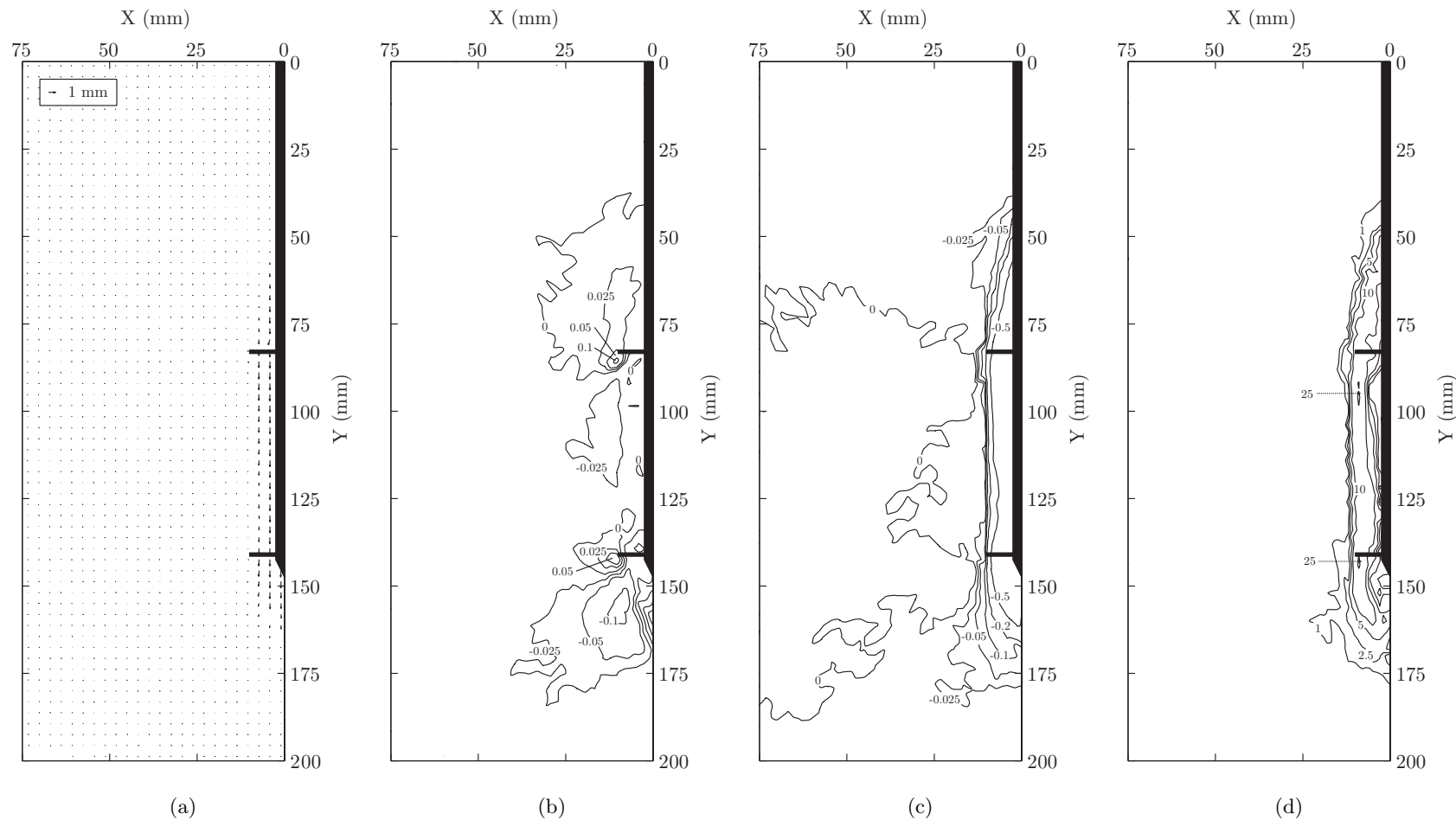


Figure 5.37: C2-60 incremental PIV results from 4mm to 5mm axial compressive displacement: vector (a), horizontal displacement (b), vertical displacement (c) and shear strain contours (d) with displacements in mm and shear strains expressed as a percentage.

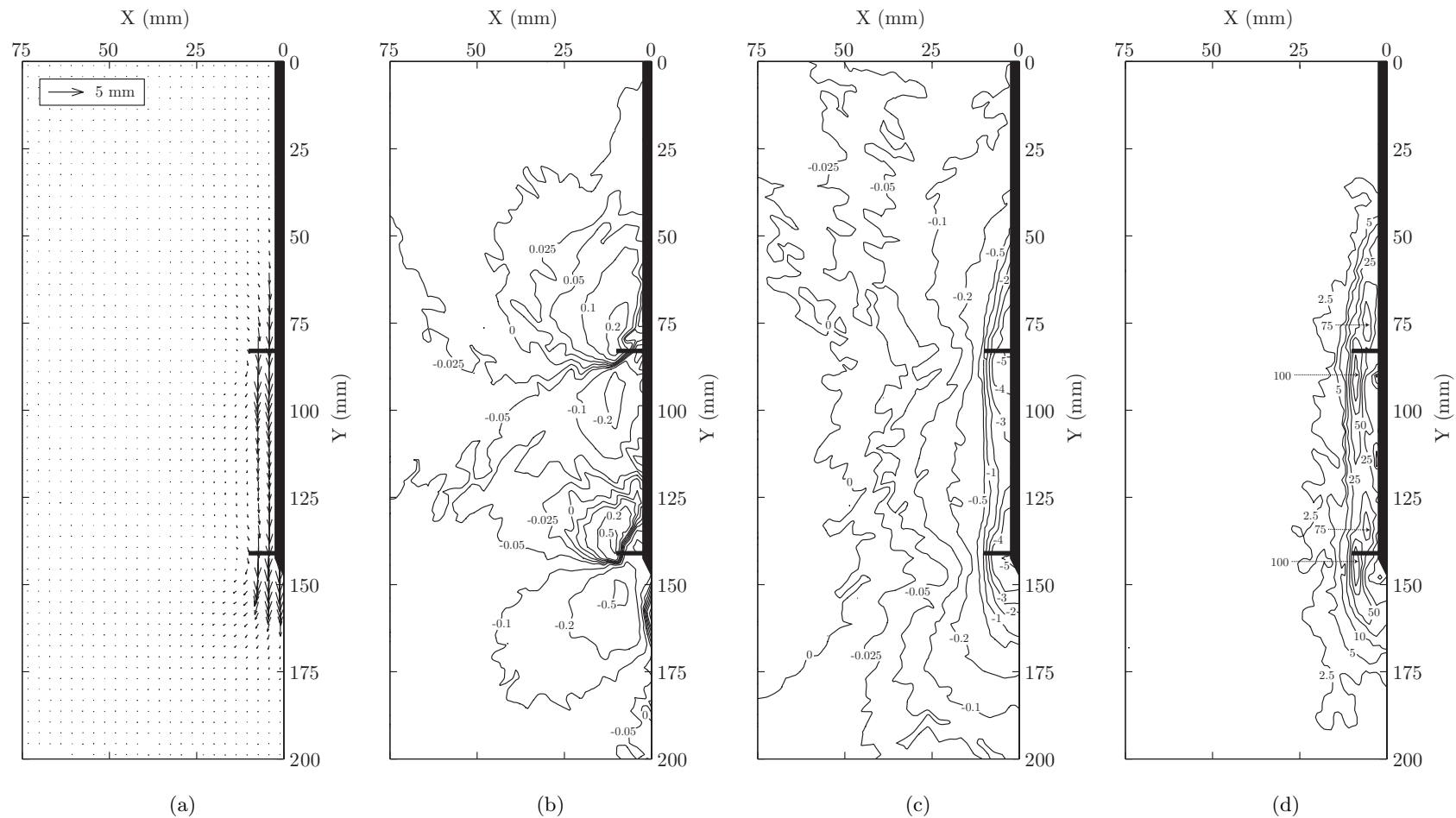


Figure 5.38: C2-60 cumulative PIV results at 5mm axial compressive displacement: vector (a), horizontal displacement (b), vertical displacement (c) and shear strain contours (d) with displacements in mm and shear strains expressed as a percentage.

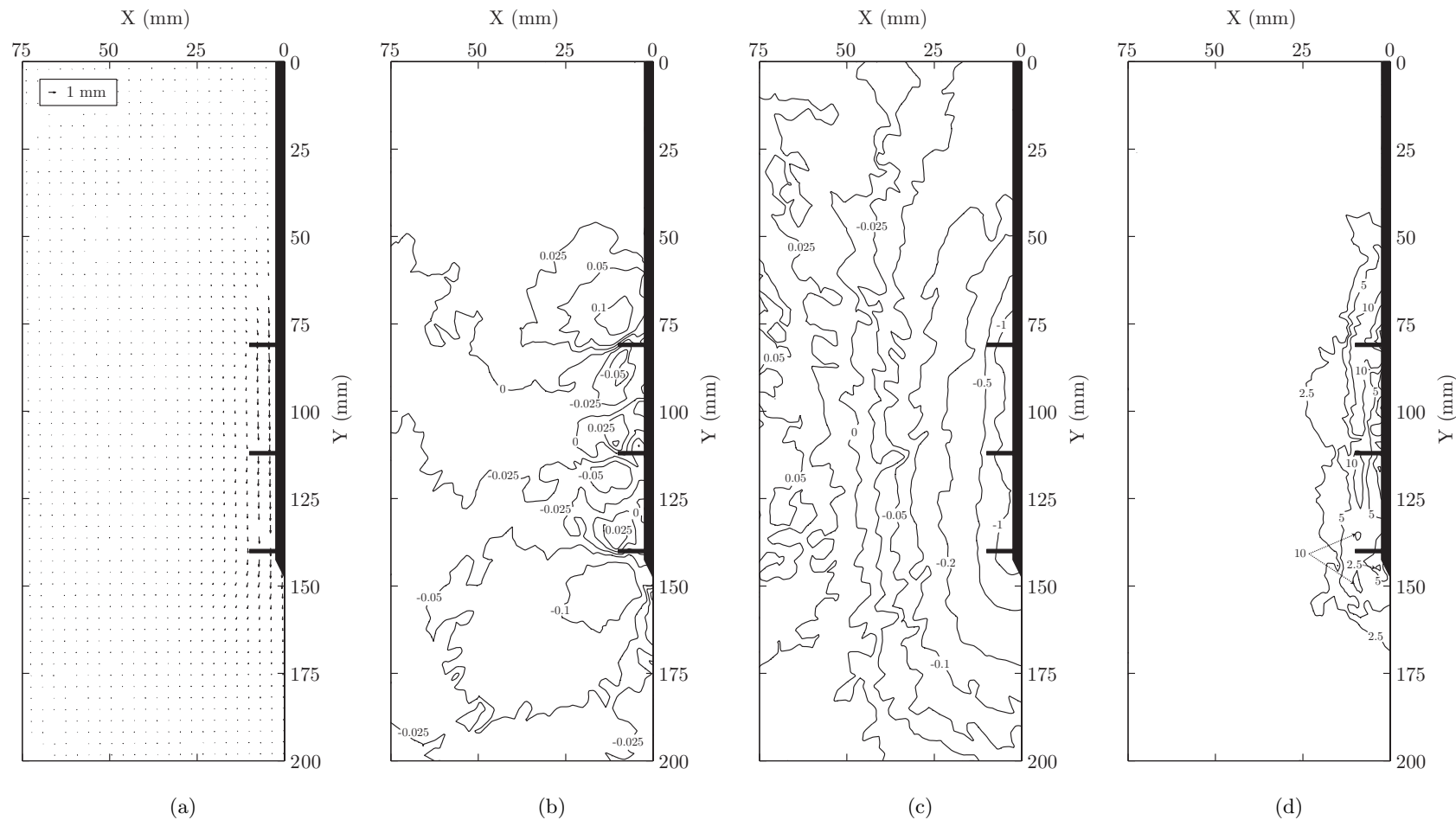


Figure 5.39: C3 cumulative PIV results at 1mm axial compressive displacement: vector (a), horizontal displacement (b), vertical displacement (c) and shear strain contours (d) with displacements in mm and shear strains expressed as a percentage.

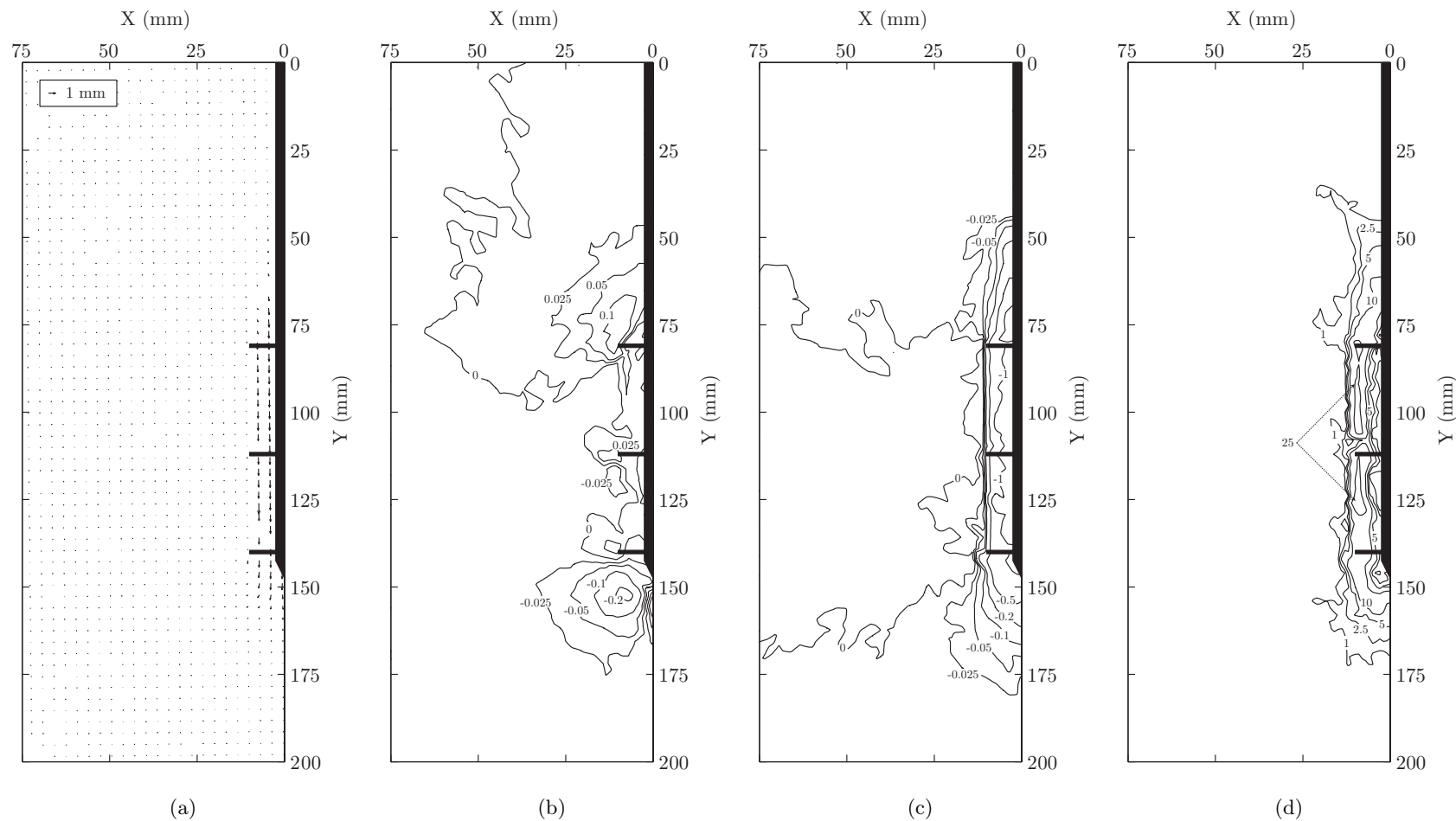


Figure 5.40: C3 incremental PIV results from 1mm to 2mm axial compressive displacement: vector (a), horizontal displacement (b), vertical displacement (c) and shear strain contours (d) with displacements in mm and shear strains expressed as a percentage.

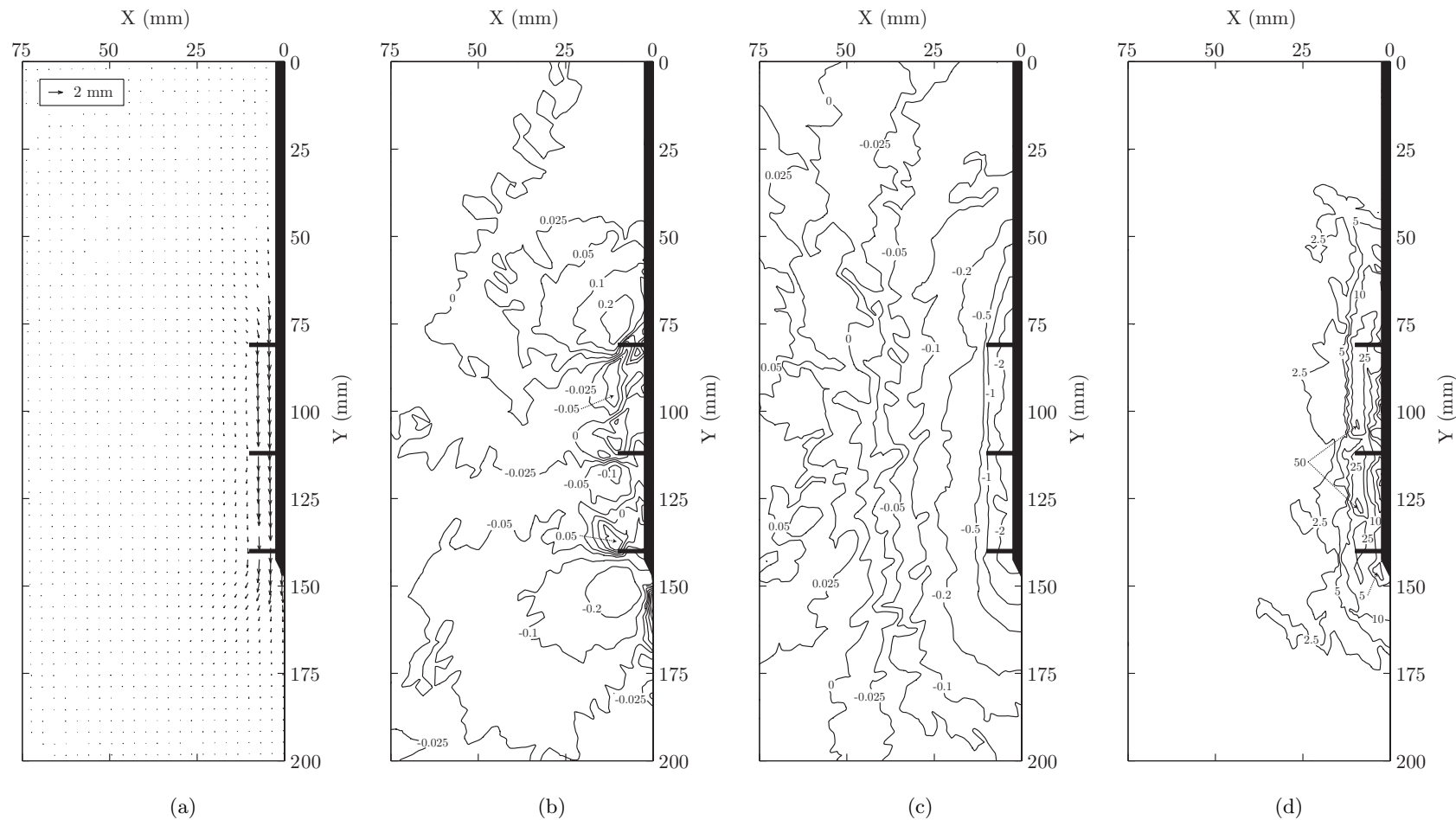


Figure 5.41: C3 cumulative PIV results at 2mm axial compressive displacement: vector (a), horizontal displacement (b), vertical displacement (c) and shear strain contours (d) with displacements in mm and shear strains expressed as a percentage.

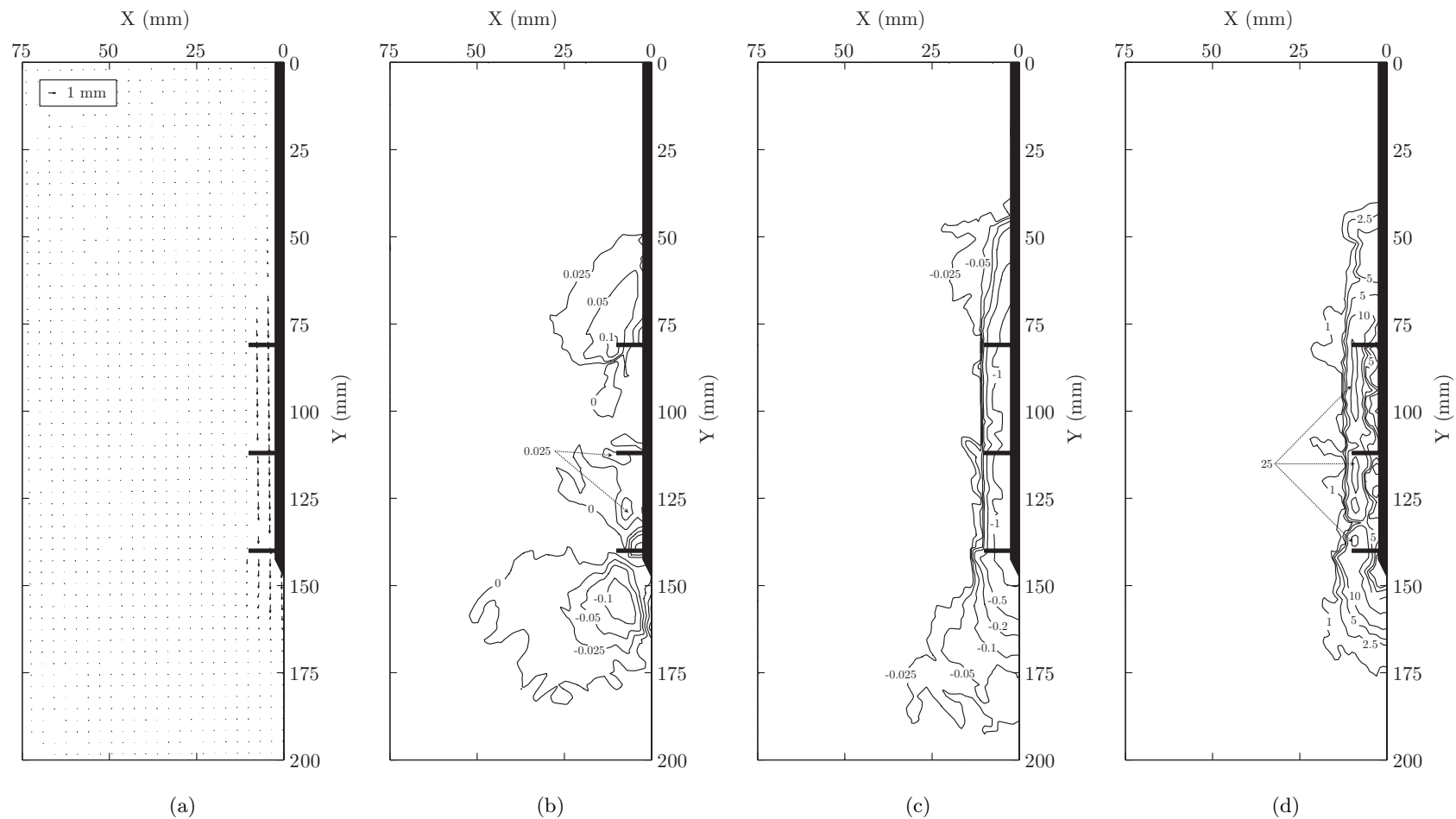


Figure 5.42: C3 incremental PIV results from $2mm$ to $3mm$ axial compressive displacement: vector (a), horizontal displacement (b), vertical displacement (c) and shear strain contours (d) with displacements in mm and shear strains expressed as a percentage.

230

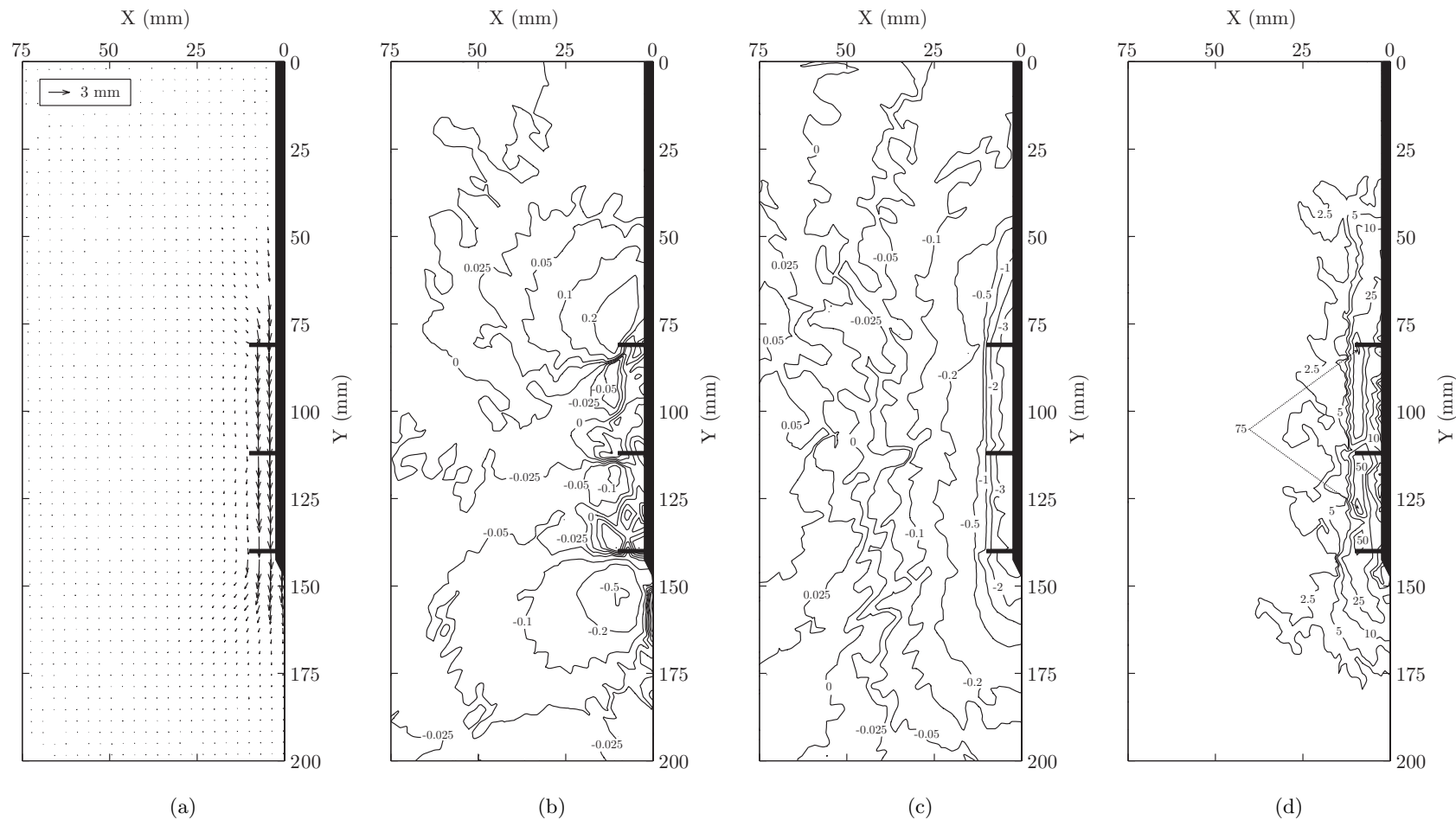


Figure 5.43: C3 cumulative PIV results at 3mm axial compressive displacement: vector (a), horizontal displacement (b), vertical displacement (c) and shear strain contours (d) with displacements in mm and shear strains expressed as a percentage.

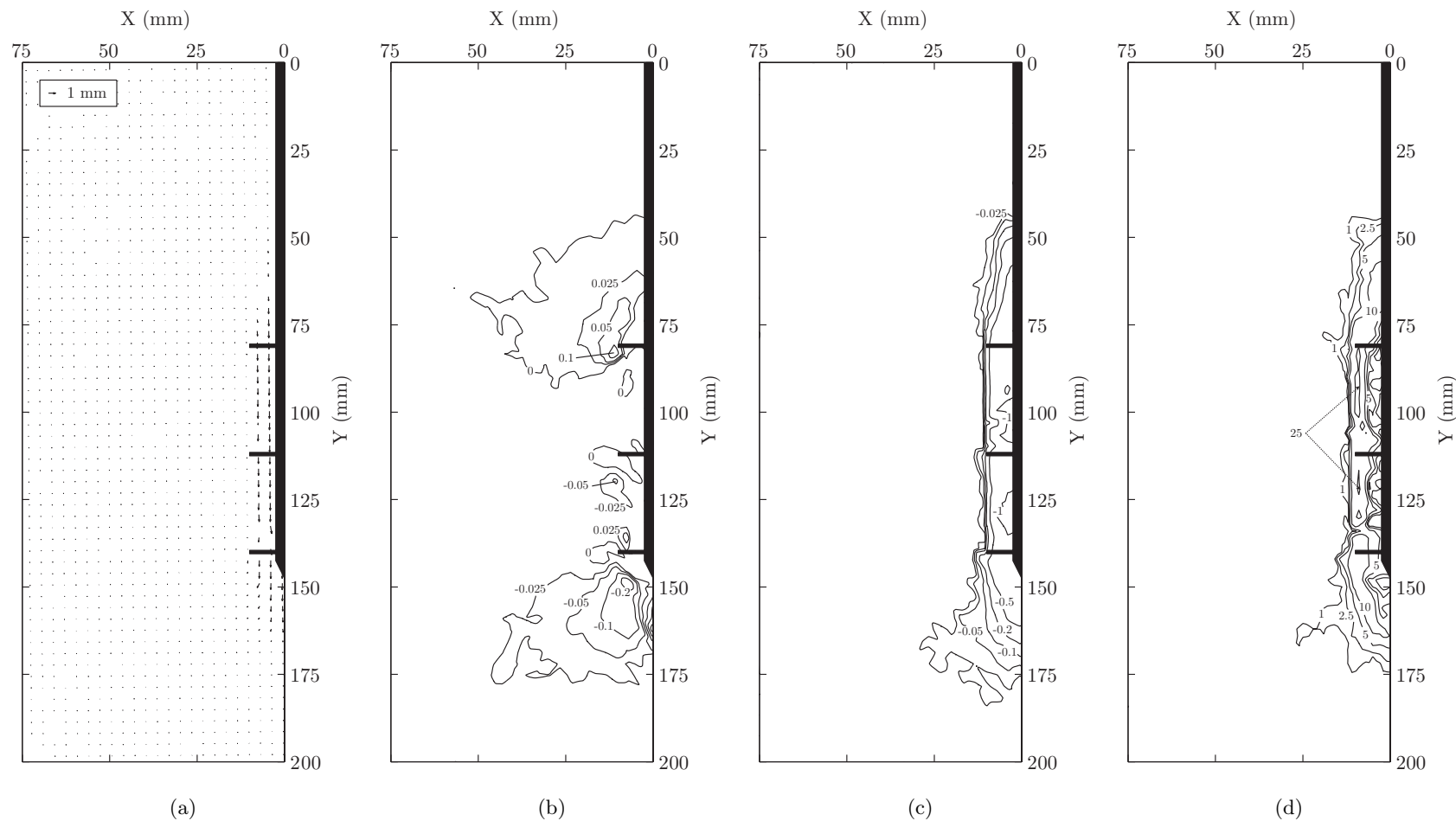


Figure 5.44: C3 incremental PIV results from 3mm to 4mm axial compressive displacement: vector (a), horizontal displacement (b), vertical displacement (c) and shear strain contours (d) with displacements in mm and shear strains expressed as a percentage.

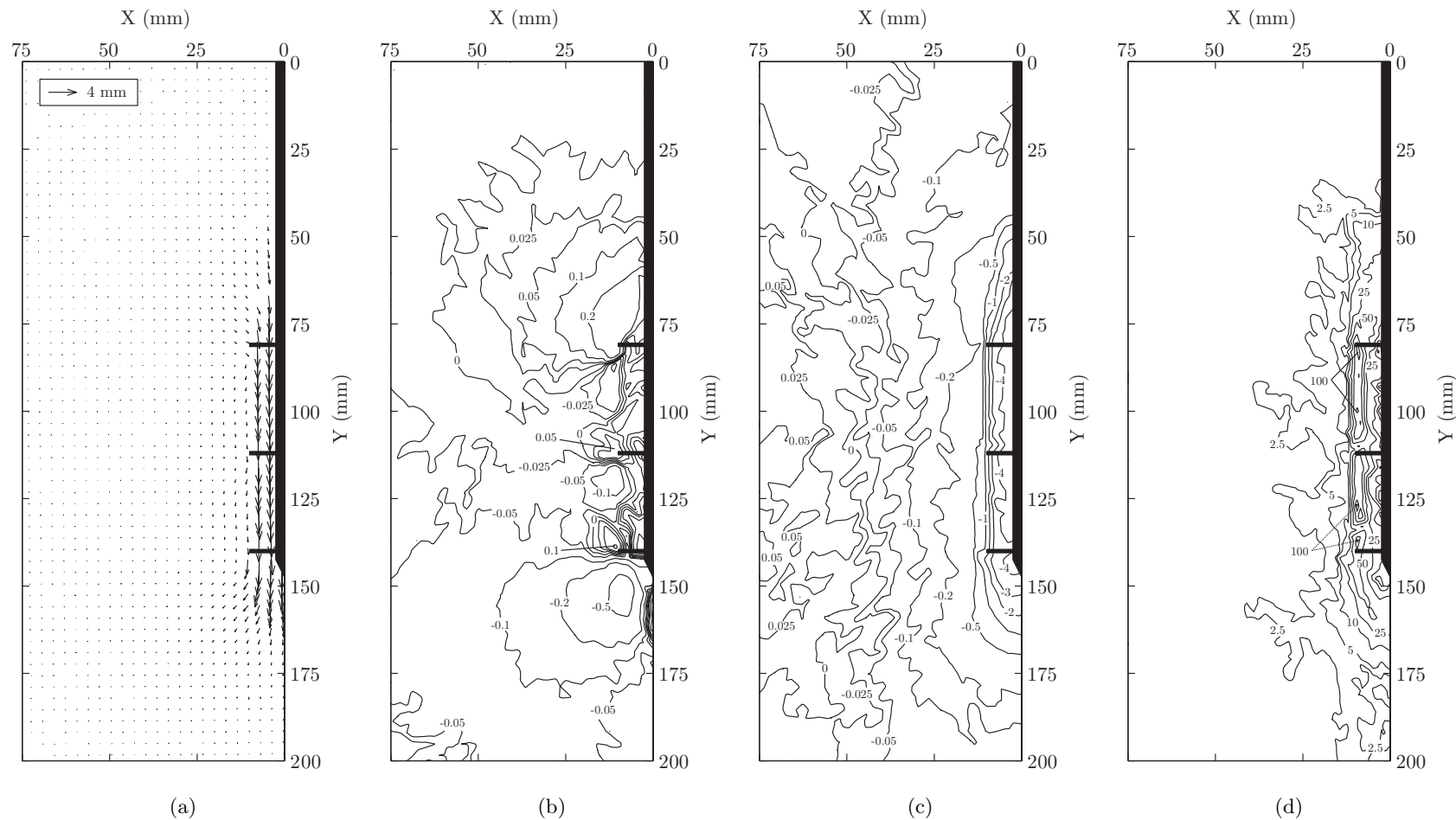


Figure 5.45: C3 cumulative PIV results at 4mm axial compressive displacement: vector (a), horizontal displacement (b), vertical displacement (c) and shear strain contours (d) with displacements in mm and shear strains expressed as a percentage.

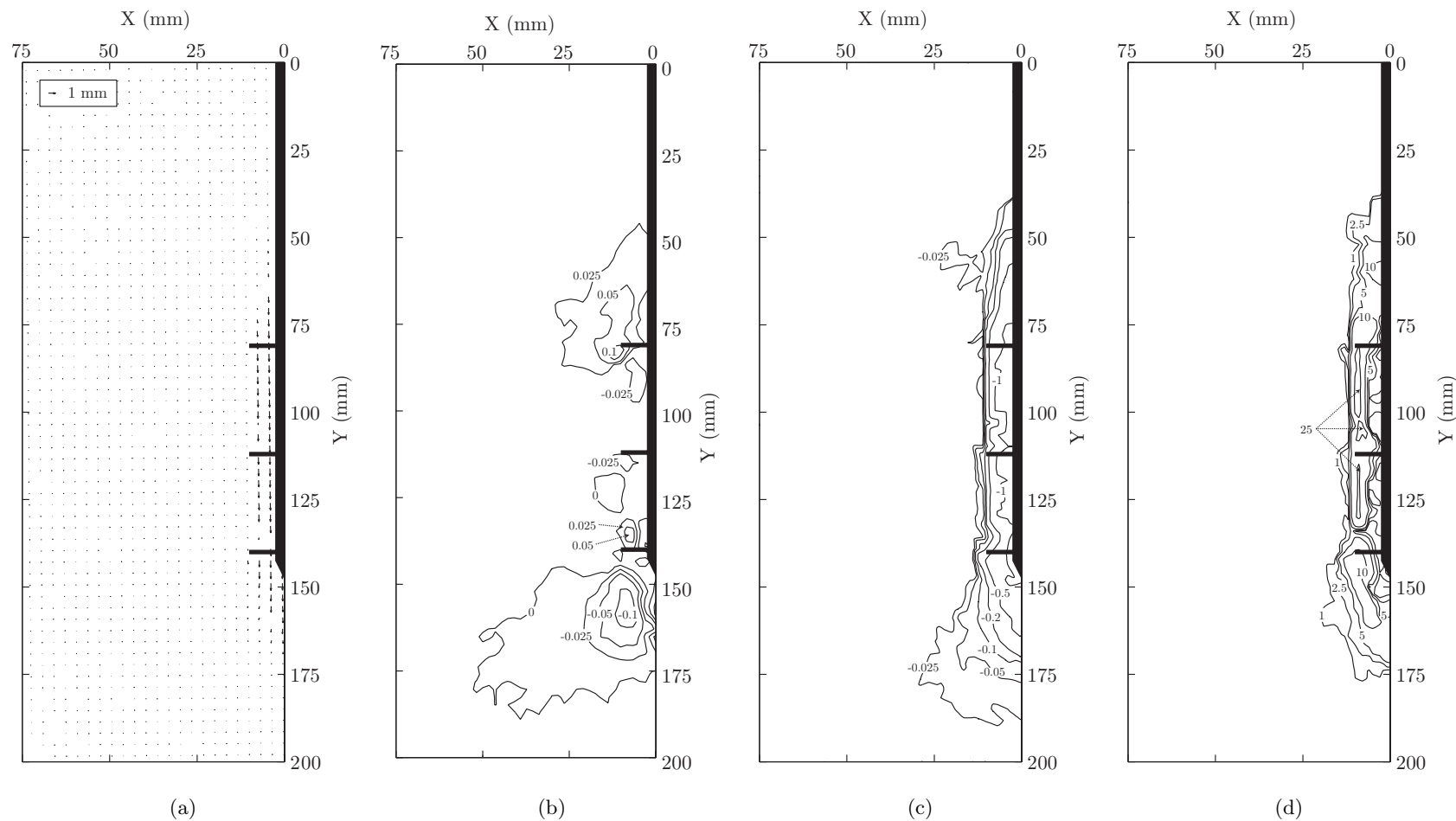


Figure 5.46: C3 incremental PIV results from 4mm to 5mm axial compressive displacement: vector (a), horizontal displacement (b), vertical displacement (c) and shear strain contours (d) with displacements in mm and shear strains expressed as a percentage.

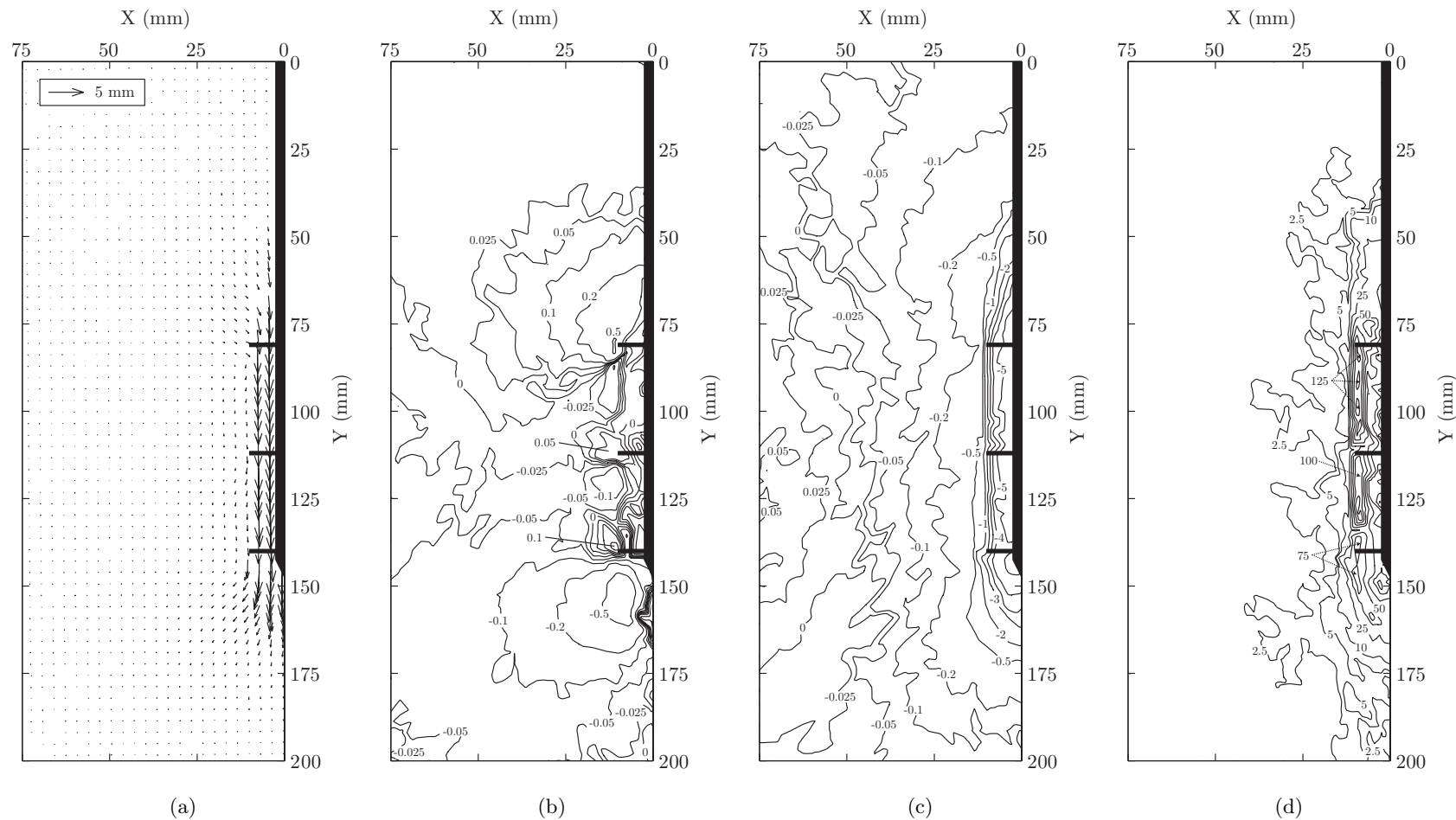


Figure 5.47: C3 cumulative PIV results at 5mm axial compressive displacement: vector (a), horizontal displacement (b), vertical displacement (c) and shear strain contours (d) with displacements in mm and shear strains expressed as a percentage.

5.3.4.2 Tension Results

The following section contains PIV derived displacement and shear strain fields of tensile loading tests conducted on helical screw piles. Figures 5.48-5.56 relate to test T1. Figures 5.57-5.65 relate to test T2-30. Figures 5.66-5.74 relate to test T2-60. Lastly, figures 5.75-5.83 relate to test T3.

For all tests both cumulative and incremental displacement and shear strain fields are presented for the same absolute magnitudes of axial displacements as for the compressive results in Section 5.3.4.1.

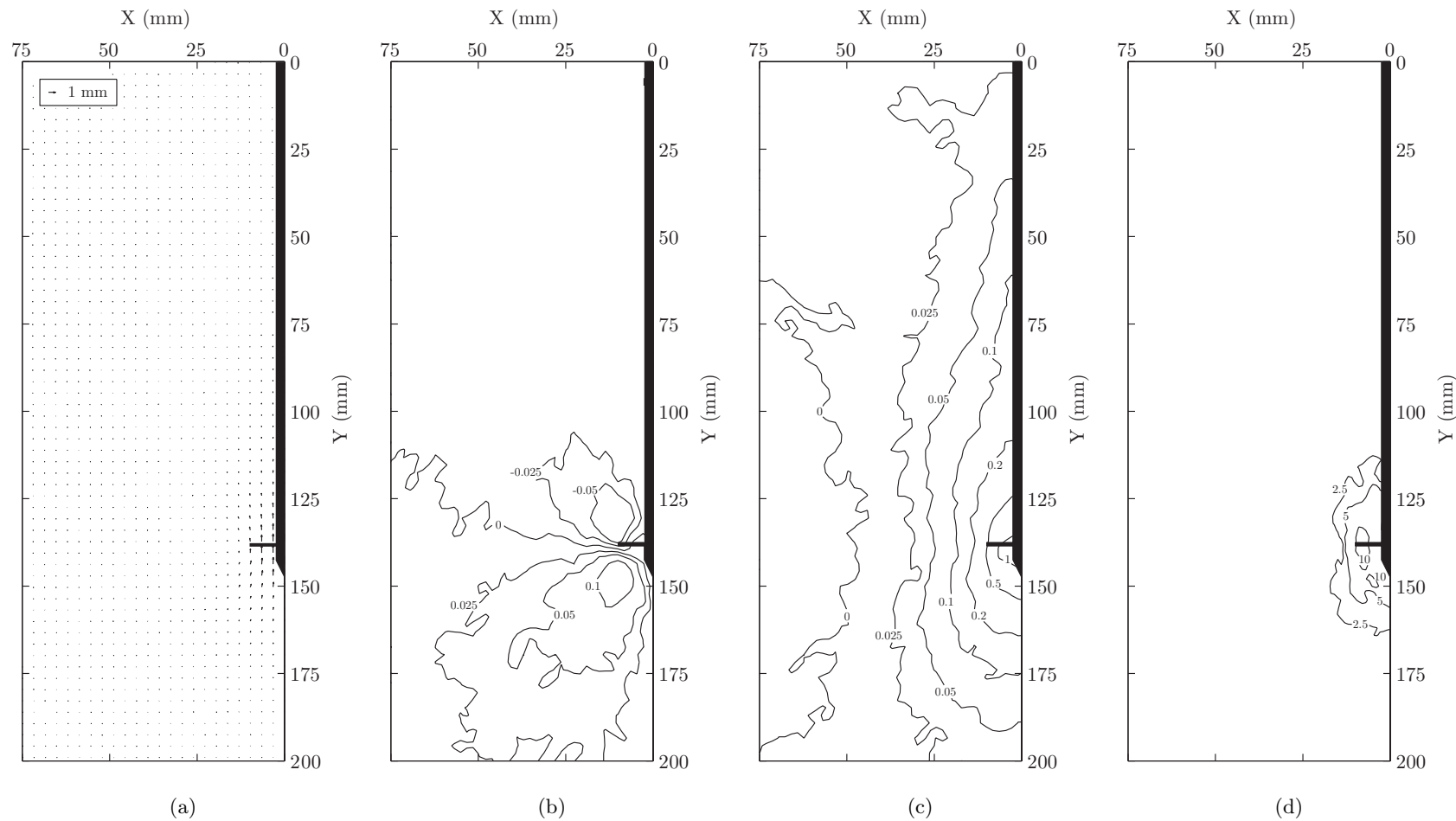


Figure 5.48: T1 cumulative PIV results at 1mm axial tensile displacement: vector (a), horizontal displacement (b), vertical displacement (c) and shear strain contours (d) with displacements in mm and shear strains expressed as a percentage.

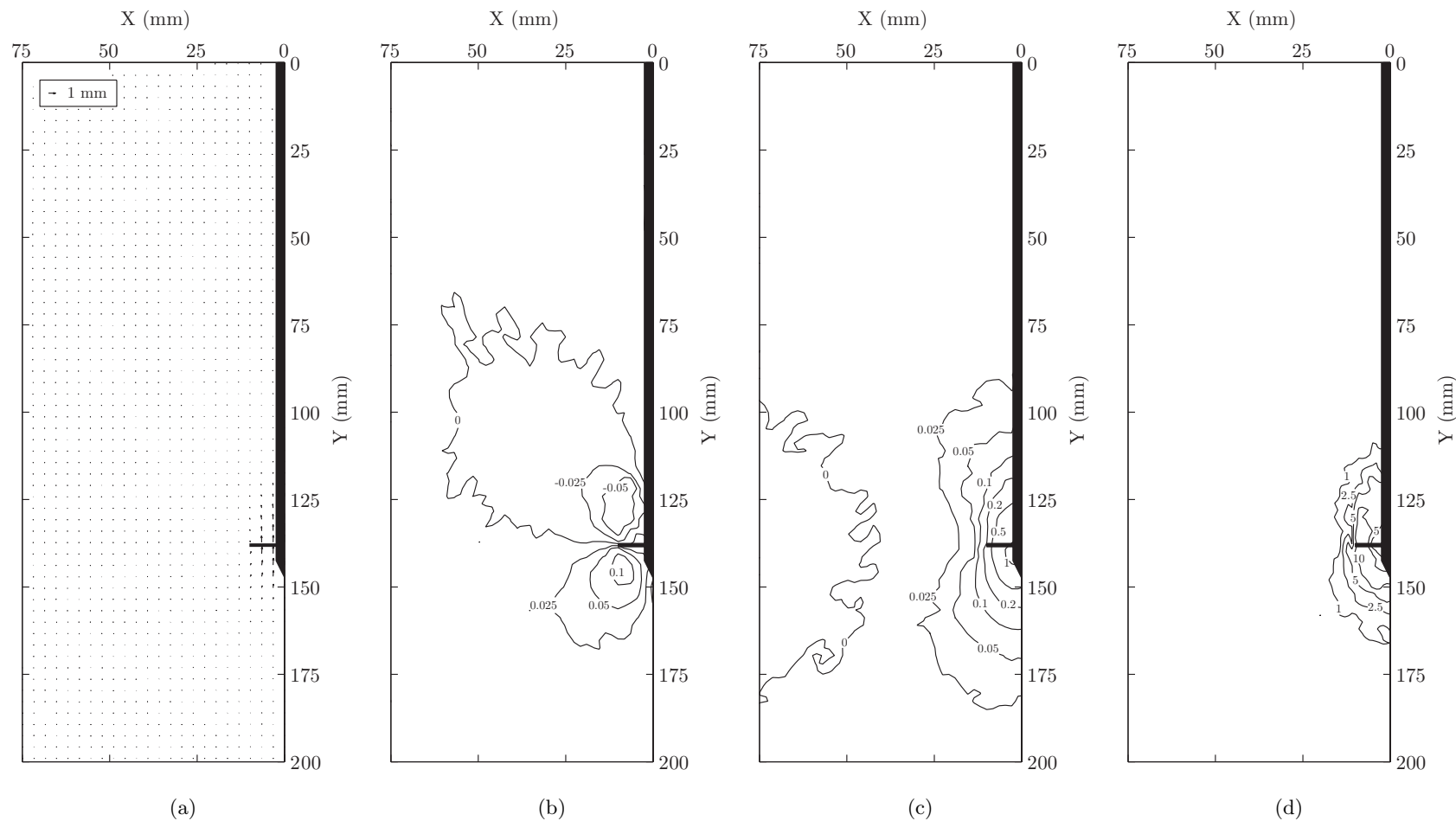


Figure 5.49: T1 incremental PIV results from 1mm to 2mm axial tensile displacement: vector (a), horizontal displacement (b), vertical displacement (c) and shear strain contours (d) with displacements in mm and shear strains expressed as a percentage.

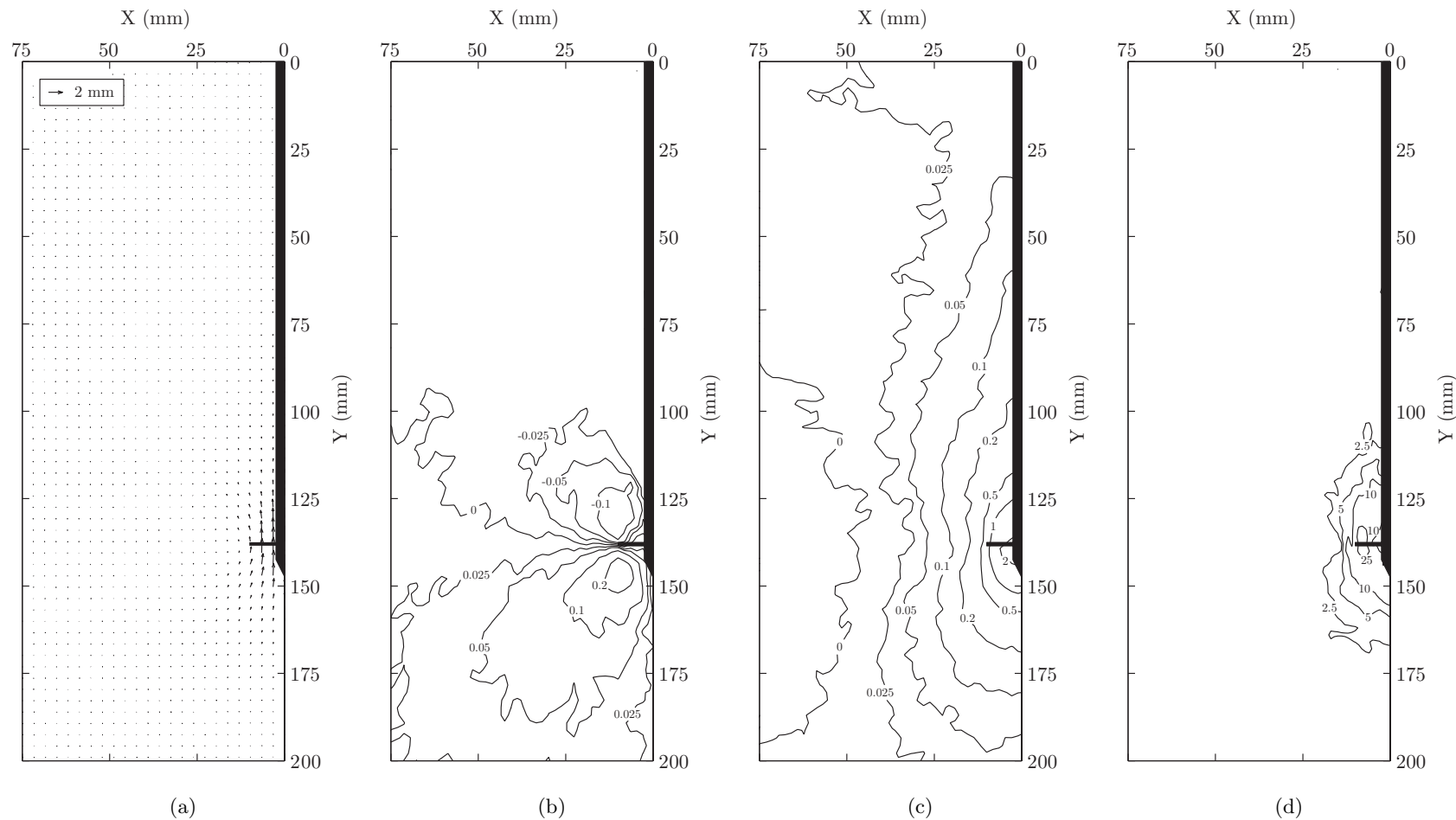


Figure 5.50: T1 cumulative PIV results at 2mm axial tensile displacement: vector (a), horizontal displacement (b), vertical displacement (c) and shear strain contours (d) with displacements in mm and shear strains expressed as a percentage.

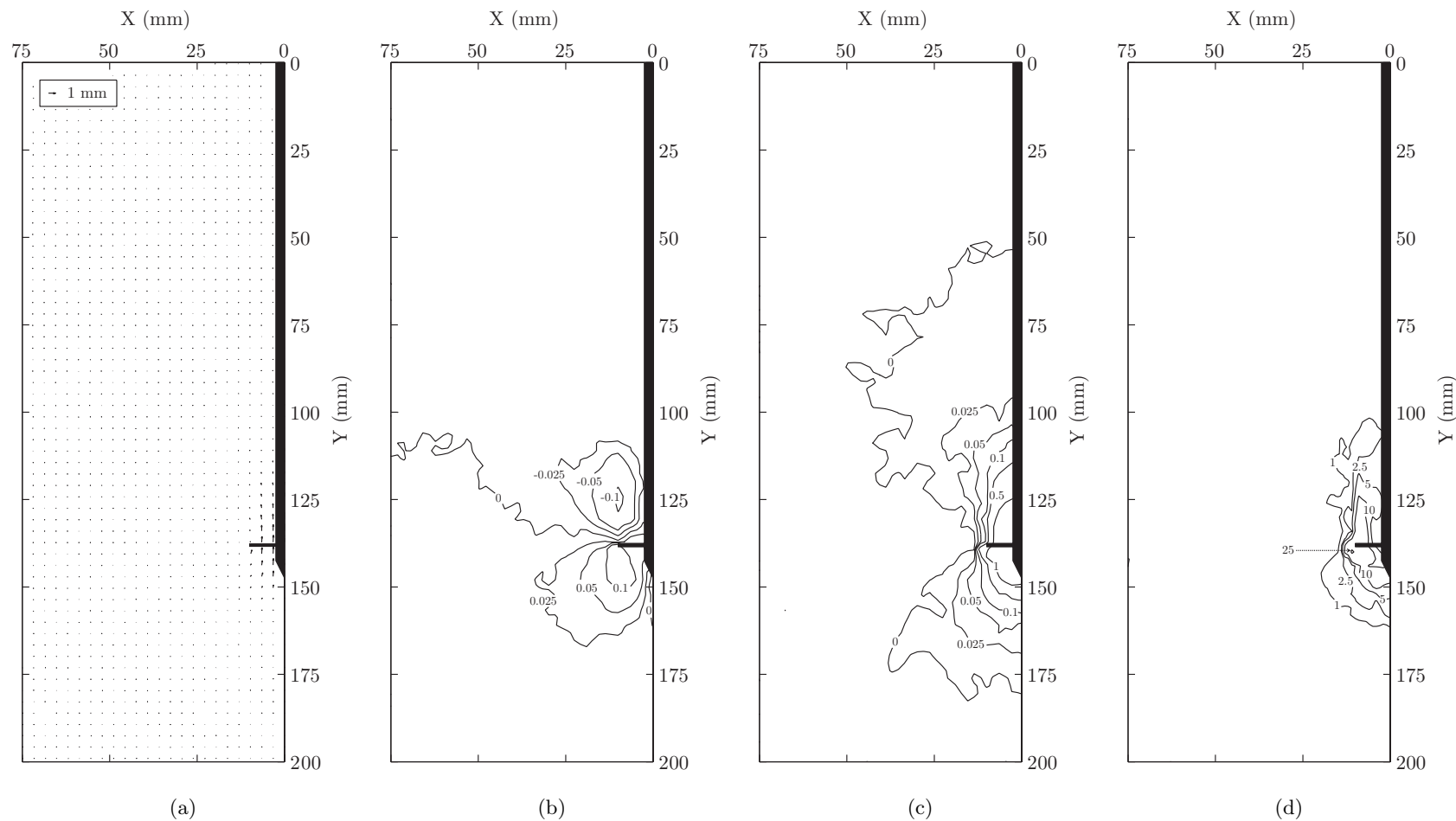


Figure 5.51: T1 incremental PIV results from 2mm to 3mm axial tensile displacement: vector (a), horizontal displacement (b), vertical displacement (c) and shear strain contours (d) with displacements in mm and shear strains expressed as a percentage.

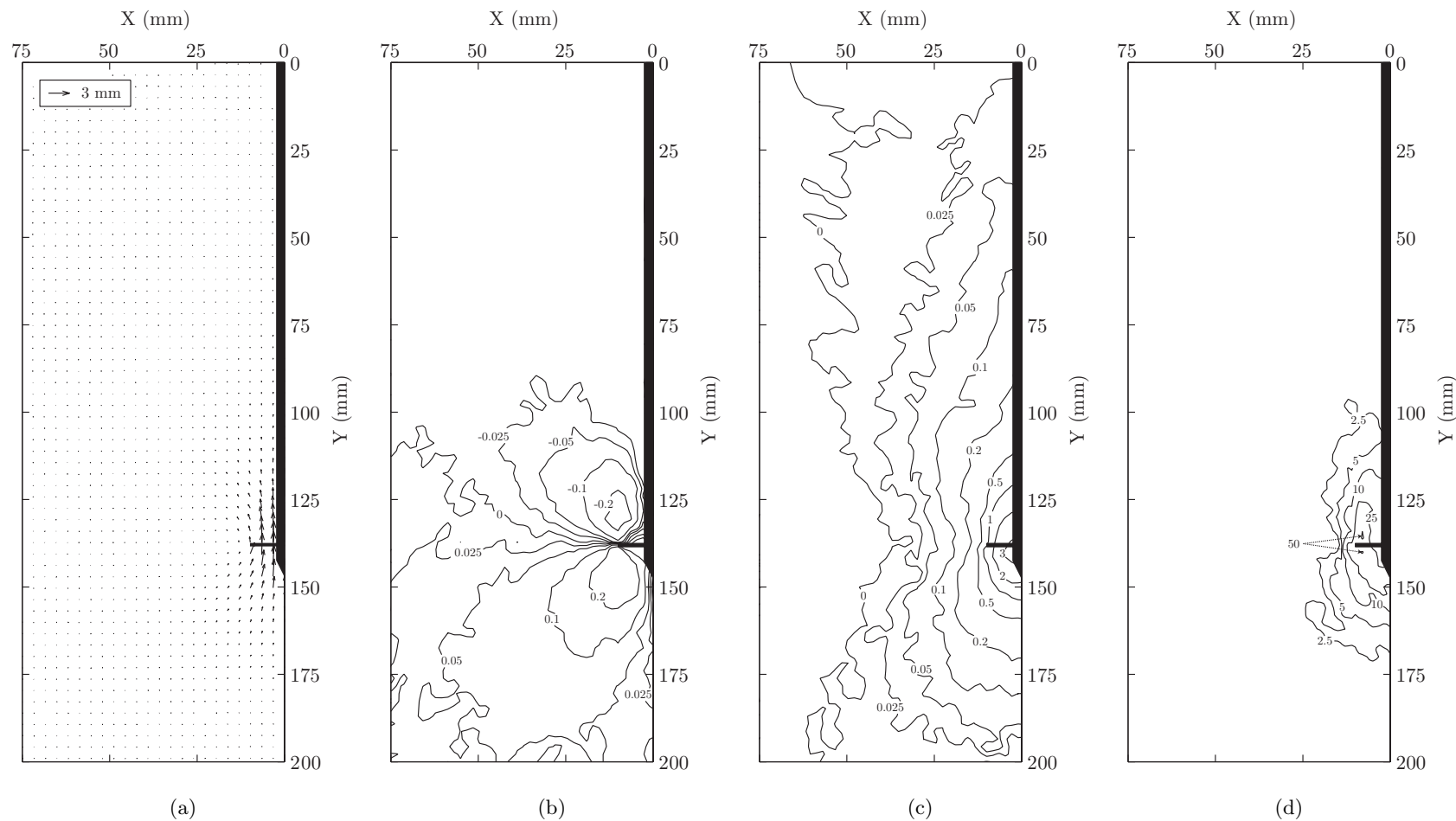


Figure 5.52: T1 cumulative PIV results at 3mm axial tensile displacement: vector (a), horizontal displacement (b), vertical displacement (c) and shear strain contours (d) with displacements in mm and shear strains expressed as a percentage.

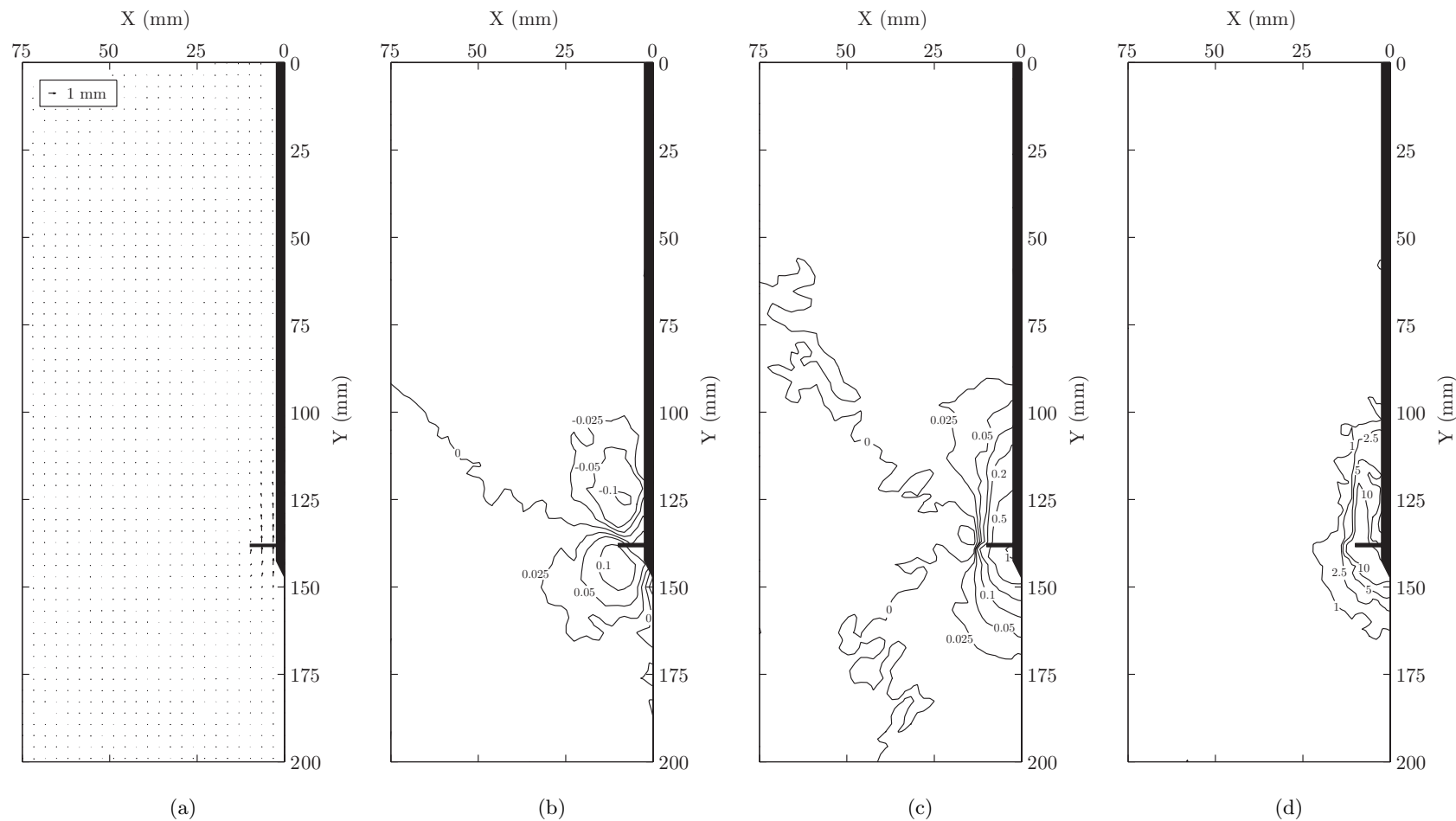


Figure 5.53: T1 incremental PIV results from 3mm to 4mm axial tensile displacement: vector (a), horizontal displacement (b), vertical displacement (c) and shear strain contours (d) with displacements in mm and shear strains expressed as a percentage.

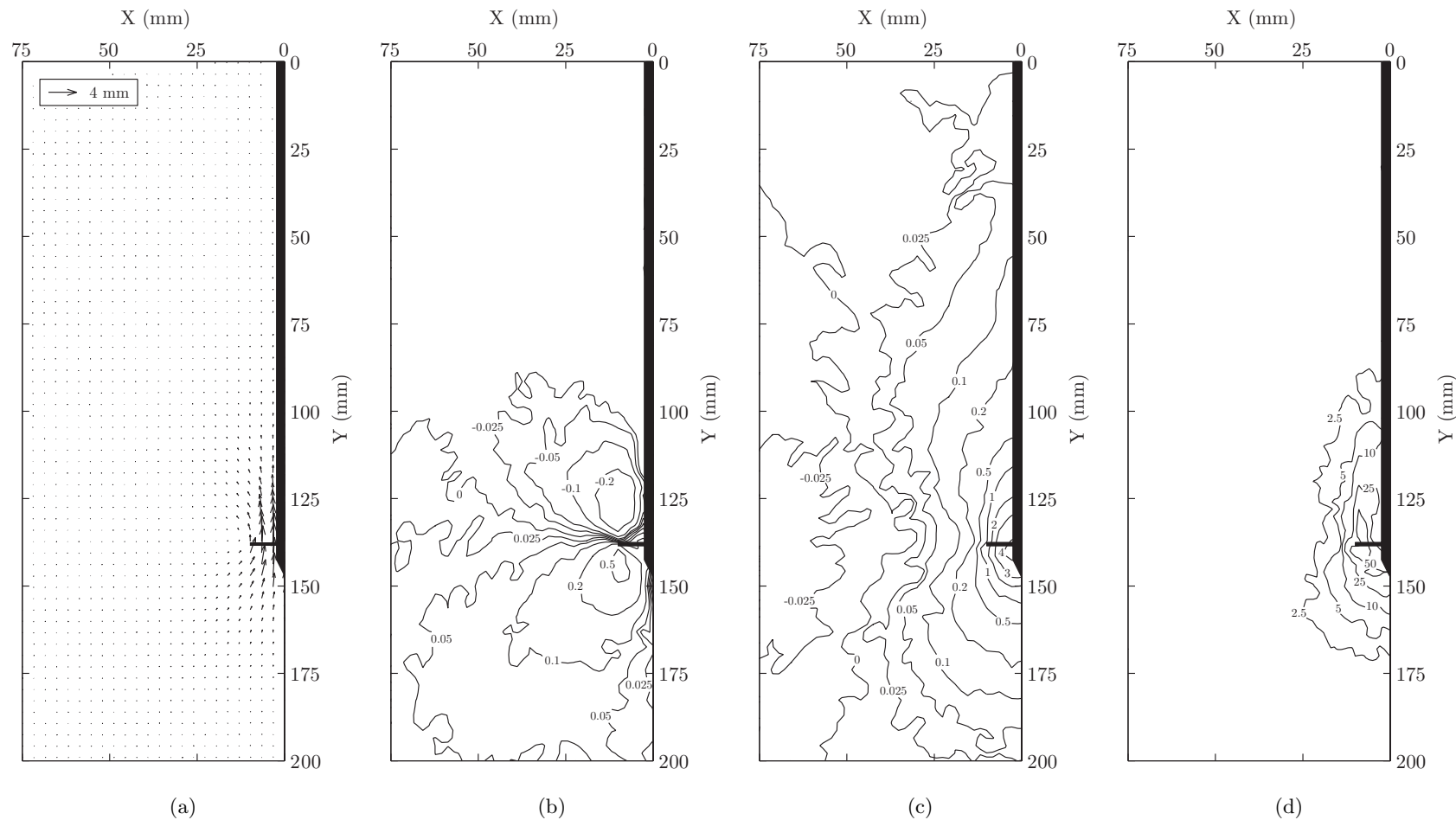


Figure 5.54: T1 cumulative PIV results at 4mm axial tensile displacement: vector (a), horizontal displacement (b), vertical displacement (c) and shear strain contours (d) with displacements in mm and shear strains expressed as a percentage.

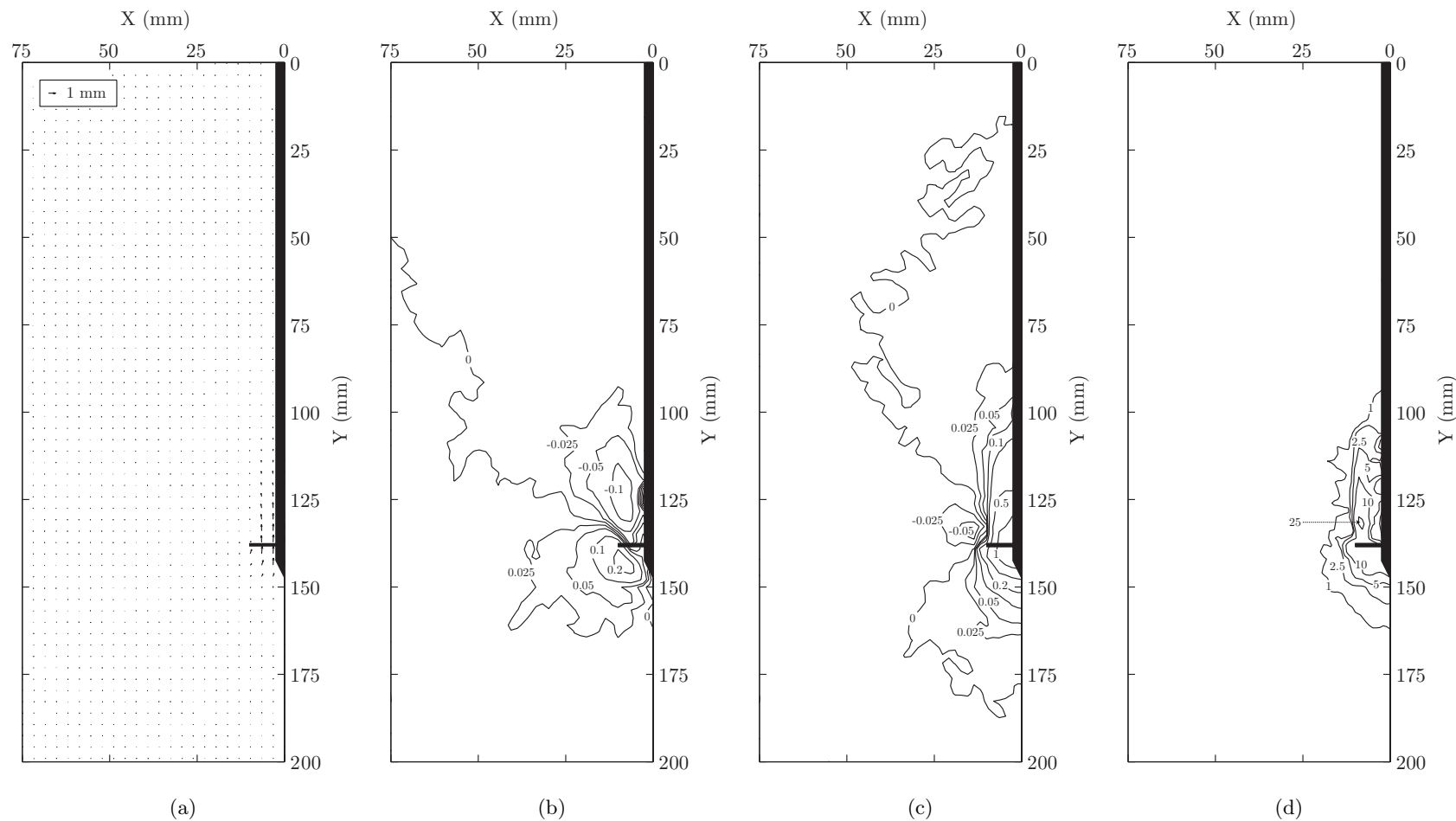


Figure 5.55: T1 incremental PIV results from 4mm to 5mm axial tensile displacement: vector (a), horizontal displacement (b), vertical displacement (c) and shear strain contours (d) with displacements in mm and shear strains expressed as a percentage.

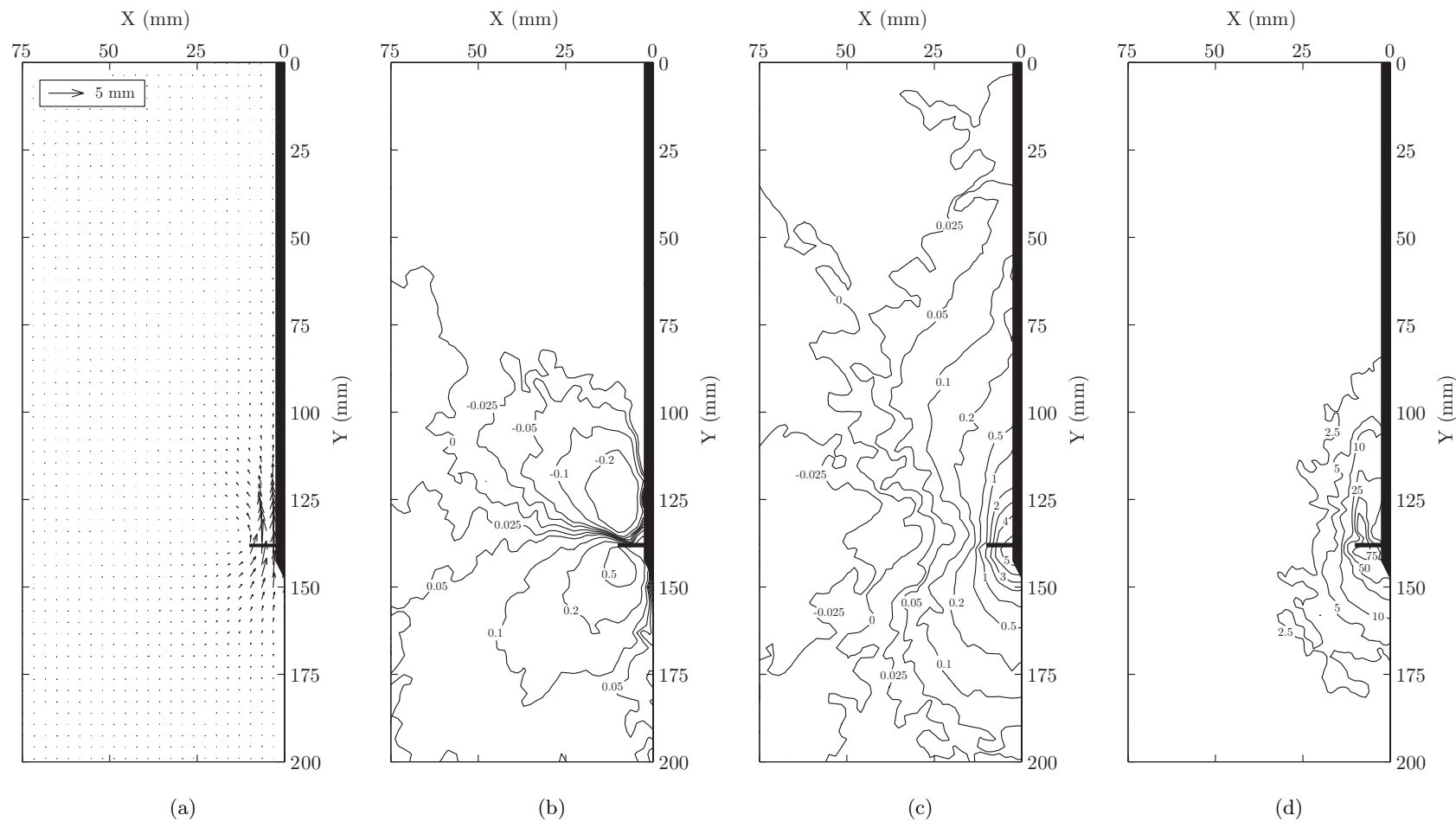


Figure 5.56: T1 cumulative PIV results at 5mm axial tensile displacement: vector (a), horizontal displacement (b), vertical displacement (c) and shear strain contours (d) with displacements in mm and shear strains expressed as a percentage.

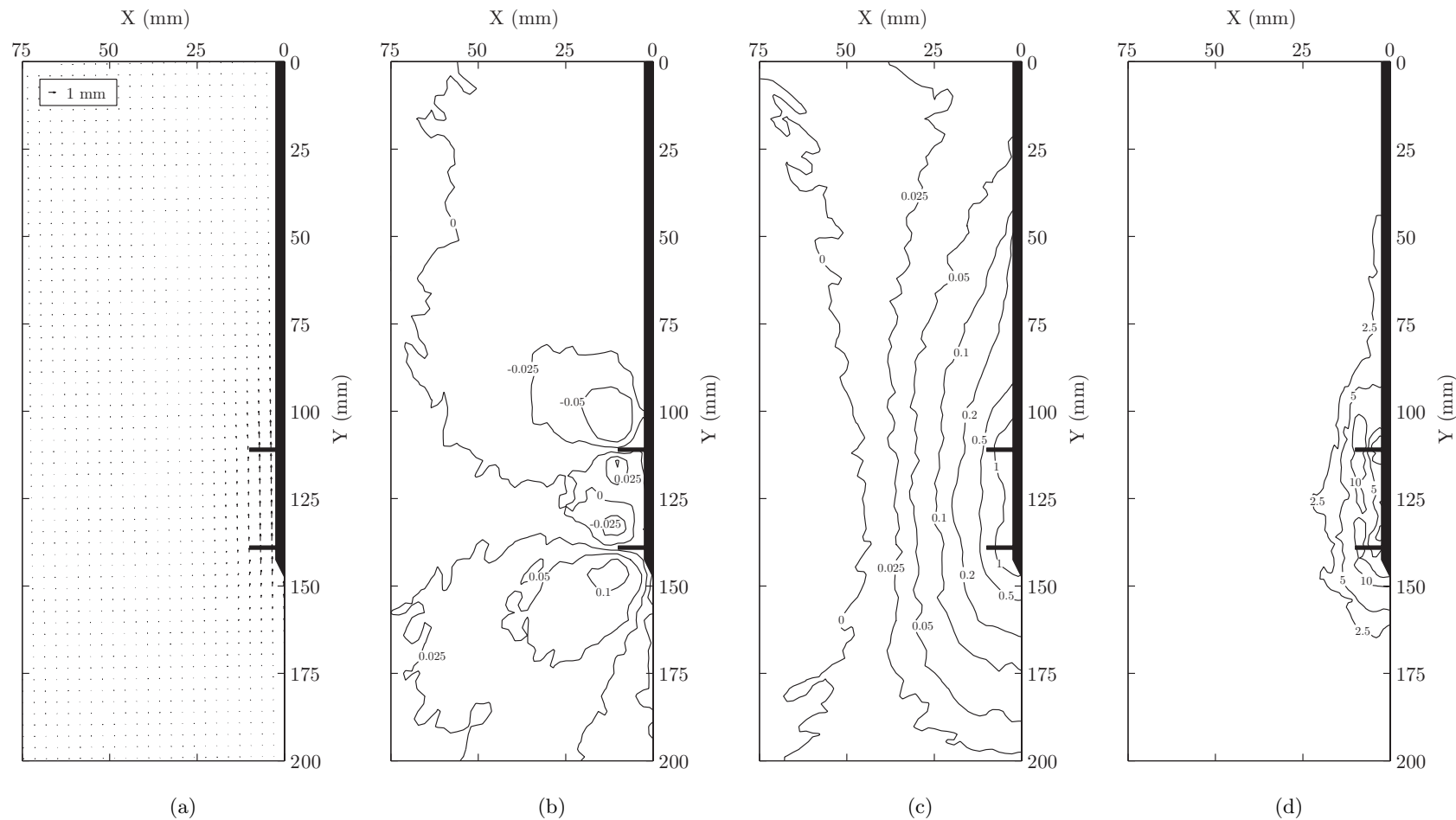


Figure 5.57: T2-30 cumulative PIV results at 1mm axial tensile displacement: vector (a), horizontal displacement (b), vertical displacement (c) and shear strain contours (d) with displacements in mm and shear strains expressed as a percentage.

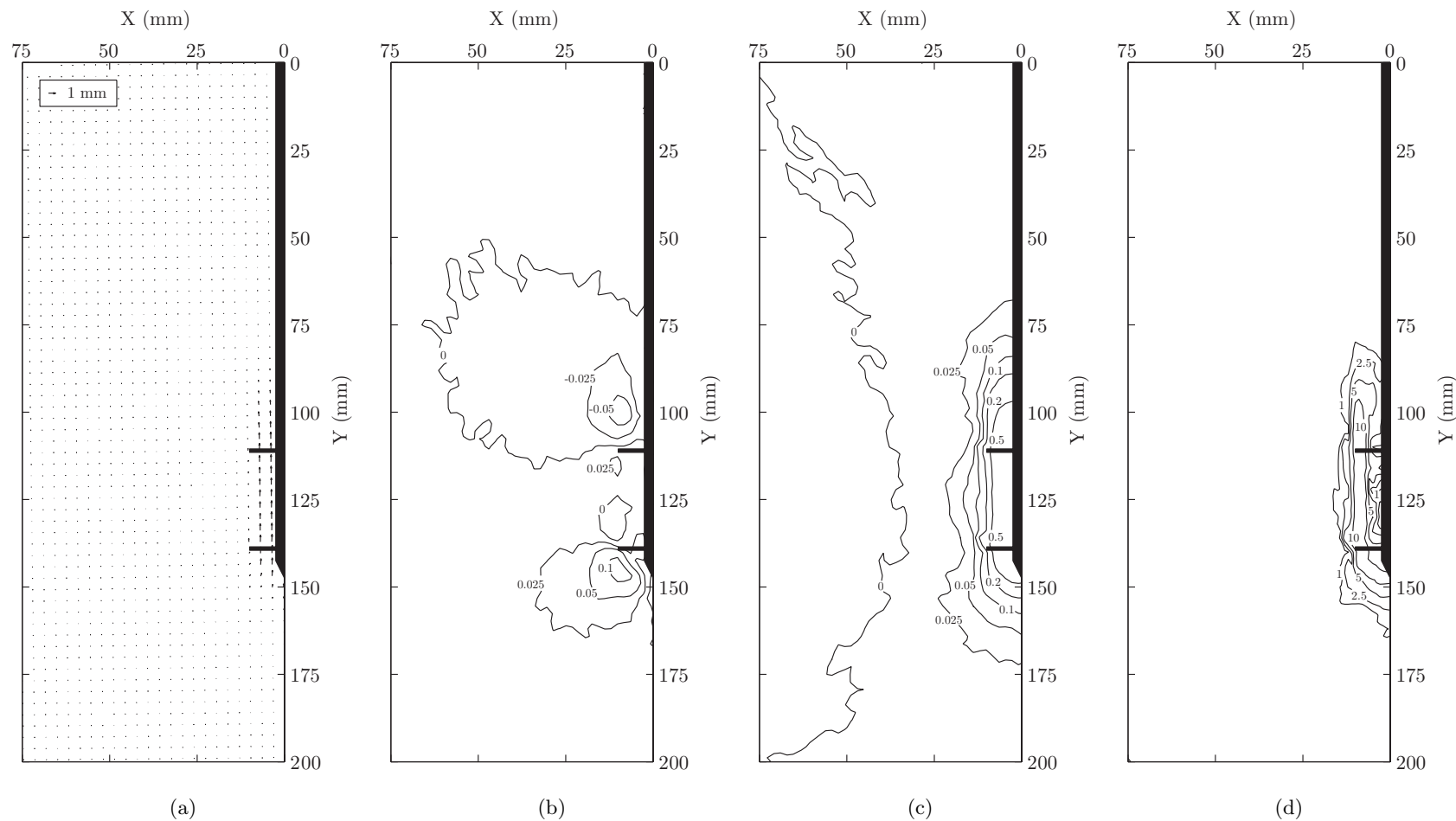


Figure 5.58: T2-30 incremental PIV results from 1mm to 2mm axial tensile displacement: vector (a), horizontal displacement (b), vertical displacement (c) and shear strain contours (d) with displacements in mm and shear strains expressed as a percentage.

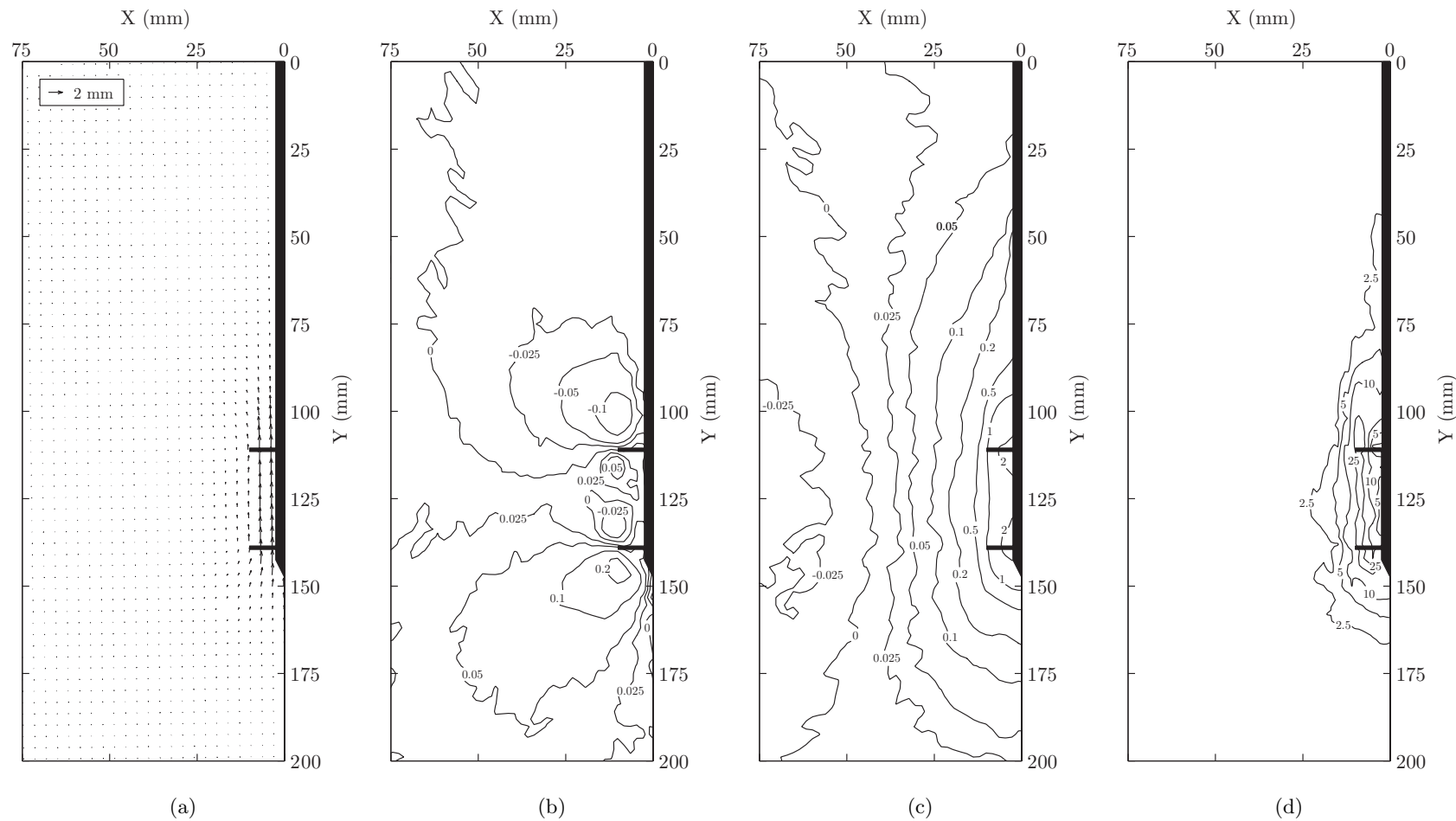


Figure 5.59: T2-30 cumulative PIV results at 2mm axial tensile displacement: vector (a), horizontal displacement (b), vertical displacement (c) and shear strain contours (d) with displacements in mm and shear strains expressed as a percentage.

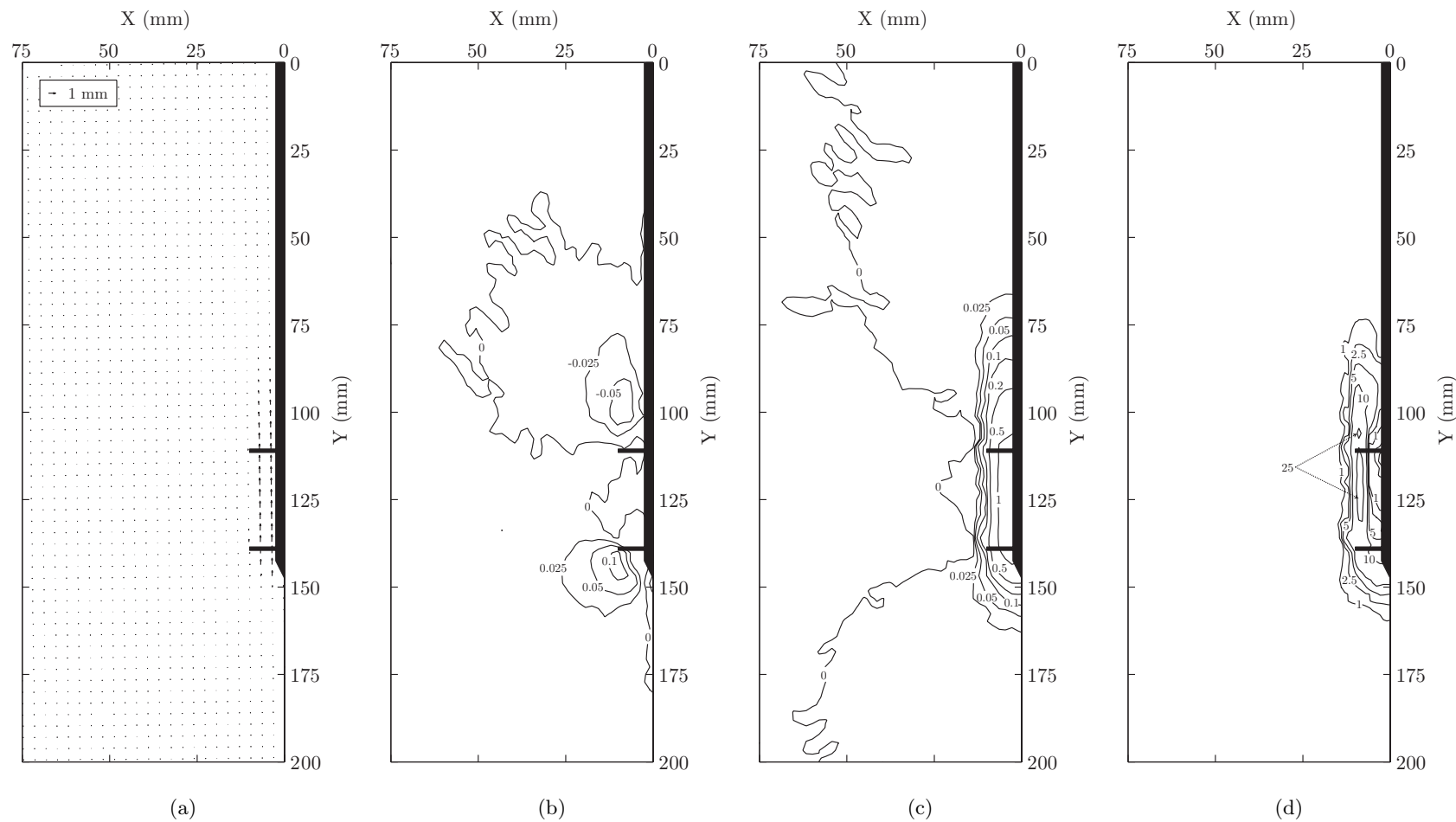


Figure 5.60: T2-30 incremental PIV results from 2mm to 3mm axial tensile displacement: vector (a), horizontal displacement (b), vertical displacement (c) and shear strain contours (d) with displacements in mm and shear strains expressed as a percentage.

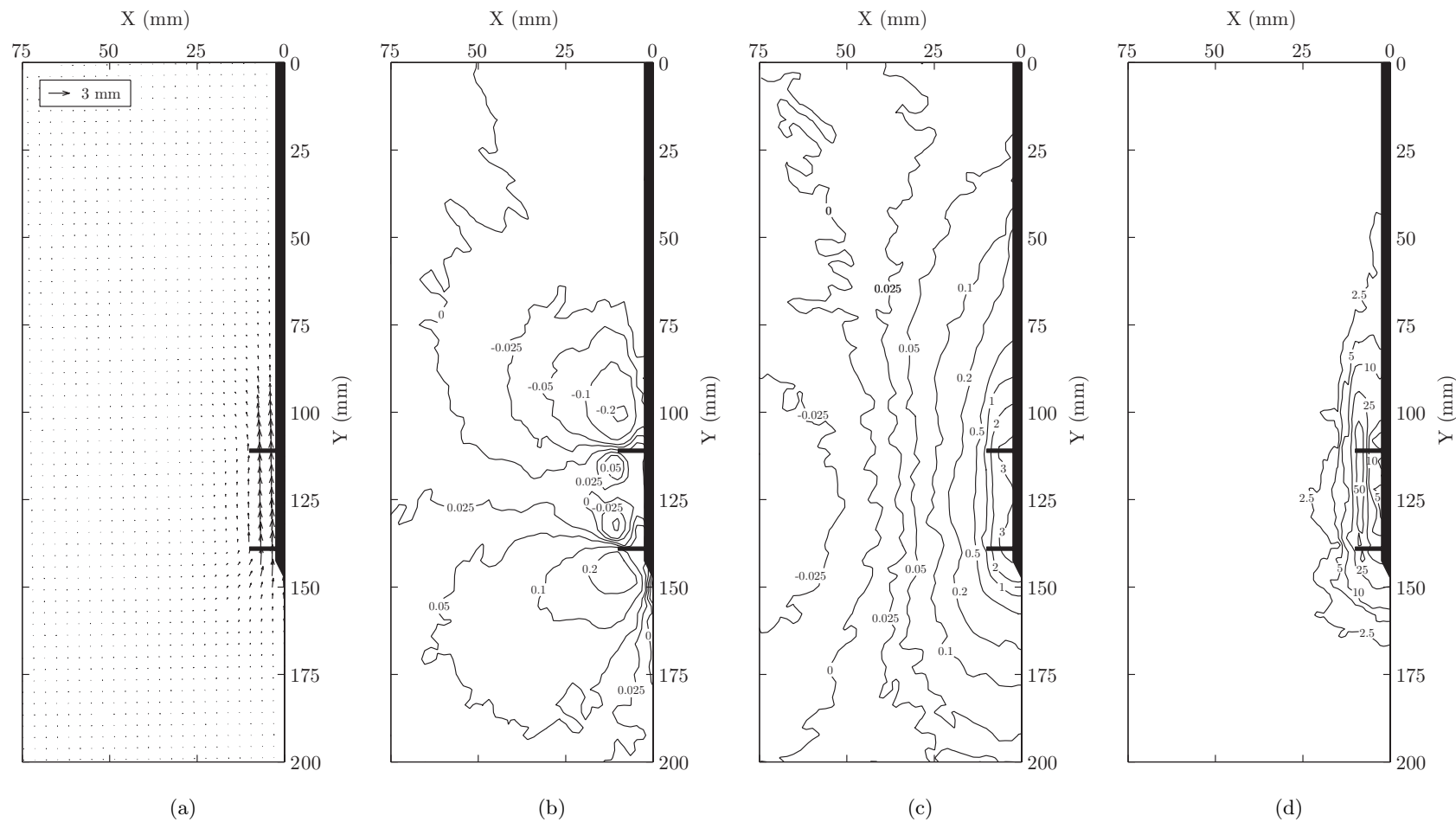


Figure 5.61: T2-30 cumulative PIV results at 3mm axial tensile displacement: vector (a), horizontal displacement (b), vertical displacement (c) and shear strain contours (d) with displacements in mm and shear strains expressed as a percentage.

250

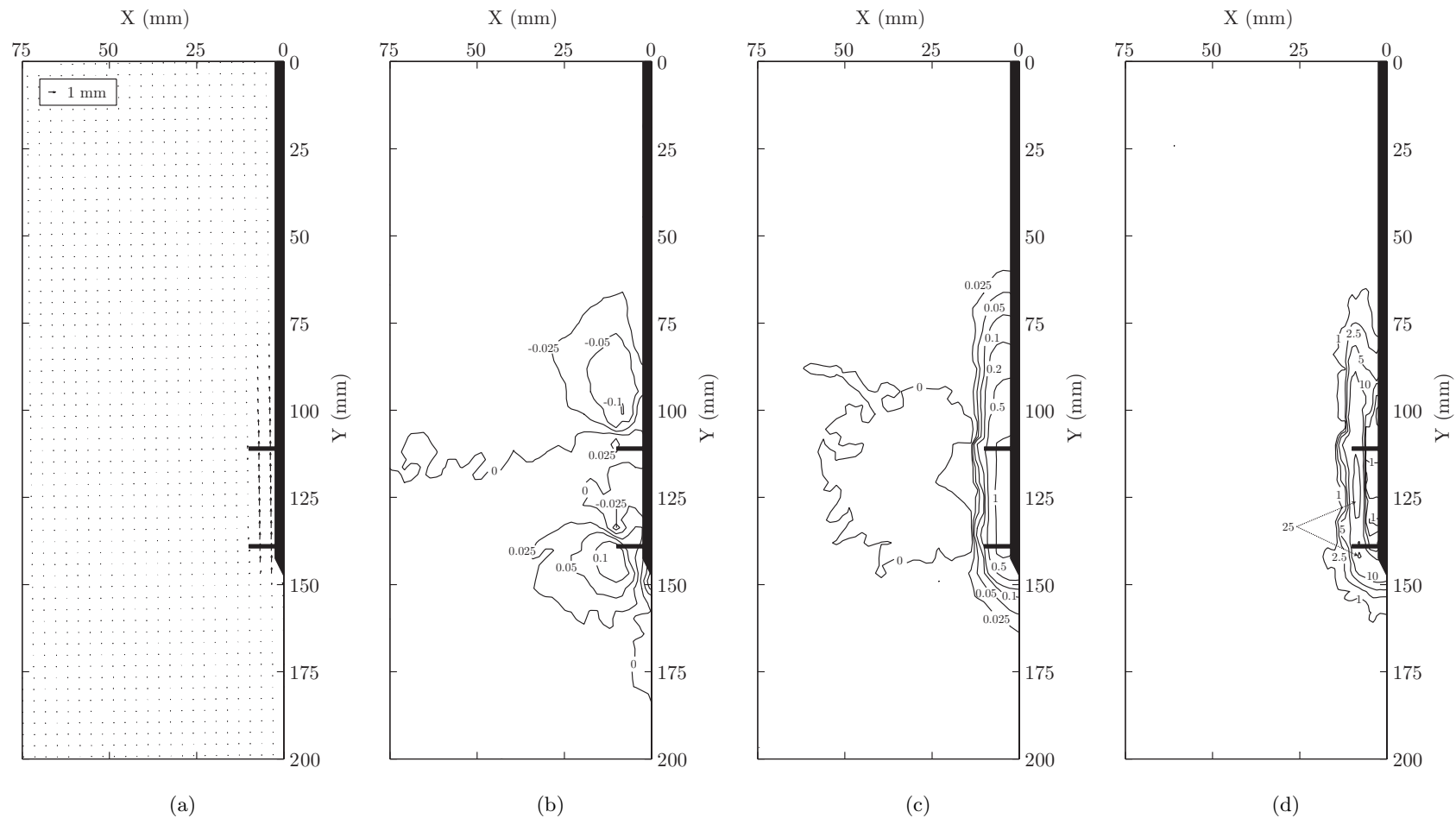


Figure 5.62: T2-30 incremental PIV results from 3mm to 4mm axial tensile displacement: vector (a), horizontal displacement (b), vertical displacement (c) and shear strain contours (d) with displacements in mm and shear strains expressed as a percentage.

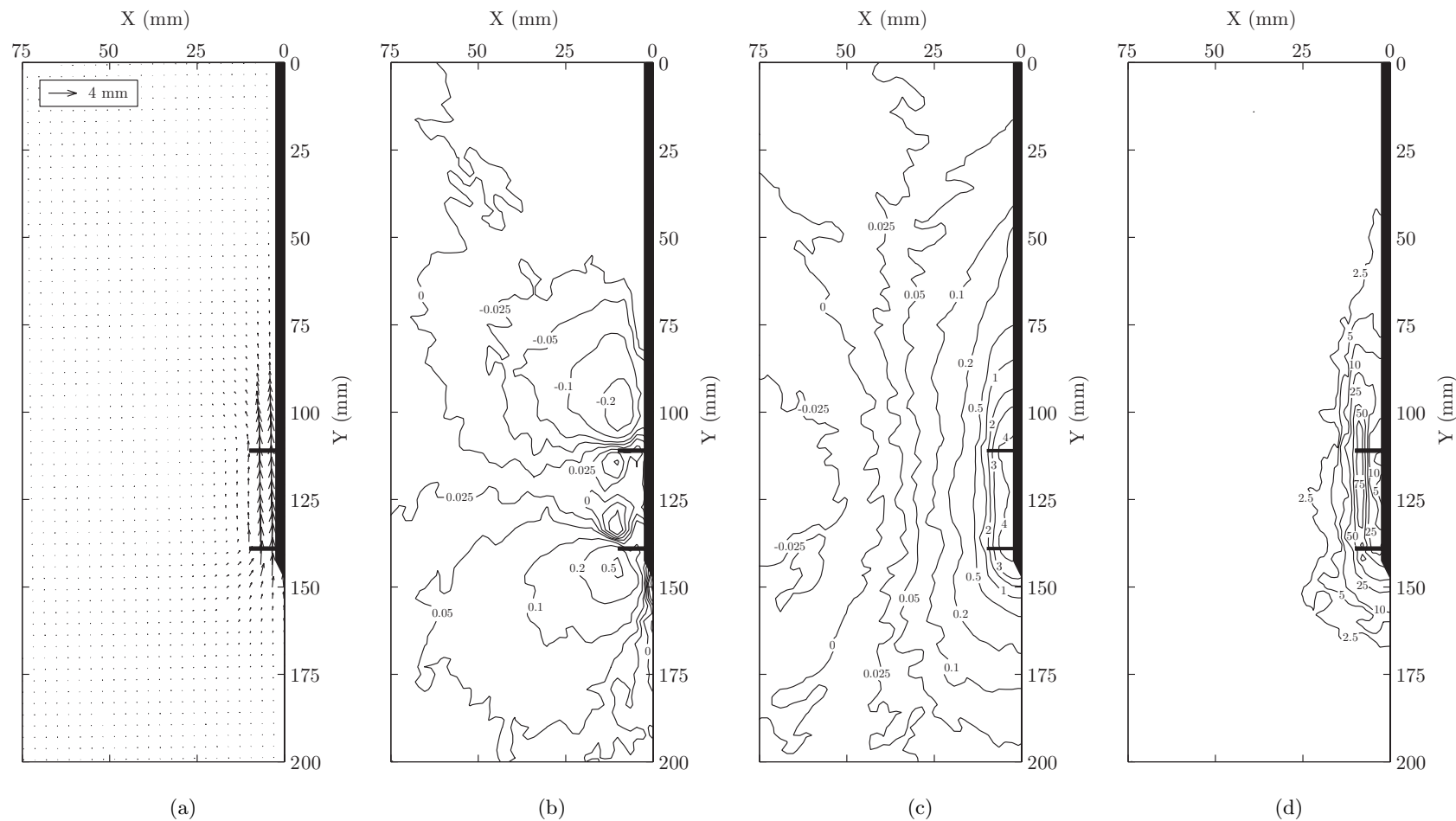


Figure 5.63: T2-30 cumulative PIV results at 4mm axial tensile displacement: vector (a), horizontal displacement (b), vertical displacement (c) and shear strain contours (d) with displacements in mm and shear strains expressed as a percentage.

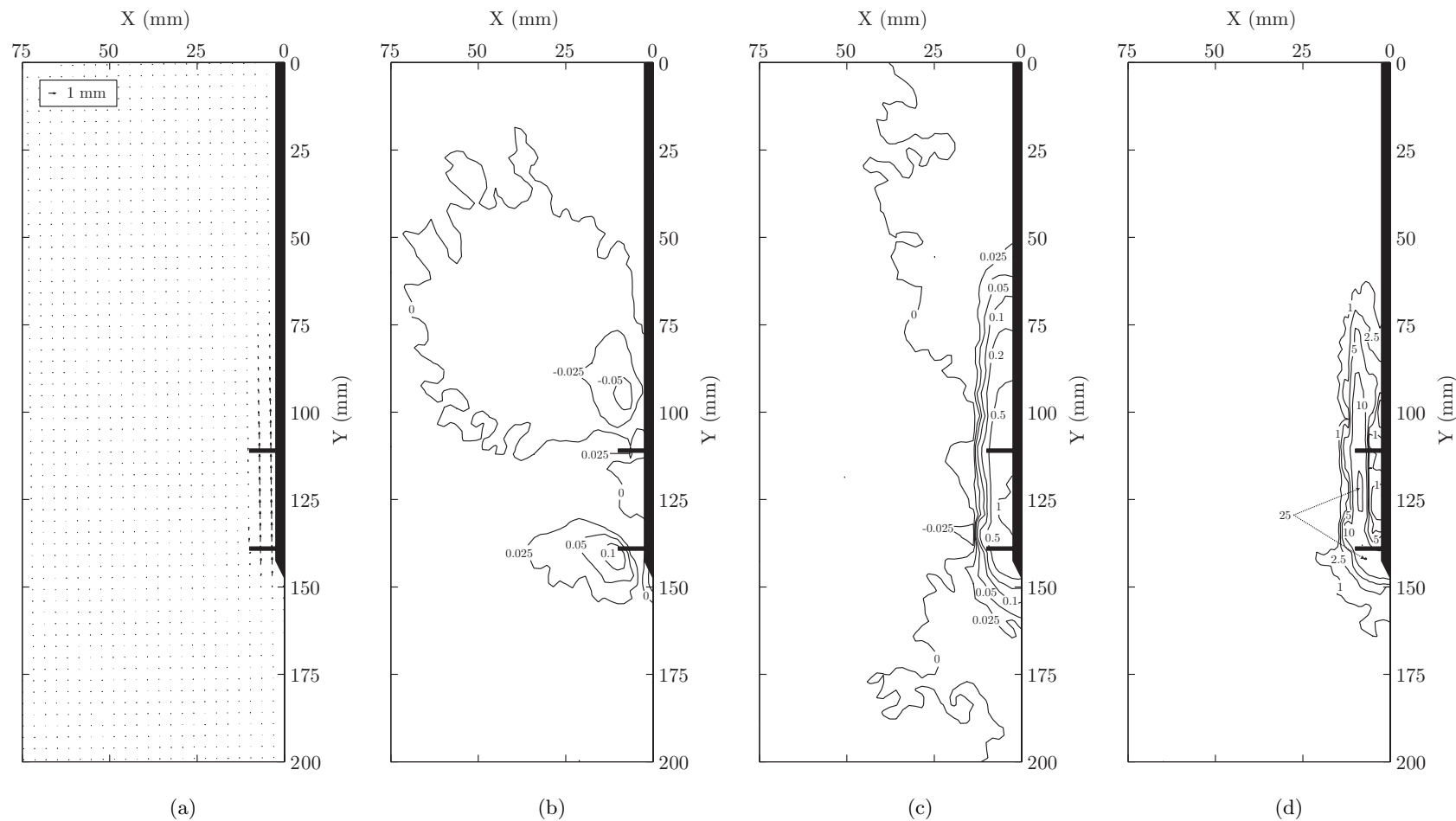


Figure 5.64: T2-30 incremental PIV results from 4mm to 5mm axial tensile displacement: vector (a), horizontal displacement (b), vertical displacement (c) and shear strain contours (d) with displacements in mm and shear strains expressed as a percentage.

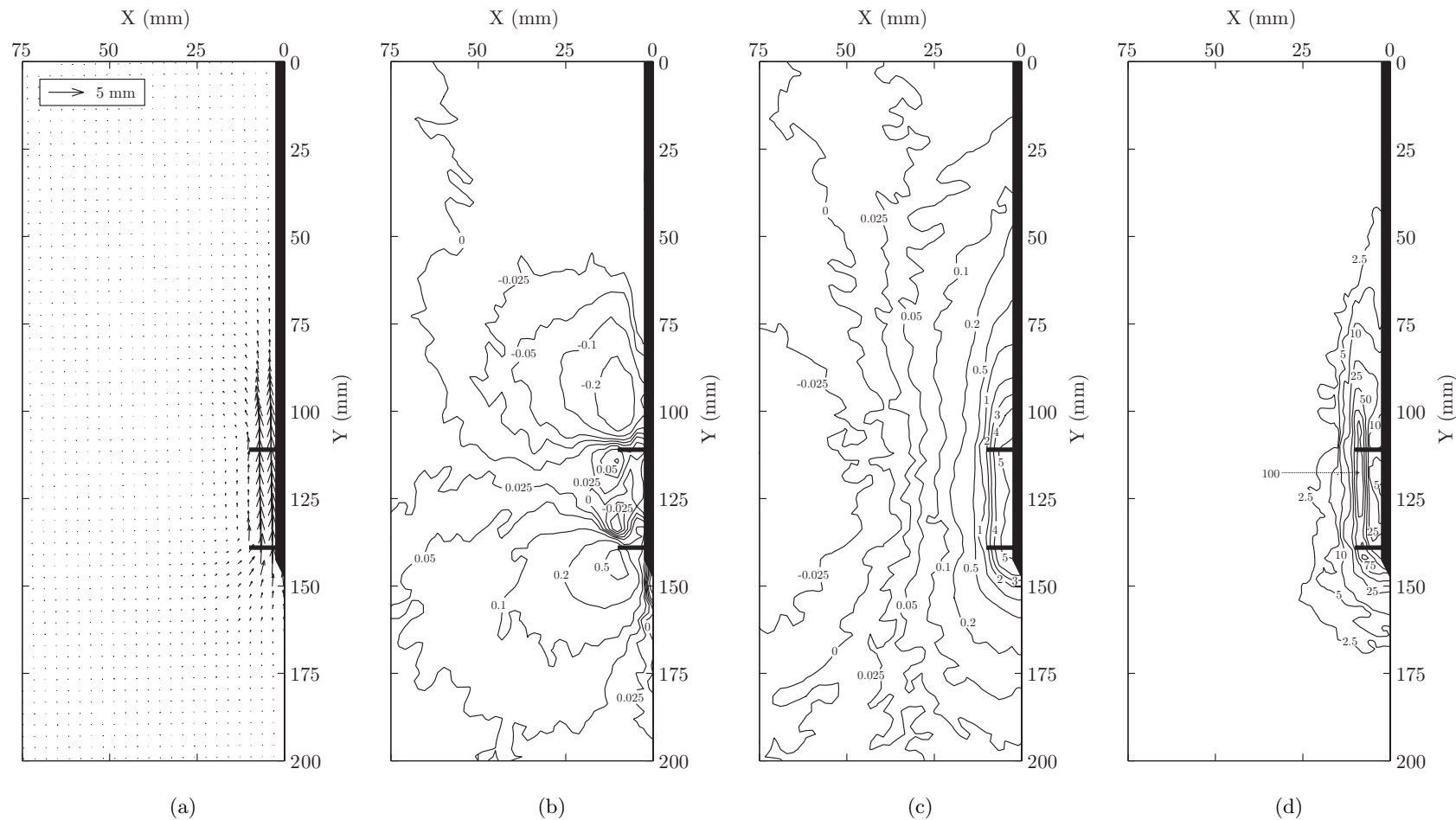


Figure 5.65: T2-30 cumulative PIV results at 5mm axial tensile displacement: vector (a), horizontal displacement (b), vertical displacement (c) and shear strain contours (d) with displacements in mm and shear strains expressed as a percentage.

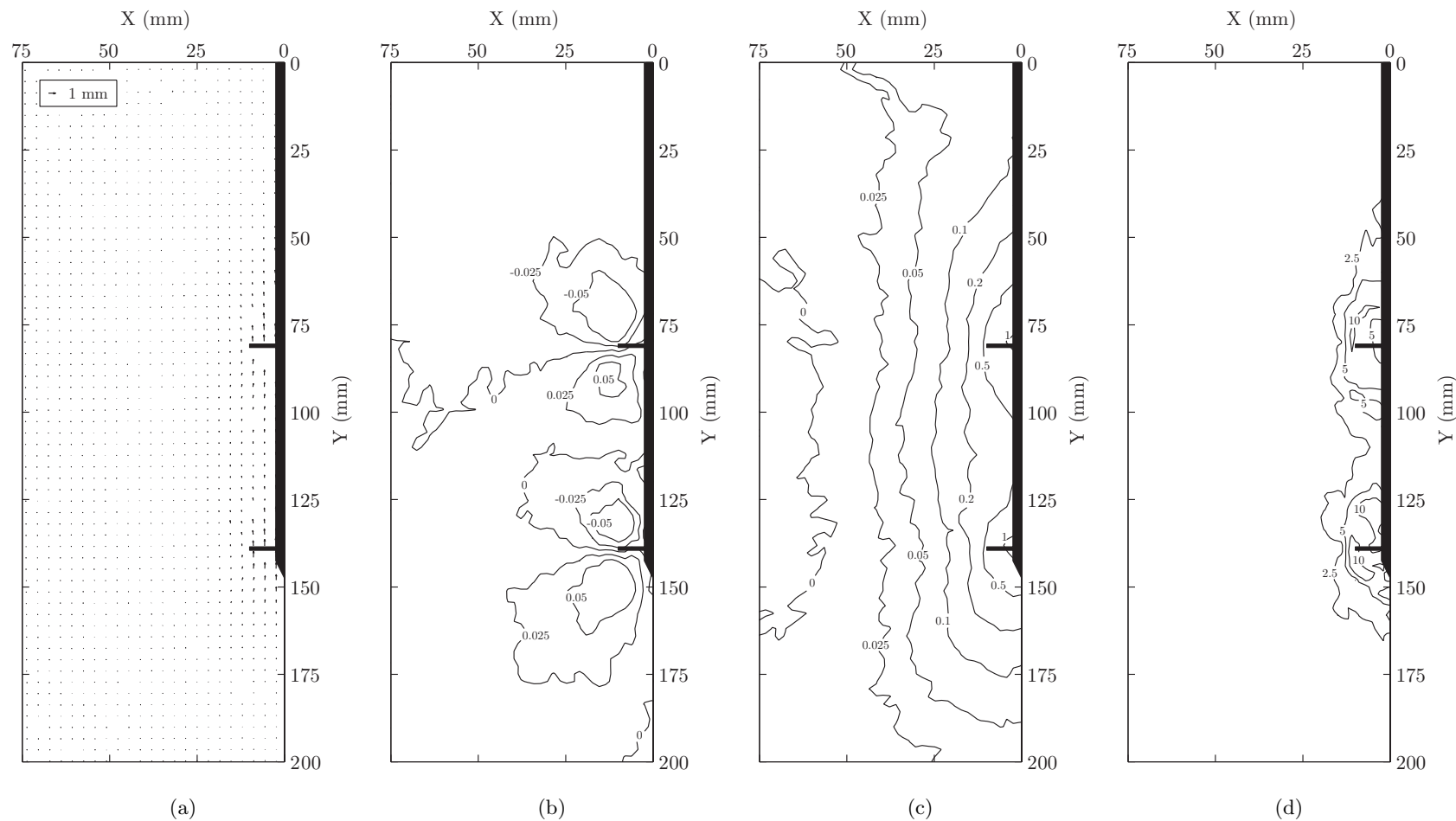


Figure 5.66: T2-60 cumulative PIV results at 1mm axial tensile displacement: vector (a), horizontal displacement (b), vertical displacement (c) and shear strain contours (d) with displacements in mm and shear strains expressed as a percentage.

255

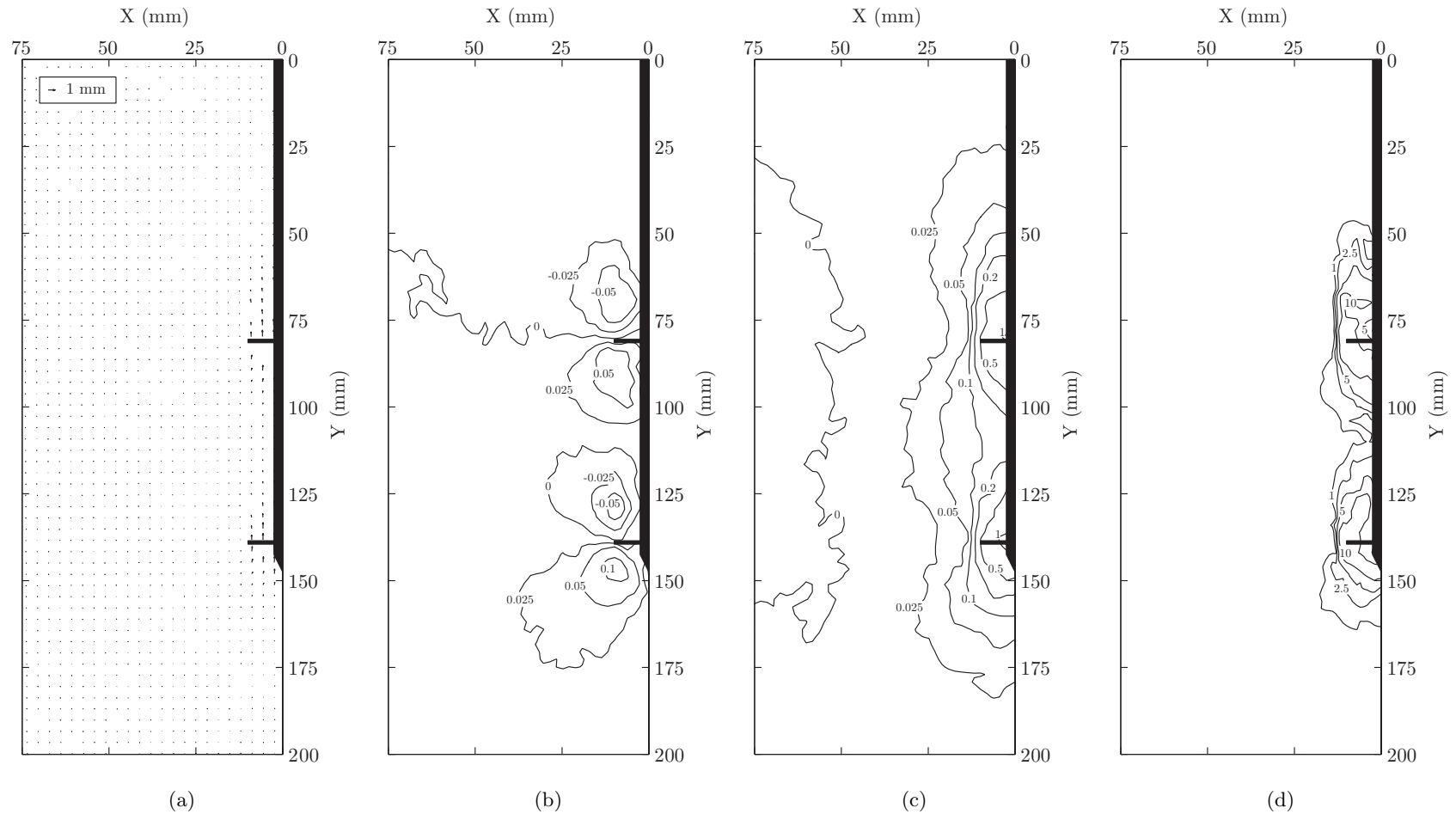


Figure 5.67: T2-60 incremental PIV results from 1mm to 2mm axial tensile displacement: vector (a), horizontal displacement (b), vertical displacement (c) and shear strain contours (d) with displacements in mm and shear strains expressed as a percentage.

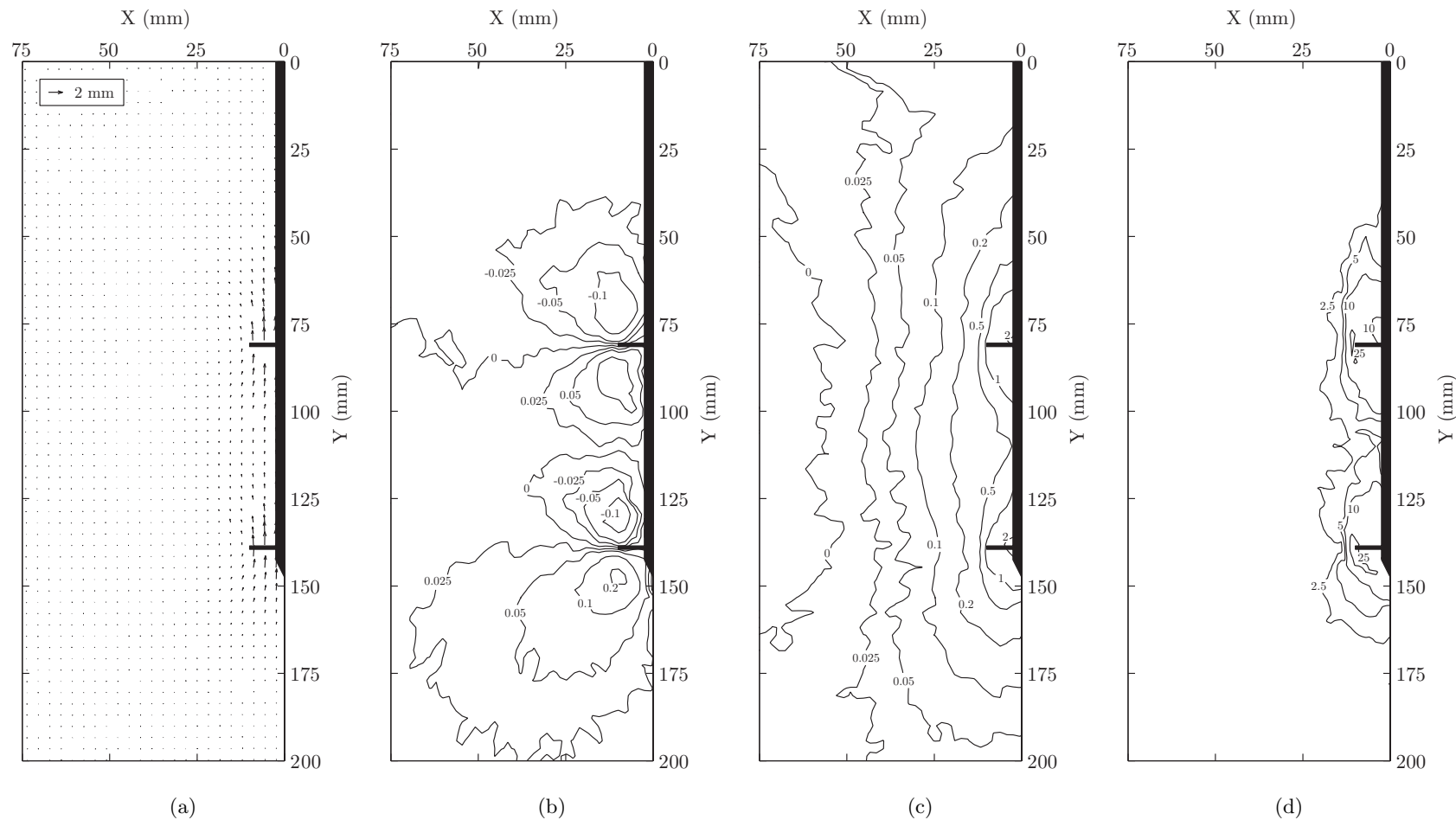


Figure 5.68: T2-60 cumulative PIV results at 2mm axial tensile displacement: vector (a), horizontal displacement (b), vertical displacement (c) and shear strain contours (d) with displacements in mm and shear strains expressed as a percentage.

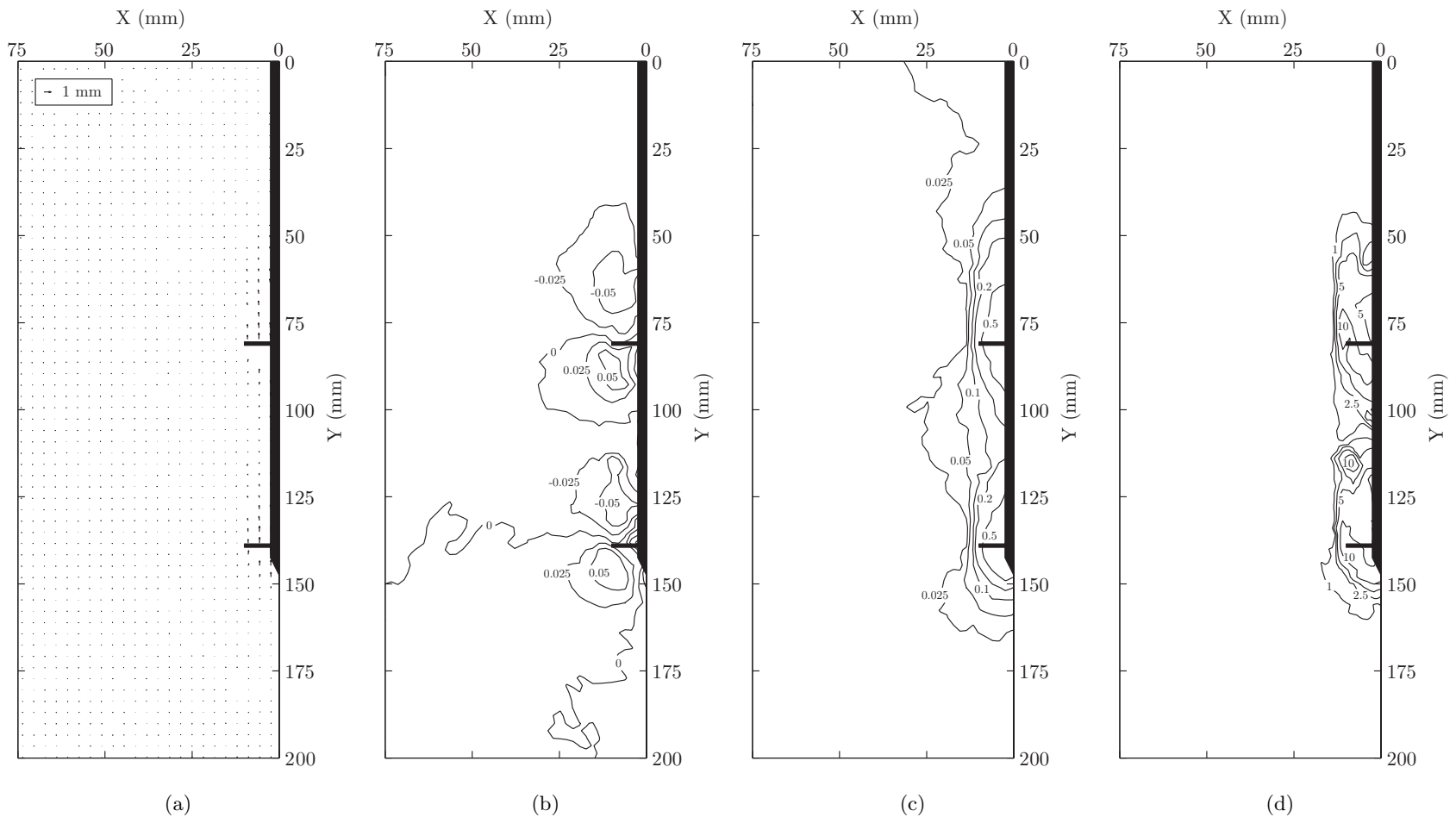


Figure 5.69: T2-60 incremental PIV results from 2mm to 3mm axial tensile displacement: vector (a), horizontal displacement (b), vertical displacement (c) and shear strain contours (d) with displacements in mm and shear strains expressed as a percentage.

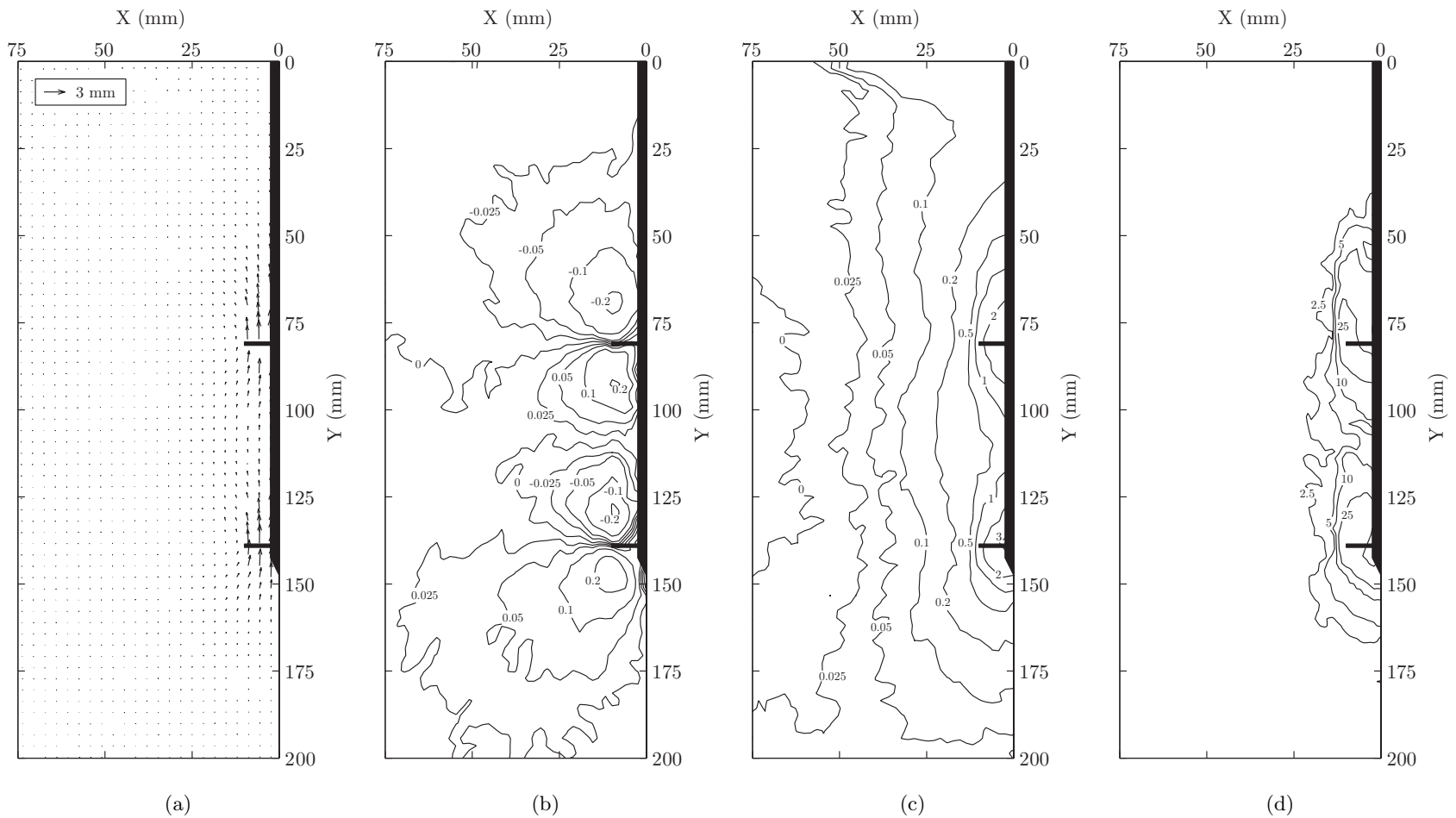


Figure 5.70: T2-60 cumulative PIV results at 3mm axial tensile displacement: vector (a), horizontal displacement (b), vertical displacement (c) and shear strain contours (d) with displacements in mm and shear strains expressed as a percentage.

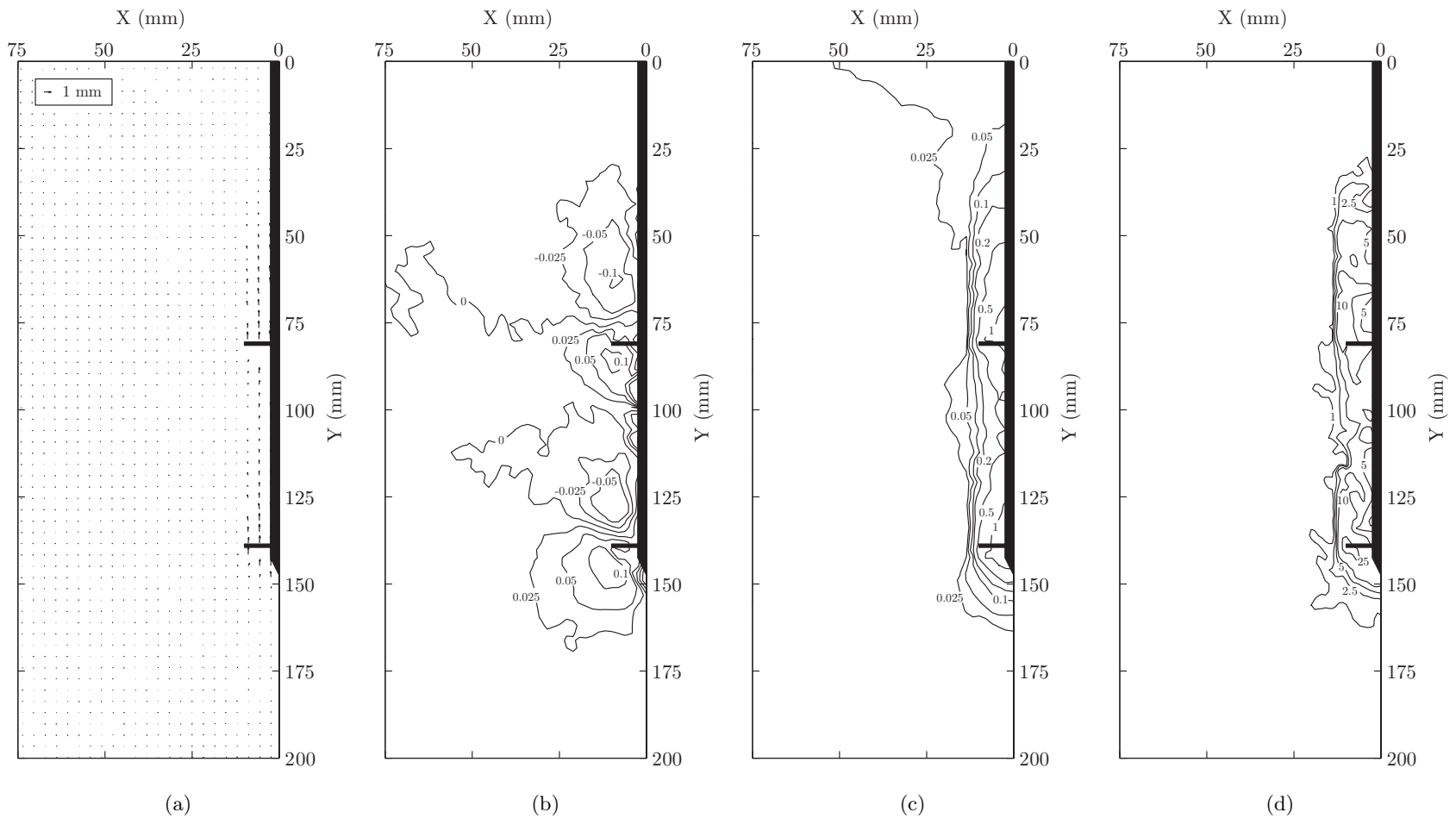


Figure 5.71: T2-60 incremental PIV results from 3mm to 4mm axial tensile displacement: vector (a), horizontal displacement (b), vertical displacement (c) and shear strain contours (d) with displacements in mm and shear strains expressed as a percentage.

260

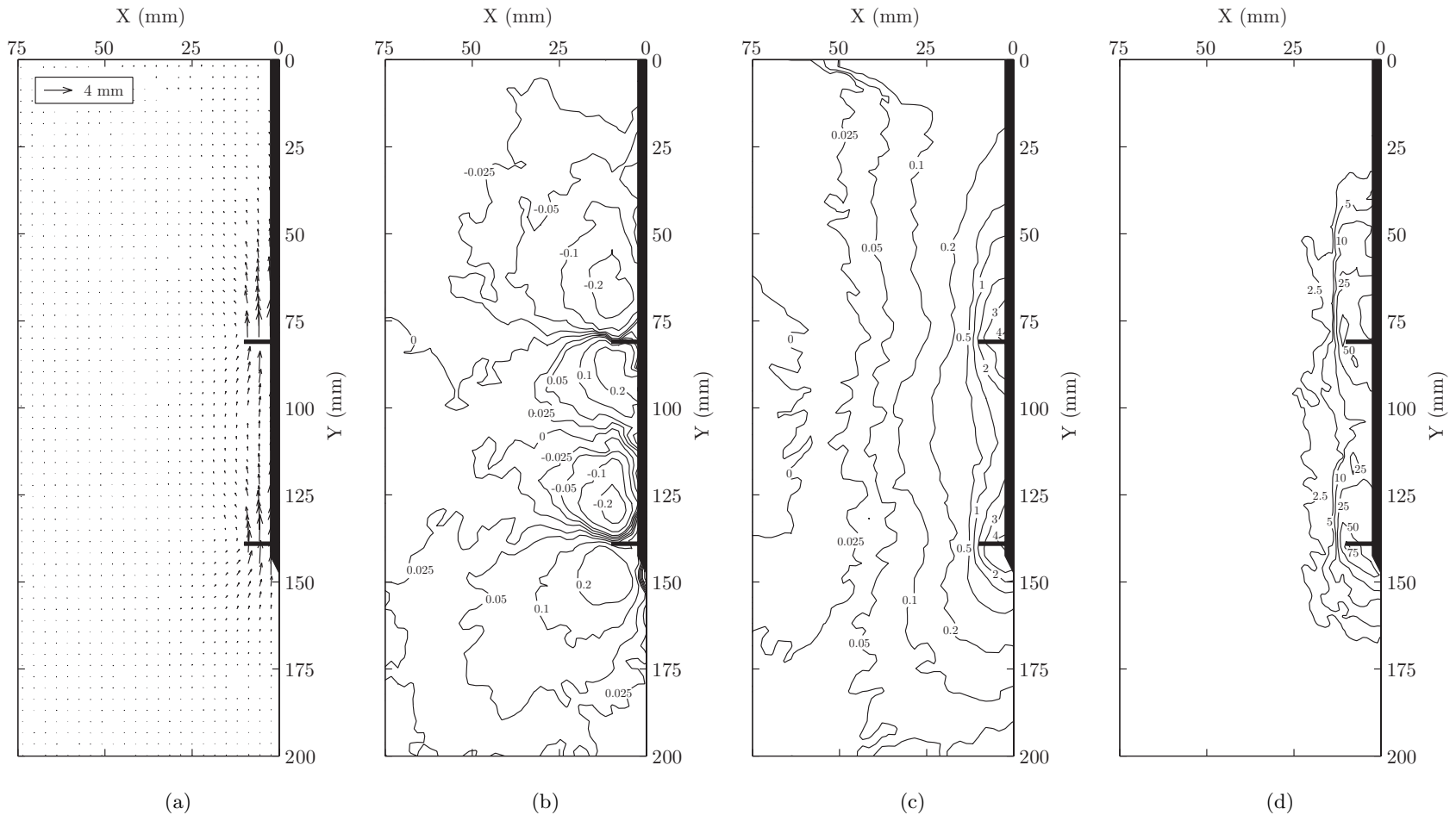


Figure 5.72: T2-60 cumulative PIV results at 4mm axial tensile displacement: vector (a), horizontal displacement (b), vertical displacement (c) and shear strain contours (d) with displacements in mm and shear strains expressed as a percentage.

261

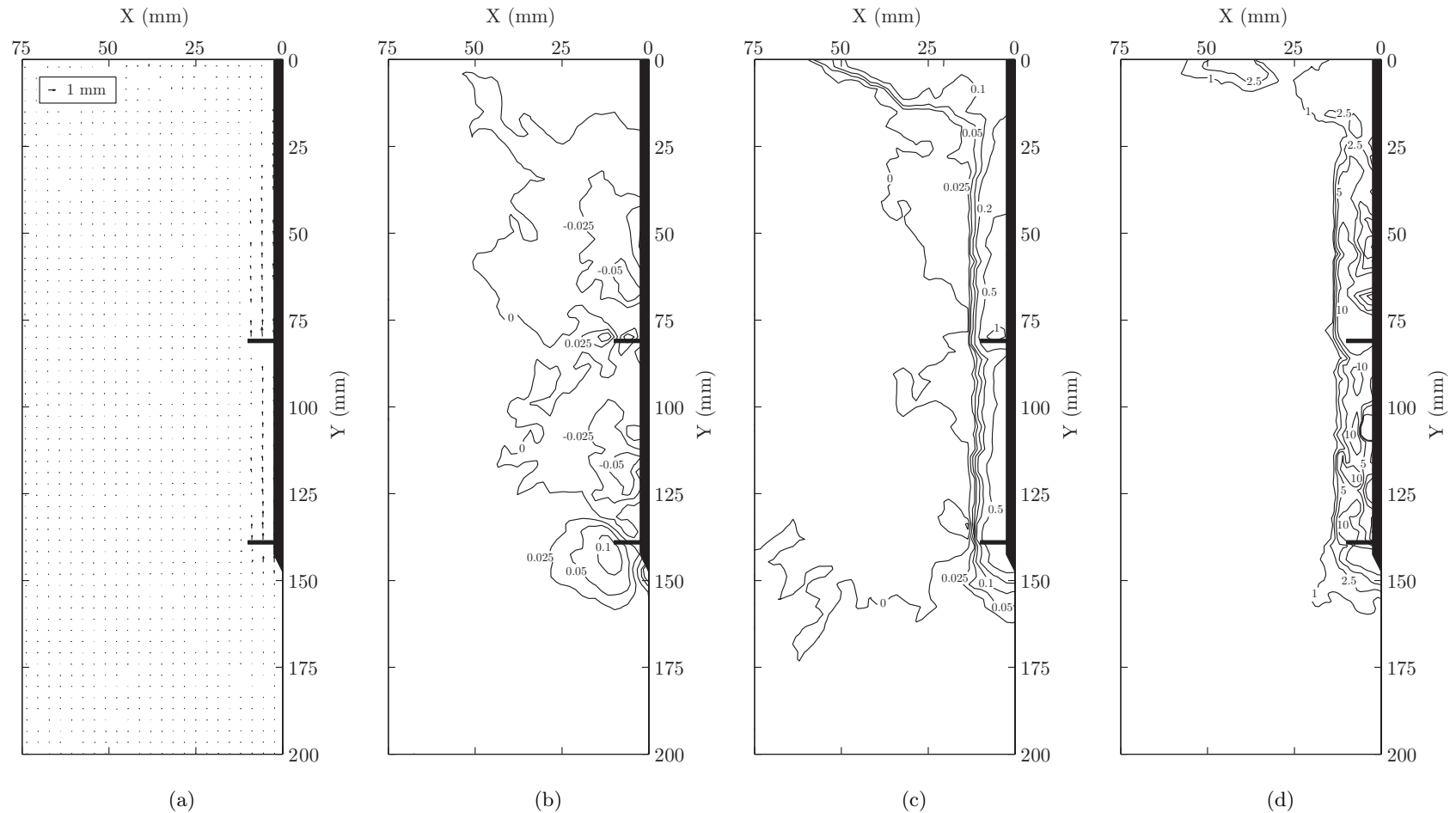


Figure 5.73: T2-60 incremental PIV results from 4mm to 5mm axial tensile displacement: vector (a), horizontal displacement (b), vertical displacement (c) and shear strain contours (d) with displacements in mm and shear strains expressed as a percentage.

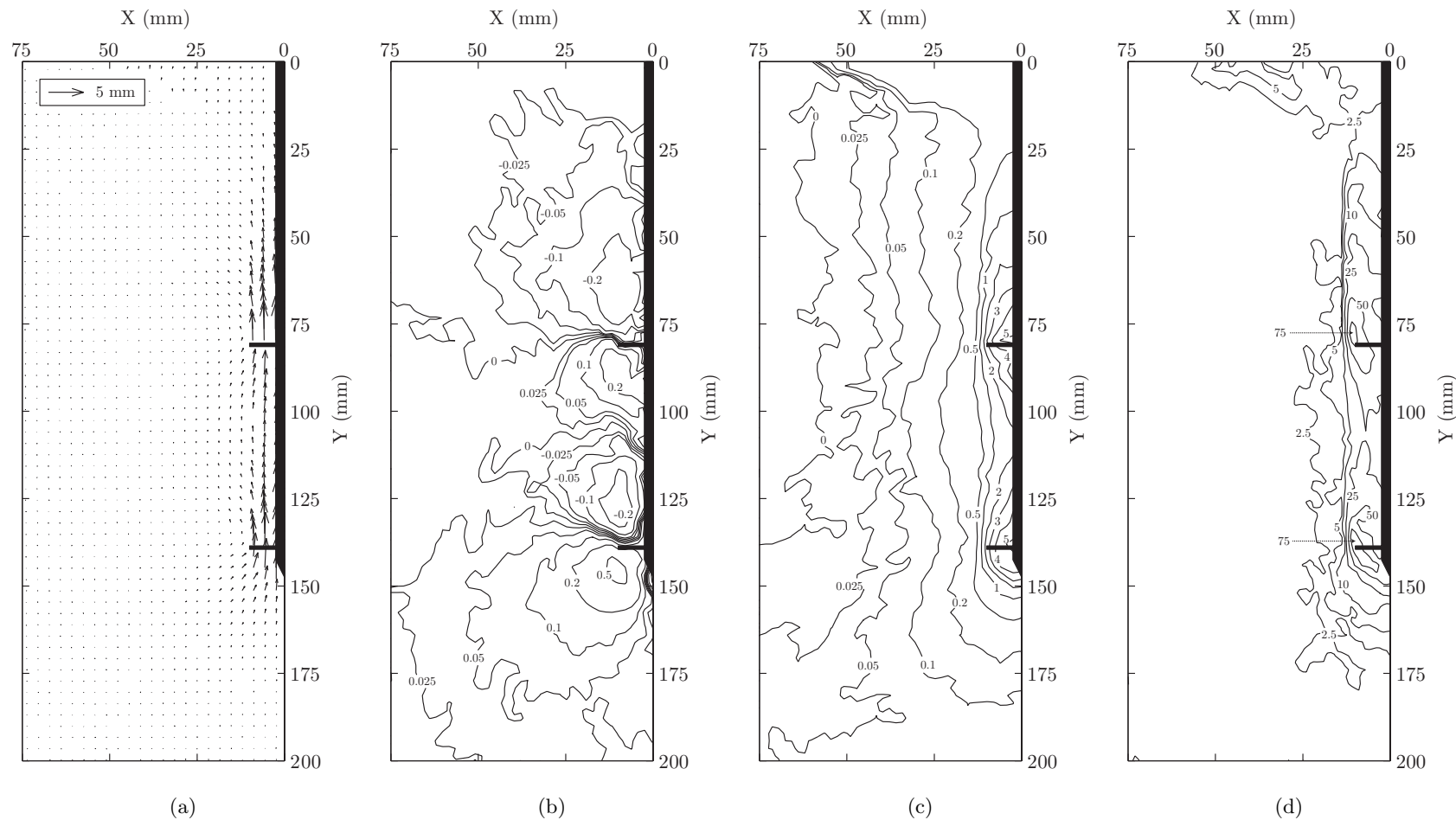


Figure 5.74: T2-60 cumulative PIV results at 5mm axial tensile displacement: vector (a), horizontal displacement (b), vertical displacement (c) and shear strain contours (d) with displacements in mm and shear strains expressed as a percentage.

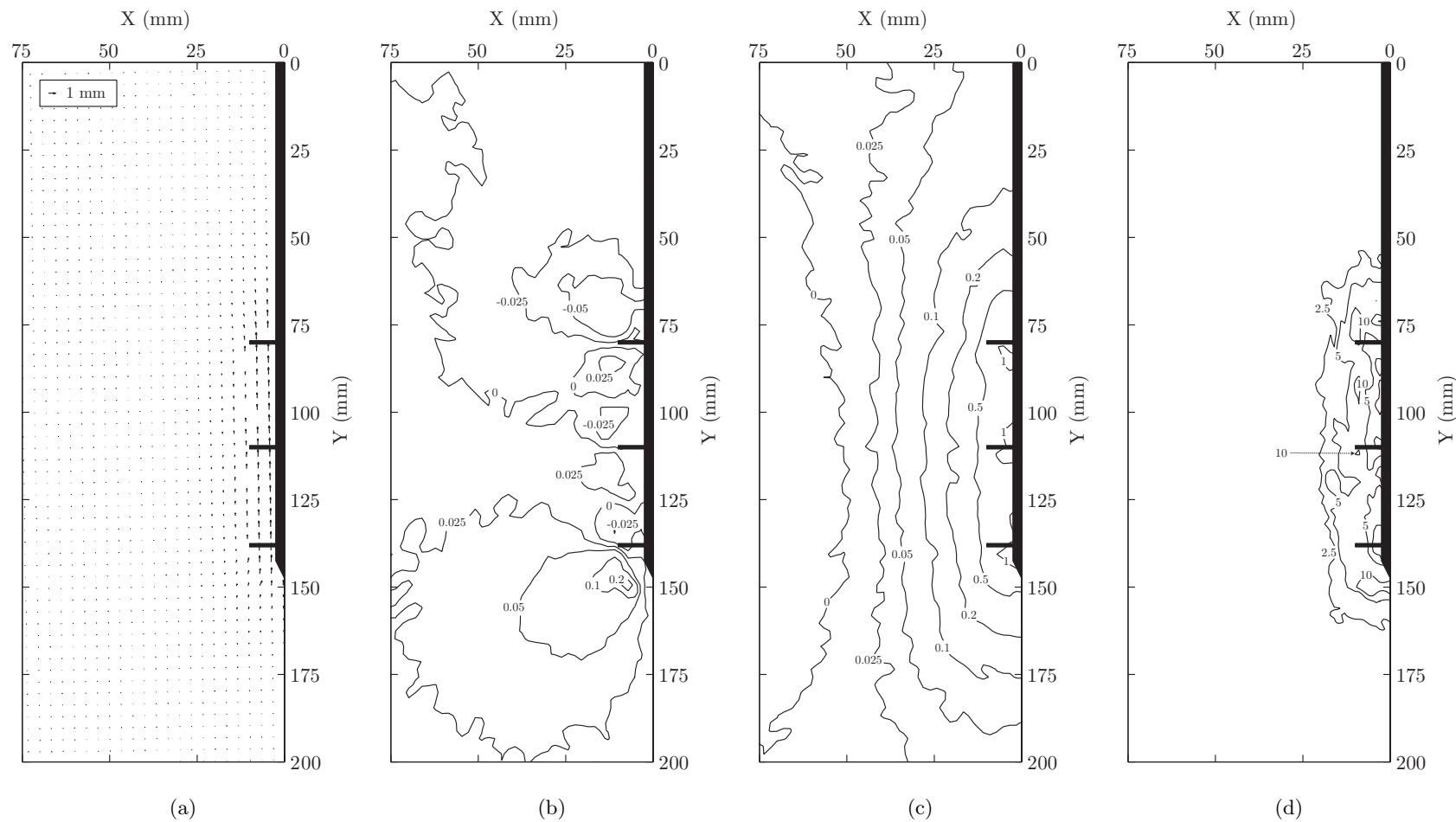


Figure 5.75: T3 cumulative PIV results at 1mm axial tensile displacement: vector (a), horizontal displacement (b), vertical displacement (c) and shear strain contours (d) with displacements in mm and shear strains expressed as a percentage.

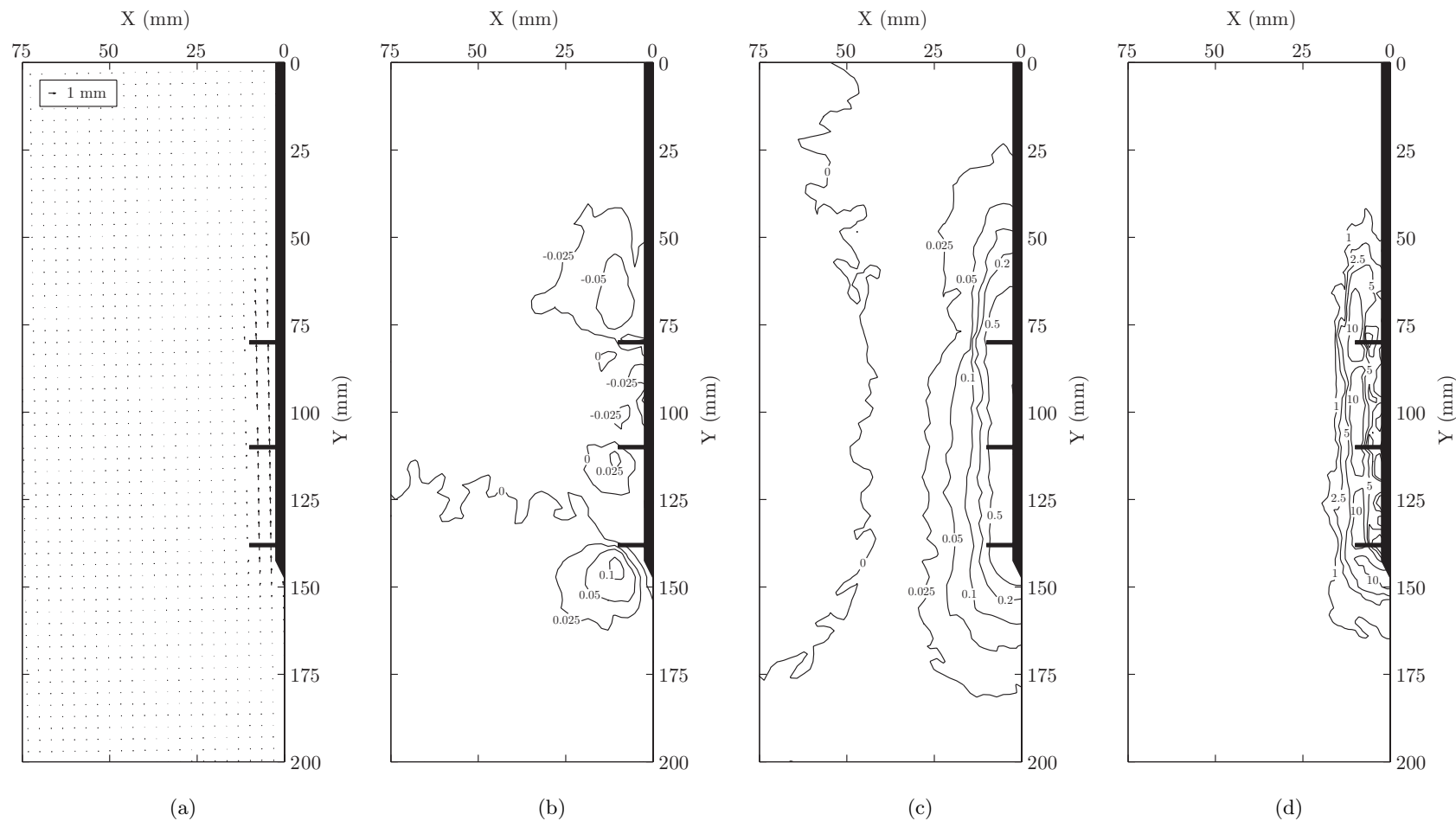


Figure 5.76: T3 incremental PIV results from 1mm to 2mm axial tensile displacement: vector (a), horizontal displacement (b), vertical displacement (c) and shear strain contours (d) with displacements in mm and shear strains expressed as a percentage.

265

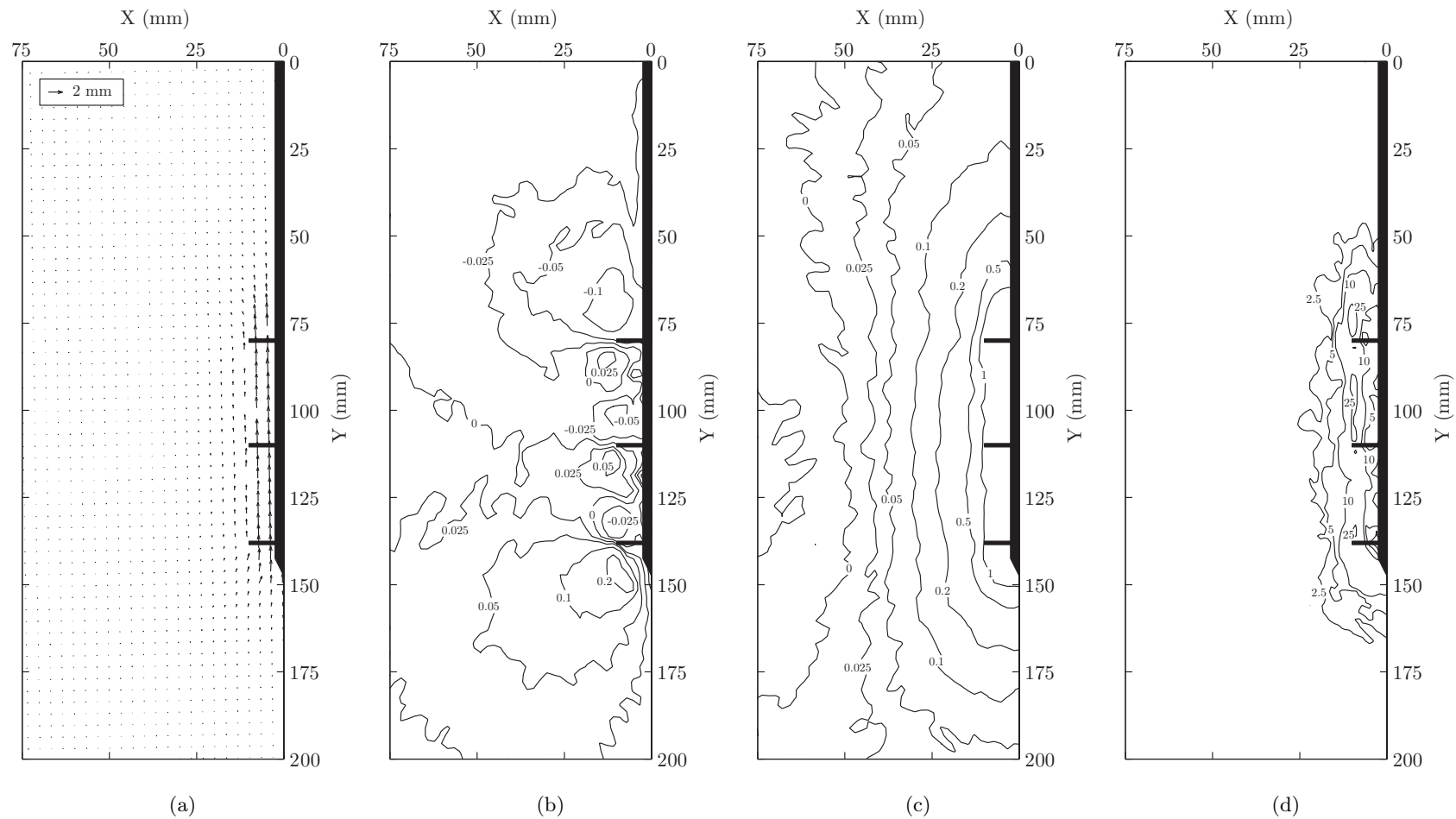


Figure 5.77: T3 cumulative PIV results at 2mm axial tensile displacement: vector (a), horizontal displacement (b), vertical displacement (c) and shear strain contours (d) with displacements in mm and shear strains expressed as a percentage.

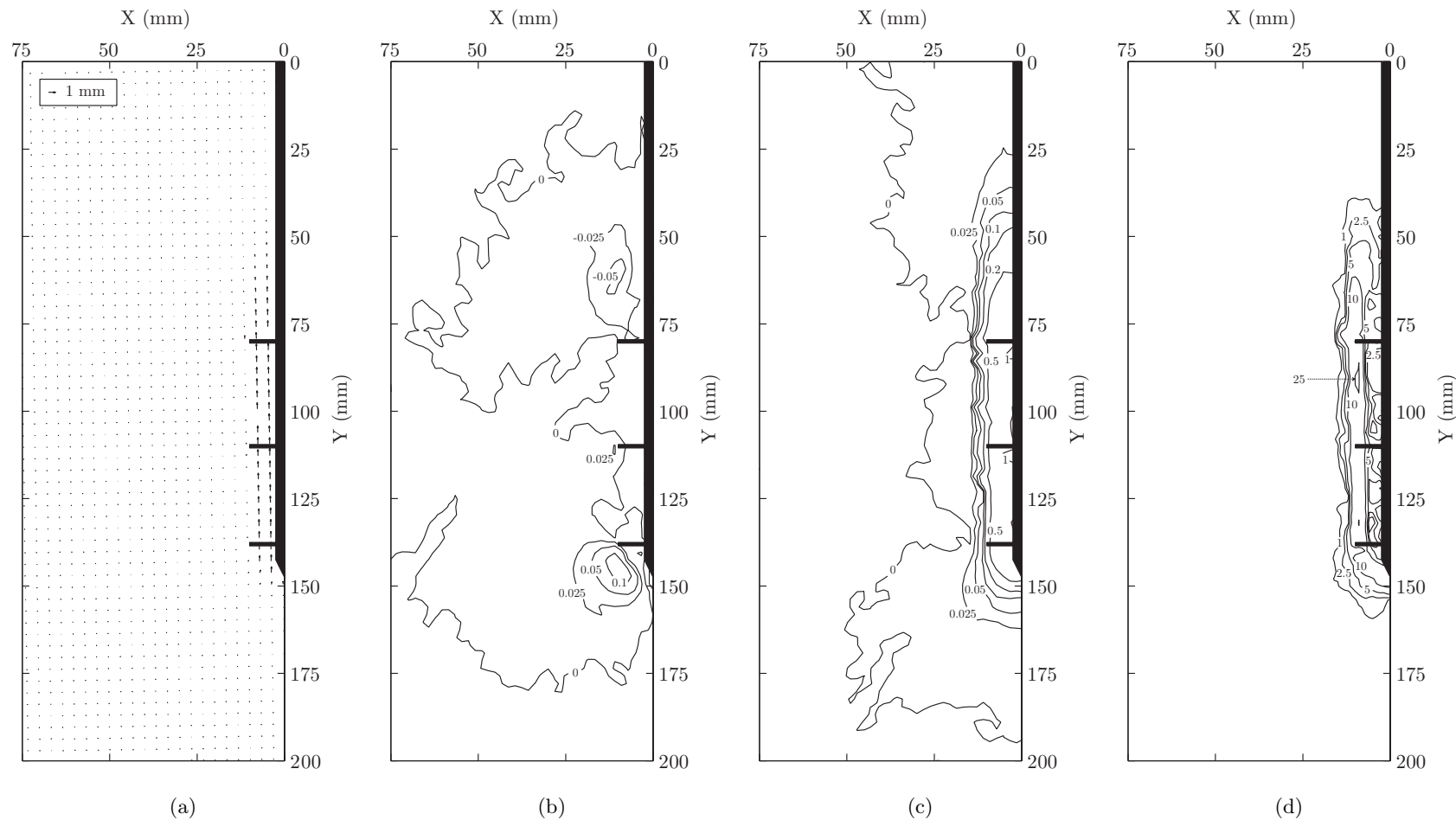


Figure 5.78: T3 incremental PIV results from 2mm to 3mm axial tensile displacement: vector (a), horizontal displacement (b), vertical displacement (c) and shear strain contours (d) with displacements in mm and shear strains expressed as a percentage.

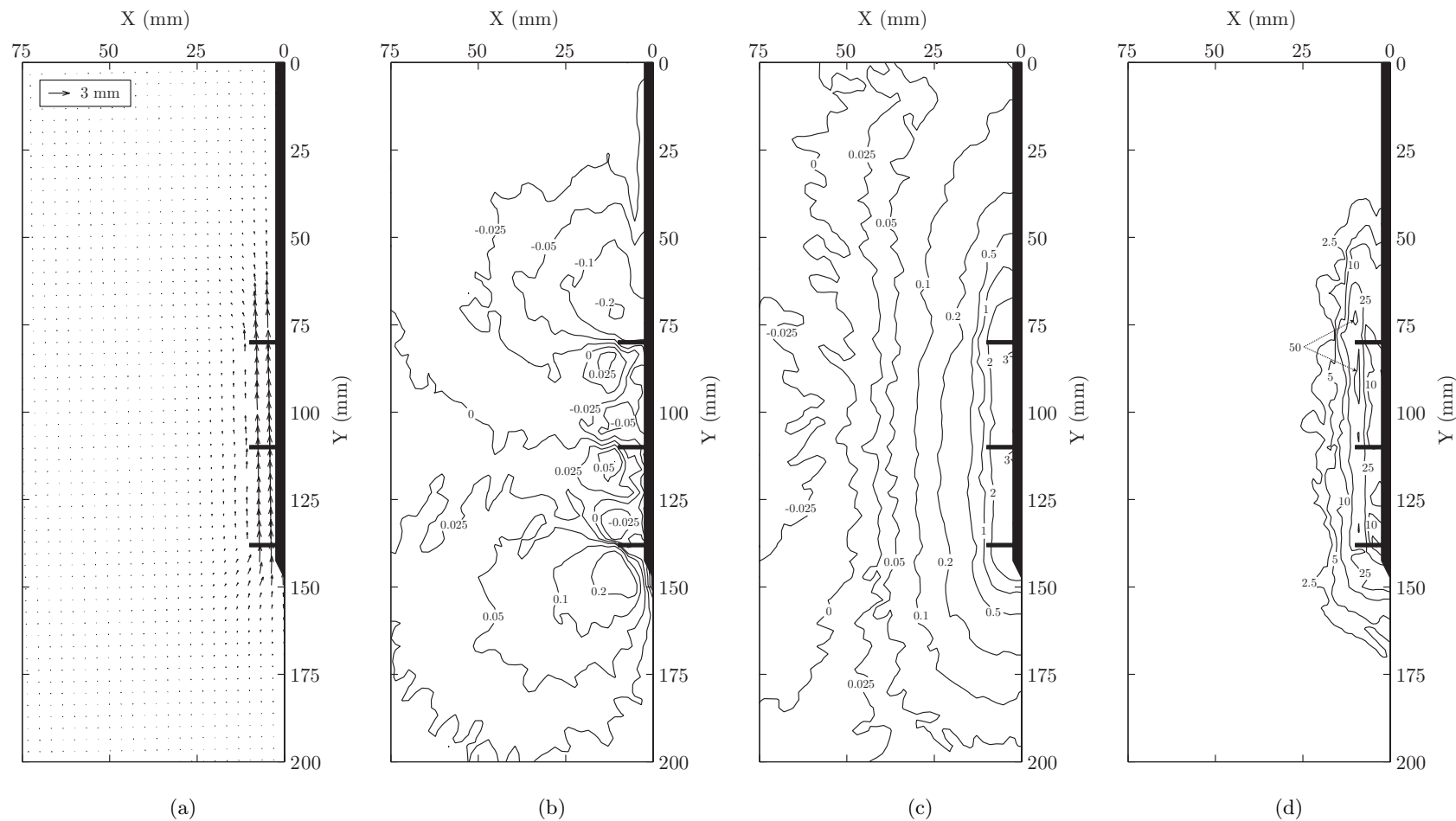


Figure 5.79: T3 cumulative PIV results at 3mm axial tensile displacement: vector (a), horizontal displacement (b), vertical displacement (c) and shear strain contours (d) with displacements in mm and shear strains expressed as a percentage.

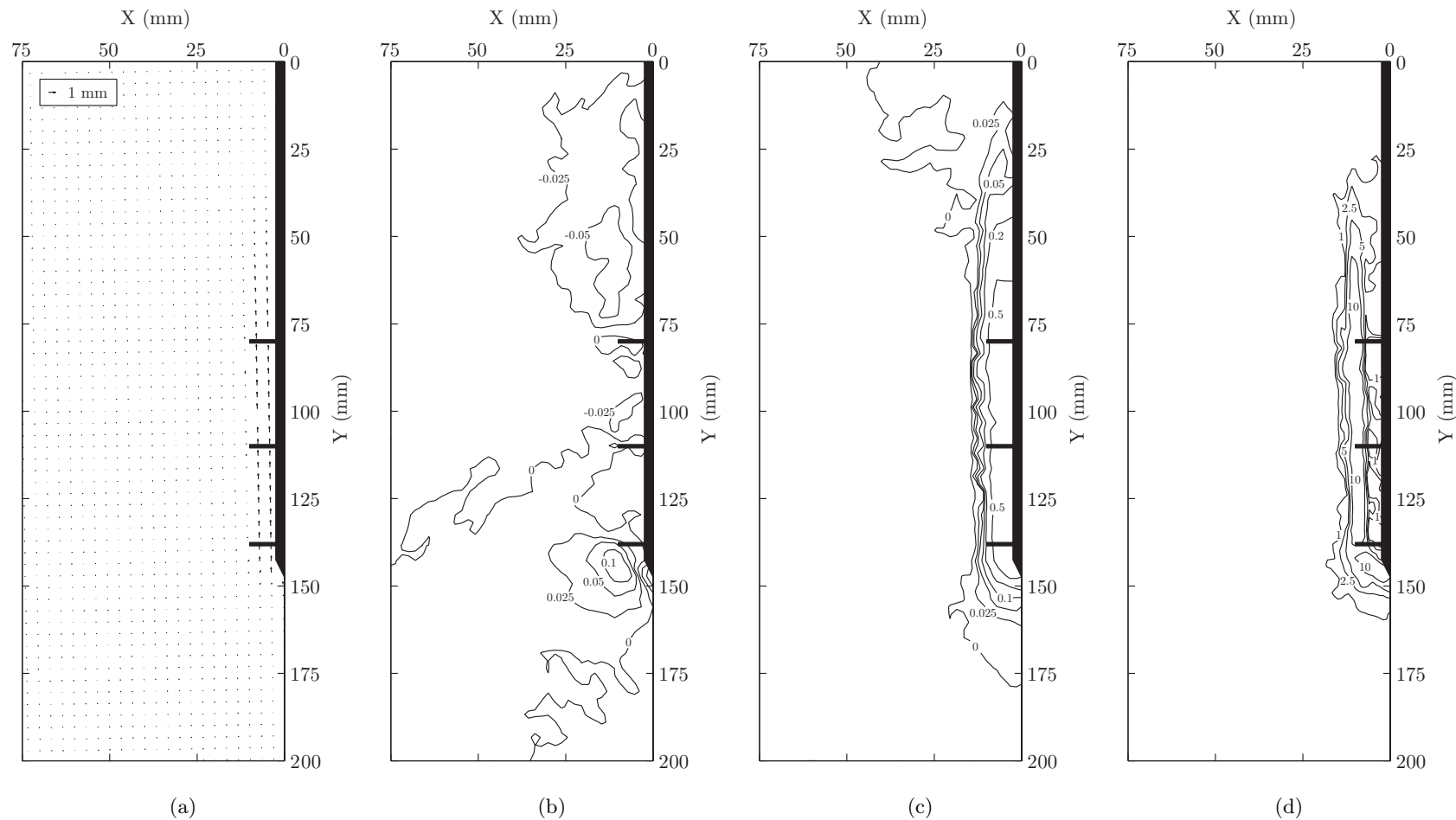


Figure 5.80: T3 incremental PIV results from 3mm to 4mm axial tensile displacement: vector (a), horizontal displacement (b), vertical displacement (c) and shear strain contours (d) with displacements in mm and shear strains expressed as a percentage.

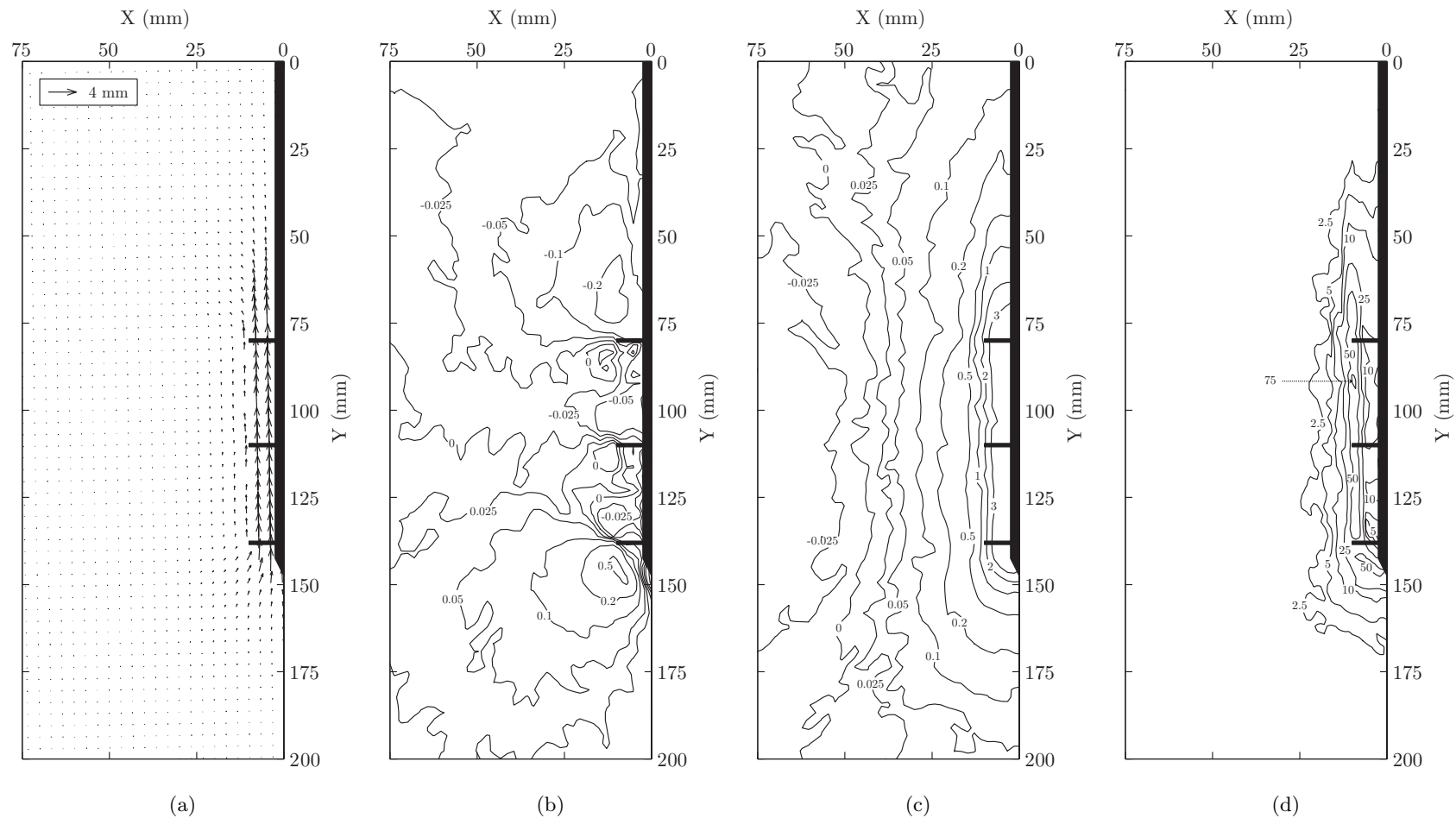


Figure 5.81: T3 cumulative PIV results at 4mm axial tensile displacement: vector (a), horizontal displacement (b), vertical displacement (c) and shear strain contours (d) with displacements in mm and shear strains expressed as a percentage.

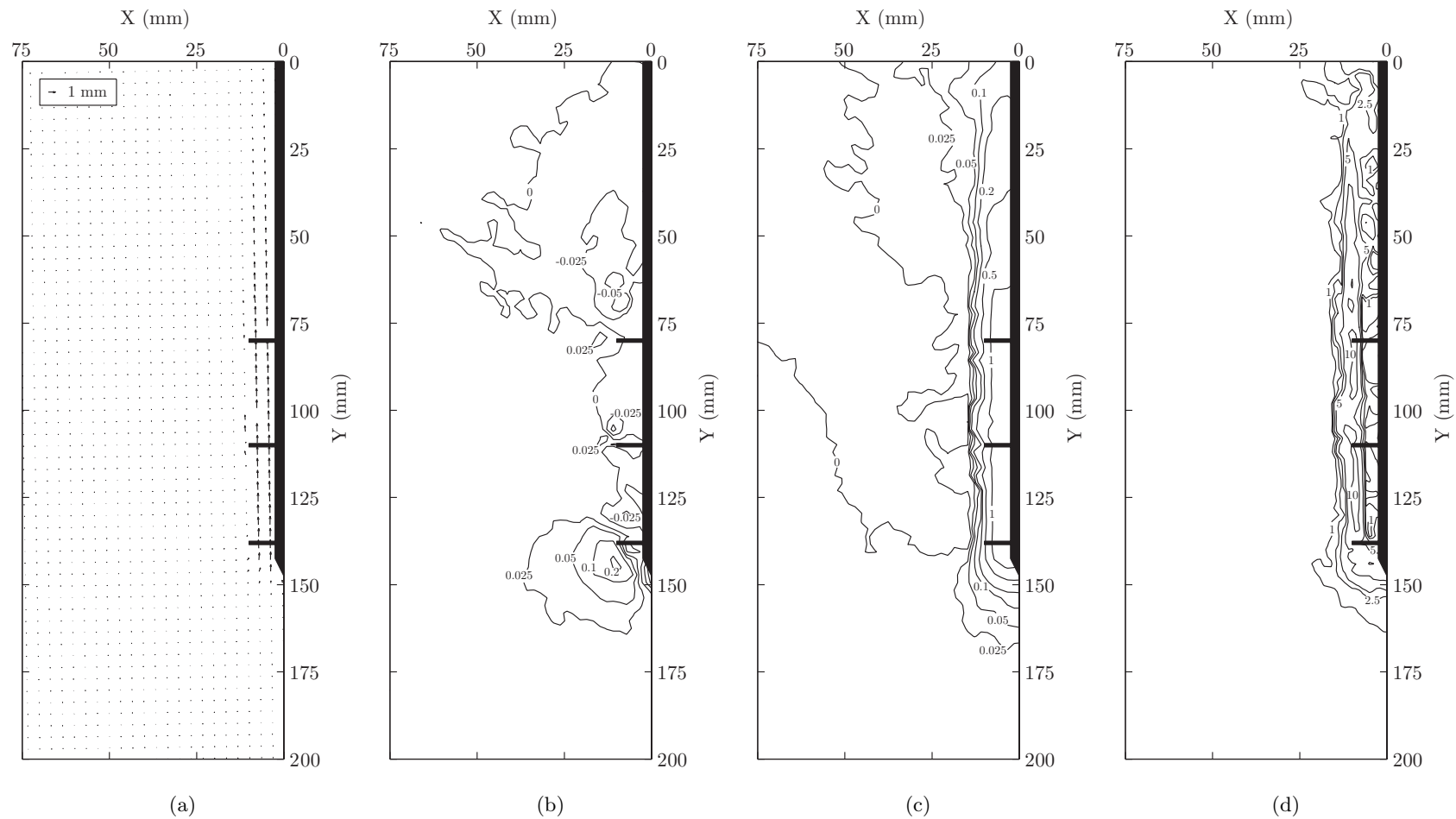


Figure 5.82: T3 incremental PIV results from 4mm to 5mm axial tensile displacement: vector (a), horizontal displacement (b), vertical displacement (c) and shear strain contours (d) with displacements in mm and shear strains expressed as a percentage.

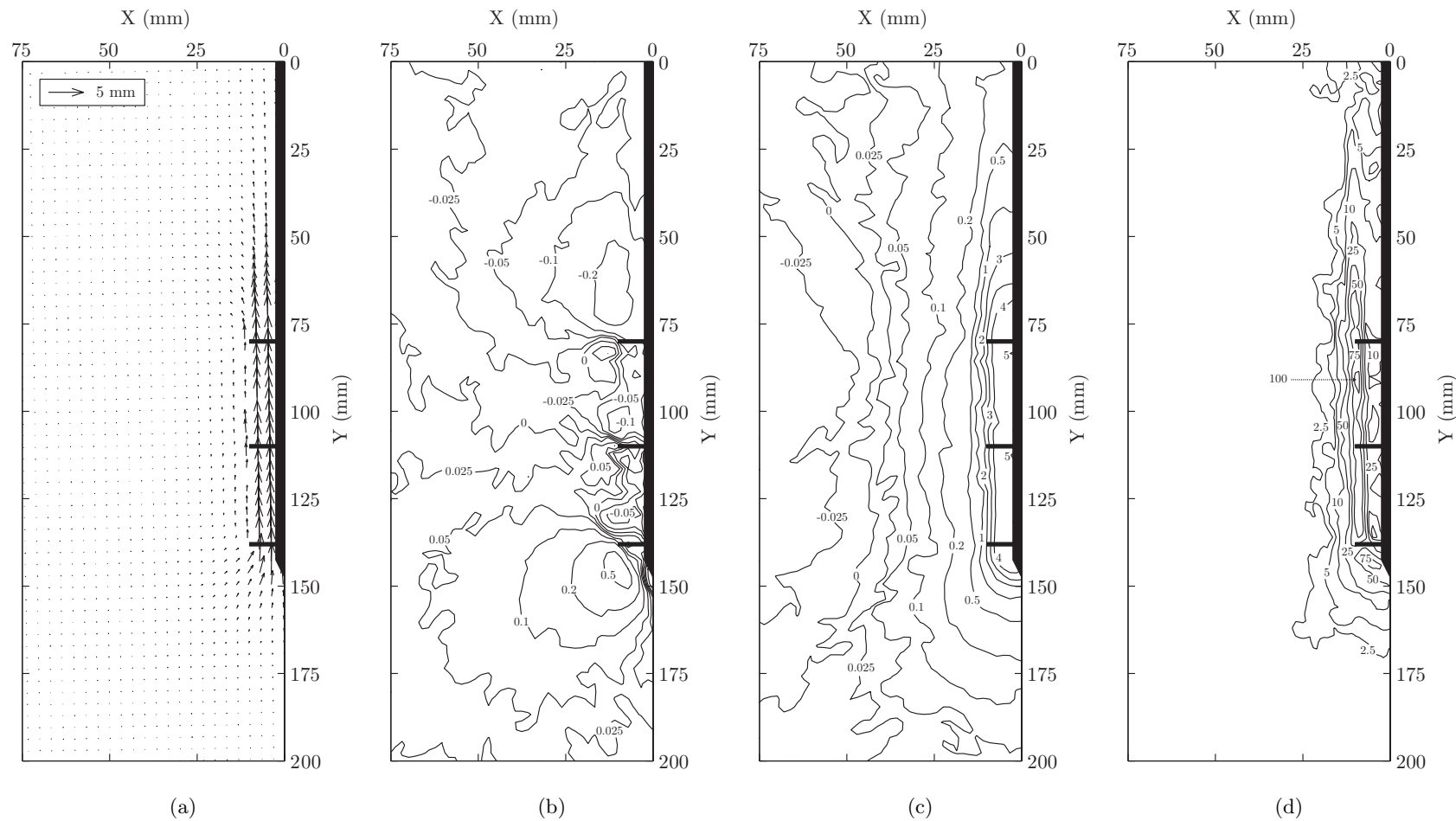


Figure 5.83: T3 cumulative PIV results at 5mm axial tensile displacement: vector (a), horizontal displacement (b), vertical displacement (c) and shear strain contours (d) with displacements in mm and shear strains expressed as a percentage.

5.3.5 Observations

5.3.5.1 Displacement Asymmetry

One of the first observations that can be made is in relation to the horizontal displacement fields for all test configurations. In Figures 5.12(b), 5.21(b), 5.30(b), 5.39(b), 5.48(b), 5.57(b), 5.66(b) and 5.75(b) it is immediately apparent that the horizontal displacement occurring above the uppermost helical plate is slightly smaller in absolute magnitude than that occurring immediately below the lowermost helical plate. This horizontal displacement asymmetry occurs in all tests, regardless of whether the pile is loaded in compression or tension.

One potential reason for the systematic displacement asymmetry is the geometry of the model piles. Considering the lowermost helix for each pile configuration, the upper surface of the helix is less than the that of the underside due to the termination of the shaft in a cone shaped tip. Given that the helix is displaced axially by a known amount, the volume of soil displaced by the underside of the lowermost helix could be expected to be greater than that displaced by the upper surface of the other helices at any other location on the pile shaft. The cone shape of the shaft tip would have also generated greater horizontal displacements than if the shaft tip had been flat, further contributing to the displacement asymmetry.

5.3.5.2 Development of Ultimate Limit State (ULS)

Development of the ULS should be signified in two ways. Firstly, the load-deflection response ought to demonstrate failure by there being no further increase in capacity evident, for an increase in axial displacement. Secondly, the displacement and shear strain fields for successive increments of equal displacement magnitude ought to be similar if the ULS has been reached, thus assuming that a perfectly plastic mechanism is formed.

Figure 5.7 indicates that mobilisation of the ultimate limit state substantially occurs over the range of axial compressive or tensile displacement of $\pm 5\text{mm}$, for all of the configurations of helical screw pile presented here. No further significant increase in capacity was evident at greater displacement magnitudes.

Displacement and shear strain fields were analysed and calculated for axial displacements up to $\pm 5\text{mm}$. As a case study, test T1 is considered, since Figure 5.7 indicated

that the mobilisation of the ULS was most gradual for the single helix pile loaded in tension. It is reasonable to expect that any discrepancy between successive incremental displacement and shear strain fields would be most significant for this test.

Figure 5.48 shows the initial cumulative displacement and shear strain fields for an axial displacement of $1mm$. Figures 5.49, 5.51, 5.53 and 5.55 are the subsequent incremental displacement and shear strain fields for sequential increments of axial displacement of $1mm$. Since the increment of axial displacement is equal to $1mm$ for all cases, the results are directly comparable and can be used to indicate whether the ULS mechanism has been mobilised. Table 5.9 summarises the capacities after each $1mm$ displacement increment and the corresponding percentage of capacity mobilised by each increment.

Table 5.9: Capacity of model pile in test T1 after each displacement increment.

δ (mm)	Capacity (N)	Capacity (%)	Gain (%)
1	-35.3	51.0	51.0
2	-53.26	76.9	25.9
3	-61.89	89.3	12.5
4	-66.6	96.1	6.8
5	-69.29	100	3.9

The first $1mm$ of axial displacement generated 51.0% of the ultimate capacity and yielded, after PIV analysis, the vector fields displayed in Figure 5.48(a). The horizontal displacement field in Figure 5.48(b) shows small displacement magnitudes above and below the helical plate in opposing directions. Soil is being drawn into the pile below the helical plate and away from it above with the displacement asymmetry described in Section 5.3.5.1 being apparent. The corresponding vertical displacement field in Figure 5.48(c), indicates that a bulb of soil around the helical plate is being displaced vertically, with reducing magnitude with distance from the helical plate. The shear strain field in Figure 5.48(d) indicates that maximum shear straining in the soil is evident towards the outer radius of the helical plate.

The second increment of $1mm$ axial displacement mobilised a further 25.92% of the ultimate capacity, almost half of the gain in capacity made during the initial increment. This generated the vector field in Figure 5.49(a). The horizontal displacement field in Figure 5.49(b) is almost symmetrical (with opposed directions of movement) indicating that the effect of displacement asymmetry is less evident. The vertical displacement field in Figure 5.49(c) is becoming more

localised around the helical plate than in the first increment of displacement, with almost symmetrical displacements around the elevation of the helical plate. The shear strain field in Figure 5.49(d) indicates that maximum shearing is still evident towards the outer radius of the helical plate but over an increased area for the same magnitude of shear strain, which in this instance is 10%. The displacement and shear strain contours are different for these first two increments than for subsequent increments of displacement and the gain in capacity is very large. Hence up until this point in the test the failure mechanism was still developing.

In the third increment of 1mm axial displacement, the gain in capacity reduced by half again to 12.46%. The resultant vector field is displayed in Figure 5.51(a). The horizontal displacement field in Figure 5.51(b) is again almost symmetric (with opposed directions of movement) and displacement asymmetry is minimal. The horizontal displacements induced are very similar to the previous increment. The vertical displacement field in Figure 5.51(c) is also very similar to that of the previous increment. Minor discrepancies of magnitude are indicated by the slightly reduced area over which displacements have been tracked. However, this can be attributed in part to wander of the zero contour caused by the summated camera-soil movement errors described in Section 5.3.3. The zero vertical displacement contour also appears to have moved in towards the outer radius of the helix, indicating upward soil movement adjacent to the outer radius of the helix and thus the onset of backflow around the helical plate. However, the magnitude of displacement at this point is very small ($\leq 25\mu m$). The shear strain field in Figure 5.51(d) is also very like that of the previous increment, with maximum shear strain again indicated towards the outer radius of the helical plate.

The latter two increments of 1mm displacement continue this trend of reducing capacity gain as it reduced further to 6.80% and the finally 3.88% for the final increment of 1mm displacement. The resultant vector fields are presented in Figures 5.53(a) and 5.55(a). The corresponding horizontal displacement fields in Figures 5.53(b) and 5.55(b) are once again almost symmetric about the elevation of the helical plate. The magnitudes of displacement above and below the helical plate are very similar, but in different directions. Backflow around the helical plate appears once more but at very small magnitudes. Figures 5.53(c) and 5.55(c) indicate that the trend of a localised bulb of soil being displaced by the pile continues.

The above observations are evidence that the failure mechanism apparent at the ULS has been mobilised since sequential increments of displacement have yielded extremely similar displacement and shear strain fields that differ from those for the initial two increments of displacement. This demonstrates that the mechanism has evolved during the incremental displacement of the model pile towards mobilisation of the ultimate capacity. Similar trends can be seen for all other tests presented here (C1, C2-30, C2-60, C3, T2-30, T2-60 and T3), when sequential increments of 1mm displacement are considered. As a result, the development of the ULS will not be described for the remaining cases.

5.3.5.3 Effect of Spacing Ratio

The effect of the spacing ratio is most apparent if the shear strain fields are compared for multi-helix piles with varied s/D , where L_a is maintained. For this case study, results from the pairs of tests C2-60 and C3 and T2-60 and T3 can be compared, where L_a is 60mm and s/D is 3.0 and 1.5 respectively.

Firstly, comparing the initial shear strain fields in Figures 5.30(d) and 5.39(d) and Figures 5.66(d) and 5.75(d), a shear band is more clearly defined, extending between the outer radius of the uppermost and lowermost helical plates, when s/D is equal to 1.5. This is a direct effect of s/D and leads to increased capacity for a given axial displacement (i.e. a stiffer response). This is even more pronounced for the next sequential 1mm increment of axial displacement shown by comparing Figures 5.31(d) and 5.40(d) and Figures 5.67(d) and 5.76(d), where maximum shearing is localised around the outer radius of each helical plate in tests C2-60 and T2-60. Conversely, maximum shearing is observed between the helical plates along the active length of the pile in tests C3 and T3.

These two initial increments of displacement are in the region of the load-deflection response where the capacity of the pile increases most significantly. As the axial displacement approaches $\pm 3\text{mm}$ the capacities begin to converge. This is also seen in the shear strain fields in Figures 5.33(d) and 5.42(d) and Figures 5.69(d) and 5.78(d) for the 1mm increment of displacement from $\pm 2\text{mm}$ to $\pm 3\text{mm}$, as the shear band, particularly in test C2-60, is beginning to extend over the full active length of the pile. The presence of a continuous shear band is less marked in the data from test T2-60. This is partially due to the deletion of some wild random vectors directly between the outer radii of the helical plates. Comparison of Figures 5.35(d)

and 5.44(d) and 5.71(d) and 5.80(d) shows that this trend continues over a further 1mm increment of axial displacement. The shear band is now fully developed between the helical plates in test C2-60 and, aside from areas of wild random vector removal, mostly developed in test T2-60. This explains the convergence of the ultimate capacities of the double helix piles with those of the triple helix piles as the cumulative displacement increases.

Lastly, comparison of Figures 5.35(d) and 5.44(d) and 5.71(d) and 5.80(d) explains why over the range of axial displacement of $\pm 4\text{-}5\text{mm}$ the ultimate capacities for the double helix and triple helix piles with L_a of 60mm converge to within about 2% of the ultimate capacity of the similarly loaded (compression or tension) triple helix pile on average. The total volume of soil being subjected to shear straining is very similar for both the double and triple helix piles. The shear band between the uppermost and lowermost helical plates for both geometries and loading configurations is now fully formed. The mobilisation of this shear band helps to explain the convergence of ultimate capacities for these two configurations of a pile with equal L_a .

5.3.5.4 Effect of Active Length

The effect of L_a on helical screw pile performance can be examined by comparing piles with maintained s/D and varied L_a . For this purpose test pairs C2-30 and C3 and T2-30 and T3 can be compared, where s/D is 1.5 and L_a is 30mm and 60mm respectively.

Given that the development of a shear band between multiple helical plates was demonstrated in the previous section, the development of the failure mechanism will not be demonstrated again for this analysis. Comparison of the shear strain fields for a 1mm axial displacement increment from $\pm 4\text{mm}$ to $\pm 5\text{mm}$ is used to illustrate the impact of L_a on capacity. This is best shown by Figures 5.28(d) and 5.46(d) and Figures 5.64(d) and 5.82(d), which show the shear strain field apparent for a double helix pile with L_a of 30mm compared to a triple helix pile with L_a of 60mm. These results show that for s/D of 1.5, a distinct shear band is generated between all helical plates for both compressive and tensile loading regardless of L_a .

It is worth noting that the appearance of closed contours at the mid point of the active length in Figure 5.28(d) is a product of data being manually removed due to the vectors being wild and random. This leads to a local absence of shear

strain measurement, which when interpolated to allow plotting of contours of shear strain leads to the closing of contours due to incorrect interpolation at the point of the data loss. Irrespective of this, the presence of a shear band is still clearly evident.

In Section 5.3.1 active length was linearly related to ultimate capacity for both compressive and tensile loading. The shear strain fields provide evidence of the effect of active length on ultimate capacity, since the volume of soil mobilised during loading appears to be governed by L_a . The maximum shear strain mobilised with the two pile configurations for the same orientation of loading (C2-30 and C3 and T2-30 and T3) is very similar and thus is a function of s/D rather than L_a .

5.3.5.5 Soil-Shaft Interface Behaviour

Inspection of the vertical displacement contour plots for all tests at $\pm 1\text{mm}$ axial displacement (see Figures 5.12(c), 5.21(c), 5.30(c), 5.39(c), 5.48(c), 5.57(c), 5.66(c) and 5.75(c)) indicates that the model pile shaft is moving independently of the soil, since vertical displacements adjacent to the shaft are very small, indicating that slippage is occurring between the soil and the shaft surface. This observation is important with respect to the formulation of numerical models of helical screw piles using Finite Elements (FE), which is explained in greater depth in Chapter 7.

5.3.5.6 Compressive-Tensile Comparison

The discrepancy between the ultimate capacity of compressive and tensile load-deflection testing was discussed in Section 5.3.1, where the hypothesis was made that reducing H/D during loading caused a reduction in ultimate capacity for the pile loaded in tension, compared to the compression test with the same pile configuration. To assess the validity of this hypothesis, comparison of tests C2-60 and T2-60 and C3 and T3 can be conducted. In these cases H was 80mm and D was 20mm . Thus H/D was 4 at the onset of loading. This was the minimum embedment depth tested in this investigation and hence ought to be most likely to reveal any propagation of the failure mechanism toward the surface of the sample for a pile subjected to tensile loading.

Figures 5.38(d) and 5.74(d) and 5.47(d) and 5.83(d) present the cumulative shear strain fields, which clearly extend towards the surface of the sample for the tension tests. This validates the hypothesis that the embedment depth may not have been sufficient for piles loaded in tension causing upward vertical displacement and a

consequent reduction of H/D . At this point in the test the embedment depth was reduced by 5mm, thus reducing the embedment ratio to 3.75. This reduction of H/D is further amplified by the installation process. Figures 5.2, 5.3, 5.4 and 5.5 indicate that breakout occurred at the soil surface during installation for all configurations of pile. This occurred during the initial keying of the lowermost helical plate with the ground. Typically up to 10mm of breakout was evident. This potentially reduced H/D further to approximately 3.25.

The horizontal displacements in Figures 5.38(b) and 5.74(b) and 5.47(b) and 5.83(b), also show evidence of propagation of the failure mechanism towards the surface of the sample. In tests T2-60 and T3 greater horizontal displacement above the uppermost helical plate is observed compared to that observed in tests C2-60 and C3.

Comparison of the position of the vertical displacement contours in the Figures 5.38(c) and 5.74(c) and 5.47(c) and 5.83(c) also shows movement of the failure mechanism towards the sample surface in tests T2-60 and T3. In test T2-60 even some breakout at the sample surface is apparent which serves as further evidence that the breakout caused by installation coupled with the reduction of H/D due to the direction of applied displacement during tensile testing impacted on the failure mechanism. This reduction of H/D is most likely the cause of discrepancies between the compressive and tensile ultimate capacities highlighted in Figure 5.8 and Table 5.5.

Final confirmation of this can be found by examining the displacement and shear strain fields for T1 and T2-30, where H/D was 7 and 5.5 respectively (summarised in Table 5.5). In these two cases with larger H/D , the cumulative shear strain fields shown in Figures 5.56(d) and 5.65(d), indicate that the failure mechanism did not propagate to the surface. The result of this is that the tensile and compressive ultimate capacities for these two configurations of pile were very similar, with a discrepancy of less than 1% of the ultimate compressive capacity for each geometric configuration of pile. Thus in these two cases the embedment ratio, H/D was sufficient to ensure that the failure mechanism did not propagate to the surface of the sample. The minimum embedment ratio at any point in the test was 6.75 for test T1 and 5.25 for test T2-30 assuming no installation induced breakout. Even assuming that up to 10mm of material at the soil surface was ineffective due to breakout, the minimum embedment ratios would only be reduced to 6.5 for test

T1 and 5 for test T2-30. Therefore, there was a significant margin between the apparent H/D and the ratio of 4 considered by Rao et al. (1993a) to constitute deep embedment.

Therefore, if the investigation were to be repeated or further tests on deep helical screw piles in soft clay are conducted, it is advised that the embedment ratio, H/D , be increased somewhat above the minimum value utilised here of 4. In this instance the maximum capacity of the apparatus available was being utilised, so formation of a deeper sample was not possible and the reduction in quality of PIV output that would have been the result of reducing the size of the model pile was deemed unacceptable.

5.3.6 Repeatability

Assessment of repeatability was assessed by performing repeat tests for the two extreme configurations of helical screw pile: single helix and triple helix with L_a of 60mm and s/D of 1.5. Both repeat tests were compressively loaded and the load deflection responses and percentage discrepancy from the original test response is presented in Figure 5.84.

The repeat single helix pile test yielded a maximum absolute discrepancy of about 7% of the ultimate capacity of the initial test, with an average absolute discrepancy of about 3%. The repeat triple helix pile test exhibited a maximum absolute discrepancy of about 6%, with an average absolute discrepancy of about 5% of the ultimate capacity of the initial test. This indicates generally good repeatability. In both cases the ultimate capacity of the repeat test was slightly less than for the initial test, in particular for the triple helix pile repeat test. The calibrations performed at the beginning and upon completion of the testing process that were presented in Chapter 3, illustrated that the discrepancy between initial and repeat tests was almost certainly not due to drift in the calibrations of the transducers with time.

Therefore, one other possible cause of the discrepancy could be the slightly lower shear strengths measured in the repeat samples (see Figures 6.3(a) and 6.3(i) and Figures 6.3(d) and 6.3(j) in Chapter 6), where the difference in shear strength is most apparent for the triple helix pile case. The cause for the slightly lower shear strength in the samples is not known but offers a plausible explanation for why the repeat tests both yielded a lower ultimate capacity compared to the initial tests.

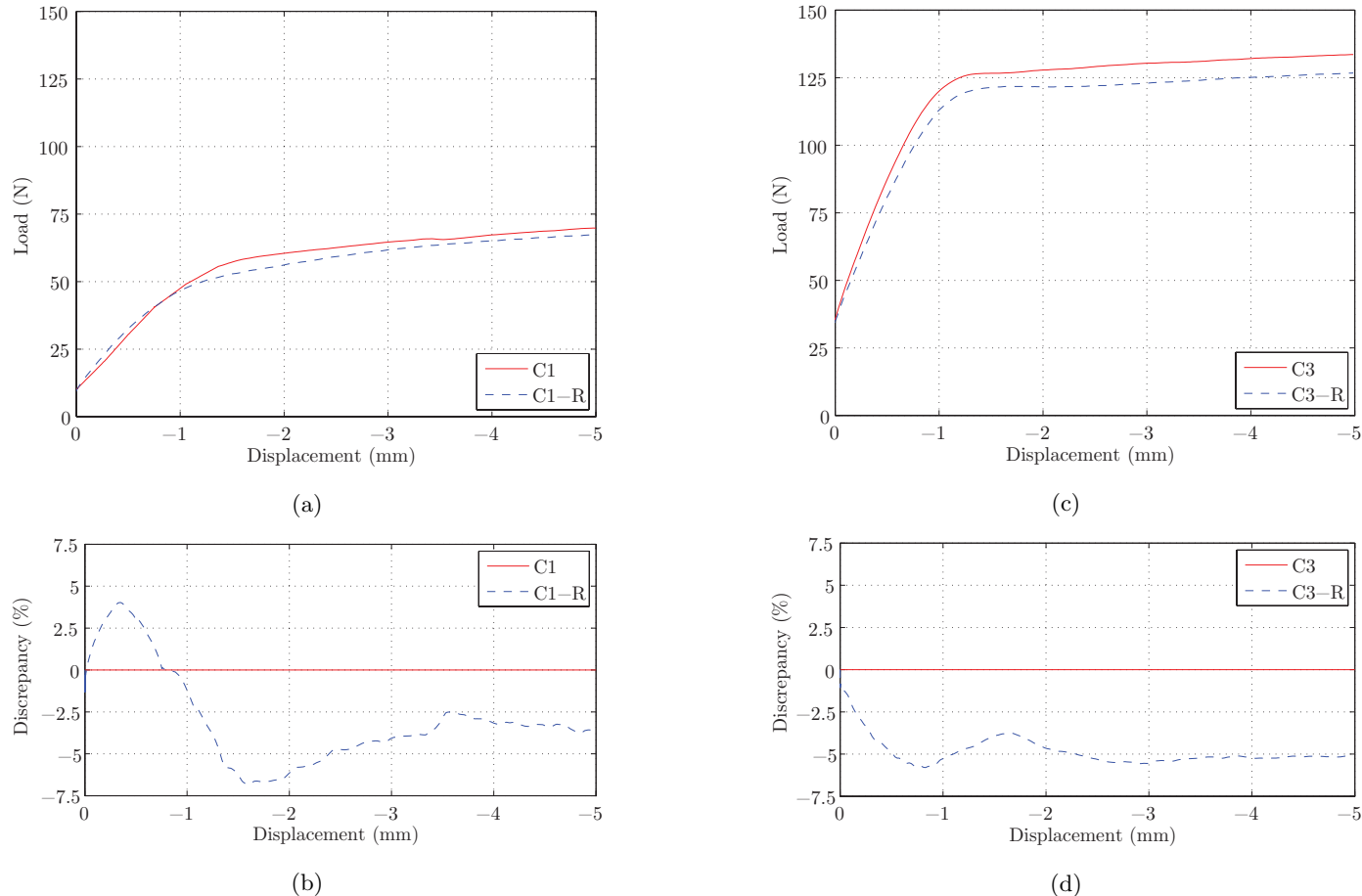


Figure 5.84: Repeatability of performance of: (a) single helix pile under axial compression; (b) corresponding percentage discrepancy; (c) triple helix pile under axial compression; and (d) corresponding percentage discrepancy.

Table 5.10 summarises the camera-soil movement corrections applied to the repeat test datasets. The magnitudes of correction and percentage of vectors of modal magnitude are modest compared to those applied to the initial tests shown in Table 5.7 indicating that camera-soil movements were minimal during the repeat tests.

Table 5.10: Magnitude of horizontal (u_c) and vertical (v_c) correction specified by modal movement correction process for repeat compressive response tests.

Test	δ (mm)	Correction			
		Horizontal		Vertical	
		u_c (μm)	$\%_u$	v_c (μm)	$\%_v$
C1-R	-5	-12	4.57	-7	3.17
C3-R	-5	0	2.08	-9	2.03

Comparison of displacement and shear strain fields from the original and repeat tests at an axial displacement of 5mm demonstrates the repeatability of the testing process. Comparing Figures 5.20 and 5.85 and Figures 5.47 and 5.86 shows that modelling of the single helix pile was particularly consistent with respect to the PIV output as no significant discrepancies are observed. Greater discrepancies can be observed in the PIV output from the triple helix pile repeat test. There is greater heave apparent in the far field away from the model pile in the repeat data set. However, this difference is less than $25\mu m$, or 0.1% of the axial displacement of the model pile and thus relatively insignificant. Comparison of Figures 5.47(d) and 5.86(d) highlights a more significant discrepancy in the shear strain fields observed. Although the pattern of a shear band forming between the outermost edge of each helix is apparent in both data sets, more soil appears to be experiencing shearing in the initial data set. The maximum magnitude of shear strain is also larger in the initial data set, albeit in very localised regions.

One, possible reason for the discrepancy may be the ambient noise in the dataset. Data yielded by the initial test was significantly noisier than data yielded by the repeat test. Hence the ragged profile of the small magnitude (2.5%) shear strain contours in Figure 5.47(d) from the initial test, compared to the smoother contours exhibited in Figure 5.86(d) from the repeat test. However, regardless of the relatively minor discrepancies, the repeat tests served their purpose well in that they prove the repeatability of the test process both in relation to the load-deflection response and PIV derived measurements. This shows that the sample preparation, model pile installation and test process is fit for purpose and can be used effectively to analyse behaviour of model helical screw piles at small scale in the laboratory.

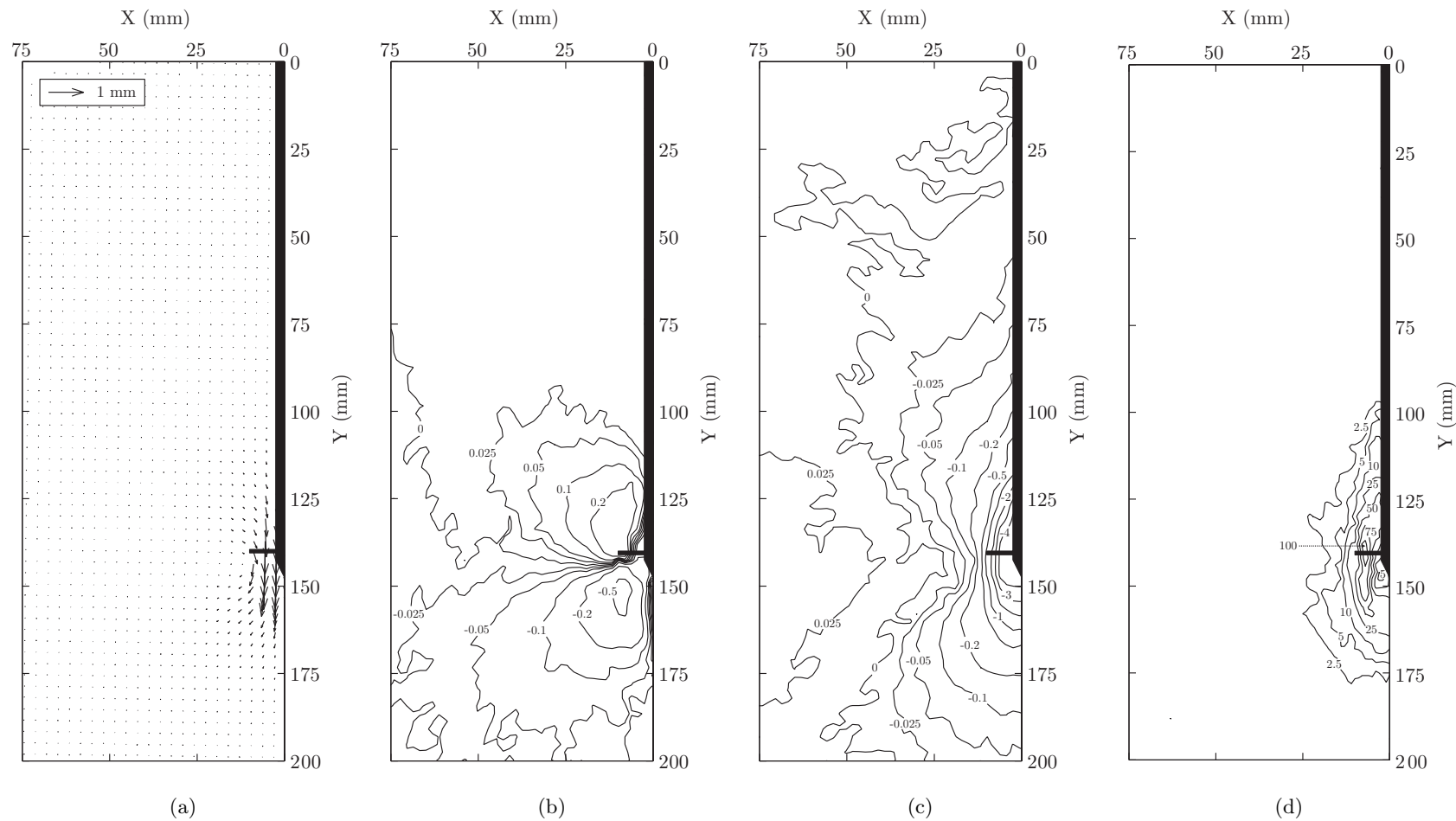


Figure 5.85: C1-R cumulative PIV results at 5mm axial compressive displacement: vector (a), horizontal displacement (b), vertical displacement (c) and shear strain contours (d) with displacements in mm and shear strains expressed as a percentage.

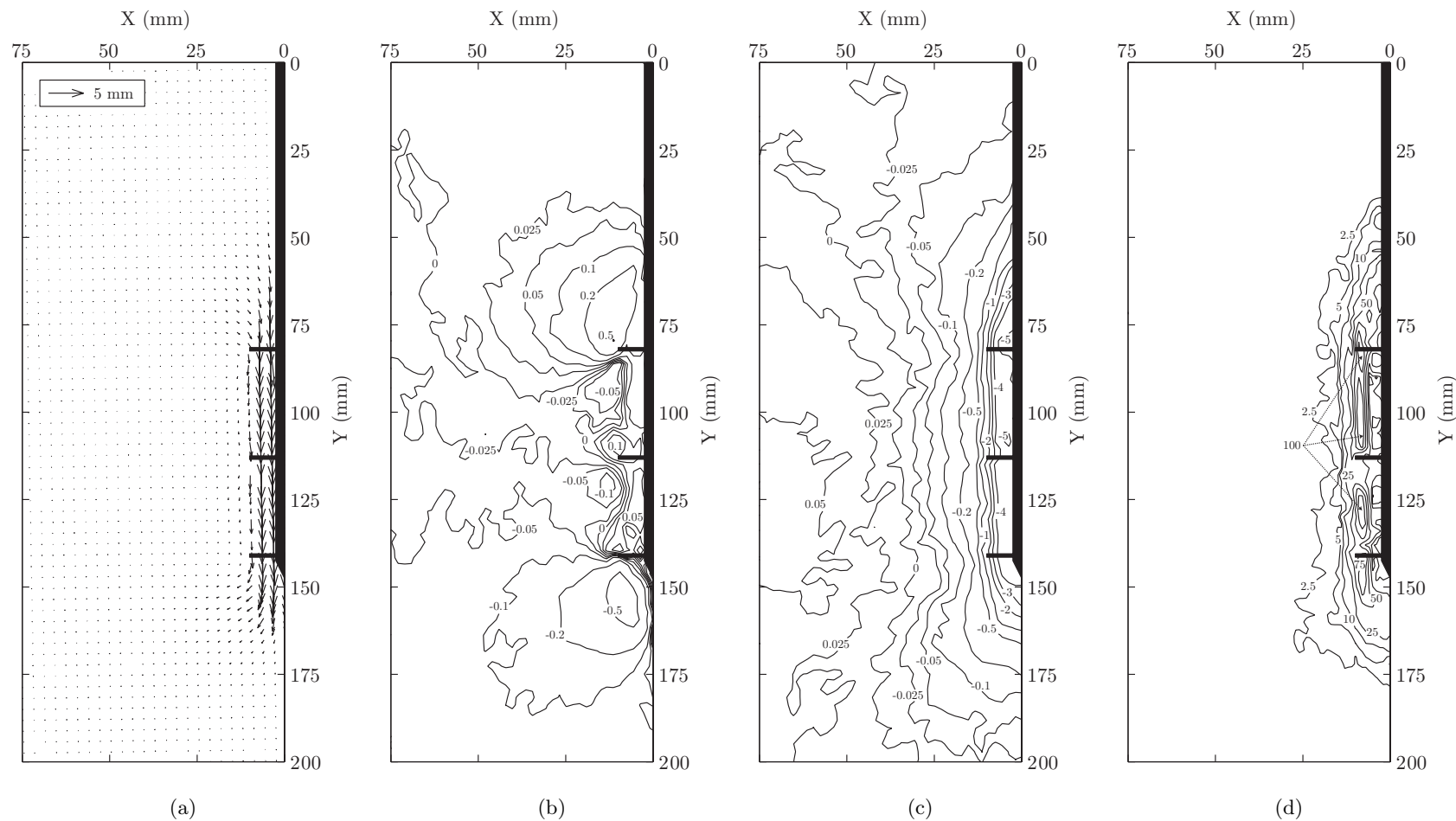


Figure 5.86: C3-R cumulative PIV results at 5mm axial compressive displacement: vector (a), horizontal displacement (b), vertical displacement (c) and shear strain contours (d) with displacements in mm and shear strains expressed as a percentage.

5.4 Summary

Results from small scale $1g$ physical models of helical screw piles loaded in compression and tension have been presented. Data in the form of load-deflection responses and PIV derived displacement and shear strain fields have been used to highlight key facets of behaviour.

Shear bands have been shown to be generated between helical plates. Where $s/D < 1.5$ shear bands form very quickly after relatively small amounts of displacement. Where $s/D > 1.5$ more displacement is required to enable a shear band between the helical plates to fully form.

s/D has been shown to control the stiffness of the response of helical screw piles. Tests with maintained L_a and differing s/D were used to demonstrate that lower s/D results in increased capacity for a given axial displacement compared to higher s/D . This is consistent with the observations made by Rao et al. (1993a).

L_a has been demonstrated to control the ultimate capacity of the helical screw pile configurations tested. Tests where s/D was maintained and L_a was varied, in conjunction with the resultant shear strain fields, demonstrated this clearly.

The presence of a sliding interface between the shaft of a helical pile and the surrounding soil was established by using PIV analysis. This will significantly impact the formulation of numerical modelling of the physical models using the FE method, which is presented in Chapter 7.

The similarity of the compressive and tensile performance of deeply installed helical screw piles in soft clay was demonstrated. Only when H/D was 4 was there any discrepancy between the compressive and tensile behaviour. PIV derived displacement and shear strain fields were then used to attribute these discrepancies to the reduction in H/D caused by installation induced breakout at the soil surface and tensile loading, as the failure mechanisms where H/D was equal to 4 were shown to eventually begin to propagate towards the surface of the sample.

Chapter 6

Derivation of Stress-Strain Characteristics of Transparent Soil

6.1 Introduction

To perform a numerical simulation of the observations derived from the physical modelling tests presented in the previous chapter, parameters are required to describe the stress-strain response of the transparent soil.

This chapter presents in-situ post-test shear strength data from hand vane shear strength tests and an UU triaxial test, facilitating the development of relationships to describe the shear strength profile with depth and the stress-strain behaviour of the transparent soil.

An alternative method of deriving the stress-strain behaviour is then proposed based upon the coupling of an equilibrium and kinematic solution for the undrained settlement of a circular foundation on clay soil, using the Mobilisable Strength Design (MSD) framework developed by Osman and Bolton (2005). Transparent soil is used to assess the deformation mechanism apparent during undrained settlement of a circular footing on clay. The load-deflection response of the footing is used to derive a stress-strain curve allowing a simple Mohr-Coulomb constitutive model to be calibrated. This procedure uses closed form axis translations proposed by Osman and Bolton (2005) to relate axial strain (ϵ_a) to footing settlement (δ) and deviator stress (q) to mobilised stress (σ_{mob}).

A combination of this data is used to calibrate a FE model of the problem allowing confirmation of the displacement and shear strain fields observed in the transparent soil based physical model. A series of parallel analyses is then presented to demonstrate the sensitivity of the process to assumptions made during formulation of the FE model, variability of the properties of the samples used in the physical modelling and aspects particular to the modelling process adopted.

6.2 Post-Test Investigation of Sample Properties

After completion of each helical screw pile test investigation of the properties of the sample was conducted to derive parameters to describe the relationship between shear stress and shear strain for the transparent soil. Initially it was felt that this would be best achieved by using thin walled sampling tubes to extract 38mm diameter samples from the test chamber. These samples could then be subjected to simple UU tests in triaxial apparatus.

Results from UU tests are presented in Figure 6.1, illustrating that the stress-strain response of the transparent soil could be modelled as linear elastic perfectly plastic. The undrained stiffness (E_u) and undrained shear strength (S_u) were then fitted by taking the average gradient of the ‘elastic’ range and average deviator stress q for the ‘plastic’ range, yielding E_u of 533.62kPa and S_u of 15.90kPa. Therefore the Rigidity Index ($I_R=E_u/S_u$) was equal to 33.56.

However, deriving strength data in this way presented two problems. First, the size of the thin wall sampling tubes made it very difficult to extract the samples from the chamber without inducing significant disturbance to the samples during extraction. For the initial UU tests presented, this was avoided by carefully dismantling the chamber, before extracting the sampling tubes by carving away the excess material surrounding them. However, this was not a practical approach for all tests. Second and more importantly, due to the length of sample required for a 38mm triaxial test and the difficulty encountered when extracting samples only one set of triaxial tests could be performed per sample, such that the behaviour was representative of the mid-height of the sample. This meant that, had the strategy of performing post-test UU tests been followed, no data would have been derived describing the homogeneity of the stress-strain behaviour of the material with respect to sample depth.

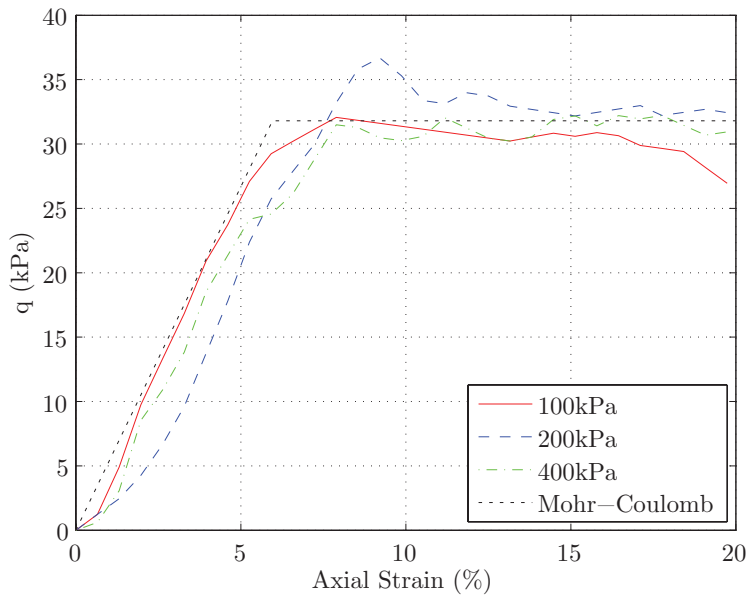


Figure 6.1: Triaxial response of transparent soil from UU test and fitted Mohr-Coulomb constitutive model.

Hence, another method of deriving undrained stiffness and strength at an alternative depth in the model was required, so that a relationship for both stiffness and strength with respect to sample depth could be postulated with the benefit of experimentally derived evidence. Therefore, strength profiles for each sample were estimated from a combination of post-test hand vane tests and the triaxial data derived from the initial UU tests. The shear strength data is summarised in Figure 6.2 with corresponding plots of shear strength data from each individual test presented in Figure 6.3. Maximum and minimum, upper and lower vane shear strength measurements have been used to define the upper and lower bound shear strength gradients. The mean strength gradient is created using the average values of the upper and lower bound shear strengths calculated using the vane shear strength data from all the samples tested. In all three cases this strength gradient with depth (k) was about -30 kPa/m . This reducing strength profile with depth is likely to be a result of the high aspect ratio of the test chamber as discussed in Chapter 3 and the associated effects of sidewall friction potentially reducing the effective stress applied to the sample with depth during consolidation.

Deriving the undrained stiffness profile with depth in such a small model was a significantly more difficult task. One possibility was to use the transparent soil material to investigate the validity of the Mobilisable Strength Design (MSD) concept conceived

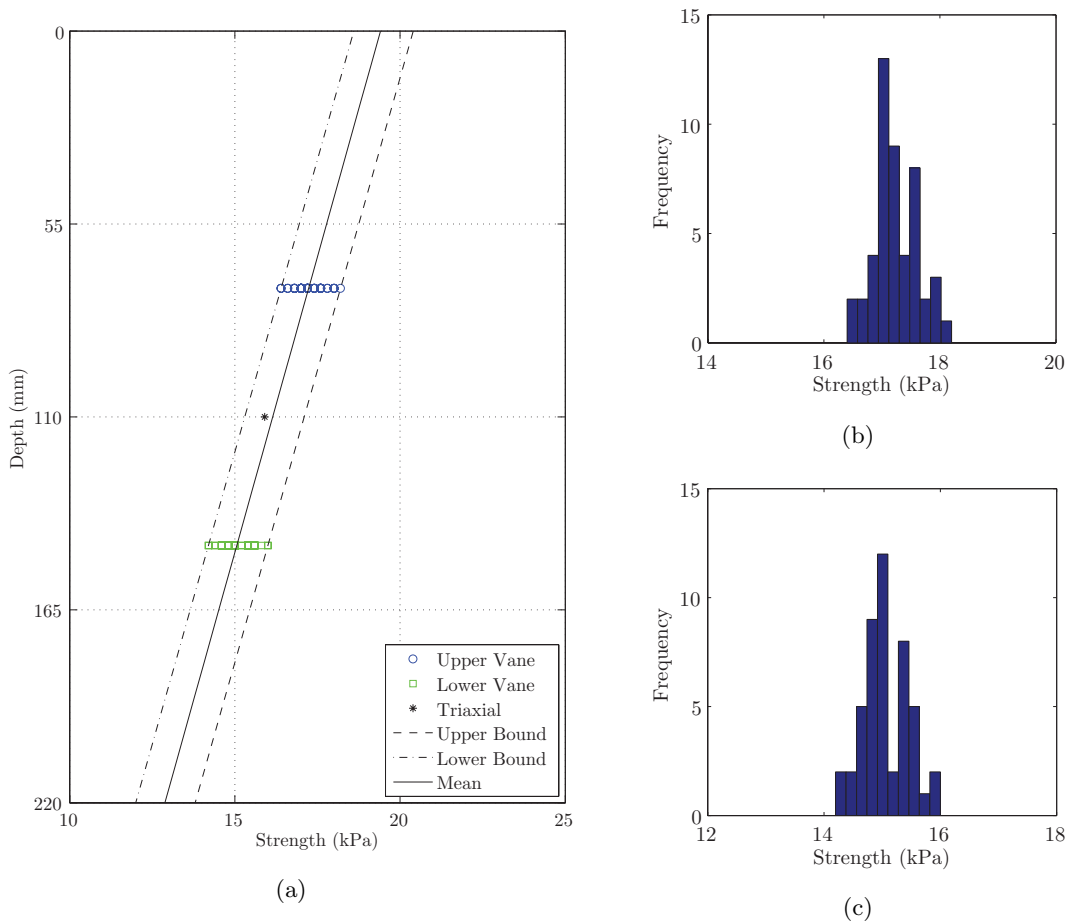


Figure 6.2: Shear strength data: (a) summary; (b) upper vane shear strength histogram; and, (c) lower vane shear strength histogram.

6.2 Post-Test Investigation of Sample Properties

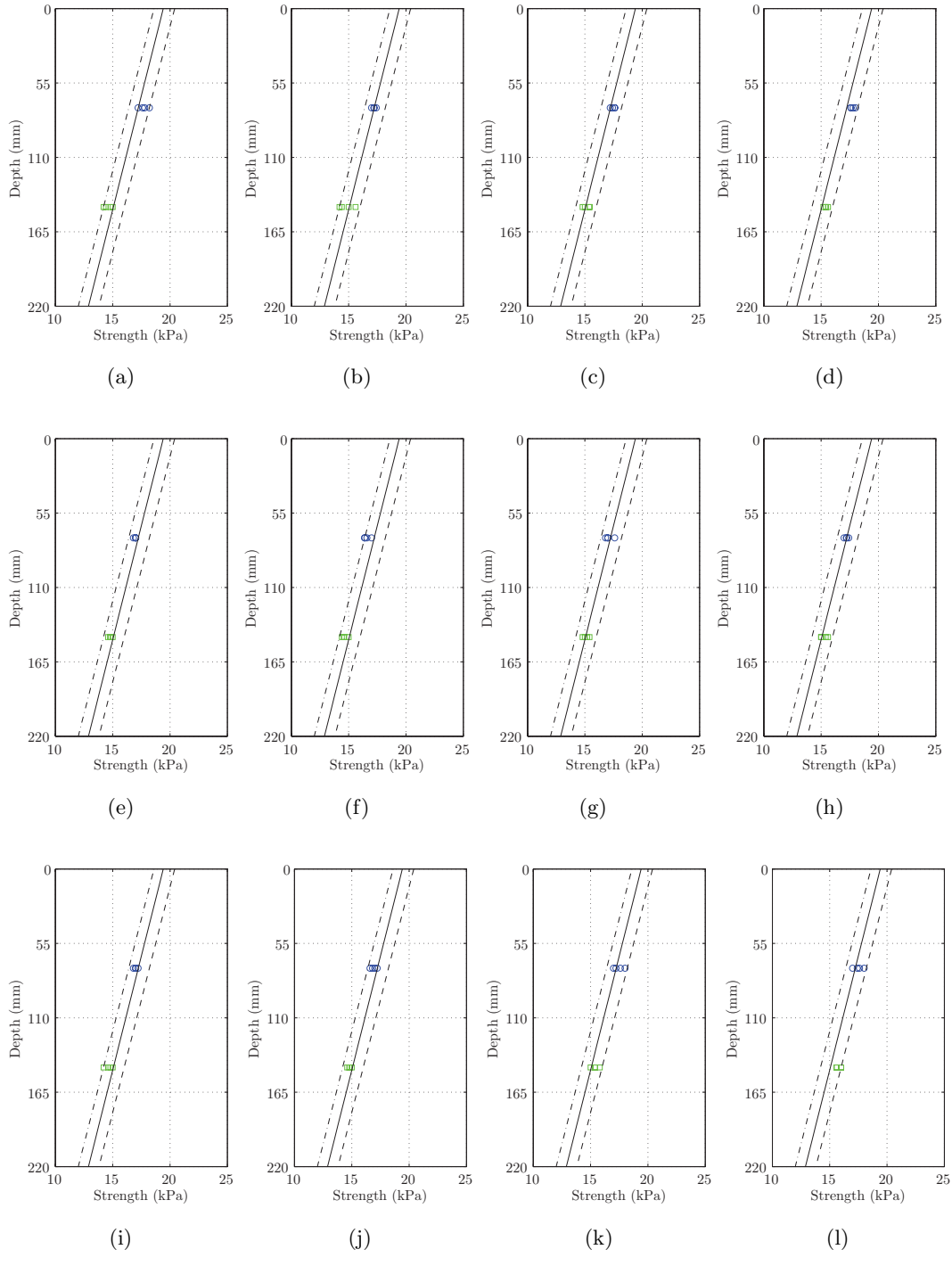


Figure 6.3: Shear strength data from individual tests: (a) C1; (b) C2-30; (c) C2-60; (d) C3; (e) T1; (f) T2-30; (g) T2-60; (h) T3; (i) C1-R; (j) C3-R; (k) F; and, (l) F-R.

by Osman and Bolton (2005). This theory postulates that the undrained settlement of a circular footing can be estimated directly from a representative stress-strain curve using axis translation. Hence non-linearity evident in the stress-strain curve, typically taken from a UU triaxial test or similar test, is incorporated in the footing settlement predictions. Due to the closed form nature of the solution, it ought to be possible to derive a theoretical UU triaxial response, allowing a non-linear constitutive model to be fitted to the data if the concept is valid. The transparent soil utilised in this investigation represents the only way in which the displacement field below a circular footing can be observed in a physical model without the boundary effects caused by a Perspex viewing window in a half space axisymmetric model, as would be required were a traditional modelling material such as kaolin used.

6.3 Mobilisable Strength Design (MSD)

Bolton and Powrie (1988) and later Osman and Bolton (2004a) developed an approach using plasticity theory and the concept of mobilisable soil strength to design retaining walls. The design method entails selecting a representative soil element for the problem, whereby the stress-strain curve for that element can be used in conjunction with a simple plastic deformation mechanism to predict displacements of the retaining wall. This methodology was later extended to predict undrained settlement of a circular footing on clay (Osman and Bolton, 2005) and was termed MSD.

This latter work proposed a plastic deformation mechanism (see Figure 6.4) consisting of a deformation boundary imposed by the Prandtl mechanism. Within this rigid boundary, the soil is split into three distinct zones, active, passive and fan, in which shearing is distributed continuously. Soil in these regions is assumed to shear and deform with no relative sliding at the boundaries of each of these three zones, such that compatibility is maintained.

Displacement components were proposed within the boundaries of the deformation mechanism that ensured compatibility and these are found in Osman (2004) and Osman and Bolton (2005). All displacements within the mechanism are proportional to the radius of the footing. Hence, the average shear strain apparent beneath the centre of the footing, $\epsilon_{s,mob}$, was calculated and related to the vertical displacement of the footing, δ , yielding a compatibility factor, M_c , which was shown in Osman (2004) to be equal to 1.35 using the relationship in Equation 6.1.

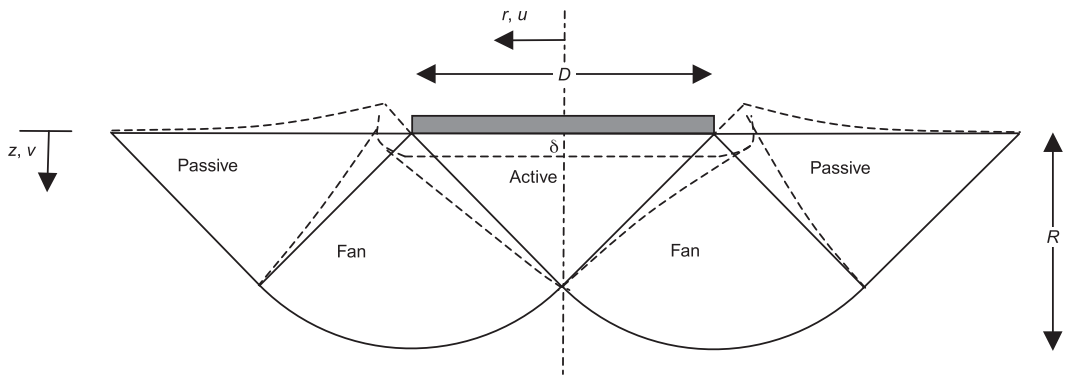


Figure 6.4: Plastic deformation mechanism for shallow circular foundation on clay, as proposed by Osman and Bolton (2005).

$$\epsilon_{s,mob} = \frac{\int \epsilon_s dvol}{\int dvol} = M_c \frac{\delta}{D} \quad (6.1)$$

The shear stresses mobilised beneath the centre of the footing, c_{mob} , were similarly related to the stress applied to the footing, σ_{mob} using the usual bearing capacity factor, N_c :

$$\sigma_{mob} = N_c \cdot c_{mob} \quad (6.2)$$

where the bearing capacity factor, N_c was calculated as 5.86 for the proposed displacement field which is only 3% greater than that calculated by Housby and Wroth (1983) of 5.69. This suggested that the solution may be a reasonable approximation for the displacement field apparent beneath a circular footing on clay. Thus, through the use of the normalisation factors M_c and N_c the load-settlement performance of a circular footing on clay can be estimated from a stress-strain curve. Given that the engineering shear strain, ϵ_s , is 1.5 times the axial strain, ϵ_a , the displacement of the footing can be expressed as:

$$\delta = \frac{1.5\epsilon_a \cdot D}{M_c} \quad (6.3)$$

This allows axis translation from axial strain, ϵ_a from a triaxial response to footing displacement, δ . Similarly, given that for an axisymmetric case the change in deviatoric stress, Δq_{mob} , is 2 times the change in mobilised shear stress, Δc_{mob} , the following axis translation can be derived to convert a change in deviatoric stress, Δq_{mob} , to a mobilised stress, σ_{mob} or force applied to the circular footing:

$$\sigma_{mob} = \frac{q_{mob} \cdot N_c}{2} \quad (6.4)$$

6.3.1 Previous Validation

Osman and Bolton (2005) used a number of case studies to validate the MSD method. Firstly an axisymmetric FE model of a 6m diameter circular footing was used in conjunction with the Strain Dependent Modified Cam Clay (SDMCC) constitutive model for clay. The 19 parameters required to calibrate the model were fitted using the triaxial compression data in Figure 6.5(a) for London clay derived experimentally by Yimsiri (2002). In-situ conditions comprised a stress history of one-dimensional consolidation to an effective stress of 1100kPa before unloading to generate a heavily overconsolidated material with the earth pressure coefficient (K_0) profile shown in Figure 6.5(b).

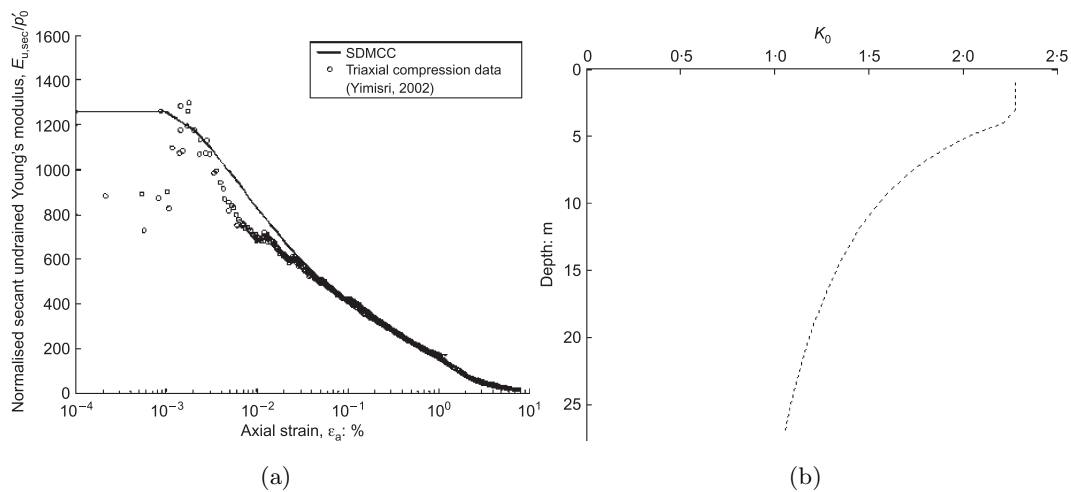


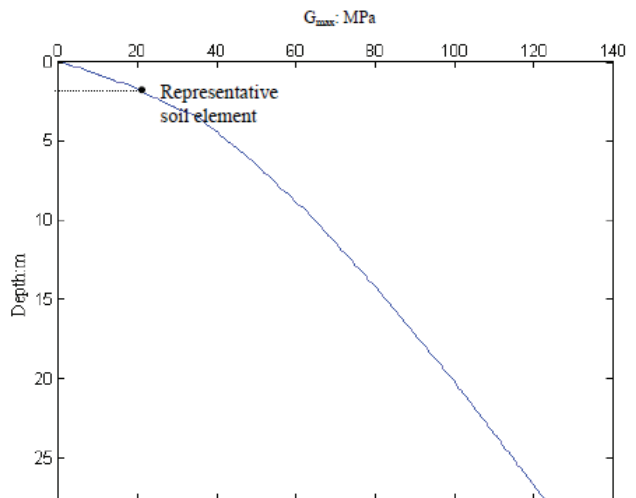
Figure 6.5: Stiffness data (a) and K_0 profile (b) assumed in FE validation of MSD concept by Osman and Bolton (2005).

The profiles of strength and stiffness with depth assumed in the FE model are shown in Figures 6.6(a) and 6.6(b), making it clear that the problem modelled

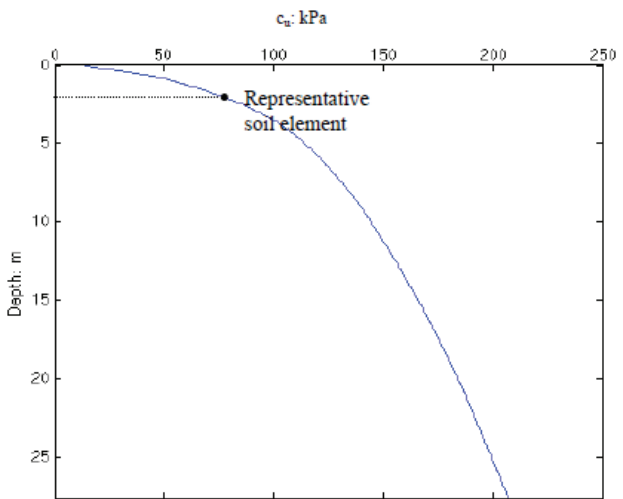
is non-linear not only in terms of the stress-strain response of the soil, but also with respect to strength and stiffness with depth. This increase of strength with depth is quite dramatic from about $10kPa$ at the surface to about $110kPa$ at the maximum depth of the assumed deformation mechanism at $\sqrt{2r^2}$ or $4.24m$. Therefore the shear strength gradient k was estimated as about $25kPa/m$, leading to the dimensionless group $\frac{kD}{S_{u_{surface}}}$ being about 15.

Choice of the representative depth at which to derive the stress-strain response using the triaxial apparatus is therefore difficult, since the deformation mechanism was derived initially for a unique stress strain response in a soil with constant S_u with depth. For simplicity it has been suggested that the representative sample for MSD calculations ought to be taken at a depth of $0.3D$ below the centreline of the footing, since this is close to the centroid of the plastic deformation zone at $0.273D$ (Osman and Bolton, 2005), or alternatively because it is close to the mid-depth of the deformation mechanism at $0.35D$ (Osman, 2004). Figure 6.6(c) is the representative stress-strain curve derived by FE simulation of a UU triaxial test for an element at a depth of $0.3D$ or $1.8m$.

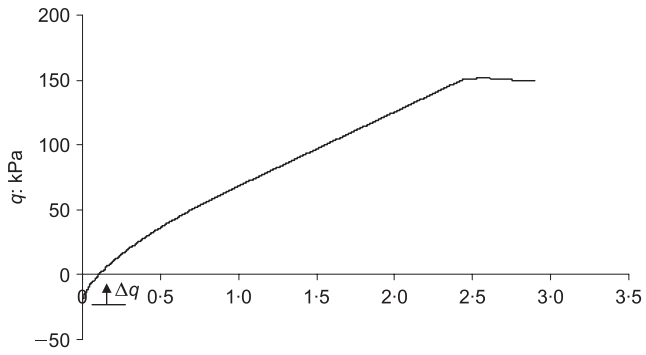
This assumption seemed to produce very good agreement with the FE simulation of the undrained settlement of the circular footing. Figure 6.7(a) illustrates that the majority of significant displacements ($< 1mm$ or $\frac{D}{6000}$) occurs within the region bounded by the Prandtl mechanism, so it was concluded that the assumed deformation mechanism reasonably approximated displacements occurring due to the undrained settlement of a smooth circular footing. However, Figure 6.7(b) shows the effect of assuming different depths at which the representative stress-strain curve is derived using an FE simulation. The settlement prediction derived using a representative sample at a depth of $0.3D$ yields good agreement between FE and MSD to within 10% over the settlement range presented. However, selecting representative depths other than $0.3D$ produced significant discrepancies between the FE and MSD derived settlement predictions. This illustrates how sensitive the choice of representative depth assumed is to the settlement predictions derived. It also serves as validation for this case that the representative depth ought to be at a depth close to either the centroid or mid-depth of the assumed deformation mechanism.



(a)



(b)



(c)

Figure 6.6: Variation of soil stiffness (a), undrained shear strength (b) and representative stress-strain curve (c) selected by Osman (2004).

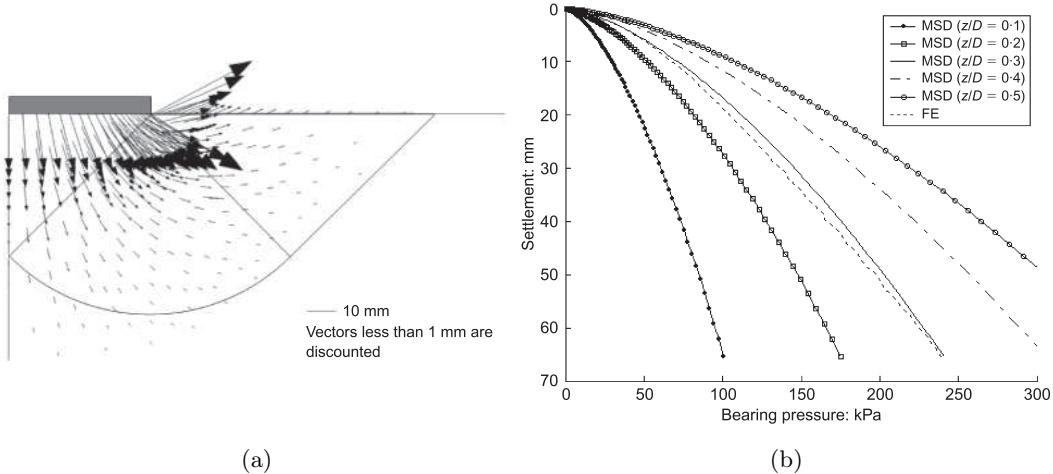


Figure 6.7: Displacement vector field at a bearing pressure of 100kPa (a) and the effect of choice of representative depth on settlement predictions (b) from Osman and Bolton (2005).

Osman and Bolton (2005) then proceeded to use back analyses of field problems relating to the undrained settlement of footings reported in the literature, at Bothkennar in Scotland and Kinnegar in Northern Ireland, to demonstrate the practical use of the MSD method. The Bothkennar site consists of a deep layer of soft clay of uncomplicated profile. The Kinnegar site consists of a depth of relatively homogeneous soft clayey silt overlain by 1m of topsoil. In both cases $\frac{kD}{S_{u_{surface}}}$ can be assumed to be relatively low. Data yielded by field tests performed on square footings at both sites were used in the MSD calculations by assuming that square and circular footings are comparable if bearing area similarity is maintained. In contrast to the original FE analysis where the footing was assumed to be smooth (implying $N_c=5.69$), the footings for these two back analyses were assumed to be rough. Hence, N_c was assumed to be 6.05 (Eason and Shield, 1960; Houlsby and Wroth, 1983) plus a correction for embedment depth (f_d) after Brinch Hansen (1970):

$$f_d = 1 + \frac{0.4z}{D} \quad (6.5)$$

However, no parallel adjustment was made to the assumed deformation mechanism to account for the fact that the footings were assumed to be rough. Consequently, the normalisation factor M_c was assumed to remain equal to 1.35. Stress-strain curves were estimated from element test data reported in the literature, to be

representative of the stress-strain response that would be observed for a soil element at the required representative depth. Both triaxial compression and extension data were used for this purpose. Settlement predictions made using the MSD method versus field measurements for the back analyses of the Bothkennar and Kinnegar data are shown in Figures 6.8(a) and 6.8(b). The results indicate that the triaxial compression and extension data appear to generate settlement prediction bounds that, for both back analyses, bracket the field measurements reasonably well.

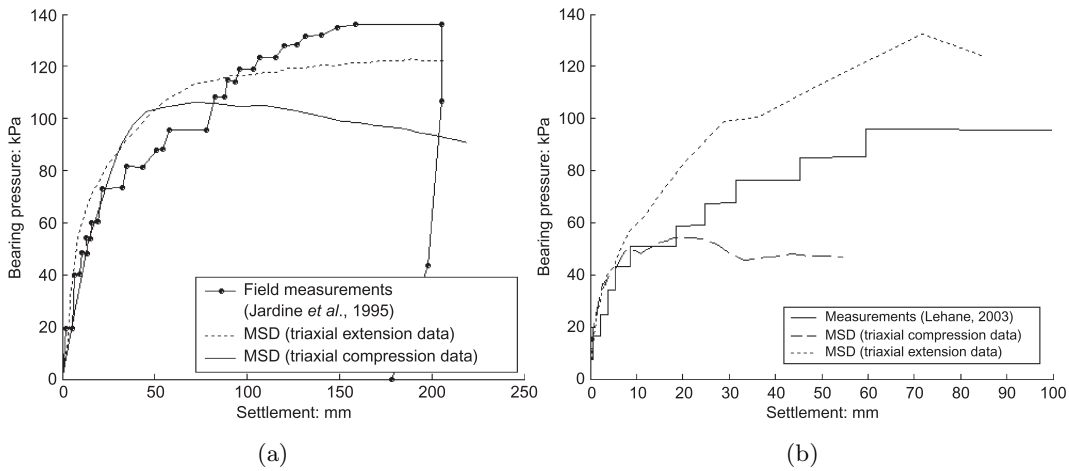


Figure 6.8: Comparison of MSD settlement predictions and field measurements at Bothkennar (a) and Kinnegar from (b) from Osman and Bolton (2005).

The question is: can the MSD framework be used to derive a non-linear stress-strain response for clay soil from the load-settlement performance of a circular footing? Is the proposed deformation mechanism a reasonable approximation of the displacement field beneath a circular footing and how valid is the assumption that N_c can be varied between 5.69 for a smooth footing and 6.05 for a rough footing without accounting for any change in the mechanics of the deformation mechanism? The following section presents a short series of small scale physical modelling tests, using transparent soil, that allow for the first time an insight into the validity of the assumptions made by Osman and Bolton (2005) and the idea that the MSD framework can be used in reverse to derive a non-linear stress strain curve for soil at shallow depths.

6.4 Physical Modelling of Undrained Settlement of a Circular Footing on Clay

A 25mm radius footing was used to investigate displacements due to the undrained settlement of a circular footing on clay soil. The Prandtl mechanism assumes displacements are limited to a radial zone of influence of $3r$ which is equal to 75mm in the model, leaving a free boundary distance of $1r$ or 25mm between the assumed extent of the deformation mechanism and the boundary. Maximising the footing size was important to maximise the size of the mechanism in the digital images captured during loading of the footing.

The test rate was defined by maintaining the dimensionless velocity factor V used in the physical modelling of the helical screw pile tests. Thus for the footing tests the test rate was reduced to 0.08mm/s, given that the footing diameter was 2.5 times the diameter of the helical plates. The values of V were checked using Equation 3.17 and the appropriate c_v values for each sample (test nomenclature for the footing tests was F for the initial test and F-R for the repeat test), from Table 3.8, which are summarised in Table 6.1. The values for V meet the same criterion suggested in Section 3.7, as V is greater than 20 in both cases, ensuring the test rate was undrained.

Table 6.1: Drainage estimation using normalised velocity approximation from Lehane et al. (2008) for footing tests.

Test	Dimensionless Velocity (V)
F	30.68
F-R	30.47

As a result of the footing diameter specified, $\frac{kD}{S_{u_{surface}}}$ was equal to -0.08, close to zero, indicating high strength homogeneity over the assumed depth of influence of the footing. All footing tests presented herein were performed in 200mm by 200mm by 220mm (W by D by H) samples, for which consolidation properties are presented in Chapter 3.

6.4.1 Load-Deflection Response

The consolidated sample exhibited a curved surface, as a result of post-consolidation swelling and sidewall friction within the test chamber. This is illustrated by Figure

6.4 Physical Modelling of Undrained Settlement of a Circular Footing on Clay

6.9 which is an extract of the first digital image used in the analysis process.

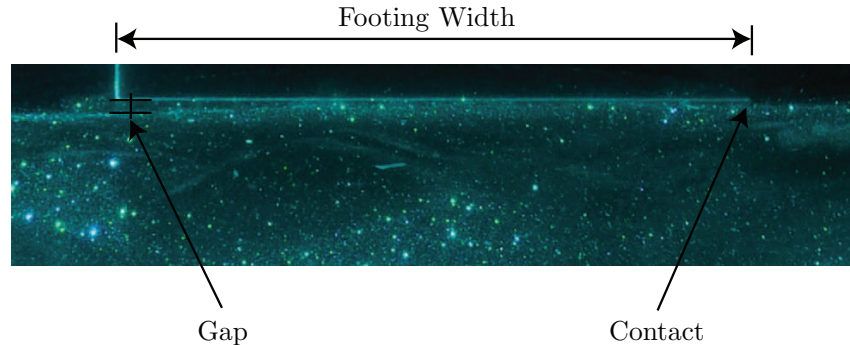


Figure 6.9: Curved sample surface and resulting uneven initial contact of footing.

This led to significant bedding errors in the load-deflection response as illustrated by Figure 6.10(a). To correct for this error, the linear portion of the response was extrapolated back to the horizontal axis and the displacement measurements were then corrected, such that the corrected response intersects the origin of the plot. The corrected response is presented in Figure 6.10(b). The ultimate capacity was reached at a settlement of about 8-10mm.

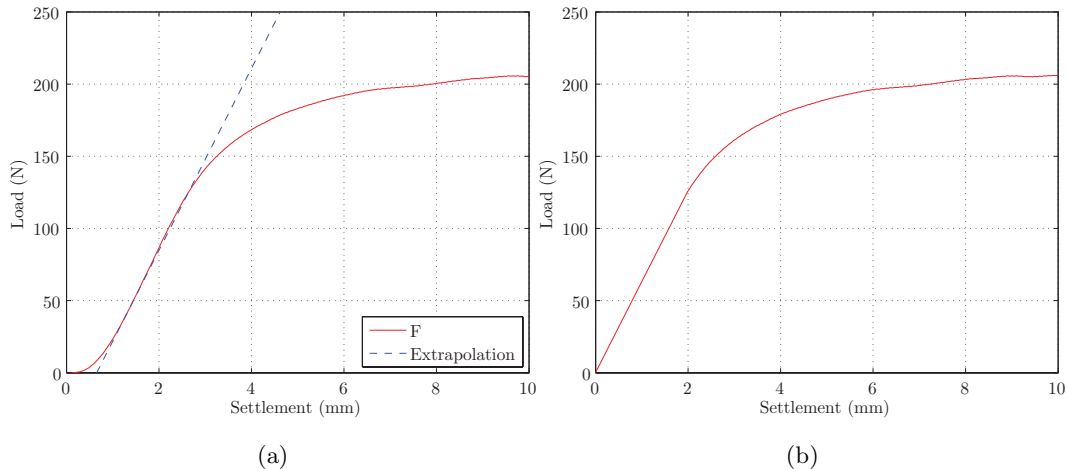


Figure 6.10: Footing load-deflection response under axial compressive loading: (a) raw response with linear extrapolation to account for bedding errors; and, (b) corrected response.

6.4.2 Analysis Method

During loading of the circular footing digital images were recorded at a rate of 3fps up to a maximum settlement of 20mm. The ULS was mobilised (identified

6.4 Physical Modelling of Undrained Settlement of a Circular Footing on Clay

by levelling off in load-deflection response) at a settlement of about $8mm$. In this instance data is plotted for increments up to $10mm$ to demonstrate that the ULS deformation mechanism has been mobilised meaning that a series of about 375 images was identified, over which PIV analysis was conducted in increments of $2mm$ settlement.

The ‘leapfrog’ parameter within GeoPIV was set to 10 for analysis of images recorded during footing settlement testing. The ‘searchzone’ parameter was set to 10px or $0.65mm$ when converted to metric units using the approximate linear scaling factor introduced in Chapter 4. Since the axial displacement rate was $0.08mm/s$ and the camera frame rate was 3fps, the maximum displacement present within the model must be less than the displacement rate divided by the camera frame rate, or about $0.027mm$. This is significantly smaller than the ‘searchzone’ defined within GeoPIV and leaving a margin for error regarding the size of ‘searchzone’ chosen. Table 6.2 presents the displacement and shear strain contours plotted in the PIV analyses of settlements below a circular footing on clay.

Table 6.2: Contours of displacement and shear strain presented in footing test contour plots.

Plot	Increments
Horizontal Displacement (mm)	-3, -2, -1, -0.5, -0.2, -0.1, -0.05, -0.025, 0, 0.025, 0.05, 0.1, 0.2, 0.5, 1, 2, 3
Vertical Displacement (mm)	-10, -9, -8, -7, -6, -5, -4, -3, -2, -1, -0.5, -0.2, -0.1, -0.05, -0.025, 0, 0.025, 0.05, 0.1, 0.2, 0.5, 1, 2, 3, 4, 5, 6
Shear Strain (%)	1, 2.5, 5, 10, 25, 50, 75, 100, 125, 150, 175, 200

Due to the increased value of ‘leapfrog’ used in this analysis compared to the PIV analyses conducted on the helical pile test data, it has been possible to plot the 1% shear strain contour. A higher value of ‘leapfrog’ was suitable for use without generating wild random vectors because the mechanism is more evenly divided into horizontal and vertical components. Therefore the shear strain field is less concentrated than for the helical pile analyses. This preserved correlation between the initial patch in the first image and the search patch in the target image as each patch was distorting less significantly between PIV computations.

To account for the bedding errors apparent in the load-deflection response, all displacements were zeroed at an axial displacement of the footing equal to the axis

translation used to remove the bedding errors from the load-deflection response. Vectorial displacement plots in this instance are not amplified, as the displacements are sufficiently large in their natural state.

6.4.3 Data Appraisal

Data quality was assessed by considering the magnitudes of movement correction applied to the raw data to account for non-coplanarity in the same manner as for previous PIV analyses presented previously. Table 6.3 presents a summary of the horizontal and vertical camera-soil movement corrections applied to the settlement increment data presented in Section 6.4.4. The percentage of vectors with modal magnitude of displacement are larger for this case than for the helical pile tests as the associated deformation mechanism is more localised. The value of the camera-soil movement correction was demonstrated in Section 5.3.3, so is not repeated here.

Table 6.3: Magnitude of horizontal (u_c) and vertical (v_c) correction specified by modal movement correction process for footing test.

Test	δ (mm)	Correction			
		Horizontal		Vertical	
		u_c (μm)	$\%_u$	v_c (μm)	$\%_v$
F	2	3	16.22	3	14.32
	4	14	4.53	19	3.65
	6	15	2.66	38	3.28
	8	8	2.34	26	2.71
	10	1	2.45	10	2.60

6.4.4 Displacement and Shear Strain Fields

The following section contains PIV derived displacement and shear strain fields for the circular footing settlement test. The cumulative displacements and shear strain fields are presented for settlements of 2, 4, 6, 8 and 10mm. In addition to this incremental results are shown for 2-4mm, 4-6mm, 6-8mm and 8-10mm settlement, since these results best demonstrate development of the ULS deformation mechanism, where successive incremental displacement and shear strain fields are similar.

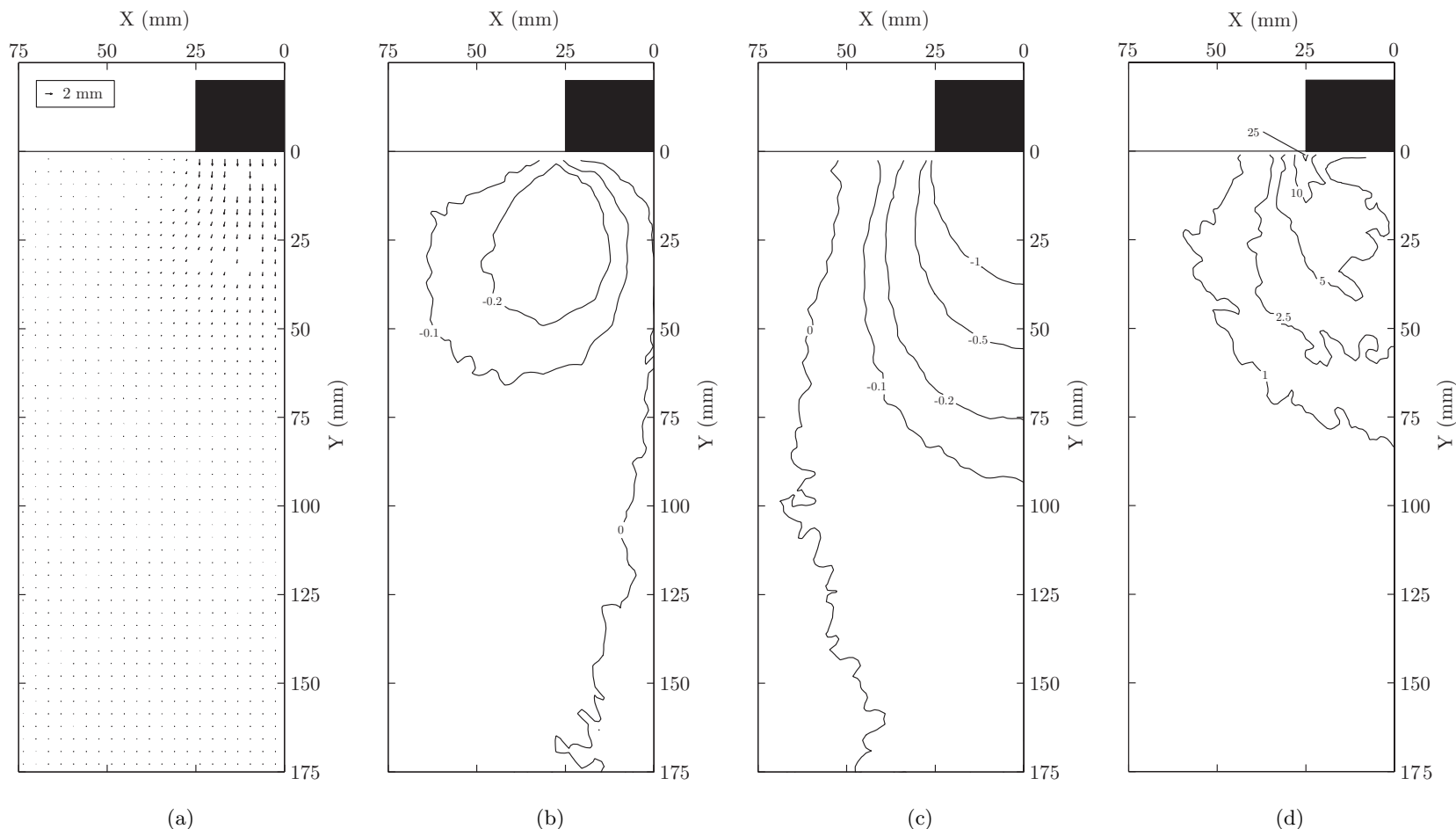


Figure 6.11: Footing tests (F) PIV results for 2mm settlement: vector (a), horizontal displacement contours (b), vertical displacement contours (c) and shear strain contours (d) with displacements in mm and shear strains expressed as a percentage.

6.4 Physical Modelling of Undrained Settlement of a Circular Footing on Clay

302

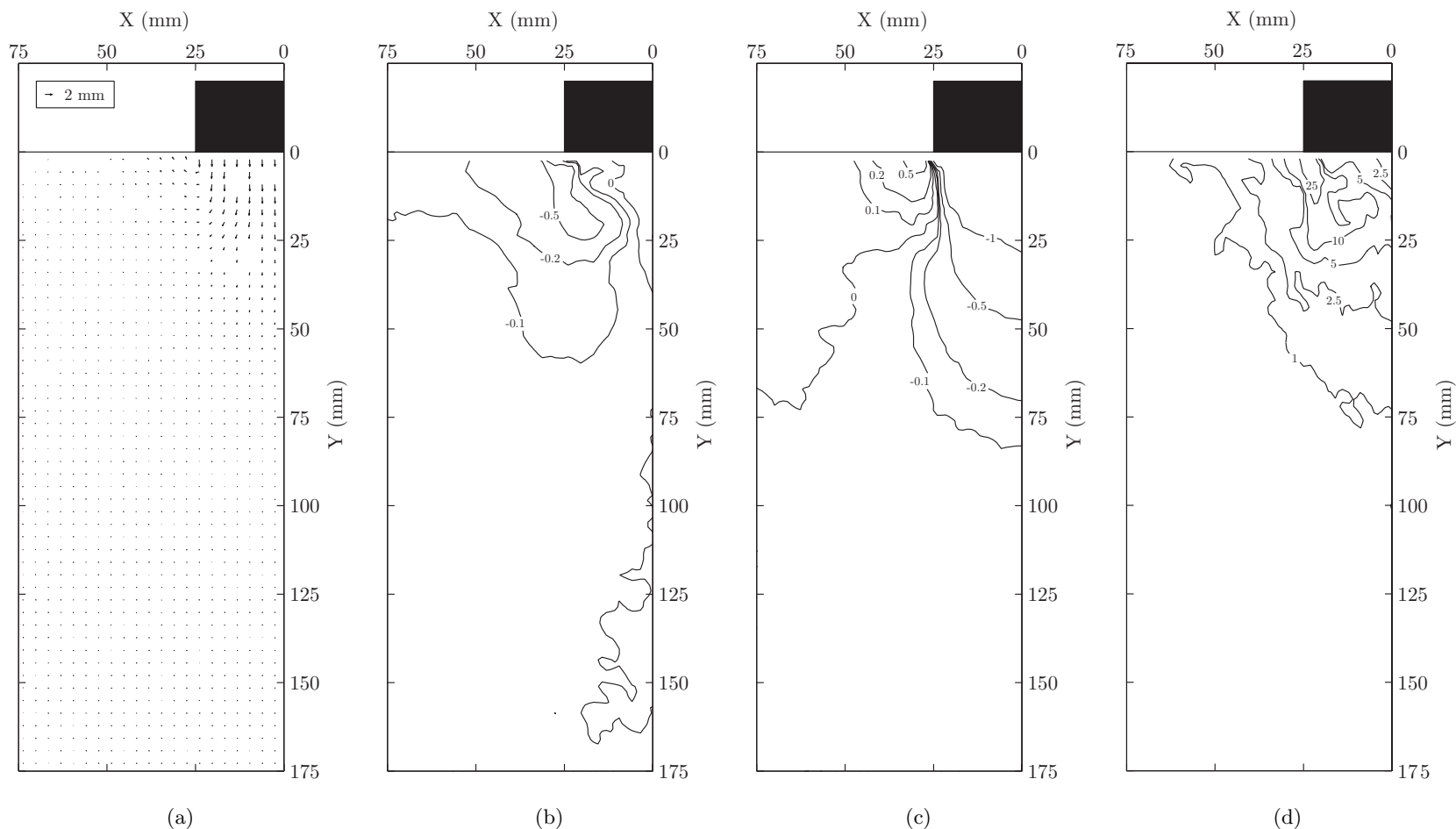


Figure 6.12: Footing test (F) PIV results for 2-4mm settlement increment: vector (a), horizontal displacement contours (b), vertical displacement contours (c) and shear strain contours (d) with displacements in mm and shear strains expressed as a percentage.

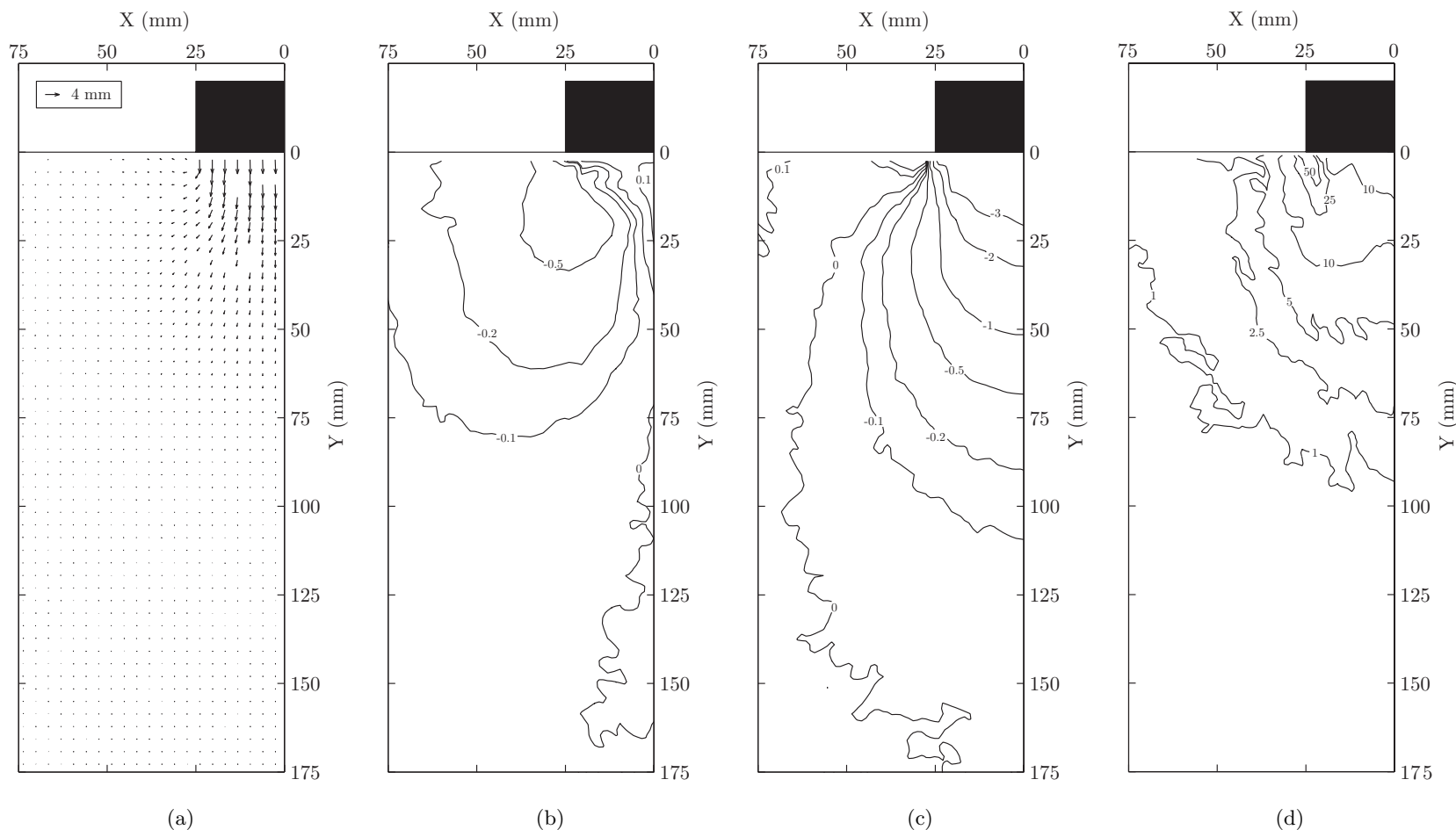


Figure 6.13: Footing tests (F) PIV results for 4mm settlement: vector (a), horizontal displacement contours (b), vertical displacement contours (c) and shear strain contours (d) with displacements in mm and shear strains expressed as a percentage.

6.4 Physical Modelling of Undrained Settlement of a Circular Footing on Clay

304

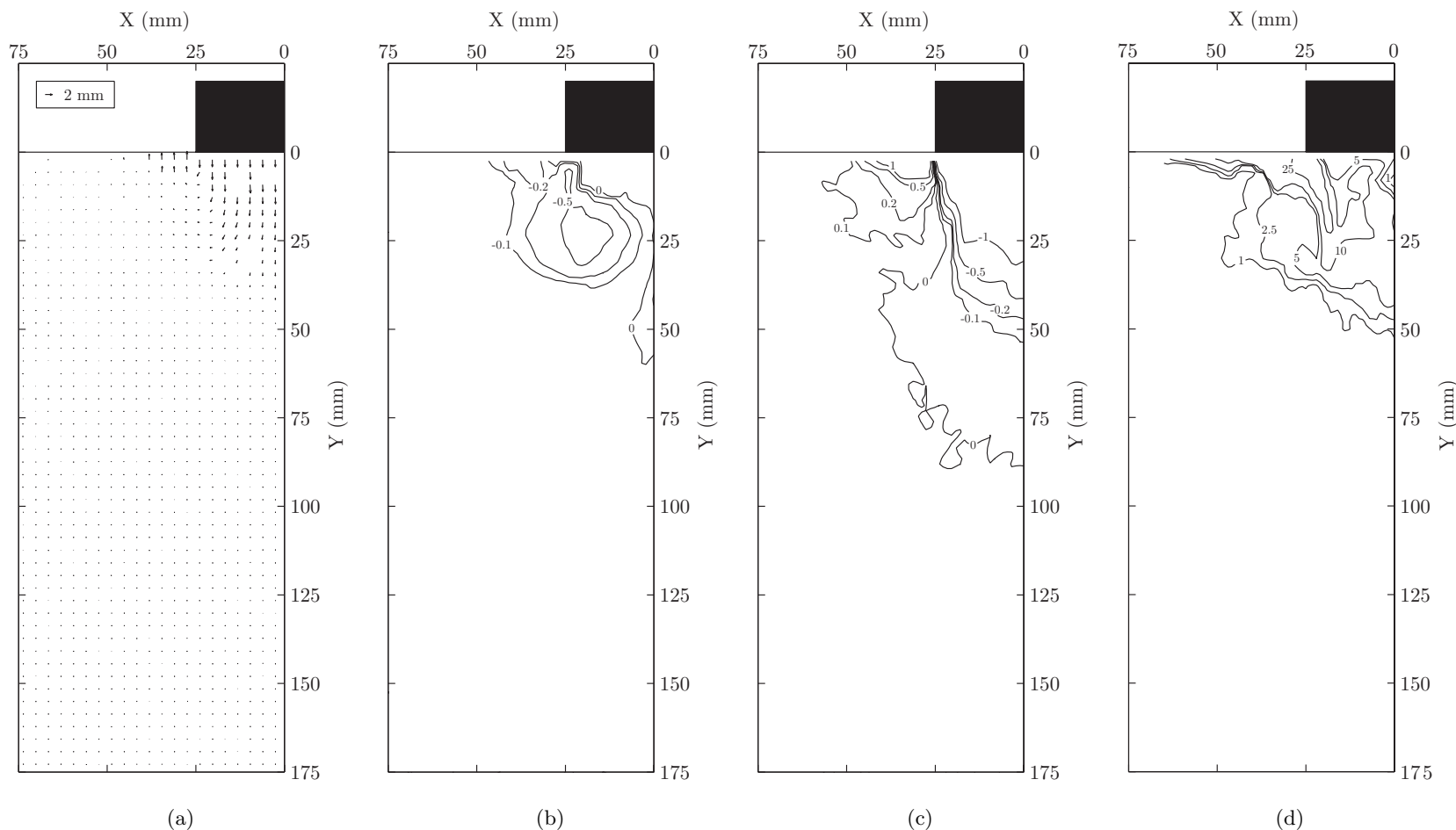


Figure 6.14: Footing test (F) PIV results for 4-6mm settlement increment: vector (a), horizontal displacement contours (b), vertical displacement contours (c) and shear strain contours (d) with displacements in mm and shear strains expressed as a percentage.

6.4 Physical Modelling of Undrained Settlement of a Circular Footing on Clay

305

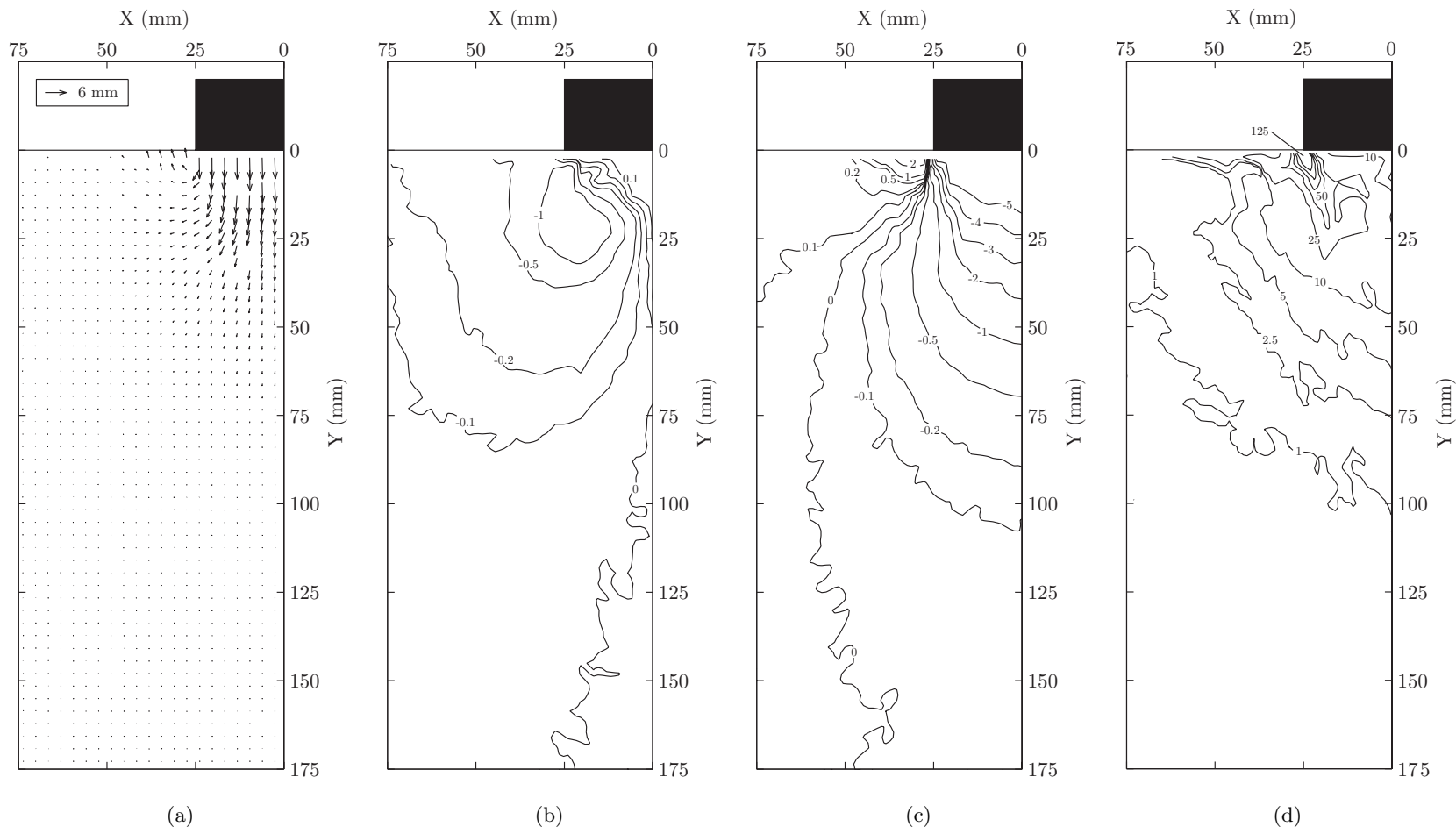


Figure 6.15: Footing test (F) PIV results for 6mm settlement: vector (a), horizontal displacement contours (b), vertical displacement contours (c) and shear strain contours (d) with displacements in mm and shear strains expressed as a percentage.

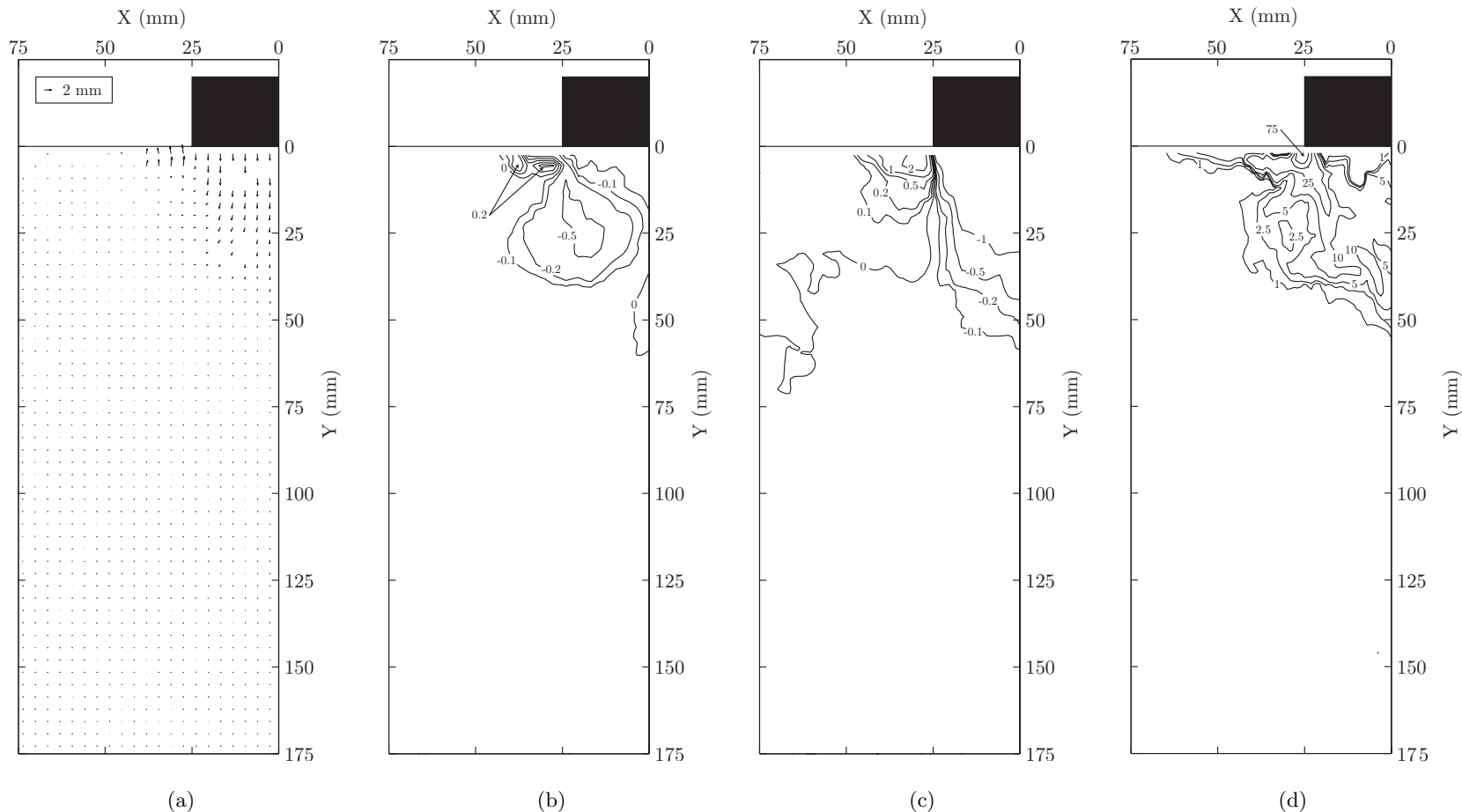


Figure 6.16: Footing test (F) PIV results for 6-8mm settlement increment: vector (a), horizontal displacement contours (b), vertical displacement contours (c) and shear strain contours (d) with displacements in mm and shear strains expressed as a percentage.

6.4 Physical Modelling of Undrained Settlement of a Circular Footing on Clay

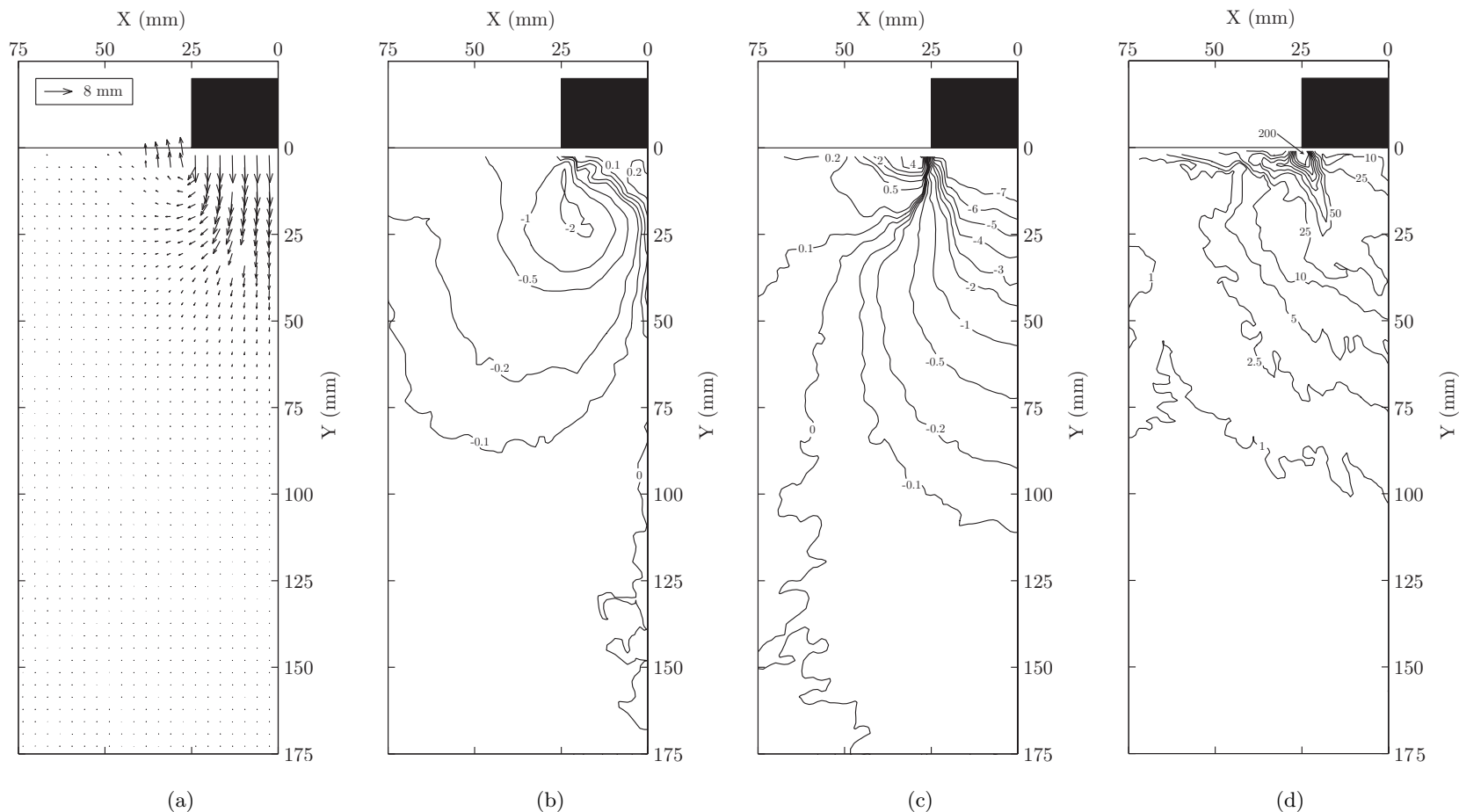


Figure 6.17: Footing test (F) PIV results for 8mm settlement: vector (a), horizontal displacement contours (b), vertical displacement contours (c) and shear strain contours (d) with displacements in mm and shear strains expressed as a percentage.

6.4 Physical Modelling of Undrained Settlement of a Circular Footing on Clay

308

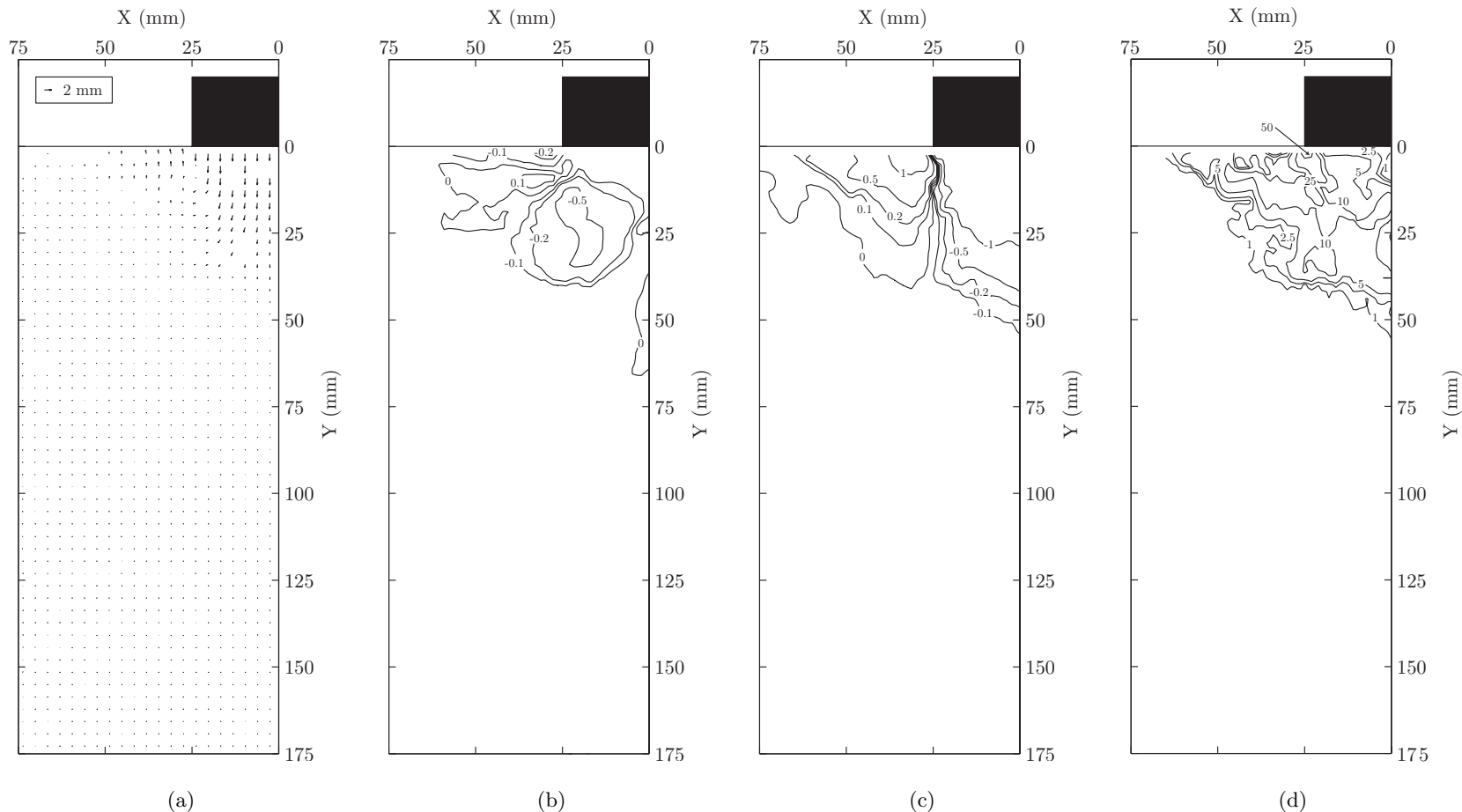


Figure 6.18: Footing test (F) PIV results for 8-10mm settlement increment: vector (a), horizontal displacement contours (b), vertical displacement contours (c) and shear strain contours (d) with displacements in mm and shear strains expressed as a percentage.

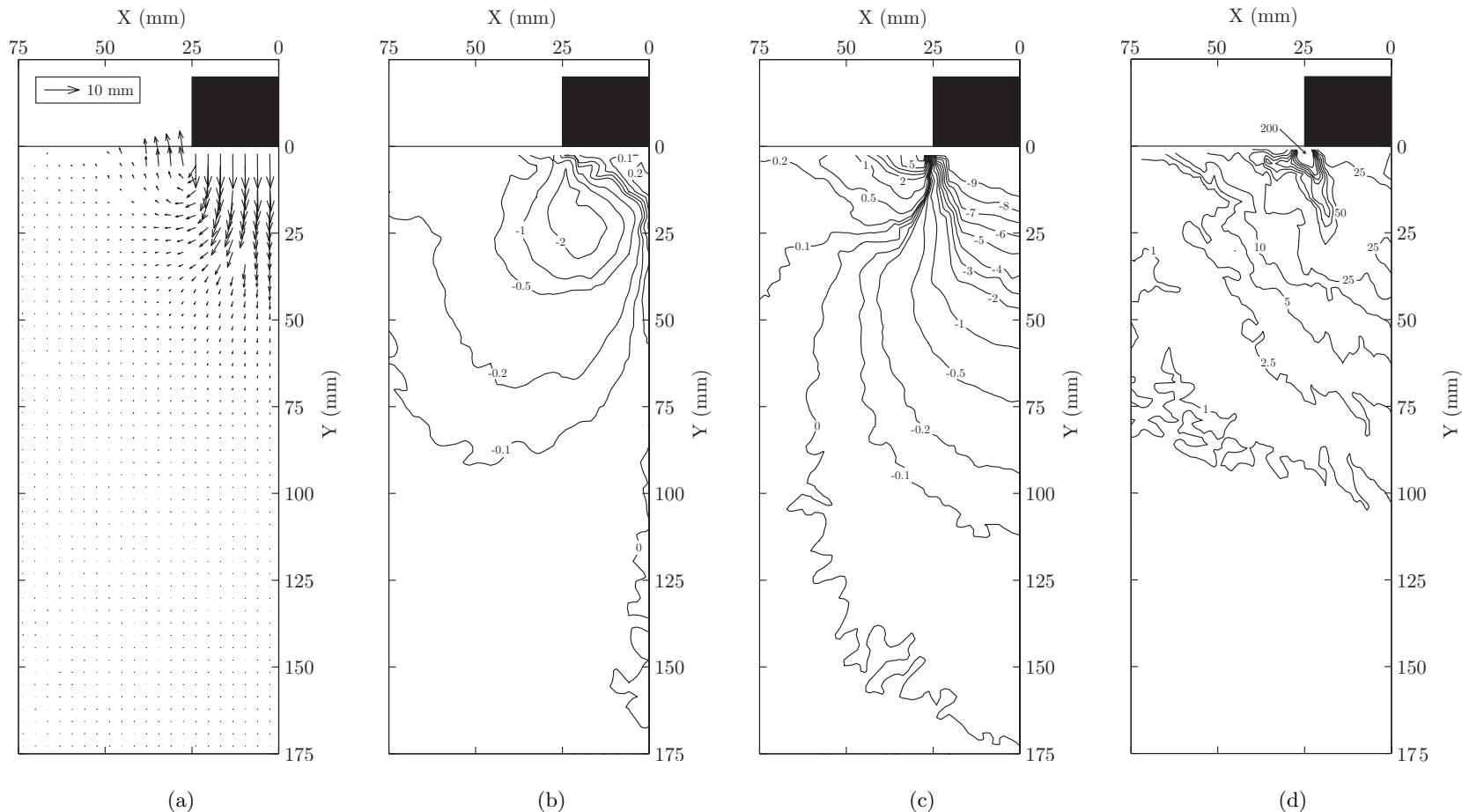


Figure 6.19: Footing test (F) PIV results for 10mm settlement: vector (a), horizontal displacement contours (b), vertical displacement contours (c) and shear strain contours (d) with displacements in mm and shear strains expressed as a percentage.

6.4.5 Observations

6.4.5.1 Development of Ultimate Limit State

In Section 6.4.1 the ULS was signified by there being no increase in capacity for an increasing increment of settlement. This state was reached at around $8mm$ settlement. The PIV derived displacement and shear strain fields can also be used to illustrate the mobilisation of the ULS and the formation of a deformation mechanism.

Figure 6.11 is a set of plots presenting the displacement and shear strain fields caused by the initial $2mm$ settlement of the model footing. Figures 6.12, 6.14, 6.16 and 6.18 are plots of the displacement and shear strain fields due to subsequent increments of $2mm$ settlement. Since the settlement of the footing for all these results is $2mm$ at different stages of the load-deflection response, the displacement and shear strain fields are all directly comparable and can be used to assess the development of the ULS.

Figure 6.11(a) is a plot of the vectorial displacements caused by the first $2mm$ of settlement. Figures 6.11(b) and 6.11(c) are contour plots of the horizontal and vertical displacements induced by the settlement. These show that the initial mechanism extends to a significant depth within the sample and that soil immediately adjacent to the footing at the soil surface also experiences settlement. A small amount of heave is apparent in the far field of the sample. Horizontal displacements are largest at a depth of $25mm$ below the toe of the footing. Figure 6.11(d) is a contour plot of the shear strains caused by the initial settlement showing the zone of influence extends to a depth of up to $75mm$ below the centre of the footing. The largest concentration of shearing is at the toe of the footing as would be expected.

The second increment of $2mm$ settlement, from $2-4mm$ settlement, yields the vector field in Figure 6.12(a). The components of horizontal and vertical displacement are presented in the contour plots in Figures 6.12(b) and 6.12(c). The horizontal displacements are more highly concentrated around the toe of the footing and have a smaller area of influence in this increment. The vertical displacements show that the mechanism is localising and beginning to generate concentrated heave at the toe of the footing. This is highlighted by the reduced area of influence apparent in the shear strain contour plot in Figure 6.12(d) where maximum shearing is apparent beneath the toe of the footing in a very concentrated region.

6.4 Physical Modelling of Undrained Settlement of a Circular Footing on Clay

The third increment of $2mm$ settlement from $4-6mm$ settlement further demonstrates the trend of increasing localisation of the displacement and shear strain fields. Figure 6.14(a) is a plot of the vectorial displacements showing clear heave at the soil surface towards the toe of the footing. The horizontal and vertical displacement contours in Figures 6.14(b) and 6.14(c) illustrate the fact that the mechanism has localised further. Horizontal displacements are limited to an area immediately beneath the toe of the footing and the extent of the vertical displacement field has reduced further. The shear strain field in Figure 6.14(d) illustrates that the depth of influence of the mechanism is reducing as the ULS is reached, whilst maximum shearing is apparent, as expected, in a band beneath the toe of the footing.

The fourth and fifth increments of $2mm$ settlement from $6-8mm$ and $8-10mm$ show that the deformation mechanism is fully formed and that the ULS is mobilised. Figures 6.16(a) and 6.18(a) are the vector fields for these increments of settlement. The corresponding horizontal and vertical displacement fields in Figures 6.16(b) and 6.18(b) and Figures 6.16(c) and 6.18(c) are almost identical to those apparent for the previous $2mm$ increment of settlement from $4mm$ to $6mm$ settlement. The shear strain fields in Figures 6.16(d) and 6.18(d) are also very consistent with those for the previous increment.

6.4.5.2 Soil-Footing Interface

Another interesting observation relates to the horizontal displacements apparent immediately beneath the footing. Figures 6.11 and 6.19(b) are alternately the cumulative and incremental horizontal displacement plots caused by the footing settlement. In all of these plots immediately beneath the centre of the footing it is apparent that the horizontal movement is non-zero. Rightward movement of soil is apparent which increases in magnitude with increasing settlement.

Ordinarily the horizontal displacement immediately beneath the centre of the footing would be expected to be zero. Figure 6.9 illustrated that the soil surface was uneven, subsequently causing contact between the soil and the footing to occur first on the right hand side of the footing, leaving a small gap on the left hand side. It is this uneven initial contact that is responsible for the non-zero horizontal displacement immediately beneath the centre of the footing.

6.4.5.3 Depth of Deformation Mechanism

Reference to the Prandtl mechanism proposed by Osman and Bolton (2005) suggests that the maximum depth of the deformation mechanism immediately beneath the centre a circular footing can be assumed to be at a depth of $D/2$. In this instance where the footing diameter is 50mm, the depth of the deformation mechanism might have been expected to be no greater than 25mm.

However, Figure 6.19(d) is a plot of the cumulative shear strain caused by 10mm settlement, indicating that soil up to a depth of almost 100mm or 2D has been subjected to some shear straining. Similarly, Figure 6.18(d), which is a plot of shear strain for a 2mm increment of displacement at the ULS, shows that even when the deformation mechanism is fully formed, the depth of the deformation mechanism extends to 50mm or 1D, which is twice that suggested by the deformation mechanism proposed by Osman and Bolton (2005).

6.4.6 Repeatability

The repeatability of modelling the undrained settlement of a circular footing on clay was assessed by performing a repeat test, test F-R. Figure 6.20(a) is a plot of the load-deflection response and extrapolation of the linear portion of the initial response to correct for bedding errors. Figure 6.20(b) is the resulting load-deflection response post-correction.

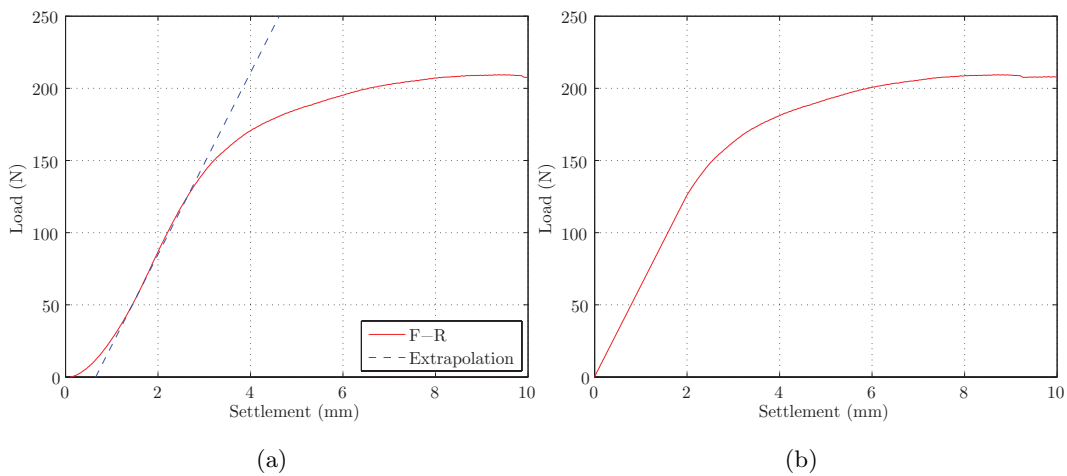


Figure 6.20: Footing repeat load-deflection response under axial compressive loading: (a) raw response with linear extrapolation to account for bedding errors; and, (b) corrected response.

6.4 Physical Modelling of Undrained Settlement of a Circular Footing on Clay

Comparison between the initial and repeat test is summarised in Figures 6.21(a) and 6.21(b), which include a mean response and an analysis of the percentage discrepancy of the capacity, in relation to the ultimate capacity of the mean response. This shows that the load-deflection response, after correction for bedding errors, is clearly repeatable as the maximum discrepancy between the two tests is about 4%. The maximum deviation from the mean response is $\pm 2\%$. This is not surprising since the measured strength of the samples for the initial test (F) and repeat test (F-R) are very similar, as indicated by the plots in Figures 6.3(k) and 6.3(l) in Section 6.2.

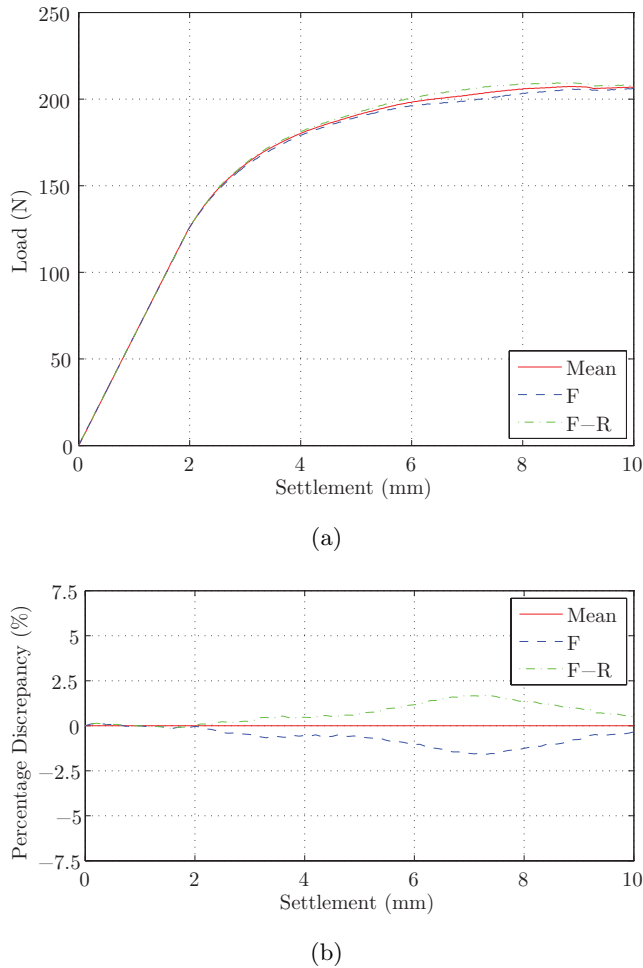


Figure 6.21: Repeatability of footing test: (a) versus mean response; and, (b) associated percentage discrepancy.

A further assessment of the repeatability of the modelling procedure is provided by assessing the displacement and shear strain fields generated at a settlement of 10mm in the repeat test in comparison to the corresponding data from the initial test presented in Section 6.4.4. Table 6.4 is a summary of the camera-soil movement correction applied and the percentage of vectors with modal magnitude, at a settle-

ment of 10mm. The magnitudes of correction are slightly larger and the percentage of vectors with modal magnitude slightly smaller than for the initial test. This indicates that camera-soil movement was more prevalent in this data set compared to the initial test.

Table 6.4: Magnitude of horizontal (u_c) and vertical (v_c) correction specified by modal movement correction process for repeat footing test.

Test	δ (mm)	Correction			
		Horizontal		Vertical	
		u_c (μm)	$\%_u$	v_c (μm)	$\%_v$
F-R	10	-10	1.64	31	2.96

Figure 6.22 presents the displacement and shear strain fields apparent at a settlement of 10mm, which are directly comparable to those presented in Figure 6.19. Due to poor texture near to the toe of the footing, a significant number of vectors required removal from the output data. This results in apparently reduced strain at the toe of the footing at the soil surface in Figure 6.22(d) compared to Figure 6.19(d). This also causes the amount of heave at the soil surface at the toe of the footing to appear to be reduced in Figure 6.22(c) compared to Figure 6.19(c). It is unfortunate that the texture was poor in this critical region in this test and multiple attempts were made to perform the PIV analysis with different mesh positions with no success. This only served to prove that it is the poor texture rather than patch positioning that is responsible for the poor tracking in this zone.

Aside from the differences arising from the problems caused by poor texture quality at the toe of the footing, the results are generally similar. The extent of the deformation mechanism is very consistent and indicated by comparing the shear strain fields in Figures 6.22(d) and 6.19(d), where the depth of the deformation mechanism appears to extend to about 100mm depth beneath the centre of the footing.

The magnitudes of horizontal and vertical displacement are also very similar as illustrated by comparing Figures 6.22(b) and 6.19(b) and Figures 6.22(c) and 6.19(c). The general trends apparent in both the initial and repeat tests are the same. The maximum magnitude of horizontal displacement and extent of vertical displacement in the repeat test was slightly greater than that seen in the initial test, but not significantly so. The contour of 3mm horizontal displacement seen in

6.4 Physical Modelling of Undrained Settlement of a Circular Footing on Clay

Figure 6.22(b) is likely to be due to a single measurement point. The discrepancy of the extent of vertical displacements is likely due to different bedding errors being apparent in each case.

One other minor discrepancy is the magnitude of horizontal movement apparent beneath the centre of the footing. In this repeat test the magnitude of horizontal displacement immediately beneath the centre of the footing is about $0.2mm$, which is greater than that seen in the initial test. In Section 6.4.5.2 non-zero horizontal movement at the centre of the footing was attributed to the curved surface profile of the sample and uneven contact of the footing during bedding in and this was even more significant in the repeat test. The gap at the left hand side of the footing was even greater in the repeat test when initial contact was made on the right hand side of the footing. This is further evidence that the curved surface of the sample caused the non-zero horizontal displacements apparent immediately beneath the centre of the footing.

Irrespective of the minor discrepancies documented, the repeat test shows that particularly in respect to the general deformation mechanism, its extent and associated load-deflection response, the modelling process adopted here is repeatable. The next stage was to investigate the use of the closed form axis translations proposed by Osman and Bolton (2005) to relate a stress-strain response to the load-deflection response of a circular footing on clay. For this purpose due to the similarity of the two load-deflection responses presented in Figure 6.21(a) the mean response will be considered in all further analysis and referred to as the ‘MSD’ response.

6.4 Physical Modelling of Undrained Settlement of a Circular Footing on Clay

316

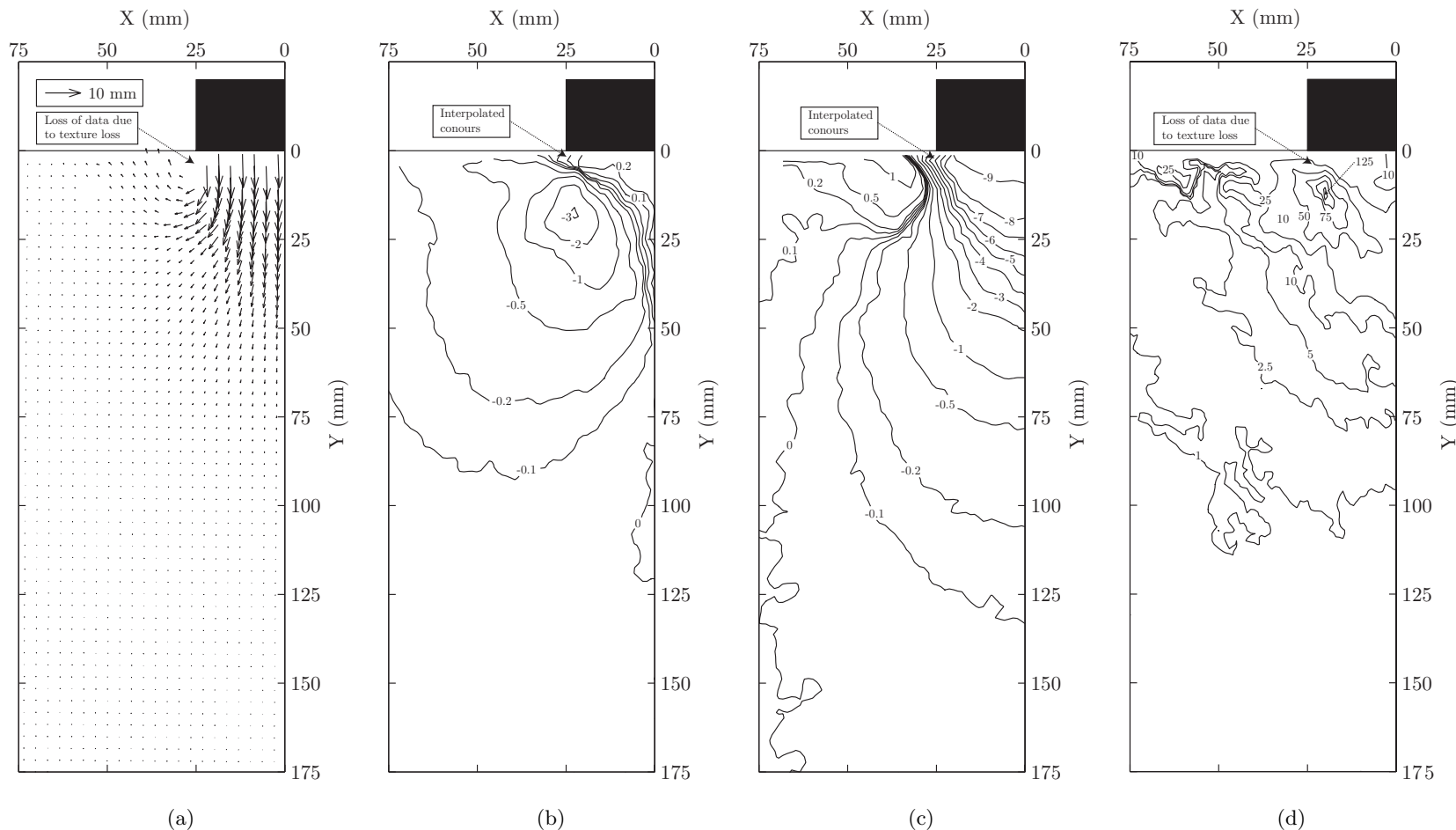


Figure 6.22: Repeat footing test (F-R) PIV results for 10mm settlement: vector (a), horizontal displacement contours (b), vertical displacement contours (c) and shear strain contours (d) with displacements in mm and shear strains expressed as a percentage.

6.5 Comparison with MSD Mechanism

Figure 6.23 shows plots of the displacement and shear strain fields predicted by the deformation mechanism proposed in Figure 6.4, using the equations for displacement in the active, fan and passive zones given by Osman and Bolton (2005). The shear strain was calculated using the ‘GeoSTRAINS’ routine (White and Take, 2002) using a nodal spacing and density similar to that used in the PIV analysis so the effects of strain smearing are constant. Hence, the results are directly comparable with those from the PIV analysis at mobilisation of the ULS such as in Figure 6.18. The contours of displacement and shear strain are the same as those used to present the PIV data in Section 6.4.4 which are summarised in Table 6.2.

Comparing Figures 6.23(a) and 6.18(a) shows that in the assumed deformation mechanism larger magnitudes of horizontal displacement are predicted along the soil-footing interface than are observed in the physical model. Contrasting Figures 6.23(b) and 6.18(b) demonstrates the effect of this on the horizontal displacement fields. In the proposed deformation mechanism, maximum horizontal displacement is concentrated at the toe of the footing at the soil surface. In the physical model maximum horizontal displacement occurs at a depth of $D/2$ beneath the toe of the footing. Comparison of Figures 6.23(c) and 6.18(c) potentially illustrates that the effect of reduced horizontal displacement at the soil-footing interface is to induce greater vertical displacement within the physical model. Correspondingly the depth of influence apparent in the physical model was significantly greater than the deformation mechanism proposed by Osman and Bolton (2005). Lastly, comparison of Figures 6.23(d) and 6.18(d) shows that maximum shearing is apparent in both cases immediately beneath the toe of the footing. However the magnitude predicted by the assumed deformation mechanism is much greater than that observed, but the extent of the shear strain fields is correspondingly reduced. Contrasting velocity fields coupled with comparable failure loads is evident in the classical solution that forms the basis of the mechanism assumed by the MSD method, that of a circular punch on plastic material. Prandtl (1921), Hill (1950) and Levin (1955) all used differing velocity fields to derive very similar bearing capacity factors for the failure load of a circular surface foundation.

More recently, White et al. (2005) presented evidence of the same phenomenon in drum centrifuge modelling tests of eccentrically loaded skirted foundations, as

velocity field dissimilarity and failure load similarity was also observed. The authors inferred that, since there are numerous mechanisms that may yield a similar failure load for any given problem in a perfectly plastic material, that rate effects or strain softening of the soil may have caused the velocity field discrepancies observed during their investigation. These experiences potentially help to account for the mechanistic dissimilarity seen here between the behaviour observed in the physical models, and that predicted by the MSD method.

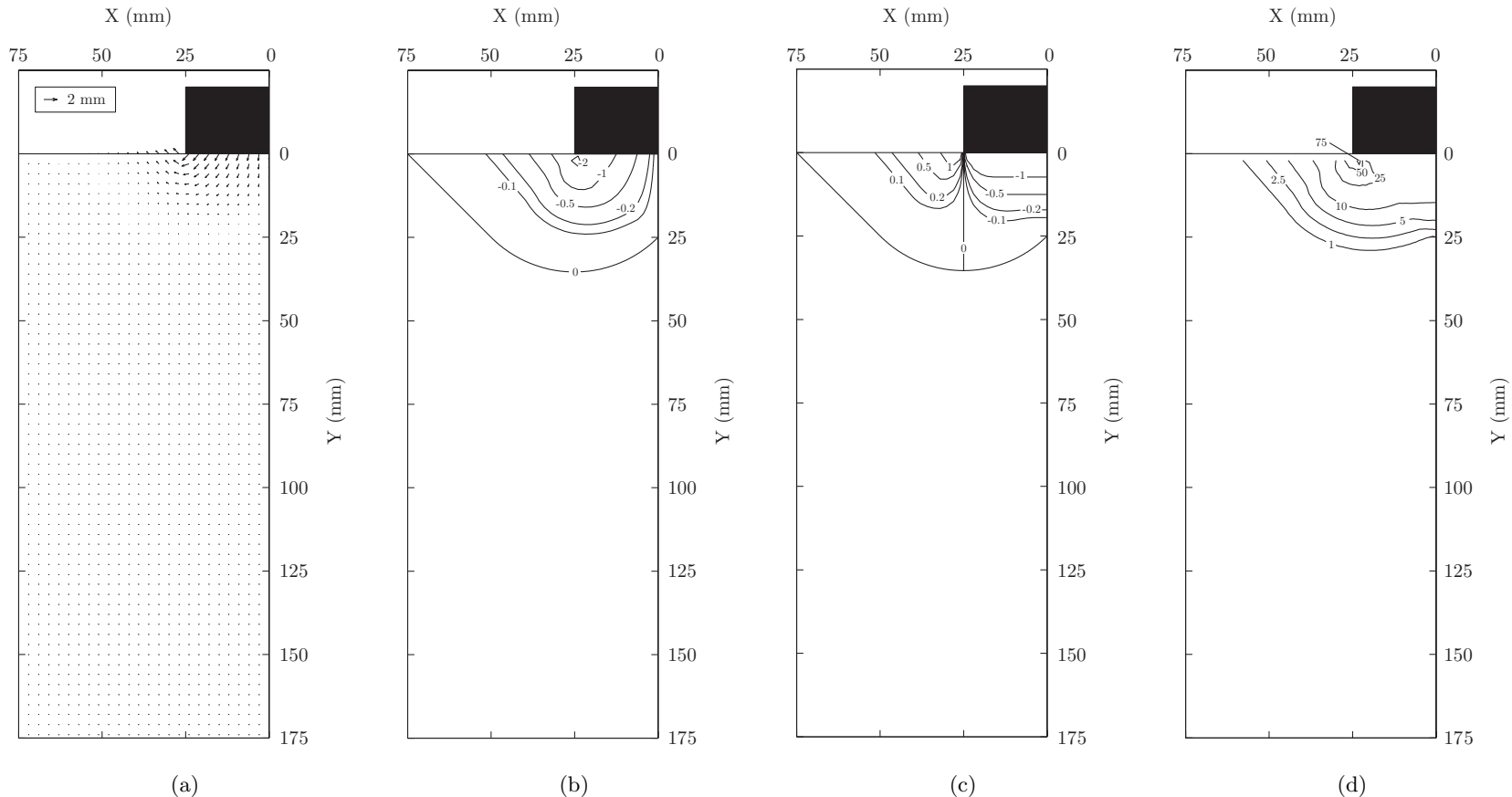


Figure 6.23: MSD deformation mechanism results for 2mm settlement increment: vector (a), horizontal displacement contours (b), vertical displacement contours (c) and shear strain contours (d) with displacements in mm and shear strains expressed as a percentage.

6.6 Derivation of Stress-Strain Response

The discrepancy between the observed displacement and shear strain fields presented in Section 6.4.4 and those predicted by the deformation mechanism proposed by Osman and Bolton (2005), necessitated a numerical simulation of the observations derived from the physical model. This was approached using the Finite Element (FE) method. To calibrate an FE model various parameters are required to describe the stress-strain behaviour of the soil. By rearranging Equations 6.3 and 6.4 the load-settlement behaviour of a circular footing that is subjected to undrained loading, can be used to derive a theoretical triaxial response in terms of the mobilised deviatoric stress, q_{mob} , and axial strain, ϵ_a :

$$\epsilon_a = \frac{M_c \delta}{1.5D} \quad (6.6)$$

$$q_{mob} = \frac{2\sigma_{mob}}{N_c} \quad (6.7)$$

Constitutive models can then be fitted directly to this data, most simply in the form of the Mohr-Coulomb parameters, E_u and S_u . However, it is not possible to define from the PIV derived displacement and shear strain fields whether the footing modelled was smooth or rough. Hence, choice of the bearing capacity factor (N_c) to adopt is difficult. Potts and Zdravković (2001) provide an example FE analysis, an excerpt of which is shown in Figure 6.24, of a strip footing on soft clay with reducing strength with depth, where both a smooth and rough footing interface are considered.

The resulting incremental displacement fields demonstrate that it is the reducing strength profile with depth that controls the depth and form of the deformation mechanism. This shows that it is not possible to assume a value for N_c by assessing the displacement field apparent beneath the footing; a lack of horizontal displacement along the interface between the soil and the footing is not evidence that the footing is rough, nor is it evidence that the footing is not smooth. Therefore a range of N_c between the values derived for a smooth footing of 5.69 and a rough footing of 6.05 (Eason and Shield, 1960; Housby and Wroth, 1983) ought to be considered when deriving the representative stress-strain curve from the mean footing load-deflection response in Figure 6.21(a) using Equations 6.6 and 6.7.

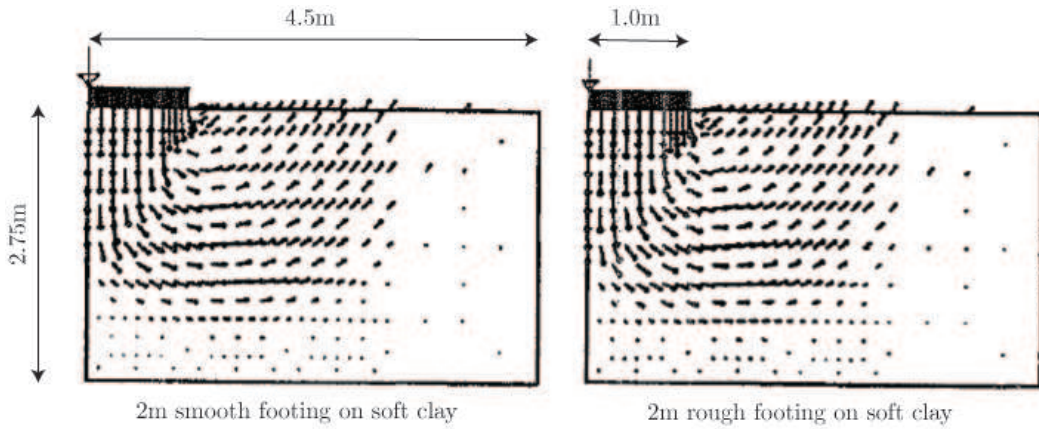


Figure 6.24: Deformation mechanisms beneath smooth (*l*) and rough (*r*) strip footings on soft clay with reducing strength with depth from Potts and Zdravković (2001).

Figure 6.25 is a plot of the stress-strain curves derived using Equations 6.6 and 6.7, assuming lower and upper bound values of N_c of 5.69 and 6.05 and M_c equal to 1.35. To these curves the parameters E_u and S_u have been fitted and are summarised in Table 6.5.

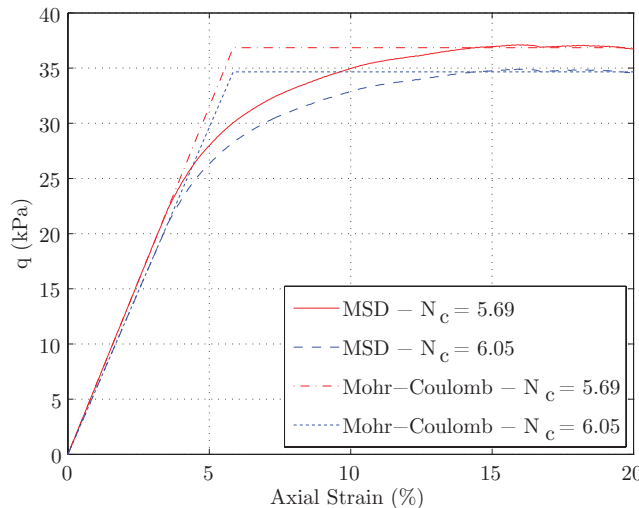


Figure 6.25: MSD derived theoretical triaxial response and fitted Mohr-Coulomb constitutive model.

Figure 6.26 is a plot comparing the shear strength derived using the reverse MSD method and the post-test data from vane shear and UU triaxial testing. The plot shows that at a depth of $0.3D$ or 15mm, which is close to both the centroid and mid-depth of the deformation mechanism proposed by Osman and Bolton (2005),

Table 6.5: E_u , S_u and I_R derived using reversed MSD method for smooth and rough bearing capacity factors.

N_c	E_u (kPa)	S_u (kPa)	$I_R = E_u/S_u$
5.69	629.35	18.43	34.16
6.05	591.90	17.33	34.16
Mean	610.63	17.88	34.16

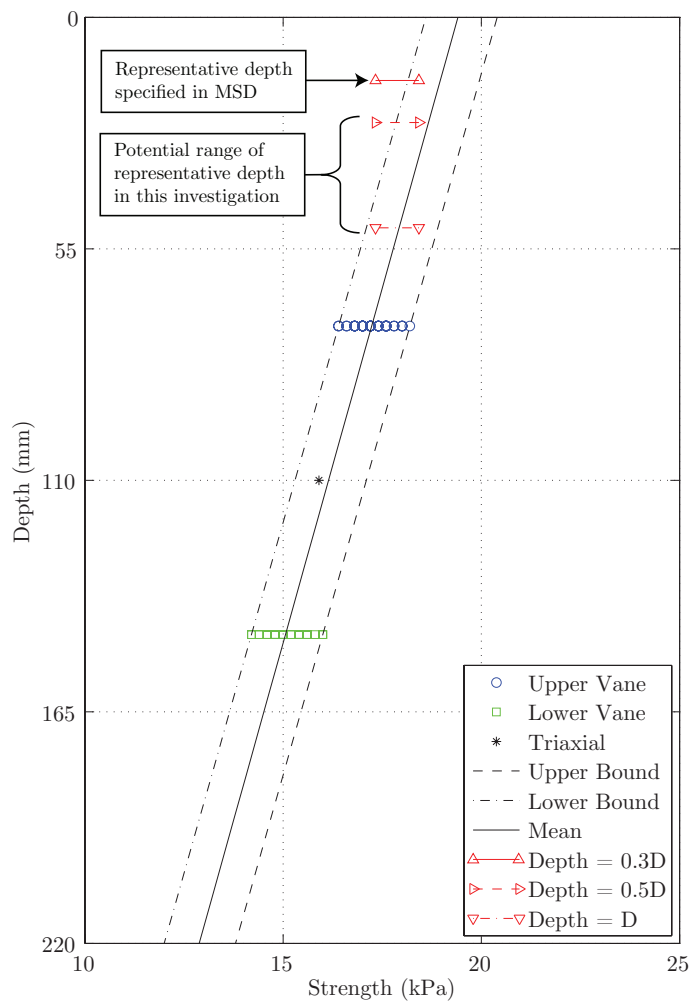


Figure 6.26: Strength derived from reverse MSD compared to lower, upper and mean strength profiles derived from post-test vane shear data and UU triaxial data.

the range of reverse MSD derived strength is less than that derived from the linear extrapolation of the strength profile fitted using the vane shear strength data.

However, in Section 6.4.5.3 it was shown that the deformation mechanism in the physical model extended to a greater depth than that proposed by Osman and Bolton (2005). Shear straining was apparent at depths of up to 100mm below the centre of the footing in the cumulative shear strain plots at 10mm settlement in Figure 6.19(d) and a depth of 50mm in the incremental shear strain plots for 8mm to 10mm settlement in Figure 6.18(d). The corresponding mid-depth of the mechanism is therefore between 25-50mm or 0.5-1D. At these greater depths the strength bounds calculated using reverse MSD are much more favourably comparable with the strength profiles estimated using the vane shear data. The average discrepancy of the reverse MSD derived strength measurements, compared to the mean strength bound at the representative depth specified by MSD of 0.3D, is only 5.7%. At a depth of 0.5-1D this discrepancy reduces to about 2.18% on average. The lack of sensitivity of this simulation to the strength profile apparent in the physical models is demonstrated in Section 6.7.4.

Selection of the representative depth can be assumed to be more critical in soil with rapidly changing properties with depth. The validation of MSD performed by Osman and Bolton (2005) was very sensitive to the representative depth assumed, as $\frac{kD}{S_{u_{surface}}}$ was about 15 over the depth of influence of the assumed deformation mechanism. This signified rapidly increasing strength with depth. In this investigation the samples were effectively homogeneous with respect to the footing diameter and depth of influence of the observed deformation mechanism, as $\frac{kD}{S_{u_{surface}}}$ was only -0.08, signifying only slightly reducing strength with depth. Therefore, it is not surprising that there is a far greater range of depths that could be taken as representative with relatively small associated errors (<5%) than was observed in the validation performed by Osman and Bolton (2005). It is also noticeable in Table 6.5 that I_R is the same regardless of the choice of N_c . This is because it is the horizontal axis translation (Equation 6.6) that controls I_R . The compatibility factor, M_c , therefore governs the calculation of I_R as it relates ϵ_a to δ/D . In this investigation it was taken as the value calculated by Osman (2004) of 1.35. The effect of varying M_c was considered as part of a FE simulation based sensitivity analysis which is summarised in Section 6.7.

Since there was significant uncertainty regarding the appropriate choice of N_c and representative depth to assume, the shear strength profile adopted in the FE model was governed by the vane shear strength data. The average I_R derived from the reverse MSD process and the UU triaxial test data, which is equal to 33.86, was used to describe undrained stiffness, E_u , with respect to undrained shear strength, S_u . The shear strength gradient k was shown in Section 6.2 to be equal to $-30\text{kPa}/\text{m}$. As a result Equations 6.8 and 6.9 are the relationships used to describe the stress-strain response of the transparent soil in the FE simulation of the physical model.

$$S_u = S_{u_{surface}} + k.z = S_{u_{surface}} - 30z \quad (6.8)$$

$$E_u = I_R.S_u = 33.86S_u \quad (6.9)$$

where z is the depth within the model from the soil surface, which is expressed in metres, and the undrained shear strength S_u is expressed in kPa .

6.7 Finite Element Simulation

To validate the observations presented in the preceding section, an axisymmetric analysis of the problem was performed to predict the undrained settlement of a circular footing on transparent soil, with stress-strain response governed by Equations 6.8 and 6.9. Excess pore pressure was assumed not to dissipate during loading; hence Poisson's ratio (ν) was assumed to be close to 0.5. The analysis was conducted in ABAQUS/STANDARD version 6.7, using the Mohr-Coulomb plasticity model for soil. Strength (S_u) and stiffness (E_u) profiles were varied with respect to model depth (z) using ABAQUS Subroutine 'USDFLD' in the Fortran 77 programming language.

The footing, a billet of aluminium, was represented in the FE simulation as a linear elastic material with E equal to 69GPa , ν equal to 0.3 and density, ρ , of 2700kg/m^3 (MatWeb, 2010). The mean soil strength at the surface of the sample was taken from Figure 6.2(a) as 19.41kPa . S_u and E_u for the transparent soil were derived using the relationships in Equations 6.8 and 6.9. The soil density, ρ , was derived experimentally for the consolidated soil as 942kg/m^3 . Gravitational acceleration

(g) was taken as $9.81m/s^2$.

The geometry of the problem was split into four regions as shown in Figure 6.27(a), to allow control of the nodal seeding and resultant mesh densities in key regions of the problem. Nodal seeding densities were increased near to the toe of the footing since this is the area where the changes of stresses and strains are highly concentrated. The problem was modelled using hybrid quadratic tetrahedral elements, since these allow convergence of problems where ν is approaching 0.5. In this instance ν was taken as 0.49, as convergence problems were experienced if this value was increased further. Since horizontal displacement at the soil-footing interface was minimal in the PIV analyses, the nodes along this interface surface were tied. The bottom boundary of the problem was restrained horizontally and vertically. The side boundary was restrained only horizontally such that heave or settlement could occur. The potential effect of these assumptions in comparison to the baseline response was investigated in a sensitivity analysis that is summarised in Section 6.7.4.

Details of the resulting mesh are shown in Figure 6.27(b). The average aspect ratio of the elements was 1.18 and the worst ratio was 1.93. Ideally these numbers ought to be as close to unity as possible. However for the average aspect ratio to be unity, the mesh would need to be populated entirely with elements of equal size. This was deemed to be unreasonably computationally intensive so the element size in regions of lesser interest within the model was decreased. The total number of elements was 597.

The model was first initialised before the footing was displaced vertically downwards, under displacement control. At convergence of each increment of displacement, the resultant forces at the nodes at the surface of the footing were summated to calculate the load applied to mobilise the displacement increment. Displacement field data was extracted from the results database at increments of displacement of $2mm$ for comparison of the resulting displacement and shear strain fields with the PIV data presented in Section 6.4.4. This data was extracted using ‘Python’ routines executed via MATLABTM.

For comparability with the PIV output, displacements at the nodes of each element were interpolated back to a regular grid of points of similar spacing to the

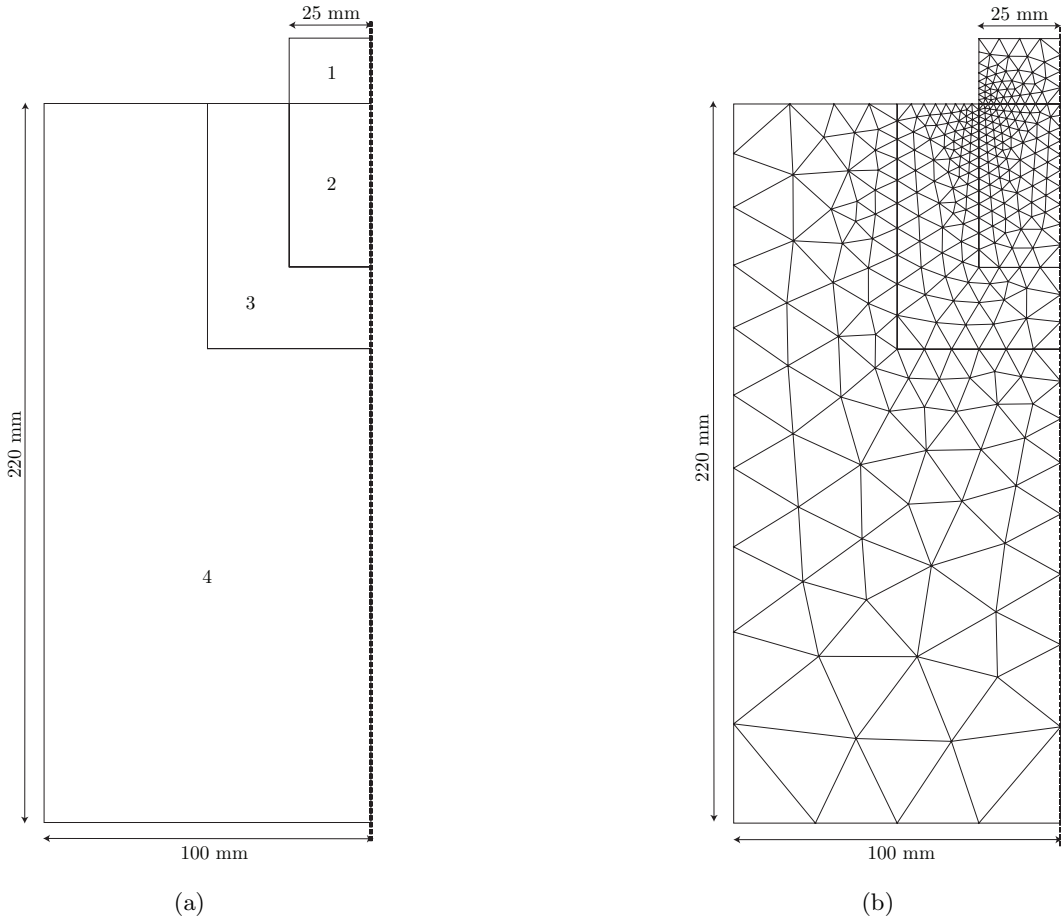


Figure 6.27: FE regions (a) and mesh (b) for baseline case.

PIV measurement points. This allowed computation of shear strain fields using the ‘GeoSTRAINS’ routine (White and Take, 2002) so that the resultant data exhibited the same shear strain smearing as that derived from the PIV analysis. As a result all plots from the PIV analysis and FE simulation are directly comparable. Throughout the following sections this analysis is referred to as the ‘Baseline’ analysis.

6.7.1 Load-Deflection Response

Figure 6.28(a) is a plot of the settlement predictions from the ‘Baseline’ FE analysis compared to the settlement measured in the physical model. Figure 6.28(b) is a plot of the percentage discrepancy as a function of the ultimate capacity of the baseline analysis (at δ equal to 10mm). It shows that the prediction of displacements is within 5%, over a range of settlement of 0-10mm or 0-0.2D. In the original validation analysis performed by Osman and Bolton (2005), a discrepancy of 10% was found over a range of settlement of 0-65mm or 0-0.011D. Therefore, the calibration

of a simple Mohr-Coulomb constitutive model using a strength profile relationship derived by in-situ testing and I_R from the reverse MSD procedure appears to have captured relatively accurately the stress-strain characteristics of the transparent soil. That is, if the uncertainty regarding the assumption of the representative depth is accepted, as discussed in Section 6.6, and I_R is assumed to be constant with depth.

The range of displacement over which the predictions are valid as a function of the footing diameter is an order of magnitude greater than that previously presented in Osman and Bolton (2005). However, as settlement increases towards mobilisation of the ULS the experimental and FE simulation responses begin to diverge, with the FE simulation overpredicting the capacity of the footing. This is likely to be due to the simplification adopted in describing the apparent shear strength profile with depth in the physical models and the small-strain nature of the FE simulation. The load-deflection response derived from this analysis is only a true simulation if the deformation mechanism computed by the FE method is similar to that observed in the physical model, particularly in respect to the depth of influence of the deformation mechanism. In the following section this will be assessed.

6.7.2 Displacement and Shear Strain Fields

Figures 6.29, 6.31, 6.33, 6.35 and 6.37 are plots of the cumulative displacement and shear strain fields from the FE simulation analysis at increments of 2mm settlement. Similarly, Figures 6.30, 6.32, 6.34 and 6.36 are plots of the incremental displacement and shear strain fields for increments of 2mm settlement. The contours of displacement and shear strain are the same as those used to present the PIV data in Section 6.4.4 which are summarised in Table 6.2.

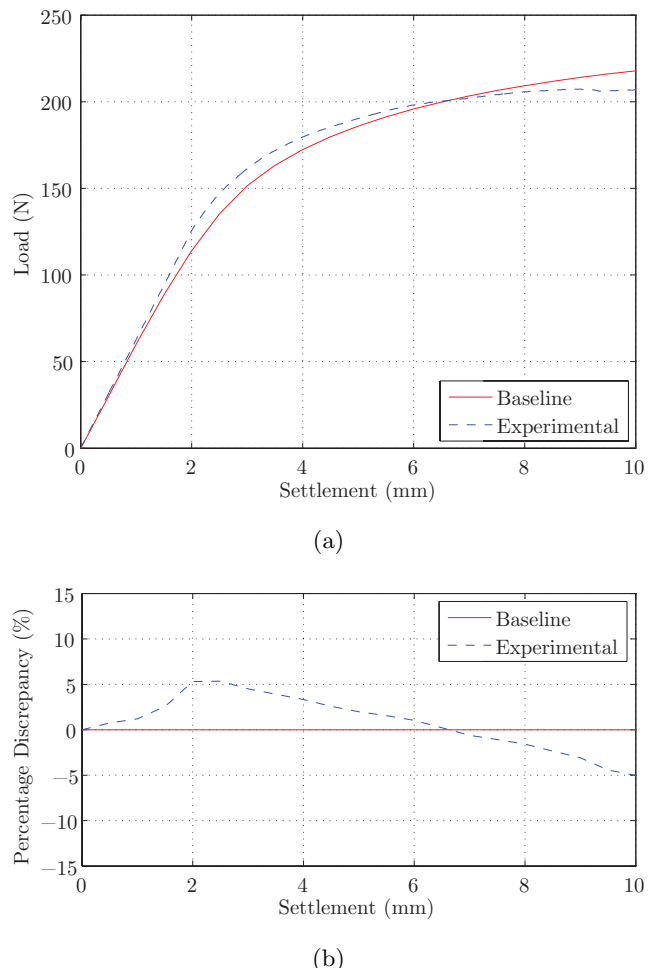


Figure 6.28: Comparison of FE and experimental (a) footing response and (b) percentage discrepancy as a function of capacity at $\delta=10\text{mm}$.

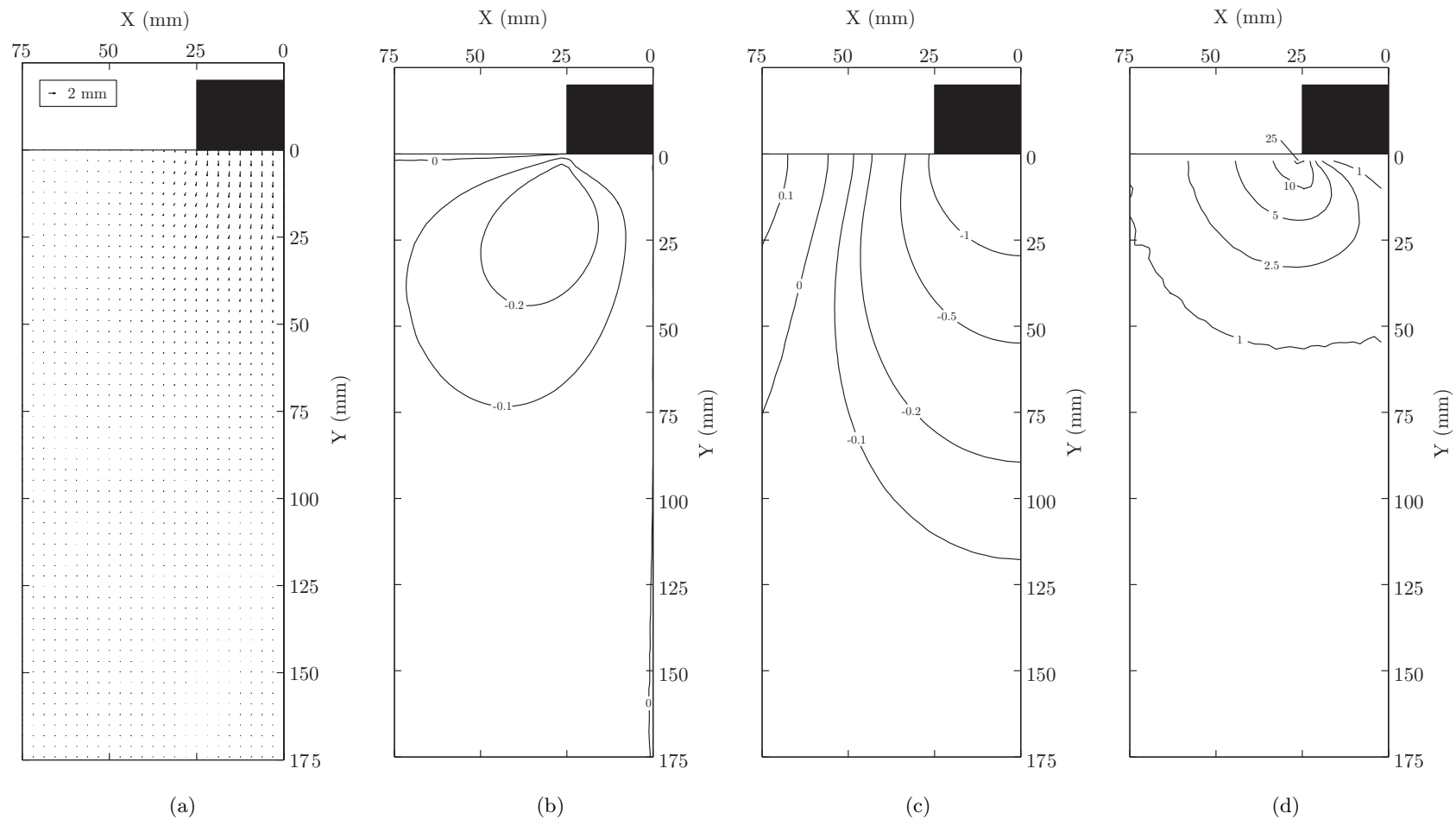


Figure 6.29: Baseline FE analysis results at 2mm settlement: vector (a), horizontal displacement contours (b), vertical displacement contours (c) and shear strain contours (d) with displacements in mm and shear strains expressed as a percentage.

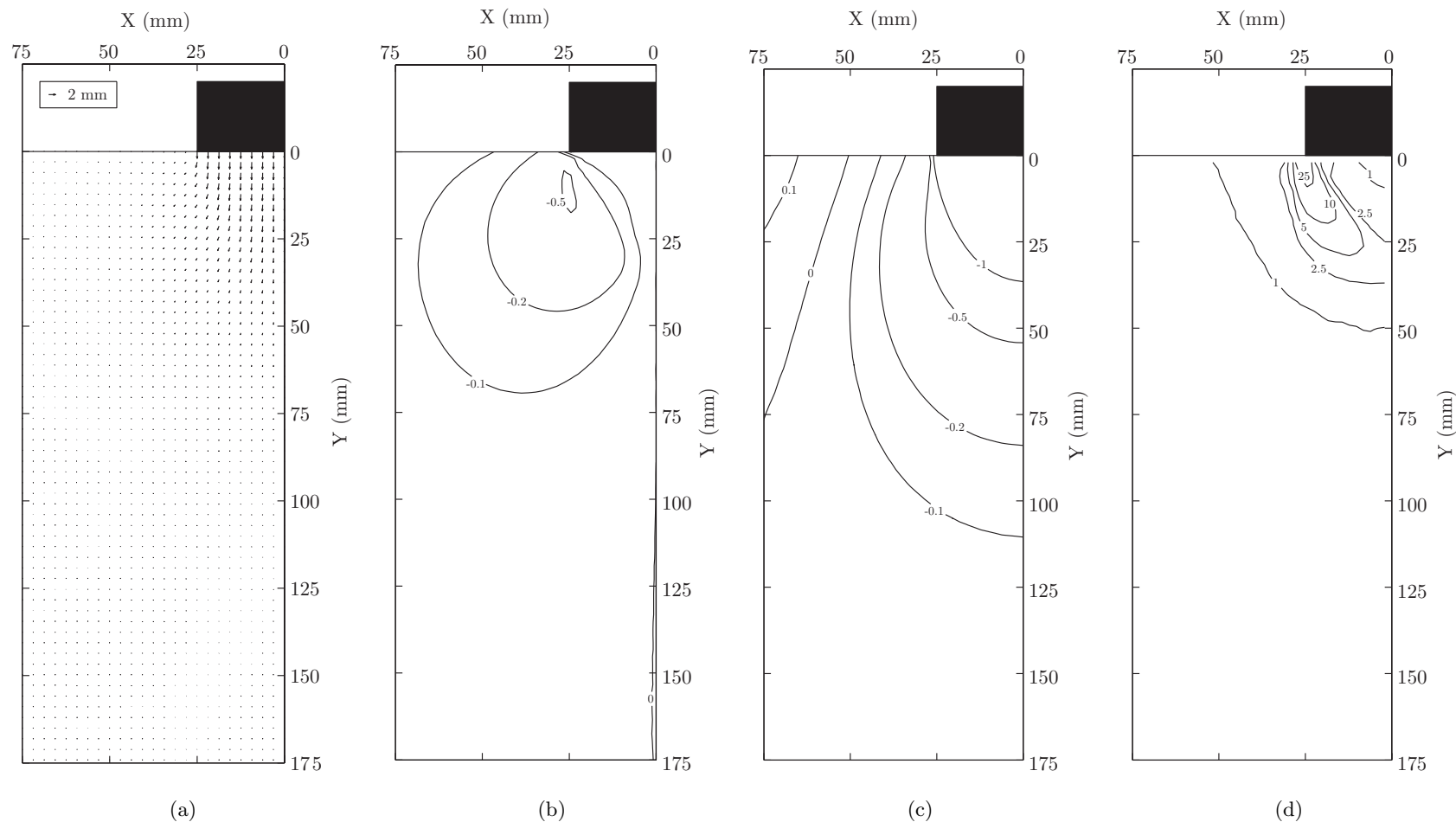


Figure 6.30: Baseline FE analysis results for 2-4mm settlement increment: vector (a), horizontal displacement contours (b), vertical displacement contours (c) and shear strain contours (d) with displacements in mm and shear strains expressed as a percentage.

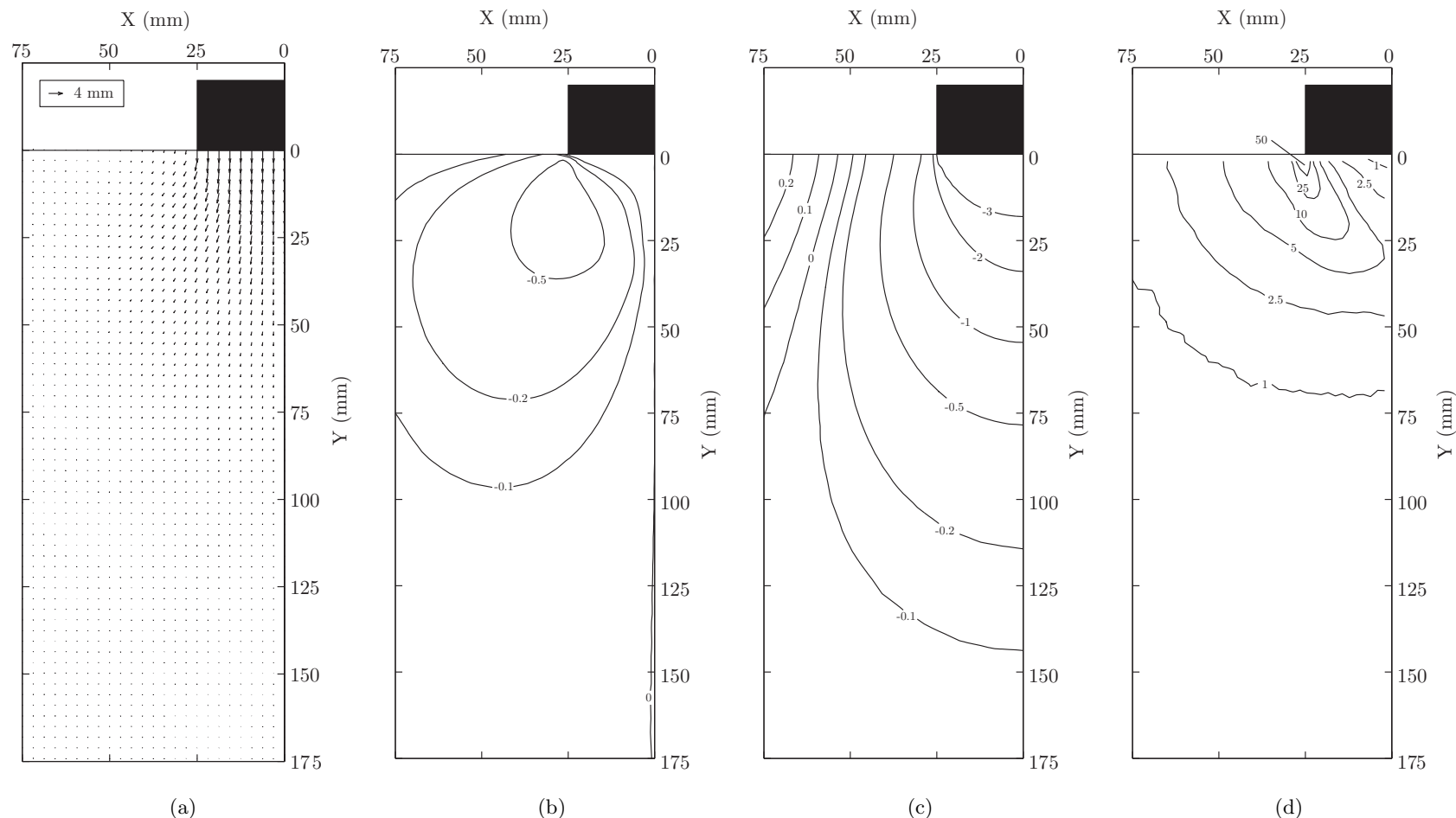


Figure 6.31: Baseline FE analysis results at 4mm settlement: vector (a), horizontal displacement contours (b), vertical displacement contours (c) and shear strain contours (d) with displacements in mm and shear strains expressed as a percentage.

6.7 Finite Element Simulation

332

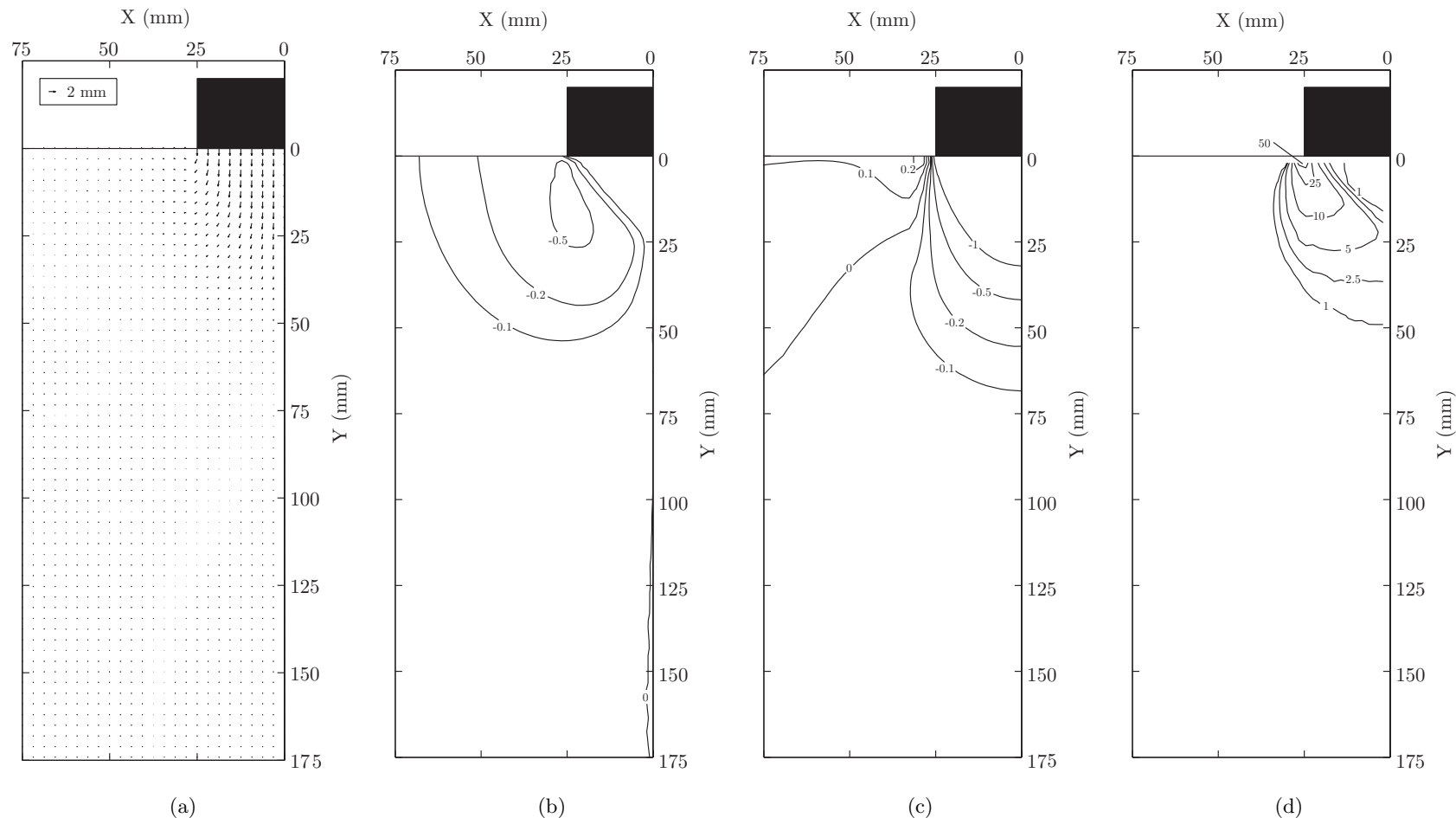


Figure 6.32: Baseline FE analysis results for 4-6mm settlement increment: vector (a), horizontal displacement contours (b), vertical displacement contours (c) and shear strain contours (d) with displacements in mm and shear strains expressed as a percentage.

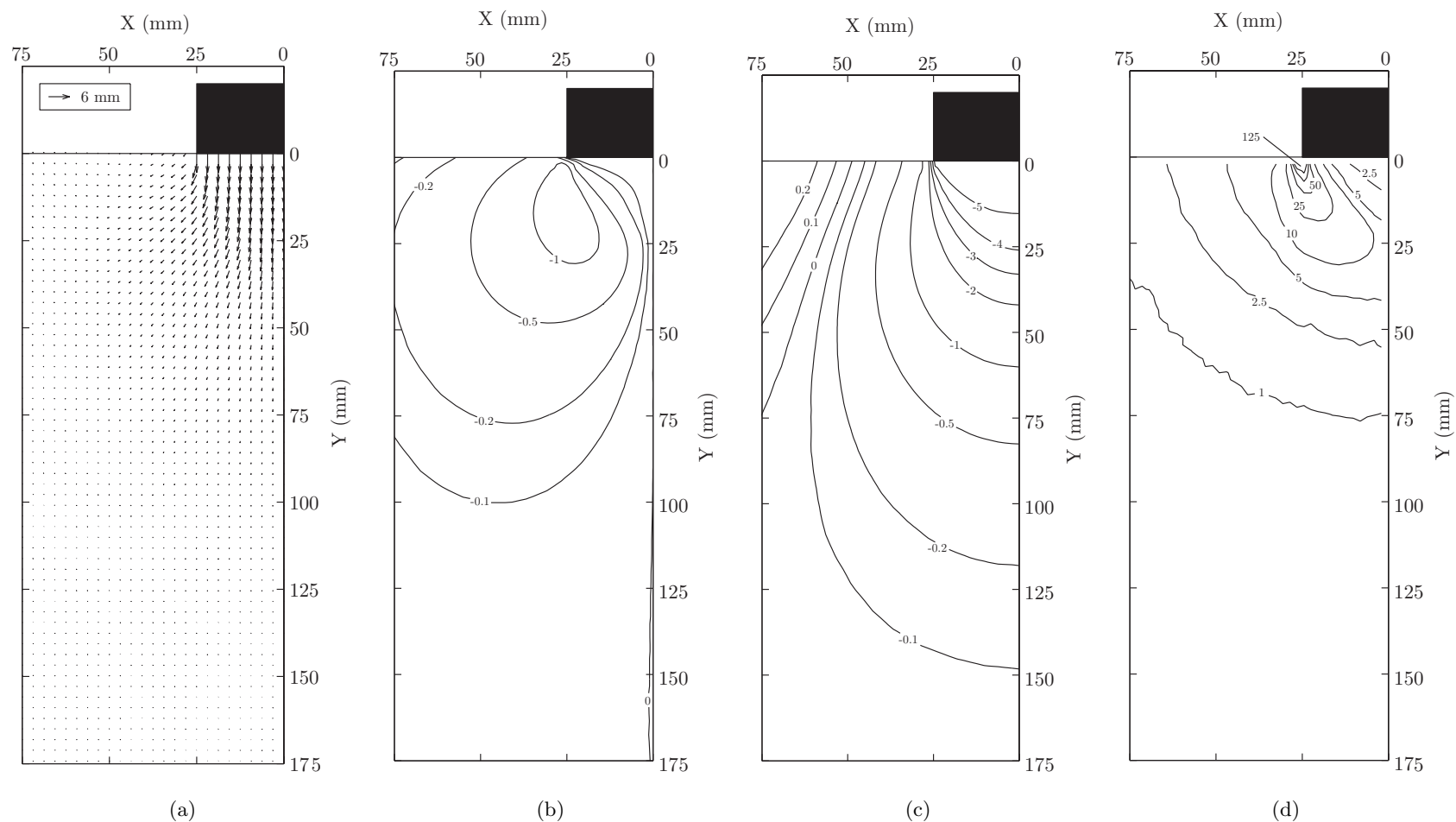


Figure 6.33: Baseline FE analysis results at 6mm settlement: vector (a), horizontal displacement contours (b), vertical displacement contours (c) and shear strain contours (d) with displacements in mm and shear strains expressed as a percentage.

6.7 Finite Element Simulation

334

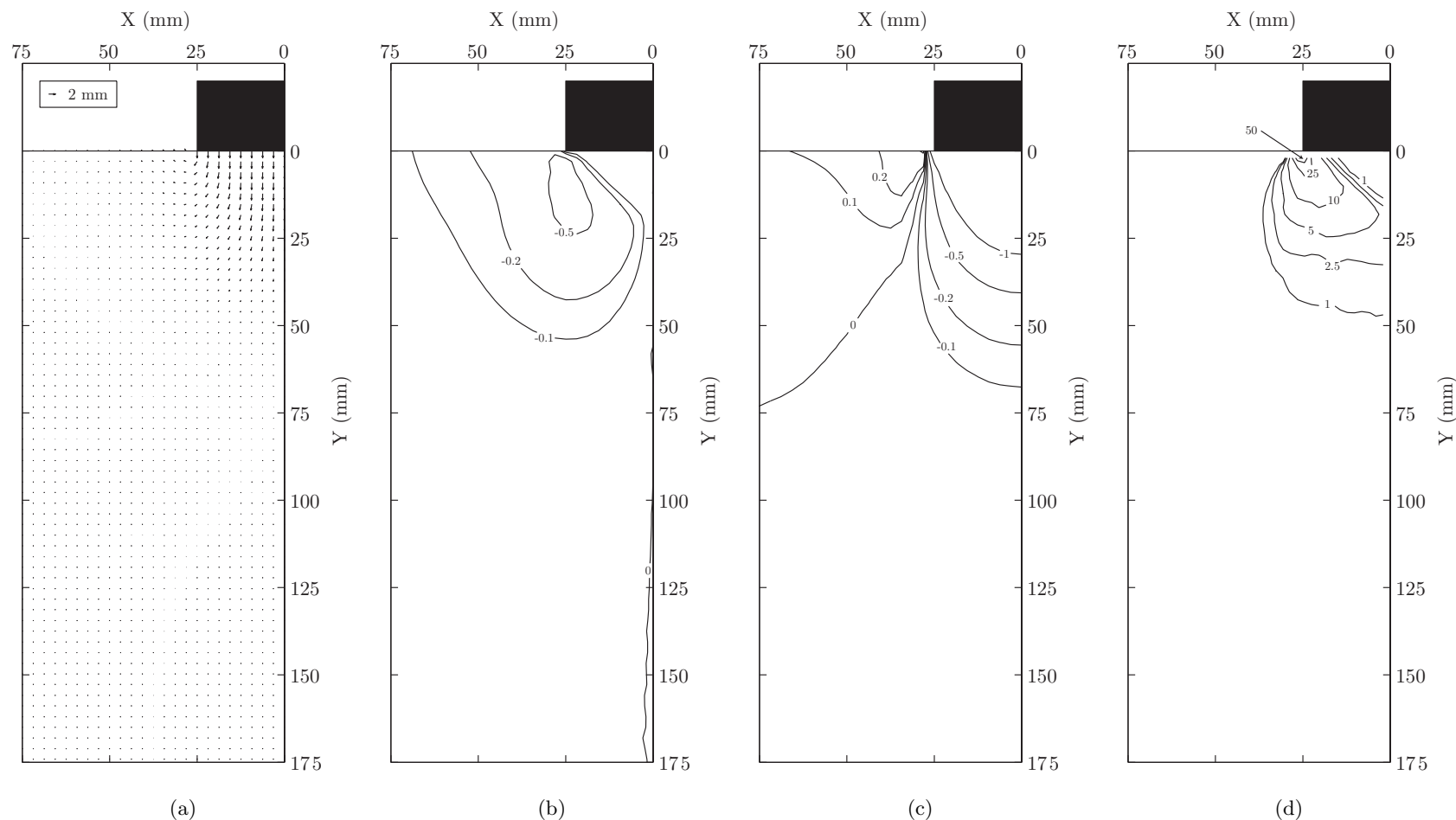


Figure 6.34: Baseline FE analysis results for 6-8mm settlement increment: vector (a), horizontal displacement contours (b), vertical displacement contours (c) and shear strain contours (d) with displacements in mm and shear strains expressed as a percentage.

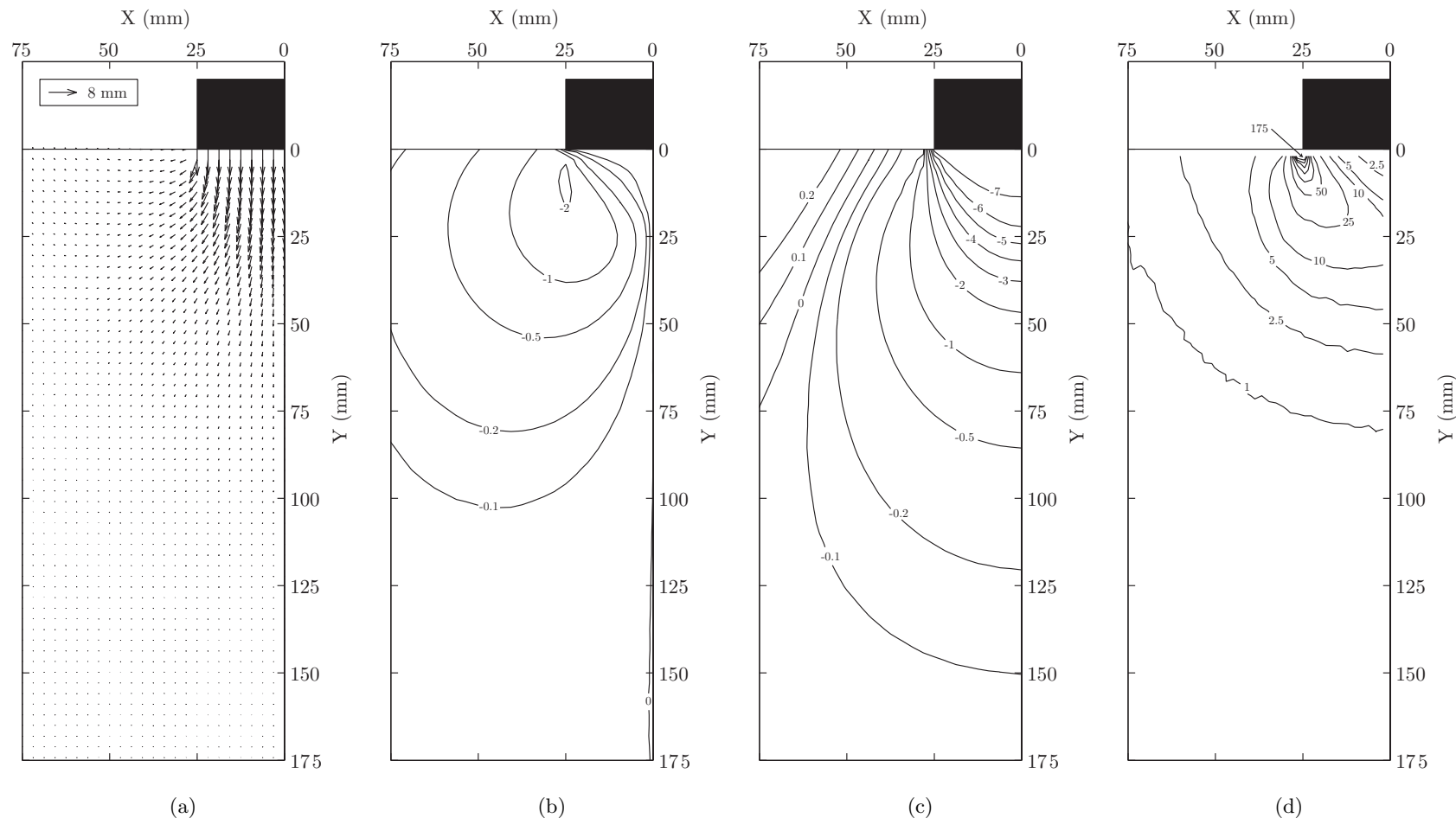


Figure 6.35: Baseline FE analysis results at 8mm settlement: vector (a), horizontal displacement contours (b), vertical displacement contours (c) and shear strain contours (d) with displacements in mm and shear strains expressed as a percentage.

6.7 Finite Element Simulation

336

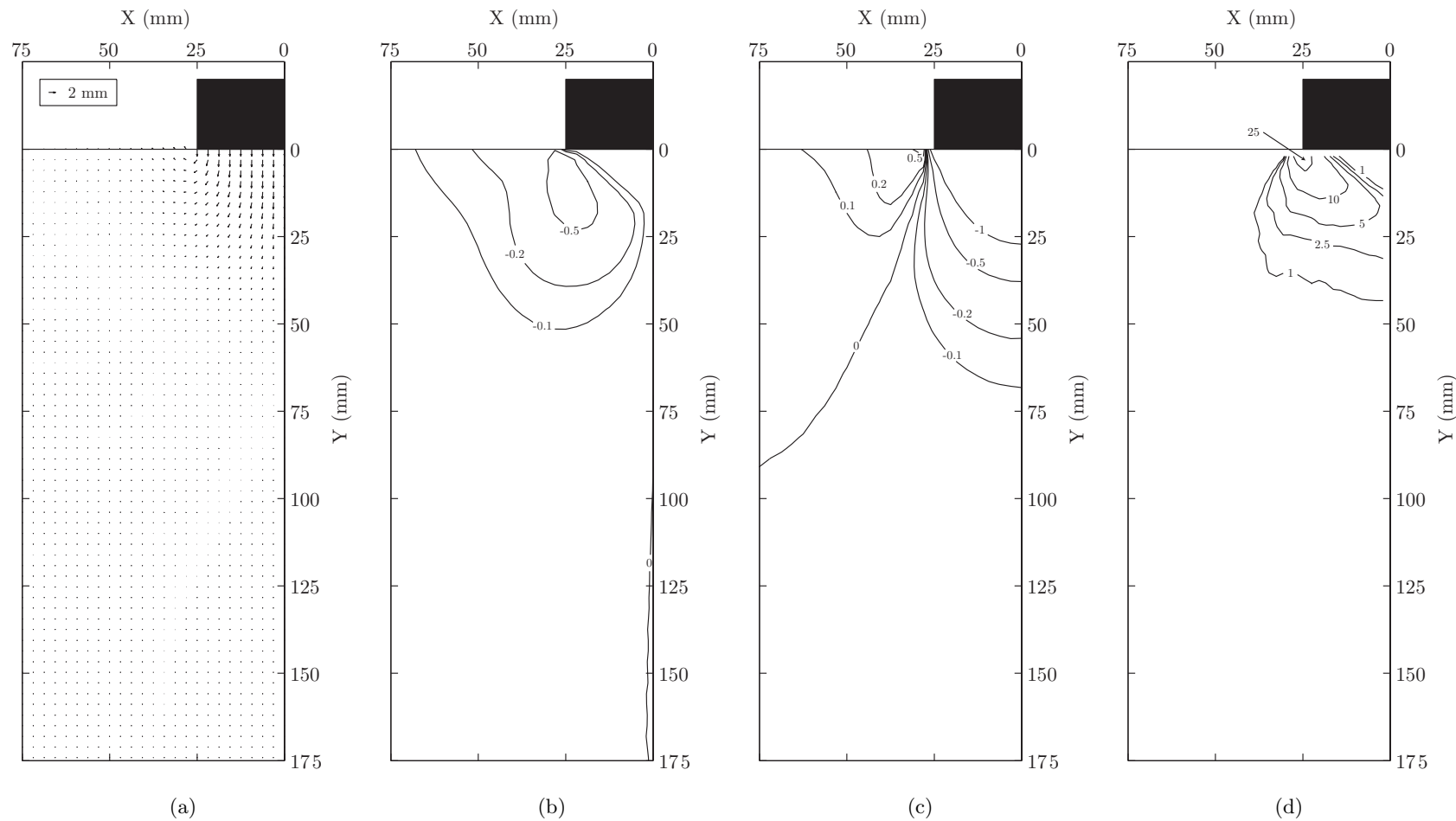


Figure 6.36: Baseline FE analysis results for 8-10mm settlement increment: vector (a), horizontal displacement contours (b), vertical displacement contours (c) and shear strain contours (d) with displacements in mm and shear strains expressed as a percentage.

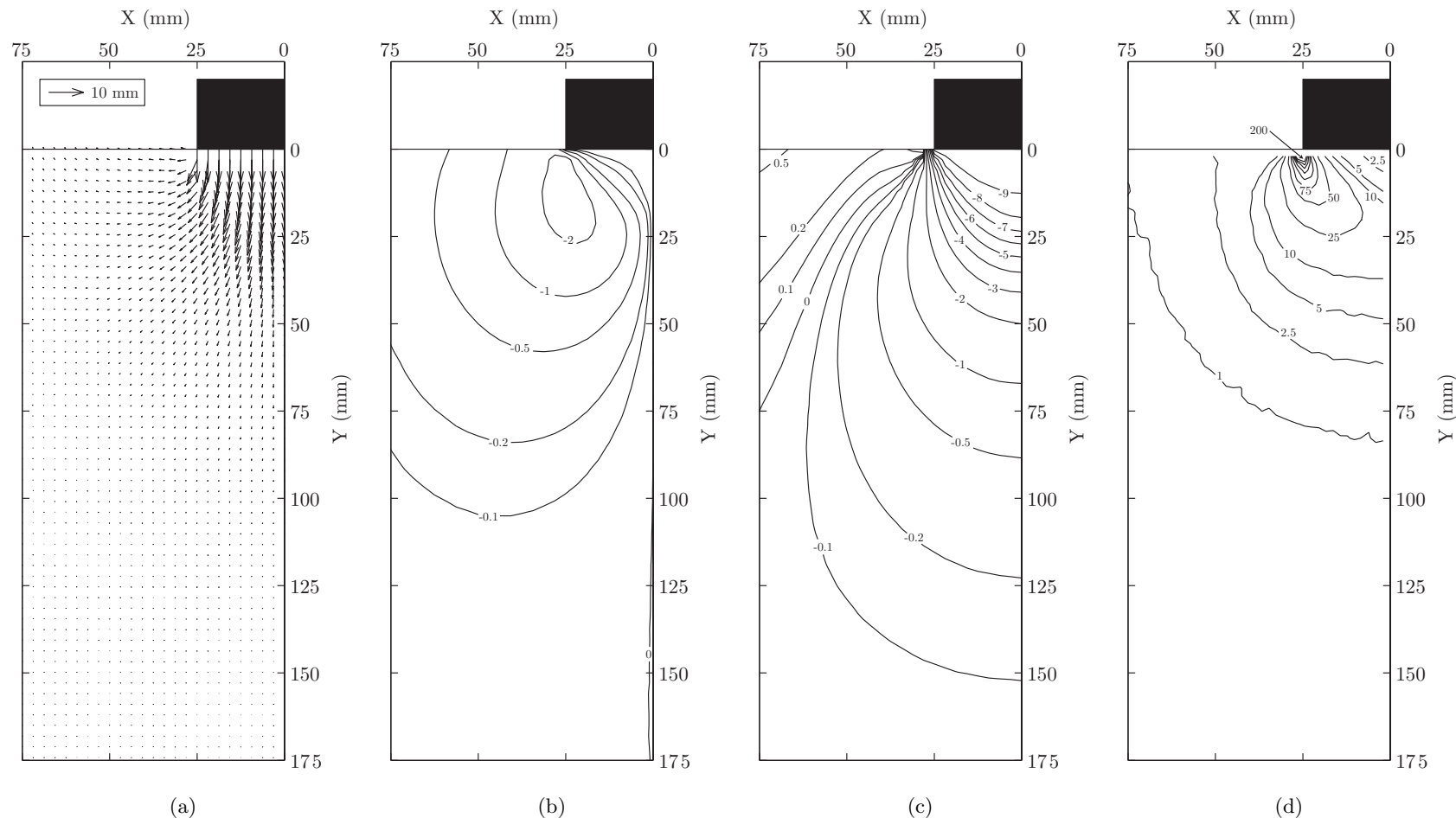


Figure 6.37: Baseline FE analysis results at 10mm settlement: vector (a), horizontal displacement contours (b), vertical displacement contours (c) and shear strain contours (d) with displacements in mm and shear strains expressed as a percentage.

6.7.3 Observations

6.7.3.1 Displacement Field Discrepancy

The horizontal displacements evident in the FE analysis are generally spread over a larger area of the model than is observed in the PIV measurements. Comparison of Figures 6.18(b) and 6.36(b) and Figures 6.19(b) and 6.37(b) showing horizontal displacement for the increment of 8-10mm settlement and at 10mm settlement indicate this trend most clearly. In both cases the maximum horizontal displacement is well predicted and has a similar area of influence. However, displacements less than about 0.2mm or $\frac{D}{250}$ for the settlement increment results and 0.5mm or $\frac{D}{100}$ for the total settlement results are not so well predicted.

A similar trend is apparent when the vertical displacement fields are compared. Figures 6.18(c) and 6.36(c) and Figures 6.19(c) and 6.37(c) show vertical displacement for the increment of 8-10mm settlement and at 10mm settlement. Once again, in both cases the extent of vertical displacements for magnitudes less than about 0.5mm or $\frac{D}{100}$ for the settlement increment results and 1mm or $\frac{D}{50}$ for the total settlement results are not so similar.

It is most likely that these discrepancies were a result of the bedding errors, evident in both the initial (F) and repeat (F-R) footing tests as documented in Sections 6.4.5.2 and 6.4.6.

6.7.3.2 Development of Ultimate Limit State

Comparison of displacement and shear strain field plots, after acceptance of the displacement field discrepancies at small magnitudes, shows that for both total and incremental settlement the FE predictions are very similar to those observed using PIV. Of key importance is assessing the similarity of the deformation mechanism at the ULS.

Comparison of Figures 6.18(b) and 6.36(b) and 6.18(c) and 6.36(c) shows that the deformation mechanism is generally very similar. This is confirmed by the similarity between Figures 6.18(d) and 6.36(d), which show the shear strain fields beneath the footing for a settlement increment of 2mm.

6.7.3.3 Soil Footing Interface

The most rigorous demonstration of the validity of the assumption that the nodes along the soil-footing interface can be tied in the FE simulation is by comparison of horizontal displacement fields at maximum settlement. Figures 6.19(b) and 6.37(b) show the horizontal displacement fields at 10mm settlement. Ignoring the non-zero horizontal displacement induced by the bedding errors as discussed in Section 6.4.5.2, the horizontal displacement fields are in generally good agreement. Thus assuming that the nodes at the soil-footing interface are tied, appears to be a reasonable assumption for this case.

6.7.3.4 Depth of Deformation Mechanism

In contrast to the deformation mechanism proposed by Osman and Bolton (2005), Figures 6.18(c) and 6.36(c) illustrate that the depth of the deformation mechanism is significantly greater than $\frac{D}{2}$ at $r=0$ (note that $r=X$ in the PIV output presented due to the axisymmetric geometry of the circular footing being investigated). The depth of the shear strain field in Figures 6.18(d) and 6.36(d) is further evidence that the maximum depth of the deformation mechanism beneath a circular footing on clay cannot necessarily be assumed to be $\frac{D}{2}$. The agreement between the PIV observations and FE simulation suggest that the representative depth for the reverse MSD derived measurement in this investigation ought to be at a lower depth than $0.3D$.

6.7.3.5 Heave at Toe of Footing

One aspect of the physical model that is not evident in the FE simulation is heave at the toe of the footing. Comparison of Figures 6.19(c) and 6.37(c) demonstrates the extent of this discrepancy at a total settlement of 10mm. In the physical model heave at the toe of the footing is apparent with a magnitude of 5-6mm. In contrast only 0.2-0.5mm heave is apparent in the FE simulation.

The significance of the discrepancy is reduced for increments of settlement once the ULS has been mobilised. This is demonstrated by comparing Figures 6.18(c) and 6.36(c) where about 1-2mm of heave is apparent in the physical model compared to 0.5-1mm heave in the FE simulation. The prediction of reduced heave in both the total settlement and incremental settlement results is most likely caused by the tieing of nodes along the soil-footing interface and the lack of adaptivity in the FE analysis method adopted (i.e. no periodic remeshing).

6.7.4 Sensitivity of Finite Element Simulation

The observations presented in the previous section, illustrated the validity of the physical modelling results using a ‘Baseline’ FE simulation. However, during formulation of the numerical model used in the simulation various assumptions were made. Some of these were investigated through a sensitivity analysis involving the variation of isolated parameters or assumptions to allow assessment of their impact. The effect of the following assumptions was considered:

- Compressibility:
 - ν varied from 0.49 to 0.49999 using an alternative FE package (Oasys Geo SAFE).
- Mesh density:
 - 50% and 200% nodal seeding densities considered.
- Assumed geometric simplification:
 - Axisymmetric and 3D geometry simulations compared.
- Assumed vertical boundary condition:
 - Results attained using fixed and sliding boundary conditions compared.
- Strength uncertainty:
 - Upper and lower strength profiles from post-test data used.
- Rigidity Index:
 - The influence of M_c investigated by varying I_R by $\pm 10\%$.
- Shear strength gradient:
 - The influence of k investigated by assessing the impact of values for k of 30, 0 and $-30 kPa/m$.

Throughout, the results were considered by comparing load-deflection responses predicted for the circular footing and by assessing the percentage sensitivity as a function of the capacity of the ‘Baseline’ case at a settlement of 10mm. In all cases, the deformation mechanism observed at the ULS was imperceptibly different to that presented in Section 6.7.2.

The following findings were generated by the sensitivity analysis:

1. Repeating the analysis in OASYS Geo SAFE confirmed the results of the simulation to within $\pm 1\%$ over the range of displacement assessed.
2. The mesh was shown to be appropriately element rich as refining it by increasing the seeding density by a factor of two had a negligible ($< 1\%$ of capacity) impact on the result.
3. The axisymmetric geometric simplification caused only a 2% increase in footing capacity at the ULS.
4. Assuming that the vertical boundary was sliding rather than fixed caused a small reduction in potential capacity at the ULS of about 2%.
5. The strength profile assumed (upper, mean or lower) from the post-test property data had the most significant impact as it affected the computed ULS capacity by $\pm 10\%$.
6. Varying I_R by $\pm 10\%$ impacted most significantly on the linear portion of the load deflection response by $\pm 5\%$ at the worst case but minimally on the ULS capacity where the impact was less than 1.5%.
7. Varying k between values of 30, 0 and $-30 kPa/m$ only impacted significantly on the ULS capacity causing a variance in capacity of about 2%.

These findings provided some confidence in the parameters assumed for the elasto-plastic constitutive model as they show that the FE analysis was generally insensitive to the assumptions made during formulation of the simulation. They also show that the greatest uncertainties relate to the choice of S_u and I_R .

6.8 Summary

Post-test in-situ property data and UU triaxial test data has been used to define lower, mean and upper bounds to describe the strength profile apparent in the physical models used to investigate the behaviour of deep helical screw piles in a clay soil. E_u , S_u and subsequently I_R were then calculated from the UU test data indicating that a simple Mohr-Coulomb constitutive model was adequate in describing the stress-strain response of the transparent soil.

An alternative method of deriving E_u , S_u and I_R was then presented, which used the MSD procedure of Osman and Bolton (2005) in reverse to derive a stress-strain curve from the undrained settlement of a circular footing. A physical model of a 50mm diameter footing was then used to investigate the deformation mechanism apparent beneath the footing, with the use of transparent soil allowing quantification of displacement and shear strain fields beneath a circular footing without the boundary effects associated with a Perspex viewing window that is a feature of half-space axisymmetric modelling.

The displacement and shear strain fields from the physical model differed somewhat from the deformation mechanism assumed by Osman and Bolton (2005), as the depth of influence observed was much greater in the physical model. As a result a FE simulation of the observations was performed using ABAQUS, which indicated generally good agreement with the physical modelling results in relation to both load-settlement performance and the displacement and shear strain fields beneath the footing.

Sensitivity analyses were then performed to assess the effect of various assumptions made during formulation of the FE model used for the simulation. Confirmation of the simulation was performed using an alternative FE package. The simulation was generally insensitive to the assumptions made when formulating the FE model, with it being most sensitive to the shear strength profile assumed. Variation from the lower to upper bound shear strength induced an absolute variation of 10% of the capacity of the ‘Baseline’ simulation at a settlement of 10mm. Hence discrepancies between the physical models’ behaviour and FE predictions of up to 5% are unsurprising and are due primarily to sample variability.

The reverse MSD method presented appears to show promise. However, uncertainty regarding the choice of N_c , M_c and the representative depth of the measurement derived, limits its current application in the manner proposed here, where stress-strain characteristics of clay soils can be derived from a simple undrained footing test. Further experimental and parallel numerical investigation is required to further develop understanding of the impact of these choices and assumptions. Therefore, in its current state the methodology has been used to derive I_R which is unaffected by the choice of N_c . This has then been used to calculate E_u as a function of the S_u profile with depth, which was derived from post-test in-situ vane shear tests.

Chapter 7

Numerical Modelling of Helical Screw Piles

7.1 Introduction

The following chapter documents the development of a series of FE based simulations of the physical modelling presented in Chapter 5, alongside some simple analytical models based on previously published theories.

ABAQUS/STANDARD was used to develop the FE work, using the Mohr-Coulomb elasto-plastic constitutive model to describe the stress-strain response of the transparent soil, coupled with undrained strength and stiffness parameters derived from in-situ post-test property testing and the reverse MSD procedure investigated in Chapter 6.

In these simulations the helical plates are idealised as circular plates and the helical pile is ‘wished’ into place, due to the associated difficulty of modelling the installation process using the FE method. As a result, axisymmetric simplification is assumed. Load-deflection responses and displacement and shear strain fields computed by the FE models are compared to the results obtained from the physical modelling investigations documented in Chapter 5.

The FE simulations developed do not account for installation induced effects. However, a series of sensitivity analyses are presented to differentiate the discrepancies in observed and computed behaviour due to assumptions made during development of the FE models from installation induced effects. Some of the possible causes of the discrepancies attributable to the installation process are then discussed

including stiffening and strengthening of material local to the helical piles due to consolidation caused by dissipation of installation induced excess pore pressures.

A simple analytical model, using simple previously published theories is developed and used to calculate the ultimate capacity of each of the configurations of helical screw pile tested under compressive and tensile loading. The capacities predicted by the analytical and FE simulations at the ULS are then compared and discussed.

Lastly, different design methodologies are compared. A traditional approach based upon ‘permissible stress’ is compared to alternative methods of design capacity estimation including Eurocode 7. The impact of designing pile capacities using ULS calculation models is then discussed with reference to a case study focussing on the initial displacement of helical screw piles upon application of design loads.

7.2 Finite Element Simulation

To facilitate comparisons with the observations presented in Chapter 5, axisymmetric analyses were developed to predict the load-deflection performance of the model helical screw piles in transparent soil. The stress-strain behaviour of the soil was governed by the Mohr-Coulomb constitutive model. The analysis was conducted in ABAQUS/STANDARD version 6.7 and S_u and E_u profiles were varied with respect to model depth using ABAQUS Subroutine ‘USDFLD’ in the Fortran 77 programming Language. As in Chapter 6, excess pore pressure was assumed not to dissipate during loading. Hence ν was assumed to be close to 0.5 at 0.49 which is the maximum value for which ABAQUS/STANDARD can achieve convergence.

The helical piles were ‘wished’ into place in the FE simulation, thus the effects of the installation process were not modelled. Discrepancies in behaviour observed between the experimental and numerical investigations are therefore partly due to a combination of installation induced effects, which are difficult to quantify, and assumptions made during formulation of the FE models. Some of the assumptions outlined in the following paragraphs were explored in a sensitivity analysis summarised in Section 7.2.4. Causes of the remaining discrepancies, that cannot be accounted for by any of the assumptions made during development of the simulations, are discussed in Sections 7.2.1 and 7.2.3.

The helical screw piles were modelled as aluminium in the FE simulations, using a linear elastic constitutive model with E equal to $69GPa$, ν equal to 0.3 and ρ equal to $2700kg/m^3$ (MatWeb, 2010). The mean soil strength at the surface of the sample was taken from Figure 6.2(a) as $19.41kPa$. S_u and E_u for the transparent soil were derived using the relationships in Equations 6.8 and 6.9. The soil density, ρ , was derived experimentally for the consolidated soil as $942kg/m^3$. Gravitational acceleration, g , was taken as $9.81m/s^2$.

Figure 7.2 illustrates the regions defined for the four configurations of helical screw pile tested. Displacement fields derived from the physical models using PIV in Section 5.3 indicated that differential sliding was apparent along the soil-shaft interface above the uppermost helical plate for all cases. Hence, in the FE simulation, sliding was allowed along this boundary between the pile shaft and the soil. This was facilitated using a sliding contact interaction law within ABAQUS, along the boundary between regions 1 and 3, shown in Figure 7.2. 5mm of the shaft above the uppermost helical plate was tied to the adjacent soil to facilitate convergence of the problem, as errors were experienced if the full length of shaft to the helical plate intersection was free to slip. Contact between the soil and pile shaft was maintained throughout the analysis to mirror the observations seen in the physical modelling results, i.e. no cavity was allowed to form adjacent to the model pile at any depth within the problem over the range of displacement investigated. This assumption was justified from photographic evidence, i.e. in the photographs used in the PIV analysis no cavity was formed for axial displacements of the pile over the range of $\pm 5mm$.

Tomlinson (2001) suggested, using field data from pile tests performed in Boulder clay, that an adhesion factor, α , of unity can be assumed in clay where S_u is less than $80kPa$. In this instance the shear strength was approximately $20kPa$ at the top of the strength profiles measured using post-test in-situ hand vane shear testing. This, coupled with the inability of ABAQUS/STANDARD to model contact sliding with $\alpha < 1$, led to α being assumed to be equal to unity in the FE simulations. Along the remaining inter-region boundaries all nodes were assumed to be tied, meaning no differential slippage was allowed.

Nodal seeding densities were increased near to the outer radii of the helical plates and along the pile shaft as these are the areas where the changes of stresses and

7.2 Finite Element Simulation

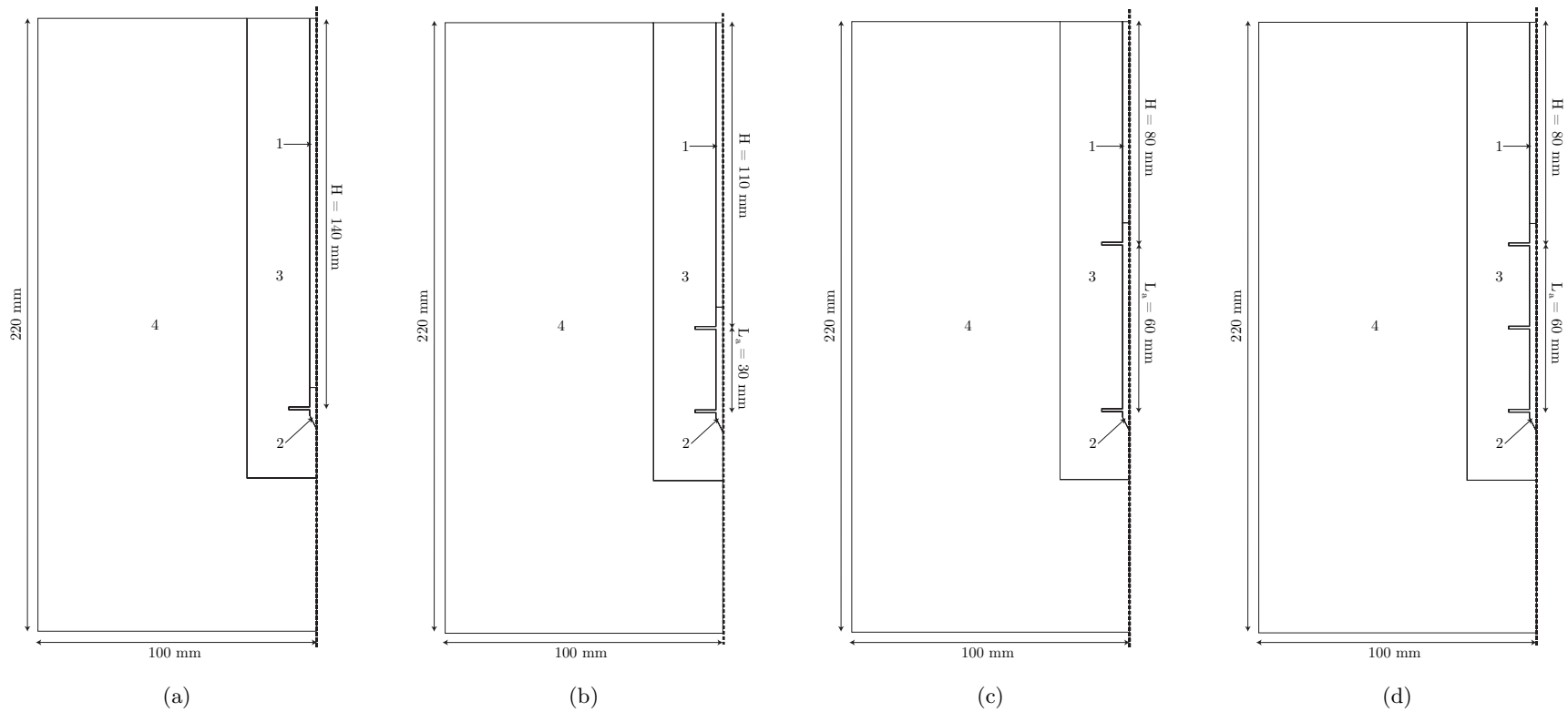


Figure 7.1: Single helix (a); double helix with L_a of 30mm (b); double helix with L_a of 60mm (c); and triple helix with L_a of 60mm (d) axisymmetric baseline FE model mesh regions.

7.2 Finite Element Simulation

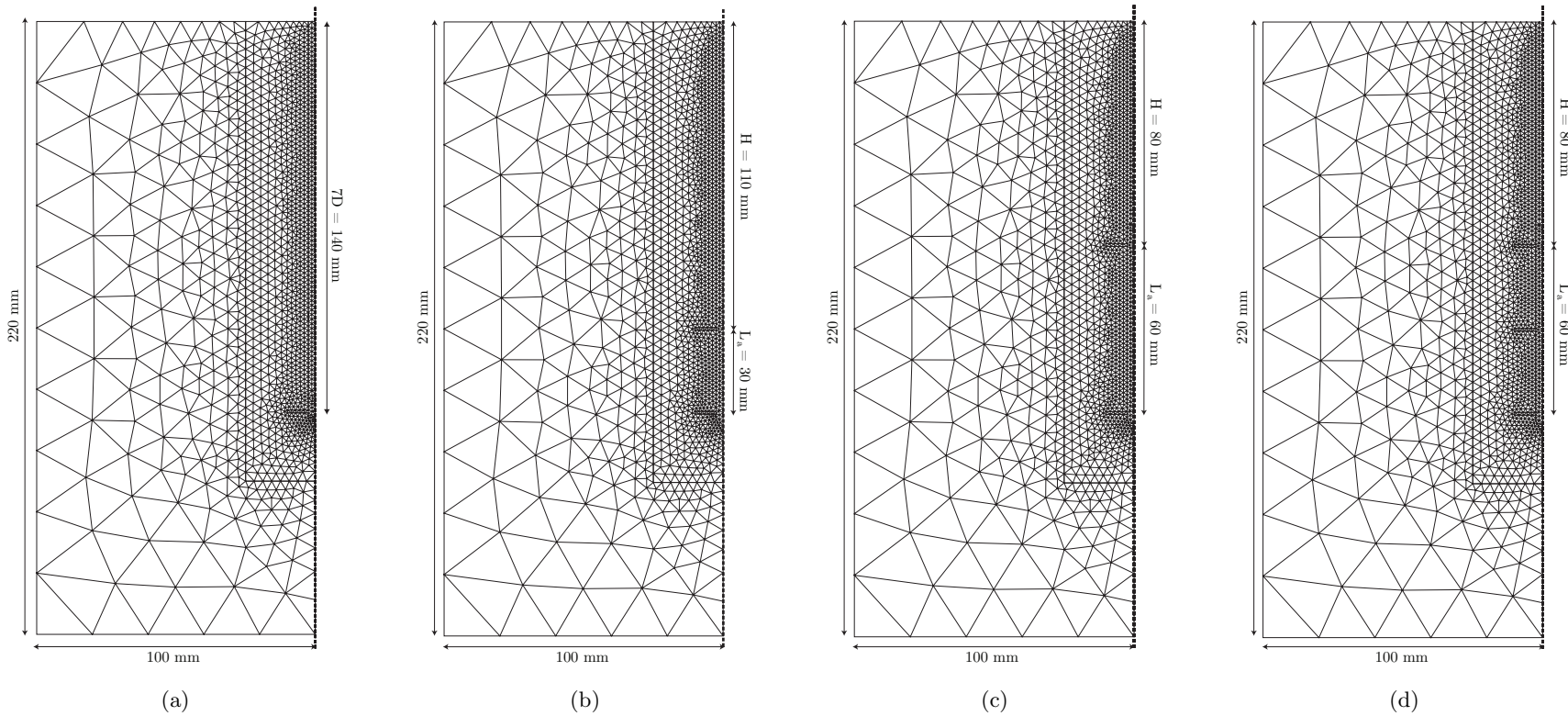


Figure 7.2: Single helix (a); double helix with L_a of 30mm (b); double helix with L_a of 60mm (c); and triple helix with L_a of 60mm (d) axisymmetric baseline FE model mesh.

strains were assumed to be highly concentrated. As in Chapter 6, the problem was modelled using hybrid quadratic tetrahedral elements. The vertical model boundary was assumed to be restrained horizontally, whilst permitting vertical sliding. The horizontal model boundary was assumed to be restrained both horizontally and vertically. The potential effect of these assumptions was investigated in a sensitivity analysis that is summarised in Section 7.2.4.

Details of the resulting meshes are shown in Figure 7.2. Table 7.1 shows a summary of the average and worst case aspect ratio of the meshes. In all cases the average is close to unity. The worst case is in the range of 2.12-2.47. The elements exhibiting worst case aspect ratio were located at the tip of the pile shaft.

Table 7.1: Helical screw pile axisymmetric FE mesh aspect ratio summary.

Configuration	Number of Elements	Mean	Worst Case
Single Helix	2531	1.14	2.47
Double Helix ($L_a=30mm$)	2833	1.14	2.12
Double Helix ($L_a=60mm$)	2829	1.15	2.12
Triple Helix ($L_a=60mm$)	2817	1.15	2.12

Simulation of the application of the post-installation residual force was required to ensure that load-deflection data from the physical model testing and numerical investigations were comparable. To achieve this stress control was required initially before switching to strain control. Strain control is preferable for all loading after application of the post-installation residual force so that the displacement could be controlled accurately, allowing the generation of displacement and shear strain fields that are directly comparable with the PIV derived data presented in Chapter 5. To achieve this the required post-installation residual force was applied at the centre of the surface of the pile shaft. Upon convergence, the displacement of the surface of the pile shaft was obtained, allowing use of the ABAQUS subroutine ‘DISP’ to maintain the displacement at the magnitude induced by the post-installation residual force. Subsequently increments of displacement up to $\pm 5mm$ were applied using strain control. The resultant reaction forces at the nodes of the surface of the pile shaft were summated, thus calculating the load required to mobilise the displacement increment applied and generating the load-deflection response.

Displacement field data is presented at increments of displacement of $\pm 1mm$ to allow comparison of the resulting displacement and shear strain fields with the

PIV data presented in Section 5.3.4. This data was extracted from the output database using ‘Python’ routines executed via Matlab. Given that experimental measurement of displacements using PIV started when the applied axial load was equal to the post-installation residual force, in the FE simulations displacements were zeroed after application of the post-installation residual force.

As in Chapter 6, the displacements apparent at the nodes of each element were interpolated back to a regular grid of points of similar spacing to the PIV measurement points. This allowed computation of shear strain fields using the ‘GeoSTRAINS’ routine (White and Take, 2002), so that the resultant data exhibited the same shear strain smearing as that derived from the PIV analysis. A part of this process involved disregarding displacements within the shaft volume defined by region 1 in Figure 7.2. Calculation of shear strains using nodal displacements in this section of the pile shaft and the adjacent soil in region 3 would have led to an erroneous representation of shear straining, since the soil was slipping along this boundary rather than being bonded to the pile. This was not a problem in the PIV analysis where, because the model piles were painted matt black, all patches covering the helical pile shaft became wild due to lack of texture and were manually removed from the dataset.

As a result of the processes described above, all plots from the PIV analysis and FE simulation are directly comparable. For completeness, the 1% shear strain contour has been presented for both cumulative and incremental results in the FE simulation output presented here. Throughout the following sections these initial FE analyses are referred to as the ‘Baseline’ analyses.

7.2.1 Load-Deflection Response

Figures 7.3(a), 7.3(c), 7.4(a) and 7.4(c) show comparisons of the load-deflection responses of the physical models versus the FE simulations. The percentage discrepancy is also presented as a function of the ultimate capacity (at $\pm 5\text{mm}$ axial displacement) in Figures 7.3(b), 7.3(d), 7.4(b) and 7.4(d) for the single helix pile (C1/T1), double helix pile with L_a of 30mm (C2-30/T2-30), double helix pile (C2-60/T2-60) and triple helix pile (C3/T3) with L_a of 60mm respectively.

Comparison of the experimental load-deflection responses and those from the corresponding simulations indicates that the responses are generally very similar for both

compressive and tensile loading. This supports many of the observations relating to the performance of helical screw piles made in Chapter 5. The greatest discrepancies are apparent in the initial stages of loading. For example, at an axial displacement of $\pm 1\text{mm}$ or $\pm 0.05D$, the FE validations underpredict the capacity for all configurations of helical screw pile, regardless of the type of loading (compressive or tensile), by 15-25%. As the ULS mechanism is mobilised further, this discrepancy generally reduces to lie between an underprediction of 11% and overprediction of 5%. Table 7.2 contains a summary of the absolute capacities observed from FE validation analyses with comparison to the experimental capacities, at the ULS taken at axial displacements of $\pm 5\text{mm}$.

Table 7.2: Percentage discrepancy between experimental and FE validation derived absolute capacity of helical screw piles, expressed as a percentage of the capacity at the ULS for the experimental case ($\delta=\pm 5\text{mm}$).

Test	Absolute Capacity (N)		Discrepancy (%)
	Experimental	Finite Element	
C1	69.8	66.0	-5.5
T1	69.3	61.8	-10.9
C2-30	99.4	93.0	-6.4
T2-30	98.9	90.4	-8.6
C2-60	131.8	130.7	-0.8
T2-60	119.2	125.3	5.1
C3	132.8	127.5	-4.0
T3	121.0	124.3	2.7

One trend is immediately apparent. The tensile capacity of the helical screw piles with L_a of 60mm (T2-60 and T3), is overpredicted by the FE validation. In Chapter 5 it was postulated that the reduction in capacity of tensile tests T2-60 and T3 relative to the comparable compressive tests, C2-60 and C3, was due to propagation of the failure mechanism to the surface of the sample. Evidence of this occurring was provided in the form of PIV derived displacement and shear strain fields in Section 5.3.4.2. However, this behaviour was not reproduced in the FE validations, as is demonstrated by the displacement and shear strain fields presented in Section 7.2.2. Hence, it can be concluded that propagation of the failure mechanism to the surface of the sample in tests T2-60 and T3 was most likely the product of pile installation induced breakout of soil at the surface of the sample leading to a reduction in H/D . The discrepancies in the FE analyses themselves are summarised in Table 7.3 and graphically in Figure 7.5 as a function of L_a .

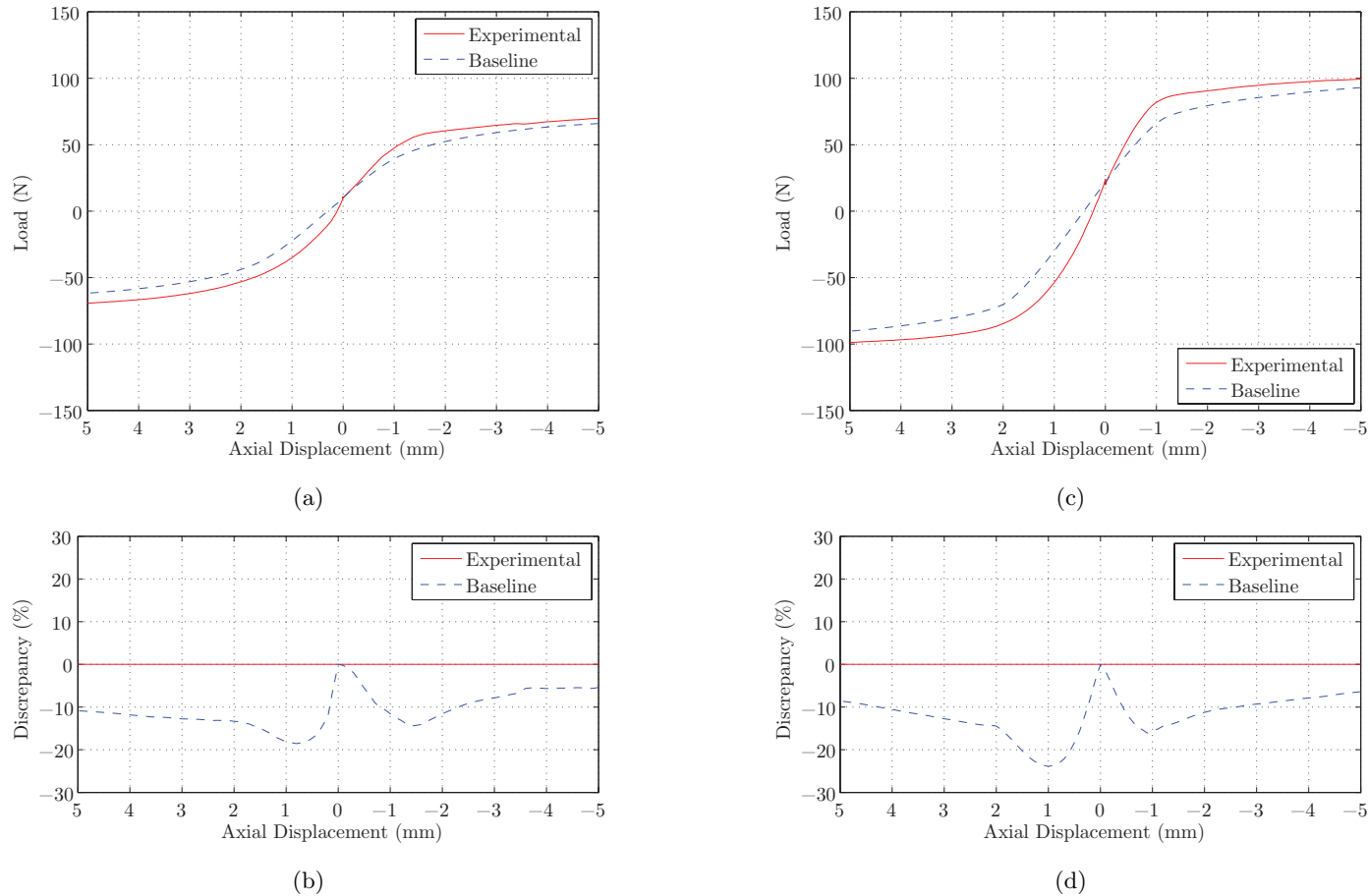


Figure 7.3: Comparison of experimental and ‘Baseline’ FE derived load deflection response for: single helix pile, response (a) and discrepancy (b); and double helix pile with L_a of 30mm, response (c) and discrepancy (d).

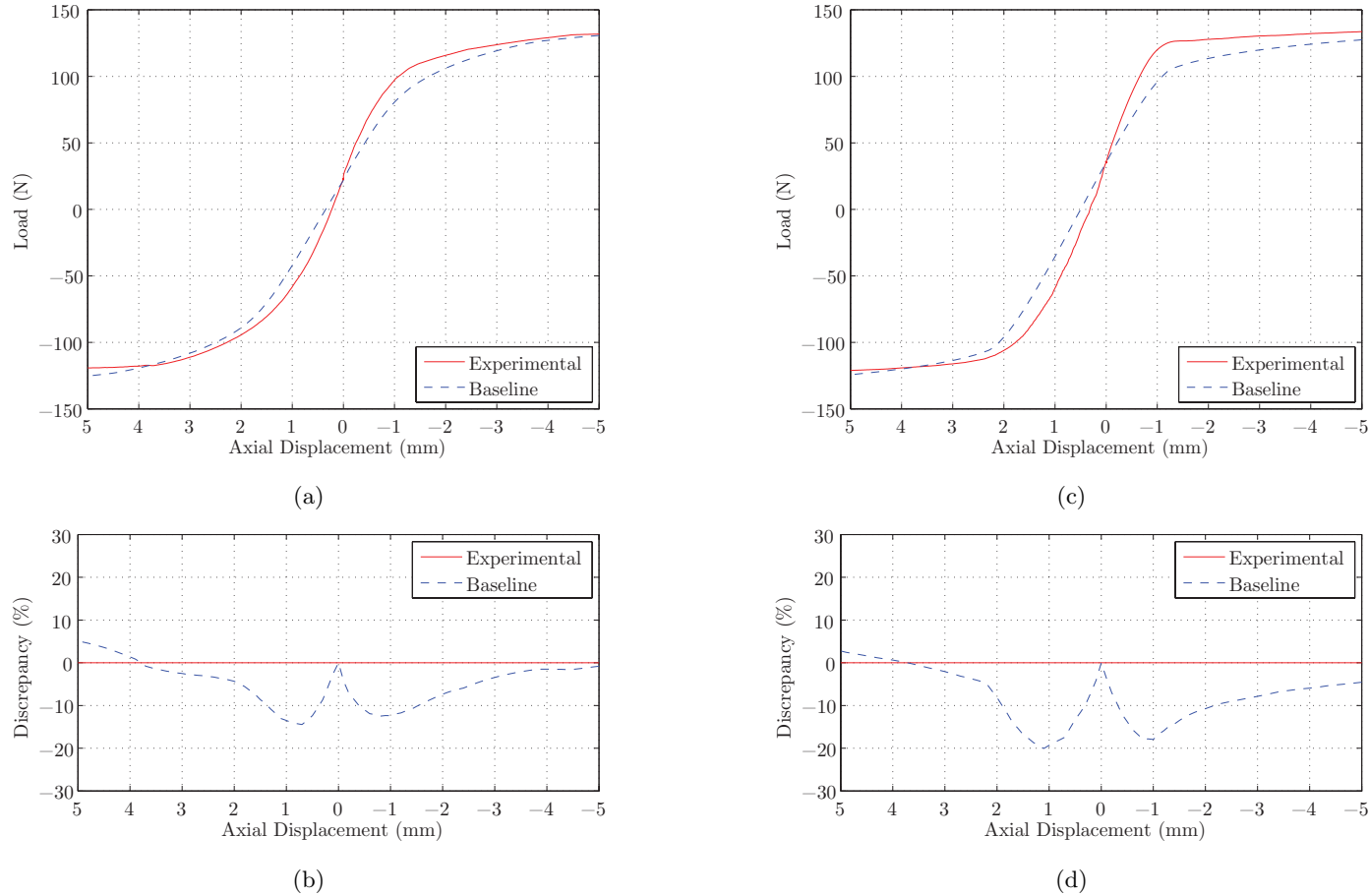


Figure 7.4: Comparison of experimental and ‘Baseline’ FE derived load deflection response for: double helix pile with L_a of 60mm, response (a) and discrepancy (b); and triple helix pile with L_a of 60mm, response (c) and discrepancy (d).

Table 7.3: Percentage discrepancy between FE validation derived compressive and tensile capacity of helical screw piles, expressed as a percentage of the ultimate compressive capacity ($\delta=-5\text{mm}$).

Test	H/D	Absolute Capacity (N)	Discrepancy (%)
C1	7	66.0	6.36
T1		61.8	
C2-30	5.5	93.0	2.80
T2-30		90.4	
C2-60	4	130.7	4.12
T2-60		125.3	
C3	4	127.5	2.51
T3		124.3	

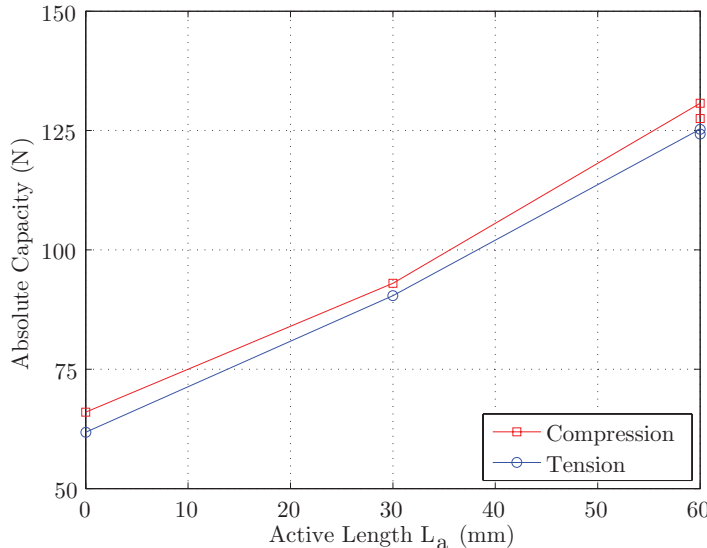


Figure 7.5: Effect of L_a on absolute ultimate capacity derived from FE validation.

The discrepancies are relatively consistent, regardless of the embedment ratio H/D , at between 2.51-6.36%. Therefore, they are most likely a result of the method adopted in the FE modelling. For example, modelling the residual force caused by the installation process was achieved by applying an axial compressive load equal to the post-installation residual force to the helical pile. This was done before displacement increments were applied to failure. Given that measurement of the displacement and shear strain fields began after application of the post-installation residual force, the load-deflection response is offset from the datum by the magnitude of displacement required to generate the post-installation residual force.

Modest further increases in capacity were evident beyond axial displacements of $\pm 5mm$, causing some divergence of the absolute ultimate capacity between the FE simulations and experimental observations. Ordinarily this might suggest that the ULS was not reached in the FE simulation. However, recent comparison of deeply embedded circular plate anchor capacities in uniform clay using small strain FE and Large Deformation FE (LDFE) methods provides a potential explanation for this divergence in calculated capacity beyond the ULS.

Wang et al. (2010) performed analyses on a circular anchor, embedded to a depth of $4D$ and subjected to uplift. This was achieved using both small strain and LDFE methods in ABAQUS and AFENA. The LDFE method was implemented using the Recovered Equilibrium of Patches (REP) method in ABAQUS and the Modified Unique Element Method (MUEM) in AFENA, within the Remeshing and Interpolation Technique with Small Strain (RITSS) framework proposed by Hu and Randolph (1998). This allows remeshing of the problem between computation increments, facilitated by interpolating the stress-state to gauss points in the new mesh using the stress data from the old mesh. This is achieved using Delaunay triangulation and Laplacian smoothing algorithms, thus preserving element quality, as the shape of elements at points of high strain within the problem being modelled are not distorted wildly during the analysis. This is in contrast to a small strain FE analysis where typically a single mesh is used and elements in zones of high straining can be distorted significantly leading to calculation errors.

Figure 7.6, where F is the capacity, A is the area of the plate anchor, w is its displacement and D is its diameter, is a comparison of the normalised load-deflection responses of the anchor using the different analysis methods. It illustrates that small strain FE methods, such as those utilised here, begin to overpredict the capacity of deeply embedded circular plate anchors at displacements greater than $0.2D$. In contrast the two LDFE solutions, where mesh distortion mitigated, both converge to a lower normalised capacity.

Given that in the simulations presented in this chapter, the helical plates are idealised as deeply buried circular plates, a similar limit on the accuracy of the small strain FE method can be assumed to be relevant here. In the helical screw pile tests, an axial displacement of $\pm 5mm$ is equal to $\pm 0.25D$. Therefore, it is perhaps

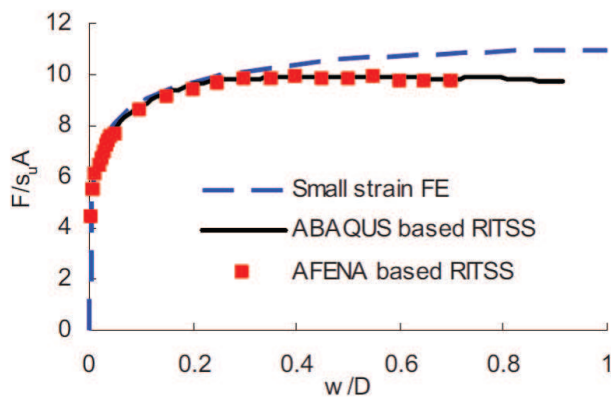


Figure 7.6: Comparison of normalised load deflection response of deeply embedded circular foundations in a uniform clay using small strain and LDFE methods, from Wang et al. (2010).

not surprising that the capacity computed by the small strain FE simulations continued to increase modestly beyond axial displacements of $\pm 5\text{mm}$.

This justifies the decision to present data only up to axial displacements of $\pm 5\text{mm}$ for the FE simulations. The average discrepancy between the experimental observations and FE simulations is -3.55%, i.e. underprediction for most cases. Increasing the range of displacement analysed would have led to further increases of the predicted capacity in the FE validations at the ULS. This in turn would have led to a reduction in the apparent average discrepancy. However, this would have been misleading, as it would have been a product of the analysis technique used (small strain versus LDFE).

Given the limitations of the small strain FE simulations performed, the maximum axial displacement analysed is $\pm 0.25D$. Therefore, it can be assumed that the load-deflection behaviour presented here is not significantly affected by the lack of remeshing between displacement increments. The discrepancy between the experimental data and FE simulation data must therefore be an effect of pile installation or constitutive model or parameter choice, i.e. choice of strength and stiffness.

The parameters utilised were derived from the in-situ post-test property data presented in Chapter 6. They have been shown to be appropriate for predicting the undrained settlement of a circular footing to a gross settlement of $0.2D$, within $\pm 5\%$ of the ultimate capacity observed in the physical models. However, only

two measurement points were used to define the relationship between strength and stiffness, I_R , with depth within the model. One was derived from a UU triaxial test performed on samples extracted from the mid-depth of a sample, whilst the other was derived from a similarity analysis based on the MSD theory of Osman and Bolton (2005) employed in reverse. Therefore, it is possible that the relationship between E_u and S_u may not have been constant over the whole depth of the physical models, as has been assumed here. However, there were insignificant numbers of data points to support any other relationship. Furthermore constant I_R is often assumed in FE based numerical modelling validations (Hu and Randolph, 1998; Song et al., 2010; Hossain and Randolph, 2009). However, the effect of varying I_R was investigated as part of the sensitivity analysis summarised in Section 7.2.4.

Aside from the discrepancies highlighted above, the trends in behaviour observed in the FE simulations are generally similar to those observed in the physical modelling presented in Chapter 5. For example, comparison of Figures 7.3(c) and 7.4(c), where s/D is constant at 1.5, whilst L_a is varied from 30mm to 60mm, indicates that the ultimate capacity mobilised is a function of L_a , which confirms the conclusion reached in Chapter 5.

Comparison of Figures 7.4(a) and 7.4(c), where s/D varied from 3.0 to 1.5, whilst L_a is maintained at 60mm or 3D, indicates that the ultimate capacity mobilised is very similar in both the experimental and FE simulation output regardless of the change in s/D . A faster rate of capacity gain (i.e. increased stiffness of load-deflection response) is also indicated in the FE simulations for cases where L_a is constant and s/D is equal to 1.5, compared to when s/D is equal to 3. This confirms the observation made relating to the effect of s/D in Chapter 5, namely that s/D governs the rate of capacity gain of multi-helix screw piles.

7.2.2 Comparison of Displacement and Shear Strain Fields

The following section contains FE simulation derived displacement and shear strain fields of helical screw piles subjected to compressive and tensile loading compared to selected results from Chapter 5. All plots are directly comparable with the experimentally derived results and are used to provide evidence to reinforce the observations discussed.

7.2.3 Observations

7.2.3.1 Initial Displacement Increment

Comparison of the displacement and shear strain fields from the FE simulations and the physical models, for the first $1mm$ increment of axial displacement, can reinforce many of the observations discussed in Chapter 5.

Firstly, consider the C1-T1 test pair. By comparing the horizontal displacement contour plots for test C1 in Figures 7.7(a) and 7.7(b) and test T1 in Figures 7.7(c) and 7.7(d), it is possible to validate the hypothesis made in Chapter 5, that the differential projected areas of the upperside of the uppermost helical plate and the lowerside for the lowermost helical plate caused the asymmetrical horizontal displacement fields. This trend was generally evident when the other physical modelling results are compared with those from the FE simulations. This is seen by comparing Figures 7.8(a) and 7.8(b) and Figures 7.8(c) and 7.8(d) for tests C2-30 and T2-30, Figures 7.9(a) and 7.9(b) and Figures 7.9(c) and 7.9(d) for tests C2-60 and T2-60 and Figures 7.10(a) and 7.10(b) and Figures 7.10(c) and 7.10(d) for tests C3 and T3. In all cases the asymmetry is less significant in the FE simulations than the experimental results and the reason for this is unknown. However, the discrepancy of the magnitude of the asymmetry is less than about $50\mu m$. The most significant difference between the FE and PIV results can be seen by comparing Figures 7.9(c) and 7.9(d) for test T2-60, where the maximum magnitude of displacement and its extent beneath the lowermost helical plate is reduced in the experimental output compared to the FE simulation. There is also no obvious explanation for this discrepancy, although it ought to be noted that it is also less than $50\mu m$ as a worst case and thus relatively small. Reassuringly in all cases with multiple helical plates the horizontal displacements evident between the helical plates are in generally good agreement.

The vertical contour plots generally indicate better agreement, since the effects of asymmetry of displacement in the physical model are less evident because the magnitude of vertical displacement is significantly greater than horizontal displacement. This is due to the geometry of the helical screws piles and the axial loading applied. Taking tests C1 and T1, by comparing Figures 7.11(a) and 7.11(b) and Figures 7.11(c) and 7.11(d), this positive agreement can be demonstrated, as the vertical displacement fields are very similar for both compressive and tensile loading. The decision to allow slippage between the coincident nodes along the

358

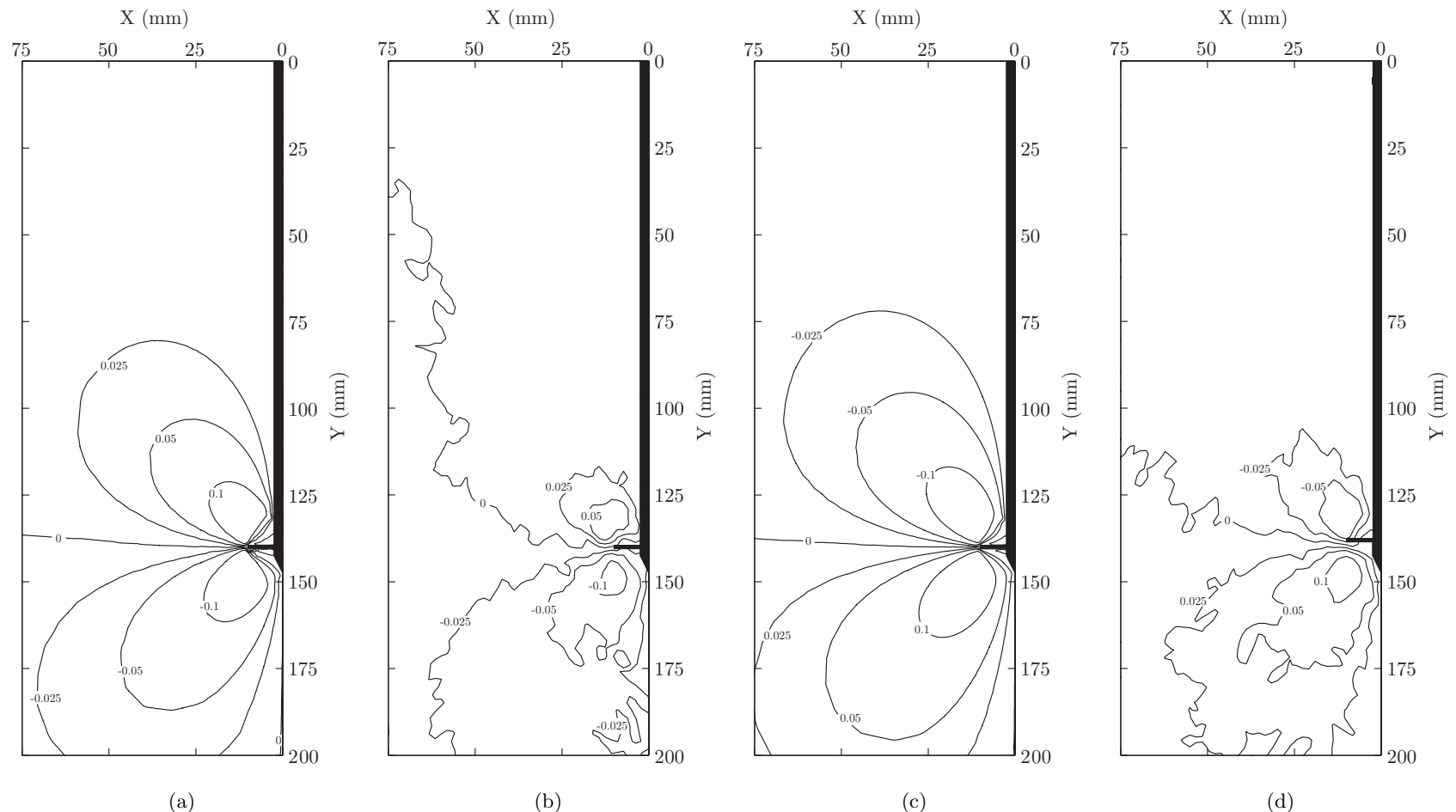


Figure 7.7: Comparison of initial horizontal displacement increment: C1 FE (a), C1 PIV (b), T1 FE (c) and T1 PIV (d) with displacements in mm.

359

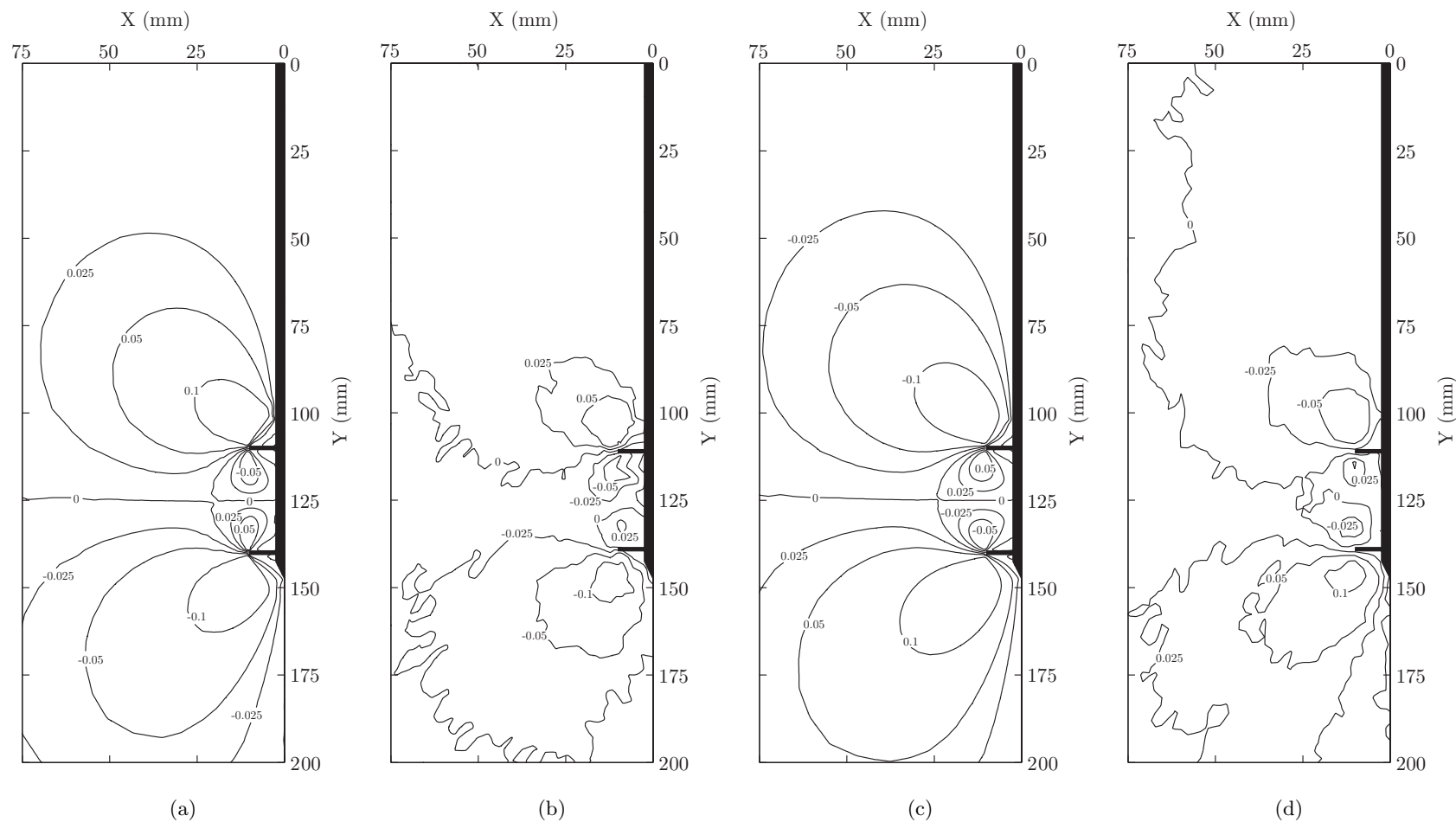


Figure 7.8: Comparison of initial horizontal displacement increment: C2-30 FE (a), C2-30 PIV (b), T2-30 FE (c) and T2-30 PIV (d) with displacements in mm.

360

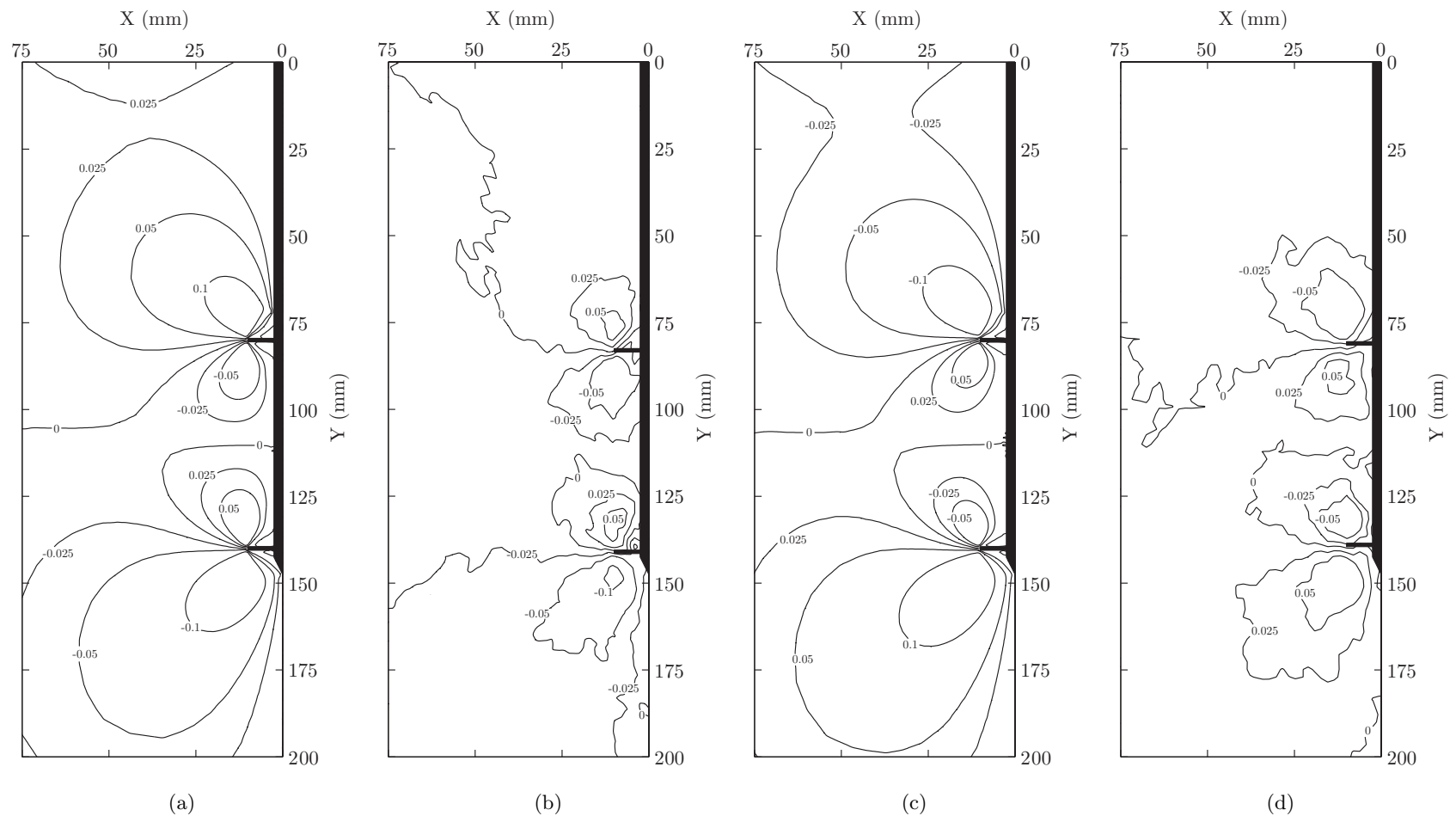


Figure 7.9: Comparison of initial horizontal displacement increment: C2-60 FE (a), C2-60 PIV (b), T2-60 FE (c) and T2-60 PIV (d) with displacements in mm.

7.2 Finite Element Simulation

361

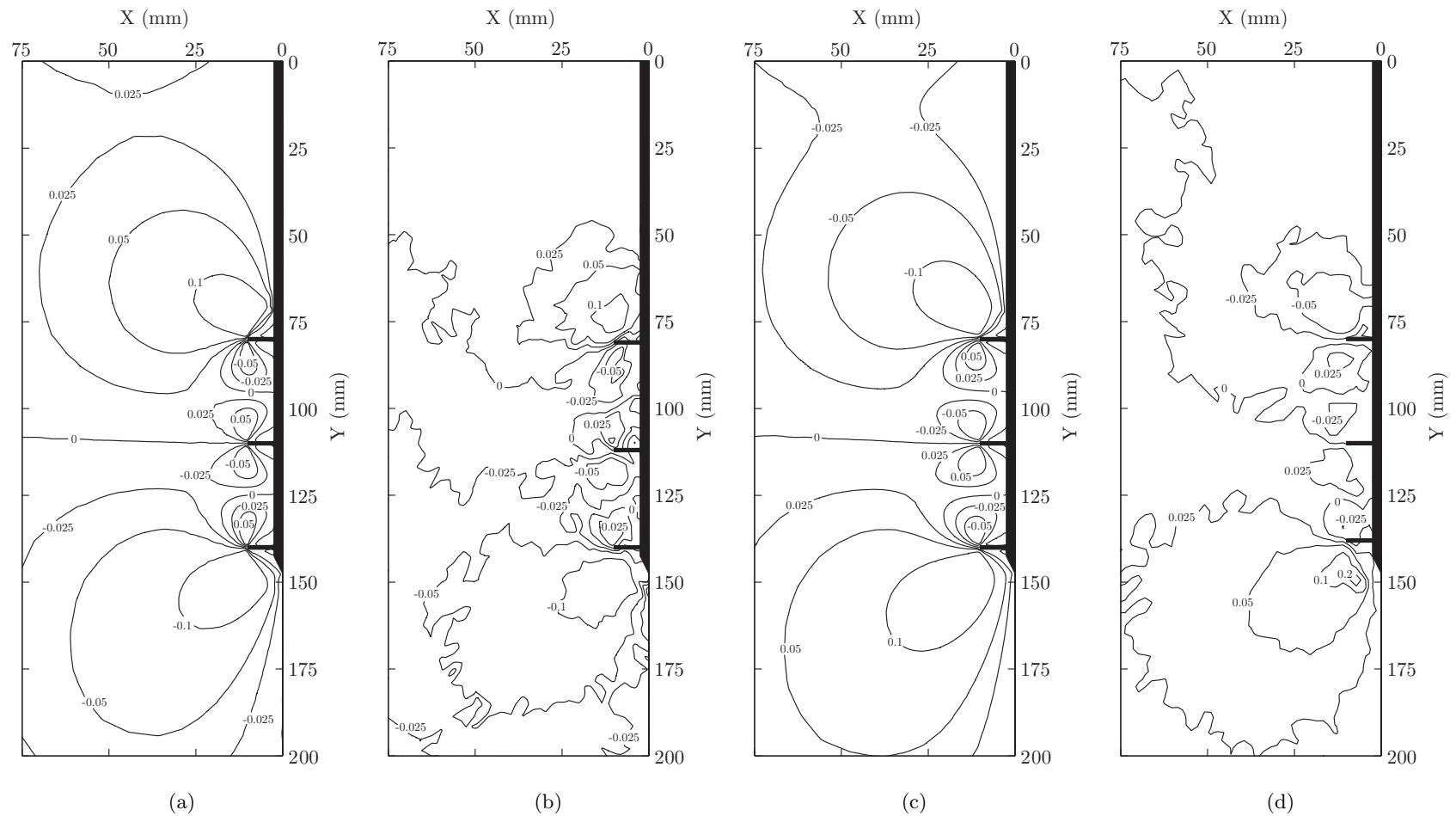


Figure 7.10: Comparison of initial horizontal displacement increment: C3 FE (a), C3 PIV (b), T3 FE (c) and T3 PIV (d) with displacements in mm.

soil-shaft interface (boundary between regions 1 and 3 in Figure 7.2) in the FE models is justified by the similar pattern of vertical displacement apparent along this boundary when the FE simulation and experimental outputs are compared. The amount of heave evident in the FE analyses is typically greater than that observed in the physical model, though the discrepancy is only about $25\mu m$. Comparison of the same type of data for the other tests demonstrates similar trends, as can be seen by comparing Figures 7.12(a) and 7.12(b) and Figures 7.12(c) and 7.12(d) for tests C2-30 and T2-30, Figures 7.13(a) and 7.13(b) and Figures 7.13(c) and 7.13(d) for tests C2-60 and T2-60 and Figures 7.14(a) and 7.14(b) and Figures 7.14(c) and 7.14(d) for tests C3 and T3. The most notable exception is seen in the comparison of Figures 7.13(a) and 7.13(b) and Figures 7.13(c) and 7.13(d) for tests C2-60 and T2-60. Here, a greater volume of soil is experiencing vertical displacement between the helical plates. In the physical modelling data two distinct bulbs of soil were displaced at the depth of each helical plate, whereas in the FE simulations, this zone covers the whole of the area between the helical plates after the initial displacement increment. This could be caused by the assumption that soil between multiple helical plates is bonded to the pile along the soil-shaft interface.

Lastly, the shear strain fields from the FE simulation can be compared to the experimental output. Using tests C1 and T1 by comparing Figures 7.15(a) and 7.15(b) and 7.15(c) and 7.15(d), it can be concluded that the shear strains generated due to the first $1mm$ increment of displacement are very well modelled in the FE simulation. For test C1 the maximum shear strain is practically identical with respect to position and extent. In the case of test T1, the same maximum shear strain is evident, but over a slightly smaller volume in the FE simulation. Reduced shear strains at the outer radii of the helical plates in the tensile case are also evident in the FE simulations for other configurations of pile. The application of the post-installation residual force in the FE analysis is the most likely cause of this systematic discrepancy. After the application of the first $1mm$ increment of displacement, the compressive pile has mobilised a larger proportion of its ultimate capacity than its tensile counterpart. Further evidence of this can be seen for tests C2-30 and T2-30 by comparing Figures 7.16(a) and 7.16(b) and 7.16(c) and 7.16(d), tests C2-60 and T2-60 by comparing Figures 7.17(a) and 7.17(b) and 7.17(c) and 7.17(d) and tests C3 and T3 by comparing Figures 7.18(a) and 7.18(b) and 7.18(c) and 7.18(d). The greatest discrepancy in the shear strain fields can be seen by comparing Figures 7.17(a) and 7.17(b) and 7.17(c) and 7.17(d) which relate to tests

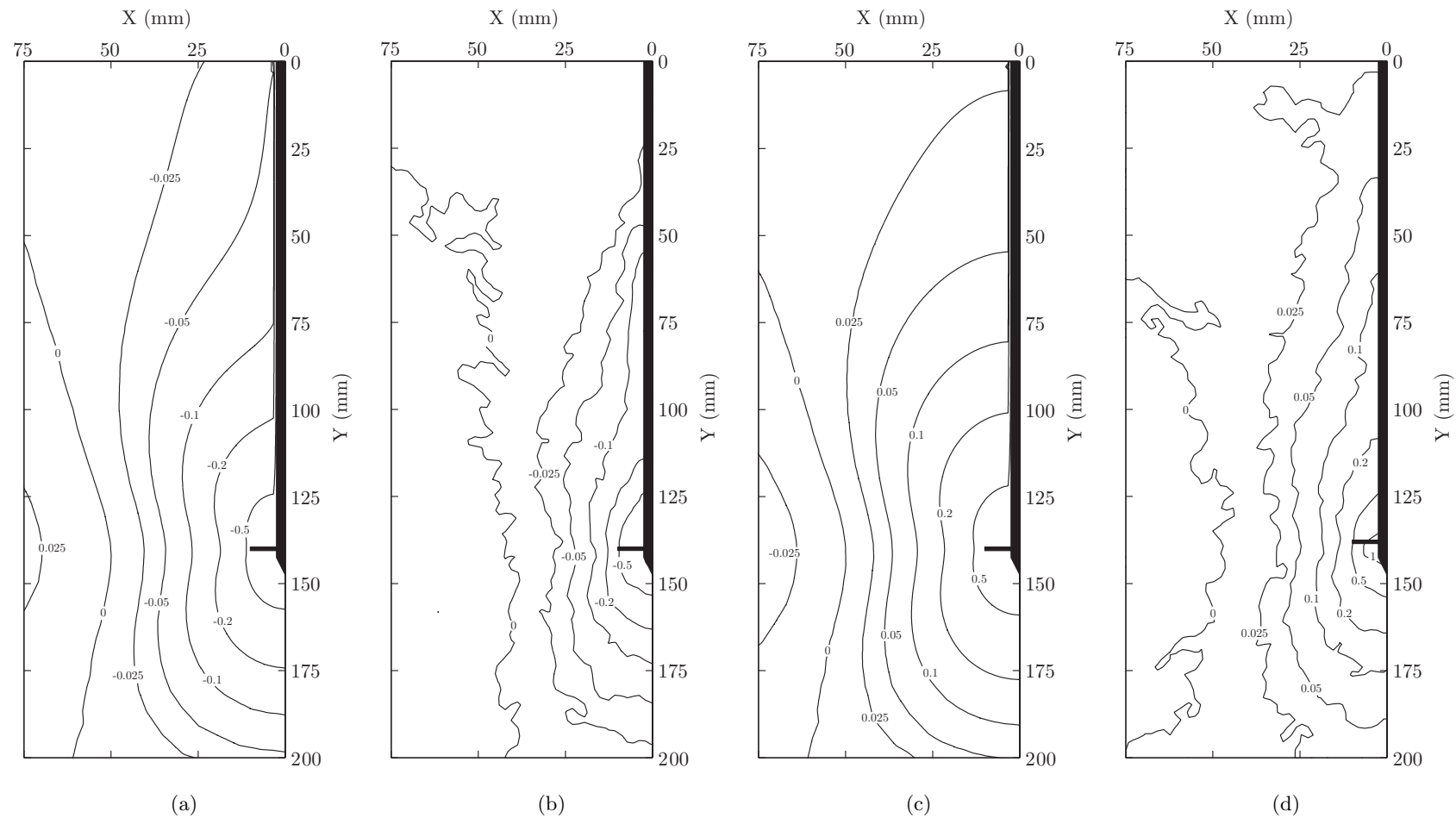


Figure 7.11: Comparison of initial vertical displacement increment: C1 FE (a), C1 PIV (b), T1 FE (c) and T1 PIV (d) with displacements in mm.

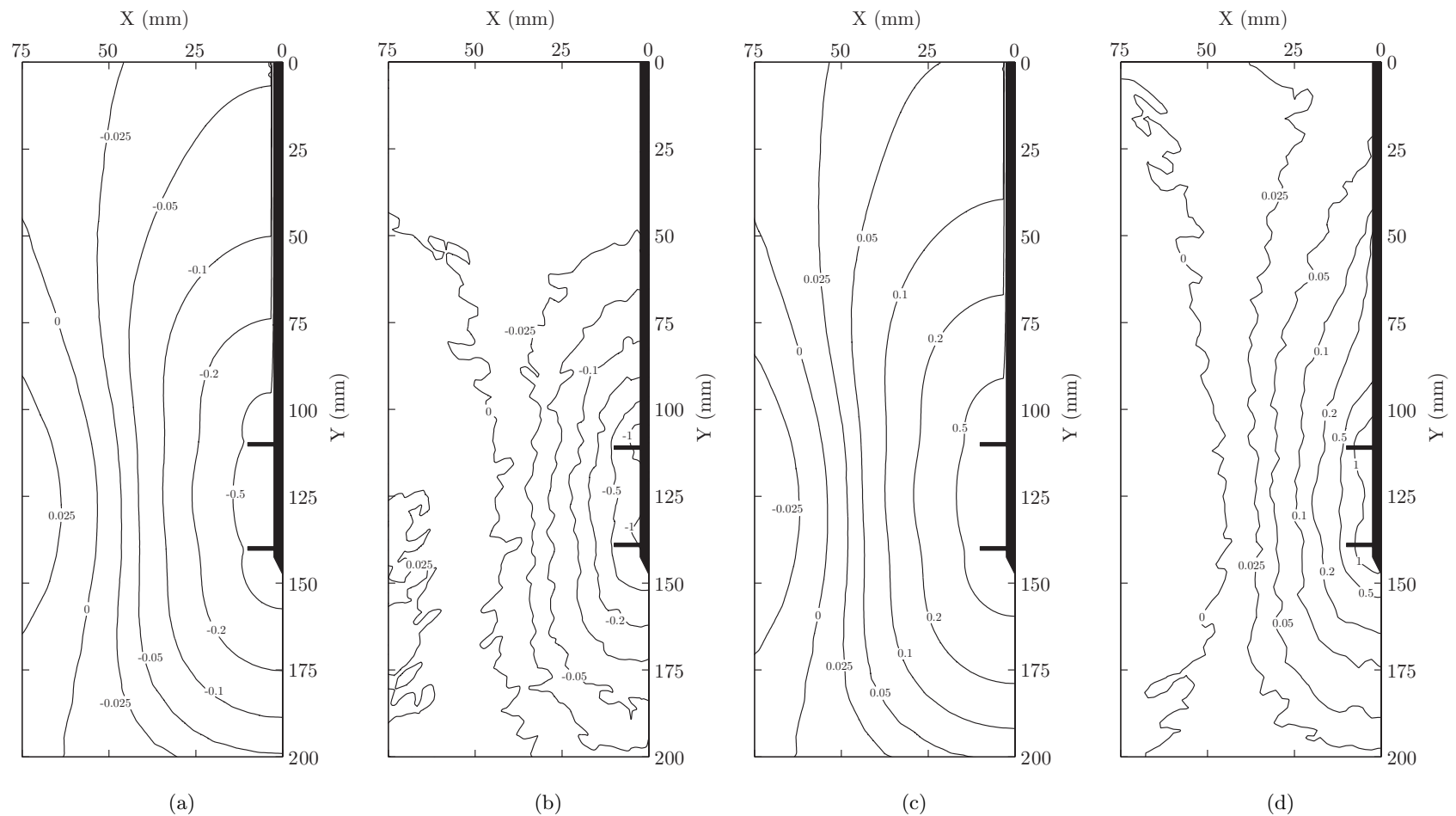


Figure 7.12: Comparison of initial vertical displacement increment: C2-30 FE (a), C2-30 PIV (b), T2-30 FE (c) and T2-30 PIV (d) with displacements in mm.

7.2 Finite Element Simulation

365

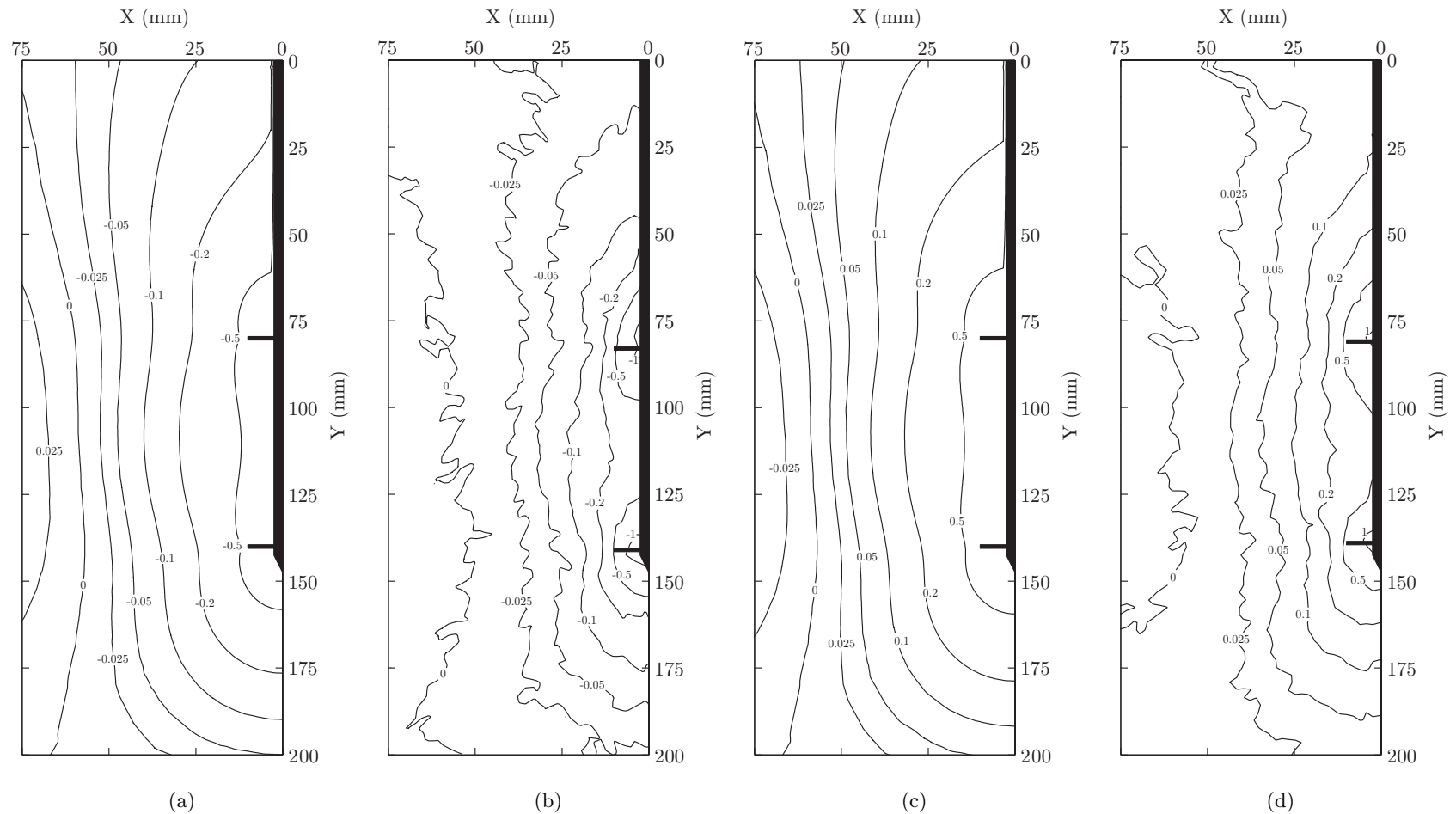


Figure 7.13: Comparison of initial vertical displacement increment: C2-60 FE (a), C2-60 PIV (b), T2-60 FE (c) and T2-60 PIV (d) with displacements in mm.

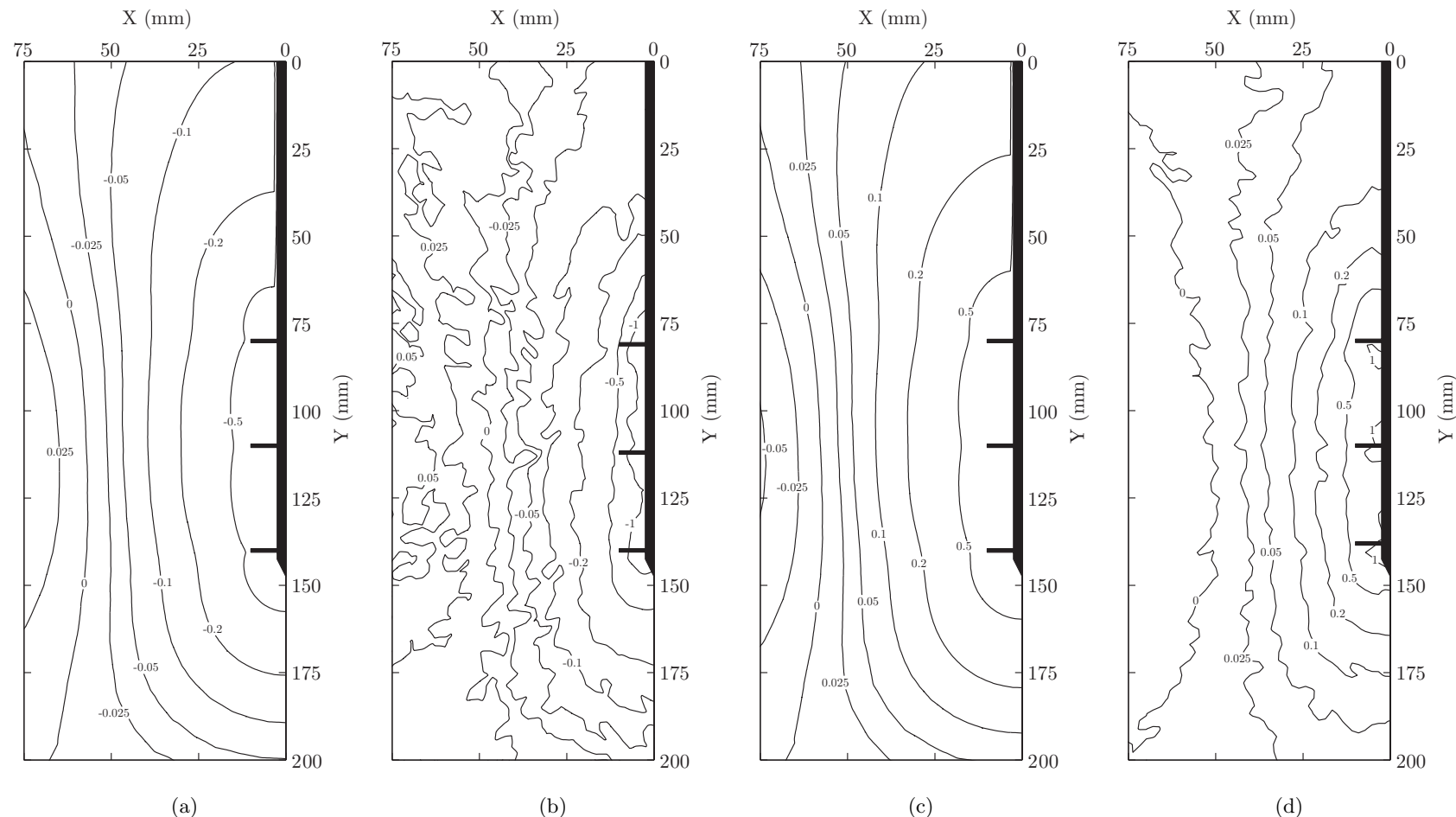


Figure 7.14: Comparison of initial vertical displacement increment: C3 FE (a), C3 PIV (b), T3 FE (c) and T3 PIV (d) with displacements in mm.

C2-60 and T2-60. In the FE simulation output, shear strains are evident near the soil-shaft interface between the helical plates. This was not evident in the physical model and there are two possible explanations. Firstly, the assumption that the soil can be tied to the pile shaft along this part of the pile could be unrealistic. Secondly, it may be that the behaviour was apparent in the physical model but was not captured by the PIV analysis, due to the matt black coating applied to the model pile and the limiting measurement density caused by the use of 50px patches in the analysis mesh with no overlapping. Nevertheless, the region experiencing maximum shear strains is correctly predicted to be at the outer radii of the helical plates.

7.2.3.2 Development of Ultimate Limit State

To assess the development of the ULS in the FE simulations, the test with the greatest percentage discrepancy has been selected for study. The appropriate tests can be identified by referring to the load-deflection response discrepancy plots in Figures 7.3(b), 7.3(d), 7.4(b) and 7.4(d). On average over the duration of each test the largest discrepancy was apparent for test T2-30. Hence it was assumed that the FE simulation and experimentally derived displacement and shear strain fields would differ most significantly for this case. The distribution of shear strains due to sequential $1mm$ increments of displacement can be compared to assess the similarity of the development of the ULS mechanism in the FE simulation and experimental output.

Figures 7.16(c) and 7.16(d) present the FE simulation and experimentally derived shear strain fields for the first $1mm$ increment of displacement. The general trend in behaviour is similar. However, the maximum magnitude of shear strains apparent in the physical modelling data is greater than that seen in the FE validation. This is potentially due to erroneous selection of the final image using PIV measurement of pile displacement in the PIV analysis, since Figure 5.57(c) indicates that the axial displacement applied must have been slightly more than $1mm$, as a $1mm$ vertical displacement contour is present. Alternatively the method in which the post-installation residual force was applied as a step in the FE analysis may have contributed to this as the post-installation residual force was applied as a compressive load. Subsequently loading the pile in tension first causes unloading before net tensile loading to failure. Hence during this initial $1mm$ displacement increment the pile was effectively unloaded before being loaded in tension. Due

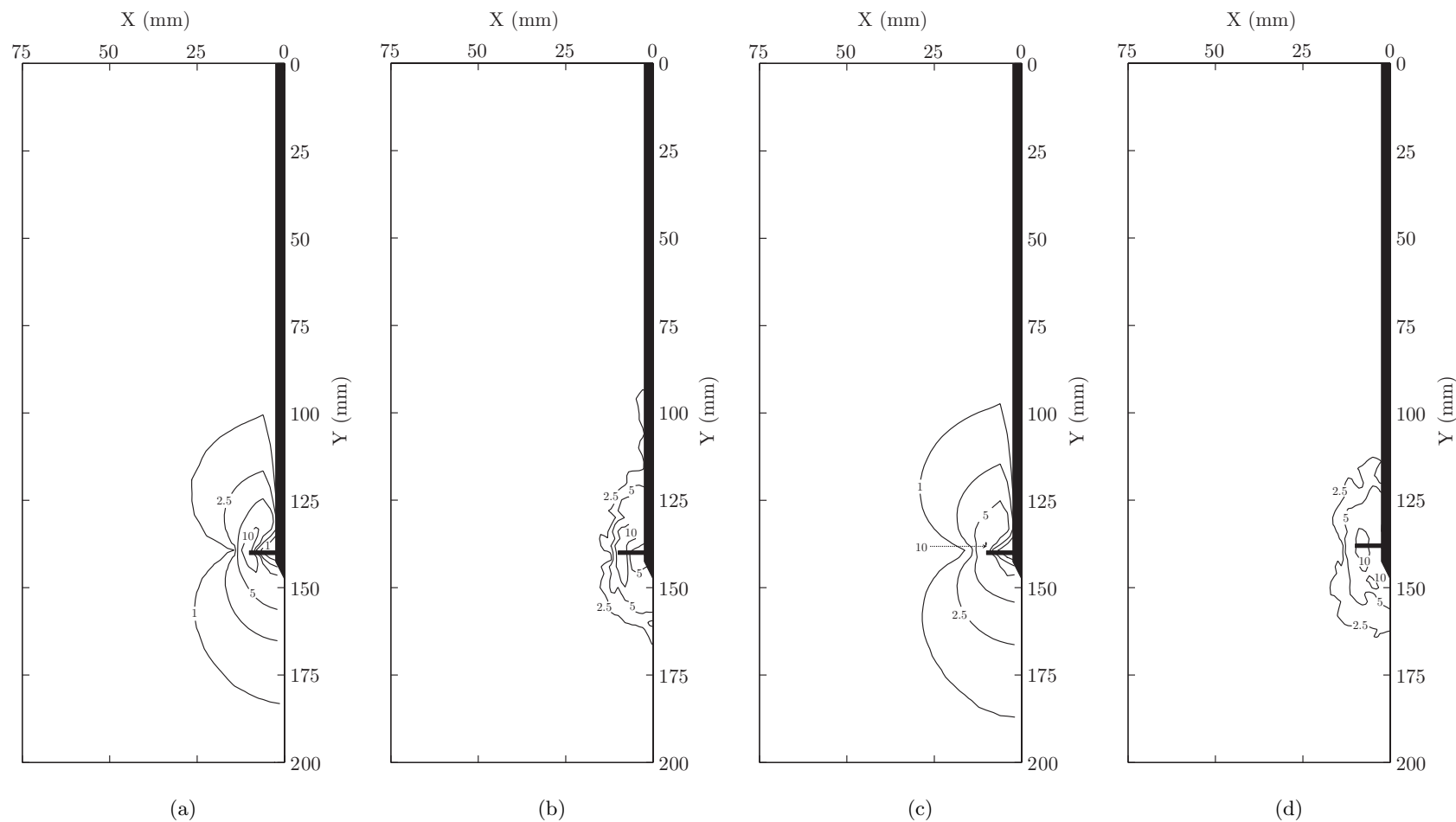


Figure 7.15: Comparison of shear strain fields at 1mm cumulative displacement: C1 FE (a), C1 PIV (b), T1 FE (c) and T1 PIV (d) with shear strains expressed as a percentage.

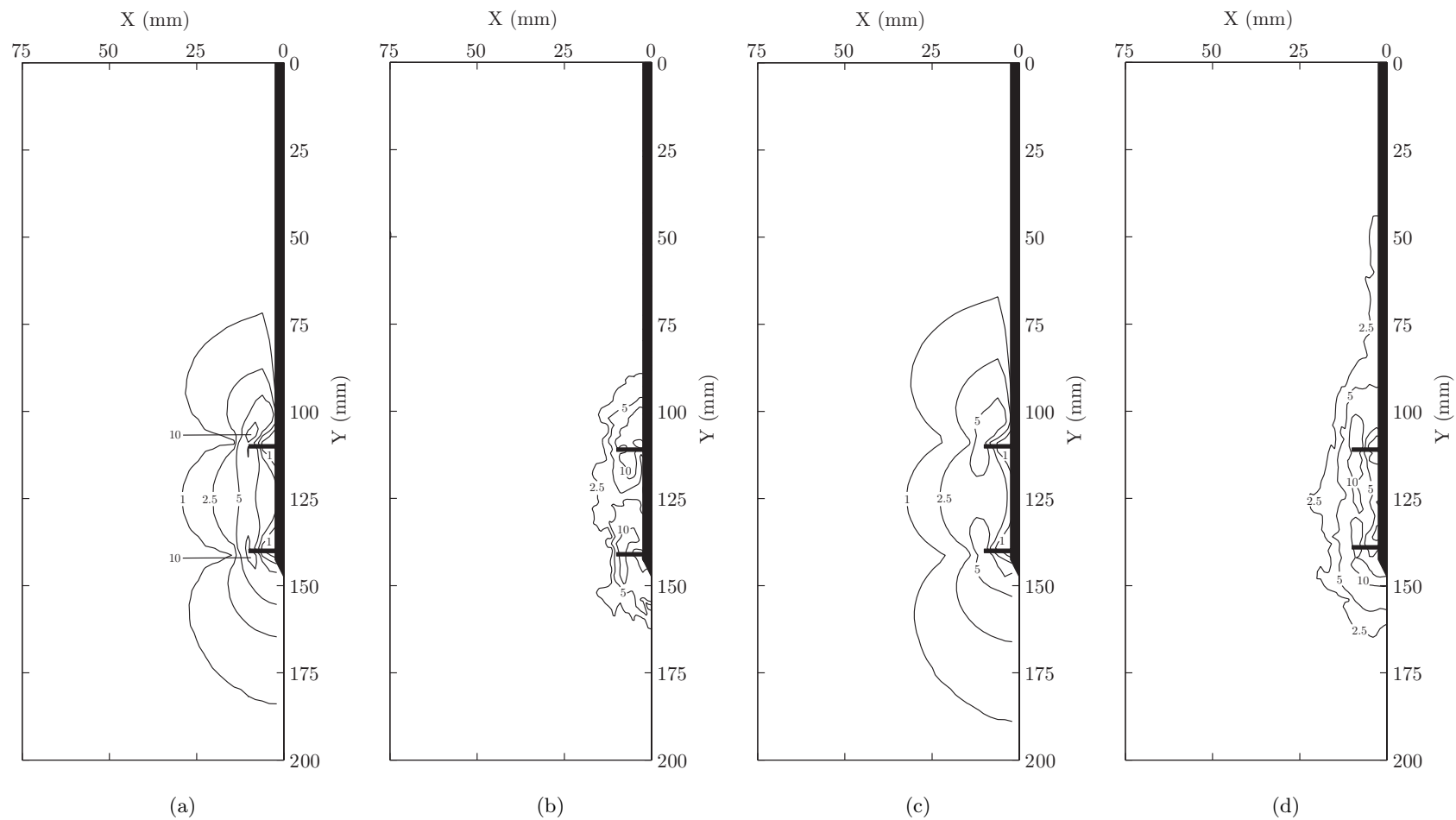


Figure 7.16: Comparison of shear strain fields at 1mm cumulative displacement: C2-30 FE (a), C2-30 PIV (b), T2-30 FE (c) and T2-30 PIV (d) with shear strains expressed as a percentage.

370

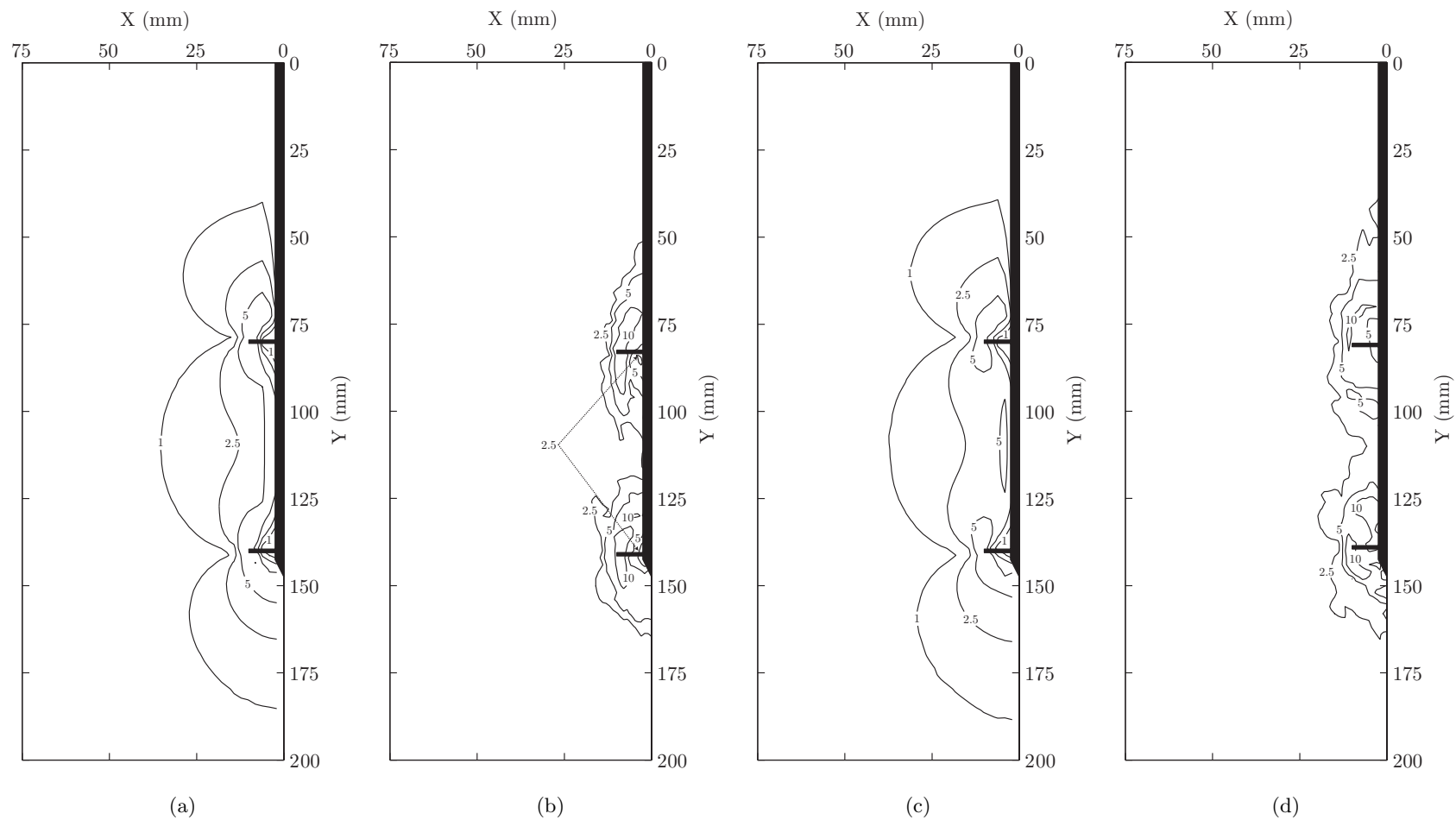


Figure 7.17: Comparison of shear strain fields at 1mm cumulative displacement: C2-60 FE (a), C2-60 PIV (b), T2-60 FE (c) and T2-60 PIV (d) with shear strains expressed as a percentage.

7.2 Finite Element Simulation

371

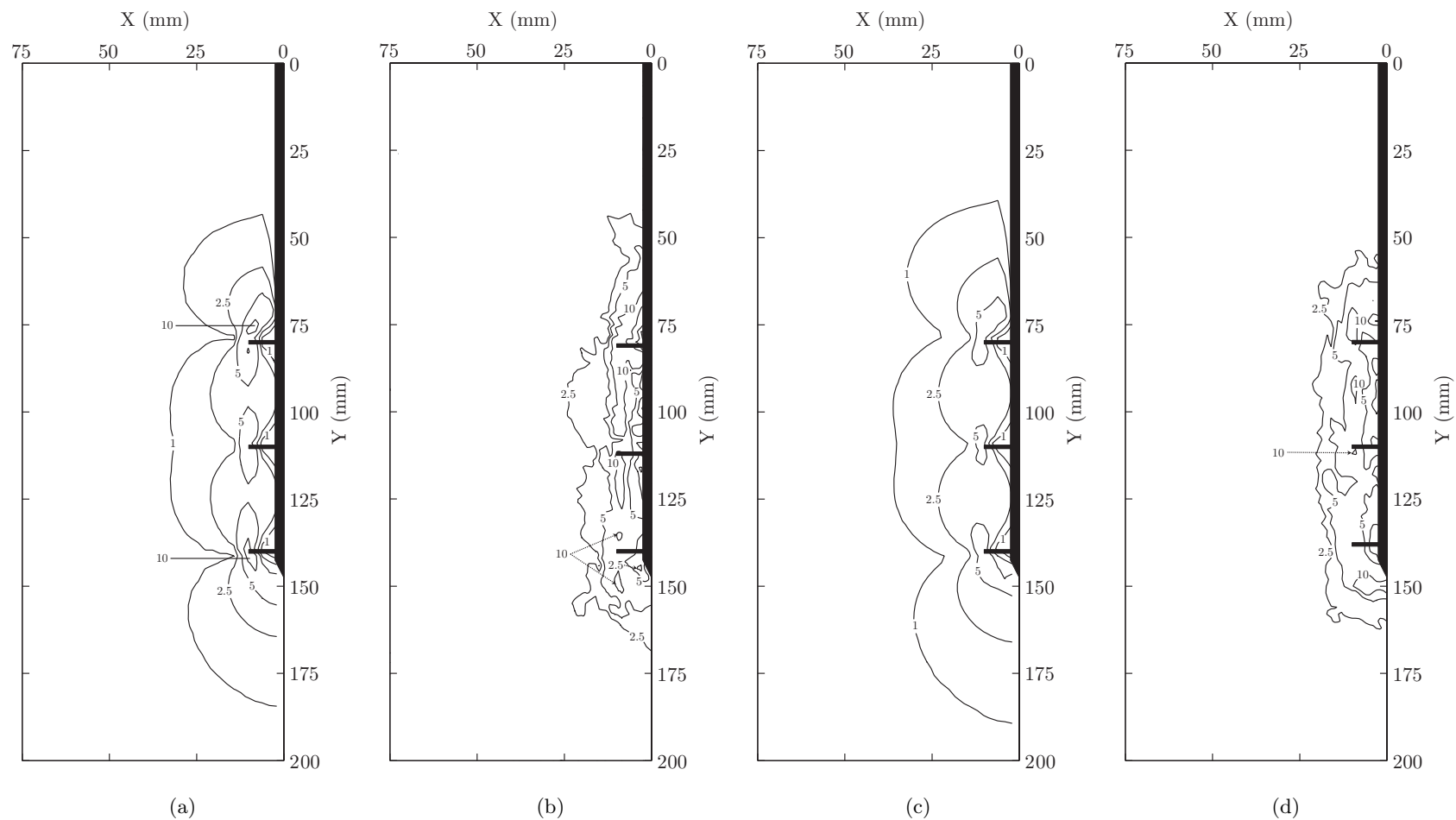


Figure 7.18: Comparison of shear strain fields at 1mm cumulative displacement: C3 FE (a), C3 PIV (b), T3 FE (c) and T3 PIV (d) with shear strains expressed as a percentage.

to either, or a combination, of these potential causes, the shear band developing between the uppermost and lowermost helical plates in the physical model is more developed and continuous than in the FE simulation.

Figures 7.19(a) and 7.19(b) illustrate the shear strain due to the next $1mm$ increment of axial displacement, which produces a cumulative displacement of $2mm$. The same trend is evident, although a more defined shear band is apparent in the FE simulation and the maximum shear strain is the same in both physical and numerical models at 10%. The extent of shear straining is greater in the FE simulation compared to the physical model, i.e. the mechanism is more localised in the physical model. This is evidence that a preferential shear band may have developed due to the legacy of the installation process in the physical model. In contrast, in the FE simulation the pile is ‘wished’ into place, so no such band is present.

After application of the next $1mm$ increment of axial displacement, generating a cumulative displacement of $3mm$, similarity between the shear strain contour plots improves drastically, as is illustrated by comparing Figures 7.19(a) and 7.19(d). The maximum shear strain in the FE simulation is 10%, along a shear band extending between the uppermost and lowermost helical plates. The maximum shear strain in the physical model is greater at around 25% at the centre of the developing cylindrical failure mechanism. However, the extent of the shear strain field is in far better agreement. The last two computed increments of $1mm$ axial displacement produce almost the same predicted behaviour, as can be seen by comparing Figures 7.20(a) and 7.20(b) and Figures 7.26(c) and 7.26(d).

Aside from the slight difference in maximum shear strain, that is apparent for some increments, the only notable discrepancy is that in the physical model the shear strain field is shown to propagate further above the uppermost helical plate than is observed in the FE simulation. Again this is evidence of a preferential shear band being caused by the installation process, along the path of installation at the outer radii of the helical plates. In general, the same trends can be seen for all other configurations of helical pile under compressive or tensile loading. The initial increments of displacement show some discrepancies between the physical modelling and FE simulation output. This is not surprising since the load-deflection response

7.2 Finite Element Simulation

373

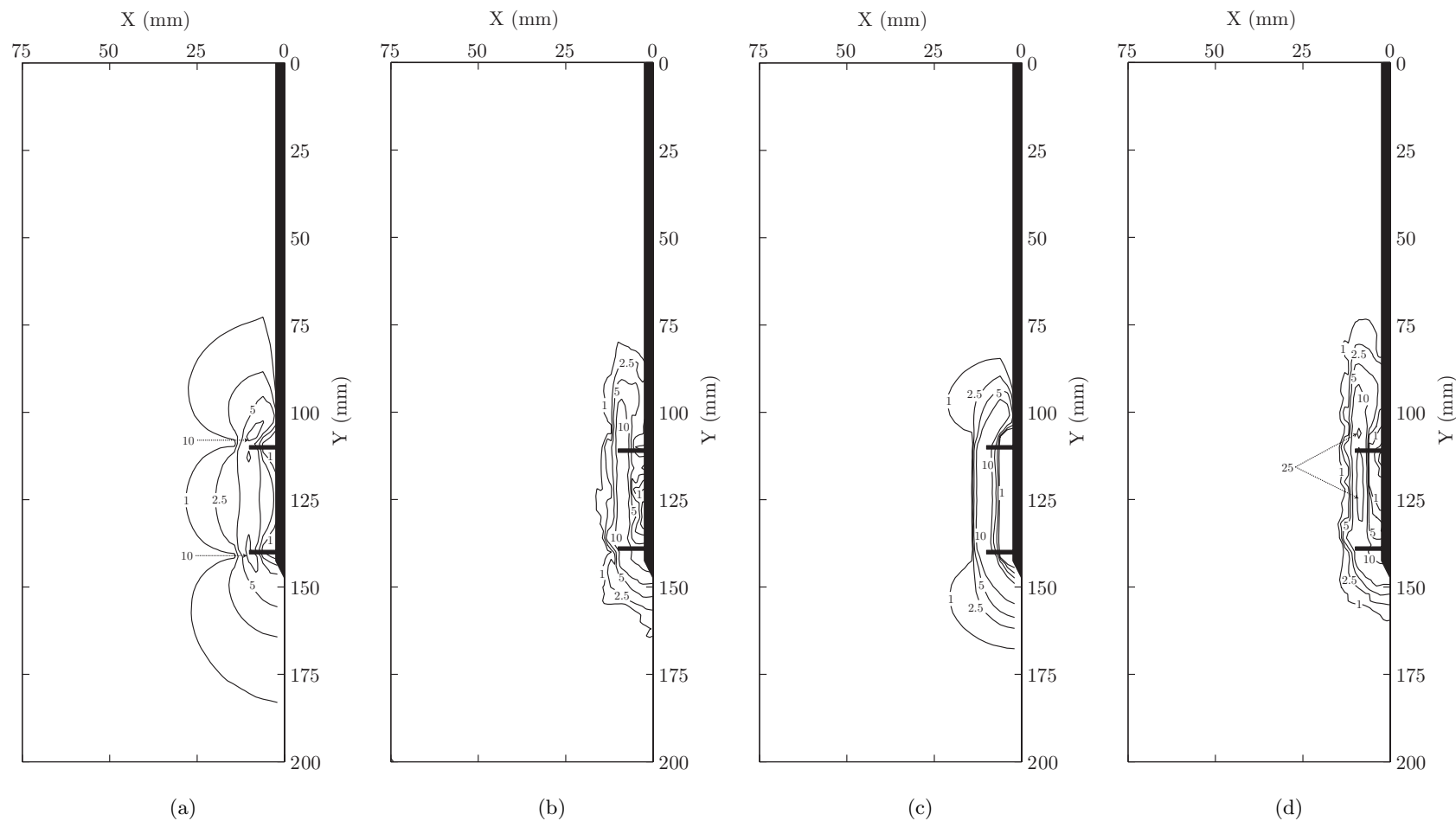


Figure 7.19: Comparison of shear strain fields for 1-2mm and 2-3mm incremental displacements: T2-30 1-2mm FE (a), T2-30 1-2mm PIV (b), T2-30 2-3mm FE (c) and T2-30 2-3mm PIV (d) with shear strains expressed as a percentage.

7.2 Finite Element Simulation

374

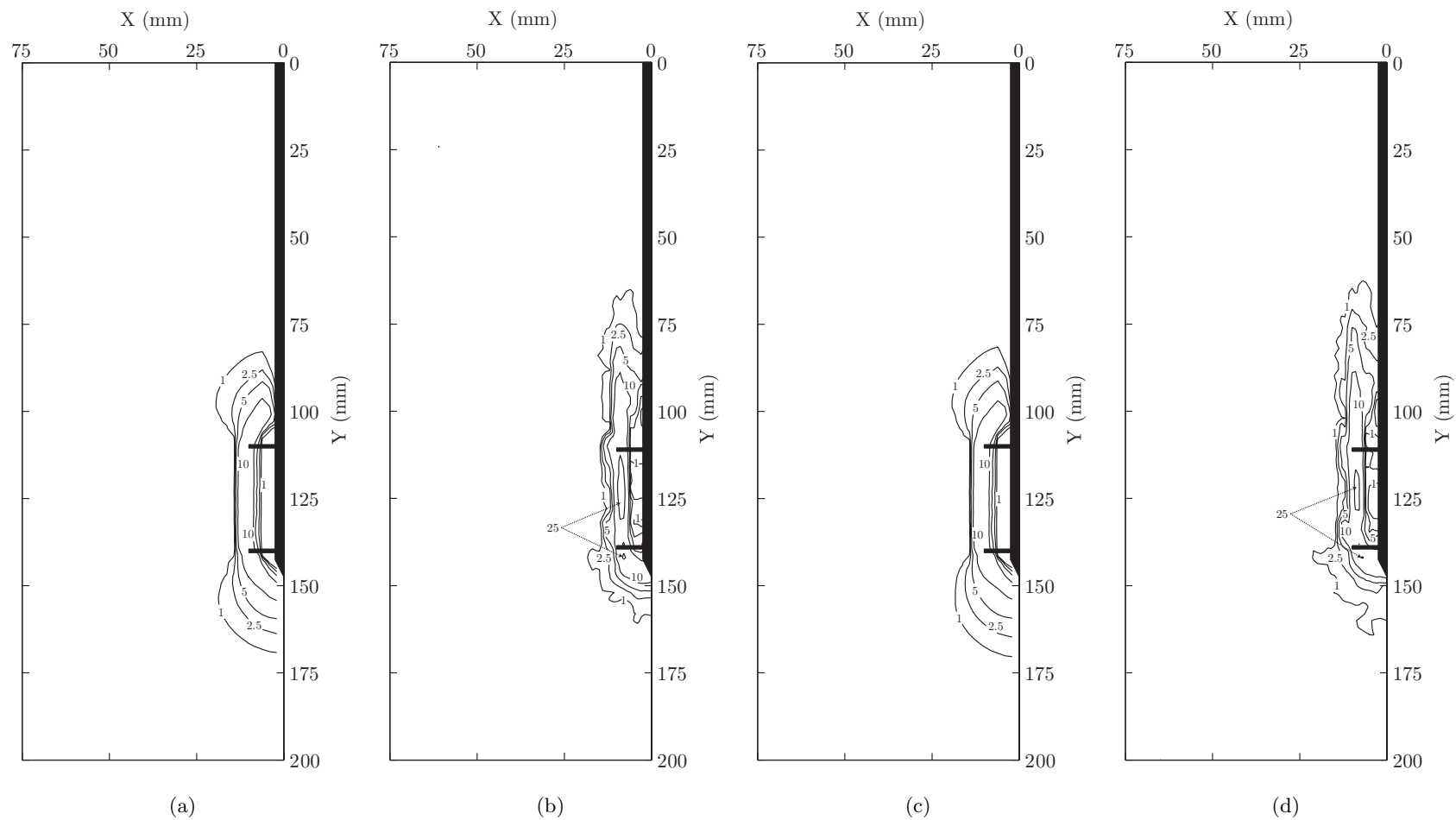


Figure 7.20: Comparison of shear strain fields for 3-4mm and 4-5mm incremental displacements: T2-30 3-4mm FE (a), T2-30 3-4mm PIV (b), T2-30 4-5mm FE (c) and T2-30 4-5mm PIV (d) with shear strains expressed as a percentage.

discrepancy is greatest for these initial displacement increments in all cases, yet reduces significantly as the ULS is approached.

7.2.3.3 Comparison of ULS Deformation Mechanisms

In the previous section the development of the ULS in the FE validation and physical models was compared. Now, the ULS deformation mechanisms observed using PIV and computed by the FE simulations are compared for all configurations of helical screw pile and loading.

Firstly, consider the single helix pile in tests C1 and T1. For both compressive and tensile loading the ULS failure mechanism predicted in the FE simulations is similar to that observed in the physical models. The shear strain contour plots in Figures 7.23(a) and 7.23(b) and Figures 7.23(c) and 7.23(d) indicate that the deformation mechanism for a single helix pile is characterised by a zone of concentrated shear strains at the outer radii of the helical plate. Shear strains are local to the helical plate and extend vertically by $\pm 1-2D$ above and below the plate and horizontally by $\pm 1D$. The horizontal displacement contours in Figures 7.21(a) and 7.21(b) and Figures 7.21(c) and 7.21(d) and the vertical displacement contours in Figures 7.22(a) and 7.22(b) and Figures 7.22(c) and 7.22(d), show almost identical magnitude and extent of horizontal displacements and similar vertical displacements.

For the double helix pile with L_a of 30mm investigated in tests C2-30 and T2-30, the ULS deformation mechanisms computed in the FE simulations and observed in the physical models, consist of a shear band extending between the uppermost and lowermost helical plates. The shear strain contour plots in Figures 7.26(a) and 7.26(b) and Figures 7.26(c) and 7.26(d) best demonstrate this. However, the shear band in the physical model extends further above the uppermost helical plate than is computed in the FE simulation. As previously discussed, this is most likely due to the installation process generating a preferential shear band in the model, that is activated in tension but not when the pile is loaded in compression. Above and below the uppermost and lowermost helical plates the shear strain field in the FE validation extends over a greater area than was observed in the physical model. Figures 7.24(a) and 7.24(b) and Figures 7.24(c) and 7.24(d) indicate that greater horizontal displacement above and below the uppermost and lowermost helical plates was computed by the FE simulations. Figures 7.25(a) and 7.25(b) and Figures 7.25(c) and 7.25(d) show that the FE simulation computes very similar

376

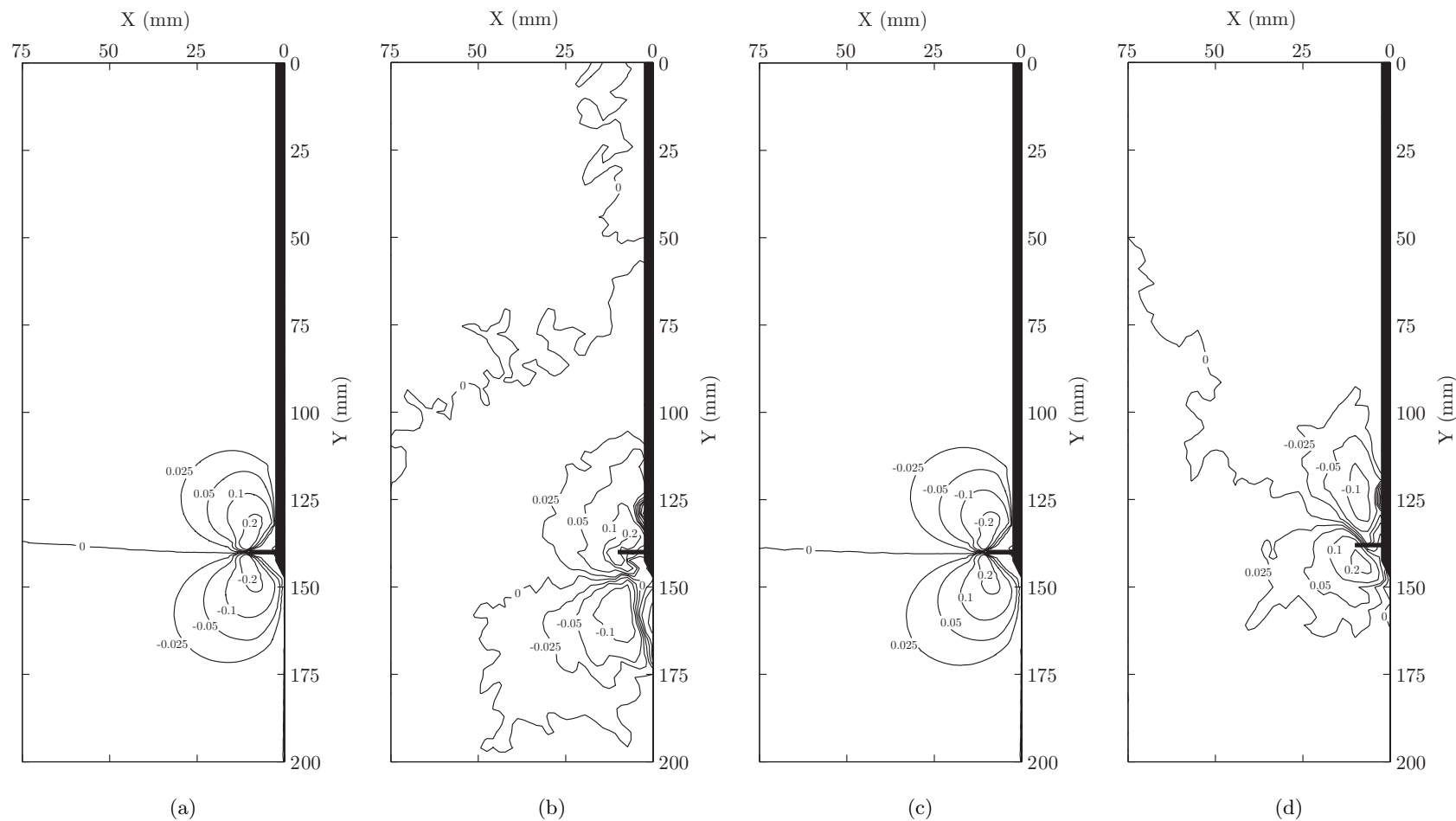


Figure 7.21: Comparison of ULS horizontal displacement field for 4-5mm displacement increment: C1 FE (a), C1 PIV (b), T1 FE (c) and T1 PIV (d) with displacements in mm.

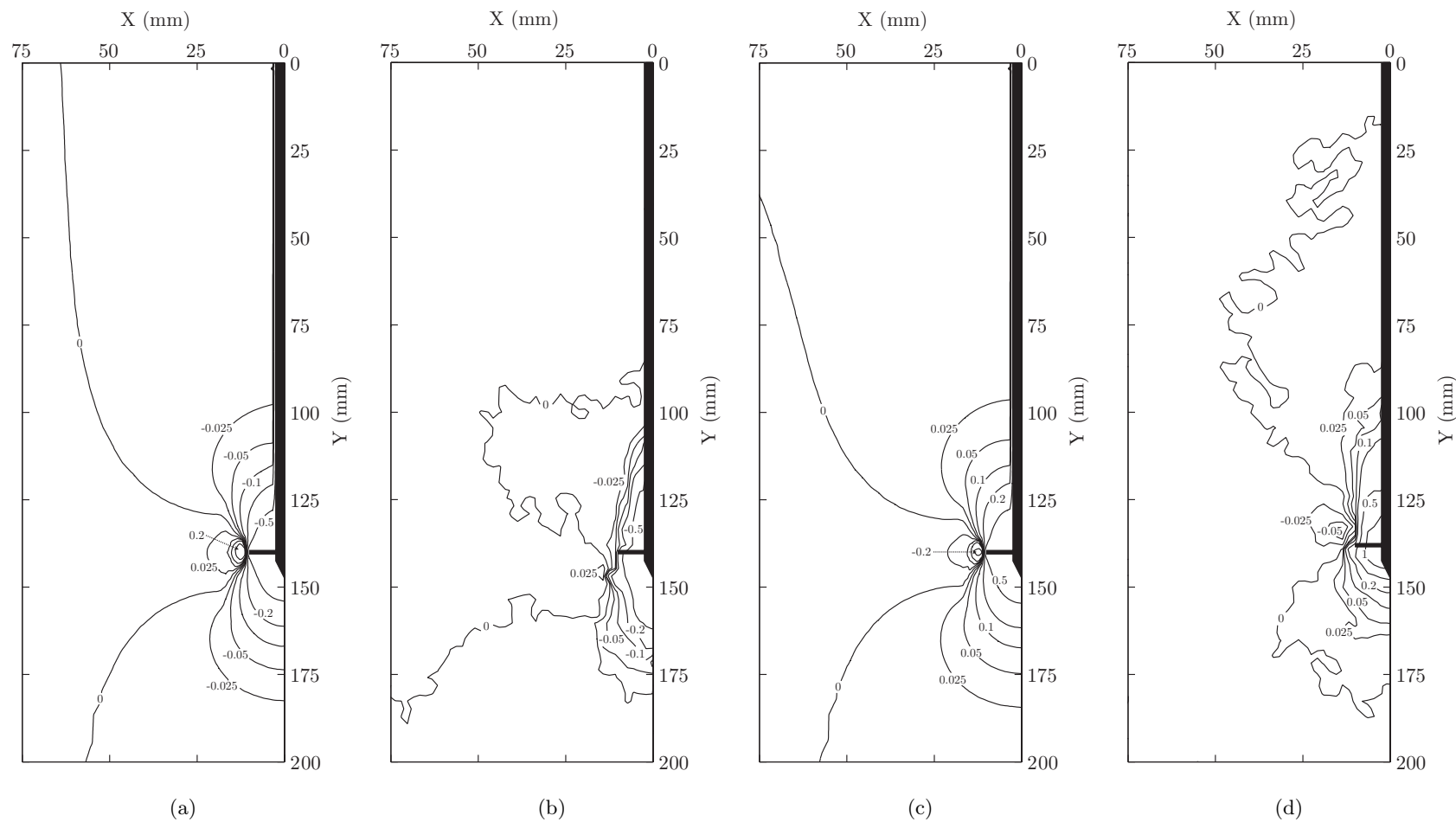


Figure 7.22: Comparison of ULS vertical displacement field for 4-5mm displacement increment: C1 FE (a), C1 PIV (b), T1 FE (c) and T1 PIV (d) with displacements in mm.

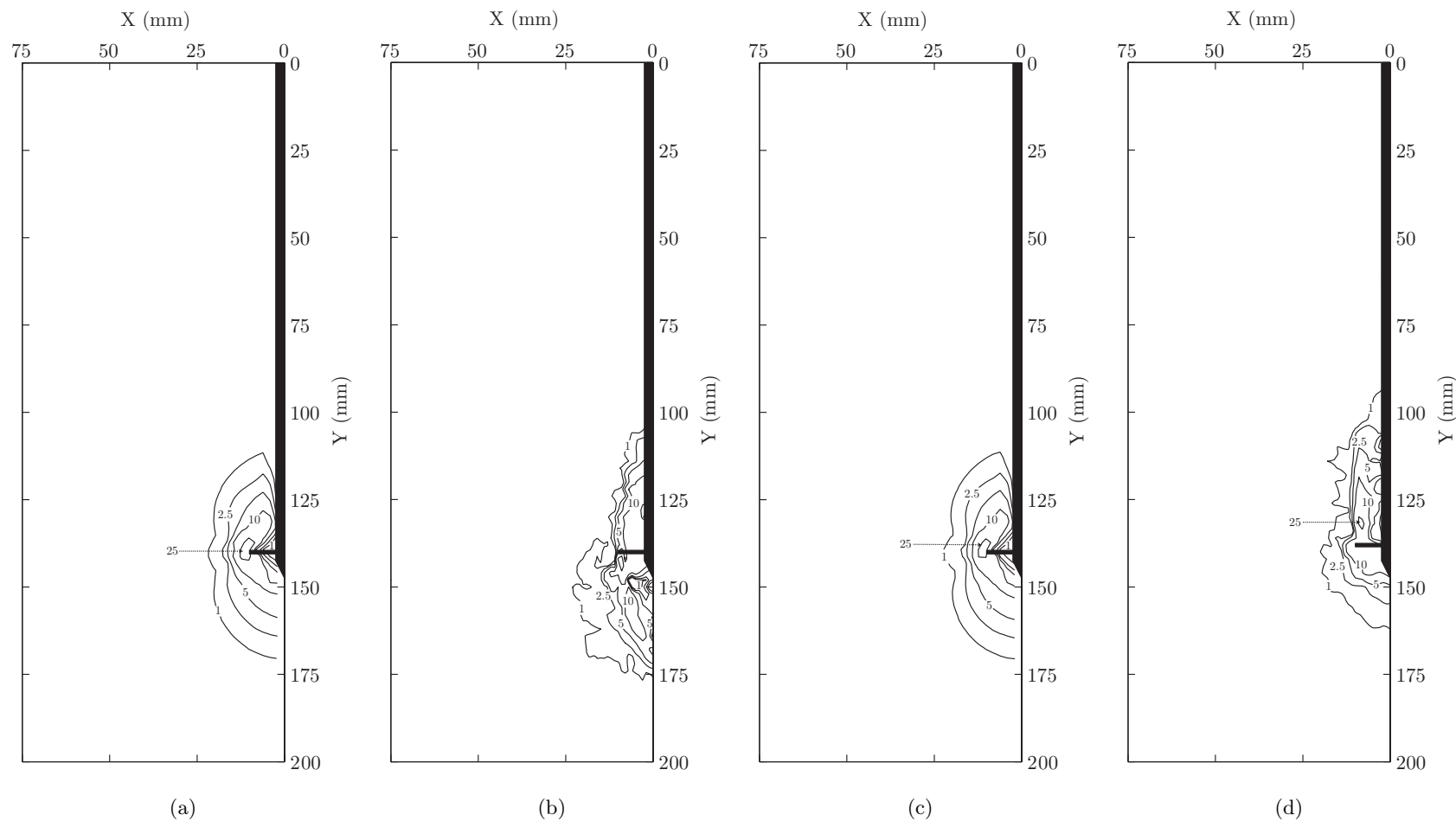


Figure 7.23: Comparison of ULS shear strain field for 4-5mm displacement increment: C1 FE (a), C1 PIV (b), T1 FE (c) and T1 PIV (d) with shear strains expressed as a percentage.

vertical displacements for both compressive and tensile loading at the ULS. The discrepancies in the vertical component of displacement are very small, being generally less than $25\mu m$ in the compressive loading case and slightly more in the tensile case where vertical displacements propagated further above the uppermost helical plate.

The ULS deformation mechanism for the double helix pile with $60mm$ L_a loaded in compression, investigated by test C2-60, shows generally good agreement between the FE simulation and experimental observations. Comparison of the shear strain contour plots in Figures 7.29(a) and 7.29(b) indicates that in both the FE simulation and experimental result a continuous shear band is generated between the uppermost and lowermost helical plates. Aside from small sections of the shear band, the magnitude of shear strains is in good agreement. The vertical displacement contours in Figures 7.28(a) and 7.28(b) are almost identical, except that in the physical model small pockets of upward movement at the outer radii of the helical plates were not apparent. This could be caused by there not being enough measurement points in these areas in the PIV analysis to capture these small areas of heave. Comparison of the horizontal contour plots in Figures 7.27(a) and 7.27(b) indicates that horizontal movements between the helical plates and above the uppermost helical plate are slightly overpredicted by the FE simulation.

In contrast, the discrepancies are more significant for the same pile loaded in tension, investigated in test T2-60. Comparing the shear strain contour plots in Figures 7.29(c) and 7.29(d) illustrates that in the FE validation a continuous band of shearing is predicted adjacent to the pile shaft between the helical plates. This is in contrast to the compressive case where the shear band was evident some distance away from the pile shaft. In the physical model of test T2-60 this shear band was less continuous. However, Figure 5.73(a) indicates that this may be a result of the patches in the PIV analysis overlapping the model pile shaft, the associated vectors becoming wild and being removed from the dataset manually. This leaves gaps in the shear strain dataset which, when interpolated back to a regular grid to allow the contour plot to be formed, leads to closed contours of shear strain. The shear band then appears as discrete pockets rather than a continuous band. The shear band in the physical model also extends further towards the surface of the sample.

380

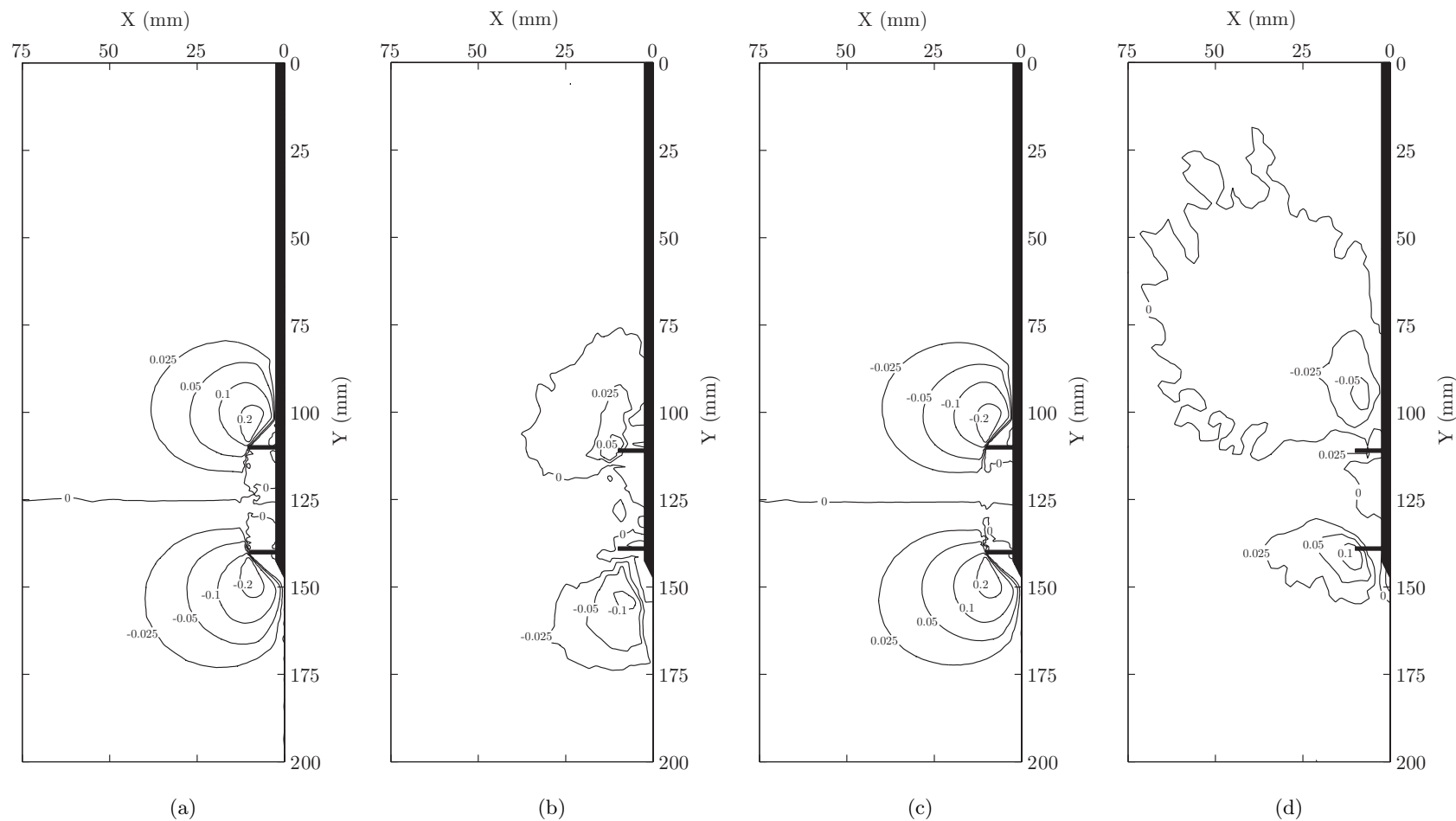


Figure 7.24: Comparison of ULS horizontal displacement field for 4-5mm displacement increment: C2-30 FE (a), C2-30 PIV (b), T2-30 FE (c) and T2-30 PIV (d) with displacements in mm .

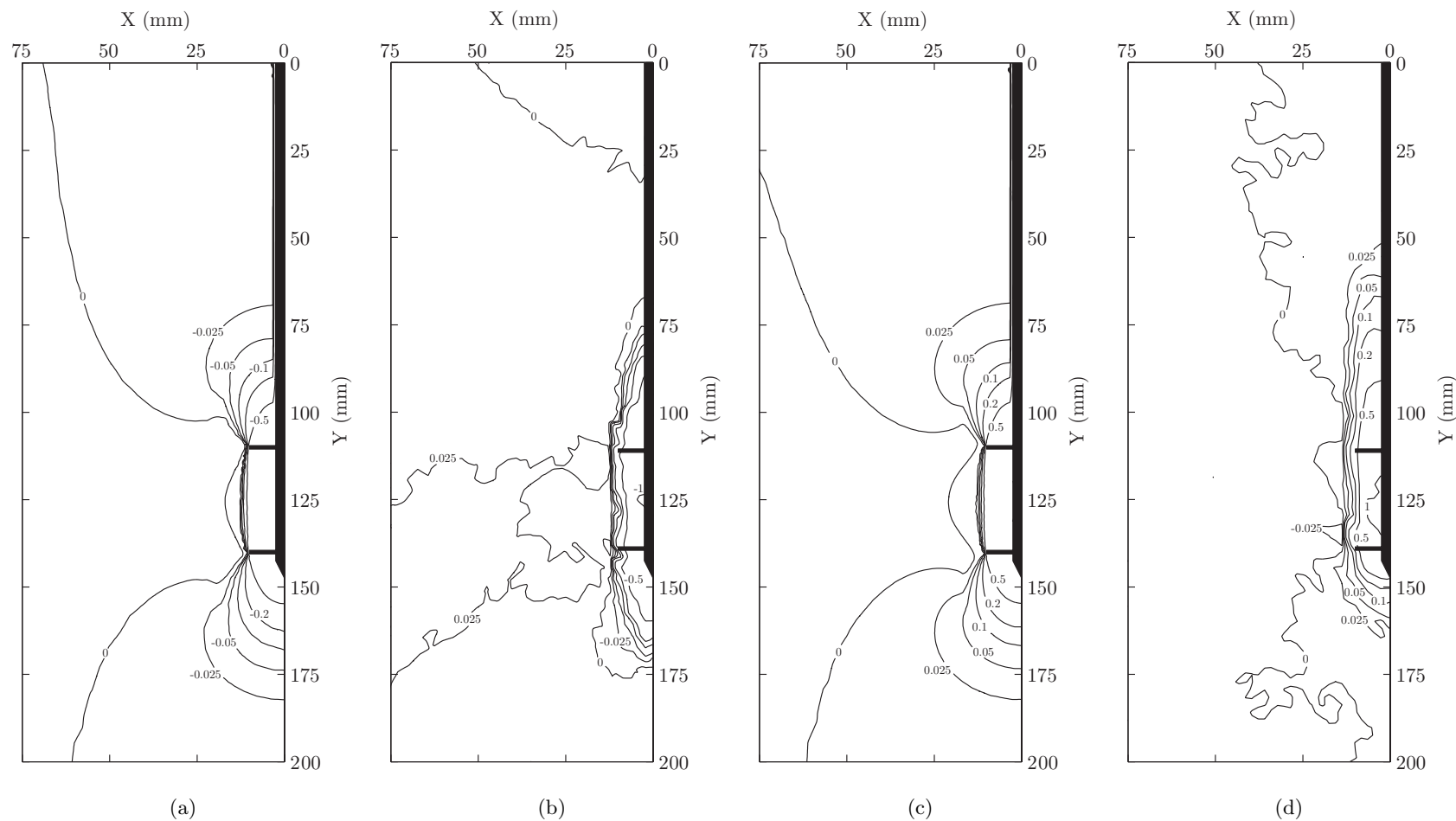


Figure 7.25: Comparison of ULS vertical displacement field for 4-5mm displacement increment: C2-30 FE (a), C2-30 PIV (b), T2-30 FE (c) and T2-30 PIV (d) with displacements in mm.

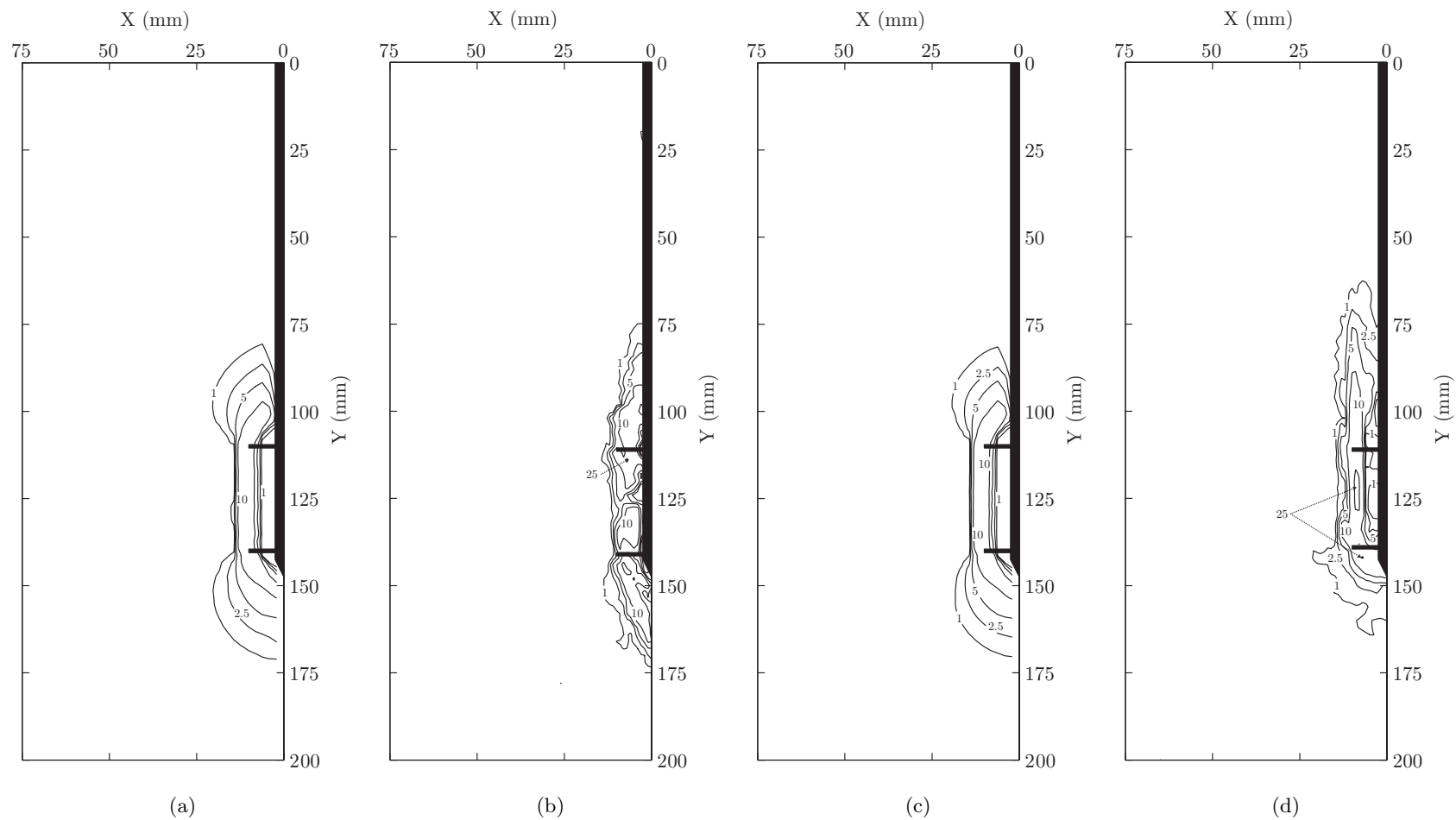


Figure 7.26: Comparison of ULS shear strain field for 4-5mm displacement increment: C2-30 FE (a), C2-30 PIV (b), T2-30 FE (c) and T2-30 PIV (d) with shear strains expressed as a percentage.

The experimental vertical displacement contours are also slightly different to those from the compressive FE simulation, as is demonstrated by comparing Figures 7.28(c) and 7.28(d). Here, the $0.5mm$ contour appears to be tending towards the pile shaft. Hence, the shear band is closer to the pile shaft at the mid-depth of the L_a . This distribution of vertical displacement is similar to that observed for the previous increment of compressive displacement for $3-4mm$. Therefore, the difference in the deformation mechanism at this point in the analysis is most likely a product of the methodology adopted. For example, application of the post-installation residual force in the FE simulation, induced some settlement of the model pile. Compressive loading generated further settlement. In contrast, tensile loading caused, firstly reduction in settlement, before net uplift with reference to the original position of the pile before any form of loading (post-installation residual force or displacement increments) was applied. Therefore, the compressively loaded pile has experienced greater net settlement than the corresponding tensile test has experienced net uplift. The discrepancy in net settlement/uplift is equal to twice the settlement induced by application of the post-installation residual force. In this instance, the total difference can be estimated by doubling the offset of the FE simulation derived load-deflection response in Figure 7.4(a) from the graphical datum. This yields a total difference of about $0.7mm$. It is therefore likely that a further $1mm$ increment of tensile displacement would have generated a deformation mechanism similar to that in the compressive test shown in Figure 7.29(a), where a continuous shear band was evident some distance away from the pile shaft. This may be evidence that in this instance the ULS deformation mechanism may not have fully stabilised. Comparison of the horizontal displacement contours in Figures 7.27(c) and 7.27(d) indicates that the trend of displacement is similar but the magnitudes of movement are overpredicted by the FE simulation. In particular, this is true in the zone of soil between the helical plates.

The ULS deformation mechanisms for the triple helix pile tests, C3 and T3, were well predicted by the FE simulations. Comparisons of the shear strain contours in Figures 7.32(a) and 7.32(b) and Figures 7.32(c) and 7.32(d) illustrate that the shear band at the outer radii of the helical plates extends from the uppermost to the lowermost helical plate in both the FE simulation and experimental output. The computed magnitudes and extent of shear strain are very similar for both compressive and tensile loading. For the tensile case, the experimental shear band extends further vertically above the uppermost helical plate. The horizontal

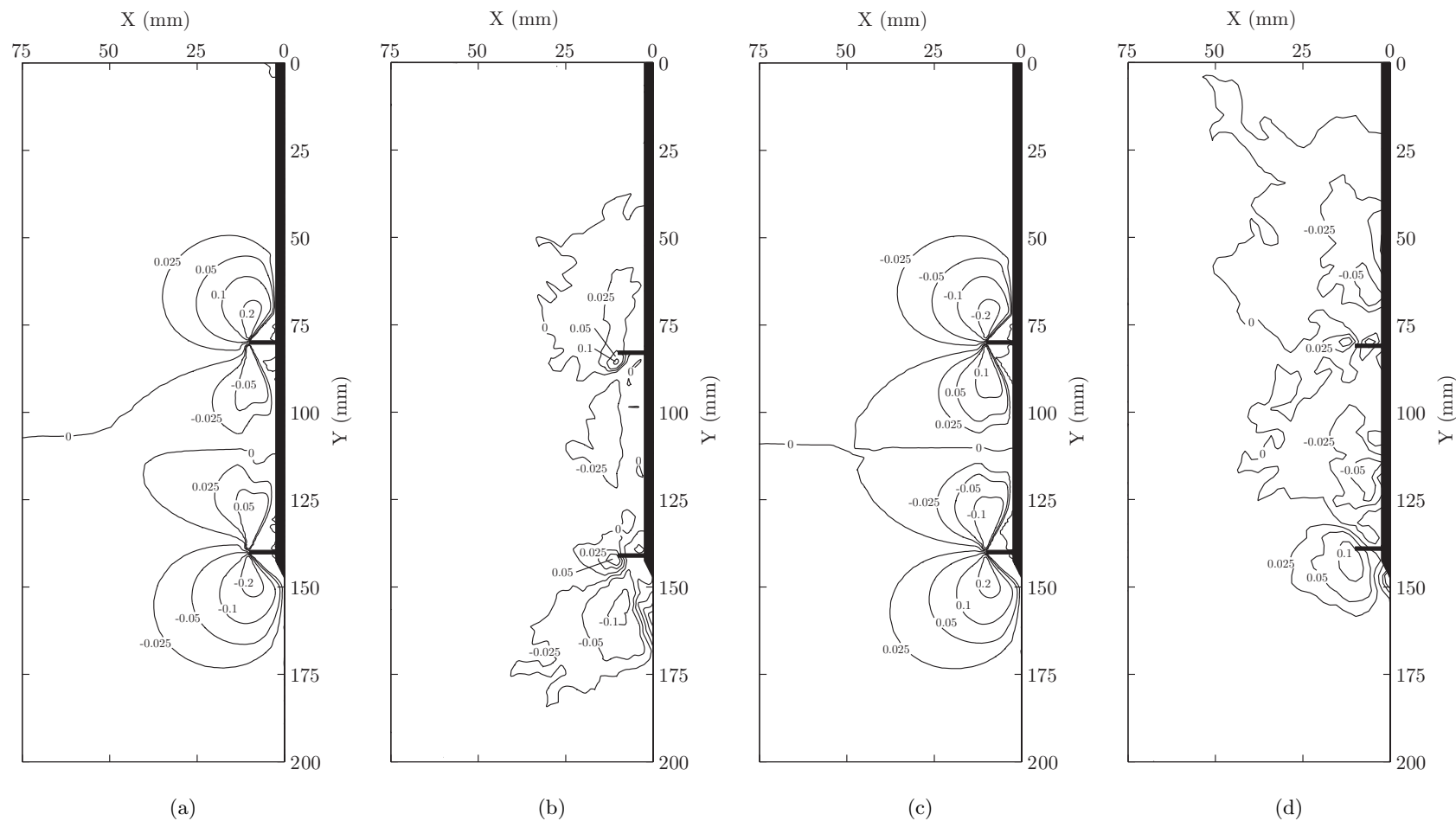


Figure 7.27: Comparison of ULS horizontal displacement field for 4-5mm displacement increment: C2-60 FE (a), C2-60 PIV (b), T2-60 FE (c) and T2-60 PIV (d) with displacements in mm.

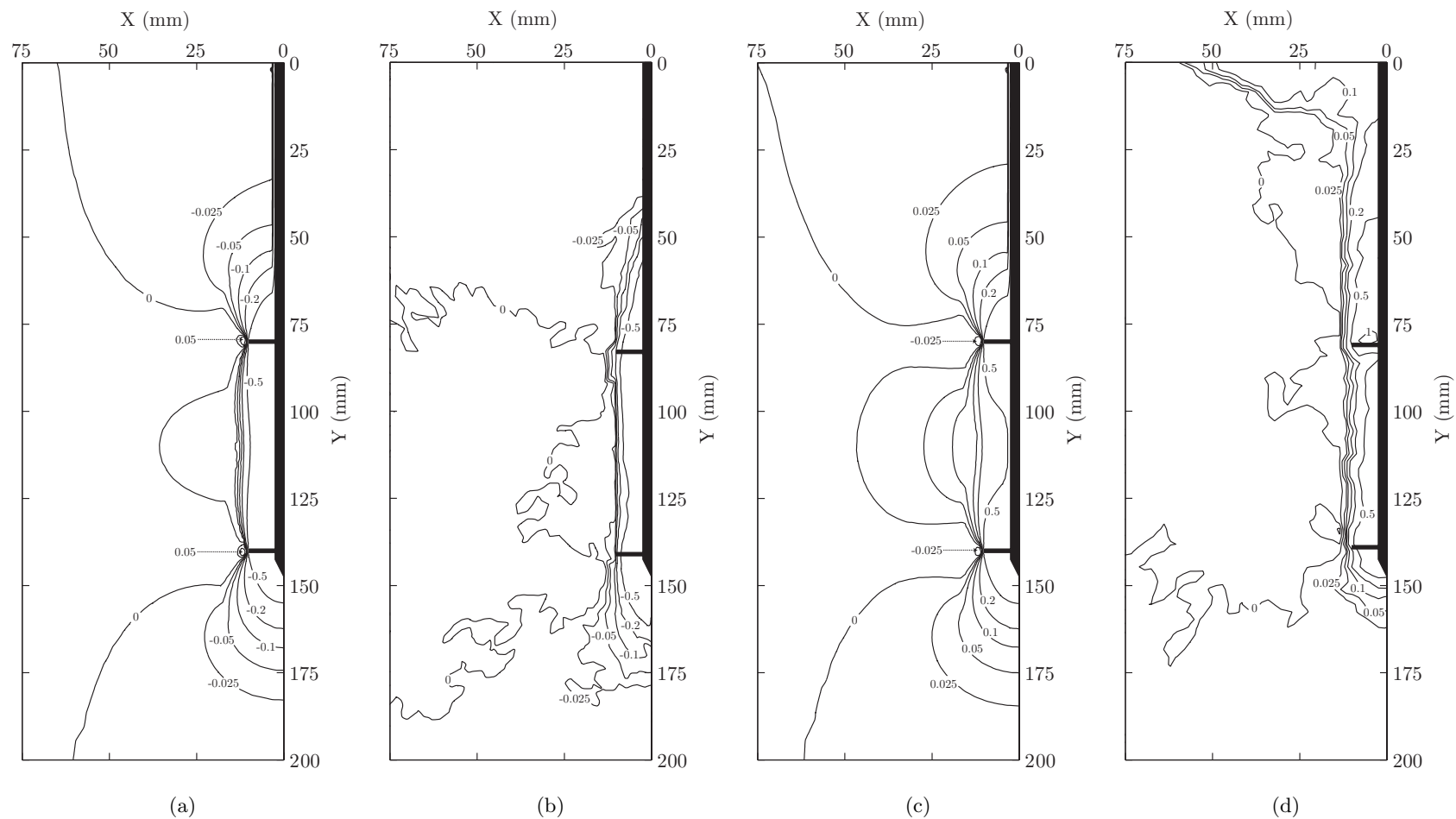


Figure 7.28: Comparison of ULS vertical displacement field for 4-5mm displacement increment: C2-60 FE (a), C2-60 PIV (b), T2-60 FE (c) and T2-60 PIV (d) with displacements in mm.

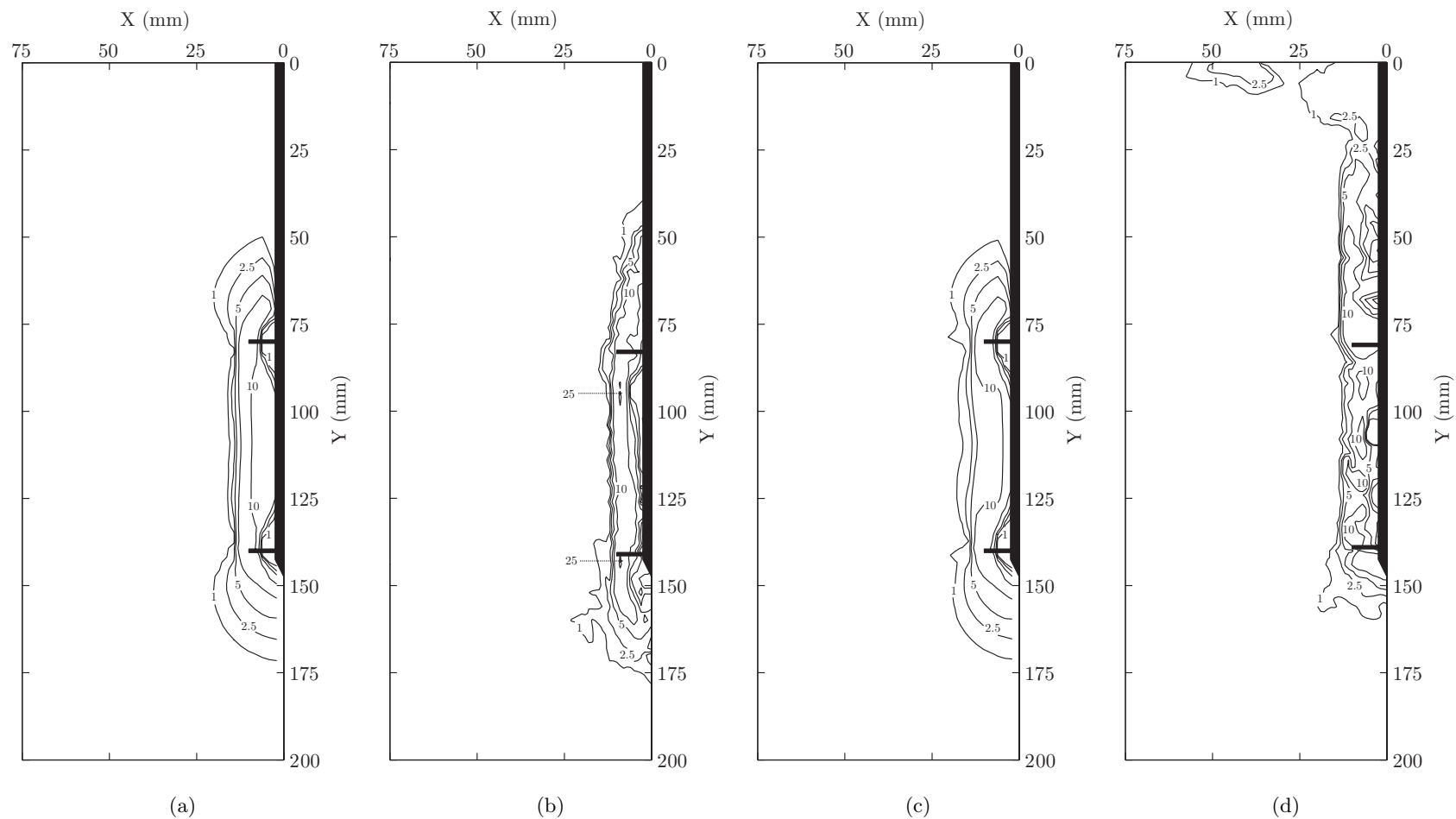


Figure 7.29: Comparison of ULS shear strain field for 4-5mm displacement increment: C2-60 FE (a), C2-60 PIV (b), T2-60 FE (c) and T2-60 PIV (d) with shear strains expressed as a percentage.

displacement contour plots in Figures 7.30(a) and 7.30(b) and Figures 7.30(c) and 7.30(d) and the vertical displacement contour plots in Figures 7.31(a) and 7.31(b) and Figures 7.31(c) and 7.31(d) are also very similar.

The evidence presented above allows a number of conclusions to be made. Firstly the transparent soil is a useful modelling material for investigating soil-structure interaction phenomena, where half-space axisymmetry or plane strain simplification cannot be utilised. Problems with complex installation processes are particularly well suited to investigations using the transparent soil physical modelling methodologies utilised here. The behaviour of the material can be adequately described using simple elasto-plastic constitutive models, such as the Mohr-Coulomb model employed here. The FE method can then be used to simulate the physical models, with good comparability of results in general. Discrepancies between the physical and numerical modelling output can then be used to develop hypotheses relating to the effect of processes that are difficult to model using the FE method, such as the installation process for a helical screw pile as has been demonstrated in this thesis.

Furthermore, a numerical model such as the FE models described would allow a comparative appraisal of the effects of other variables such as constitutive model choice, non-linearity or soil anisotropy. Unfortunately, this was not achieved during this research but is a potential avenue for further work. However, to assess the reliability of the FE simulations a sensitivity analysis was performed using different target variables primarily related to choices and assumptions made during formulation of the models. This allowed some qualitative appraisal of the effects of these choices and assumptions and the following section summarises the findings.

7.2.4 Sensitivity of Finite Element Simulation

In Chapter 6 a sensitivity analysis was conducted to assess the variations in response caused by various assumptions and parameter choices made during formulation of the ‘Baseline’ FE simulation model of the surface footing test. A similar sensitivity analysis is presented here relating to the helical screw pile FE simulations presented in the preceding sections. However, an investigation into the impact of compressibility was not possible since the alternative FE package used (Oasys Geo SAFE) was not capable of modelling a sliding soil-shaft interface, which was seen as a critical component of the FE simulations. Assessment of the impact of the geometric

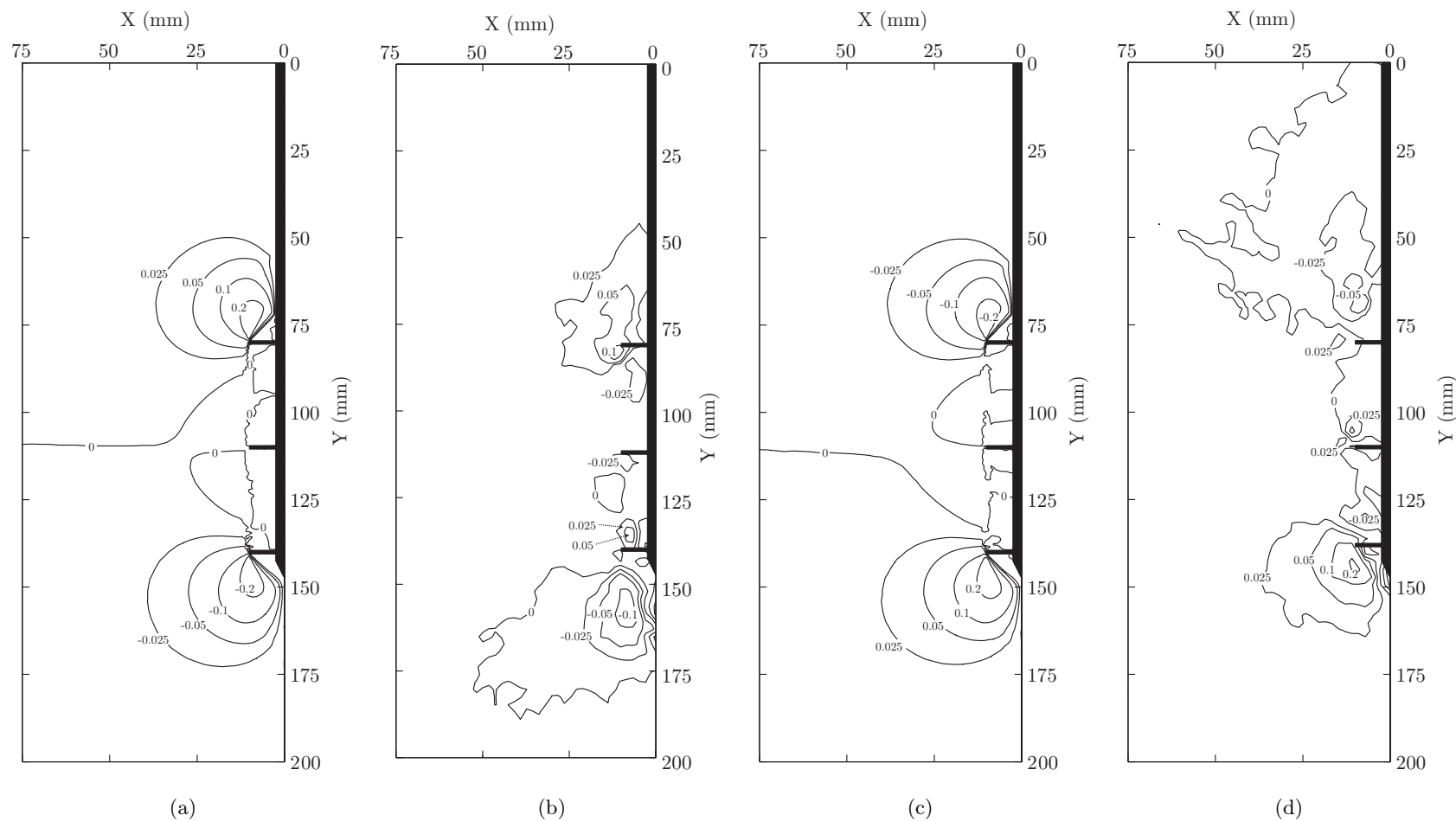


Figure 7.30: Comparison of ULS horizontal displacement field for 4-5mm displacement increment: C3 FE (a), C3 PIV (b), T3 FE (c) and T3 PIV (d) with displacements in mm.

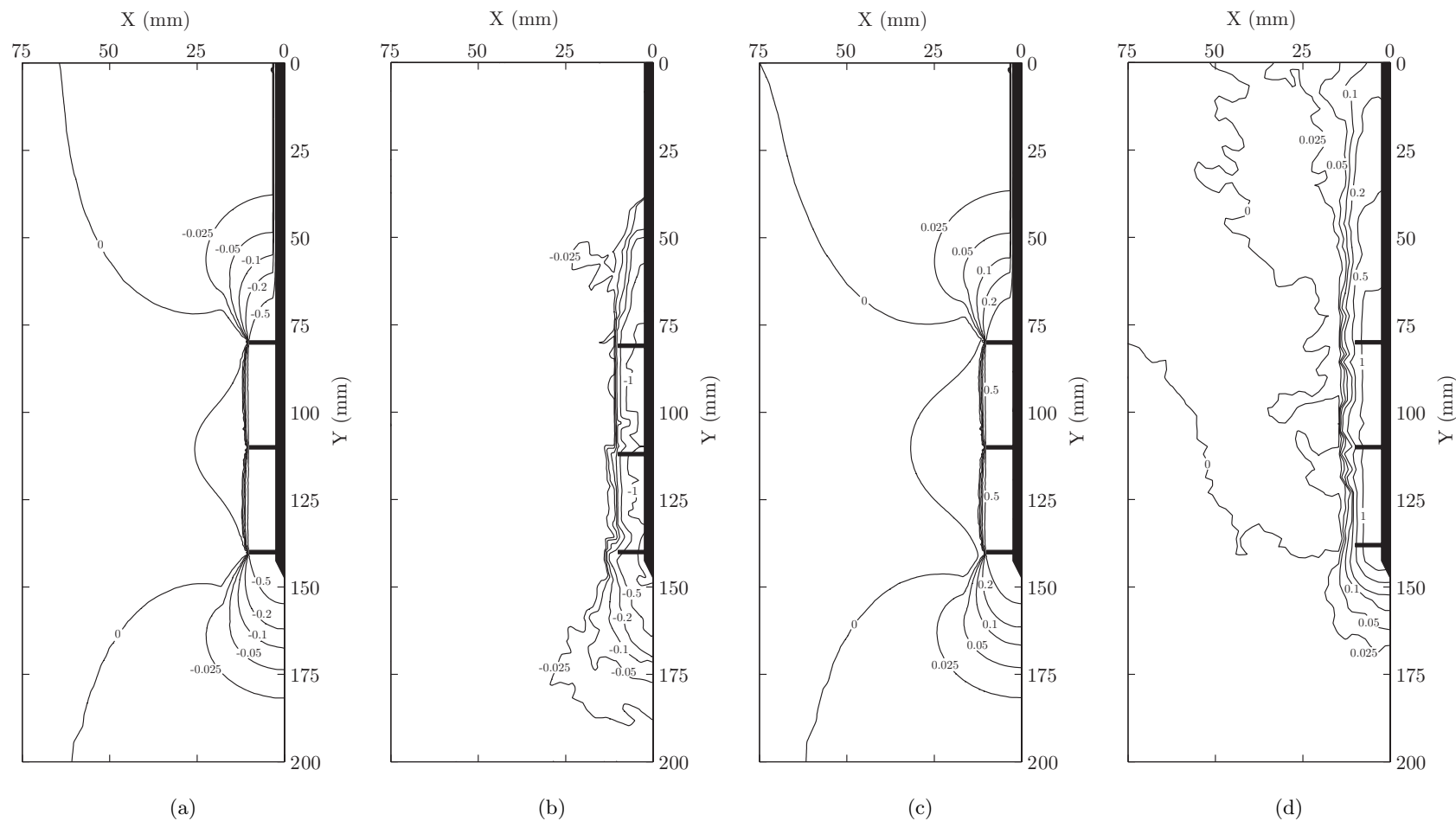


Figure 7.31: Comparison of ULS vertical displacement field for 4-5mm displacement increment: C3 FE (a), C3 PIV (b), T3 FE (c) and T3 PIV (d) with displacements in mm.

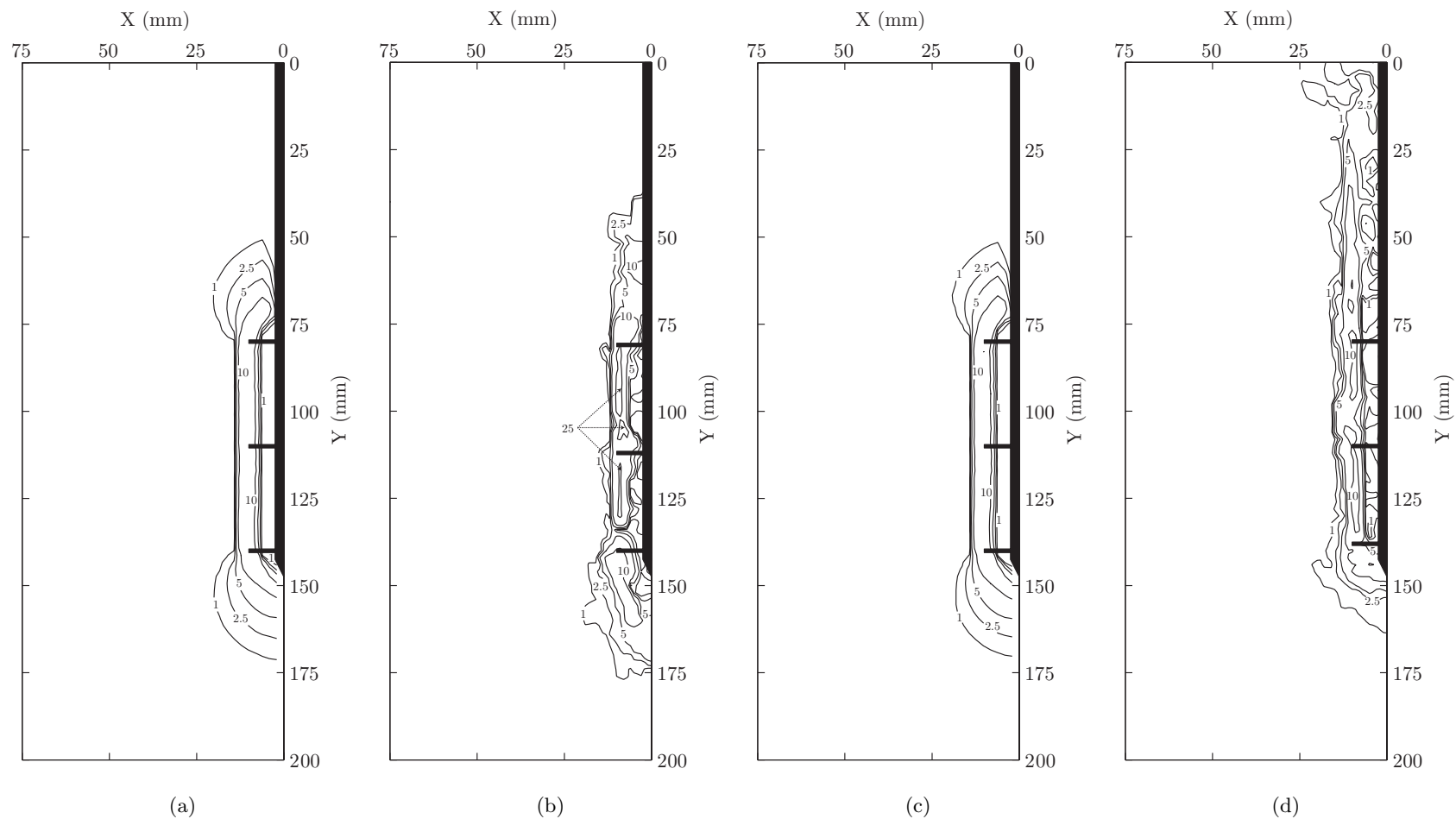


Figure 7.32: Comparison of ULS shear strain field for 4-5mm displacement increment: C3 FE (a), C3 PIV (b), T3 FE (c) and T3 PIV (d) with shear strains expressed as a percentage.

simplification employed was also not achieved as 3D simulations of the helical screw pile tests encountered significant convergence problems that were not resolved.

The remaining variables studied were:

- Mesh density:
 - 50% and 200% nodal seeding densities used.
- Assumed vertical boundary condition:
 - Results using fixed and sliding boundary conditions.
- Strength uncertainty:
 - Upper and lower strength profiles post-test property data used.
- Rigidity Index:
 - Influence of M_c investigated by varying I_R by $\pm 10\%$.

Throughout, the results were considered by comparing load-deflection responses predicted for the helical screw piles and by assessing the percentage sensitivity as a function of the capacity of the ‘Baseline’ case at a settlement of $\pm 5mm$. In all cases, the deformation mechanisms observed at the ULS were insignificantly different to those found for the ‘Baseline’ analyses. The following findings were generated by the sensitivity analysis:

1. The meshes were shown to be sufficiently element rich as refining them by increasing the seeding densities by a factor of two only reduced the computed ULS capacities by less than 2.5% whereas reducing the seeding densities by a factor of two increased the computed capacities at the ULS by about 4%.
2. Assuming that the vertical boundaries permitted sliding rather than fixity caused reductions in the computed capacities at the ULS that were no greater than 0.5%.
3. The strength profile assumed (upper, mean or lower) from the post-test property data had the most significant impact as it affected the computed ULS capacities as much as $\pm 6\%$.

4. Varying I_R by $\pm 10\%$ impacted most significantly over a certain initial range of displacement ($\delta = \pm 0.2mm$) with a maximum sensitivity of $\pm 5\%$ and a sensitivity of $\pm 1.5\%$ at the ULS.

The sensitivity analyses summarised here show that the FE simulations are not overly sensitive to variation of the modelling assumptions. They do indicate that the greatest uncertainty relates to the choice of the constitutive modelling parameters, S_u and I_R , yet cannot explain the poor simulation of the physical models over the initial range of displacements of $\pm 2mm$ seen in Figures 7.3(b), 7.3(d), 7.4(b) and 7.4(d). A much more significant increase in I_R would have been required to better simulate the initial load-deflection responses. The fact that the simulation of the model footing in Chapter 6 was more successful for a similar range of normalised displacement suggests that poor simulation in this instance could be caused by variability of I_R with depth or installation induced effects that were not measurable during post-test property investigation and thus were not modelled in the FE simulation.

7.3 Analytical Model

Equations suggested by Rao et al. (1991) have been used as a basis to assess the validity of simple analytical expressions for predicting the ULS capacity of helical screw piles. It is assumed that a cylindrical failure surface forms between the uppermost and lowermost helical plates of multi-helix piles. This assumption is justified by the observations made in Chapter 5 and the FE simulations presented here. Therefore, neglecting the contribution of suction and pile self weight, the net compressive (Q_c) and tensile (Q_t) capacities of a helical screw pile can be assumed to be derived from three separate components:

$$Q_c = Q_{base} + Q_{shear} + Q_{shaft} \quad (7.1)$$

$$Q_t = Q_{uplift} + Q_{shear} + Q_{shaft} \quad (7.2)$$

where Q_{base} or Q_{uplift} is the bearing or uplift capacity of the projected area of the lowermost or uppermost helical plate, Q_{shear} is the capacity of the cylindrical failure surface generated between the uppermost and lowermost helical plates and Q_{shaft} is the capacity mobilised by shaft adhesion. These components can be described using the following expressions:

$$Q_{base} = \left[\frac{\pi \cdot D^2}{4} \right] \cdot N_{cu} \cdot S_{u_{lower}} \quad (7.3)$$

$$Q_{uplift} = \left[\frac{\pi \cdot (D^2 - d^2)}{4} \right] \cdot N_c \cdot S_{u_{upper}} \quad (7.4)$$

$$Q_{shear} = S_f \cdot \pi D \cdot L_a \cdot S_{u_{shear}} \quad (7.5)$$

$$Q_{shaft} = \alpha \cdot \pi \cdot d \cdot H_{eff} \cdot S_{u_{shaft}} \quad (7.6)$$

where D , d , N_c , N_{cu} , H , L_a , S_f , α and H_{eff} are as defined in Chapter 2. $S_{u_{lower}}$, $S_{u_{upper}}$, $S_{u_{shear}}$ and $S_{u_{shaft}}$ are the undrained shear strengths at the depths of the lowermost and uppermost helical plates and the average strengths over the cylindrical failure surface and the active shaft length respectively. Rao et al. (1991) assumed that all of these strengths were equal to the average bed strength obtained using a hand vane. However, in this investigation a linearly decreasing strength with depth relationship was apparent. Hence, Equations 7.3-7.6 can be modified to describe each strength as a function of $S_{u_{surface}}$ by substituting in Equation 6.8. The soil strength at the depth of the uppermost and lowermost helical plates is used in the calculation of uplift and bearing capacity. Integration is used to describe the S_u as a function of depth in the calculation of the contributions of the cylindrical failure surface and shaft adhesion to the total capacity. This leads to the following expressions:

$$Q_{base} = \left[\frac{\pi \cdot D^2}{4} \right] \cdot N_c \cdot (S_{u_{surface}} + k \cdot (H + L_a)) \quad (7.7)$$

$$Q_{uplift} = \left[\frac{\pi \cdot (D^2 - d^2)}{4} \right] \cdot N_{cu} \cdot (S_{u_{surface}} + k \cdot H) \quad (7.8)$$

$$\begin{aligned} Q_{shear} &= S_f \cdot \pi \cdot D \cdot \int_H^{(H+L_a)} (S_{u_{surface}} + k \cdot z) \, dz \\ &= S_f \cdot \pi \cdot D \cdot \left(\left[S_{u_{surface}} \cdot (H + L_a) + \frac{k \cdot (H + L_a)^2}{2} \right] - \right. \\ &\quad \left. - \left[S_{u_{surface}} \cdot H + \frac{k \cdot H^2}{2} \right] \right) \end{aligned} \quad (7.9)$$

$$\begin{aligned}
 Q_{shaft} &= \alpha \cdot \pi \cdot d \cdot \int_0^{H_{eff}} (S_{u_{surface}} + k \cdot z) \, dz \\
 &= \alpha \cdot \pi \cdot d \cdot \left(\left[S_{u_{surface}} \cdot H_{eff} + \frac{k \cdot H_{eff}^2}{2} \right] - 0 \right)
 \end{aligned} \tag{7.10}$$

Rao et al. (1993a) proposed a spacing ratio modification factor S_f to account for the difference in observed ultimate capacities for helical screw piles with maintained L_a and varied s/D . The relationships in Equation 7.11 were proposed by fitting a relationship to normalised capacities from experimental data reported in Rao et al. (1991). The capacities were normalised by the pile capacity with minimal s/D . Figure 7.33 is plot of the S_f relationship fitted to experimental data from Rao et al. (1991), presented by Rao and Prasad (1993). The relationship is described by the three best fit lines in Equation 7.11.

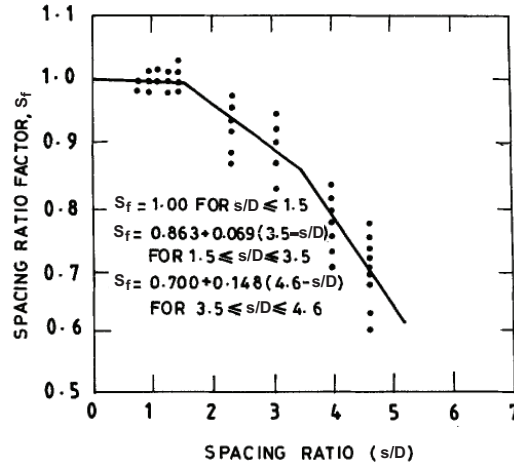


Figure 7.33: Spacing ratio factor relationship S_f determined by fitting to experimental data from Rao et al. (1991) by Rao and Prasad (1993).

$$s/D \leq 1.5 \implies S_f = 1.0$$

$$1.5 \leq s/D \leq 3.5 \implies S_f = 0.863 + 0.069(3.5 - s/D) \tag{7.11}$$

$$3.5 \leq s/D \leq 4.6 \implies S_f = 0.700 + 0.148(4.6 - s/D)$$

However, in this investigation the difference in capacity at the ULS for tests C2-60 and C3 and T2-60 and T3 was minimal. This may be attributable to

the differing testing methodologies used. In the present investigation undrained constant displacement rates were adopted (see Section 3.7), whereas Rao et al. (1991) used load control and a threshold displacement rate of 0.02mm/s to define when the next loading increment ought to be applied. It can be assumed that in the later investigation by Rao et al. (1993a) that a similar strategy was employed. In that instance it is also possible that partial drainage was apparent around the helical piles. The relationships in Equation 7.11, describing S_f with respect to s/D , were fitted using test data from helical piles with shallow, transition and deep embedment conditions. The cases considered in the present investigation are all deeply embedded, where $H/D \geq 4$. There is significant scatter in the data used to fit the relationship. S_f would only be relevant to tests C2-60 and T2-60 in this investigation, where s/D is equal to 3.0, making S_f equal to 0.90 according to Equation 7.11. This would reduce the contribution of the cylindrical failure surface to the total capacity of the pile by 10%. However, no significant discrepancy was seen between the capacities for tests C2-60 and C3 or T2-60 and T3 in either the physical models or FE simulations. For all of these reasons, S_f has been assumed to be equal to unity in this investigation.

The H_{eff} parameter was introduced by Rao et al. (1993a) to factor down the shaft length over which shaft adhesion is assumed to be mobilised during tensile loading. The rationale behind this was that the uppermost helical plate, which develops capacity through uplift by mobilising soil lying above, would render some proportion of the shaft unable to generate capacity through frictional sliding between the pile shaft and soil. In their investigation H_{eff} was taken as:

$$H_{eff} = H - xD \quad (7.12)$$

where, x is the ineffective shaft length and was varied between 1.4 and 2.3. The ineffective shaft lengths reported by Rao et al. (1993a) appear to show variation between each test over this range without justification. In this investigation, with the benefit of PIV derived vertical displacement fields, it is possible to provide more robust justification for the choice of ineffective shaft length assumed. For compressive and tensile loading , Figures 5.19(c), 5.28(c), 5.37(c) and 5.46(c) and Figures 5.55(c), 5.64(c), 5.73(c) and 5.82(c) can be examined. These plots show the vertical displacement due to a $\pm 1\text{mm}$ increment of displacement at the ULS.

The compressive loading cases exhibit differential sliding between the pile shaft and adjacent soil over a smaller length of shaft above the uppermost helical plate when compared to the tensile loading cases. It is difficult to define a threshold of differential displacement beyond which adhesion can be assumed to be fully mobilised. However, given that the differential displacement was apparent over a greater shaft length for the compression tests, the ineffective shaft lengths assumed in this investigation were estimated as $1.0D$ for piles loaded in compression and $2.0D$ for piles loaded in tension. These values are similar to the values assumed by Rao et al. (1993a) but are kept constant for all tests of each loading configuration.

Table 7.6 contains a summary of parameters common for all the analytical capacity calculations. The bearing capacity factor, N_c , and uplift capacity factor, N_{cu} , were assumed to be equal to 9.0, since where $H/D \geq 4$, deep embedment conditions have been assumed and uplift capacity is assumed to be similar to bearing capacity (Rao et al., 1993a). For a deeply embedded vanishingly thin circular plate anchor, the exact solution for N_c has been shown by Martin and Randolph (2001) to be equal to 12.42 for a smooth and 13.11 for a rough soil-anchor interface using the method of characteristics. Independent collapse mechanisms for the same problem yielded values for N_c within 2% of these exact solutions. These values are greater than the values assumed here for both N_c and N_{cu} . However, they were derived assuming a homogeneous soil profile of infinite extent and the flow mechanisms proposed by Martin and Randolph (2001) were not observed at the depth of each helical plate in either the physical models or FE simulations. Therefore the values used here (Table 7.6), perhaps represent a conservative estimate for N_c and N_{cu} . They are consistent with the values used by Rao et al. (1993a) and that usually assumed as suitable for calculating the bearing resistance of a driven pile in clay (Tomlinson, 2001). α was taken as unity for consistency with the assumptions in the FE simulation.

Tables 7.4 and 7.5 present capacities predicted using Equations 7.1 and 7.2 coupled with the parameters in Table 7.6. The calculated capacities are compared with the experimental ULS capacities in Table 7.7. The analytically predicted capacities are all within $\pm 10\%$ of the experimental capacities. The maximum overprediction was 9.2% for test C1 and the maximum underprediction was -8.8% for test C3.

Table 7.4: Absolute compressive capacity calculated using analytical methods and mean strength.

Configuration	s/D	S_f	H (m)	H_{eff} (m)	L_a (m)	Q_{base} (N)	Q_{shear} (N)	Q_{shaft} (N)	Q_c (N)
C1	∞	1	0.14	0.12	0.0	43.0	0.0	33.2	76.20
C2-30	1.5	1	0.11	0.09	0.03	43.0	29.6	25.5	98.1
C2-60	3	1	0.08	0.06	0.06	43.0	60.7	17.5	121.2
C3	1.5	1	0.08	0.06	0.06	43.0	60.7	17.5	121.2

Table 7.5: Absolute tensile capacity calculated using analytical methods and mean strength.

Configuration	s/D	S_f	H (m)	H_{eff} (m)	L_a (m)	Q_{uplift} (N)	Q_{shear} (N)	Q_{shaft} (N)	Q_t (N)
T1	∞	1	0.14	0.12	0.0	40.3	0.0	28.1	68.5
T2-30	1.5	1	0.11	0.09	0.03	42.7	29.6	20.2	92.4
T2-60	3	1	0.08	0.06	0.06	45.1	60.7	11.8	117.6
T3	1.5	1	0.08	0.06	0.06	45.1	60.7	11.8	117.6

Table 7.6: Parameters common to all analytical calculations.

Parameter	Value
$S_{u_{surface}}$ (kPa)	19.41
k (kPa/m)	-30
α	1
N_c	9
N_{cu}	9
d (m)	0.005
D (m)	0.02

Table 7.7: Percentage discrepancy between experimental and analytical validation derived absolute capacity of helical screw piles, expressed as a percentage of the capacity at the ULS for the experimental case ($\delta = \pm 5\text{mm}$).

Test	Absolute Capacity (N)		Discrepancy (%)
	Experimental	Analytical	
C1	69.8	76.2	9.2
T1	69.3	68.5	-1.2
C2-30	99.4	98.1	-1.3
T2-30	98.9	92.4	-6.6
C2-60	131.8	121.2	-8.1
T2-60	119.2	117.6	-1.3
C3	132.8	121.2	-8.8
T3	121.0	117.6	-2.8

7.4 Discussion

Comparison of the ULS capacities predicted by the FE and analytical methods are presented in Figure 7.34. The discrepancy is calculated as a percentage of the experimentally derived ULS capacity for each test.

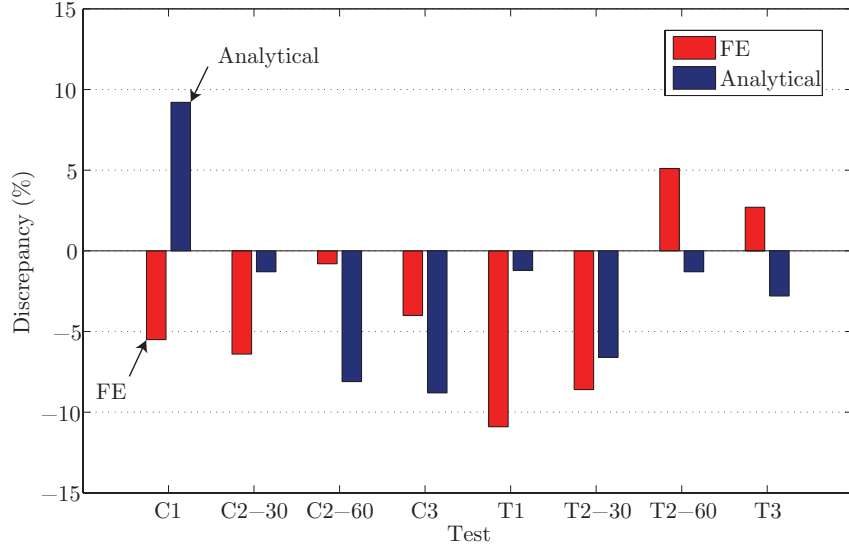


Figure 7.34: Discrepancy summary.

The FE method appears to be conservative for all cases apart from the tensile tests with L_a of 60mm (tests T2-60 and T3), where propagation of the failure mechanism to the surface of the sample was observed in the physical models. Using the assumed value of H_{eff} , the analytical method is also conservative for all configurations except the single helix pile loaded in compression (test C1). However, prediction of the ULS capacities for tests C1 and T1 were very sensitive to the choice of H_{eff} since a large proportion of Q_c and Q_t was derived from shaft capacity. For the other configurations of pile the contribution of shaft adhesion was reduced and therefore the capacity predicted was less sensitive to the H_{eff} assumed. Given the underprediction of the capacities using the analytical approach, assuming S_f equal to unity for tests C2-60 and T2-60 appears to be justified.

The lack of a need for the spacing ratio correction factor, S_f , compared with the results of Rao and Prasad (1993), could be due to differences in test procedure. For example dissipation of excess pore pressures during loading could potentially have occurred in the test procedure adopted by Rao et al. (1991) as load control was used in a step wise manner. Also the range of s/D tested here was limited to 1.5

and 3.0, which is significantly less than that investigated by Rao and Prasad (1993), meaning the smallest value for S_f would have been 0.9 (using Equation 7.11), in turn meaning that 10% of the contribution of the cylindrical shear failure surface to the overall capacity would be subtracted. Tables 7.4 and 7.5 indicate that this correction at a maximum would be only $4.5N$ in any case since the contribution of shaft friction to the net capacity is $45.1N$ for both cases.

The FE method was demonstrated to be able to predict the failure mechanisms of deeply installed helical screw piles in soft clays. The load-deflection performance is somewhat underpredicted and most likely due to the lack of facility to model installation induced effects on the surrounding soil properties using the FE method. The initial stiffness response of the piles was also quite seriously underpredicted. The cause of this underprediction is not known since increasing I_R in the sensitivity analysis by 10% did not significantly improve the results. This perhaps indicates that the choice of I_R in the FE simulations of the helical piles was inadequate, even though it was shown to be adequate when simulating the performance of the circular surface foundation in Chapter 6. This may suggest that I_R varied significantly with depth in a way that was not obviously apparent in the post-test property data or that installation effects induced significant change in the I_R of the soil.

The sensitivity of the transparent soil has been shown to be about 2 (Gill, 1999). This was confirmed by performing disturbed hand vane measurements, following BS1377-9:1990 (1990), immediately after taking the peak the measurements presented in Chapter 6. This yielded from a total of forty eight measurements a mean sensitivity of 1.92 and corresponding standard deviation of 0.13. However, the FE simulations and analytical model predictions indicate that in this investigation the transparent soil recovered a significant proportion of its strength during the holding period between completion of the installation process and commencement of testing, which was allowed to facilitate dissipation of installation induced excess pore pressures.

Reassuringly, simplifying the geometry of the helical plates to simple circular plates, allowing the use of axisymmetric FE meshes, was shown to produce results very similar to the physical models where the helical plates were three dimensional. This

is useful as it may allow practitioners to use the FE method, with axisymmetric geometries, to estimate capacities of single isolated helical screw piles for complicated ground conditions such as layered soils.

Care ought to be taken if the FE method is used to predict helical pile capacities in more sensitive materials, where a reduced α value and S_u may be more appropriate to ensure conservatism. It is also important to note that the FE method used here is only valid if similar scaled setup time is allowed in the field. This is unlikely to be allowed as helical screw piles are often used due to their fast and simple installation methods and purportedly short setup times. Therefore, care ought to be taken if FE methods are to be used to estimate capacities of piles loaded soon after installation in soft clays. Further research is required into the effects of the setup time allowed before loading on the ULS capacity. Such further research would also provide insights into the effects of the installation process on material strength within the path of installation.

Use of the analytical method to predict capacities of helical screw piles shows promise. However, appropriate choice of H_{eff} is important, particularly for piles with a large contribution to ultimate capacity due to shaft capacity. It is important to choose the values of H_{eff} and α conservatively in such cases, if safe design is to be assured. The discrepancies in capacity between the physical models and analytical predictions are very consistent with those reported in the literature using similar techniques (Rao et al., 1991; Rao and Prasad, 1993; Rao et al., 1993a). This is apparent even though different assumptions were made relating to the definition of S_u , H_{eff} and α and the testing methodologies were different.

The analytical method can provide a reasonable first estimate of helical screw pile capacity. The underlying validity of the method, assuming a cylindrical failure mechanism, is confirmed by the experimental observations made in Chapter 5. However, the need for $S_f < 1$ is questioned by the findings presented here since both the physical modelling and FE simulation results did not indicate that there was a need for it. However, it is noted that the range of s/D investigated here was limited. As with the FE method consideration ought to be given to the setup time allowed in the field if this analytical method of capacity estimation is to be relied upon. If the setup time allowable in the field is particularly short, the use of reduced strength and adhesion factor may be appropriate.

7.5 Design Methodology

An interesting exercise, with implications for practicing engineers wishing to use helical screw piles, is to assess the impact of different design methodologies on the calculation of a design capacity. The following sections compare the design loads and predicted immediate settlements with reference to the physical model tests of this investigation, when calculated using the traditional ‘permissible stress’ approach, a simple bearing/uplift capacity in reserve method and the more complicated partial factor method of Eurocode 7. First the calculation methods are outlined for each of the design methodologies before comparison of the computed design capacities and discussion of the results. In all cases the calculation model assumed is that presented in Section 7.3.

7.5.1 Permissible Stress

The ‘permissible stress’ design methodology uses a calculation model to define the ultimate capacity of the pile, to which a global safety factor, F , is then applied to factor down the ultimate capacity and generate an allowable design capacity. For the helical screw piles investigated here the calculation model proposed in Section 7.3 is assumed and factored as follows, with all symbols as previously defined:

$$Q_{c\ d} = \frac{(Q_{base} + Q_{shear} + Q_{shaft})}{F} \quad (7.13)$$

$$Q_{t\ d} = \frac{(Q_{uplift} + Q_{shear} + Q_{shaft})}{F} \quad (7.14)$$

where $Q_{c\ d}$ and $Q_{t\ d}$ are the design capacities for compressive and tensile loading. The value taken for F is dependent upon the uncertainty surrounding the parameters used in the calculation model or the quality and consistency of pile test data from the site. It is common to apply the safety factor F as either a single global factor or as separate independent factors on the base and shaft capacities. For simplicity a global factor of safety is assumed here. According to Bond and Harris (2008), if on-site pile testing to failure has been conducted, it is thought reasonable for the global factor of safety to be assumed to be 2. However, in cases where pile testing has been conducted to ‘proof loads’ only, a value of 2.5 is recommended. Where no testing at all has been conducted on full scale piles a larger value of 3 is often assumed to ensure conservatism. For this investigation it is assumed that only laboratory

test data was available for the ‘site’ as this simplifies comparison with the Eurocode methodologies where the data used in the design process impacts upon the partial factors assumed. Hence a value of 3 has been assumed.

7.5.2 Uplift/Base Capacity in Reserve

An alternative method of predicting design capacities for helical screw piles could be to disregard the contribution of either the bearing capacity generated by the lowermost helical plate when loaded in compression, or the uplift capacity generated by the uppermost helical plate when loaded in tension. The potential validity for this methodology relies on the commonly accepted fact that piles mobilise shaft capacity much more quickly than base capacity.

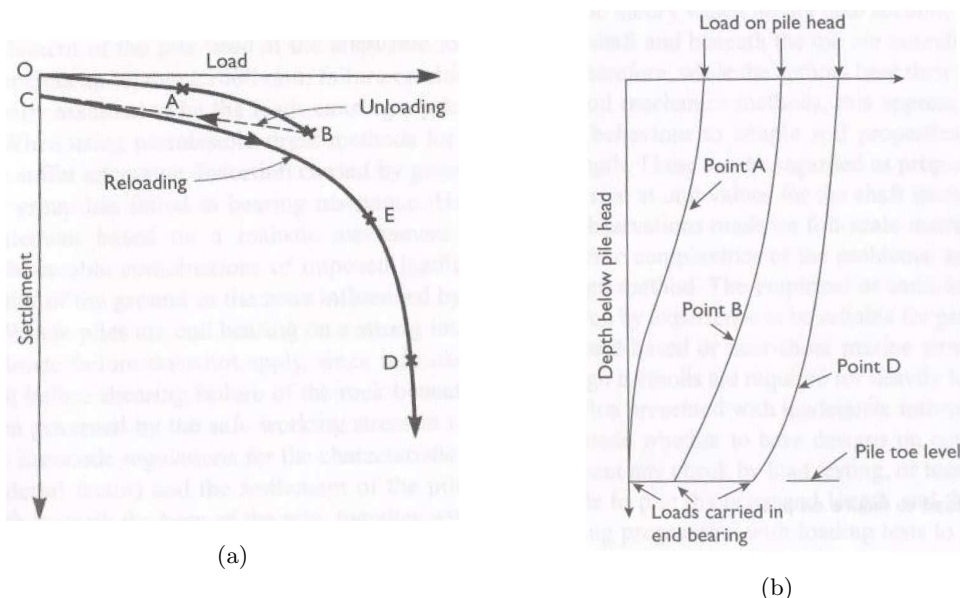


Figure 7.35: Idealised load-settlement (a) and load-transfer (b) phenomena for compressive loading of a pile to failure from Tomlinson and Woodward (2008).

Figure 7.35 illustrates the transfer of the pile load to the ground with relation to the idealised load-settlement response of a pile undergoing compressive loading to failure. As the pile is loaded and subsequently unloaded, it is the shaft resistance that is predominantly mobilised. Only as the pile approaches failure upon reloading is the base capacity significantly mobilised.

The validity of keeping the uplift or base capacity in reserve when calculating allowable design loads is reliant upon this phenomena. If this assumption is deemed valid the design capacities, $Q_{c\ d}$ and $Q_{t\ d}$ can be derived using the calculation model

proposed in Section 7.3 by disregarding the uplift and base capacities of the piles as shown in Equations 7.15 and 7.16.

$$Q_{c,d} = Q_{shear} + Q_{shaft} \quad (7.15)$$

$$Q_{t,d} = Q_{shear} + Q_{shaft} \quad (7.16)$$

7.5.3 Eurocode 7

Eurocode 7 uses a different approach to design by utilising partial factors on a combination of actions, resistances and material properties. Fundamentally Eurocode 7 defines the ULS adequacy by comparing design actions F_d with design resistances R_d :

$$F_d \leq R_d \quad (7.17)$$

where adequacy is assumed if the above statement is true, given that F_d is equal to:

$$F_d = \sum F_k \cdot \gamma_F \quad (7.18)$$

where F_k are the characteristic actions and γ_F are the appropriate partial factors. Table 7.8 contains a summary of the partial factors for permanent and variable actions for both favourable and unfavourable scenarios according to Eurocode 7. The design resistance R_d for the pile is obtained using:

$$R_d = \sum \frac{R_k}{\gamma_R} \quad (7.19)$$

where R_k are the characteristic resistances and γ_R are the appropriate partial factors for each component of resistance. Partial factors for resistances are defined in Eurocode 7 for three different types of pile: driven, bored and CFA. For these pile types partial factors for base resistance R_b , shaft resistance R_s , total resistance R_t and tensile resistance R_{st} are summarised in Table 7.9.

The characteristic resistance R_k is calculated using:

$$R_k = \frac{R_{cal}}{\xi} \quad (7.20)$$

where R_{cal} is the calculated resistance, which is governed by the calculation model assumed and ξ , which is the appropriate correlation factor. This factor is dependent on the source and amount of data used to obtain the calculated resistances. Sources of data that can be used for adequacy assessment in Eurocode 7 include in-situ and laboratory testing of soil properties and on-site static or dynamic pile testing. Table 7.10 summarises the correlation factors according to EN 1997-1. To satisfy Eurocode 7 both mean and minimum resistances need to be assessed, with the lower characteristic resistance, R_k , of the two being carried forward in the calculation of design resistance, R_d .

In this investigation, it can be assumed that all samples consolidated were representative of the same site given that the stress history for each of the samples was identical. For in-situ derived data Eurocode 7 defines tests that provide a strength profile with depth as a single independent test. Hence, based upon this criteria, each pair of upper and lower vane shear measurements constitute a shear strength profile in this investigation. Four pairs of vane shear measurements were taken per sample, of which there were ten in total. This provides 40 independent measurements of strength with depth, hence, given that the number of tests exceeds 10, the appropriate values for ξ in this instance are ξ_3 and ξ_4 , which are 1.25 and 1.08 respectively.

The calculation model used to derive the calculated resistance, R_{cal} , must incorporate the appropriate partial factors for material properties, γ_M , which are summarised in Table 7.11.

For the helical screw piles investigated here the calculated resistance R_{cal} can be taken as (after Section 7.3) Equation 7.21 where $R_{cal\ base}$ is the base resistance, $R_{cal\ uplift}$ is the uplift resistance, $R_{cal\ shear}$ is the cylindrical failure surface shear resistance and $R_{cal\ shaft}$ is the shaft resistance.

$$\begin{aligned} R_{cal} &= R_{c\ cal} \text{ or } R_{t\ cal} \\ &= (R_{cal\ base} + R_{cal\ shear} + R_{cal\ shaft}) \text{ or } (R_{cal\ uplift} + R_{cal\ shear} + R_{cal\ shaft}) \end{aligned} \quad (7.21)$$

Table 7.8: Partial factors for actions as specified by EN 1997-1.

Action		Partial Factor	Set	
			A1	A2
Permanent (G)	Unfavourable	γ_G	1.35	1.0
	Favourable	$\gamma_{G_{fav}}$	1.0	1.0
Variable (Q)	Unfavourable	γ_Q	1.5	1.3
	Favourable	$\gamma_{Q_{fav}}$	0	0

Table 7.9: Partial factors for resistance specified by EN 1997-1.

Component	Partial Factor	Pile Type	Set			
			R1	R2	R3	R4
Base Resistance (R_b)	γ_b	Driven	1.0	1.1	1.0	1.3
		Bored	1.25	1.1	1.0	1.6
		CFA	1.1	1.1	1.0	1.45
Shaft Resistance (R_s)	γ_s	All	1.0	1.1	1.0	1.3
Total Resistance (R_t)	γ_t	Driven	1.0	1.1	1.0	1.3
		Bored	1.15	1.1	1.0	1.5
		CFA	1.1	1.1	1.0	1.4
Tensile Resistance (R_{st})	γ_{st}	All	1.25	1.15	1.0	1.6

Table 7.10: Correlation factors specified by EN 1997-1.

Number	Static Load Tests		Ground Tests		Number	Dynamic Impact				
	ξ_1 (Mean)	ξ_2 (Min.)	ξ_3 (Mean)	ξ_4 (Min.)		ξ_5 (Mean)	ξ_6 (Min.)			
1	1.4	1.4	1.4	1.4	N/A	N/A	N/A			
2	1.3	1.2	1.35	1.27						
3	1.2	1.05	1.33	1.23	2 – 4	1.6	1.5			
4	1.1	1.0	1.31	1.20						
5	1.0	1.0	1.29	1.15	5 – 9	1.5	1.35			
7	1.0	1.0	1.27	1.12						
10	1.0	1.0	1.25	1.08	10 – 14	1.45	1.3			
≥ 10	1.0	1.0	1.25	1.08						
≥ 10	1.0	1.0	1.25	1.08	15 – 19	1.42	1.25			
≥ 10	1.0	1.0	1.25	1.08	≥ 20	1.4	1.25			

Table 7.11: Partial factors for material properties as specified by EN 1997-1.

Property	Partial Factor	Set	
		M1	M2
Angle of Friction ($\tan\phi$)	γ_ϕ	1.0	1.25
Effective Cohesion (c')	$\gamma_{c'}$	1.0	1.25
Unconfined Compressive Strength (q_u)	γ_{q_u}	1.0	1.4
Undrained Shear Strength (S_u)	γ_{S_u}	1.0	1.4
Unit Weight (γ)	γ_γ	1.0	1.0

Equations 7.7, 7.8, 7.9 and 7.10 can be used to describe the resistance generated by helical screw piles of various geometries. These equations describe the net capacity under undrained loading in a clay soil. Hence the only relevant partial factor for material properties is γ_{Su} . By incorporating this partial factor into the original equations the following are obtained:

$$R_{cal\ base} = \left[\frac{\pi \cdot D^2}{4} \right] \cdot N_c \cdot \left(\left(\frac{S_{u_{surface}}}{\gamma_{Su}} \right) + k \cdot (H + L_a) \right) \quad (7.22)$$

$$R_{cal\ uplift} = \left[\frac{\pi \cdot (D^2 - d^2)}{4} \right] \cdot N_{cu} \cdot \left(\left(\frac{S_{u_{surface}}}{\gamma_{Su}} \right) + k \cdot H \right) \quad (7.23)$$

$$R_{cal\ shear} = S_f \cdot \pi \cdot D \cdot \left(\left[\left(\frac{S_{u_{surface}}}{\gamma_{Su}} \right) \cdot (H + L_a) + \frac{k \cdot (H + L_a)^2}{2} \right] - \left[\left(\frac{S_{u_{surface}}}{\gamma_{Su}} \right) \cdot H + \frac{k \cdot H^2}{2} \right] \right) \quad (7.24)$$

$$R_{cal\ shaft} = \alpha \cdot \pi \cdot d \cdot \left(\left[\left(\frac{S_{u_{surface}}}{\gamma_{Su}} \right) \cdot H_{eff} + \frac{k \cdot H_{eff}^2}{2} \right] - 0 \right) \quad (7.25)$$

where all symbols are taken as defined previously in Section 7.3 and all pile geometries and soil properties are as defined in Tables 3.3 and 7.6. In this instance the mean and minimum strength profiles in Figure 6.2 were assumed to define the mean and minimum soil surface shear strength, $S_{u_{surface}}$, and shear strength gradient, k , values for which are summarised in Table 7.12.

Table 7.12: Mean and minimum soil surface shear strength and gradients.

Parameter	Mean	Minimum
$S_{u_{surface}}$ (kPa)	19.4	18.6
k (kPa/m)	-30	-30

The resistance partial factor sets given by Eurocode 7 do not currently cater for helical screw piles. Therefore, suitable partial factors need to be proposed and

applied for each of the individual resistance components (base or uplift resistance, cylindrical failure surface shear resistance and shaft resistance) to calculate the characteristic resistance R_k .

The shaft friction mobilised by a helical screw pile perhaps can be assumed to be similar in nature to the shaft friction mobilised by a driven pile. The base resistance mobilised by a helical screw pile, similarly, could be assumed to be most like that of a driven pile. Therefore for these two components of resistance it is logical to assume the same values as those stated for driven piles in Table 7.9. The helical screw piles investigated here were all deeply installed. Hence, the uplift capacity factor N_{cu} was assumed to be equal to the bearing capacity factor N_c . Following this assumption it is reasonable to assume that the partial factors for the uplift resistance, which are referred to here as γ_u , ought to equal those assumed for the base resistance, i.e. $\gamma_u = \gamma_b$.

Given that a shear band has been shown to develop in the physical models at the outer radii of the helical plates over the L_a of the pile, it can be assumed for simplicity that this may be mechanically similar in nature to the development of shearing resistance along the effective shaft length, H_{eff} . γ_{sh} could thus be assumed to be equal to γ_s as a first estimate. A summary of the partial factors assumed herein for helical screw piles is presented in Table 7.13. It can be seen that these assumptions lead to all partial factors being equal for all sets. With further data, preferably derived from full scale testing, these partial factors could be redefined with increased confidence and values for the total resistance, γ_t , and tensile resistance, γ_{st} , could be proposed.

Table 7.13: Partial factors for resistances generated by helical screw piles propose by the author.

Component	Partial Factor	Set			
		R1	R2	R3	R4
Base Resistance (R_b)	γ_b	1.0	1.1	1.0	1.3
Uplift Resistance (R_u)	γ_u	1.0	1.1	1.0	1.3
Shaft Resistance (R_s)	γ_s	1.0	1.1	1.0	1.3
Cylindrical Shear Resistance (R_{sh})	γ_{sh}	1.0	1.1	1.0	1.3

Carrying forward the minimum characteristic resistance and incorporating the appropriate partial factors from Table 7.13, leads to the compressive and tensile design resistances, $R_{c\ d}$ and $R_{t\ d}$, being defined as:

$$R_{c\ d} = \left(\frac{R_{k\ base}}{\gamma_b} \right) + \left(\frac{R_{k\ shear}}{\gamma_{sh}} \right) + \left(\frac{R_{k\ shaft}}{\gamma_s} \right) \quad (7.26)$$

$$R_{t\ d} = \left(\frac{R_{k\ uplift}}{\gamma_u} \right) + \left(\frac{R_{k\ shear}}{\gamma_{sh}} \right) + \left(\frac{R_{k\ shaft}}{\gamma_s} \right) \quad (7.27)$$

Eurocode 7 allows for three separate Design Approaches (DA's) to be used by the practitioner to investigate different scenarios by applying different groups of partial factors. There are three DA's defined by Eurocode 7: DA1, DA2 and DA3. There was a need for three separate DA's due to some member nations preferring to apply load and material factors, whilst others preferred to apply load and resistance factors. Table 7.14 outlines the partial factor combinations for each DA and the primary variables that are being factored during pile design. DA1 considers two separate combinations of factors, referred to as 'Combination 1' and 'Combination 2', where the actions and resistances are the primary variable being factored respectively. DA2 simultaneously factors the actions and resistances, whilst DA3 takes a different approach by factoring the actions and material properties. Consequently for DA3 the action partial factors can be taken from either set A1 or A2, a choice which is dependent on whether the action in question is a structural action or a geotechnical action. Here, the capacities calculated for the helical screw piles are net capacities. Hence all actions are considered structural actions. For other cases a table of potential geotechnical scenarios and whether an action ought to be considered structural or geotechnical is provided by Bond and Harris (2008).

Table 7.14: Eurocode 7 Design Approach partial factor sets and primary variables.

Design Approach	DA1		DA2	DA3
	Combination 1	Combination 2		
Partial Factor Sets	A1 + M1 + R1	A2 + M1 + R4	A1 + R2 + M1	A1 or A2 + M2 + R3
Primary Variable	Actions	Resistances	Actions and Resistances	Actions and Material Properties

For an adequacy factor of unity, Equation 7.17 can be rewritten as:

$$F_d = R_d \quad (7.28)$$

where if the loads applied during this investigation are all assumed to be permanent unfavourable loads, the design load F_d can be simplified as follows:

$$F_d = (F_{k_G} \cdot \gamma_G) \quad (7.29)$$

Hence the characteristic load can be calculated by dividing the design load F_d by the appropriate partial factor:

$$F_{k_G} = \frac{F_d}{\gamma_G} \equiv Q_{c\ d} \text{ or } Q_{t\ d} \quad (7.30)$$

This can be taken as equivalent to the design loads ($Q_{c\ d}$ or $Q_{t\ d}$) derived using the ‘permissible stress’ and ‘uplift/base capacity in reserve’ methods and thus allows comparison of the maximum safe capacity calculated using each of the design methodologies.

7.5.4 Comparison of Methods

The design loads calculated using the ‘permissible stress’, ‘uplift/base capacity in reserve’ and Eurocode 7 DA’s are summarised in Table 7.15. Negative signs have been assigned to denote tensile loads. The range in capacities is similar to the minimum predicted capacity for all pile configurations. This indicates that there is significant variation in the design capacity for helical screw piles using different design methodologies.

An alternative method of displaying the data is to normalise the experimental capacities in Table 7.7 by the design capacities, as shown in Figure 7.36. The ‘permissible stress’ method is seen to consistently be the most conservative of the methodologies, with Eurocode 7 DA3 second most conservative. The ‘uplift/base capacity in reserve’ method and Eurocode 7 DA1, combinations 1 and 2, and DA2 are, in contrast, consistently less conservative.

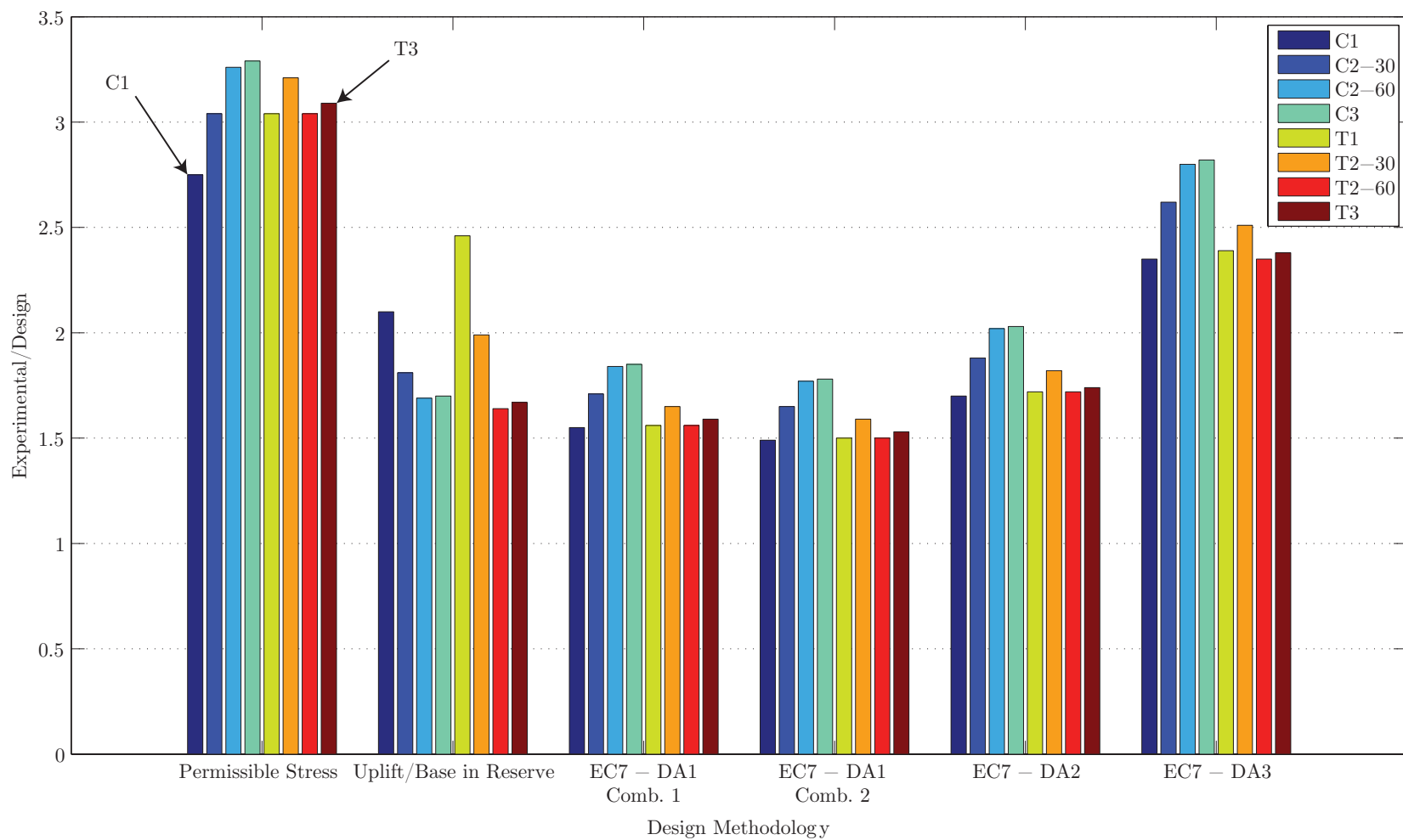


Figure 7.36: Experimental/design capacity for various design methodologies.

Table 7.15: Design capacities calculated using various design methodologies.

Methodology	Design Capacity (N)							
	C1	C2-30	C2-60	C3	T1	T2-30	T2-60	T3
Permissible Stress	25.4	32.7	40.4	40.4	-22.8	-30.8	-39.2	-39.2
Base/Uplift in Reserve	33.2	55.1	78.2	78.2	-28.1	-49.7	-72.6	-72.6
Eurocode 7 - DA1 - Comb. 1	45.2	58.1	71.8	71.8	-44.3	-59.9	-76.3	-76.3
Eurocode 7 - DA1 - Comb. 2	46.9	60.3	74.6	74.6	-46.1	-62.2	-79.3	-79.3
Eurocode 7 - DA2	41.1	52.8	65.3	65.3	-40.3	-54.5	-69.4	-69.4
Eurocode 7 - DA3	29.7	38.0	47.0	47.0	-29.0	-39.5	-50.8	-50.8
Range	21.5	27.7	37.8	37.8	23.2	31.4	40.1	40.1

It is noticeable that the ‘overdesign’ factors are relatively consistent for each pile geometry for all design methodologies except the ‘uplift/base capacity in reserve’ method. This is due to the fact that as L_a is increased the proportion of total capacity provided by either the base or uplift capacity reduces, and consequently this leads to reducing conservatism with increasing L_a . This limits the validity of this method as a design approach, since its conservatism is dependent upon the proportion of total capacity contributed by either base or uplift capacity of the uppermost or lowermost helical plate.

An interesting exercise is to back-calculate the immediate displacements that would have been induced had the design loads been applied to the model piles using load control. Given that the post-installation residual force, discussed in Chapter 5, was generated by the physical modelling process adopted, the horizontal offset from the graphical datum has been removed. This was achieved within MATLABTM, with Figure 7.37 showing the resulting corrected load-deflection curves, where zero load indicates zero axial displacement for all pile configurations.

Using this corrected data and interpolation, it was possible to calculate the immediate displacement that would have been induced due to the application of the design loads summarised in Table 7.15. Figure 7.38 illustrates the immediate displacement for all pile configurations using all of the design methodologies. There is significant scatter in the predicted immediate displacements. As expected the ‘permissible stress’ method, which was the most conservative, leads to the smallest immediate displacements. The largest displacements are indicated for Eurocode 7 DA1, combinations 1 and 2.

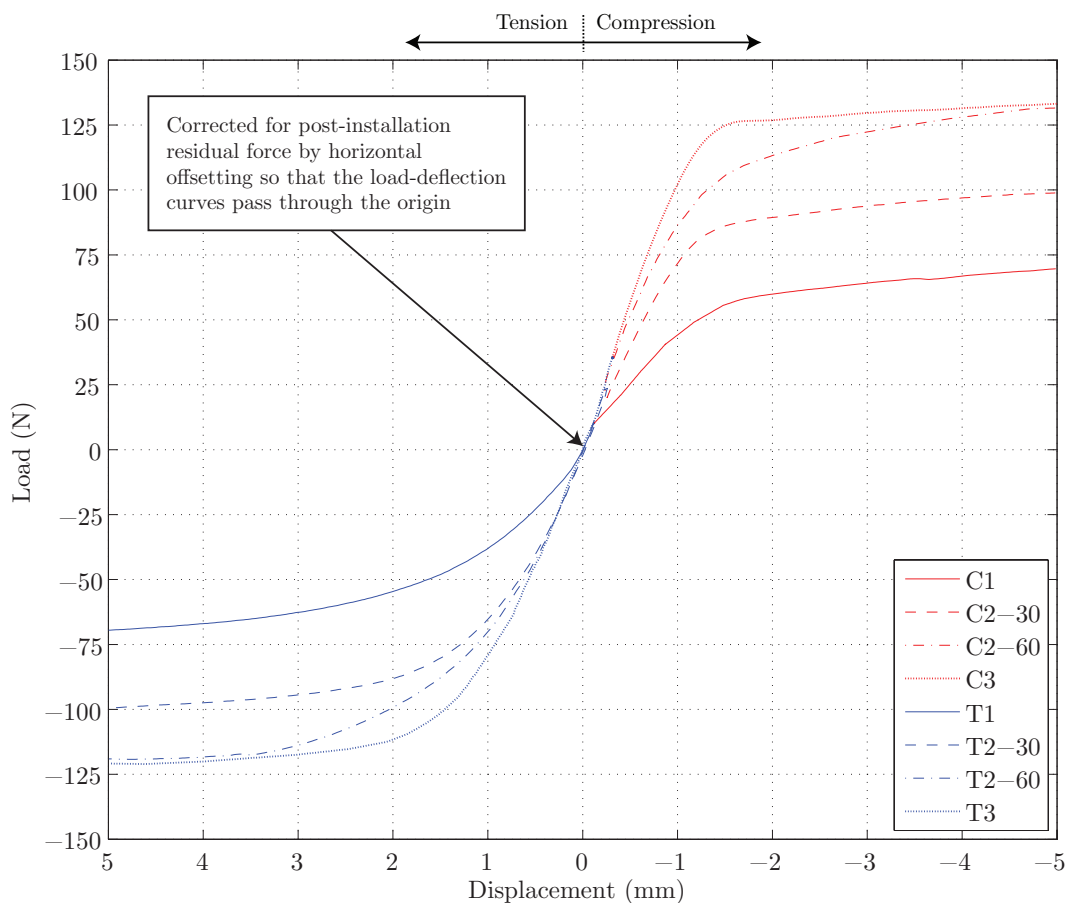


Figure 7.37: Load-deflection curves for model piles after correction for the effect of the post-installation residual force.

Figure 7.38 can be used to illustrate the importance of the initial stiffness of the load-deflection response of the helical screw piles (i.e. the early portion of the load-deflection response). For example, comparing the extreme cases of the single helix (C1/T1) and triple helix (C3/T3) piles, it can be seen that the low stiffness configuration (single helix) is very sensitive to small increases in applied load. In contrast the high stiffness configuration (triple helix) is far more tolerant of increases in applied load without significant increases in the immediate displacement of the pile.

If simple ULS calculations are, in addition to checking the ULS, to be used by practitioners to indicate serviceability or the SLS, this is an important point. For example, the double helix pile with S_f of 3.0 and the triple helix pile with S_f of 1.5 both have the same L_a , and hence the ULS capacities predicted are the same when the calculation model proposed in Section 7.3 is used. However, Figure 7.38 shows that the immediate displacement of the double helix pile would be greater due to the reduced stiffness of its initial load-deflection response compared to the triple helix pile. Therefore in practice, if the aim is to minimise displacement of the pile under loading, s/D ought to be minimised.

Figure 7.39 is a graphical summary of the estimated immediate percentage displacement of each of the configurations of pile as a function of the helical plate diameter, for the design loads calculated using each of the design methodologies. Lastly, Table 7.16 gives the standard deviation of the percentage immediate displacement for each of the design methodologies. The trend that is obvious in these immediate displacement estimates is that the design methodologies that are the least conservative not only lead to larger immediate displacements but also a greater range in immediate displacement due to the application of design loads. Therefore it suggested that for the design of helical screw piles, where Eurocode methods in particular are to be used (which are by design less conservative so as to be more economical), it is important that this effect is considered. Increases in design economy make it increasingly important to conduct separate SLS checks that are not reliant upon ULS capacity predictions.

A further observation is that the immediate percentage displacements estimated here are quite large. In Chapter 6 it was shown that an elasto-plastic constitutive model can capture the behaviour of the transparent soil reasonably well. However,

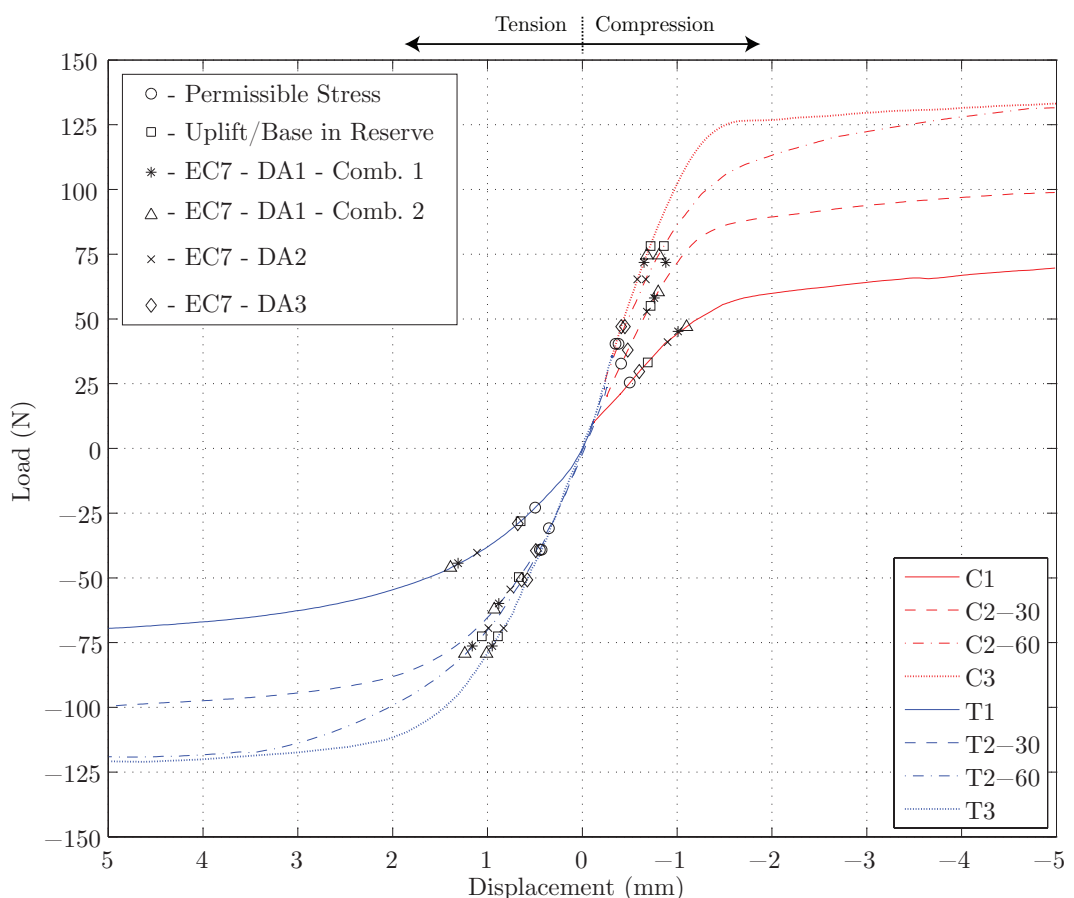


Figure 7.38: Estimation of immediate displacement of model piles for design capacities calculated using various design methodologies.

although the soil exhibits a similar shear strength to that of soft clays, its stiffness is less representative of real soil. For example the stiffness of silica based transparent soils is considerably lower than natural clays (Iskander et al., 2002), meaning that a greater shear strain must be mobilised before full strength is reached. Real soil exhibits highly non-linear stress-strain behaviour and thus is not modelled realistically using simple elasto-plastic models (Potts and Zdravković, 1999; Wood, 2004). These differences between transparent soil and real soil behaviour, probably explain the large immediate displacements estimated. Therefore, it would be imprudent to extrapolate the immediate percentage displacement estimates given here to problems in real soils at prototype scale. Thus, further research into both the immediate displacement response and long term uplift/settlement performance of helical screw piles is required.

Table 7.16: Standard deviation of percentage immediate displacement estimated to be caused by application of design loads using different design methodologies.

Methodology	Standard Deviation (%)
Permissible Stress	0.29
Base/Uplift in Reserve	0.72
Eurocode 7 - DA1 - Comb. 1	1.05
Eurocode 7 - DA1 - Comb. 2	1.21
Eurocode 7 - DA2	0.88
Eurocode 7 - DA3	0.49

7.6 Summary

FE based numerical simulations of the observations derived from small scale physical models using transparent soil and PIV have been formulated. The displacement and shear strain fields derived from the FE simulations show generally good agreement with the PIV measurements. The ULS failure mechanisms are generally well predicted by the FE method. This demonstrates both the usefulness of transparent soils for investigating problems where complex installation or failure mechanisms require investigation and the FE method in simulating the behaviour observed in the physical models.

The load-deflection response computed by the FE method is generally conservative compared to that measured in the physical model tests. It is poor at simulating the initial stiffness of the response but more adept at predicting the ULS capacity.

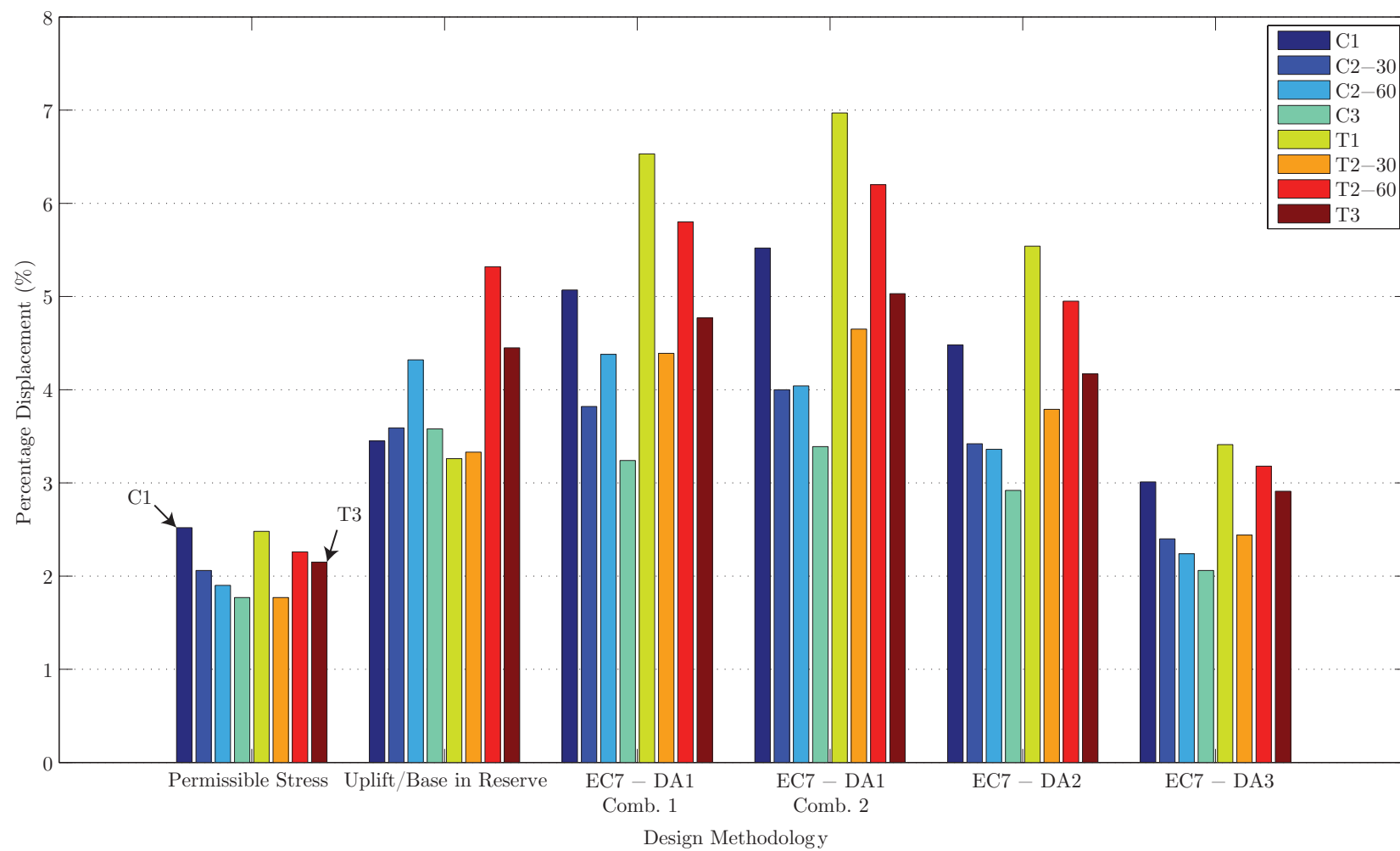


Figure 7.39: Percentage absolute immediate displacement as a function of helical plate diameter estimated using design capacities derived using various design methodologies and the corresponding load-deflection response from the model tests.

It is suggested that this may be due to variability of I_R with depth which was not measured during the post-test sample property investigations conducted. Alternatively it could be caused by an installation induced effect that could not be modelled in the FE analyses. Investigation into the sensitivity of the FE simulations indicated that increasing I_R by 10% did not fully mitigate the poor modelling of the initial stiffness of the response. To simulate the initial stiffness of the helical piles more accurately it is estimated that I_R may need to be increased by about 20-25%.

To assess the impact of the assumptions made during formulation of the FE simulations, a sensitivity analysis was conducted. This investigated the effect of the mesh density, vertical boundary fixity, strength and rigidity index. The sensitivity was shown to be most susceptible to changes in the shear strength bounds assumed and I_R , or more generally the parameters used to describe the constitutive behaviour of the soil. All other assumptions impacted upon the outcomes of the analyses less than the discrepancy between the experimental and FE simulation load-deflection responses. Therefore for most of the configurations of pile tested the discrepancies are most likely attributable to the soil in the physical models exhibiting variable strength/stiffness properties. The two exceptions were the double and triple helix piles with L_a of 60mm where the presence of a preferential shear band has been demonstrated which facilitated propagation of the failure mechanism to the surface in tests T2-60 and T3.

An analytical method of predicting capacity based on the failure mechanisms observed in the physical models was then developed based upon formulations suggested in the literature (Rao et al., 1991; Rao and Prasad, 1993; Rao et al., 1993a). These formulations were modified to account for the strength profile apparent in the physical models tested. The predicted capacities were then compared to the physical modelling derived capacities for all configurations of pile under compressive and tensile loading. The results generally indicate good predictions of capacity. However, the method is very dependent on the assumed values of H_{eff} and α , particularly for piles dependent on the mobilisation of shaft adhesion for a significant proportion of their ultimate capacity (tests C1 and T1).

The ULS capacities computed using these two prediction methods are generally conservative. However, care still needs to be taken when utilising either of the

methods to predict the capacity of helical screw piles deeply installed in soft clays. Further research is required into the dependency of the ultimate capacity of the piles on the setup time allowed after installation before loading. If this setup time is reduced it is possible that S_u and α ought to also be reduced if predictions are to remain conservative.

Lastly, a series of design methodologies has been used to calculate design capacities for each of the configurations of helical screw pile. Traditional ‘permissible stress’, a proposed ‘uplift/base capacity in reserve’ methodology and the three design approaches of Eurocode 7 were considered. In the absence of enough evidence to propose suitable partial factors with authority, values for partial factors on uplift and cylindrical shear resistance have been tentatively proposed to facilitate comparison of the design methodologies.

The ‘permissible stress’ method, perhaps as expected, was shown to be most conservative. Correspondingly, Eurocode DA1 was shown to be least conservative. By estimating the immediate displacement that would have been induced by application of the calculated design loads under stress control, the importance of the s/D has been demonstrated. Helical piles with equal L_a and differing s/D have been shown to exhibit the same ULS, but with differing immediate displacement estimated for the application of design loads. This has highlighted the need for independent SLS checks on the immediate, and also potentially the long-term, uplift/settlement of helical screw piles. The consistency of the estimated percentage immediate displacements has also illustrated that the less conservative but more economic Eurocode design methods may in general lead to less consistent immediate displacements under design loads.

Chapter 8

Conclusion

8.1 Introduction

The main aim of this research was to model the behaviour of helical screw piles and assess their failure mechanisms. To achieve this transparent soil has been used in conjunction with non-intrusive physical modelling techniques to assess the failure mechanisms of various geometries of helical screw pile. Supplementary numerical modelling has then been presented to assess the similarity of the observations made using the physical models and predictions made using the FE method. A simple analytical model has then been assessed with comparison to the physical and numerical models before some discussion of the impacts of the findings on practice. To guide the research a series of objectives were outlined in Chapter 1, by which the success of the project ought to be appraised. The following section revisits these objectives in turn and summarises the key findings and conclusions generated by the research.

8.2 Research Outcomes

The first objective of the research was:

1. *To assess the potential capacity of transparent soils for the investigation of geotechnical problems using small scale physical modelling by conducting a thorough review of published literature.*

A review of published literature showed that fine grained transparent soil afforded the greatest opportunity for modelling geotechnical problems at small scale in the laboratory. Two fine grained transparent soils were compared, one used previously in conjunction with PIV analysis techniques and a new formulation comprising of

fumed amorphous silica aggregates and a pore fluid of improved optical clarity. This development led to the following conclusions:

- Fine grained transparent soil has been developed using fumed amorphous silica rather than precipitated amorphous silica aggregates, which when coupled with mineral oil of improved optical clarity compared to that previously used (Hird et al., 2008; Ni et al., 2010) exhibits significantly improved consolidated transparency.
- The volume of soil used in each model in this investigation was four times greater than the maximum that was previously used by Ni et al. (2010).
- These improvements significantly increase the potential of the material for investigating geotechnical phenomena and the development of displacements and subsequently strains around geotechnical structures.

The literature review highlighted the possibility of using transparent soil based modelling techniques to investigate the failure mechanisms of helical screw piles in fine grained soils representative of soft clay. This work was encompassed within the following objective which was:

2. To design small scale physical modelling experiments that maximise the modelling capacity of transparent soils and allow observation of the failure mechanisms of helical screw piles.

This objective was met by modifying and designing equipment, where necessary, to allow transparent soils to be used to facilitate observation of soil displacements around small model helical screw piles. Model helical screw piles with 20mm diameter helical plates and 5mm shaft diameter were manufactured, to allow investigation of the impact of L_a over the range of 0-60mm and s/D over the range of 1.5-3.0, on the observed failure mechanisms and performance. Transparent soil beds with dimensions of 200mm (W) by 200mm (D) by 220mm (H) were prepared to facilitate the proposed investigations with minimal boundary effects. Experiences gained during the modelling process led to the following key conclusions in relation to the modelling techniques adopted:

- Soil beds with controlled stress history can be readily created in the laboratory for non-intrusive physical modelling investigations.

- The consolidation process highlighted the importance of slowly unloading the consolidated soil bed during sample preparation to preserve the intactness of the samples.
- A test methodology has been developed for which adequate repeatability has been demonstrated using two repeat tests.
- The apparatus facilitated investigations into:
 - Installation induced disturbance caused by helical screw piles of varying geometry.
 - Displacement fields generated by compressive and tensile loading of deeply installed helical screw piles.

After developing the non-intrusive physical modelling methodology to allow observation of the failure mechanisms of deeply installed helical screw piles in a transparent soil representative of soft clay, techniques for measuring the observed displacements were required that utilised the digital images recorded during the tests. The objective related to displacement measurement was:

3. To measure accurately the displacement and shear strain fields generated during loading of model helical screw piles of varying geometry using Particle Image Velocimetry (PIV) and photogrammetry.

This entailed using PIV measurement techniques and adapting close-range photogrammetry methods to specifically cater for the modelling of geotechnical phenomena using transparent soils. Rigorous calibration of the PIV measurement techniques was conducted. Previously published close-range photogrammetry techniques were then adapted to allow conversion of PIV derived image space measurements to object space output using only two points with coincident image space and object space coordinates (i.e. the tip of the model piles at the commencement and completion of the installation process or the edges of the circular footing). A rigorous assessment of the capabilities of the PIV measurement and photogrammetric correction system was then conducted via a validation process leading to the following conclusions:

- An improved photogrammetric correction method (compared to that previously used by Ni et al. (2010)) has been described, which utilises the pinhole camera model (Heikkilä and Silvén, 1997) to resolve and correct for erroneous soil-camera movements and mathematical models to correct for camera induced radial and tangential distortions.

- A novel approach has been proposed and validated that alleviates the problems caused by a lack of coincident image space and object space coordinates for the LED control points used.
 - This allowed the advantages of close range photogrammetry to be harnessed, whilst ensuring that all measurements made relate to the plane of interest.
- Non-coplanarity between the control and target planes has been mitigated using a simple statistical approach which has been partly validated.
- These improvements have led to a measurement resolution of $25\mu m$ for a FOV of $75mm$ by $200mm$, with an accuracy on average of $50\mu m$ and precision of $5\text{--}20\mu m$.

These improvements to the PIV measurement and photogrammetric correction techniques allowed the installation and performance of helical screw piles with a range of geometries to be investigated non-intrusively. The results allowed following conclusions to be made in relation to the installation of the helical screw piles:

- Installation of helical screw piles was observed to cause breakout at the soil surface during initial penetration of the lowermost helix of the pile which was thought to be exacerbated by the low unit weight of the material and the low stress profiles induced by the $1g$ modelling procedure adopted.
- Helical piles with greater numbers of helices were shown to induce greater lateral disturbance to the soil into which they are installed which was thought to have been caused by the increased volume of the piles which was a result of the increased numbers of helical plates.
- The vertical disturbance caused by installation was greatest for piles with minimum s/D which was thought to be caused by the increased confinement of soil between the helical plates for low s/D .
- The advance of the lowermost helical plate was shown to cause the majority of disturbance to the soil into which the pile is being installed which highlighted the importance of driving multi helix screw piles at a screw rate of installation (vertical advancement of the pitch of the helical plates per revolution) in practice if soil disturbance is to be minimised.

Following helical pile installation, a setup period of 24 hours was allowed to facilitate dissipation of installation induced excess pore pressures in the transparent soil. The piles were then loaded to failure using displacement control in either compression or tension. A series of 8 tests and 2 repeat tests were conducted that allowed the following conclusions to be drawn from the results:

- The compressive and tensile performance of deeply installed helical screw piles in soft clay is very similar.
 - Discrepancies in capacity due to the configuration of loading applied were generally only observed where H/D was 4 and were attributed to a combination of installation induced breakout and reducing H/D during tensile loading caused by the displacement induced by loading.
- Shear bands have been shown to be generated between the outer radii of the helical plates for multi helix piles.
 - $s/D < 1.5$ led to rapid generation of these shear bands whereas $s/D > 1.5$ necessitated greater displacement to be induced before the shear band between the outer radii of the helical plates was fully formed.
- s/D was shown to control the stiffness of the initial load-deflection response as comparing tests with constant L_a but differing s/D demonstrated that lower s/D resulted in increased capacity for the same axial displacement compared to piles with greater s/D .
- L_a was shown to influence the ULS capacity of the helical screw piles as comparing tests where s/D was maintained and L_a was varied demonstrated that piles with greater L_a consistently exhibited greater ULS capacities.
- The interface between the pile shaft and surrounding soil was shown to be a sliding interface and was significant as it governed a principal assumption made during the formulation of the simulations of the physical model experiments using the FE method.

The next objective of the investigation was to generate numerical simulations of the experiments, allowing assessment of the similarity of the experimental observations and numerical predictions of behaviour. For this purpose the FE method was used. To facilitate this the constitutive behaviour of the transparent soil had to be characterised and this was governed by the following objective which was:

-
4. To derive suitable soil parameters to allow calibration of a suitable constitutive model for use in Finite Element (FE) simulations of the physical model tests.

This objective was met initially using a combination of in-situ and element testing processes. Firstly, hand vane shear tests were performed in the samples after testing of the helical screw piles. UU triaxial tests were also performed on samples taken from another sample with identical stress history allowing estimation of E_u and S_u and subsequently I_R . This allowed fitting of a simple elasto-plastic constitutive model in the form of the Mohr-Coulomb model. An alternative method of deriving the stress-strain behaviour of the transparent soil was then proposed and investigated. This utilised the MSD theory of Osman and Bolton (2005) and small scale models of the undrained settlement of a circular footing (50mm diameter) on a bed of transparent soil. This work led to the following key conclusions:

- Displacement and shear strain fields derived using PIV analysis of digital images recorded during the physical model tests differed to those assumed by Osman and Bolton (2005) as the depth of influence observed was much greater in the physical model.
- Consequently an axisymmetric FE simulation of the physical model test was performed using ABAQUS which indicated generally good agreement with the physical modelling results in relation to both load-settlement performance and the displacement and shear strain fields apparent beneath the footing.
- A sensitivity analysis conducted on the FE simulation employed showed that the simulation was generally insensitive to the assumptions made when formulating the FE model.
 - The simulation was found to be most sensitive to the shear strength profile assumed as variation from the lower to upper bound shear strength induced an absolute variation of 10% of the capacity of the ‘Baseline’ simulation at a settlement of 10mm.
 - Thus discrepancies between the physical models’ behaviour and FE predictions of up to 5% of the maximum capacity were deemed unsurprising and thought most likely to be due to sample variability.
- The reverse MSD method has been demonstrated to show promise, although the uncertainty regarding the choice of N_c , M_c and the representative depth

of the measurement derived limits confidence in its application in the manner proposed here.

- Further experimental and parallel numerical investigation is deemed necessary to improve understanding of the impact of the choice of N_c and M_c .
- The stress-strain response of the transparent soils utilised in this investigation has been demonstrated to be adequately captured by a simple elasto-plastic constitutive model.

Characterisation of the stress-strain response of the transparent soil allowed simulation of the physical modelling tests using the FE method in ABAQUS, which was motivated by the following objective:

5. *To perform FE simulations of the physical models to allow comparison of the experimentally derived load-deflection performance and displacement and shear strain fields with a numerically derived solution.*

To achieve this objective the helical screw piles were idealised as circular plates allowing axisymmetric simplification to be assumed. The same elasto-plastic constitutive model that was employed in the simulation of the aforementioned footing test was used again. The pile was ‘wished’ into place in the FE simulations and thus no installation induced effects were modelled. The results of the simulations and comparison to the observations made using data from the physical model tests led to the following conclusions:

- The displacement and shear strain fields derived from the FE simulations demonstrate generally good agreement with the PIV measurements.
- The ULS failure mechanisms are generally well predicted by the FE method.
- The simulations demonstrate both the usefulness of transparent soils for investigating problems where complex installation or failure mechanisms require investigation and the FE method in simulating behaviour observed in the physical models.
- The load-deflection response computed by the FE method is generally conservative compared to that measured using the physical models.
- The FE method was poor at simulating the initial stiffness of the load-deflection response but more adept at predicting the ULS capacity.

- It was suggested that this may be due to variability of I_R with depth which was not measured during the post-test sample property investigations conducted or could alternatively be caused by an installation induced effect that could not be modelled in the FE analyses.
- A sensitivity analysis was conducted which investigated the effect of the mesh density, vertical boundary fixity, strength and rigidity index on the FE simulations.
 - The sensitivity was shown to be most susceptible to changes in the shear strength bounds assumed and I_R .
 - Increasing I_R by 10% did not fully mitigate the poor modelling of the initial stiffness of the response.
 - * To more accurately simulate the initial stiffness of the helical piles it is estimated that I_R may need to be increased by about 20-25%.
- The FE simulations confirmed that the installation process, and resulting reduction of H/D caused by breakout at the surface of the sample and installation induced disturbance, contributed to the ULS capacity discrepancy seen for multi helix piles with H/D equal to 4 (piles C2-60 and C3 and piles T2-60 and T3) .

After confirming the similarity of the physical modelling and FE based numerical modelling derived results, a key objective was:

6. To assess the validity of capacity prediction methods reported in published literature by comparing the predictions with capacities derived from the physical modelling experiments and FE simulations.

This is a critical objective in relation to practice in the construction industry. Relatively simple yet accurate models for predicting the capacity of helical screw piles are required. The first stage in developing such models is to define a suitable mechanism. Previous work suggested that a cylindrical failure surface could be assumed to form between the outer radii of helical plates on a multi helix pile. The validity of this assumption was confirmed by both the physical and numerical modelling conducted as part of this investigation. By taking this basic assumption a simple analytical model for capacity prediction was developed and its ability assessed through comparison of its predictions with those derived from the physical model tests and FE simulations. These comparisons led to the following conclusions.

- The comparisons generally indicate good predictions of capacity by the calculation model investigated.
- The method is very dependent on the assumed values of H_{eff} and α in particular for piles dependent on the mobilisation of shaft adhesion for a significant proportion of their ultimate capacity (tests C1 and T1).
- The ULS capacities calculated are generally conservative.
- Further research is required into the dependency of the ultimate capacity of the piles on the setup time allowed after installation before loading.
 - If this setup time is reduced it is possible that S_u and α ought to also be reduced if predictions are to remain conservative.

Lastly, after demonstrating the generally good capacity prediction of the cylindrical shear surface failure model assumed the final objective of the research was:

7. To utilise the findings of the research to guide industrial practice relating to the prediction of helical screw pile capacities and definition of appropriate pile geometries during design.

This was achieved by incorporating the calculation model developed into common design methodologies. These design methodologies included the traditional ‘permissible stress’ approach, a novel ‘base/uplift capacity in reserve’ method and the partial factor approach of Eurocode 7. Firstly design capacities were calculated using the three methods allowing appraisal of conservatism, economy and consistency of each design methodology. Following this, in conjunction with the load-deflection responses recorded during the physical modelling tests, the immediate displacement induced by application of the design capacity calculated by each of the design methodologies was compared. This work led to the following conclusions:

- The ‘permissible stress’ method was shown to be most conservative.
- Eurocode DA1 was shown to be least conservative using the proposed partial factors.
- The importance of s/D has been demonstrated by estimating the immediate displacement that would have been induced by application of the calculated design loads under stress control.

- Helical piles with equal L_a and differing s/D have been shown to exhibit the same ULS, but with differing immediate displacement estimated for the application of design loads.
- This has highlighted the need for independent SLS checks on the immediate, and also potentially the long-term, uplift/settlement of helical screw piles.
- The consistency of the estimated percentage immediate displacements has also illustrated that the less conservative but more economic Eurocode design methods in general lead to less consistent immediate displacements under design loads.

8.3 Recommendations for Further Research

There remain areas related to the research presented here that require further development. These potential avenues for further work encompass both further investigation into helical screw pile behaviour and the modelling techniques employed here and include:

- The failure mechanisms in coarse grained soils such as sands are not definitively known. Fused silica or silica gel afford an opportunity to potentially observe the failure mechanisms of helical screw piles in coarse grained soils using similar techniques to those employed here (Sadek et al., 2002; Iskander et al., 2002a; Iskander et al., 2002b; Liu et al., 2002; Iskander et al., 2003). However since the behaviour of coarse grained soils is typically stress dependent, if small scale models are to be used, the use of a geotechnical centrifuge to artificially increase the self weight of the transparent soil may be deemed necessary.
- In light of the previous suggestion, incorporation of transparent soils into geotechnical centrifuge models where the self weight of the soil is significant, represents a potential future direction for research. This has already been partly achieved by Song et al. (2010). However, their lack of PIV based displacement measurement leaves scope for further improvement of the techniques they reported.
- The long-term displacement performance of helical screw piles in fine grained soils provides another potentially fruitful direction for future research. As yet there has been very little study of the long term performance of helical screw piles. Research, in particular, into the dependence of capacity on the setup

period allowed after installation is seen as an area of importance with respect to guidance for the practicing engineer. As yet there is very little guidance related to the setup period that ought to be allowed after installation of helical screw piles into fine grained soils.

- Further investigation into the undrained settlement of a circular footing on clay soils is required to further explore the validity of the MSD concept of Osman and Bolton (2005) and its potential use in reverse as has been demonstrated in this thesis. Further physical modelling using different footing geometries and soil bed strength profiles and parallel numerical studies is suggested to facilitate this.
- Lastly, in Chapter 4 it was highlighted that dynamically changing the ‘leapfrog’ parameter within GeoPIV dependent upon the gradient of displacement may improve GeoPIV’s ability to simultaneously track both small and large magnitudes of movement within the same analysis. Research into methods to improve GeoPIV such as the one suggested, could potentially improve its capabilities and/or consistency.

References

- Adrian, R. (1991). Particle-imaging technique for experimental fluid dynamics, *Annual Reviews in Fluid Mechanics* **23**: 261–304.
- Adrian, R. (2005). Twenty years of particle image velocimetry, *Experiments in Fluid Mechanics* **39**: 159–169.
- Ahmed, M. & Iskander, M. (2010). Analysis of tunneling induced ground movements using transparent soil models, *Journal of Geotechnical and Geoenvironmental Engineering - Available online ahead of print*.
- Ali, B., Kumar, C. & Pushpavanam, S. (2008). Analysis of liquid circulation in a rectangular tank with a gas source at a corner, *Chemical Engineering Journal* **144**, No. 3: 442–452.
- Allersma, H. (1982). Photoelastic investigation of the stress distribution during penetration, *Proc. 2nd European Symposium on Penetration Testing* pp. 411–418.
- Andrawes, K. & Butterfield, R. (1973). The measurement of planar displacements of sand grains, *Géotechnique* **23**, No. 5: 571–576.
- Atkinson, J. & Potts, D. (1977). Stability of a shallow circular tunnel in cohesionless soil, *Géotechnique* **27**, No. 2: 203–215.
- Black, J. (2007). *The settlement of a footing on soft clay reinforced with vibrated stone columns*, PhD thesis, Queen's University Belfast.
- Bolton, M. & Powrie, W. (1987). The collapse of diaphragm walls retaining clay, *Géotechnique* **37**, No. 3: 335–353.
- Bolton, M. & Powrie, W. (1988). Behaviour of diaphragm walls in clay prior to collapse, *Géotechnique* **38**, No. 2: 167–189.

- Bolton, M., Gui, M., Garnier, J., Corte, J., Bagge, G., Laue, J. & Renzi, R. (1999). Centrifuge cone penetration tests in sand, *Géotechnique* **49**, No. 4: 543–552.
- Bond, A. & Harris, A. (2008). *Decoding Eurocode 7*, Taylor and Francis, London.
- Bouget, J. (2008). Camera calibration toolbox for matlab. Available online at http://www.vision.caltech.edu/bougetj/calib_doc/.
- Bransby, P. & Milligan, G. (1975). Soil deformations near cantilever sheet pile walls, *Géotechnique* **25**, No. 2: 175–195.
- Brinch Hansen, J. (1970). A revised and extended formula for bearing capacity, *Danish Geotechnical Institute Bulletin* **28**: 5–11.
- Brown, M., Anderson, W. & Hyde, A. (2004). Statnamic testing of model piles in a clay calibration chamber, *International Journal of Physical Modelling in Geotechnics* **1**: 11–24.
- BS1377-9:1990 (1990). Bs1377-9 - methods of test for soils for civil engineering purposes - in-situ tests.
- Butterfield, R., Harkness, R. & Andrawes, K. (1970). A stereo-photogrammetric method for measuring displacement fields, *Géotechnique* **20**, No. 3: 308–314.
- Chance Construction Ltd. (2008). Helical screw piling supplier website found at <http://www.abchance.com>.
- Cheuk, C., White, D. & Bolton, M. (2008). Uplift mechanisms of pipes buried in sand, *Journal of Geotechnical and Geoenvironmental engineering* **134**, No. 2: 154–163.
- Chung, S. & Kim, S. (2008). Digital particle image velocimetry studies of nasal airflow, *Respiratory Physiology and Neurobiology* **163**: 111–120.
- Clemence, S. & Pepe, F. (1984). Measurement of lateral stress around multi-helix anchors in sand, *Geotechnical Testing Journal* **7**, No. 3: 145–152.
- Davies, E. (2005). *Machine vision: Theory, algorithms and practicalities*, Oxford: Morgan Kaufmann.
- Eason, G. & Shield, R. (1960). The plastic indentation of a semi-infinite solid by a perfectly rough circular punch, *Journal of Applied Mathematics and Physics (ZAMP)* **11**, No. 1: 33–43.

- Effendi, R. (2007). *Modelling of the settlement interaction of neighbouring buildings on soft ground*, PhD thesis, University of Sheffield.
- Ghaly, A. (1995a). Drivability and pullout resistance of helical units in saturated sands, *Soils and Foundations* **35**, No. 2: 61–66.
- Ghaly, A. & Clemence, S. (1998). Pullout performance of inclined helical screw anchors in sand, *Journal of Geotechnical and Geoenvironmental Engineering* **124**, No. 7: 617–627.
- Ghaly, A. & Hanna, A. (1991a). Experimental and theoretical studies on installation torque of screw anchors, *Canadian Geotechnical Journal* **28**, No. 3: 353–364.
- Ghaly, A. & Hanna, A. (1992). Stresses and strains around helical screw anchors in sand, *Soils and Foundations* **32**, No. 4: 27–42.
- Ghaly, A. & Hanna, A. (1994). Ultimate pullout resistance of single vertical anchors, *Canadian Geotechnical Journal* **31**, No. 5: 673–682.
- Ghaly, A. & Hanna, A. (1994a). Model investigation of the performance of single anchors and groups of anchors, *Canadian Geotechnical Journal* **31**, No. 2: 273–284.
- Ghaly, A., Hanna, A. & Hanna, M. (1991). Installation torque of screw anchors in dry sand, *Soils and Foundations* **31**, No. 2: 77–92.
- Ghaly, A., Hanna, A. & Hanna, M. (1991c). Uplift behaviour of screw anchors in sand I: Dry sand, *Journal of Geotechnical Engineering* **117**, No. 5: 773–793.
- Ghaly, A., Hanna, A. & Hanna, M. (1991d). Uplift behaviour of screw anchors in sand II: Hydrostatic and flow conditions, *Journal of Geotechnical Engineering* **117**, No. 5: 794–808.
- Ghaly, A., Hanna, A., Ranjan, G. & Hanna, M. (1991b). Helical anchors in dry and submerged sand subjected to surcharge, *Journal of Geotechnical Engineering* **117**, No. 10: 1463–1470.
- Gill, D. (1999). *Experimental and theoretical investigations of pile and penetrometer installation in clay*, PhD thesis, Trinity College, Dublin.
- Gill, D. & Lehane, B. (2001). An optical technique for investigating soil displacement patterns, *Geotechnical Testing Journal* **24**, No. 3: 324–329.

- GTL Partnership Ltd. (2008). Helical screw piling contractor website found at <http://www.gtl-partnership.com>.
- Gui, M., Bolton, M., Garnier, J., Corte, J., Bagge, G., Laue, J. & Remzi, R. (1998). Guidelines for cone penetration tests in sands, *Proceedings of Centrifuge 1998* pp. 155–160.
- Guler, M., Edil, T. & Bosscher, P. (1999). Measurement of particle movement in granular soils using image analysis, *Journal of Computing in Civil Engineering* **13**, No. 2: 116–122.
- Hanna, A. & Ghaly, A. (2007). Ultimate pullout resistance of groups of vertical anchors, *Canadian Geotechnical Journal* **31**, No. 5: 673–682.
- Hanna, A., Ayadat, T. & Sabry, M. (2007). Pullout resistance of single vertical shallow helical and plate anchors in sand, *Geotechnical and Geological Engineering* **25**: 559–573.
- Haralick, R. & Shapiro, L. (1992). *Computer and robot vision, vol. 1*, Wokingham: Addison-Wesley Publishing Co.
- Hassan, Y. & Dominguez-Ontiveros, E. (2008). Flow visualization in a pebble bed reactor experiment using PIV and refractive index matching techniques, *Nuclear Engineering and Design* **238**, No. 11: 3080–3085.
- Heikkilä, J. (2000). Geometric camera calibration using circular control points, *IEEE Transactions on Pattern Analysis and Machine Intelligence* **22**, No. 10: 1068–1077.
- Heikkilä, J. (2000a). Camera calibration toolbox for Matlab Version 3.0 at <http://www.ee.oulu.fi/~jth/calibr>.
- Heikkilä, J. & Silvén, O. (1997). A four-step camera calibration procedure with implicit image correction, *Proceedings of the 1997 Conference on Computer Vision and Pattern Recognition* pp. 1106–1112.
- Hill, R. (1950). *The mathematical theory of plasticity*, Clarendon Press, Oxford.
- Hird, C., Ni, Q. & Guymer, I. (2008). Physical modelling of displacements around continuous augers in clay, *Proc. 2nd British Geotechnical Association International Conference on Foundations* **1**: 565–574.

- Hossain, M. & Randolph, M. (2009). New mechanism based design approach for spudcan foundations on single layer clay, *Journal of Geotechnical and Geoenvironmental Engineering* pp. 1624–1274.
- Houlsby, G. & Wroth, C. (1983). Calculation of stresses on shallow penetrometers and footings, *Proc. of the IUTAM/IUGG symposium on seabed mechanics* pp. 107–112.
- Hu, Y. & Randolph, M. (1998). A practical numerical approach for large deformation problems in soil, *International Journal of Numerical and Analytical Methods in Geomechanics* **22**: 327–350.
- Iskander, M., Lai, J., Oswald, C. & Mannheimer, R. (1994). Development of a transparent material to model the geotechnical properties of soils, *Geotechnical Testing Journal* **17**, No. 4: 425–433.
- Iskander, M., Liu, J. & Sadek, S. (2002). Transparent amorphous silica to model clay, *Journal of Geotechnical and Geoenvironmental Engineering* **128**, No. 3: 262–273.
- Iskander, M., Sadek, S. & Liu, J. (2002a). Optical measurement of deformation using transparent silica gel to model sand, *International Journal of Physical Modelling in Geotechnics* **4**: 13–126.
- Iskander, M., Sadek, S. & Liu, J. (2002b). Displacement field measurement in transparent soils, *15th ASCE Engineering Mechanics Conference* pp. 1–8.
- Iskander, M., Sadek, S. & Liu, J. (2003). Soil structure interaction in transparent synthetic soils using digital image correlation, *TRB 2003 Session on Recent Advances in Modelling Techniques in Geomechanics (Committee A2K05) Paper Number: 03-2360* pp. 1–23.
- Jain, R., Kasturi, R. & Schunck, B. (1995). *Machine vision*, Singapore: McGraw-Hill Inc.
- Kang, J. & Lee, S. (2008). Improvement of natural ventilation in a large factory building using a louver ventilator, *Building and Environment* **43**, No. 12: 2132–2141.
- Klotz, E. & Coop, M. (2001). An investigation of the effect of soil state on the capacity of driven piles in sands, *Géotechnique* **51**, No. 9: 733–751.

- Konagai, K., Tamura, C., Rangelow, P. & Matsushima, T. (1992). Laser aided tomography: A tool for visualization of changes in the fabric of granular assemblage, *Structural Engineering/Earthquake Engineering* **9**, No. 3: 193–201.
- Ladd, C. & Foott, R. (1977). New design procedure for stability of soft clays, *Journal of the Geotechnical Engineering Division* **100**, No. 4: 763–779.
- Laguerre, O., Remy, D. & Flick, D. (2009). Airflow, heat and moisture transfers by natural convection in a refrigerating cavity, *Journal of Food Technology* **91**, No. 2: 197–210.
- Lehane, B. & Gill, D. (2004). Displacement fields induced by penetrometer installation in an artificial soil, *International Journal of Physical Modelling in Geotechnics* **1**: 25–36.
- Lehane, B., Gaudin, C., Richards, D. & Rattley, M. (2008). Rate effects on the vertical uplift capacity of footings founded in clay, *Géotechnique* **58**, No. 1: 13–21.
- Levin, A. (1955). Indentation pressure of a smooth circular punch, *Quarterly of Applied Mathematics* .
- Liu, J. & Iskander, M. (2004). Adaptive cross correlation for imaging displacements in soils, *Journal of Computing in Civil Engineering* **18**, No. 1: 46–57.
- Liu, J. & Iskander, M. (2010). Modelling capacity of transparent soil, *Canadian Geotechnical Journal* **47**: 451–460.
- Liu, J., Iskander, M. & Sadek, S. (2002). Optical measurement of deformation under foundations using a transparent soil model, *Physical Modelling in Geotechnics: ICPMG 2002* pp. 155–159.
- Liu, J., Iskander, M. & Sadek, S. (2003). Consolidation and permeability of transparent amorphous silica, *Geotechnical Testing Journal* **26**, No. 4: 1–12.
- Livneh, B. & El Naggar, M. (2008). Axial testing and numerical modelling of square shaft helical piles under compressive and tensile loading, *Canadian Geotechnical Journal* **45**, No. 8: 1142–1155.
- Lutenegger, A. (2008). Tension tests on single-helix screw-piles in clay, *Proc. 2nd British Geotechnical Association International Conference on Foundations* **1**: 201–211.

- Lyndon, A. & Schofield, A. (1970). Centrifuge model test of a short-term failure in London Clay, *Géotechnique* **20**, No. 4: 440–442.
- Martin, C. & Randolph, M. (2001). Applications of the lower and upper bound theorems of plasticity to collapse of circular foundations, *Proc. 10th International Conference of IACMAG* **2**: 1417–1428.
- MatWeb (2010). Material property database found at <http://www.matweb.com>.
- McKelvey, D. (2002). *The performance of vibro stone column reinforced foundations in deep soft ground*, PhD thesis, Queens University, Belfast.
- McKelvey, D., Sivakumar, V., Bell, A. & Graham, J. (2004). Modelling vibrated stone columns in soft clay, *Proc. Institution of Civil Engineers: Geotechnical Engineering* **3**: 137–149.
- Ni, Q., Hird, C. & Guymer, I. (2010). Physical modelling of pile penetration in clay using transparent soil and particle image velocimetry, *Géotechnique* **60**, No. 2: 121–132.
- Nunez, I. (1989). *Tension piles in clay*, PhD thesis, University of Cambridge.
- Osman, A. (2004). *Predicting ground displacements in clay during construction*, PhD thesis, Cambridge University.
- Osman, A. & Bolton, M. (2004a). A new design method for retaining walls in clay, *Canadian Geotechnical Journal* **41**, No. 3: 451–466.
- Osman, A. & Bolton, M. (2005). Simple plasticity-based prediction of the undrained settlement of shallow circular foundations on clay, *Géotechnique* **55**, No. 6: 435–447.
- Parkes, P. (2003). The use of iron in foundations. Article published online by the Institution of Civil Engineers at http://www.ice.org.uk/downloads/iron_foundations.pdf.
- Philips, R. & Valsangkar, A. (1987). An experimental investigation of factors affecting penetration resistance in granular soils in centrifuge modelling, *CUED Technical Report, University of Cambridge*.
- Potts, D. & Zdravković, L. (1999). *Finite element analysis in geotechnical engineering: theory*, Thomas Telford Limited.

- Potts, D. & Zdravković, L. (2001). *Finite element analysis in geotechnical engineering: application*, Thomas Telford Limited.
- Prandtl, L. (1921). Über die eindringungsfestigkeit plastisher baustoffe und die festigkeit von schneiden, *Zeitschrift für Angewandte Mathematik und Mechanik* **1**, 1: 15–20.
- Prasad, Y. (1996a). Discussion of ‘drivability and pullout resistance of helical units in saturated sand’ by ghaly, a.m., *Soils and Foundations* **36**, No. 2: 139–140.
- Prasad, Y. & Rao, S. (1994). Pullout behaviour of model pile and helical pile anchors subjected to lateral cyclic loading, *Canadian Geotechnical Journal* **31**, No. 1: 110–119.
- Rao, S. & Prasad, Y. (1993). Estimation of uplift capacity of helical anchors in clays, *Journal of Geotechnical Engineering* **119**, No. 2: 352–357.
- Rao, S., Prasad, Y. & Shetty, M. (1991). The behaviour of model screw piles in cohesive soils, *Soil and Foundations* **31**, No. 2: 35–50.
- Rao, S., Prasad, Y. & Veeresh, C. (1993a). Behaviour of embedded model screw anchors in soft clays, *Géotechnique* **43**, No. 4: 605–614.
- Roscoe, K. (1970). Tenth rankine lecture: The influence of strains in soil mechanics, *Géotechnique* **20**, No. 2: 129–170.
- Rowe, P. & Barden, L. (1966). A new consolidation cell, *Géotechnique* **16**, No. 2: 162–170.
- Sadek, S., Iskander, M. & Liu, J. (2002). Geotechnical properties of transparent silica, *Canadian Geotechnical Journal* **39**, No. 1: 111–124.
- Sadek, S., Iskander, M. & Liu, J. (2003). Accuracy of digital image correlations for measuring deformations in transparent media, *Journal of Computing in Civil Engineering* **17**, No. 2: 88–96.
- Sagaseta, C., Whittle, A. & Santagata, M. (1997). Deformation analysis of shallow penetration in clay, *International Journal for Numerical and Analytical Methods in Geomechanics* **21**: 687–719.
- Sakr, M. (2010). Performance of helical piles in oil sand, *Canadian Geotechnical Journal* **46**, No. 9: 1046–1061.

- ScrewFast Foundations UK Ltd. (2008). Helical screw piling supplier website found at <http://www.screwfast.com>.
- Slama, C. (1980). *Manual of photogrammetry (4th Edition)*, American Society of Photogrammetry: 105 North Virginia Avenue, Falls Church, VA.
- Smith, M. (1993). *A laboratory study of the Marchetti Dilatometer*, PhD thesis, University of Oxford.
- Song, Z., Hu, Y., O'Loughlin, C. & Randolph, M. (2010). Loss in anchor embedment during plate anchor keying in clay, *Journal of Geotechnical and Geoenvironmental Engineering* **135**, No. 10: 1475–1485.
- Springman, S. (1989). *Lateral loading on piles due to simulated embankment construction*, PhD thesis, University of Cambridge.
- Stanier, S. (2006). *Geotechnical modelling using a transparent synthetic soil*, Master's thesis, University of Sheffield.
- Take, W. (2003). *The influence of seasonal moisture cycles on clay slopes*, PhD thesis, University of Cambridge.
- Tani, K. & Craig, W. (1995). Bearing capacity of circular foundations on soft clay of strength increasing with depth, *Soils and Foundations* **35**, No. 4: 21–35.
- Toiya, M., Hettinga, J. & Losert, W. (2007). 3D imaging of particle motion during penetrometer testing: From microscopic to macroscopic soil mechanics, *Granular Matter* **9**: 323–329.
- Tomlinson, M. (2001). *Foundation design and construction*, Pearson Education Limited.
- Tomlinson, M. & Woodward, J. (2008). *Pile design and construction practice*, Taylor and Francis, London.
- Udwari, J., Rodgers, T. & Singh, H. (1979). A rational approach to the design of high capacity multi-helix screw anchors, *Proc. 7th Annual IEEE/PES Transmission and Distribution Exposition* pp. 606–610.
- Wang, D., Hu, Y. & Randolph, M. (2010). Three-dimensional Large Deformation Finite Element analysis of plate anchors in uniform clay, *Journal of Geotechnical and Geoenvironmental Engineering* **136**, No. 2: 355–365.

- Welker, A., Bowders, J. & Gilbert, R. (1999). Applied research using a transparent material with hydraulic properties similar to soil, *Geotechnical Testing Journal* **22**: 266–270.
- White, D. (2002a). *An investigation into the behaviour of pressed-in piles*, PhD thesis, University of Cambridge.
- White, D. (2008). Contributions to Géotechnique 1948-2008: Physical modelling, *Géotechnique* **58**, No. 5: 413–421.
- White, D. & Bolton, M. (2004). Displacement and strain paths during plane-strain model pile installation in sand, *Géotechnique* **54**, No. 6: 375–397.
- White, D. & Take, W. (2002). GeoPIV: Particle Image Velocimetry (PIV) software for use in geotechnical testing, *CUED Technical Report, University of Cambridge*.
- White, D., Gaudin, C., Boylan, N. & Zhou, H. (2010). Interpretation of t-bar penetrometer tests at shallow embedment and in very soft soils, *Canadian Geotechnical Journal* **47**: 218–229.
- White, D., Randolph, M. & Thompson, B. (2005). An image-based deformation measurement system for the geotechnical centrifuge, *International Journal of Physical Modelling in Geotechnics* **3**: 1–12.
- White, D., Richards, D. & Lock, A. (2003a). The measurement of landfill settlement using digital imaging and PIV analysis, *Proc. 9th International Waste Management and Landfill Symposium* pp. 1–10.
- White, D., Take, W. & Bolton, M. (2001a). Measuring soil deformation in geotechnical models using digital images and PIV analysis, *Proc. 10th International Conference on Computer Methods and Advances in Geomechanics* pp. 997–1002.
- White, D., Take, W. & Bolton, M. (2003). Soil deformation measurement using Particle Image Velocimetry (PIV) and photogrammetry, *Géotechnique* **53**, No. 7: 619–631.
- White, D., Take, W. & Bolton, M. (2005a). Discussion of ‘Accuracy of digital image correlations for measuring deformations in transparent media’ by samer sadek, magued g. iskander and jinyuan liu, *Journal of Computing in Civil Engineering* **19**, No. 2: 217–219.

- White, D., Take, W., Bolton, M. & Munachen, S. (2001). A deformation measurement system for geotechnical testing based on digital imaging, close-range photogrammetry, and PIV image analysis, *Proc. 15th International Conference on Soil Mechanics and Geotechnical Engineering* **1**: 539–542.
- Wood, D. (2004). *Geotechnical modelling*, Oxfordshire: Spon Press.
- Yasufuku, N. & Hyde, A. (1995). Pile end-bearing capacity in crushable sands, *Géotechnique* **45**, No. 4: 663–676.
- Yimsiri, S. (2002). *Stiffness of fine-grained soil at very small strains*, PhD thesis, University of Cambridge.
- Zelikson, A. (1969). Geotechnical models using the hydraulic gradient similarity method, *Géotechnique* **19**, No. 4: 495–508.